MOLECULAR BIOMARKERS AND IMAGING MARKERS IN THE PREDICTION, DIAGNOSIS, AND PROGNOSIS OF BLADDER CANCER

EDITED BY: Yongwen Luo, Yi Zhang, Yu Xiao and Fang-Ming Deng
PUBLISHED IN: Frontiers in Cell and Developmental Biology

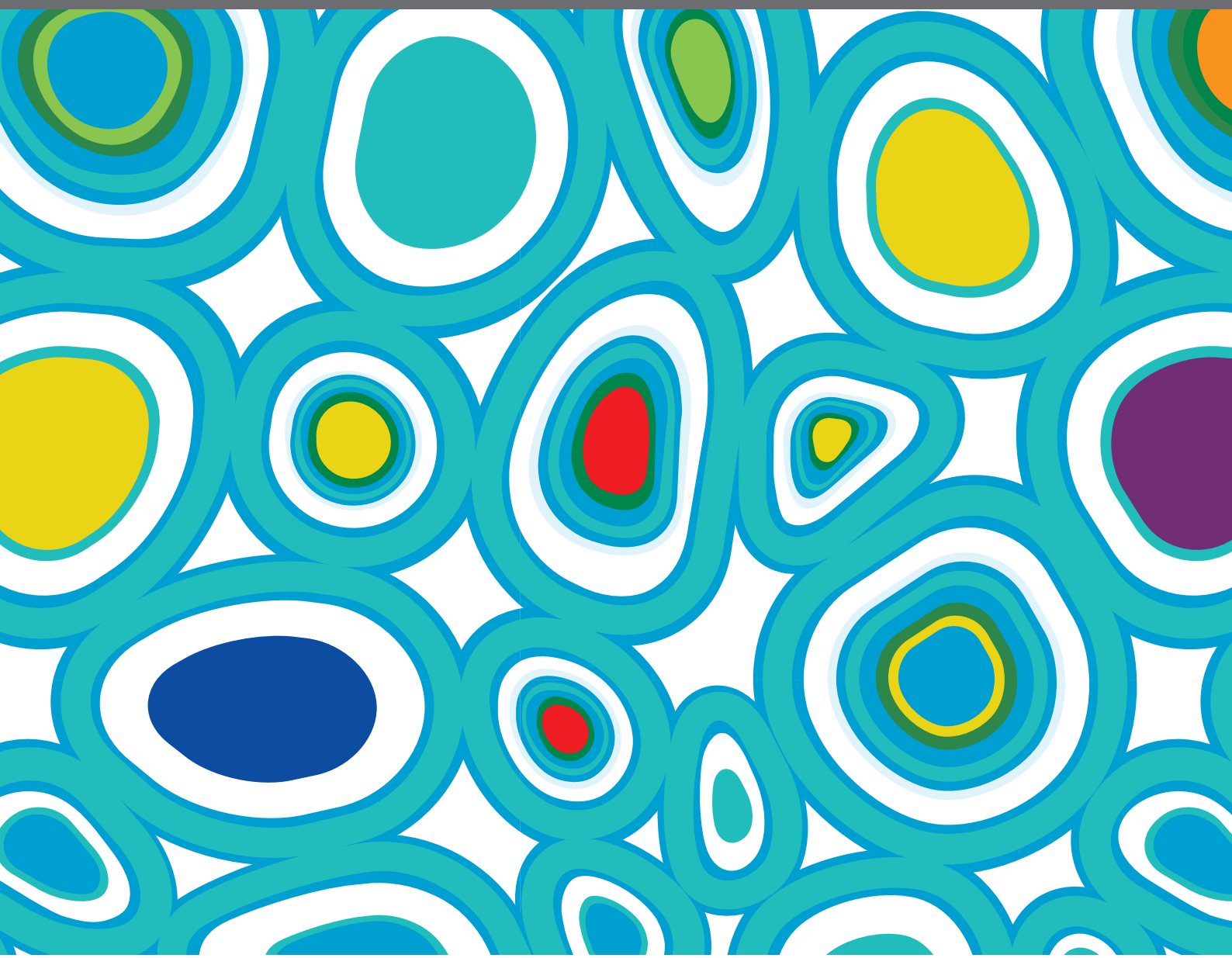

frontiers Research Topics

frontiers

ISSN 1664-8714
ISBN 978-2-88976-629-1
DOI 10.3389/978-2-88976-629-1

About Frontiers

Frontiers is more than just an open-access publisher of scholarly articles: it is a pioneering approach to the world of academia, radically improving the way scholarly research is managed. The grand vision of Frontiers is a world where all people have an equal opportunity to seek, share and generate knowledge. Frontiers provides immediate and permanent online open access to all its publications, but this alone is not enough to realize our grand goals.

Frontiers Journal Series

The Frontiers Journal Series is a multi-tier and interdisciplinary set of open-access, online journals, promising a paradigm shift from the current review, selection and dissemination processes in academic publishing. All Frontiers journals are driven by researchers for researchers; therefore, they constitute a service to the scholarly community. At the same time, the Frontiers Journal Series operates on a revolutionary invention, the tiered publishing system, initially addressing specific communities of scholars, and gradually climbing up to broader public understanding, thus serving the interests of the lay society, too.

Dedication to Quality

Each Frontiers article is a landmark of the highest quality, thanks to genuinely collaborative interactions between authors and review editors, who include some of the world's best academicians. Research must be certified by peers before entering a stream of knowledge that may eventually reach the public - and shape society; therefore, Frontiers only applies the most rigorous and unbiased reviews.
Frontiers revolutionizes research publishing by freely delivering the most outstanding research, evaluated with no bias from both the academic and social point of view. By applying the most advanced information technologies, Frontiers is catapulting scholarly publishing into a new generation.

What are Frontiers Research Topics?

Frontiers Research Topics are very popular trademarks of the Frontiers Journals Series: they are collections of at least ten articles, all centered on a particular subject. With their unique mix of varied contributions from Original Research to Review Articles, Frontiers Research Topics unify the most influential researchers, the latest key findings and historical advances in a hot research area! Find out more on how to host your own Frontiers Research Topic or contribute to one as an author by contacting the Frontiers Editorial Office: frontiersin.org/about/contact

MOLECULAR BIOMARKERS AND IMAGING MARKERS IN THE PREDICTION, DIAGNOSIS, AND PROGNOSIS OF BLADDER CANCER

Topic Editors:
Yongwen Luo, Wuhan University, China
Yi Zhang, Euler Technology, China
Yu Xiao, Wuhan University, China
Fang-Ming Deng, New York University, United States

Citation: Luo, Y., Zhang, Y., Xiao, Y., Deng, F.-M., eds. (2022). Molecular Biomarkers and Imaging Markers in the Prediction, Diagnosis, and Prognosis of Bladder Cancer. Lausanne: Frontiers Media SA. doi: 10.3389/978-2-88976-629-1

Table of Contents

frontiers | Frontiers in Cell and Developmental Biology

TYPE Editorial
PUBLISHED 14 October 2022
DOI 10.3389/fcell.2022.1014565

OPEN ACCESS

EDITED BY
Daniel R. Principe,
University of Illinois at Chicago,
United States

REVIEWED BY
Xiangpeng Dai,
Jilin University, China

*CORRESPONDENCE
Yu Xiao,
yu.xiao@whu.edu.cn

SPECIALTY SECTION
This article was submitted to Molecular and Cellular Pathology, a section of the journal Frontiers in Cell and Developmental Biology

RECEIVED 08 August 2022
ACCEPTED 21 September 2022
PUBLISHED 14 October 2022

CITATION
Luo Y, Deng F-M, Zhang Y and Xiao Y (2022), Editorial: Molecular biomarkers and imaging markers in the prediction, diagnosis, and prognosis of bladder cancer.
Front. Cell Dev. Biol. 10:1014565.
doi: 10.3389/fcell.2022.1014565

Editorial: Molecular biomarkers and imaging markers in the prediction, diagnosis, and prognosis of bladder cancer

Yongwen Luo[1,2,3], Fang-Ming Deng[4], Yi Zhang[5,6] and Yu Xiao[1,2,3]*

[1]Department of Urology, Zhongnan Hospital of Wuhan University, Wuhan, China, [2]Department of Biological Repositories, Zhongnan Hospital of Wuhan University, Wuhan, China, [3]Human Genetics Resource Preservation Center of Hubei Province, Wuhan, China, [4]Department of Pathology, New York University Medical Center, New York, NY, United States, [5]Center of Life Sciences, Peking University, Beijing, China, [6]Euler Technology, Beijing, China

KEYWORDS

bladder cancer, immunotherapy, metabolic reprogramming, immune microenvironment, biomarker

Editorial on the Research Topic
Molecular biomarkers and imaging markers in the prediction, diagnosis, and prognosis of bladder cancer

Bladder cancer (BLCA) is a common malignant tumor in the urinary system. BLCA is divided into muscle-invasive bladder cancer (MIBC) and non-muscle-invasive bladder cancer (NMIBC) (Sanli et al., 2017). Approximately 70% of BLCA patients are initially diagnosed with NMIBC, but 50%–70% of patients relapse after treatment, and 10%–20% of patients progress to MIBC. The 5-year survival rate for patients with MIBC is about 50% (Lenis et al., 2020; Wilson et al., 2022). Nowadays there is still a lack of public recognized, universally applicable diagnosis and prognostic markers for BLCA.

In this Research Topic, we compiled seventeen research articles and one review that summarized new advances about molecular biomarkers and imaging markers in the prediction, diagnosis, and prognosis of BLCA.

For the diagnosis of BLCA, Jeong and Ku systematically reviewed research progress of non-invasive diagnosis of BLCA. Urine cytology shows high sensitivity and specificity in high-grade urothelial cancer diagnosis. Moreover, nuclear matrix protein-22 (NMP-22), bladder tumor antigen (BTA), BTAstat and BTA-TRAK, UroVysion in Fluorescence *in situ* Hybridization, urine miRNA and urine cell-free DNA show high clinical application value for the diagnosis of BLCA. Xu et al. developed a novel urine cytology test (UCT) by mixing urine with mNPs (Nano-cytology) to harvest more tumor cells during UCT procedures. The Nano-cytology assay had a significantly improved sensitivity compared with UCT for detecting BLCA patients. It represents a promising tool for diagnosis of BLCA in clinical practice. Ye et al. utilized non-negative matrix factorization (NMF)

algorithm to construct a radiomics signature based on CT images, and the radiomics signature is a potential biomarker to predict BCG response and relapse free survival (RFS) after BCG treatment in patients with high-risk NMIBC.

Increasing evidence have demonstrated that tumor microenvironment (TME), such as immune cells and cancer-associated fibroblasts (CAFs) affect tumor progression, prognosis and chemotherapy resistance (Biffi and Tuveson, 2019; Huang et al., 2022). Huang et al. identified three distinct immune cell infiltration (ICI) subtypes based on the TME immune infiltration pattern of 584 BLCA patients. The ICI score represented an effective prognostic predictor for evaluating the response to immunotherapy. Yang et al. identified four subtypes of BLCA based on immune profiling including immune ignorant, cold tumor, immune inactive, and hot tumor. CCL4 may be the key molecule functioning in immune cell infiltration in the hot tumor subtype. Moreover, neutrophils may function as an important suppressor in the TME of the immune ignorant and immune inactive subtypes. Chu et al. identified three types of TME patterns (stromal-activation subtype, immune-enriched subtype and immune-suppressive subtype). Then the tumor microenvironment signature (TMSig) was constructed by modified Lasso penalized regression. Patients in low-TMSig score groups had a better prognosis, higher M1 macrophage infiltration, better response to immunotherapy, and more similar molecular characteristics to the luminal (differentiated) subtype. Zheng et al. found that CD3E and LCK were potential biomarkers for MIBC. High-LCK and high-CD3E expression patients had a higher percentage of responders than the low-expression groups for immunotherapy. Tumor necrosis factor (TNF) family members play vital roles in cancer development and antitumor immune responses (Freeman et al., 2021). Li et al. developed and validated a robust TNF-based risk score, which could predict prognostic outcomes, TME, and molecular subtypes of BLCA. Ye et al. systematically assessed the DNA methylation modes in BLCA, and identified three DNA methylation modes. These modes are related to diverse clinical outcomes, immunophenotypes, aggressiveness, and immune responses of BLCA. DMRscore could serve as a signature to predict prognosis outcomes and immune responses. Taken together, these studies provided novel immunotherapy biomarkers and therapeutic targets for BLCA.

Additionally, amounting evidence indicates that ferroptosis may serve as a new target for BLCA (Kong et al., 2021; Lei et al., 2022). Xia et al. comprehensively evaluated the ferroptosis patterns of BLCA. They identified four distinct ferroptosis patterns, and verified ferroptosis is associated with TMB, TME immune cell infiltration, chemotherapy, and immunotherapy in BLCA. Wang et al. identified a prediction model containing five ferroptosis-related lncRNAs through integrated bioinformatics. This prediction model performed a good predictive ability, and can be used as an independent prognostic indicator.

Metabolic reprogramming is a unique hallmark of tumor cells. Accumulating evidence suggests that tumor metabolism plays a critical role in maintaining tumorigenesis and progression (Martínez-Reyes and Chandel, 2021; Raggi et al., 2022). Zhang et al. evaluated correlation between the metabolic status and the outcome of patients with BLCA using data from TCGA and GEO databases. Two clusters were identified using a consensus clustering algorithm based on an energy metabolism-related signature. The established energy metabolism-related gene signature was able to predict survival in patients with BLCA. Song et al. found iron metabolism is a pivot of tumor occurrence, progression, and TME in BLCA. They clustered the TCGA-BLCA cohort into four distinct iron metabolism patterns based on 95 prognosis-related iron metabolism-related genes (IMRGs), and then constructed the IMRG prognosis signature (IMRGscore), which could be utilized as an independent prognostic indicator.

Moreover, some authors have explored and studied biomarkers about progression, prognosis and treatment of BLCA. Tao et al. found that BRCC3 is upregulated in BLCA and indicates a negative survival prognosis. In BLCA cells, BRCC3 depletion dramatically attenuated cell proliferation, viability and migration. Mechanistically, BRCC3 binds with TRAF2 to activate NF-κB pathway. This finding points to BRCC3 as a potential target in BLCA patients. Mao et al. found ID2 expression was significantly downregulated in TCGA database and clinical samples, and high ID2 expression was associated with low-grade tumor staging and correlated with better overall survival, disease specific survival (DSS) and progress free interval (PFI). Mechanistically, ID2 acts as a tumor suppressor through PI3K/AKT signaling pathway to inhibit the progression and metastasis of BLCA. Du et al. found cancer-associated myofibroblasts (myCAFs) participate in extracellular matrix remodeling, tumor metabolism, cancer stemness, and oncological mutations. myCAFs have potential as potential diagnostic biomarkers and therapeutic targets for BLCA. Gu and Liang constructed a 15-top-prognostic gene-based signature based on TCGA-BLCA and GSE13507 cohorts, and this gene signature indicated a highly prognostic efficacy for BLCA. Moreover, the prognostic signature has a favorable predictive value for treatment with gemcitabine, doxorubicin, cisplatin, paclitaxel, and vinblastine. Song et al. identified key biomarkers in gemcitabine (GEM)-resistant BLCA and investigate their associations with tumor-infiltrating immune cells in a tumor immune microenvironment through integrative bioinformatics analysis. They reported that CAV1, COL6A2, FABP4, FBLN1, PCOLCE, and CSPG4 were critical biomarkers through regulating the immune cell infiltration in an immune microenvironment of GEM-resistance and could act as promising treatment targets for GEM-resistant MIBC.

In conclusion, the collections of research articles and reviews under this Research Topic present novel insights on the

prediction, diagnosis, and prognosis of bladder cancer. It will hopefully encourage us to explore molecular targets from various perspectives and ultimately promote the diagnosis and treatment of BLCA.

Author contributions

All authors listed have made a substantial, direct, and intellectual contribution to the work and approved it for publication.

Funding

This work was supported by Zhongnan Hospital of Wuhan University Science, Technology and Innovation Seed Fund (CXPY2020014), Zhongnan Hospital of Wuhan University and Excellent Doctor Fund Project (ZNYB2020005), and Zhongnan Hospital of Wuhan University Medical Science and Technology Innovation Platform Construction Support Project (PTXM2022018).

Acknowledgments

The authors would like to thank all the authors, reviewers, and editors who contributed to this Research Topic and Editorial Office for their assistance and support.

Conflict of interest

Author YZ was employed by Euler Technology.

The remaining authors declare that the research was conducted in the absence of any commercial or financial relationships that could be construed as a potential conflict of interest.

Publisher's note

References

Biffi, G., and Tuveson, D. A. (2019). Diversity and biology of cancer-associated fibroblasts. *Physiol. Rev.* 101, 147–176. doi:10.1152/physrev.00048.2019

Freeman, A. J., Kearney, C. J., Silke, J., and Oliaro, J. (2021). Unleashing TNF cytotoxicity to enhance cancer immunotherapy. *Trends Immunol.* 42, 1128–1142. doi:10.1016/j.it.2021.10.003

Huang, H., Wang, Z., Zhang, Y., Pradhan, R. N., Ganguly, D., Chandra, R., et al. (2022). Mesothelial cell-derived antigen-presenting cancer-associated fibroblasts induce expansion of regulatory T cells in pancreatic cancer. *Cancer Cell* 40, 656–673. doi:10.1016/j.ccell.2022.04.011

Kong, N., Chen, X., Feng, J., Duan, T., Liu, S., Sun, X., et al. (2021). Baicalin induces ferroptosis in bladder cancer cells by downregulating FTH1. *Acta Pharm. Sin. B* 11, 4045–4054. doi:10.1016/j.apsb.2021.03.036

Lei, G., Zhuang, L., and Gan, B. (2022). Targeting ferroptosis as a vulnerability in cancer. *Nat. Rev. Cancer* 22, 381–396. doi:10.1038/s41568-022-00459-0

Lenis, A. T., Lec, P. M., Chamie, K., and Mshs, M. D. (2020). Bladder cancer: A review. *Jama* 324, 1980–1991. doi:10.1001/jama.2020.17598

Martínez-Reyes, I., and Chandel, N. S. (2021). Cancer metabolism: Looking forward. *Nat. Rev. Cancer* 21, 669–680. doi:10.1038/s41568-021-00378-6

Raggi, C., Taddei, M. L., Rae, C., Braconi, C., and Marra, F. (2022). Metabolic reprogramming in cholangiocarcinoma. *J. Hepatol.* 77, 849–864. doi:10.1016/j.jhep.2022.04.038

Sanli, O., Dobruch, J., Knowles, M. A., Burger, M., Alemozaffar, M., Nielsen, M. E., et al. (2017). Bladder cancer. *Nat. Rev. Dis. Prim.* 3, 17022. doi:10.1038/nrdp.2017.22

Wilson, F., Joseph, N., and Choudhury, A. (2022). Biomarkers in muscle invasive bladder cancer. *Adv. Clin. Chem.* 107, 265–297. doi:10.1016/bs.acc.2021.07.005

frontiers in Cell and Developmental Biology

ORIGINAL RESEARCH
published: 11 March 2021
doi: 10.3389/fcell.2021.596484

Immune Profiling Reveals Molecular Classification and Characteristic in Urothelial Bladder Cancer

Li Yang[1], Aitian Li[1], Fengsen Liu[1], Qitai Zhao[1], Shaofei Ji[2], Wen Zhu[3], Weina Yu[1], Ru Zhang[1], Yaqing Liu[1], Wencai Li[3] and Yi Zhang[1]**

[1] Biotherapy Center, The First Affiliated Hospital of Zhengzhou University, Zhengzhou, China, [2] Emergency Intervention Department, Orthopaedic Hospital of Zhengzhou City, Zhengzhou, China, [3] Department of Urology, The First Affiliated Hospital of Zhengzhou University, Zhengzhou, China

Urothelial bladder cancer (UBC) is the most common malignant tumor of the urinary system. Most patients do not benefit from treatment with immune checkpoint inhibitors, which are closely associated with immune profiling in the context of UBC. Therefore, we aimed to characterize the immune profile of UBC to identify different immune subtypes that may influence therapy choice. We identified four subtypes of UBC based on immune profiling including immune ignorant, cold tumor, immune inactive, and hot tumor. After excluding the cold tumor subtype because of its unique pathology distinct from the other types, a high correlation between patient survival and immune characteristics was observed. Most immune cell types had highly infiltrated the hot tumor subtype compared to other subtypes. Interestingly, although immune cells infiltrated the tumor microenvironment, they exhibited an exhaustion phenotype. CCL4 may be the key molecule functioning in immune cell infiltration in the hot tumor subtype. Moreover, neutrophils may function as an important suppressor in the tumor microenvironment of the immune ignorant and immune inactive subtypes. Furthermore, different tumor-intrinsic signaling pathways were involved in immune cell infiltration and exclusion in these four different subtypes. Immune profiling could serve as a prognostic biomarker for UBC, and has potential to guide treatment decisions in UBC. Targeting tumor-intrinsic signaling pathways may be a promising strategy to treat UBC.

Keywords: urothelial bladder cancer, immune profiling, immune cell infiltration, tumor-intrinsic signaling pathway, prognosis

OPEN ACCESS

Edited by:
Cathy Tournier, The University of Manchester, United Kingdom

Reviewed by:
Emanuele Giurisato, University of Siena, Italy
Ana Cuenda, Consejo Superior de Investigaciones Científicas (CSIC), Spain

****Correspondence:***
Li Yang
fccyangl1@zzu.edu.cn
Yi Zhang
yizhang@zzu.edu.cn

Specialty section:
This article was submitted to Signaling, a section of the journal Frontiers in Cell and Developmental Biology

Received: *20 August 2020*
Accepted: *18 February 2021*
Published: *11 March 2021*

Citation:
Yang L, Li A, Liu F, Zhao Q, Ji S, Zhu W, Yu W, Zhang R, Liu Y, Li W and Zhang Y (2021) Immune Profiling Reveals Molecular Classification and Characteristic in Urothelial Bladder Cancer. Front. Cell Dev. Biol. 9:596484. doi: 10.3389/fcell.2021.596484

INTRODUCTION

Urothelial bladder cancer (UBC) is the most common malignant tumor of the urinary system and is one of the ten most common tumors (Ferlay et al., 2015), but the treatment of UBC has seen little progress (von der Maase et al., 2005). However, some patients with advanced cancer have shown durable remission, owing to the introduction of checkpoint inhibitors and other

Abbreviations: UBC, urothelial bladder cancer; ORR, objective response rate; IRGs, immune-related genes; TCGA, The Cancer Genome Atlas; MSigDB, Molecular Signature Database; GSEA, Gene Set Enrichment Analysis; PPI, Protein protein interaction; PCA, principal component analysis; UMAP, uniform manifold approximation and projection; GO, gene ontology; KEGG, Kyoto Encyclopedia of Genes and Genomes; OS, overall survival; Tcm, central memory T cells; Tem, effector memory T cells; Tgd, gamma delta T; Th1, T helper 1; Th2, T helper 1; Tregs, regulatory T cells; pDC, plasmacytoid dendritic cells; aDC, activated dendritic cells; cDC, conventional dendritic cells; iDC, immature dendritic cells; NKT, natural killer T cell; TGF, transforming growth factor.

immunotherapies (Bracarda et al., 2015; Carosella et al., 2015; Kim et al., 2015). When treated with immune checkpoint inhibitors, the objective response rate (ORR) in PD-L1$^+$ bladder cancer patients was 52%, whereas the ORR in PD-L1$^-$ patients with bladder cancer was only 11% (Powles et al., 2014). Therefore, most patients with UBC do not benefit from immune checkpoint inhibitors, and further study of the resistance mechanisms is needed.

The antitumor T cell response is crucial for immunotherapy, such as immune checkpoint inhibitors, to function (Harlin et al., 2009; Ji et al., 2012; Liu, 2019). In UBC, increased T cell infiltration has been found to be correlated with longer patient survival (Sharma et al., 2007). Hot tumors filled with T cells and other immune cells are often considered to be more sensitive to immunotherapy compared to cold tumors with fewer T cells; however, it is unclear why this may be the case. Variations in immune profiles have been linked to the subtypes, prognosis, and therapeutic responses of cancer (Iglesia et al., 2014; Gentles et al., 2015; Li et al., 2016). Therefore, it is critical to understand the immune profile of UBC.

Efforts have now been focused on understanding the mechanisms driving T cell exclusion and immunosuppressive cell infiltration. Immune aberrations have been shown to be closely associated with inter-tumor heterogeneity (Verhaak et al., 2010; Lehmann et al., 2011; Kim et al., 2019). Interestingly, activation of the β-catenin signaling pathway can lead to a non-T cell-inflamed phenotype in melanoma (Spranger et al., 2015). It is not yet known if tumor-intrinsic features affect the immune phenotype in UBC.

Therefore, the aim of this study was to further characterize the immune profile of UBC to identify subtypes that may be relevant for therapy choice.

PATIENTS AND METHODS

Clinical Samples and Data Collection

A total of 2,498 immune-related genes (IRGs) were obtained from the ImmPort database[1]. RNA-seq data and clinical data from 408 UBC patients were obtained from The Cancer Genome Atlas (TCGA)[2]. All data were processed using software (version 3.6.0) or GSEA software (version 4.0.3). In addition, Molecular Signature Database (MSigDB) gene sets were downloaded from the Gene Set Enrichment Analysis (GSEA) browser[3]. Protein protein interaction (PPI) network analysis was performed based on the STRING database in http://string-db.org/cgi/input.pl.

Identification of Immune Subtypes

Sample clustering and comparisons were performed with the R package Seurat. Transcripts per kilobase million values of UBC patients were first log-transformed and normalized, then gene expression data were analyzed by principal component analysis (PCA). The Seurat JackStrawPlot function was used to identify the number of significant principal components for each cluster. Seurat's FindClusters function was used to generate clusters from the data, with a resolution of 0.5. We performed uniform manifold approximation and projection (UMAP) for data visualization in Seurat. Each sample yielded four clusters. The FindAllMarkers function was used to identify differentially expressed genes between the four clusters based on the following cut-off values: adjusted $P < 0.05$ and $|\log2\ FC| > 0.5$.

Cell Infiltration and Differentially Expressed Gene Analysis

Gene expression data were used to estimate cell infiltration levels for 34 types of immune cells by R package xCell. Differentially expressed genes among subtypes were determined and estimated using the R package limma with significance criteria of adjusted P-value < 0.05.

Signaling Pathway Analysis

Gene set enrichment analysis software was used to estimated significant gene ontology (GO) functions and Kyoto Encyclopedia of Genes and Genomes (KEGG) pathways enriched in each immune subtype with the significance criteria ($|NES| > 1$, NOM p-val < 0.05, FDR q-val < 0.25). The enrichment levels of GO functions or KEGG pathways were quantified by single-sample GSEA in the R package gsva, based on transcripts per kilobase million values of the TCGA samples. The single-sample GSEA in our study was performed with the C2 and C5 gene sets that are involved in KEGG pathways and GO functions, respectively. The C2 and C5 gene sets were retrieved from MSigDB (see text footnote 3).

Immunohistochemistry and Immunofluorescence Staining

Human UBC tissues were obtained from The First Affiliated Hospital of Zhengzhou University in 2019, all tissues were fixed, embedded in paraffin and serially sliced. Paraffin-embedded tissue slides were dewaxed in 65°C for 1 h, hydrated in alcohol with different concentrations, heated in citrate buffer for antigen retrieval, and incubated with hydrogen peroxide for 10 min to inactivate endogenous peroxidases. Anti-human CD8 (1:200, abcam, ab199016), DSG2 (1:300, abcam, ab150372), CACNB2 antibody (1:200, abcam, ab93606) were added on slides and incubated at 4°C overnight. On the next day, slides were stained with HRP-conjunct anti-rabbit/mouse antibody (ZSGB-BIO, SP-9000). These protein expressions were visualized by DAB staining (ZSGB-BIO, ZLI-9018) following slides being counterstained with hematoxylin. The photos were recorded by microscope (PerkinElmer, Vectra).

For immunofluorescence, the sections were treated with 1% Triton X100 in 0.01 M PBS. Anti-human CD8 (1:200, abcam, ab199016), CCL4 antibody (1:100, abcam, ab45690) were added on slides and incubated at 4°C overnight. On the next day, Alexa Fluor 488-AffiniPure Donkey Anti-Mouse IgG (1:1000, Jackson, 715-545-150) and Alexa Fluor 594-AffiniPure Donkey Anti-Rabbit IgG (1:1000, Jackson, 711-585-152) were used to detect the primary antibodies. Nuclear staining was performed with

[1]https://www.immport.org/home

[2]https://portal.gdc.cancer.gov/

[3]https://www.gsea-msigdb.org/gsea/index.jsp

DAPI (C0060, Solarbio). The stained cells were observed under microscope (PerkinElmer, Vectra), and photos were recorded.

Statistical Analysis

The prognostic values of the four clusters, IRGs, and immune cell infiltration were estimated using the Kaplan-Meier curve and log-rank test with the R packages survival[4] and survminer[5]. UBC samples were classified into high and low groups for IRG expression and immune cell infiltration based on the optimal cutoff value. Correlation coefficients (r) were calculated by Spearman's correlation analysis. For comparisons of more than two groups, Kruskal–Wallis tests were used to estimate the differences. For all statistical methods, $P < 0.05$ was considered to be significantly different.

RESULTS

Classifying Subtypes of UBC by Immune Profiling

First, we determined whether T cell-inflamed and non-T cell-inflamed UBCs could be identified using the IRG expression signature from the Immport website (1187 genes). Next, these genes were screened by survival analysis, which revealed 752 IRGs to be significantly differentially expressed with $P < 0.05$. Furthermore, these 752 genes were analyzed using PCA (**Figure 1A**). In total, ten principal components were identified, and, among them, six principal components had significant differences with $P < 0.05$ (**Figure 1B**). These six principal components were then analyzed using UMAP (**Figure 1C**). The results identified four subtypes: immune ignorant, cold tumor, immune inactive, and hot tumor (subtype 1–4, **Figure 1D**). Among these subtypes, tumors with an immunosuppressive phenotype were defined as immune ignorant (subtype 1, $n = 117$), tumors that were completely devoid of immune infiltration were defined as a so-called cold tumor (subtype 2, $n = 110$), tumors that lack activation of the interferon signaling pathway and have no response to immunotherapy were categorized as immune inactive (subtype 3, $n = 107$), and tumors infiltrated by T cells and other immune cells were referred to as a hot tumor (subtype 4, $n = 57$). Overall survival (OS) analysis revealed that UBC patients with tumors belonging to different subtypes exhibited differential survival (**Figure 1E**). Patient survival in subtypes 2 and 4 was better than that of subtypes 1 and 3 (**Figure 1E**). Therefore, UBCs could be grouped based on their expression of genes indicative of an immune cell-inflamed tumor microenvironment.

We further evaluated the relationship between populations of the four subtypes and clinical pathological parameters. The results indicated that the pathology of most patients in the cold tumor subtype (subtype 2) were papillary, whereas other subtypes were primarily non-papillary (**Supplementary Figure 1A**). Moreover, other clinical parameters, including grade, clinical stage, tumor (T) status, and lymph node (N) status, of patients in the cold tumor subtype were significantly different compared to patients in other subtypes (**Supplementary Figures 1B–E**), indicating that patients in the cold tumor subtype were in the early stage of the tumor. This explains why patients in the cold tumor subtype exhibited good survival.

Next, we analyzed the correlation between the expression of T cell signature genes (CCL4, CCL5, CCL8, CCL13, CCL18, CCR5, CD3D, CD3E, CD4, and CD8A) and patient survival. For this analysis, patients in the cold tumor subtype were excluded due to their unique pathological type and early clinical stage. The results revealed that low expression levels of these genes were associated with poor OS (**Supplementary Figure 2**). These data demonstrate that the T cell signature genes could serve as potential prognostic biomarkers.

Characteristics of Immune Cell Infiltration in UBC

To further investigate and confirm the immune cell infiltration in different subtypes of UBC, we analyzed and estimated the following 34 subpopulations of immune cells: activated T cells, including $CD4^+$ and $CD8^+$ naïve T cells, central memory T cells (Tcm) and effector memory T cells (Tem), gamma delta T (Tgd) cells, T helper 1 (Th1) cells, Th2 cells, regulatory T cells (Tregs); naïve, class-switched memory, memory, and pro-B cells; along with cell subtypes related to innate immunity, such as monocytes, M1/M2-like macrophages, mast cells, eosinophils, neutrophils, plasmacytoid, activated, and conventional, immature dendritic cells (pDC, aDC, cDC, and iDC), NK cells, and natural killer T (NKT) cells.

We observed heterogeneity across these four subtypes of UBC. The hot tumor subtype (subtype 4) was enriched for immune cell infiltration; however, the other three subtypes were lacking immune cell infiltration (**Figure 2A**). Excluding the cold tumor subtype, we further compared the degree of immune cell infiltration between the other three subtypes. The results revealed that most immune cells had highly infiltrated the hot tumor subtype compared with the other subtypes (**Figure 2B**). These findings suggest that patients in the hot tumor subtype have a high degree of immune cell infiltration and have good antitumor immunity, which may explain why patients in the hot tumor subtype exhibited good survival.

Additionally, the correlation between immune cells and patient survival was further analyzed. We found that immune cell profiling was positively associated with survival, high levels of immune cell infiltration, and specifically related to adaptive immunity, including CD4 + T cells, Tcm and Tem CD4 + and CD8 + T cells, naïve CD8 + T cells, cDC, DC, and class switched memory B cells, resulting in a good prognosis (**Supplementary Figure 3**). In summary, immune cell profiling could function as a prognostic biomarker for UBC.

Activated Immune Cells Exhibit an Immunosuppressive Phenotype

Based on the above results, we identified the hot tumor subtype as an immune cell-inflamed tumor, particularly a T cell-inflamed tumor. Moreover, the expression of IRGs, including CD8A, CXCL9, CXCL10, CXCL11, CCL4, CCL5, CCL13, CCL18,

[4]https://cran.r-project.org/package=survival

[5]https://cran.r-project.org/package=survminer

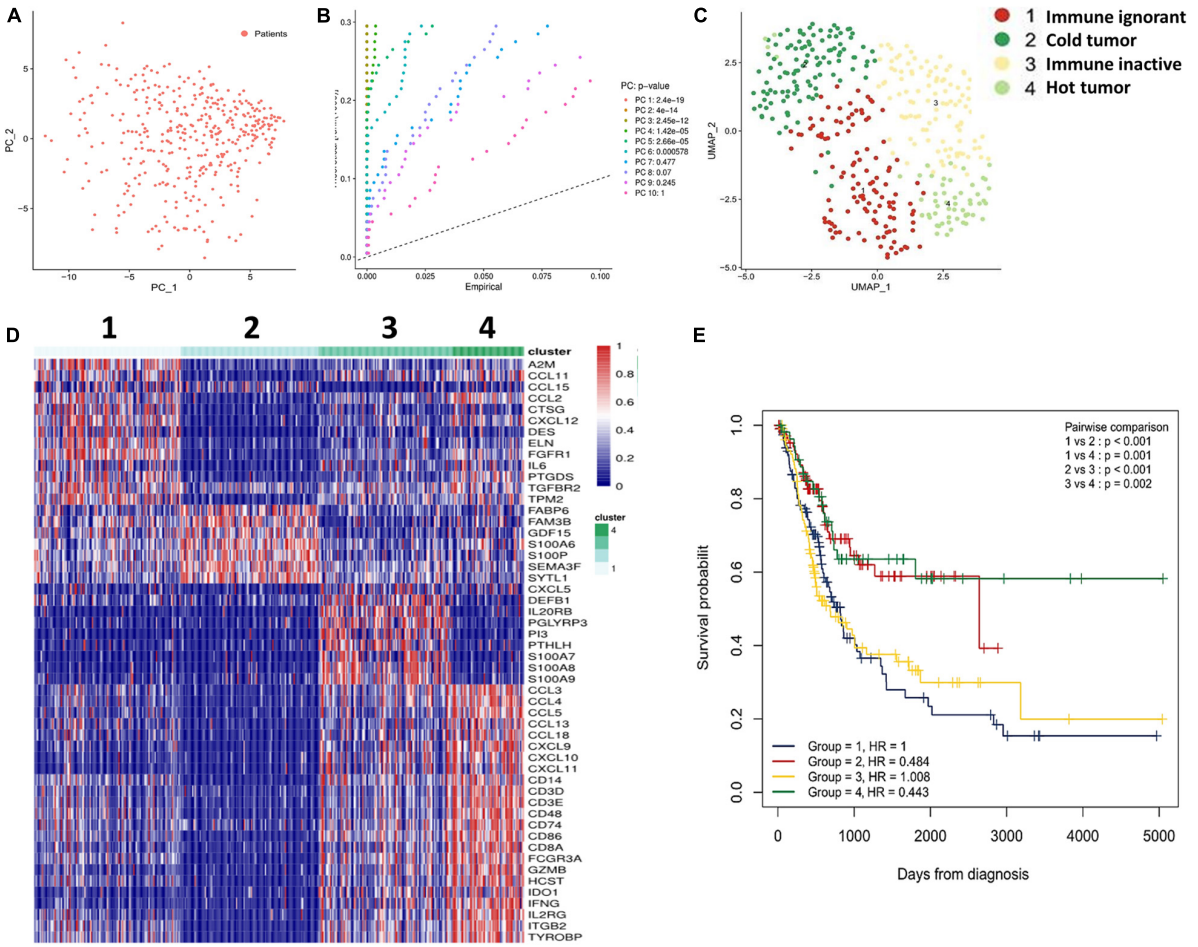

FIGURE 1 | Subtypes of UBC classified by immune profiling. **(A)** IRGs (752 genes) were analyzed by PCA. **(B)** The Seurat JackStrawPlot function was used to identify the number of significant principal components for clustering. **(C)** UMAP was performed for data visualization using Seurat. **(D)** Sample clustering and comparisons were performed using the R Package Seurat. **(E)** Subtype survival was estimated by Kaplan-Meier analysis.

IL2RG, etc., were markedly higher in the hot tumor subtype compared to the other subtypes (**Supplementary Figure 4**). Next, we investigated the correlation between the immune-related molecules highly expressed in the hot tumor subtype and immune cell infiltration in the tumor microenvironment. The results showed that the expression of IRGs was closely correlated with immune cell infiltration (**Figure 3A**), revealing that high expression of IRGs, especially of chemokines that recruit T cells, such as CXCL9, CXCL10, CXCL11, etc., could induce an increase in immune cell infiltration in bladder cancers of the hot tumor subtype.

It has been shown that increased levels of immune inhibitory molecules are associated with a T cell-inflamed phenotype (Spranger et al., 2013). Therefore, we evaluated the relationship between the expression of immune inhibitory molecules (TIGIT, PDCD1LG2, PDCD1, LAG3, HAVCR2, CTLA4, and CD274) in the immune ignorant, immune inactive, and hot tumor subtypes. This revealed that inhibitory molecules were significantly more highly expressed in immune cells (**Figures 3B–D**). Furthermore, the expression of these inhibitory molecules was positively correlated with the T cell signature gene CD8A (**Supplementary Figure 5**). Interestingly, although immune cells had infiltrated the tumor microenvironment, they exhibited an exhaustion phenotype.

Enriched Signaling Pathways Involved in T Cell Infiltration in the Hot Tumor Subtype

To validate which signaling pathways were involved in immune cell infiltration, especially in the T cell-inflamed tumor microenvironment, we further categorized two different gene populations with high and low expression in the hot tumor subtype (**Figure 4A**). Then, we assessed signaling pathway enrichment by comparing the immune ignorant versus hot tumor subtype (1 vs. 4) and the immune inactive versus hot tumor subtype (3 vs. 4). GO enrichment results revealed that 1,089 signaling pathways were screened, and 46 KEGG pathways were found to be enriched (**Figure 4B**). Based on these enriched signaling pathways, ten signaling pathways with significant

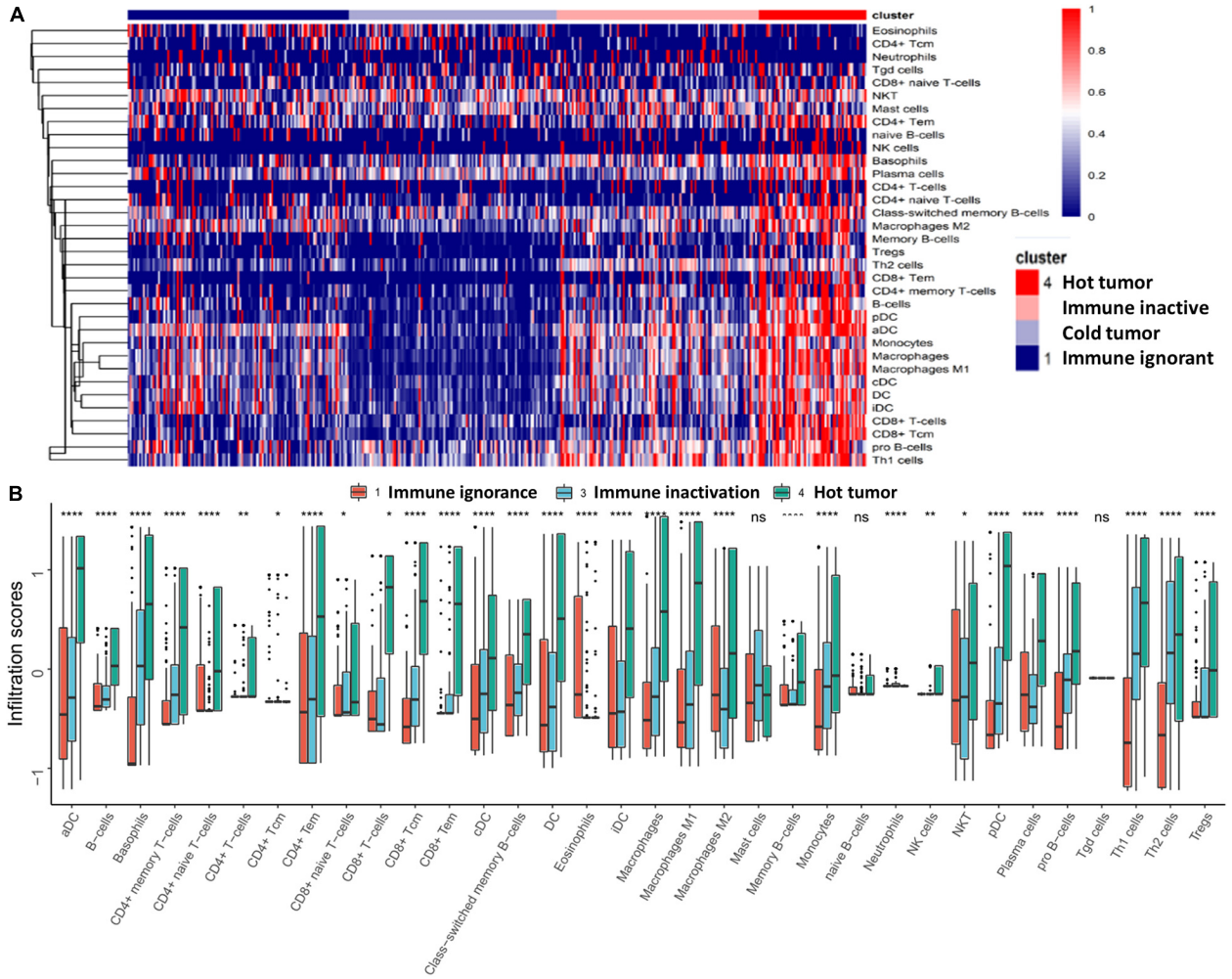

FIGURE 2 | Characteristics of immune cell infiltration in UBC. **(A)** Immune cell infiltration in the four subtypes is presented as a heatmap. **(B)** Comparison of immune cell infiltration in different subtypes. Data are shown as boxplots. $^{*}P < 0.05$, $^{**}P < 0.01$, $^{****}P < 0.0001$, ns, non-significant.

standard that survival analyses were selected and included CD4 positive alpha beta T cell activation, interferon gamma mediated signaling pathway, positive regulation of alpha beta T cell proliferation, positive regulation of T cell cytokine production, regulation of T cell differentiation, regulation of T cell receptor signaling pathway, T cell differentiation involved in immune response, antigen processing and presentation, natural killer cell mediated cytotoxicity, and T cell receptor signaling pathway (**Figure 4C**). To evaluate whether the high level of immune cell infiltration was mediated by these enriched signaling pathways, their correlation was analyzed. The results indicated that these enriched signaling pathways were positively correlated with increased infiltration of most immune cell types (**Figure 4D**), and with high expression of IRGs in the hot tumor subtype (**Figure 4E**). The above data has revealed that the regulation of the T cell differentiation and activation signaling pathways are involved in immune cell infiltration in the hot tumor subtype.

Next, we investigated the interaction of these high level immune-related molecules in the hot tumor subtype and found a strong interaction between these molecules (**Figure 4F**). Additionally, CCL4 was the most connected with other molecules (**Figure 4G**), suggesting that CCL4 could be the key molecule functioning in the immune cell infiltration of the hot tumor subtype. Moreover, immunofluorescence results showed that CCL4 level was positively correlated with CD8 level in human UBC tissues (**Figure 4H**), indicating that $CD8^{+}$ T cell infiltration is closely associated with CCL4 in the hot tumor subtype.

Enriched Signaling Pathways Involved in the Lack of Immune Cell Infiltration in the Immune Ignorant and Immune Inactive Subtypes

Tumor-intrinsic signaling pathway has been reported to mediate the immune phenotype of the tumor microenvironment. To develop new therapeutic strategies that improve the response to immunotherapies, it has been a priority to identify the molecular signaling pathways that function in tumor cells

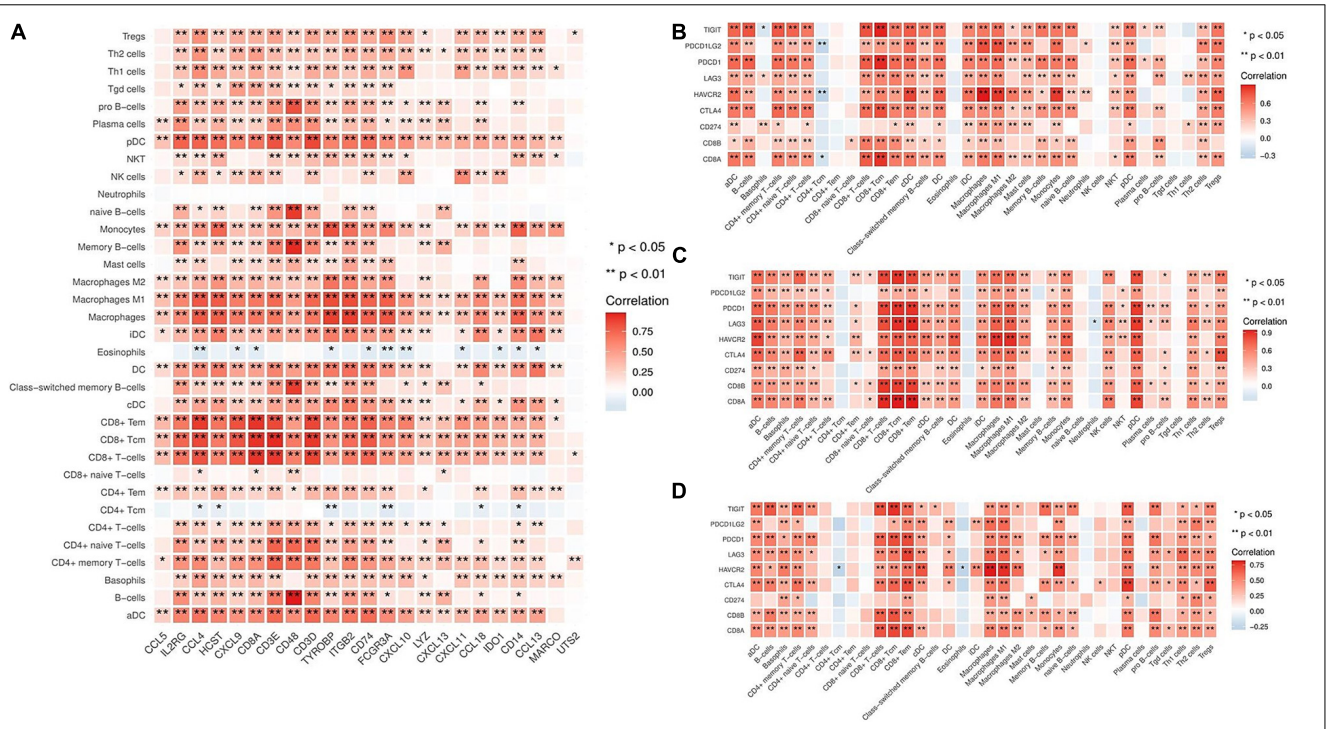

FIGURE 3 | Correlation between immune cell infiltration and IRG expression in different subtypes. **(A)** The relationship between immune cell infiltration and IRG expression in the hot tumor subtype. **(B)** The relationship between immune cell infiltration and inhibitory molecules (TIGIT, PDCD1LG2, PDCD1, LAG3, HAVCR2, CTLA4, and CD274) in the immune ignorant subtype. **(C)** The relationship between immune cell infiltration and inhibitory molecules in the immune inactive subtype. **(D)** The relationship between immune cell infiltration and inhibitory molecules in the hot tumor subtype. $^{*}P < 0.05$, $^{**}P < 0.01$.

and may capable of inducing the exclusion of immune cells, especially T cells, from the tumor microenvironment. Therefore, we hypothesized that some tumor-intrinsic signaling pathways may be involved in the exclusion of immune cells in the immune ignorant and immune inactive subtypes. First, two different gene populations were grouped based on high and low expression in the immune ignorant subtype (**Figure 5A**). Additionally, five signaling pathways that were highly expressed and had significant survival analyses were identified and included including cardiac ventricle morphogenesis, cell-cell signaling involved in cardiac conduction, cell communication involved in cardiac conduction, nephron development, regulation of cardiac muscle cell membrane repolarization, and response to BMP signaling pathway (**Figure 5B**). Correlation analysis revealed that these signaling pathways were negatively associated with decreased immune cell infiltration, particularly T cell exclusion (**Figure 5C**), and positively associated with the expression level of IRGs, which were highly expressed in the immune ignorant subtype (**Figure 5D**). Finally, the related genes (CXADR, KCNQ1, SCN4B, and CACNB2) of the cell-cell signaling involved in cardiac conduction signaling pathway, the most enriched pathway in the immune ignorant subtype, were negatively associated with $CD8^{+}$ T cell infiltration (**Figure 5E**). Furthermore, we analyzed the correlation between CD8 and CACNB2 by immunohistochemistry, showing that CACNB2 level was negatively correlated with CD8 level in human UBC tissues (**Figure 5F**). Therefore, the lack of T cells in the tumor microenvironment could be mediated by cell-cell signaling involved in cardiac conduction signaling pathway in the immune ignorant subtype.

Additionally, the mechanism underlying T cell exclusion from the tumor microenvironment in the immune inactive subtype was identified and analyzed. The significantly different genes were divided into two groups (**Figure 6A**). Three main signaling pathways were enriched in the immune inactive subtype, including desmosome, keratinocyte proliferation, and regulation of keratinocyte proliferation signaling pathway (**Figure 6B**), and these three pathways also had a strong survival significance. Correlation analysis revealed that these three signaling pathways were negatively correlated with the lack of immune cell infiltration, especially T cell exclusion (**Figure 6C**), and were also positively correlated with the levels of IRGs, which were highly expressed in the immune inactive subtype (**Figure 6D**). The related genes (PPL, DSG2, PERP, and JUP, etc.) of the desmosome signaling pathway, the most enriched pathway in the immune inactive subtype, were negatively associated with $CD8^{+}$ T cell infiltration (**Figure 6E**). And we also found that DSG2 level was negatively correlated with CD8 level in human UBC tissues (**Figure 6F**). Taken together, these results indicate that tumor-intrinsic signaling pathways are involved in the decrease of immune cell infiltration in the non-T cell-inflamed phenotype.

Immune profiling in the immune inactive subtype was similar to that of the immune ignorant subtype, demonstrating that neutrophils were increased in the tumor microenvironment

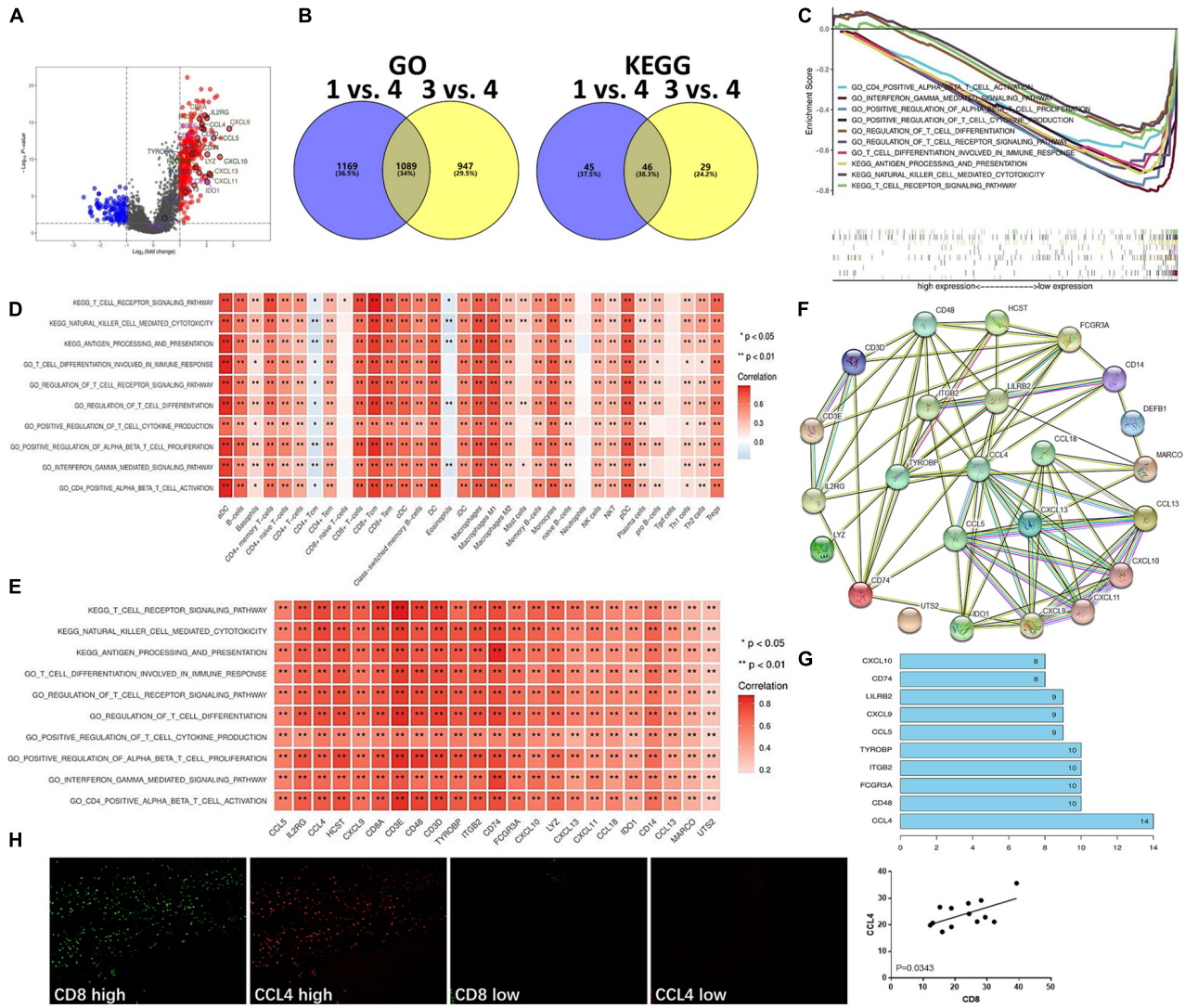

FIGURE 4 | Enriched signaling pathways involved in T cell infiltration in the hot tumor subtype. **(A)** Differentially expressed genes in the hot tumor subtype versus other subtypes (4 vs. 1 and 3). **(B)** Signaling pathway enrichment in different subtypes (1 vs. 4, and 3 vs. 4) was analyzed using GO and KEGG analysis. **(C)** Enriched signaling pathways in the hot tumor subtype were analyzed and are presented. **(D)** Correlation between enriched signaling pathways and immune cell infiltration in the hot tumor subtype. **(E)** Correlation of enriched signaling pathways and IRGs in the hot tumor subtype. **(F)** Network of the high level immune-related molecules in the hot tumor subtype. **(G)** The number of molecules linked with one another in the hot tumor subtype was analyzed. **(H)** CCL4 and CD8 expression in human UBC tissues was analyzed by immunofluorescence. Data are presented as a bar chart. $^{*}P < 0.05$, $^{**}P < 0.01$.

via the crucial signaling pathways found in both the immune ignorant and immune inactive subtypes. Neutrophils were found to function as an important suppressor, in opposition of antitumor immunity, in the tumor microenvironment of the immune ignorant and immune inactive subtypes.

DISCUSSION

The classification of bladder cancer is dependent on various types of profiling. Muscle-invasive bladder cancer patients treated with bladder-sparing trimodality therapy have been classified into luminal, luminal-infiltrated, basal, and claudin-low subtypes based on whole transcriptome expression profiling (Efstathiou et al., 2019). Sweis et al. (2016) analyzed 267 samples of UBC from a TCGA dataset and divided into the samples into T cell-inflamed and non-T cell-inflamed subtypes based on immune gene profiling. A cluster of 725 genes containing 12 T cell signature genes was used to perform consensus clustering of tumor samples. In the current study, we used 752 IRGs to classify subtypes of UBC. The results identified the following four subtypes: immune ignorant, cold tumor, immune inactive, and hot tumor. Among these subtypes, subtype 1 is defined as immune ignorant and presents an immunosuppressive phenotype and decreased immune cell infiltration; subtype 2 is defined as cold tumor due to the complete lack of immune cell

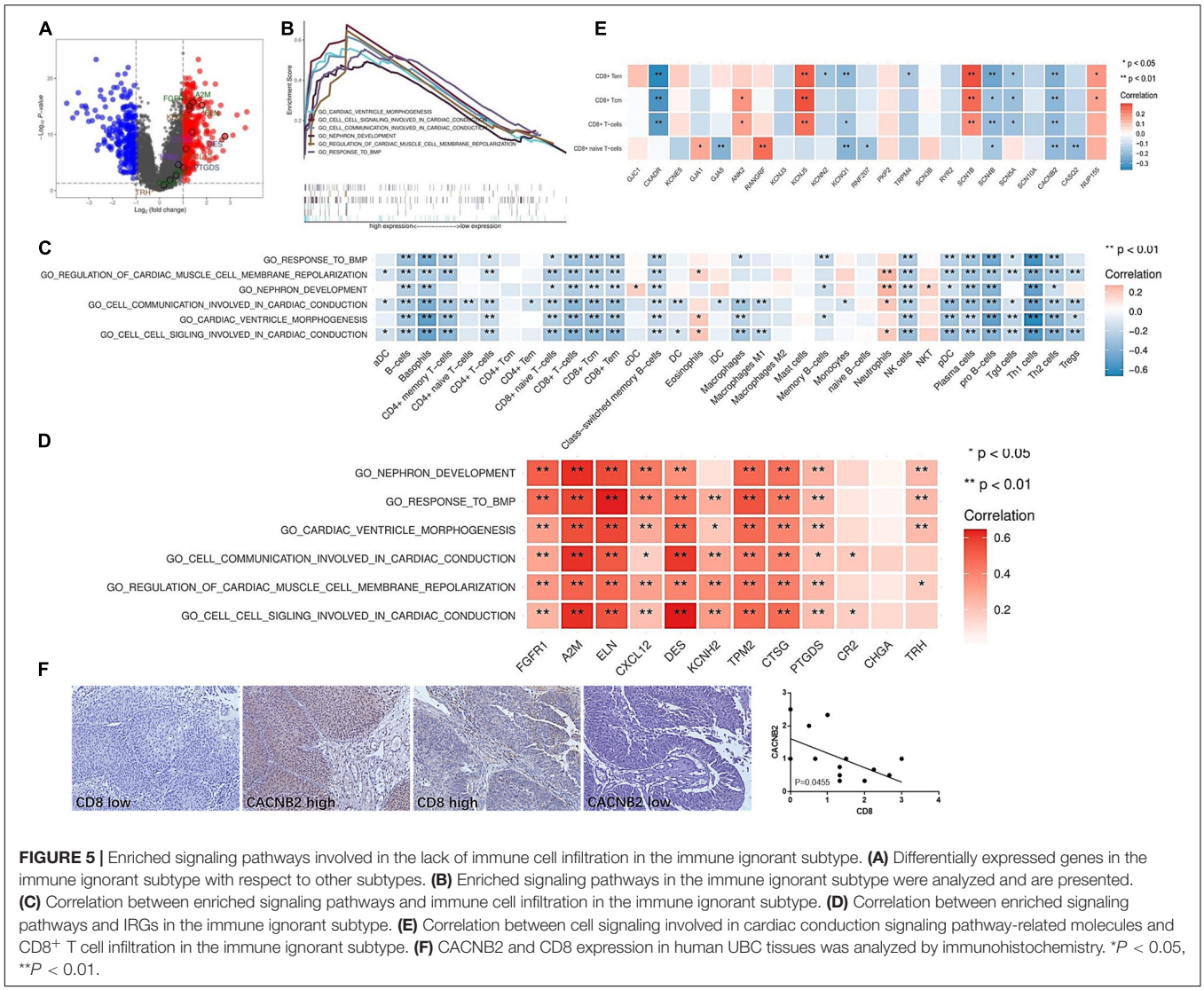

FIGURE 5 | Enriched signaling pathways involved in the lack of immune cell infiltration in the immune ignorant subtype. **(A)** Differentially expressed genes in the immune ignorant subtype with respect to other subtypes. **(B)** Enriched signaling pathways in the immune ignorant subtype were analyzed and are presented. **(C)** Correlation between enriched signaling pathways and immune cell infiltration in the immune ignorant subtype. **(D)** Correlation between enriched signaling pathways and IRGs in the immune ignorant subtype. **(E)** Correlation between cell signaling involved in cardiac conduction signaling pathway-related molecules and $CD8^+$ T cell infiltration in the immune ignorant subtype. **(F)** CACNB2 and CD8 expression in human UBC tissues was analyzed by immunohistochemistry. $^*P < 0.05$, $^{**}P < 0.01$.

infiltration; subtype 3 is referred to as immune inactive due to the lack of active interferon signaling and failure to respond to immunotherapy; subtype 4 is defined as hot tumor due to the enrichment of T cells and other immune cells in the tumor microenvironment.

Among these four subtypes, the cold tumor subtype is unique (Fang et al., 2018). The results indicated that the clinical pathology of patients in the cold tumor subtype was primarily papillary, whereas other subtypes were primarily non-papillary. Moreover, other clinical parameters, including grade and clinical stage, T and N statuses indicated that patients in the cold tumor subtype were in the early stage of UBC. This explains why patients in the cold tumor subtype exhibited good survival given the unique clinical pathology compared to other subtypes.

A variety of papers have demonstrated a close relationship between immunity and patient survival. DC-SIGN + macrophages were correlated with poor prognosis and inferior therapeutic response to fluorouracil-based adjuvant chemotherapy, and may serve as an independent prognostic factor for gastric cancer (Liu et al., 2020). In addition, intratumoral CD8 status had an obvious effect on prognosis. In patients with high levels of intratumoral CD8, PD-L1 expression revealed no significant prognostic impact; however, in patients with low levels of intratumoral CD8, the presence of PD-L1 was associated with a significantly worse prognosis compared to the control (Handa et al., 2020). Moreover, Sun et al. (2018) developed a radiomic signature for CD8 cells, and a high baseline radiomic score was correlated with improved OS. In our study, we also used IRGs as prognostic biomarkers in UBC. High levels of T cell signature genes (CCL4, CCL5, CCL8, CCL13, CCL18, CCR5, CD3D, CD3E, CD4, and CD8A) were associated with a good OS. Furthermore, we found that a high level antitumor immune cell infiltration was positively associated with survival, and provided a good prognosis, suggesting that immune cell profiling could serve as a prognostic biomarker for UBC.

In the current study, we also found that cancer patients within the four subtypes exhibited different survivals. Excluding the cold tumor subtype (the unique subtype with an early clinical stage),

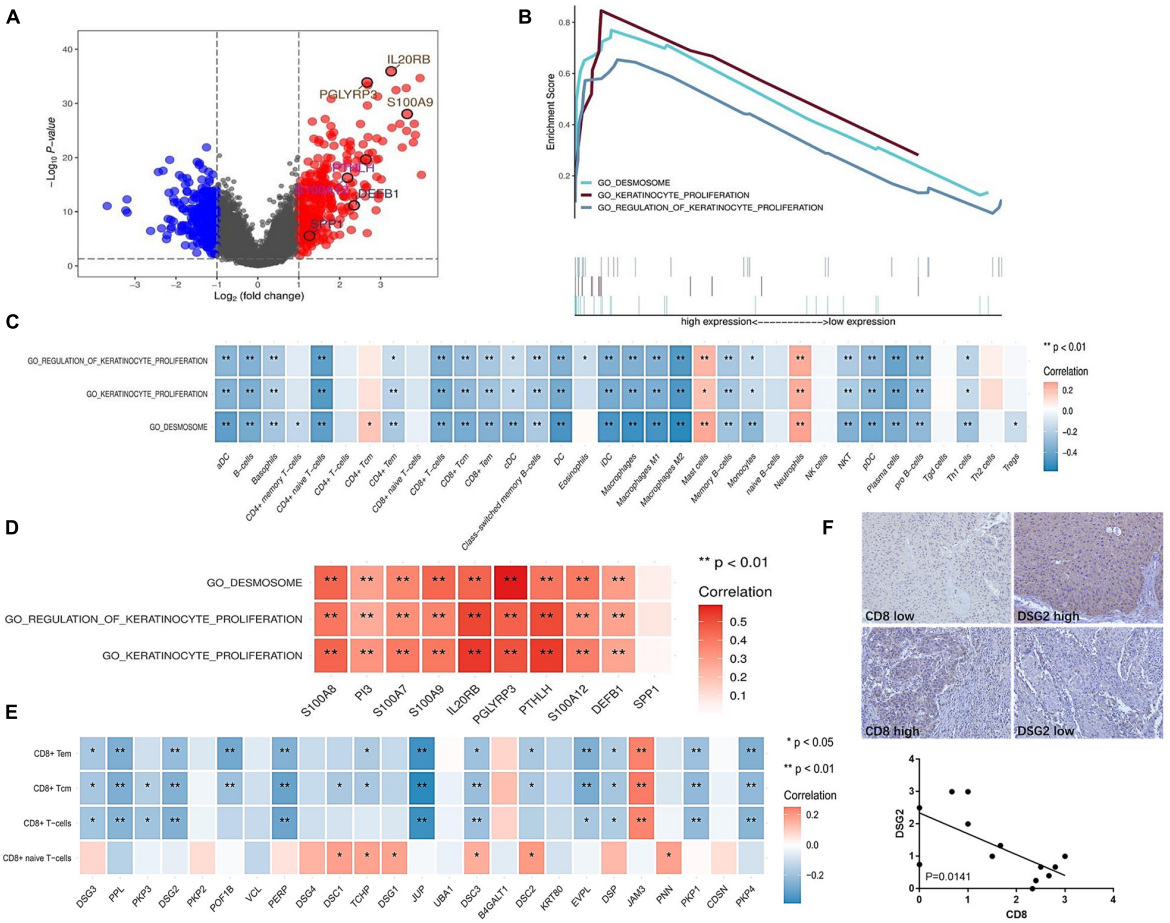

FIGURE 6 | Enriched signaling pathways involved in the lack of immune cell infiltration in the immune inactive subtype. **(A)** Differentially expressed genes in the immune inactive subtype with respect to other subtypes. **(B)** Enriched signaling pathways in the immune inactive subtype were analyzed and are presented. **(C)** Correlation between enriched signaling pathways and immune cell infiltration in the immune inactive subtype. **(D)** Correlation between enriched signaling pathways and IRGs in the immune inactive subtype. **(E)** Correlation between desmosome signaling pathway-related molecules and CD8$^+$ T cell infiltration in the immune inactive subtype. **(F)** DSG2 and CD8 expression in human UBC tissues was analyzed by immunohistochemistry. $^*P < 0.05$, $^{**}P < 0.01$.

patients in the hot tumor subtype with high immune infiltration exhibited good antitumor immunity, which may explain why patients in the hot tumor subtype demonstrated better survival. In other published papers, the immune active subtype has been associated with improved survival and shared similar genomic characteristics with those who responded to anti-PD-1 therapy (Zhou et al., 2020). In addition, the immunosuppressive subtype was found to feature high immune infiltration, stromal enrichment, and activation of the transforming growth factor (TGF)-β signaling pathway was correlated with the non-responsive signature of immune checkpoint inhibitor therapy, which may be required for the combination therapy of anti-PD-L1 and anti-TGF-β (Zhou et al., 2020).

T cell exhaustion is a hallmark of cancers and is characterized by the increase of several immune checkpoints that lead to the failure of immune checkpoint inhibitors. Woroniecka et al. (2018) observed the poor function of infiltrated T cells in the tumor microenvironment of glioblastoma. In localized clear cell renal cell carcinoma, the intratumoral infiltration of exhausted CD8$^+$ T cells with high levels of PD-1, Tim-3, and Lag-3 was investigated (Giraldo et al., 2017). The current study also found that although immune cells had infiltrated the tumor microenvironment of UBC, immune cells, especially T cells, exhibited an exhaustion phenotype.

In our previous study, the activation of specific tumor-intrinsic signaling pathways could be explained the phenomenon of immune exclusion in a subset of cancers (Yang et al., 2019). Increasing evidence has indicated that tumor-intrinsic signaling plays an important role in regulating tumor immune escape. Activation of the β-catenin signaling pathway within melanoma tumor cells excludes immune cell activation and leads to a non-T cell-inflamed tumor microenvironment (Spranger et al., 2015). Constitutively active STAT3 signaling in tumor cells has been shown to downregulate chemokine expression, including CCL5 and CXCL10, which are functionally responsible for T cell recruitment (Wang et al., 2004; Burdelya et al., 2005). Profiling the expression of IRGs identified three molecular pathways linked with the non-T cell-inflamed subtype (Fang et al., 2018).

In this study, the tumor-intrinsic signaling pathways, such as cardiac ventricle morphogenesis, cell communication involved in cardiac conduction, nephron development, regulation of cardiac muscle cell membrane repolarization, and response to BMP signaling pathway, may be involved in the non-T inflamed tumor microenvironment of the immune ignorant subtype. Moreover, desmosome, keratinocyte proliferation, and regulation of keratinocyte proliferation signaling pathway may be responsible for T cell exclusion in the immune inactive subtype.

In our study, we observed a relatively increase of neutrophils in the immune inactive subtype and immune ignorant subtype, which were found to function in opposition of antitumor immunity. Mandelli et al. (2020) reported that basal type of bladder cancer contained a significantly higher density of $CD66b^+$ tumor-associated neutrophils (TANs) compared to the luminal type, and a high density of TANs and T cells was significantly associated with a better outcome. However, Liu et al. (2018) found that elevated $CD66b^+$ TAN was correlated with an advanced T-stage, a high grade, a worse recurrence-free survival within non-muscle invasive bladder cancer subgroup and a worse overall survival within all urothelial bladder cancer cases. Therefore, Neutrophils might show different phenotypes and roles in different histological types of bladder cancers.

CONCLUSION

Urothelial bladder cancer can be classified into four subtypes by immune profiling. The hot tumor subtype has a high level of immune cell infiltration and is closely associated with good patient survival. IRGs and infiltrated immune cells can serve as potential biomarkers for prognosis. Tumor-intrinsic signaling pathways may play a key role in intratumoral T cell exclusion and poor prognosis in the immune ignorant and immune inactive subtypes. Therefore, targeting these signaling pathways represents a promising strategy for the treatment of UBC.

DATA AVAILABILITY STATEMENT

The original contributions presented in the study are included in the article/**Supplementary Material**, further inquiries can be directed to the corresponding author/s.

AUTHOR CONTRIBUTIONS

LY and YZ designed, edited, and led out this study. AL, FL, QZ, SJ, WZ, WY, and RZ conducted the data analysis and critical discussions of the results. LY, AL, FL, QZ, YL, and WL provided material support and study supervision. All authors contributed to the writing and editing of the manuscript, and approved the final draft of the manuscript.

FUNDING

This work was supported by grants from the National Natural Science Foundation of China (Nos. 91942314, U1804281, and 81602024), State's Key Project of Research and Development Plan (Nos. 2018YFC1313400 and 2016YFC1303500), and 2020 Science and Technology Project of Henan Province (No. 202102310039).

SUPPLEMENTARY MATERIAL

The Supplementary Material for this article can be found online at: https://www.frontiersin.org/articles/10.3389/fcell.2021.596484/full#supplementary-material

Supplementary Figure 1 | Clinical pathologies of the four subtypes. **(A)** The percent of papillary and non-papillary pathology observed in subtypes 1–4. **(B)** The percent of high and low grade observed in subtypes 1–4. **(C)** The percent of stage I-IV observed in subtypes 1–4. **(D)** The percent of T1-T4 observed in subtypes 1–4. **(E)** The percent of N1-N4 observed in subtypes 1–4.

Supplementary Figure 2 | The effect of IRGs on patient survival. Kaplan-Meier survival curves for UBC patients with high and low expression of IRGs.

Supplementary Figure 3 | The effect of immune cell infiltration on patient survival. Kaplan-Meier survival curves for UBC patients with high and low levels of immune cell infiltration.

Supplementary Figure 4 | Comparison of IRG expression in the immune ignorant, immune inactive, and hot tumor subtypes. IRGs included CCL13, CCL18, CCL4, CCL5, CD14, CD3D, CD3E, CD48, CD74, CD8A, CXCL10, CXCL11, CXCL13, CXCL9, FCGR3A, HCST IDO1, IL2RG, ITGB2, LYZ, MARCO, TYROBP, and UTS2. Data are shown as boxplots. $^{****}P < 0.0001$.

Supplementary Figure 5 | Correlation between CD8A and inhibitory molecules in UBC. Inhibitory molecules included PD-L1, TIM3, LAG3, CD163, CD39, CD73, IDO, IL-10, TGFB1I1, TGFB2, TGFB3, and IL6. Correlation coefficient (r) was calculated by Pearson's correlation analysis.

REFERENCES

Bracarda, S., Altavilla, A., Hamzaj, A., Sisani, M., Marrocolo, F., Del Buono, S., et al. (2015). Immunologic checkpoints blockade in renal cell, prostate, and urothelial malignancies. *Semin. Oncol.* 42, 495–505. doi: 10.1053/j.seminoncol.2015.02.004

Burdelya, L., Kujawski, M., Niu, G., Zhong, B., Wang, T., Zhang, S., et al. (2005). Stat3 activity in melanoma cells affects migration of immune effector cells and nitric oxide-mediated antitumor effects. *J. Immunol.* 174, 3925–3931. doi: 10.4049/jimmunol.174.7.3925

Carosella, E. D., Ploussard, G., LeMaoult, J., and Desgrandchamps, F. (2015). A systematic review of immunotherapy in urologic cancer: evolving roles for targeting of CTLA-4, PD-1/PD-L1, and HLA-G. *Eur. Urol.* 68, 267–279. doi: 10.1016/j.eururo.2015.02.032

Efstathiou, J. A., Mouw, K. W., Gibb, E. A., Liu, Y., Wu, C. L., Drumm, M. R., et al. (2019). Impact of immune and stromal infiltration on outcomes following bladder-sparing trimodality therapy for muscle-invasive bladder cancer. *Eur. Urol.* 76, 59–68. doi: 10.1016/j.eururo.2019.01.011

Fang, P., Li, X., Dai, J., Cole, L., Camacho, J. A., Zhang, Y., et al. (2018). Immune cell subset differentiation and tissue inflammation. *J. Hematol. Oncol.* 11:97. doi: 10.1186/s13045-018-0637-x

Ferlay, J., Soerjomataram, I., Dikshit, R., Eser, S., Mathers, C., Rebelo, M., et al. (2015). Cancer incidence and mortality worldwide: sources, methods and major patterns in GLOBOCAN 2012. *Int. J. Cancer* 136, E359–E386. doi: 10.1002/ijc.29210

Gentles, A. J., Newman, A. M., Liu, C. L., Bratman, S. V., Feng, W., Kim, D., et al. (2015). The prognostic landscape of genes and infiltrating immune cells across human cancers. *Nat. Med.* 21, 938–945. doi: 10.1038/nm.3909

Giraldo, N. A., Becht, E., Vano, Y., Petitprez, F., Lacroix, L., Validire, P., et al. (2017). Tumor-infiltrating and peripheral blood T-cell immunophenotypes predict early relapse in localized clear cell renal cell carcinoma. *Clin. Cancer Res.* 23, 4416–4428. doi: 10.1158/1078-0432.CCR-16-2848

Handa, Y., Tsutani, Y., Shiroma, N., Kai, Y., Mimae, T., Miyata, Y., et al. (2020). Prognostic impact of programmed death-ligand 1 and surrounding immune status on stage i lung cancer. *Clin. Lung Cancer*. 21, e302–e314. doi: 10.1016/j.cllc.2020.01.013

Harlin, H., Meng, Y., Peterson, A. C., Zha, Y., Tretiakova, M., Slingluff, C., et al. (2009). Chemokine expression in melanoma metastases associated with CD8+ T-cell recruitment. *Cancer Res.* 69, 3077–3085. doi: 10.1158/0008-5472.CAN-08-2281

Iglesia, M. D., Vincent, B. G., Parker, J. S., Hoadley, K. A., Carey, L. A., Perou, C. M., et al. (2014). Prognostic B-cell signatures using mRNA-seq in patients with subtype-specific breast and ovarian cancer. *Clin. Cancer Res.* 20, 3818–3829. doi: 10.1158/1078-0432.CCR-13-3368

Ji, R. R., Chasalow, S. D., Wang, L., Hamid, O., Schmidt, H., Cogswell, J., et al. (2012). An immune-active tumor microenvironment favors clinical response to ipilimumab. *Cancer Immunol. Immunother.* 61, 1019–1031. doi: 10.1007/s00262-011-1172-6

Kim, I. S., Gao, Y., Welte, T., Wang, H., Liu, J., Janghorban, M., et al. (2019). Immuno-subtyping of breast cancer reveals distinct myeloid cell profiles and immunotherapy resistance mechanisms. *Nat. Cell Biol.* 21, 1113–1126. doi: 10.1038/s41556-019-0373-7

Kim, J. W., Tomita, Y., Trepel, J., and Apolo, A. B. (2015). Emerging immunotherapies for bladder cancer. *Curr. Opin. Oncol.* 27, 191–200. doi: 10.1097/CCO.0000000000000177

Lehmann, B. D., Bauer, J. A., Chen, X., Sanders, M. E., Chakravarthy, A. B., Shyr, Y., et al. (2011). Identification of human triple-negative breast cancer subtypes and preclinical models for selection of targeted therapies. *J. Clin. Invest.* 121, 2750–2767. doi: 10.1172/JCI45014

Li, B., Severson, E., Pignon, J. C., Zhao, H., Li, T., Novak, J., et al. (2016). Comprehensive analyses of tumor immunity: implications for cancer immunotherapy. *Genome Biol.* 17:174. doi: 10.1186/s13059-016-1028-7

Liu, D. (2019). CAR-T "the living drugs", immune checkpoint inhibitors, and precision medicine: a new era of cancer therapy. *J. Hematol. Oncol.* 12:113. doi: 10.1186/s13045-019-0819-1

Liu, K., Zhao, K., Wang, L., and Sun, E. (2018). The prognostic values of tumor-infiltrating neutrophils, lymphocytes and neutrophil/lymphocyte rates in bladder urothelial cancer. *Pathol. Res. Pract.* 214, 1074–1080. doi: 10.1016/j.prp.2018.05.010

Liu, X., Cao, Y., Li, R., Gu, Y., Chen, Y., Qi, Y., et al. (2020). Poor clinical outcomes of intratumoral dendritic cell-specific intercellular adhesion molecule 3-grabbing non-integrin-positive macrophages associated with immune evasion in gastric cancer. *Eur. J. Cancer* 128, 27–37. doi: 10.1016/j.ejca.2020.01.002

Mandelli, G. E., Missale, F., Bresciani, D., Gatta, L. B., Scapini, P., Caveggion, E., et al. (2020). Tumor infiltrating neutrophils are enriched in basal-type urothelial bladder cancer. *Cells* 9:291. doi: 10.3390/cells9020291

Powles, T., Eder, J. P., Fine, G. D., Braiteh, F. S., Loriot, Y., Cruz, C., et al. (2014). MPDL3280A (anti-PD-L1) treatment leads to clinical activity in metastatic bladder cancer. *Nature* 515, 558–562. doi: 10.1038/nature13904

Sharma, P., Shen, Y., Wen, S., Yamada, S., Jungbluth, A. A., Gnjatic, S., et al. (2007). CD8 tumor-infiltrating lymphocytes are predictive of survival in muscle-invasive urothelial carcinoma. *Proc. Natl. Acad. Sci. U.S.A.* 104, 3967–3972. doi: 10.1073/pnas.0611618104

Spranger, S., Bao, R., and Gajewski, T. F. (2015). Melanoma-intrinsic beta-catenin signalling prevents anti-tumour immunity. *Nature* 523, 231–235. doi: 10.1038/nature14404

Spranger, S., Spaapen, R. M., Zha, Y., Williams, J., Meng, Y., Ha, T. T., et al. (2013). Up-regulation of PD-L1, IDO, and T(regs) in the melanoma tumor microenvironment is driven by CD8(+) T cells. *Sci. Transl. Med.* 5:200ra116. doi: 10.1126/scitranslmed.3006504

Sun, R., Limkin, E. J., Vakalopoulou, M., Dercle, L., Champiat, S., Han, S. R., et al. (2018). A radiomics approach to assess tumour-infiltrating CD8 cells and response to anti-PD-1 or anti-PD-L1 immunotherapy: an imaging biomarker, retrospective multicohort study. *Lancet Oncol.* 19, 1180–1191. doi: 10.1016/S1470-2045(18)30413-3

Sweis, R. F., Spranger, S., Bao, R., Paner, G. P., Stadler, W. M., Steinberg, G., et al. (2016). Molecular drivers of the non-T-cell-inflamed tumor microenvironment in urothelial bladder cancer. *Cancer Immunol. Res.* 4, 563–568. doi: 10.1158/2326-6066.CIR-15-0274

Verhaak, R. G., Hoadley, K. A., Purdom, E., Wang, V., Qi, Y., Wilkerson, M. D., et al. (2010). Integrated genomic analysis identifies clinically relevant subtypes of glioblastoma characterized by abnormalities in PDGFRA, IDH1, EGFR, and NF1. *Cancer Cell* 17, 98–110. doi: 10.1016/j.ccr.2009.12.020

von der Maase, H., Sengelov, L., Roberts, J. T., Ricci, S., Dogliotti, L., Oliver, T., et al. (2005). Long-term survival results of a randomized trial comparing gemcitabine plus cisplatin, with methotrexate, vinblastine, doxorubicin, plus cisplatin in patients with bladder cancer. *J. Clin. Oncol.* 23, 4602–4608. doi: 10.1200/JCO.2005.07.757

Wang, T., Niu, G., Kortylewski, M., Burdelya, L., Shain, K., Zhang, S., et al. (2004). Regulation of the innate and adaptive immune responses by Stat-3 signaling in tumor cells. *Nat. Med.* 10, 48–54. doi: 10.1038/nm976

Woroniecka, K., Chongsathidkiet, P., Rhodin, K., Kemeny, H., Dechant, C., Farber, S. H., et al. (2018). T-cell exhaustion signatures vary with tumor type and are severe in glioblastoma. *Clin. Cancer Res.* 24, 4175–4186. doi: 10.1158/1078-0432.CCR-17-1846

Yang, L., Li, A., Lei, Q., and Zhang, Y. (2019). Tumor-intrinsic signaling pathways: key roles in the regulation of the immunosuppressive tumor microenvironment. *J. Hematol. Oncol.* 12:125. doi: 10.1186/s13045-019-0804-8

Zhou, Y. J., Zhu, G. Q., Lu, X. F., Zheng, K. I., Wang, Q. W., Chen, J. N., et al. (2020). Identification and validation of tumour microenvironment-based immune molecular subgroups for gastric cancer: immunotherapeutic implications. *Cancer Immunol. Immunother.* 69, 1057–1069. doi: 10.1007/s00262-020-02525-8

Conflict of Interest: The authors declare that the research was conducted in the absence of any commercial or financial relationships that could be construed as a potential conflict of interest.

frontiers in Cell and Developmental Biology

ORIGINAL RESEARCH
published: 31 August 2021
doi: 10.3389/fcell.2021.723817

Identification of Immune-Related Subtypes and Characterization of Tumor Microenvironment Infiltration in Bladder Cancer

Mengjia Huang[1†], Lin Liu[1†], Junkai Zhu[1†], Tong Jin[1], Yi Chen[1], Li Xu[1], Wenxuan Cheng[1], Xinjia Ruan[1], Liwen Su[1], Jialin Meng[2,3], Xiaofan Lu[1]* and Fangrong Yan[1]**

[1] State Key Laboratory of Natural Medicines, Research Center of Biostatistics and Computational Pharmacy, China Pharmaceutical University, Nanjing, China, [2] Department of Urology, The First Affiliated Hospital of Anhui Medical University, Hefei, China, [3] Anhui Province Key Laboratory of Genitourinary Diseases, Institute of Urology, Anhui Medical University, Hefei, China

OPEN ACCESS

Edited by:
Yu Xiao,
Wuhan University, China

Reviewed by:
Yejinpeng Wang,
Wuhan University, China
Shaohua Xu,
Tongji University, China

***Correspondence:**
Jialin Meng
mengjialin@ahmu.edu.cn
Xiaofan Lu
xlu.cpu@foxmail.com
Fangrong Yan
f.r.yan@163.com

† These authors have contributed equally to this work

Specialty section:
This article was submitted to Molecular and Cellular Pathology, a section of the journal Frontiers in Cell and Developmental Biology

Received: *11 June 2021*
Accepted: *12 August 2021*
Published: *31 August 2021*

Citation:
Huang M, Liu L, Zhu J, Jin T, Chen Y, Xu L, Cheng W, Ruan X, Su L, Meng J, Lu X and Yan F (2021) Identification of Immune-Related Subtypes and Characterization of Tumor Microenvironment Infiltration in Bladder Cancer. Front. Cell Dev. Biol. 9:723817. doi: 10.3389/fcell.2021.723817

Tumors are closely related to the tumor microenvironment (TME). The complex interaction between tumor cells and the TME plays an indisputable role in tumor development. Tumor cells can affect the TME, promote tumor angiogenesis and induce immune tolerance by releasing cell signaling molecules. Immune cell infiltration (ICI) in the TME can affect the prognosis of patients with bladder cancer. However, the pattern of ICI of the TME in bladder cancer has not yet been elucidated. Herein, we identified three distinct ICI subtypes based on the TME immune infiltration pattern of 584 bladder cancer patients using the ESTIMATE and CIBERSORT algorithms. Then, we identified three gene clusters based on the differentially expressed genes (DEGs) between the three ICI subtypes. In addition, the ICI score was determined using single sample gene set enrichment analysis (ssGSEA). The results suggested that patients in the high ICI score subgroup had a favorable prognosis and higher expression of checkpoint-related and immune activity-related genes. The high ICI score subgroup was also linked to increased tumor mutation burden (TMB) and neoantigen burden. A cohort treated with anti-PD-L1 immunotherapy confirmed the therapeutic advantage and clinical benefit of patients with higher ICI scores. In the end, our study also shows that the ICI score represents an effective prognostic predictor for evaluating the response to immunotherapy. In conclusion, our study deepened the understanding of the TME, and it provides new ideas for improving patients' response to immunotherapy and promoting individualized tumor immunotherapy in the future.

Keywords: ICI, immune subtype, tumor microenvironment, bladder cancer, immunotherapy

INTRODUCTION

Bladder cancer is the most common malignant tumor of the urinary system. It accounts for the highest incidence of genitourinary tumors in China and is the second most common genitourinary malignancy in the United States (Kaufman et al., 2009). Bladder cancer can occur at any age, even in children, and its incidence increases with age and in those aged 50–70 years old. The incidence

of bladder cancer in males is three to four times higher than that in females (Kaufman et al., 2009; Sanli et al., 2017). According to the histological classification of urinary tract tumors in the 2004 WHO "Pathology and Genetics of Tumors in the Urological System and Male Reproduction Organ," the pathological types of bladder cancer include bladder urothelial carcinoma, bladder squamous cell carcinoma and bladder adenocarcinoma. Other rare disease subtypes include bladder clear cell carcinoma, bladder small cell carcinoma and bladder carcinoid. Among them, bladder urothelial carcinoma is the most common, accounting for more than 90% of the total number of bladder cancer patients. Urothelial carcinoma of the bladder can be divided into non-muscle invasive urothelial carcinoma (NMIBC) and muscle invasive urothelial carcinoma (MIBC), and approximately 75% of newly diagnosed patients have non-muscle invasive bladder cancer with 25% having muscle invasive bladder cancer (Kaufman et al., 2009; Sanli et al., 2017). Most patients with non-muscle invasive urothelial carcinoma receive transurethral resection of bladder tumors and bladder perfusion therapy to prevent recurrence postoperatively. Total cystectomy is often used in patients with muscle invasive urothelial carcinoma, squamous cell carcinoma and adenocarcinoma of the bladder, and partial cystectomy may be used in some patients. Neoadjuvant chemotherapy combined with surgery is also recommended for patients with muscle invasive urothelial carcinoma. Metastatic bladder cancer is primarily treated with chemotherapy. Approximately 70% of patients relapse after transurethral resection, and Bacillus Calmette-Guerin (BCG) or chemotherapy can reduce the recurrence rate to 25–40%.

Immunotherapy is a treatment method that artificially enhances or suppresses the immune function of the body to treat diseases by harnessing the immune state of the body, which is low or hyperactive. Tumor immunotherapy aims to activate the human immune system, kill tumor cells and tissues through autoimmune function, and restore the normal antitumor immune response of the body by restarting and maintaining the tumor-immune cycle to control and eliminate tumors. It includes monoclonal antibody immune checkpoint inhibitors, therapeutic antibodies, cancer vaccines, cell therapy, small molecule inhibitors and so on. Immunotherapy has evolved in recent years and has been proven to treat a variety of cancers, including melanoma, non-small cell lung cancer, kidney cancer and prostate cancer (Del Paggio, 2018). For example, ipilimumab improves survival in melanoma patients (Hodi et al., 2010; Schadendorf et al., 2015). Immunotherapy strategies for bladder cancer include intravesical administration of BCG (Alexandroff et al., 1999) and immune checkpoint inhibitors. However, studies have shown that immunotherapy is effective in only a small number of patients (Julie and Scott, 2012; Christofi et al., 2019). Therefore, new therapeutic markers are needed to identify the subgroup of patients who are suitable for immunotherapy.

The TME has been recognized as an important component of malignant tumor tissues and plays a mixed role in tumor progression, metastasis, treatment resistance and disease recurrence (Runa et al., 2017). The TME refers to the surrounding microenvironment of tumor cells, including blood vessels, immune cells, fibroblasts, bone marrow-derived inflammatory cells, various signaling molecules and the extracellular matrix (ECM). The complex interaction between tumor cells and the TME plays an indisputable role in tumor development (Pottier et al., 2015). Tumors are closely related to the TME. Tumors can affect their microenvironment, promote tumor angiogenesis and induce immune tolerance by releasing cell signaling molecules (Kerkar and Restifo, 2012). Tumor cells promote the growth and development of tumors by changing and maintaining the conditions of their survival and development through autocrine and paracrine mechanisms. Immune cells in the microenvironment include adaptive immunity, T lymphocytes, dendritic cells and accidental B cells, innate immunity, macrophages, polymorphonuclear leukocytes, and natural killer cells, which can influence tumor cell growth and development (Whiteside, 2008). Therefore, it is possible to identify different immune phenotypes by analyzing the heterogeneity and complexity of the TME, improving the ability to guide and predict responses to immunotherapy.

In this study, we identified three distinct immune ICI subtypes based on the infiltration patterns of 22 immune cells obtained using the CIBERSORT algorithm and the immune score and stroma score computed by the ESTIMATE algorithm of 584 bladder cancer tumor samples. Samples were further divided into three gene clusters based on DEGs identified based on three ICI subtypes. In addition, we established an ICI score to characterize the immune landscape of bladder cancer, which can accurately predict patients' outcomes and responses to immunotherapy. Finally, the ICI score was validated in an independent cohort. The results indicated that the ICI score can be used as an effective prognostic predictor of immunotherapy. The evaluation of ICI patterns in larger samples may provide new directions for strategies of immunotherapy in bladder cancer.

MATERIALS AND METHODS

Study Cohort and Data Pre-processing

Bladder cancer data were obtained from five publicly available datasets, TCGA-BLCA, GSE13507, GSE31684, E-MTAB-1803, and a validation cohort (GSE93527). The RNA-Seq data (fragments per kilobase million value) of the TCGA-BLCA cohort were downloaded using the R package "TCGAbiolinks," and the FPKM values were transformed into TPM values. Four hundred and fourteen samples of bladder cancer were obtained by considering only the mRNA-encoding protein. Clinical and survival information of TCGA-BLCA was extracted from pan-cancer data, including age, sex, stage, etc. Only overall survival (OS) was considered. Tumor samples lacking clinical information were excluded, and samples with 0 OS were also removed. Common samples of expression profile data and survival information were extracted, and 406 bladder cancer samples were obtained from the TCGA-BLCA cohort. The copy number variation data were downloaded from Fire Browse[1]. Mutation data were downloaded from cBioPortal[2]. The number

[1]http://firebrowse.org/

[2]https://www.cbioportal.org/

of predicted neoantigens of TCGA-BLCA samples was obtained from a published article (Rooney et al., 2015). The GSE13507 cohort and GSE93527 cohort were downloaded from the Gene Expression Omnibus database[3] on the Illumina platform. The microarray datasets (GSE31684 and E-MTAB-1803) were downloaded from the Array Express database[4] on the Affymetrix platform. Samples with non-muscle invasive bladder cancer (NMIBC) samples were excluded, and only patients with muscle invasive bladder cancer (MIBC) were retained. Similarly, tumor samples lacking clinical information and samples with 0 OS were removed. Four datasets were combined, and the "Combat" algorithm was used to eliminate the batch effect (**Supplementary Figure 2**). In the end, a total of 584 bladder cancer samples were obtained for subsequent analysis. Detailed information on 584 bladder cancer patients is shown in **Supplementary Table 1**. The validation cohort, Imvigor210, was obtained from the R package "Imvigor210coreBiologies," including survival outcomes, response results and expression profiles of patients who received immunotherapy (Mariathasan et al., 2018). The functional annotation gene set (h.all.v7.2.symbol) was downloaded from the MSigDB database[5]. The data of cell lines in bladder cancer were downloaded from DepMap[6].

Unsupervised Clustering Analysis

The level of ICI in bladder cancer was quantified by the CIBERSORT algorithm using the LM22 gene signature (Newman et al., 2015). The immune score and stroma score of each sample were calculated using the ESTIMATE algorithm (Yoshihara et al., 2013). Unsupervised clustering was applied to classify patients into distinct ICI subtypes according to the above 24 signatures. Consensus clustering was used to determine the number of clusters and stability using the R package "ConsensusClusterPlus" (Wilkerson and Hayes, 2010). We repeated 1,000 times (each using 90% of the samples) to guarantee the stability of clustering. The optimal cluster number was determined by the clustering score for the cumulative distribution function (CDF) curve and the relative changes in the area under the CDF curve.

Identification of Differentially Expressed Genes

To identify ICI pattern-related genes, patients with bladder cancer were classified into three distinct ICI subtypes. The R package "limma" was applied to determine DEGs between different ICI subtypes (Ritchie et al., 2015). The significance criteria for determining DEGs were set as adjusted $p < 0.05$ and fold change cut-off of 1.65.

Generation of ICI Score

To quantify ICI patterns of individual tumors, the ICI score was calculated. First, patients were classified into different groups using an unsupervised clustering method based on overlapping DEGs. We performed consensus clustering to determine the number of clusters that was repeated 500 times (each using 90% of the samples) of Spearman distance measurement using the PAM clustering method to enhance the stability of clustering. Second, we performed Pearson correlation analysis between DEGs and the cluster signature and obtained ICI gene signatures A and B, which were positively and negatively correlated with the cluster signature, respectively. Finally, we used the Boruta algorithm to reduce the dimension of ICI gene signatures. And then we used ssGSEA to calculate the signature scores (Barbie et al., 2009; Kursa and Rudnicki, 2010). ssGSEA was performed using the R package "GSVA." We then defined the ICI score using a method similar to the gene expression grade index (GGI) (Sotiriou et al., 2006; Zeng et al., 2019):

$$\text{ICI score} = \sum \text{Score}_A - \sum \text{Score}_B$$

Somatic Mutation Analysis

The mutation data of TCGA-BLCA tumor samples were downloaded from cBioPortal (see text footnote 2). Studies have shown that higher TMB and somatic mutation rates are correlated with stronger antitumor immunity (Rooney et al., 2015). To determine the relationship between somatic mutation and ICI score, we first classified patients into two subgroups, the high and low ICI score subgroups, and then used the R package "maftools" to identify driver genes in the high and low ICI score subgroups (Mayakonda et al., 2018). The top 25 driver genes with the highest mutation frequency were further analyzed.

Copy Number Variation Analysis

The copy number variation data of TCGA-BLCA tumor samples were downloaded from Fire Browse (see text footnote 1). The Genomic Identification of Significant Targets in Cancer (GISTIC2.0) algorithm was utilized to classify the copy number variant genes with remarkable gains and losses (Mermel et al., 2011). The confidence level was set to 0.95, and other parameters were left at default settings (Luo et al., 2020; Yang et al., 2020).

Collection of Genomic and Clinical Information With Immunotherapy

To further validate the predictive value of prognosis of the ICI score, we applied the ICI score to an independent anti-PD-L1 immunotherapy cohort, IMvigor210. The expression data and detailed clinical annotations of this cohort were obtained using the R package "IMvigor210CoreBiologies" that can be downloaded from http://research-pub.gene.com/IMvigor210CoreBiologies (Mariathasan et al., 2018). For gene expression data, the count value was also transformed into the TPM value with $\log_2$(TPM+1) for further analysis.

Statistical Analysis

All statistical analyses were conducted using R version 4.0.2. The Kruskal–Wallis test was used for statistical comparison among more than two groups, and the Wilcoxon test was used for two group comparisons (Hazra and Gogtay, 2016). Kaplan–Meier curves were used to evaluate survival time in patients with bladder cancer. The OS probability was evaluated. The log-rank test was utilized to identify significant differences. The

[3]https://www.ncbi.nlm.nih.gov/geo/

[4]https://www.ebi.ac.uk/arrayexpress/

[5]http://www.gsea-msigdb.org/gsea/msigdb

[6]https://depmap.org/portal/

Wilcoxon test was used to analyze the correlation between the ICI score subgroups and somatic mutation frequency, and Pearson analysis was used to compute the correlation coefficient. All statistical *p*-values were two-sided, with $p < 0.05$ indicating statistical significance.

RESULTS

Identification of ICI Subtypes in Bladder Cancer

The detailed workflow for ICI score construction is shown in **Supplementary Figure 1**. The abundance of 22 immune cells was estimated using the CIBERSORT algorithm, the enrichment scores of stromal cells and immune cells were estimated using the ESTIMATE algorithm, and 24 signatures were obtained for clustering analysis (**Supplementary Table 2**; Yoshihara et al., 2013; Newman et al., 2015). We identified three distinct ICI subtypes based on the above 24 signatures in 584 patients with bladder cancer, designated ICI clusters A–C (**Figure 1A** and **Supplementary Figure 3**). The OS curve of the three ICI subtypes was obtained using the Kaplan–Meier method (log-rank test, $p = 0.003$; **Figure 1B**). To visualize immune cell interactions in the TME, we also analyzed the correlations between 22 immune cells (**Figure 1C**). Additionally, we compared the composition of the TME of three distinct ICI subtypes to further elucidate differences among ICI subtypes. The infiltration levels of CD8+ T cells, activated natural killer cells, activated memory CD4+ T cells, follicular helper T cells and M1 macrophages were significantly higher in ICI cluster A. Patients in ICI cluster B were characterized by a significantly higher infiltration level of naive CD4+ T cells, gamma delta T cells and activated mast cells. ICI cluster C was marked by increased monocytes, M2 macrophages, resting memory CD4+ T cells and resting mast cells infiltration and had the poorest prognosis (**Figure 1D**). Finally, we analyzed and compared the expression levels of two important immune checkpoints of the ICI subtypes, PD-L1 and PD1. The results indicated that ICI cluster A exhibited the highest expression level of the two immune checkpoints (**Figures 1E**,**F**).

Identification of Gene Subtypes Based on DEGs

Subsequent analysis was only based on the TCGA-BLCA cohort. To elucidate the difference in biological features in ICI subtypes, we performed differential analysis using the R package "limma" to determine transcriptome differences between ICI subtypes (Ritchie et al., 2015). Finally, 857 DEGs were identified (**Supplementary Table 3**). Then, 506 gene signatures A and 351 gene signatures B were identified by Pearson correlation analysis (**Supplementary Table 4**). At the same time, we used the Boruta algorithm to reduce the dimensions of gene signatures A and B, and 97 gene signatures A and 112 gene signatures B were finally obtained (Kursa and Rudnicki, 2010). Subsequently, unsupervised clustering was applied to classify patients into three subtypes based on 857 DEGs, gene clusters A–C (**Figure 2A** and **Supplementary Figure 4**). Gene cluster A exhibited lower expression of gene signatures A and gene signatures B. Gene cluster B had a higher expression level of gene signatures A and lower expression level of gene signatures B, and gene cluster C was the opposite with higher expression of gene signatures B and lower expression of gene signatures A (**Figure 2A**). The OS curve of the three gene subtypes was obtained using the Kaplan–Meier method (log-rank test, $p < 0.001$; **Figure 2B**). We found that patients in gene cluster C had the poorest prognosis. Gene ontology (GO) enrichment analysis was executed. The significantly enriched biological processes of gene signatures A and gene signatures B are summarized in **Figures 2C**,**D**, respectively. Detailed information on the enrichment analysis is shown in **Supplementary Table 5**. We also found that gene cluster A exhibited increased activated dendritic cells, naive CD4+ T cells, and gamma delta T cell infiltration. Gene cluster B, with the highest immune score, exhibited higher infiltration of M1 and M2 macrophages, natural killer cells, activated memory CD4+ T cells, CD8+ T cells and regulatory T cells. Gene cluster C displayed an escalated stroma score and higher infiltration of M0 macrophages and resting mast cells (**Figure 2E**). Similarly, analyzing the expression level of two immune checkpoints showed that gene cluster B had the highest expression of PD1 and PD-L1 (**Figures 2F**,**G**).

Construction of the ICI Scores

To quantify the ICI patterns of individual tumors, the ICI score was constructed (Zhang et al., 2020). ssGSEA was used to calculate the score of gene signatures A and B, score A and score B, and then the prognostic signatures score was obtained. Patients were classified into two subgroups as high or low ICI score groups by the median score in the TCGA-BLCA cohort. The distribution of patients in three gene subtypes and two subgroups is shown in **Figure 3A**. We compared the expression levels of the immune checkpoint- and immune activity-related genes between the two groups to evaluate the immune activity and tolerance condition (Hugo et al., 2016; Ayers et al., 2017). We found significant overexpression of most immune checkpoint- and immune activity-related genes in the high ICI group, except TBX2 (**Figure 3B**). Gene set enrichment analysis (GSEA) was then executed (**Figures 3C**,**D**). Detailed information is provided in **Supplementary Table 6**. In addition, survival analysis revealed that the prognosis of patients in the high ICI score group was better than that in the low ICI score group (log-rank test, $p = 0.002$; **Figure 3E**).

Furthermore, the predictive value of prognosis of the ICI score was validated in the total BLCA cohort ($n = 584$), including TCGA-BLCA ($n = 406$), GSE13507 ($n = 61$), GSE31684 ($n = 74$), and E-MTAB-1803 ($n = 43$). Survival analysis showed that the prognosis of patients in the high ICI score group was better than that in the low ICI score group (log-rank test, $p = 0.017$; **Supplementary Figure 5A**). In addition, we validated the ICI score in a completely independent external cohort (GSE93527). Survival analysis revealed that the prognosis of patients in the high ICI score group was better than that in the low ICI score group (log-rank test, $p = 0.01$; **Supplementary Figure 5B**). Finally, we validated the results on cell lines of bladder cancer.

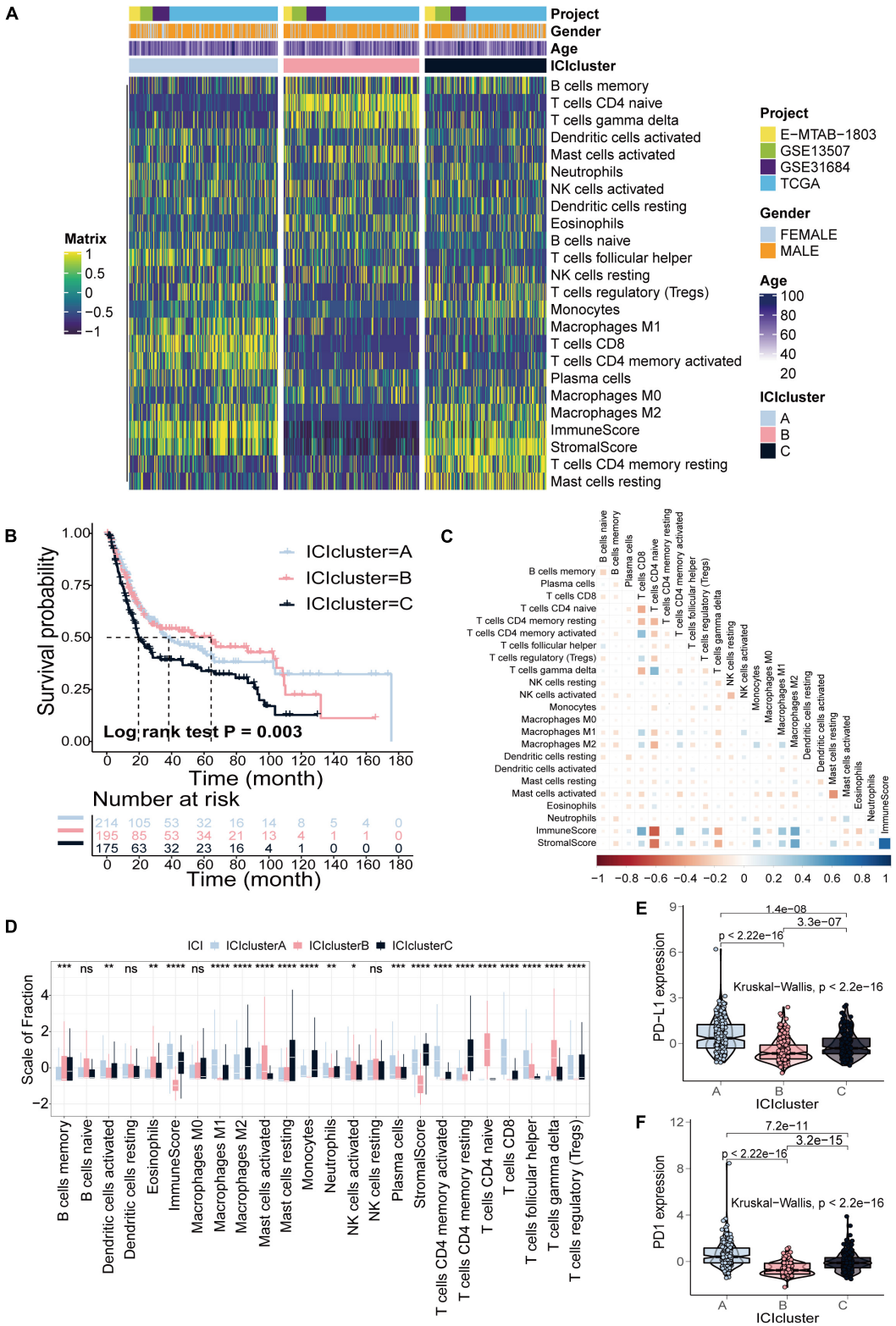

FIGURE 1 | Identification of ICI subtypes in bladder cancer. **(A)** Consensus clustering of TIICs in four BLCA cohorts. **(B)** Kaplan–Meier curves for OS of all BLCA patients with ICI clusters (log-rank test, $p = 0.003$). **(C)** Cellular interaction of the TIICs types. **(D)** The fraction of TIICs, immune score and stromal score in three ICI clusters (Kruskal–Wallis test, $^{*}p < 0.05$; $^{**}p < 0.01$; $^{***}p < 0.001$; $^{****}p < 0.0001$). **(E,F)** The difference in PD-L1 **(E)** and PD-1 **(F)** expression among three ICI clusters (Kruskal–Wallis test, $p < 2.2e\text{-}16$).

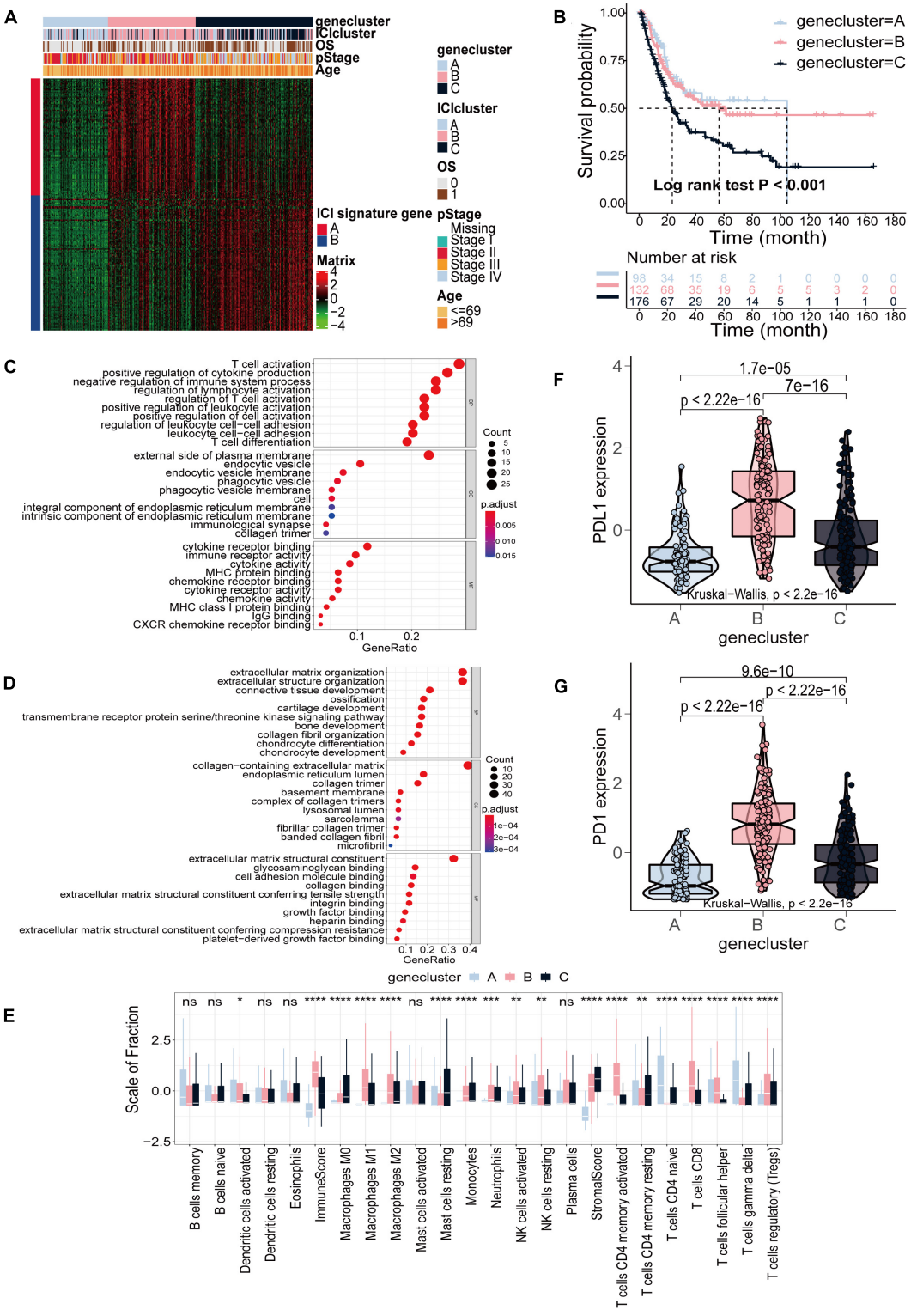

FIGURE 2 | Identification of gene subtypes based on DEGs in TCGA-BLCA cohort. **(A)** Consensus clustering of DEGs among three ICI subtypes. **(B)** Kaplan–Meier curves for OS of the three gene clusters (log-rank test, $p < 0.001$). **(C,D)** GO enrichment analysis of the two ICI-related signature genes: ICI signature genes A **(C)** and ICI signature genes B **(D)**. **(E)** The fraction of TIICs, immune score and stromal score in three gene clusters (Kruskal–Wallis test, $^{*}p < 0.05$; $^{**}p < 0.01$; $^{***}p < 0.001$; $^{****}p < 0.0001$). **(F,G)** The difference in the expression of PD-L1 **(F)** and PD-1 **(G)** among three gene clusters (Kruskal–Wallis test, $p < 2.2e\text{-}16$).

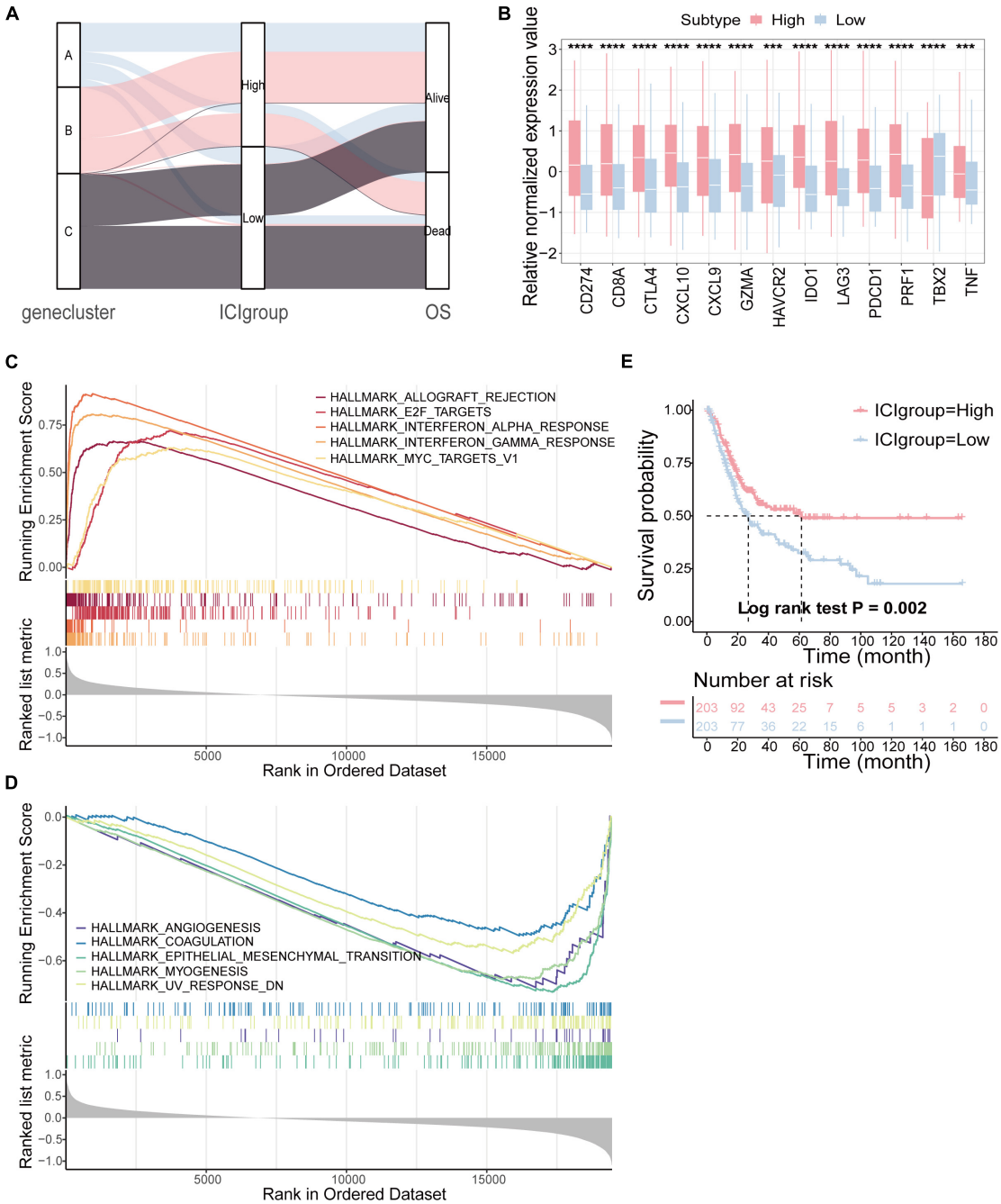

FIGURE 3 | Construction of the ICI score. **(A)** Alluvial diagram of gene cluster distribution in groups with different ICI score and survival outcomes. **(B)** The difference in the expression of immune checkpoint-related genes (IDO1, CD274, HAVCR2, PDCD1, CTLA4, and LAG3) and immune activity-related genes (CD8A, CXCL10, CXCL9, GZMA, PRF1, TBX2, and TNF) between high and low ICI score subgroups. **(C,D)** The gene set enrichment analysis (GSEA) in high **(C)** and low ICI score subgroups **(D)**. **(E)** Kaplan–Meier curves for high and low ICI score groups in the TCGA-BLCA cohort (log-rank test, $p = 0.002$). ***$p < 0.001$; ****$p < 0.0001$.

We calculated the ICI score for each cell line and grouped them into two groups by the median scores. Subsequently, we conducted differential expression analysis between the two groups and obtained 886 differentially expressed genes ($|\log2FC| > 1.65$ and p-value < 0.05). Finally, we conducted hierarchical clustering of cell lines based on these differentially expressed genes, and finally obtained two classes, class 1 and class 2 (**Supplementary Figure 5C**). We analyzed and compared the ICI score of the two classes, and the results showed that the ICI score of class 2 was significantly higher than that of class 1 (Wilcoxon test, $p = 0.019$; **Supplementary Figure 5D**). It indicated that the differentially expressed genes defined were related to the

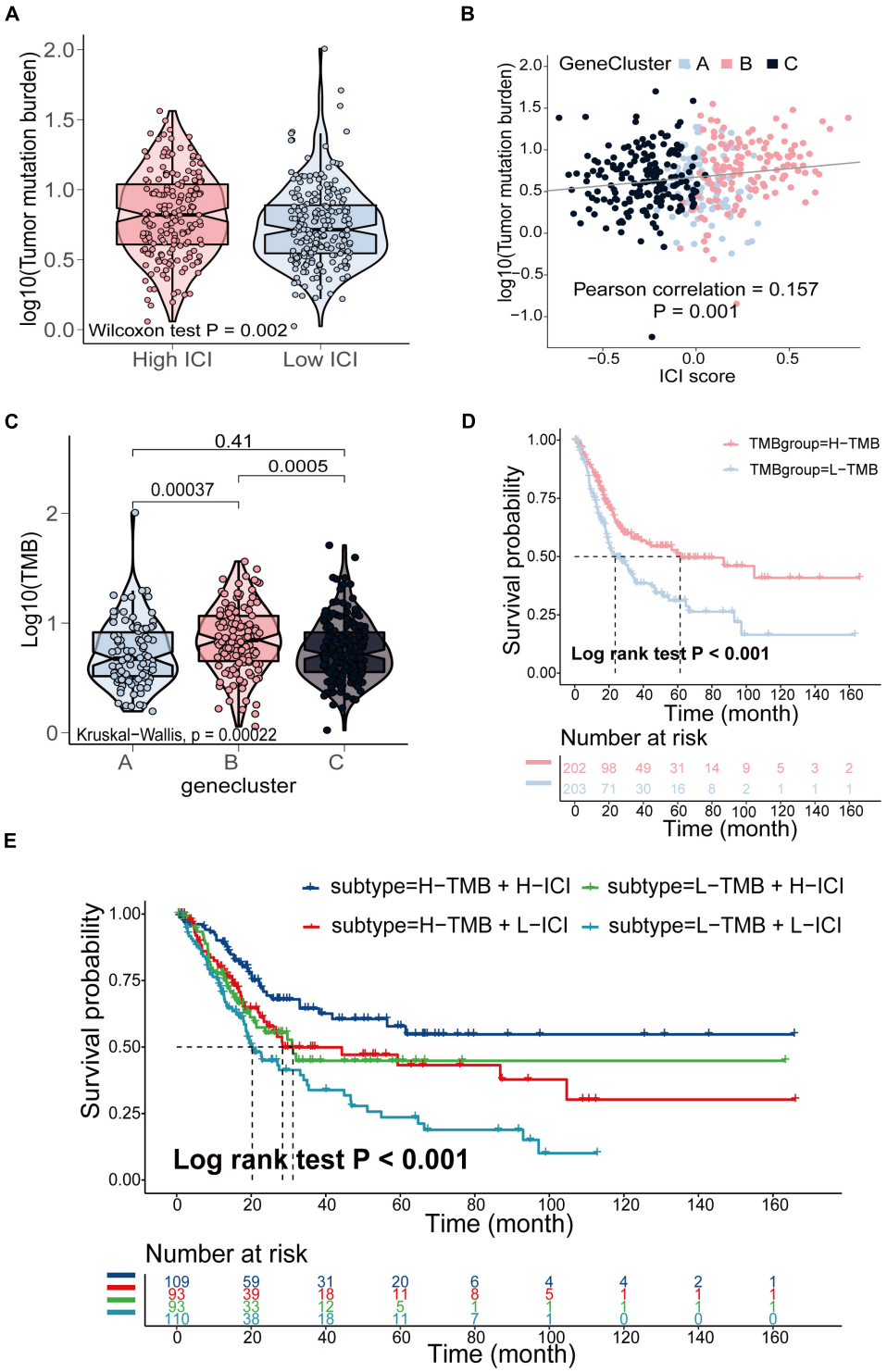

FIGURE 4 | The relationship between the ICI score and somatic mutation in the TCGA- BLCA cohort. **(A)** TMB difference in the high and low ICI score subgroups (Wilcoxon test, $p = 0.002$). **(B)** Pearson correlation analysis between ICI score and mutation load (Pearson correlation coefficient = 0.157, $p = 0.001$). **(C)** The comparison of TMB among three gene clusters (Kruskal–Wallis test, $p = 0.0002$). **(D)** Kaplan–Meier curves for high and low TMB groups of (log-rank test, $p < 0.001$). **(E)** Kaplan–Meier curves for patients stratified by both TMB and ICI score (log-rank test, $p < 0.001$).

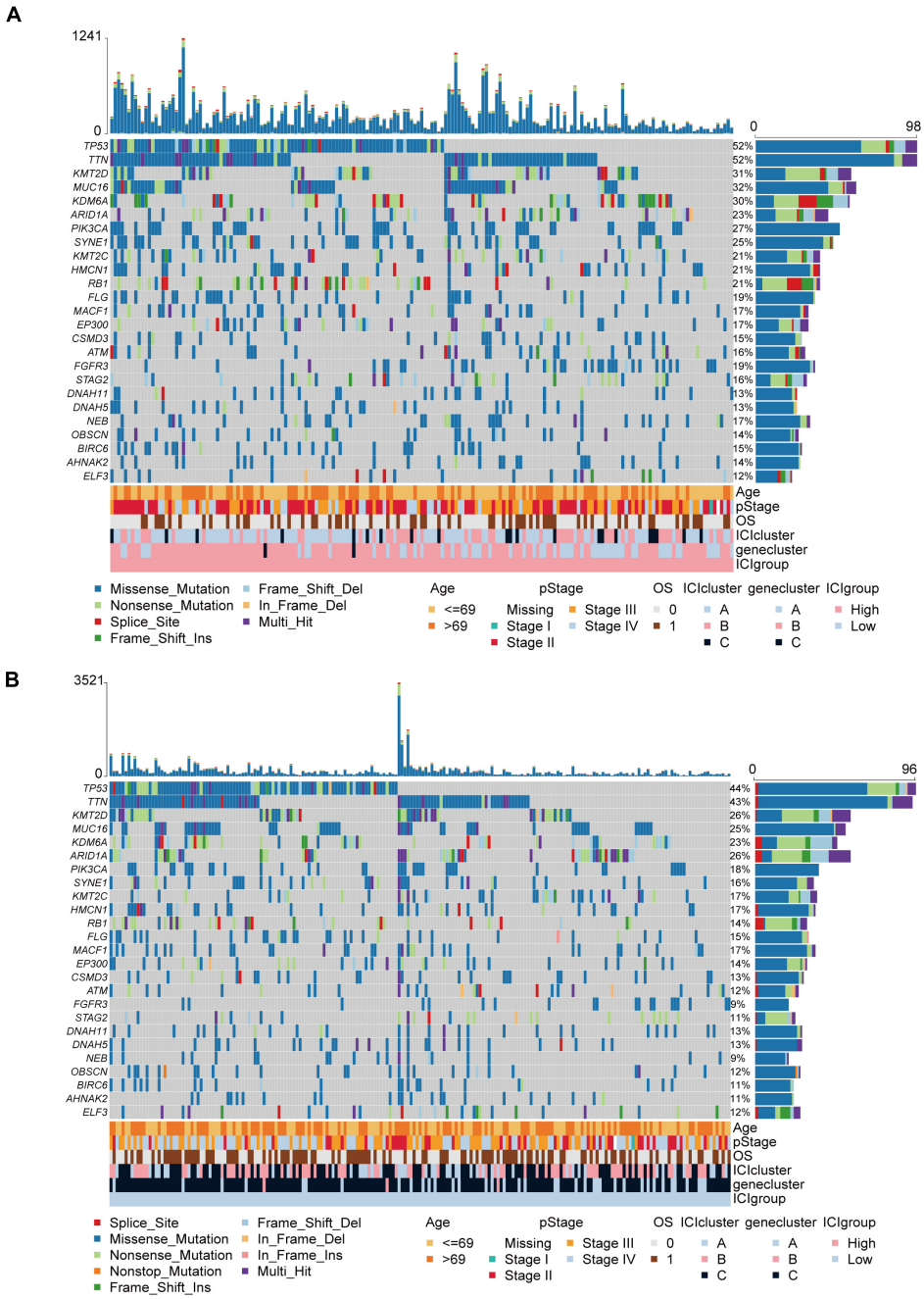

FIGURE 5 | The oncoPrint in the high **(A)** and low ICI score group **(B)**.

ICI score, and also verified the prognostic effect of ICI score from another aspect.

The Relationship Between the ICI Score and Somatic Mutation and Copy Number Variation

The TMB is a crucial biomarker in cancer immunotherapy (Chan et al., 2019). Studies show that a higher TMB is correlated with stronger antitumor immunity (Rooney et al., 2015). Our analysis revealed that patients in the high ICI score group exhibited significantly higher TMB than those in the low ICI score group (Wilcoxon test, $p = 0.002$; **Figure 4A**). Pearson correlation analysis confirmed that the ICI score was significantly and positively correlated with TMB (Pearson correlation coefficient = 0.157, $p = 0.001$; **Figure 4B**). In addition, we found significant differences in TMB between the three gene clusters. The patients in gene cluster B exhibited significantly

TABLE 1 | The association between ICI score and somatic variants.

Hugo_Symbol	High score		Low score		*p*-value
	Mutated samples	Mutation frequency	Mutated samples	Mutation frequency	
FGFR3	36	19%	20	9%	0.0042
NEB	33	17%	20	9%	0.0139
PIK3CA	51	27%	38	18%	0.0214
SYNE1	47	25%	35	16%	0.0287
KDM6A	57	30%	49	23%	0.0829
TTN	98	52%	94	43%	0.0858
RB1	39	21%	31	14%	0.0912
MUC16	61	32%	54	25%	0.0993
STAG2	31	16%	24	11%	0.1167
TP53	98	52%	96	44%	0.1256
BIRC6	28	15%	23	11%	0.2011
FLG	36	19%	32	15%	0.2470
ATM	30	16%	26	12%	0.2567
AHNAK2	27	14%	23	11%	0.2595
HMCN1	39	21%	36	17%	0.2948
KMT2D	58	31%	57	26%	0.3241
KMT2C	39	21%	37	17%	0.3557
EP300	32	17%	31	14%	0.4627
ARID1A	44	23%	57	26%	0.4874
CSMD3	28	15%	29	13%	0.5774
OBSCN	26	14%	27	12%	0.6950
ELF3	22	12%	27	12%	0.8045
DNAH11	25	13%	28	13%	0.9229
DNAH5	25	13%	28	13%	0.9229
MACF1	32	17%	36	17%	0.9268

higher TMB than those in gene cluster A and C (Kruskal–Wallis test, $p = 0.0002$; **Figure 4C**). Next, we divided patients into high and low TMB subgroups according to the median TMB value. Survival analysis showed that patients in the high TMB subgroup presented better OS than those in the low TMB subgroup (log-rank test, $p < 0.001$; **Figure 4D**). To evaluate the synergistic effect of ICI score and TMB in bladder cancer, we further classified patients into four subgroups: high TMB + high ICI score, high TMB + low ICI score, low TMB + high ICI score, and low TMB + low ICI score. The stratified analysis revealed that TMB status did not affect the prediction of ICI score, and the high ICI score group exhibited significantly better survival in both the high and low TMB subgroups (log-rank test, $p < 0.001$; **Figure 4E**). We also evaluated somatic variants of driver genes between the low and high ICI groups, which were determined using the R package "maftools." The top 25 driver genes with the highest mutation frequency in the high and low ICI score subgroups were analyzed (**Figures 5A**,**B**). The results revealed that the mutation frequency of FGFR3, NEB, PIK3CA, and SYNE1 in the high ICI score group was significantly higher than that in the low ICI score group, which provides some new ideas regarding the association between ICI and somatic mutation in immune checkpoint inhibitor therapy (**Table 1**).

Furthermore, we analyzed the relationship between the ICI score and copy number variation. GISTIC2.0 was used to analyze the copy number variation in the high and low ICI score subgroups (Mermel et al., 2011). The results were visualized using the R package "maftools" (**Figures 6A**,**B**). Significantly amplified regions in the high ICI score subgroup included 1q21.3, 1p34.2, 5p15.33, 6p24.1, etc. Significant amplified in the low ICI score subgroup included 3p25.2, 4q13.3, 6q23.3, 8p11.23, etc. In addition, we identified DEGs between the high and low ICI score groups, including 1140 genes that were highly expressed in the high ICI score group and 3419 genes that were highly expressed in the low ICI score group ($|\log2FC| > \log2(1.2)$ and $padj < 0.05$). And then we mapped the chromosomal locations of those genes. We performed Pearson correlation analysis between the expression of these genes and the copy number of the region in which the genes are located. According to the *r*-value, the correlation information of the first 24 genes in the high and low ICI score groups was plotted (**Supplementary Figures 6A**,**B**). For example, the expression of gene CD274 was positively correlated with the copy number of its region "9p24.1," and the correlation coefficient was 0.525 (**Supplementary Figure 6A**). Therefore, the high expression of this gene is significantly correlated with the copy number of its region.

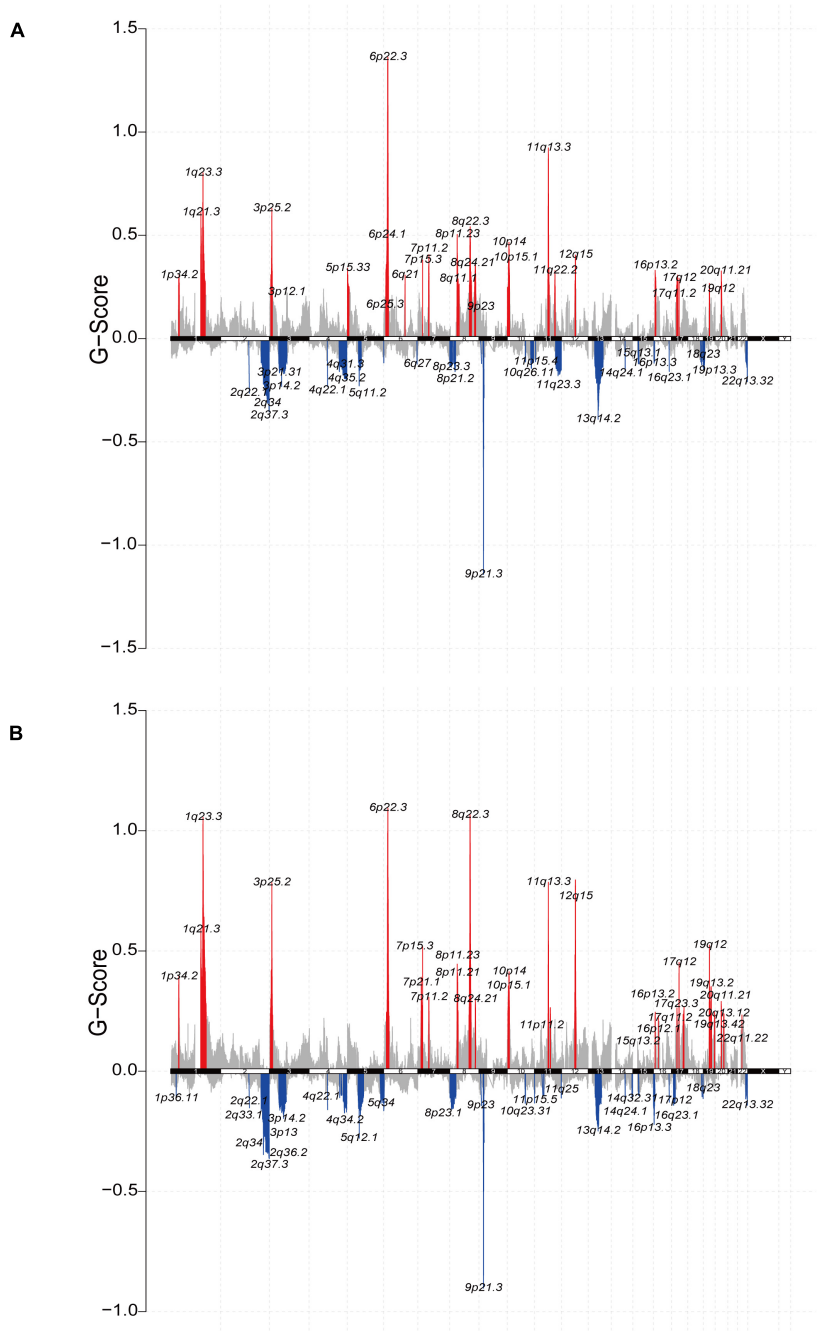

FIGURE 6 | The relationship between the ICI score and copy number variation in the TCGA-BLCA cohort. **(A,B)** The visualization of the copy number variation analysis based on GISTIC2.0 for high **(A)** and low **(B)** ICI score groups.

Detailed correlation information of these genes is shown in **Supplementary Table 7**.

The Relationship Between the ICI Score and Antitumor Immunity

To determine how the ICI score enhanced the immunogenicity of bladder cancer and activated antitumor immunity, we compared the expression of 74 immune-related genes between the high ICI score and low ICI score groups. The 74 immune-related genes were obtained from a published article (Yi et al., 2020). The results revealed that the expression of 53 immune-related genes was significantly different between the high and low ICI score group (**Supplementary Figure 7**). The detailed information of 74 immune-related genes is shown in **Supplementary Table 8**. Tumor neoantigens are abnormal proteins or antigens produced

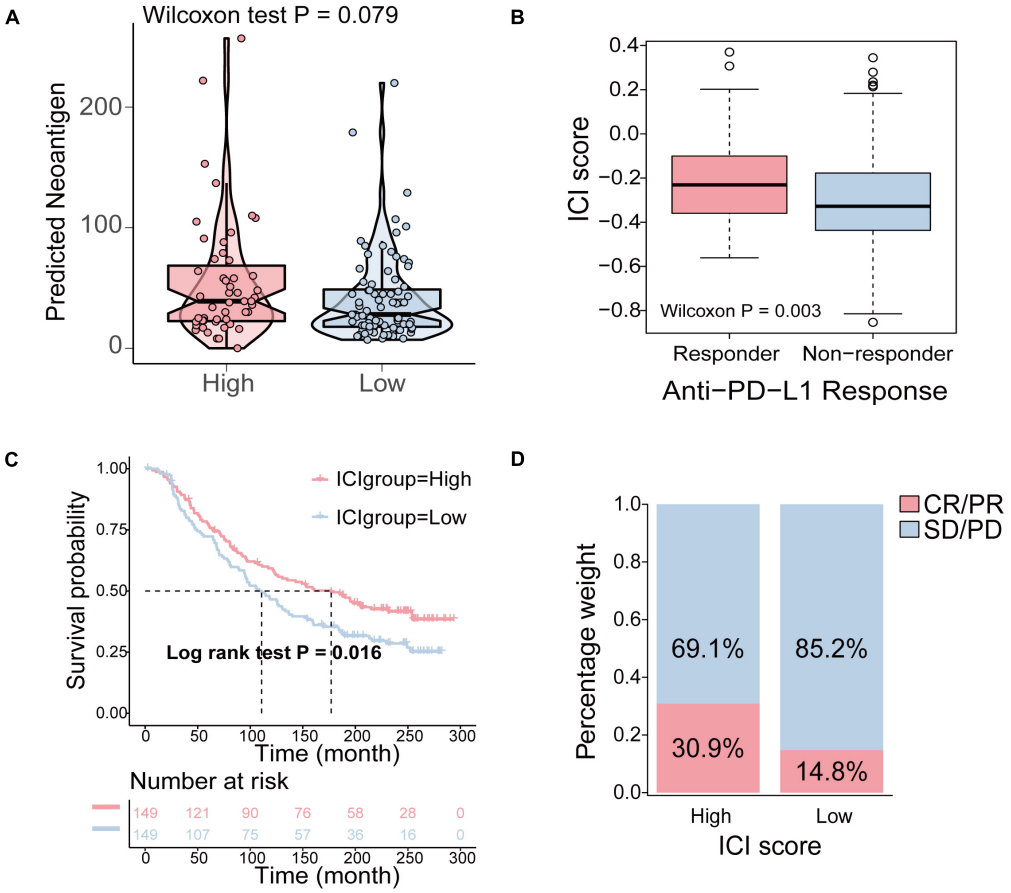

FIGURE 7 | The relationship between the ICI score and antitumor immunity and the role of ICI pattern in anti-PD-L1 immunotherapy. **(A)** The difference of the number of neoantigens in the high and low ICI score groups (Wilcoxon test, $p = 0.079$). **(B)** The comparison of the ICI score in different anti-PD-1 clinical response statuses (Wilcoxon test, $p = 0.003$). **(C)** Kaplan–Meier curves for patients in the high and low ICI score group in the IMvigor210 cohort (log-rank test, $p = 0.016$). **(D)** The rate of clinical response to anti-PD-L1 immunotherapy in the high and low ICI score groups in the IMvigor210 cohort (CR, complete response; PR, partial response; SD, stable disease; PD, progressive disease).

by mutations in the genes of tumor cells that are recognized by immune cells and can activate the immune system (Lennerz et al., 2005; Zhou et al., 2005). Neoantigens are a key target of cancer immunotherapy (Gubin et al., 2015). The feasibility of developing personalized immunotherapies based on neoantigens has been demonstrated (Nielsen et al., 2007; Mahesh, 2014). Therefore, it is necessary to explore the relationship between neoantigens and ICI score. The number of predicted neoantigens of some TCGA-BLCA samples was obtained from a published article (Rooney et al., 2015). The results demonstrated that the number of neoantigens in the high ICI score group was higher than that in the low ICI score group, but the differences were not statistically significant (Wilcoxon test, $p = 0.079$; **Figure 7A**).

The Role of ICI Pattern in Anti-PD-L1 Immunotherapy

Immune checkpoints are a series of molecules that are expressed on immune cells and regulate the degree of immune activation. They play an important role in preventing the occurrence of autoimmune action (Pardoll, 2012). Immunotherapy induced by the blockade of PD-L1 and PD-1 is undoubtedly a breakthrough in cancer treatment (Sharma et al., 2011; Hinrichs and Rosenberg, 2014). As a result, based on an anti-PD-L1 immunotherapy cohort, IMvigor210, we investigated to determine whether the ICI score predicts patients' responses to immune checkpoint inhibitors. Similarly, patients were classified into two groups as the high and low ICI score groups by the median score. We found that higher ICI score were associated with objective responses to anti-PD-L1 treatment, and patients with responses to anti-PD-L1 treatment exhibited higher ICI score in the Imvigor210 cohort (Wilcoxon test, $p = 0.003$; **Figure 7B**). Patients with high ICI score exhibited significantly prolonged OS (log-rank test, $p = 0.016$; **Figure 7C**). In addition, patients in the high ICI score group exhibited a significantly higher objective response rate (CR/PR) to anti-PD-L1 immunotherapy than those in the low ICI score group (**Figure 7D**). In conclusion, these results indicated that the ICI score is significantly associated with anti-PD-L1 immunotherapy responses and that the established ICI score can help predict the anti-PD-L1 immunotherapy response.

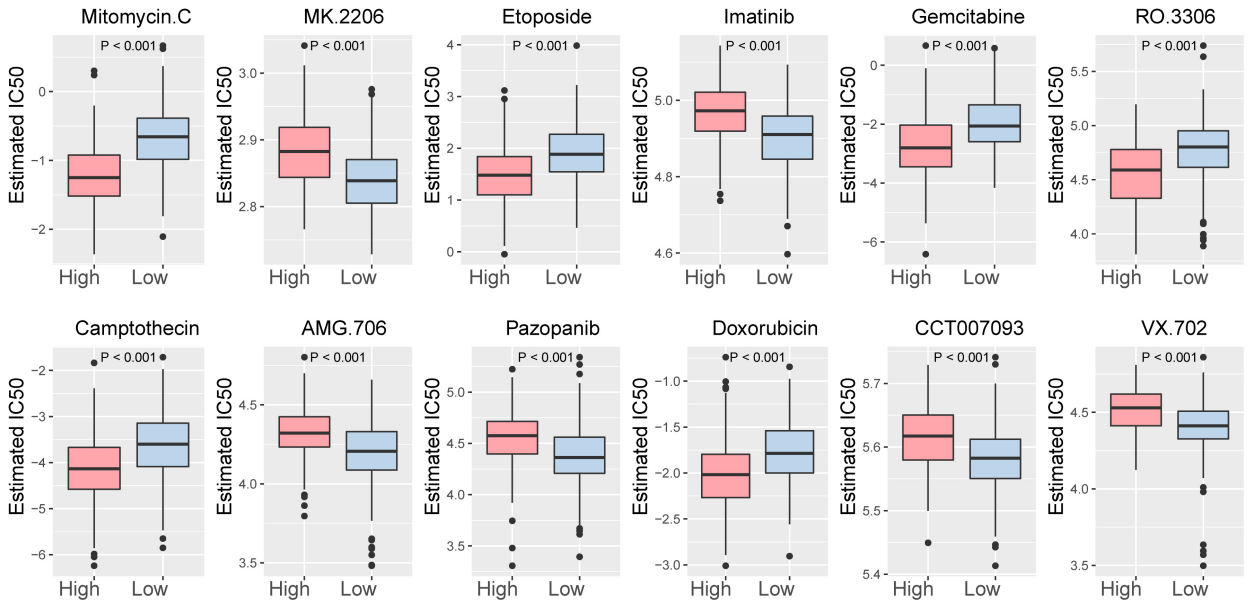

FIGURE 8 | The first 12 drugs with different responses between the high ICI score subgroup and low ICI score subgroup.

In addition, the relationship between the ICI score and the sensitivity of drug therapy was examined. We analyzed the effect of the ICI score on the sensitivity of bladder cancer cells to drug therapy in the TCGA-BLCA cohort based on Genomics of Drug Sensitivity in Cancer (GDSC)[7]. Among them, 92 drugs exhibited significantly different responses between the high and low ICI score groups (**Supplementary Figure 7**). The high ICI score group exhibited increased bladder cancer sensitivity to 50 drugs. According to the *p*-value, the first 12 drugs with different responses were plotted (**Figure 8**).

DISCUSSION

Immunotherapy has evolved in recent years and has been proven to treat a variety of cancers, including melanoma, non-small cell lung cancer, kidney cancer and prostate cancer (Del Paggio, 2018). It functions by blocking PD-L1 and PD-1. PD-1 is an inhibitory receptor expressed on the surface of activated T cells with two ligands, PD-L1 and PD-L2. PD-L1 is generally widely expressed on the surface of epithelial cells, endothelial cells, and tumor cells. PD-1/PD-L1 inhibitors have been successful in the treatment of melanoma and therefore are also being studied in urothelial carcinoma. A high level of PD-L1 expression was found in the TME of urothelial carcinoma, which increases the recognition of exogenous antigens by the host immune system (Inman et al., 2007; Chen and Mellman, 2013). A 2016 study reported that a PD-L1 monoclonal antibody, durvalumab (MEDI4736), exhibited some clinical efficacy in patients with bladder urothelial carcinoma receiving multiline therapy (Massard et al., 2016). However, studies have shown that immunotherapy is effective in only a small number of patients (Julie and Scott, 2012; Christofi et al., 2019). Therefore, new therapeutic markers are needed to identify the subgroup of patients who are suitable for immunotherapy. In this study, we identified three ICI subtypes based on ICI and then identified three gene clusters based on the DEGs between the ICI subtypes. In addition, we developed a method to quantify the tumor immune environment of individual tumors. Our results suggested that the ICI score is a valid prognostic predictor for evaluating immunotherapy response and provides a worthy reference for the immunotherapy of bladder cancer.

The TME that surrounds tumor cells is composed of tumor-infiltrating immune cells (TIICs), mesenchymal cells, endothelial cells, inflammatory mediators, and ECM molecules (Hanahan and Coussens, 2012). A large number of studies have shown that the TME has significant effects on tumor growth and development, therapeutic resistance and clinical outcome (Wu and Dai, 2017; Peltanova et al., 2019; Baghban et al., 2020). In this study, we identified three distinct ICI subtypes based on the ICI pattern of 584 bladder cancer samples. The characteristics of the TME and the proportions of 22 tumor immune infiltration cells were significantly different among the three ICI subtypes. This suggests the critical role of ICI in cancer progression. In detail, a previous study demonstrated that the functions of B cells are different in different types of cancer (Liu et al., 2018). B cells can be activated by tumor cells and then secrete immunoglobulin to inhibit tumor growth (Li et al., 2009). Some studies have shown that B cell infiltration promotes tumor invasion and metastasis in bladder cancer (Ou et al., 2015). In our study, there was no significant difference in the infiltration of naive B cells among the three ICI subtypes, while the infiltration level of memory B cells in ICI subtype C with the poorest prognosis was significantly higher than that in ICI subtypes A and B. This indicates that

[7]https://www.cancerrxgene.org/

B cell infiltration promotes tumor invasion and metastasis in bladder cancer, consistent with a previous study (Ou et al., 2015). Memory T cells, effector T cells and T cell differentiation play an important role in immune defense (Li et al., 2020). T cells can be classified into CD4+ and CD8+ T cells, and CD4+ T cells can further differentiate into regulatory T cells (Tregs) and follicular helper T cells (Tfhs). Tregs are responsible for maintaining the balance of immune responses and preventing excessive immune responses, and they are thought to be involved in the escape of tumors from the host's immune system in cancer (Whiteside, 2014). They have also been shown to have a positive prognostic effect on bladder cancer (Winerdal et al., 2018). Tfhs are thought to play a key role in coordinating humoral-related immune responses, and the abnormal regulatory behavior of Tfhs contributes to autoimmune diseases, primary immunodeficiency and acquired immunodeficiency (Jia et al., 2015). In addition, studies have shown that high expression of Tfh-related genes in colorectal cancer and breast cancer is associated with a good prognosis (Shi et al., 2018). In our study, ICI subtype A, with a better prognosis, exhibited higher immune infiltration of Treg and Tfh cells. These results imply that Tregs and Tfh cells play a positive role during the development of bladder cancer, which is consistent with previous studies (Shi et al., 2018; Winerdal et al., 2018). Macrophages, including M1 and M2 macrophages, are an important part of innate and adaptive immunity (Hao et al., 2012). Studies have shown that M1 macrophages have the opposite effect as M2 macrophages. M1 macrophages participate in a positive immune response and play the role of immune surveillance by secreting proinflammatory cytokines and chemokines and presenting antigens. M2 macrophages only have a weak antigen-presenting ability and play an important role in immune regulation by secreting inhibitory cytokines to downregulate the immune response (Chanmee et al., 2014). In this study, we found that infiltration of M1 macrophages was higher in ICI subtype A with a better prognosis, while the infiltration level of M2 macrophages was higher in ICI subtype C with a poorer prognosis, consistent with known findings.

Studies have shown that only a small number of patients respond to immunotherapy, which suggests that the immune phenotype cannot completely or accurately predict the response of patients to immunotherapy (Julie and Scott, 2012; Christofi et al., 2019). Therefore, we identified three gene clusters based on DEGs between three ICI subtypes. Gene cluster B, with the highest immune score, exhibited higher infiltration of plasma cells, CD8+ T cells and activated CD4+ T cells, and the expression levels of PD1 and PD-L1 were higher in this cluster, presenting an immune-hot phenotype. We speculate that patients in this cluster might benefit from immunotherapy. Gene cluster A had the lowest immune and stroma scores, and the infiltration level of immune-associated cells was decreased, which suggests an immune-cold phenotype. A good prognosis in this cluster may be related to the high immune infiltration of naive CD4+ T cells, which can rapidly differentiate into effector, regulatory, or memory T cells activated by antigen-presenting cells.

Considering the individual heterogeneity of the TME, it is necessary to quantify the ICI pattern of individual tumors (Runa et al., 2017). For that, we established the ICI score to evaluate the degree of individual patient immune infiltration in bladder cancer. Our analysis suggested that patients in the high ICI score group had a favorable prognosis and higher expression of checkpoint-related and immune activity-related genes. The GSEA results showed that ALLOGRAFT_REJECTION, INTERFERON_ALPHA_RESPONSE and INTERFERON_GAMMA_RESPONSE were significantly enriched in the high ICI score group, while ANGIOGENESIS, COAGULATION and EPITHELIAL_MESENCHYMAL_TRANSITION were enriched in the low ICI score group. ALLOGRAFT_REJECTION involves cytokine-cytokine receptor interactions and IL-12-mediated signal-related pathways, and upregulation of this gene set is associated with the activation of the acute immune response. Interferon is a cytokine that can trigger protective defenses of the immune system, activate immune cells, upregulate antigen presentation and prevent viral replication (Parkin and Cohen, 2001). A previous study demonstrated that an improvement in survival was observed when interferon was administered to patients with bladder cancer (Flávia et al., 2018). Conversely, tumor angiogenesis is a prerequisite for tumor growth and metastasis and is associated with reduced survival in bladder cancer (Kong et al., 2005; Agrawal et al., 2011). Increased expression of coagulation factors was observed in cancer patients, and coagulation factors may promote migration and invasion by transforming macrophages into tumor-associated macrophages in gastric cancer (Ma et al., 2011). Epithelial-mesenchymal transition (EMT) is a process in which epithelial cells with polarity are transformed into transitional mesenchymal cells and acquire the ability to invade and migrate, which exists in multiple physiological and pathological processes of the human body. EMT is closely related to the invasion and metastasis of tumor cells (Thiery, 2003).

In addition, studies have shown that increased TMB and somatic mutation rates are correlated with stronger antitumor immunity (Rooney et al., 2015). Therefore, it is necessary to explore the relationship between TMB and ICI score. Survival analysis demonstrated that the high TMB group had a better prognosis than the low TMB group. Our analysis also showed a significantly positive correlation between ICI score and TMB with a correlation coefficient of 0.157. These results were consistent with previous studies. Stratification analysis revealed that the ICI score was a potent biomarker of prognosis independent of TMB. In addition, studies have shown that FGFR3 mutations occur in 50% of primary bladder tumors and are associated with a favorable prognosis (van Rhijn et al., 2003; Oers et al., 2009; Saing et al., 2018). PIK3CA mutations were also associated with improved outcomes (Kim et al., 2015). Our results revealed that the mutation frequency of FGFR3 and PIK3CA in the high ICI score subgroup with better prognosis was significantly higher than that in the low ICI score subgroup. Finally, the prognostic value of the ICI score was validated in all BLCA cohorts.

In short, we analyzed the ICI pattern, providing a clear view of the antitumor immune or protumor immune response in bladder cancer. We found that the difference in ICI patterns was correlated with tumor heterogeneity and treatment

complexity. Thus, systematic evaluation of tumor ICI patterns in this study has crucial clinical implications. Moreover, our results provide new ideas for improving patient clinical response to immunotherapy and promoting individualized tumor immunotherapy in the future.

CONCLUSION

In this study, we identified three ICI subtypes based on ICI and then identified three gene clusters based on the DEGs among the ICI subtypes. In addition, we developed a method to quantify the tumor immune environment of individual tumors. Our results suggested that the ICI score is a valid prognostic biomarker and predictor for evaluating immunotherapy response, providing new ideas for improving patients' response to immunotherapy and promoting individualized tumor immunotherapy in the future.

DATA AVAILABILITY STATEMENT

Raw data for this study were generated at the TCGA database with the cancer type of BLCA. The datasets used and/or analyzed during the current study are available from the GEO database (GSE13507 and GSE93527) and the Array Express database (GSE31684 and E-MTAB-1803). Derived data supporting the findings are available from the corresponding author (FY) on reasonable request.

AUTHOR CONTRIBUTIONS

FY and XL designed and guided the work. MH and LL participated in data collecting, data processing, program implementation, and manuscript writing. JZ and TJ contributed to statistical analysis. YC, LX, and WC contributed to manuscript writing and article publishment. JM revised the manuscript critically. All authors provided critical advice for the final manuscript.

FUNDING

This work was supported by the National Key R&D Program of China (2019YFC1711000), National Natural Science Foundation of China (81973145), Key R&D Program of Jiangsu Province (Social Development) (BE2020694), and Active Components of Natural Medicines and Independent Research Projects of the State Key Laboratory in 2020 (SKLNMZZ202016).

ACKNOWLEDGMENTS

The results shown here are, on whole or part, based on data publicly available at the TCGA database, GEO database and the Array Express database. We thank patients and investigators who participated in these datasets for providing data.

SUPPLEMENTARY MATERIAL

The Supplementary Material for this article can be found online at: https://www.frontiersin.org/articles/10.3389/fcell.2021.723817/full#supplementary-material

REFERENCES

Agrawal, U., Mishra, A. K., Salgia, P., Verma, S., Mohanty, N. K., and Saxena, S. (2011). Role of tumor suppressor and angiogenesis markers in prediction of recurrence of non muscle invasive bladder cancer. *Pathol. Oncol. Res.* 17, 91–101. doi: 10.1007/s12253-010-9287-1

Alexandroff, A. B., Jackson, A. M., O'Donnell, M. A., and James, K. (1999). BCG immunotherapy of bladder cancer: 20 years on. *Lancet* 353, 1689–1694. doi: 10.1016/S0140-6736(98)07422-4

Ayers, M., Lunceford, J., Nebozhyn, M., Murphy, E., Loboda, A., Kaufman, D. R., et al. (2017). IFN-gamma-related mRNA profile predicts clinical response to PD-1 blockade. *J. Clin. Invest.* 127, 2930–2940. doi: 10.1172/JCI91190

Baghban, R., Roshangar, L., Jahanban-Esfahlan, R., Seidi, K., Ebrahimi-Kalan, A., Jaymand, M., et al. (2020). Tumor microenvironment complexity and therapeutic implications at a glance. *Cell Commun. Signal.* 18:59.

Barbie, D. A., Tamayo, P., Boehm, J. S., Kim, S. Y., Moody, S. E., Dunn, I. F., et al. (2009). Systematic RNA interference reveals that oncogenic KRAS-driven cancers require TBK1. *Nature* 462, 108–112. doi: 10.1038/nature08460

Chan, T. A., Yarchoan, M., Jaffee, E., Swanton, C., Quezada, S. A., Stenzinger, A., et al. (2019). Development of tumor mutation burden as an immunotherapy biomarker: utility for the oncology clinic. *Ann. Oncol.* 30, 44–56. doi: 10.1093/annonc/mdy495

Chanmee, T., Ontong, P., Konno, K., and Itano, N. (2014). Tumor-associated macrophages as major players in the tumor microenvironment. *Cancers (Basel)* 6, 1670–1690. doi: 10.3390/cancers6031670

Chen, D. S., and Mellman, I. (2013). Oncology meets immunology: the cancer-immunity cycle. *Immunity* 39, 1–10. doi: 10.1016/j.immuni.2013.07.012

Christofi, T., Baritaki, S., Falzone, L., Libra, M., and Zaravinos, A. (2019). Current perspectives in cancer immunotherapy. *Cancers (Basel)* 11:1472. doi: 10.3390/cancers11101472

Del Paggio, J. C. (2018). Immunotherapy: cancer immunotherapy and the value of cure. *Nat. Rev. Clin. Oncol.* 15, 268–270. doi: 10.1038/nrclinonc.2018.27

Flávia, C., Patrícia, C., Madeira, G. R., Karine, S., and José, O. (2018). Interferon-gamma at the crossroads of tumor immune surveillance or evasion. *Front. Immunol.* 9:847. doi: 10.3389/fimmu.2018.00847

Gubin, M. M., Artyomov, M. N., Mardis, E. R., and Schreiber, R. D. (2015). Tumor neoantigens: building a framework for personalized cancer immunotherapy. *J. Clin. Invest.* 125, 3413–3421. doi: 10.1172/JCI80008

Hanahan, D., and Coussens, L. M. (2012). Accessories to the crime: functions of cells recruited to the tumor microenvironment. *Cancer Cell* 21, 309–322. doi: 10.1016/j.ccr.2012.02.022

Hao, N. B., Lu, M. H., Fan, Y. H., Cao, Y. L., Zhang, Z. R., and Yang, S. M. (2012). Macrophages in tumor microenvironments and the progression of tumors. *Clin. Dev. Immunol.* 2012:948098. doi: 10.1155/2012/948098

Hazra, A., and Gogtay, N. (2016). Biostatistics series module 3: comparing groups: numerical variables. *Indian J. Dermatol.* 61, 251–260. doi: 10.4103/0019-5154.182416

Hinrichs, C. S., and Rosenberg, S. A. (2014). Exploiting the curative potential of adoptive T−cell therapy for cancer. *Immunol. Rev.* 257, 56–71. doi: 10.1111/imr.12132

Hodi, F. S., O'Day, S. J., Mcdermott, D. F., Weber, R. W., and Urba, W. J. (2010). Improved survival with ipilimumab in patients with metastatic melanoma. *N. Engl. J. Med.* 363, 711–723. doi: 10.1056/NEJMoa1003466

Hugo, W., Zaretsky, J. M., Sun, L., Song, C., Moreno, B. H., Hu-Lieskovan, S., et al. (2016). Genomic and transcriptomic features of response to anti-PD-1 therapy in metastatic melanoma. *Cell* 165, 35–44. doi: 10.1016/j.cell.2016.02.065

Inman, B. A., Sebo, T. J., Frigola, X., Dong, H., Bergstralh, E. J., Frank, I., et al. (2007). PD-L1 (B7-H1) expression by urothelial carcinoma of the bladder and BCG-induced granulomata. *Cancer* 109, 1499–1505. doi: 10.1002/cncr.22588

Jia, Y., Zeng, Z., Li, Y., Li, Z., Jin, L., Zhang, Z., et al. (2015). Impaired function of CD4+ T follicular helper (Tfh) cells associated with hepatocellular carcinoma progression. *PLoS One* 10:e0117458. doi: 10.1371/journal.pone.0117458

Julie, R. B., and Scott, S. T. L. Q. (2012). Safety, activity, and immune correlates of anti-PD-1 antibody in cancer. *N. Engl. J. Med.* 366, 2443–2454. doi: 10.1056/NEJMoa1200690

Kaufman, D. S., Shipley, W. U., and Feldman, A. S. (2009). Bladder cancer. *Lancet* 374, 239–249. doi: 10.1016/S0140-6736(09)60491-8

Kerkar, S. P., and Restifo, N. P. (2012). Cellular constituents of immune escape within the tumor microenvironment. *Cancer Res.* 72, 3125–3130. doi: 10.1158/0008-5472.CAN-11-4094

Kim, P. H., Cha, E. K., Sfakianos, J. P., Iyer, G., Zabor, E. C., Scott, S. N., et al. (2015). Genomic predictors of survival in patients with high-grade urothelial carcinoma of the bladder. *Eur. Urol.* 67, 198–201. doi: 10.1016/j.eururo.2014.06.050

Kong, C., Zhu, Y., Sun, C., Li, Z., Sun, Z., Zhang, X., et al. (2005). Inhibition of tumor angiogenesis during cisplatin chemotherapy for bladder cancer improves treatment outcome. *Urology* 65, 395–399. doi: 10.1016/j.urology.2004.09.041

Kursa, M. B., and Rudnicki, W. R. (2010). Feature selection with theborutapackage. *J. Stat. Softw.* 36:39234. doi: 10.18637/jss.v036.i11

Lennerz, V., Fatho, M., Gentilini, C., Frye, R. A., Lifke, A., Ferel, D., et al. (2005). The response of autologous T cells to a human melanoma is dominated by mutated neoantigens. *Proc. Natl. Acad. Sci. U.S.A.* 102, 16013–16018. doi: 10.1073/pnas.0500090102

Li, F., Guo, H., Wang, Y., Liu, B., and Zhou, H. (2020). Profiles of tumor-infiltrating immune cells and prognostic genes associated with the microenvironment of bladder cancer. *Int. Immunopharmacol.* 85:106641.

Li, Q., Teitz-Tennenbaum, S., Donald, E. J., Li, M., and Chang, A. E. (2009). In vivo sensitized and in vitro activated B cells mediate tumor regression in cancer adoptive immunotherapy. *J. Immunol.* 183, 3195–3203. doi: 10.4049/jimmunol.0803773

Liu, M., Sun, Q., Wang, J., Wei, F., Yang, L., and Ren, X. (2018). A new perspective: exploring future therapeutic strategies for cancer by understanding the dual role of B lymphocytes in tumor immunity. *Int. J. Cancer* 144, 2909–2917. doi: 10.1002/ijc.31850

Luo, H., Xu, X., Yang, J., Wang, K., Wang, C., Yang, P., et al. (2020). Genome-wide somatic copy number alteration analysis and database construction for cervical cancer. *Mol. Genet. Genomics* 295, 765–773. doi: 10.1007/s00438-019-01636-x

Ma, Y. Y., He, X. J., Wang, H. J., Xia, Y. J., Wang, S. L., Ye, Z. Y., et al. (2011). Interaction of coagulation factors and tumor-associated macrophages mediates migration and invasion of gastric cancer. *Cancer Sci.* 102, 336–342. doi: 10.1111/j.1349-7006.2010.01795.x

Mahesh, Y. (2014). Predicting immunogenic tumour mutations by combining mass spectrometry and exome sequencing. *Nature* 515, 572–576. doi: 10.1038/nature14001

Mariathasan, S., Turley, S. J., Nickles, D., Castiglioni, A., Yuen, K., Wang, Y., et al. (2018). TGFbeta attenuates tumour response to PD-L1 blockade by contributing to exclusion of T cells. *Nature* 554, 544–548. doi: 10.1038/nature25501

Massard, C., Gordon, M. S., Sharma, S., Rafii, S., and Segal, N. H. (2016). Safety and efficacy of durvalumab (MEDI4736), a PD-L1 antibody, in urothelial bladder cancer. *J. Clin. Oncol.* 34, 4502–4502. doi: 10.1200/JCO.2016.34.15_suppl.4502

Mayakonda, A., Lin, D. C., Assenov, Y., Plass, C., and Koeffler, H. P. (2018). Maftools: efficient and comprehensive analysis of somatic variants in cancer. *Genome Res.* 28, 1747–1756. doi: 10.1101/gr.239244.118

Mermel, C. H., Schumacher, S. E., Hill, B., and Meyerson, M. (2011). GISTIC2.0 facilitates sensitive and confident localization of the targets of focal somatic copy-number alteration in human cancers. *Genome Biol.* 12, R41–R41.

Newman, A. M., Liu, C. L., Green, M. R., Gentles, A. J., Feng, W., Xu, Y., et al. (2015). Robust enumeration of cell subsets from tissue expression profiles. *Nat. Methods* 12, 453–457. doi: 10.1038/nmeth.3337

Nielsen, M., Lundegaard, C., and Lund, O. (2007). Prediction of MHC class II binding affinity using SMM-align, a novel stabilization matrix alignment method. *BMC Bioinformatics* 8:238. doi: 10.1186/1471-2105-8-238

Oers, J., Zwarthoff, E. C., Rehman, I., Azzouzi, A. R., Cussenot, O., Meuth, M., et al. (2009). FGFR3 mutations indicate better survival in invasive upper urinary tract and bladder tumours. *Eur. Urol.* 55, 650–658. doi: 10.1016/j.eururo.2008.06.013

Ou, Z., Wang, Y., Liu, L., Li, L., and Chang, C. (2015). Tumor microenvironment B cells increase bladder cancer metastasis via modulation of the IL-8/androgen receptor (AR)/MMPs signals. *Oncotarget* 6, 26065–26078. doi: 10.18632/oncotarget.4569

Pardoll, D. M. (2012). The blockade of immune checkpoints in cancer immunotherapy. *Nat. Rev. Cancer* 12, 252–264. doi: 10.1038/nrc3239

Parkin, J., and Cohen, B. (2001). An overview of the immune system. *Lancet* 357, 1777–1789. doi: 10.1016/S0140-6736(00)04904-7

Peltanova, B., Raudenska, M., and Masarik, M. (2019). Effect of tumor microenvironment on pathogenesis of the head and neck squamous cell carcinoma: a systematic review. *Mol. Cancer* 18:63. doi: 10.1186/s12943-019-0983-5

Pottier, C., Wheatherspoon, A., Roncarati, P., Longuespee, R., Herfs, M., Duray, A., et al. (2015). The importance of the tumor microenvironment in the therapeutic management of cancer. *Expert Rev. Anticancer Ther.* 15, 943–954. doi: 10.1586/14737140.2015.1059279

Ritchie, M. E., Phipson, B., Wu, D., Hu, Y., Law, C. W., Shi, W., et al. (2015). limma powers differential expression analyses for RNA-sequencing and microarray studies. *Nucleic Acids Res.* 43:e47. doi: 10.1093/nar/gkv007

Rooney, M. S., Shukla, S. A., Wu, C. J., Getz, G., and Hacohen, N. (2015). Molecular and genetic properties of tumors associated with local immune cytolytic activity. *Cell* 160, 48–61. doi: 10.1016/j.cell.2014.12.033

Runa, F., Hamalian, S., Meade, K., Shisgal, P., Gray, P. C., and Kelber, J. A. (2017). Tumor microenvironment heterogeneity: challenges and opportunities. *Curr. Mol. Biol. Rep.* 3, 218–229. doi: 10.1007/s40610-017-0073-7

Saing, K. Y., Kyung, K., Ghee-Young, K., Jin, L. S., and Hoon, P. S. (2018). Fibroblast growth factor receptor 3 (FGFR3) aberrations in muscle-invasive urothelial carcinoma. *BMC Urol.* 18:68. doi: 10.1186/s12894-018-0380-1

Sanli, O., Dobruch, J., Knowles, M. A., Burger, M., Alemozaffar, M., Nielsen, M. E., et al. (2017). Bladder cancer. *Nat. Rev. Dis. Primers* 3:17022. doi: 10.1038/nrdp.2017.22

Schadendorf, D., Hodi, F. S., Robert, C., Weber, J. S., Margolin, K., Hamid, O., et al. (2015). Pooled analysis of long-term survival data from phase II and phase III trials of ipilimumab in unresectable or metastatic melanoma. *J. Clin. Oncol.* 33, 1889–1894. doi: 10.1200/JCO.2014.56.2736

Sharma, P., Wagner, K., Wolchok, J. D., and Allison, J. P. (2011). Novel cancer immunotherapy agents with survival benefit: recent successes and next steps. *Nat. Rev. Cancer* 11, 805–812. doi: 10.1038/nrc3153

Shi, W., Dong, L., Sun, Q., Ding, H., Meng, J., and Dai, G. (2018). Follicular helper T cells promote the effector functions of CD8(+) T cells via the provision of IL-21, which is downregulated due to PD-1/PD-L1-mediated suppression in colorectal cancer. *Exp. Cell Res.* 372, 35–42. doi: 10.1016/j.yexcr.2018.09.006

Sotiriou, C., Wirapati, P., Loi, S., Harris, A., Fox, S., Smeds, J., et al. (2006). Gene expression profiling in breast cancer: understanding the molecular basis of histologic grade to improve prognosis. *J. Natl. Cancer Inst.* 98, 262–272. doi: 10.1093/jnci/djj052

Thiery, J. P. (2003). Epithelial-mesenchymal transitions in development and pathologies. *Curr. Opin. Cell Biol.* 139, 871–890. doi: 10.1016/j.ceb.2003.10.006

van Rhijn, B. W., Vis, A. N., van der Kwast, T. H., Kirkels, W. J., Radvanyi, F., and Ooms, E. C. (2003). Molecular grading of urothelial cell carcinoma with fibroblast growth factor receptor 3 and MIB-1 is superior to pathologic grade for the prediction of clinical outcome. *J. Clin. Oncol.* 21, 1912–1921. doi: 10.1200/JCO.2003.05.073

Whiteside, T. L. (2008). The tumor microenvironment and its role in promoting tumor growth. *Oncogene* 27, 5904–5912. doi: 10.1038/onc.2008.271

Whiteside, T. L. (2014). Regulatory T cell subsets in human cancer: are they regulating for or against tumor progression? *Cancer Immunol. Immunother.* 63, 67–72. doi: 10.1007/s00262-013-1490-y

Wilkerson, M. D., and Hayes, D. N. (2010). ConsensusClusterPlus: a class discovery tool with confidence assessments and item tracking. *Bioinformatics* 26, 1572–1573. doi: 10.1093/bioinformatics/btq170

Winerdal, M. E., Krantz, D., Hartana, C. A., Zirakzadeh, A. A., Linton, L., Bergman, E. A., et al. (2018). Urinary bladder cancer tregs suppress MMP2 and potentially regulate invasiveness. *Cancer Immunol. Res.* 6, 528–538. doi: 10.1158/2326-6066.CIR-17-0466

Wu, T., and Dai, Y. (2017). Tumor microenvironment and therapeutic response. *Cancer Lett.* 387, 61–68. doi: 10.1016/j.canlet.2016.01.043

Yang, J., Chen, Y., Luo, H., and Cai, H. (2020). The landscape of somatic copy number alterations in head and neck squamous cell carcinoma. *Front. Oncol.* 10:321. doi: 10.3389/fonc.2020.00321

Yi, R., Lin, A., Cao, M., Xu, A., Luo, P., and Zhang, J. (2020). ATM mutations benefit bladder cancer patients treated with immune checkpoint inhibitors by acting on the tumor immune microenvironment. *Front. Genet.* 11:933. doi: 10.3389/fgene.2020.00933

Yoshihara, K., Shahmoradgoli, M., Martinez, E., Vegesna, R., Kim, H., Torres-Garcia, W., et al. (2013). Inferring tumour purity and stromal and immune cell admixture from expression data. *Nat. Commun.* 4:2612. doi: 10.1038/ncomms3612

Zeng, D., Li, M., Zhou, R., Zhang, J., Sun, H., Shi, M., et al. (2019). Tumor microenvironment characterization in gastric cancer identifies prognostic and immunotherapeutically relevant gene signatures. *Cancer Immunol. Res.* 7, 737–750. doi: 10.1158/2326-6066.CIR-18-0436

Zhang, X., Chen, T., and Zhang, B. (2020). Characterization of the immune cell infiltration landscape in head and neck squamous cell carcinoma to aid immunotherapy. *Mol. Ther. Nucleic Acids* 22, 298–309. doi: 10.1016/j.omtn.2020.08.030

Zhou, J., Dudley, M. E., Rosenberg, S. A., and Robbins, P. F. (2005). Persistence of multiple tumor-specific T-cell clones is associated with complete tumor regression in a melanoma patient receiving adoptive cell transfer therapy. *J. Immunother.* 28, 53–62. doi: 10.1097/00002371-200501000-00007

Conflict of Interest: The authors declare that the research was conducted in the absence of any commercial or financial relationships that could be construed as a potential conflict of interest.

Publisher's Note: All claims expressed in this article are solely those of the authors and do not necessarily represent those of their affiliated organizations, or those of the publisher, the editors and the reviewers. Any product that may be evaluated in this article, or claim that may be made by its manufacturer, is not guaranteed or endorsed by the publisher.

frontiers in Cell and Developmental Biology

ORIGINAL RESEARCH
published: 16 September 2021
doi: 10.3389/fcell.2021.720349

BRCC3 Promotes Tumorigenesis of Bladder Cancer by Activating the NF-κB Signaling Pathway Through Targeting TRAF2

Huangheng Tao[1,2,3†], Yixiang Liao[4,5†], Youji Yan[4,5†], Zhiwen He[1,2†], Jiajie Zhou[4,5], Xinghuan Wang[1,2‡], Jianping Peng[1,2*‡], Shangze Li[6,7*‡] and Tao Liu[1,2*‡]*

[1] Department of Urology, Zhongnan Hospital of Wuhan University, Wuhan, China, [2] Medical Science Research Center, Zhongnan Hospital of Wuhan University, Wuhan, China, [3] State Key Laboratory Breeding Base of Basic Science of Stomatology (Hubei-MOST) and Key Laboratory for Oral Biomedicine of Ministry of Education (KLOBM), School and Hospital of Stomatology, Wuhan University, Wuhan, China, [4] Jingzhou Hospital, Yangtze University, Jingzhou, China, [5] The Second Clinical Medical College, Yangtze University, Jingzhou, China, [6] Hubei Key Laboratory of Cell Homeostasis, College of Life Sciences, Wuhan University, Wuhan, China, [7] School of Medicine, Chongqing University, Chongqing, China

NF-κB signaling is very important in cancers. However, the role of BRCC3-associated NF-κB signaling activation in bladder cancer remains to be characterized. Western blotting and IHC of tissue microarray were used to confirm the abnormal expression of BRCC3 in bladder cancer. Growth curve, colony formation, soft agar assay and Xenograft model were performed to identify the role of BRCC3 over-expression or knock-out in bladder cancer. Further, RNA-Seq and luciferase reporter assays were used to identify the down-stream signaling pathway. Finally, co-immunoprecipitation and fluorescence confocal assay were performed to verify the precise target of BRCC3. Here, we found that high expression of BRCC3 promoted tumorigenesis through targeting the TRAF2 protein. BRCC3 expression is up-regulated in bladder cancer patients which indicates a negative prognosis. By *in vitro* and *in vivo* assays, we found genetic BRCC3 ablation markedly blocks proliferation, viability and migration of bladder cancer cells. Mechanistically, RNA-Seq analysis shows that NF-κB signaling is down-regulated in BRCC3-deficient cells. BRCC3 binds to and synergizes with TRAF2 to activate NF-κB signaling. Our results indicate that high BRCC3 expression activates NF-κB signaling by targeting TRAF2 for activation, which in turn facilitates tumorigenesis in bladder cancer. This finding points to BRCC3 as a potential target in bladder cancer patients.

Keywords: BRCC3, TRAF2, NF-kB, tumorigenesis, bladder cancer

Abbreviations: BCa, Bladder cancer; CHX, cycloheximide; DMEM, Dulbecco's modified Eagle's medium; DSBs, DNA double-strand breaks; ECIS, Electric Cell-substrate Impedance Sensing; EMT, epithelial-mesenchymal transition; FBS, fetal bovine serum; IHC, Immunohistochemical. K63-Ub, lysine 63-linked ubiquitin polymers; NF-κB, Nuclear factor kappa-B; PBS, phosphate-buffered saline; qRT-PCR, quantitative real-time PCR; RT, Reverse transcription; SDS-PAGE, sodium dodecyl sulfate-polyacrylamide gel electrophoresis; sgRNAs, small guide RNAs.

OPEN ACCESS

Edited by:
Fang-Ming Deng,
New York University, United States

Reviewed by:
Youliang Wang,
Beijing Institute of Technology, China
Di Cui,
Shanghai General Hospital, China
Mou Peng,
Central South University, China
Zitaiyu Li,
The Fifth Affiliated Hospital of Sun Yat-sen University, China

***Correspondence:**
Xinghuan Wang
wangxinghuan@whu.edu.cn
Jianping Peng
pengjianping@whu.eud.cn
Shangze Li
shangze.li@whu.edu.cn
Tao Liu
liutaozaiwuda@whu.edu.cn

†These authors have contributed equally to this work and share first authorship

‡These authors have contributed equally to this work and share senior authorship

Specialty section:
This article was submitted to Molecular and Cellular Pathology, a section of the journal Frontiers in Cell and Developmental Biology

Received: *04 June 2021*
Accepted: *24 August 2021*
Published: *16 September 2021*

Citation:
Tao H, Liao Y, Yan Y, He Z, Zhou J, Wang X, Peng J, Li S and Liu T (2021) BRCC3 Promotes Tumorigenesis of Bladder Cancer by Activating the NF-κB Signaling Pathway Through Targeting TRAF2. Front. Cell Dev. Biol. 9:720349. doi: 10.3389/fcell.2021.720349

INTRODUCTION

Bladder cancer (BCa) is one of the most common tumors in the urinary system. There are approximately 78,100 new cases and 32,100 bladder cancer-related deaths in China annually (Cumberbatch et al., 2018). The bladder cancer related incidence and mortality rates in China have been rising rapidly. At present, diagnosing bladder cancer mainly depends on urine exfoliative cytology, cystoscopy and live examination, of which the former has very low sensitivity and the latter is an intrusive operation increasing the suffering of the patients (Roos et al., 2008; He et al., 2018; Choudhury and Hoskin, 2019). The main method of clinical treatment for bladder cancer is surgical treatment. Once the opportunity for surgical intervention is lost or the disease recurs, treatment can rely on only traditional radiotherapy and chemotherapy, and there is no molecular targeted drug suitable for bladder cancer in the clinic. The main reason for this clinical approach is the lack of accurate and reliable molecular therapeutic markers for bladder cancer. Although triple therapy with surgery/radiotherapy/chemotherapy has recently been explored to treat advanced bladder cancer, the efficacy is still not good enough (Dudley et al., 2018; Efstathiou et al., 2019). Therefore, to explore the mechanism of bladder cancer progression, and identify specific diagnostic molecules and potential therapeutic targets for bladder cancer are quite urgently needed.

The NF-κB signaling pathway plays important roles in various kinds of chronic diseases, including cancer, inflammation and so on (Kunnumakkara et al., 2018). The aberrant activation of NF-κB signaling pathway has been noted in various human cancers (Rayet and Gelinas, 1999; Al-Halabi et al., 2011). Hence, targeting the NF-κB pathways have high potential for preventing cancers. However, most drugs targeting the NF-κB pathway have adverse side effects. Therefore, it is urgent to find a novel protein targeting NF-κB pathways that plays a crucial role in bladder cancer (Kunnumakkara et al., 2018).

BRCC3 is a member of deubiquitinase family, which can specifically cleave lysine 63-linked ubiquitin polymers (K63-Ub). The zinc-dependent JAB1/MPN/MOV4 metalloprotease domain is critical for the deubiquitylation activity of BRCC3 (Huang et al., 2015). In the DNA damage response, BRCC3 specifically cuts K63-Ub from histones H2A and H2AX. DNA double-strand breaks (DSBs) can result in genotoxic stress and promote tumorigenesis (Sun et al., 2016). Consistent with this conclusion, aberrant expression of BRCC3 has been associated with decreased sensitivity to ionizing radiation breast carcinomas and defects in the G2/M checkpoint in nasopharyngeal carcinomas (Dong et al., 2003; Tu et al., 2015). In cervical cancer, knocking down BRCC3 expression inhibits cell viability, invasion and migration via inhibition of epithelial-mesenchymal transition (EMT) progression and the expression levels of Snail family (Zhang and Zhou, 2018). Apart from its role in the DSB-associated carcinogenesis, BRCC3 regulates the type I interferon signaling pathway during antiviral responses and inflammasome activity by deubiquitinating NLRP3 (Py et al., 2013; Hu et al., 2019). Although BRCC3 has emerged as an oncogene in various tumors, the role of BRCC3 in bladder cancer is still obscure.

In this study, we reported BRCC3 as a novel oncogene in bladder cancer. We identified BRCC3 bound to TRAF2 to activate NF-κB signaling. Meanwhile, we found BRCC3 was aberrantly expressed in BCa patients with an unfavorable prognosis. BRCC3 over-expression promoted tumorigenesis and was not associated with the enzymatic activity of BRCC3. In contrast, knocking out of BRCC3 attenuated the tumorigenesis *in vitro* and *in vivo*. Our findings suggested BRCC3 as a potential target in BCa patients.

MATERIALS AND METHODS

Cell Culture

Immortalized human bladder epithelial SV-HUC1 cell; human bladder cancer cells lines including the EJ, T24, 5637, UMUC3, SW780, RT4, and J82 cell lines; and HEK293T cell line were purchased from the Stem Cell Bank, CASS, China. SV-HUC1, EJ, T24, and 5637 cells were cultured in RPMI 1640 medium containing 10% fetal bovine serum (FBS; Gibco, China), 100 U/ml penicillin-G sodium and 100 mg/ml streptomycin sulfate at 37°C under an atmosphere of 95% air and 5% CO2. UMUC3, SW780, RT4, J82, and HEK293T cells were cultured in Dulbecco's modified Eagle's medium (DMEM) (Gibco) supplemented with 10% FBS, 100 U/ml penicillin-G sodium and 100 mg/ml streptomycin sulfate at 37°C in 5% CO_2.

Reagents and Antibodies

Proteasome inhibitor MG132 (Sigma, United States); the protein translation inhibitor cycloheximide (CHX, Sigma); and low melting point agarose (Solarbio Life Sciences, Spain) were purchased. The cDNA Reverse Transcription Kit was purchased from Thermo Fisher Scientific (Thermo Fisher Scientific, United States). Antibodies against BRCC3 (1:1,000, Cat. #18215), TNFα (1:100, Cat. #8184), and Ki67 (1:200, Cat. #9449) were purchased from Cell Signaling Technologies (Danvers, MA, United States). An anti-β-actin antibody (1:1,000, Cat. #AC026) was purchased from ABclonal (ABclonal, United States). Antibodies against FLAG (1:1,000, Cat. #M185-3L) and HA (1:1,000, Cat. # M180-3) were purchased from MBL (MBL Beijing Biotech Co., Ltd.). An anti-TRAF2 antibody (1:1,000, Cat. #ab126758) was obtained from Abcam (Abcam, United Kingdom).

Plasmids and sgRNA

A plasmid expressing wild type BRCC3 and the deubiquitinating enzyme-null mutant BRCC3 (which was built by a site-directed mutation of H122Q) was generated using PCR and cloned into pHAGE/puro/3 × Flag. Plasmids expressing HA-TRAF2, HA-TNFR, HA-TAK1, HA-TAB1, HA-IKKβ, or HA-P65 were generated with pCDNA5/FRT/TO-3 × HA, respectively. pRL-TK and pGL3-NF-κB-luc were purchased from Addgene (Cambridge, MA, United States). For CRISPR-Cas9 gene editing, small guide RNAs (sgRNAs) of BRCC3 were cloned into lenti-v2 (Addgene, Cat. #92062). The sgRNA sequences:

sgRNA-F, 5′-caccGAAGTAATGGGGCTGTGCAT-3′; sgRNA-R, 5′-aaacATGCACAGCCCCATTACTTC-3′.

Genetic Knock-Out of BRCC3 in Human Bladder T24 Cells

The genetic knockout of BRCC3 in T24 cells was performed using a CRISPR-Cas9 system. Briefly, we designed BRCC3-sepcific sgRNAs[1] which was cloned into lenti-v2. HEK293T cells were transfected with two packaging vectors and the recombinant lenti-v2 vector containing the BRCC3-sepcific sgRNA sequences. After 48 h, the supernatant containing the lentivirus was harvested. 1×10^5 T24 cells were incubated with the lentivirus for 48 h and then exposed to 600 ng/ml puromycin for another 5 days. Next, the cells were put in five 96-well plates by limiting dilution method. After 14 days of growth, the single clones were screened using immunoblotting analysis with an anti-BRCC3 antibody, and the positive clones were amplified.

[1]http://www.e-crisp.org/E-CRISP/

Transient Transfections and Lentivirus-Mediated Stable Overexpression

To produce lentivirus, 293T cells were incubated with MAX transfection reagent, corresponding expression plasmids together with the packaging vectors pMD2.G (Addgene, Cat. #12259) and psPAX2 (Addgene, Cat. #12260). The transfection complex was mixed in DMEM (Gibco) without FBS, and finally dripped to cells. And the medium which contains virus was gain 72 h later. For stable transfection with pHAGE-3 × FLAG-BRCC3, 600 ng/ml puromycin was used for 5 days to kill the non-transfected cells. The efficiencies of transfection were determined by western blot.

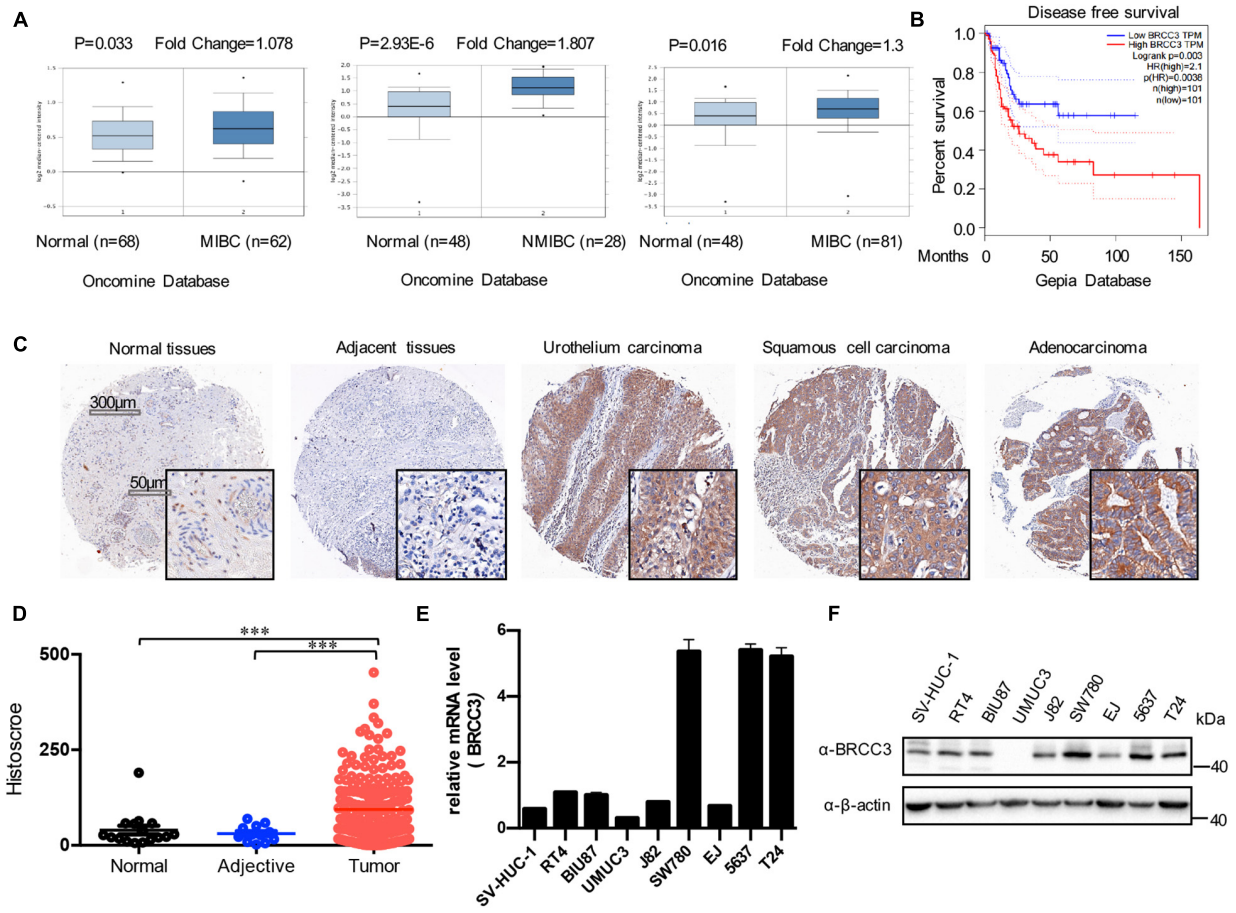

FIGURE 1 | Expression of BRCC3 in bladder cancer. **(A)** Data form Oncomine database. Three microarray datasets exhibited obvious upregulation of BRCC3 expression in muscle-invading bladder cancer tissue compared to normal. **(B)** Disease-free survival time analysis of data from the GEPIA database. The *p*-value is indicated. **(C)** Immunohistochemical staining for BRCC3 in tissue microarrays containing cancer tissue samples, adjacent tissue samples and normal bladder tissue samples from patients with chronic cystitis or a healthy urinary tract. Representative staining images for different pathological types of bladder cancer including uro-endothelial carcinoma, squamous cell carcinomas and adenocarcinoma are shown. **(D)** Tissue microarray data analysis of BRCC3 expression in 188 bladder cancer tissue samples, 12 corresponding adjacent tissue samples and 16 normal bladder tissue samples (including 8 chronic cystitis tissue samples and 8 healthy bladder tissue samples collected at autopsy). **(E)** The mRNA expression levels of BRCC3 in SV-HUC-1 and 8 bladder cancer cell lines. **(F)** The protein expression levels of BRCC3 in SV-HUC-1 and 8 bladder cancer cell lines. $^*P < 0.05$, $^{**}P < 0.001$, and $^{***}P < 0.001$ compared with controls.

Cell Proliferation Assays

We used Electric Cell-substrate Impedance Sensing (ECIS) method to perform cell proliferation assays. An ECIS system was obtained from Applied BioPhysics, Inc. The ECIS culture-ware used was 96W10idf. Briefly, the protocol was as follows: The cell suspension was prepared first, and then counted. The cell suspension was diluted to 4×10^3 cells in 200 μl, and added to a 96-well electrode plate. Then, the signal from the cells in the electrode plate was conventionally monitored for 48–72 h. The data were analyzed by the specific software matched to the ECIS system. The experiments were performed in triplicate.

Colony Formation and Soft Agar Assay

For the colony formation assay, UMUC3 cells (4×10^2 cells) or T24 cells(1×10^3 cells)were cultured in a 6-well plate. Eight days later, the cell colonies were fixed and stained with 0.3% crystal violet in ethanol, counted and photographed. For the soft agar assay, low melting point agarose and 2 ml of 0.7% lower agar-RPMI 1640 medium were plated into 6-well plates. Then, UMUC3 cells (3×10^4) or T24 cells (5×10^4 cells) was mixed with agar-RPMI 1640 medium, which were cultured for more than 14 days. Finally, the numbers of cell clones were counted and recorded (the cell colony including more than 10 cells was counted as one colony).

Luciferase Reporter Assays

For luciferase assays, a dual-luciferase kit [Promega, Cat. #E1980, Promega (Beijing) Biotech Co., Ltd.] was used. 48 h after cells were transfected with pGL3-NF-κB-luc (containing a repetitive NF-κB sequence), pRL-TK and the indicated levels of the expression constructs, the reporter assays were performed according to the standard protocol.

Real-Time PCR

Total RNA was isolated using TRIzol Reagent (Invitrogen). The RevertAid Fist Strand cDNA Synthesis Kit (Thermo Fisher Scientific) was used for the RT analysis, and 2 μg of RNA was reverse transcribed into cDNA. Real-time quantitative PCR was performed by adding 2 μl of RT reaction mixture to a final volume of 20 μl and analyzing the reaction mixture with an ABI PRISM 7500 system (Applied Biosystems, Forster City, Calif) by using the FastStart Universal SYBR Green Master protocol (ROCHE, 04913850001). Primer sequences and annealing temperatures are summarized in **Supplementary Table 1**. Values were normalized to GAPDH amplification.

Immunoblotting Analysis

Cells were washed by ice-cold phosphate-buffered saline (PBS) for three times and lysed in 1% Triton lysis buffer on ice. A BCA kit (Thermo Fisher Scientific) was then used to test the protein concentrations. 50 μg total protein (was separated by 10–15% SDS-PAGE electrophoresis (Promoton Biotechnology, shanghai, China) and transferred onto PVDF membranes (Millipore, cat# IPVH00010). After electrophoresis, PVDF membranes with protein on it were incubated with TBST (containing 5% non-fat dry milk) for 60 min at room temperature, and then incubated with specific primary antibodies overnight at 4°C followed by incubation with HRP-conjugated secondary antibodies at 37°C for 2 h at room temperature. The membranes were developed with the WesternBright ECL HRP substrate (Advansta).

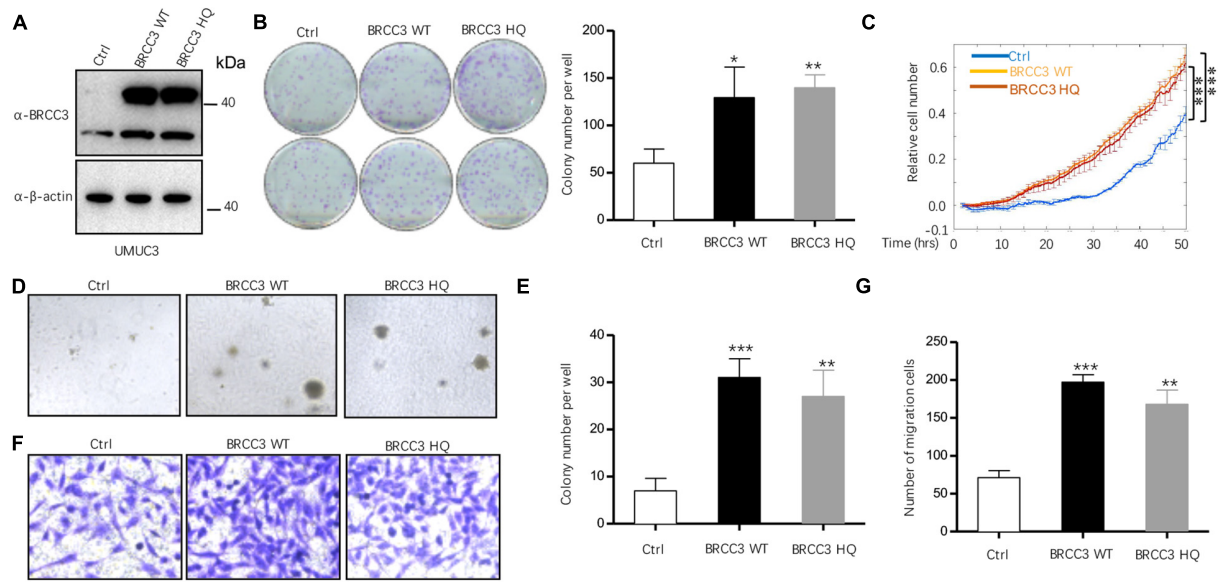

FIGURE 2 | The overexpression of BRCC3 increased tumor cell proliferation *in vitro*. **(A)** BRCC3-overexpressing cells were identified via immunoblotting. **(B)** Colony formation assays. The number of clones was counted and plotted. **(C)** An ECIS cell proliferation assay was performed. **(D)** Three-dimensional colony formation assay was performed in soft agar. The colony numbers are expressed as the means ± standard error of triplicate assays. **(E)** The Quantitative data show the colonies numbers in **(D)**. **(F)** Transwell migration assay. The relative cell numbers of migrating were statistically analyzed. **(G)** Quantitative data show the number of migrating cells in **(F)**. $^*P < 0.05$, $^{**}P < 0.001$, and $^{***}P < 0.001$ compared with controls.

Co-immunoprecipitation

NP-40 lysis buffer was used to lysed cells in immunoprecipitation assays. The indicated antibody and protein G-agarose beads (Roche) were added into the cell lysates at 4°C overnight. Then, the beads were washed three times with 500 μl of wash buffer containing 300 mM NaCl at 4°C. The precipitates were analyzed by standard western blot.

Fluorescence Confocal Assays

T24 cells were seeded in 12-mm cover-slips, and washed with PBS. After that, cells were fixed with 4% PFA for 15 min. The cells were then treated with a 0.1% Triton X-100 solution and blocked in normal goat serum for 30 min at room temperature. The fixed cells were incubated with the indicated antibodies at the proper dilution for 2 h at room temperature, washed three times with PBS, and incubated with secondary antibodies for 1 h. Nuclei were visualized by incubating with DAPI (2 μg/ml) for 10 min at room temperature, and slides were analyzed using a confocal microscope system (Nikon $C2^+$ Confocal Microscope, Japan).

Xenograft Assays

Male BALB/c-null mice (4-weeks old) were purchased from Beijing Vital River Laboratory Animal Technology Co., Ltd. (Beijing, China), and maintained in the laboratory animal facility of Zhongnan Hospital of Wuhan University. One week later for adaptive feeding, mice were subcutaneous injected with 4×10^6 wide-type T24 cells or $BRCC3^{-/-}$ T24 cells ($n = 6$). Five weeks later, the mice were sacrificed under effectively anesthetic by 2% pentobarbital sodium (30 mg/kg) and the tumors were removed and weighed. In addition, tumor volume was measured every 3 days.

Immunohistochemical (IHC) Analysis

Two tissue microarrays (Alenabio, cat. #BL2081c, and cat. #T124a, Alenabio Co., Ltd) including 188 bladder cancer tissue specimens, 12 corresponding adjacent tissues specimens and 16 normal bladder tissue specimens were used. Briefly, the paraffin-embedded sections were first deparaffinized. And then citrate buffer (pH 6.0) was used for antigen retrieval, and 0.3% H_2O_2 was used to block the endogenous peroxidase activity. The indicated primary antibody and secondary antibody were added to the sections. Nuclei were labeled with DAB. The histoscore value of BRCC3 in the paraffin-embedded sections was analyzed by fluorescence microscopy.

Statistical Analysis

SPSS version 13.0 (University of Nevada, Las Vegas, NV, United States) was used for the statistical analyses. All data are presented as the means ± standard error. Statistical analysis was performed using Student's *t*-test or one-way ANOVA, with $P < 0.05$ considered statistically significant.

RESULTS

BRCC3 Was Upregulated in Bladder Cancer

To analyze the level of BRCC3 in bladder cancer, we first searched the Oncomine and GEPIA databases. The mRNA

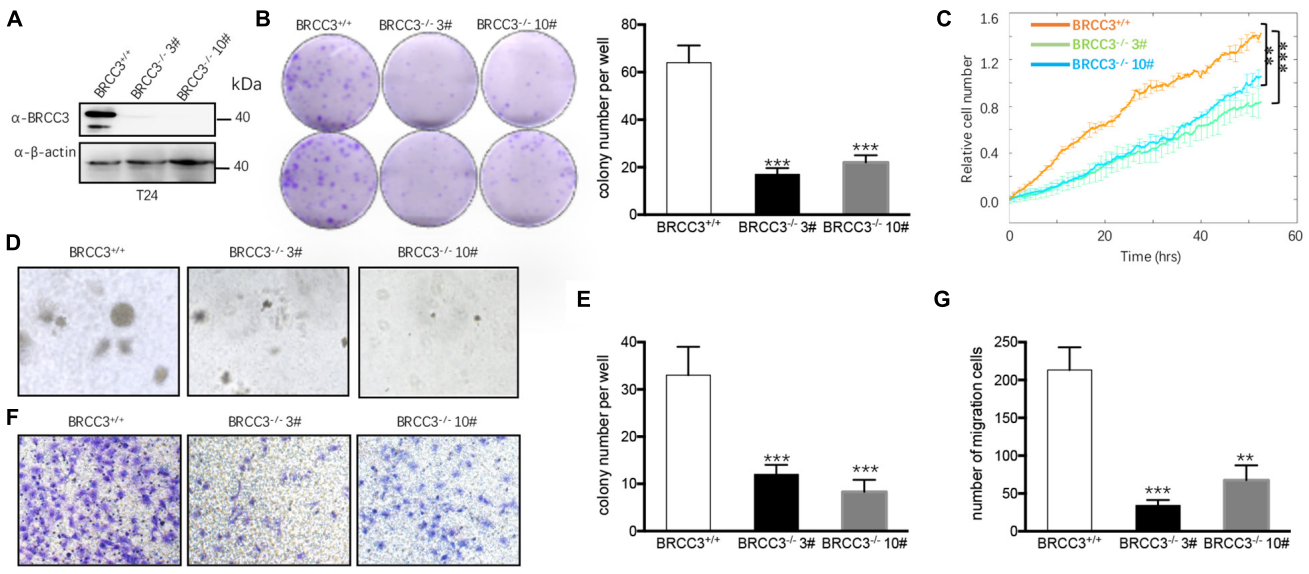

FIGURE 3 | The depletion of BRCC3 repressed tumor formation *in vitro*. **(A)** BRCC3-deficient cells were identified via Western blotting assays. **(B)** Colony formation assays. **(C)** An ECIS cell proliferation assay was performed. **(D)** Three-dimensional colony formation assay was performed in soft agar. The colony numbers are expressed as the means ± standard error of triplicate assays. **(E)** The Quantitative data show the colonies numbers in **(D)**. **(F)** Transwell migration assay. The relative cell numbers of migrating were statistically analyzed. **(G)** Quantitative data show the number of migrating cells in **(F)**. *$P < 0.05$, **$P < 0.001$, and ***$P < 0.001$ compared with controls.

levels of BRCC3 in bladder cancer tissue specimens were obviously upregulated, compared with those in normal bladder tissue samples (**Figure 1A**). And upregulated BRCC3 expression was negatively related to the diseases-free survival in patients with bladder cancer (**Figure 1B**). To confirm the results above, we performed an IHC analysis of BRCC3 using tissue

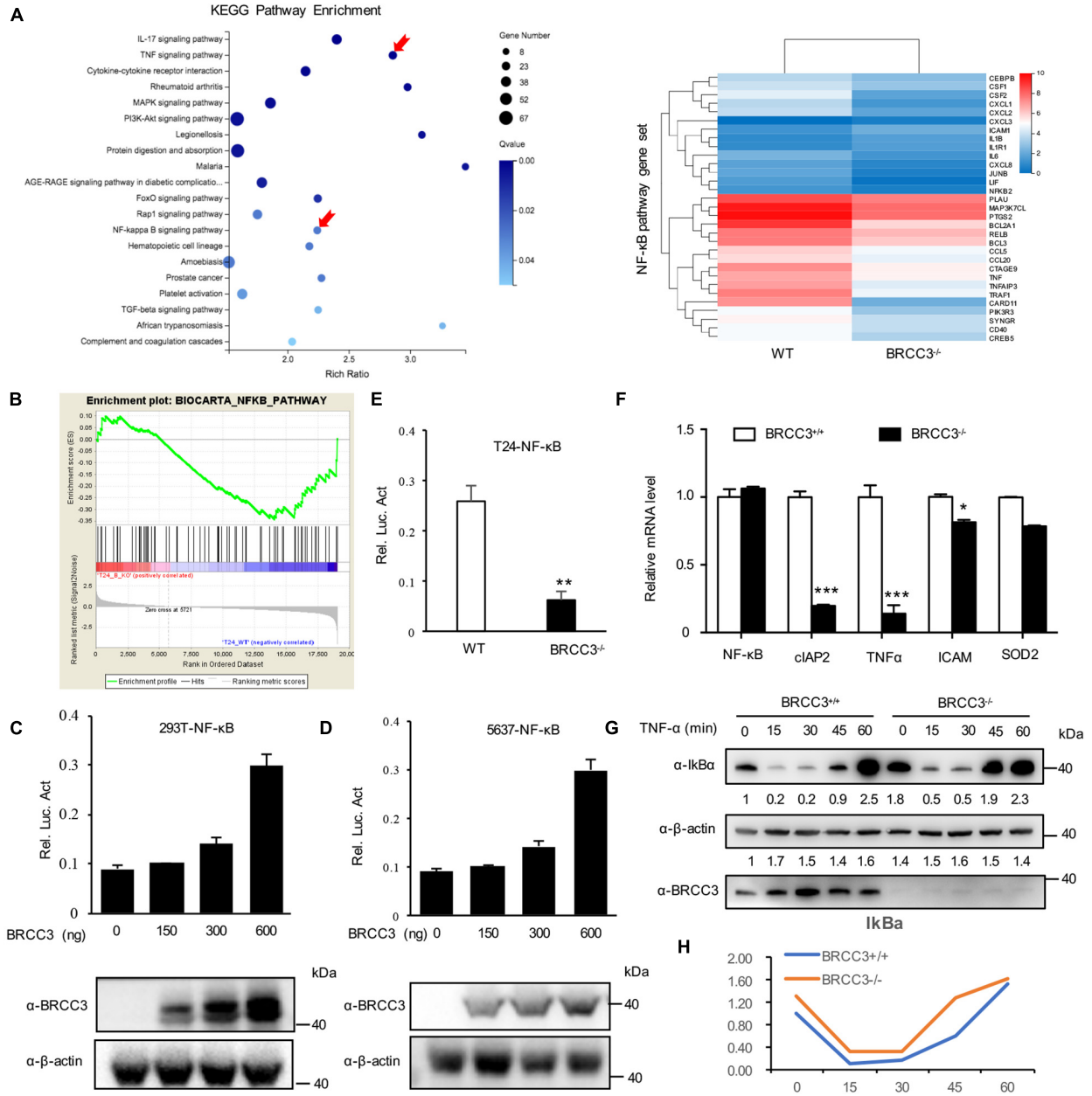

FIGURE 4 | Knocking out of BRCC3 resulted in inactivation of the NF-κB signaling pathway. **(A)** KEGG pathway enrichment analysis was used to assess wild type and BRCC3$^{-/-}$ bladder cancer cells. **(B)** GSEA identified NF-κB pathway-related gene sets enriched in the wild-type cells. **(C)** BRCC3 promotes the transcriptional activity of NF-κB. 293T cells were transfected with an NF-κB reporter firefly luciferase plasmid (200 ng), pRL-TK (10 ng) and the indicated amounts of a BRCC3 plasmid. Reporter assays were performed 48 h after transfection, and the results are presented as the NF-κB/TK luciferase activity. Data were analyzed employing one-way ANOVA and presented as the means ± standard error (n = 3/group). **(D)** BRCC3 promoted the transcriptional activity of NF-κB in bladder cancer 5637 bladder cancer cells. The experiments and data analyses were performed as in **(C)**. **(E)** BRCC3 ablation inhibited the transcriptional activity of NF-κB. **(F)** The BRCC3 deficiency blocked the transcription of NF-κB-targeted genes in the T24 cells. The expression levels of the indicated NF-κB-targeted genes were examined by RT-qPCR in BRCC3$^{-/-}$ T24 cells and wild type T24 cells. **(G)** BRCC3 deficiency reduced the degradation of IκBα under TNFα stimulation. BRCC3$^{-/-}$ T24 cells and wild type T24 cells were treated with 5 ng/ml TNFα for indicated time, and then the cell total protein lysis was analyzed by immunoblotting assays. **(H)** Quantitative data show the relative protein levels of IκBα in **(G)**. Statistical analysis was conducted using a t-test. The means ± standard error from three independent experiments is shown. *P < 0.05, **P < 0.001, and ***P < 0.001 compared with controls.

microarrays, which contained 188 bladder cancer tissue samples, 12 corresponding adjacent tissue samples and 16 normal bladder tissue samples. The results indicated a significant upregulation of the BRCC3 expression level in the cancer tissue compared to the paired adjacent and normal bladder tissue (**Figures 1C,D**). Moreover, we investigated the BRCC3 mRNA and protein levels in bladder cancer-derived cell lines and the immortalized normal uroepithelial cell line SV-HUC1, and found that 6 out of 8 cancer cell lines showed BRCC3 expression upregulation, compared with SV-HUC1 (**Figures 1E,F**). Taken together, these results implied BRCC3 was upregulated aberrantly in bladder cancer.

Overexpression of BRCC3 Increased Cell Proliferation and Migration

To study the role of BRCC3 in the biological behaviors, we created wild type BRCC3 (BRCC3 WT) overexpression and BRCC3 deubiquitinating enzyme-null mutant (H122Q, BRCC3 HQ) overexpression UMUC3 bladder cancer cell lines via lentiviral transfection. Western blotting determined the protein levels of the wild type and the mutant type BRCC3 (**Figure 2A**). The colony formation assay and cell growth assay based on the ECIS system showed that the overexpression of the wild type BRCC3 dramatically promoted cell growth and colony formation (**Figures 2B,C**). Next, we performed soft agar assays which showed a similar result to the results of the colony formation and proliferation assays (**Figures 2D,E**). Furthermore, a transwell migration assay suggested the overexpression of the wild type BRCC3 increased cell migration (**Figures 2F,G**). And meanwhile we investigated the effects of the overexpression of the deubiquitinating enzyme-null mutant BRCC3 on both cell proliferation and migration, which interestingly showed the similar effects as the wide type protein (**Figures 2B–D,F**).

Knocking Out BRCC3 Inhibited Cell Proliferation and Migration

We then knocked out the endogenous BRCC3 gene in the T24 cell line using CRISPR-Cas9 gene-editing system. Western blot analysis verified the abolition of the expression of BRCC3 protein in the knockout cells (**Figure 3A**). Colony formation assays and the ECIS proliferation system were used to measure cell proliferation. BRCC3-deficient cells showed significant inhibition of cell growth (**Figures 3B,C**). The colony numbers in soft agar assays were remarkably decreased when BRCC3 expression was depleted (**Figures 3D,E**). A transwell migration assay suggested that knocking out BRCC3 reduced cell migration obviously (**Figures 3F,G**).

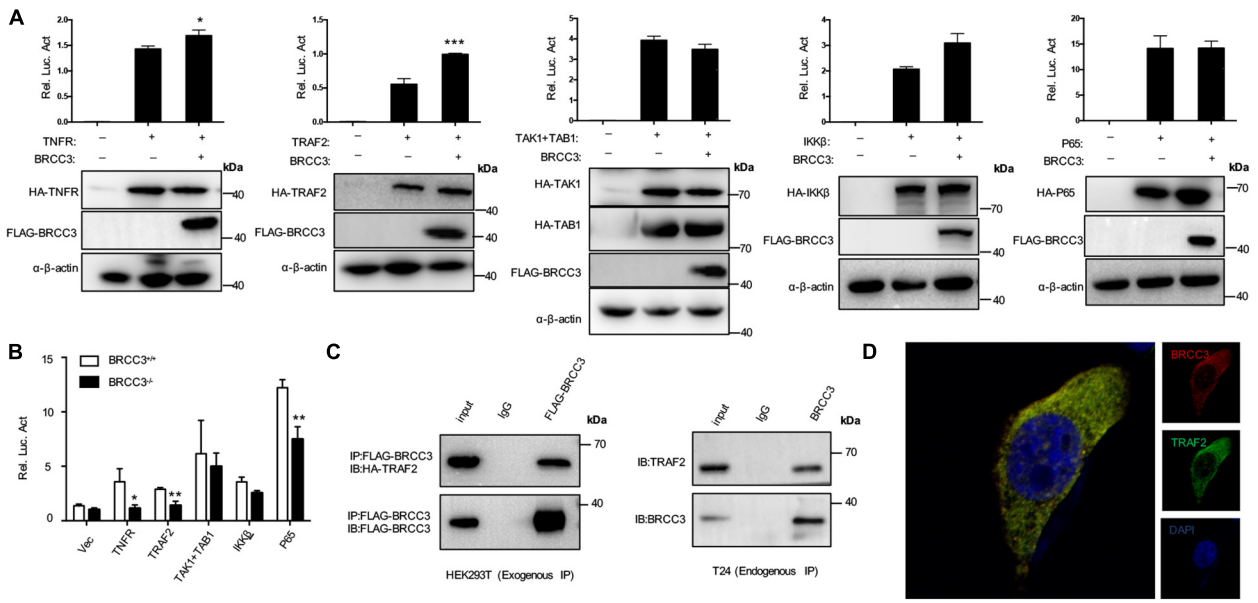

FIGURE 5 | BRCC3 activated the NF-κB signaling pathway through TRAF2. **(A)** The synergistic effects of TNFR, TRAF2, TAK1, and TAB1, IKKβ or P65 together with BRCC3 on NF-κB transcriptional activation were evaluated. HEK293T cells were co-transfected with an NF-κB reporter firefly luciferase plasmid (200 ng), pRL-TK (10 ng), the indicated component of an NF-κB pathway (300 ng) and a BRCC3 plasmid (300 ng). Reporter assays were performed 48 h after transfection, and the results are presented as the NF-κB/TK luciferase activity. Data were analyzed employing one-way ANOVA and are presented as the mean ± SE (n= 3 per group). **(B)** The influence of endogenous BRCC3 on NF-κB transcriptional activation induced by different NF-κB pathway components including TNFR, TRAF2, TAK1 and TAB1, IKKβ, and P65 was assessed. **(C)** BRCC3 interacted with TRAF2 in both exogenous and endogenous ways. The whole-cell extracts of HEK293T cells (co-transfected with BRCC3 and TRAF2 for 48 h) or the wild type T24 cells were prepared and incubated with an anti-Flag antibody or anti-BRCC3 antibody and Sepharose beads, and the immunoprecipitants were collected. The precipitates were then analyzed by SDS–PAGE, and Western blotting was performed with an anti-HA antibody or anti-TRAF2 antibody. Data are shown as the means ± standard error of technical replicates from one representative experiment out of three experiments. *P< 0.05, **P< 0.001, ***P< 0.001 compared with controls. **(D)** Immunofluorescence staining showed the co-localization of endogenous BRCC3 and TRAF2. Fluorescence confocal microscopy analysis was performed with T24 cells, using antibodies of BRCC3 and TRAF2 according to the standard immunofluorescence assays.

Genetic Deficiency in BRCC3 Resulted in Inactivation of the NF-κB Signaling Pathway

To identify the possible signaling pathway involved, we performed RNA-Seq analysis using the wild type and BRCC3-deficient T24 cell lines. Gene Set Enrichment Analysis (GSEA) was conducted using KEGG pathway enrichment models, and we found that the NF-κB signaling pathway was significantly inactivated when BRCC3 was knocked out (**Figures 4A,B**). To confirm this finding, we tested whether BRCC3 can activate the luciferase activity of an NF-κB reporter in both HEK293 cells and three bladder cancer cell lines 5637, T24, and EJ. We observed that exogenous overexpression of BRCC3 activated NF-κB pathway in a dose-dependent manner (**Figures 4C,D** and **Supplementary Figure 1**). To identify the role of endogenous BRCC3, an NF-κB reporter assay was performed with wide type and BRCC3-deficient T24 cells. The results showed that the ablation of BRCC3 vastly inhibited NF-κB activity (**Figure 4E**). In addition, Real-time PCR analyses indicated that the ablation of BRCC3 reduced the expression of the NF-κB signaling down-stream genes including cIAP2, TNFα, and ICAM (**Figure 4F**). It is well recognized that IκBα protein sequesters P65 in the cytoplasm under physiological conditions. However, under stimulation with cytokines, pathogens and so on, IκBα is degraded which makes P65 released into the nucleus, leading to NF-κB activation finally. Therefore, we also checked the influence of BRCC3 on the degradation rate of IκBα under TNFα stimulation. We found that abolition of BRCC3 reduced IκB degradation (**Figures 4G,H**), which lead to the blockade of NF-κB activation.

BRCC3 Activated NF-κB Signaling Pathway via TRAF2

To further investigate the relationship between BRCC3 and NF-κB signaling, BRCC3 was co-expressed with several NF-κB signaling protein plasmids in HEK293T cells and then analyzed the relative luciferase activity using an NF-κB signaling reporter plasmid. We found that BRCC3 increased the activation NF-κB signaling pathway together with the upstream molecules TNFR and TRAF2 (**Figure 5A**). However, BRCC3 did not increase IKKβ, P65 and TAK1/TAB1-induced activation of NF-κB signaling (**Figure 5A**). Besides, we found overexpression of TNFR, TRAF2 and P65 were able to activate the NF-κB signaling pathway in wild type ($BRCC3^{+/+}$) T24 cells, but failed to activate the signaling in BRCC3-deficient ($BRCC3^{-/-}$) T24 cells (**Figure 5B**). These results suggested the activation of the NF-κB signaling pathway was at least partially dependent on the function of BRCC3. Additionally, we used immunoprecipitation

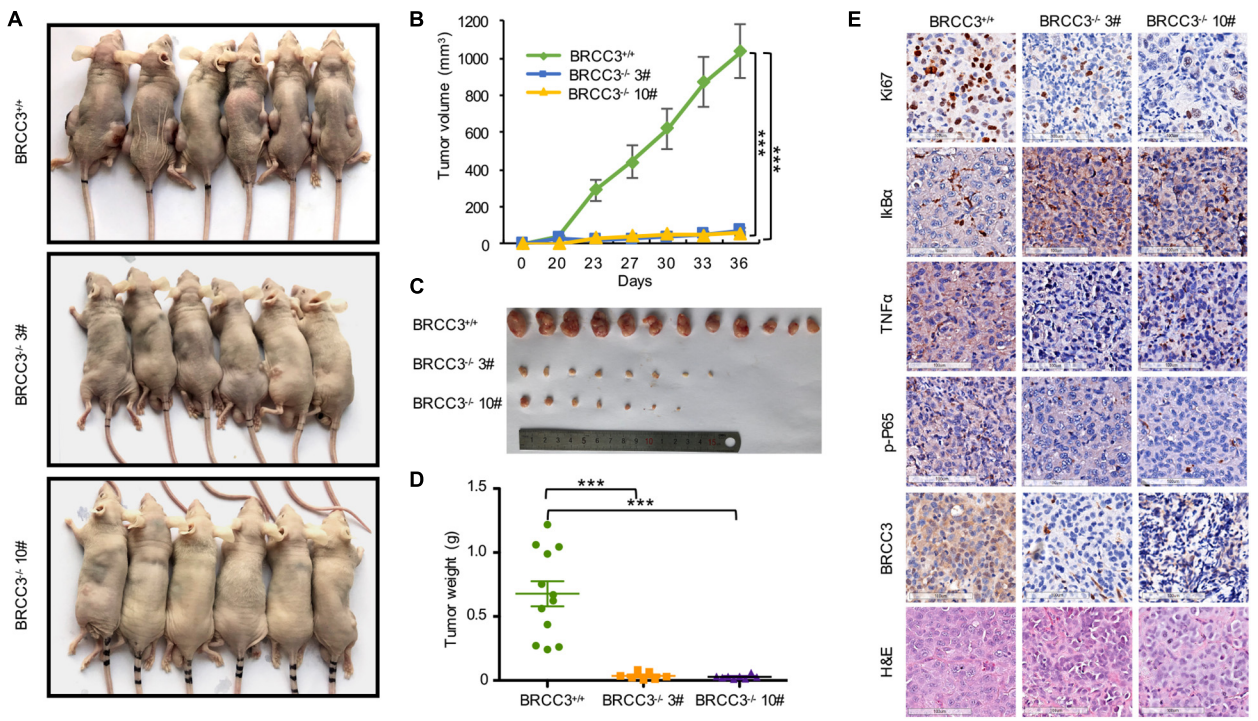

FIGURE 6 | The depletion of BRCC3 inhibits bladder cancer tumorigenesis *in vivo*. **(A)** Xenograft models ($n = 6$) were established by subcutaneously inoculating wild-type or BRCC3-KO cells and allowing the cells to grow for 5 weeks. Then the mice were sacrificed and the tumors were removed and weighed. **(B–D)** The tumor volume and weight measurements are shown. **(E)** Representative H&E staining and immunohistochemical staining of the xenograft tumors from the tumor-bearing mice in the wild-type and BRCC3-KO groups, showed the deficiency of BRCC3 (the fifth panel) and the upregulation of IκBα expression (the second panel), the downregulation of Ki67 expression (the top panel), TNFα expression (the third panel) and p-P65 expression (the fourth panel) in the BRCC3-KO groups. Statistical analysis of the tumor volume and weight were performed using one-way ANOVA. The means ± standard error of three independent experiments is shown. $^{*}P < 0.05$, $^{**}P < 0.001$, and $^{***}P < 0.001$ compared with controls.

assays to examine the interaction of BRCC3 with proteins of components of NF-κB signaling pathways such as TNFR, TRAF2, P65, and so on. We found that BRCC3 interacted with TRAF2 in both exogenous and endogenous expression models (**Figure 5C**). Moreover, the colocalization of BRCC3 and TRAF2 was proved by an endogenous immunofluorescence (**Figure 5D**).

Knocking Out BRCC3 Inhibited Bladder Cancer Growth *in vivo*

To confirm BRCC3 function *in vivo*, we constructed xenograft models. The parental T24 cells and two BRCC3-deficient T24 cell lines were injected into separate nude mice. About 1 month later, the tumors were dissected from the tumor-bearing mice. The volumes of the tumors from the parental T24 cells were much larger than those from the BRCC3$^{-/-}$ cells (**Figures 6A,B**). Accordingly, a dramatic advantage in tumor weight that agreed with the differences in tumor size was also observed (**Figures 6C,D**). These results suggested that BRCC3 played an important role in the regulation of bladder cancer tumorigenesis *in vivo*. Moreover, the dissected neoplasms were embedded in paraffin and assessed by immunohistochemistry, finding that the expression of Ki67 was lower in the BRCC3$^{-/-}$ group (**Figure 6E**). Furthermore, TNFα and phospho-P65 was decreased while the level of IκBα was increased in the BRCC3$^{-/-}$ group, which confirmed that the abolition of BRCC3 inhibited the NF-κB signaling pathway (**Figure 6E**).

DISCUSSION

The deubiquitination family is involved in a wide range of biological processes, including cancer and inflammation (Massoumi, 2011; Li et al., 2013). The function of BRCC3 in bladder cancer remains elusive. The protein level of BRCC3 in bladder cancer in The Cancer Genome Atlas (TCGA) datasets showed that BRCC3 expression is aberrantly upregulated in bladder cancer patients. Analysis of Oncomine datasets was consistent with this conclusion. To further verify these findings, IHC staining found upregulated BRCC3 expression in bladder cancer tumor tissue. Next, we determined the function of BRCC3 in the progression of bladder cancer using BRCC3 over-expressed and BRCC3 deficient cells *in vitro*. Our findings showed BRCC3 plays a crucial role in facilitating the development and progression of bladder cancer.

To reveal the way how BRCC3 promotes carcinogenesis, we analyzed BRCC3-deficient bladder cancer cell lines by RNA-Seq, and the data showed that the NF-κB inflammatory pathway was notably downregulated when BRCC3 was knockout. We

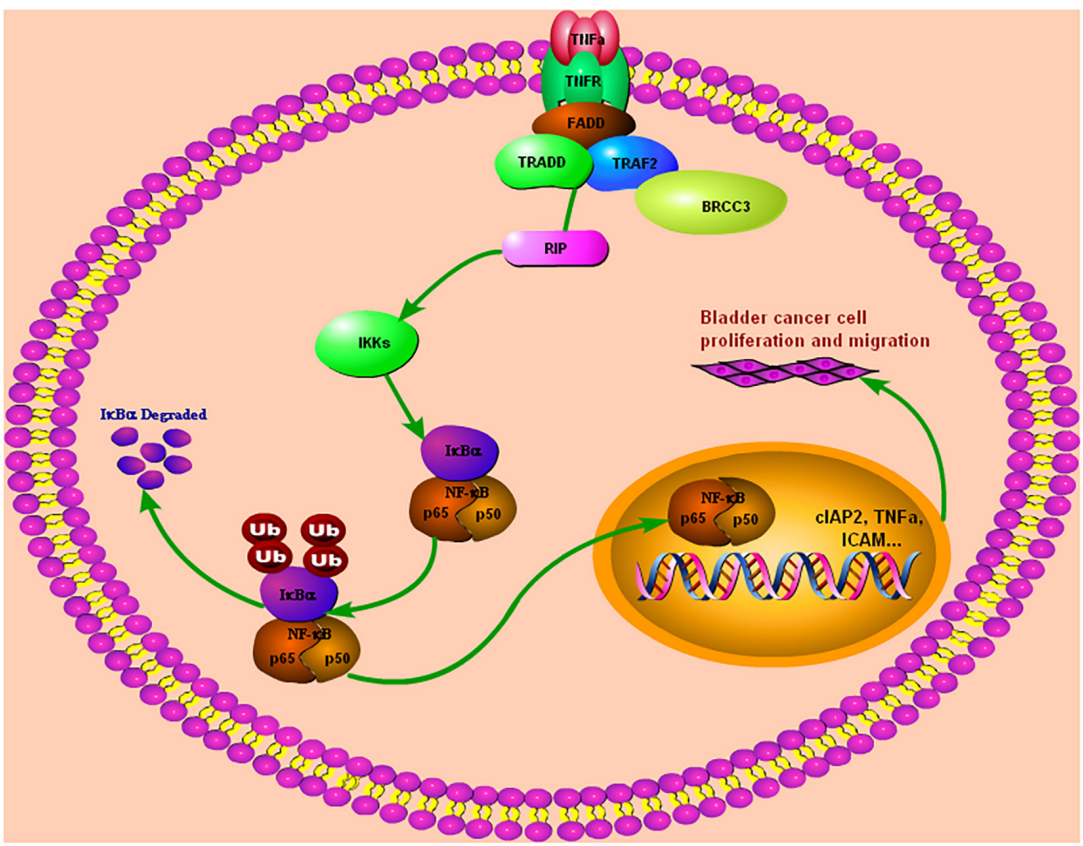

FIGURE 7 | Our study demonstrated that BRCC3 could promote BCa cells proliferation and migration both *in vitro* and *in vivo*. Furthermore, BRCC3 exerts its oncogenic role via binding to TRAF2, which in turn activates NF-κB signaling and inflammation in bladder cancer.

further confirmed this result by luciferase, qPCR and Western blotting assays. Through co-transfecting of the node protein of the NF-κB pathway, we reported that BRCC3 maximizes the potential of TRAF2 to activate the NF-κB pathway, and further exploration showed that BRCC3 binds to TRAF2. Finally, the xenograft model showed that a deficiency in BRCC3 expression significantly decreased tumorigenesis *in vivo*.

Accumulating evidence indicates that the deubiquitinase BRCC3 participates in carcinogenesis by regulating DNA stability (Huang et al., 2015). Although BRCC3 has been reported to be an important regulator of NLRP3 activity (Py et al., 2013; Hu et al., 2019), the function of BRCC3 in the NF-κB signaling pathway has not been reported. Our results showed BRCC3 promotes the NF-κB signaling in bladder cancer, therefore resulting in tumorigenesis, which is different from the previously described mechanism. TRAF2 can promote tumorigenesis in several cancers (Wu et al., 2005; Etemadi et al., 2015; Borghi et al., 2016; Wei et al., 2017). The stability and activity of TRAF2 are mediated by a large number of E3 ubiquitin ligases and deubiquitinating enzymes (Habelhah et al., 2002; Trompouki et al., 2003; Li et al., 2009; Xiao et al., 2012; Zhong et al., 2013; Borghi et al., 2016). We demonstrated that BRCC3 facilitates tumorigenesis via TRAF2 in bladder cancer. Interestingly, by using a validated deubiquitinating enzyme-null site-directed mutation (H122Q) of BRCC3 (Cooper et al., 2009; Py et al., 2013; Liu et al., 2018), we found that BRCC3 interacts with TRAF2, yet through a mechanism that is independent of the deubiquitinating enzyme activity of BRCC3.

In summary, we found that BRCC3 is overexpressed and associated with a poor prognosis in bladder cancer. BRCC3 exerts its oncogenic role via binding to TRAF2, which in turn leads the activation of NF-κB signaling in bladder cancer (**Figure 7**). Our study provides novel insight into the function of BRCC3 in the TRAF2-activating NF-κB signaling cascade in bladder cancer.

DATA AVAILABILITY STATEMENT

Oncomine data was downloaded from Thermo Fisher Scientific institute (https://www.oncomine.org/resource/login.html). Gene Expression Profiling Interactive Analysis (GEPIA) data was downloaded from Zhang's Lab of Perking university (http://gepia.cancer-pku.cn/).

ETHICS STATEMENT

The studies involving human participants were reviewed and approved by the Ethics Committee at Zhongnan Hospital of Wuhan University. Written informed consent for participation was not required for this study in accordance with the national legislation and the institutional requirements. The animal study was reviewed and approved by the Ethics Committee at Zhongnan Hospital of Wuhan University.

AUTHOR CONTRIBUTIONS

HT, YY, YL, and ZH performed the majority of the experiments and prepared the manuscript. JZ performed Luciferase reporter assays and IHC experiments. YL and TL wrote the main manuscript. TL, SL, JP, and XW designed the research. All authors read and approved the manuscript.

FUNDING

This work was supported by grants from the National Natural Science Foundation of China (Grant Nos. 81902598, 82001000, and 81970588), the China Postdoctoral Science Foundation (Grant No. 2020M670071ZX), the Fundamental Research Funds for the Central Universities (Grant No. 2042020kf0133), the Scientific Research Project of Hubei Provincial Health Commission (Grant Nos. WJ2019Q020 and WJ2021M080), and the Science and Technology Development Plan of Jingzhou (Grant Nos. 2017003 and 2017016).

SUPPLEMENTARY MATERIAL

The Supplementary Material for this article can be found online at: https://www.frontiersin.org/articles/10.3389/fcell.2021.720349/full#supplementary-material

Supplementary Figure 1 | BRCC3 promotes the transcriptional activity of NF-κB. T24 or EJ cells were transfected with an NF-κB reporter firefly luciferase plasmid (200 ng), pRL-TK (10 ng) and the indicated amounts of a BRCC3 plasmid. Reporter assays were performed 48 h after transfection, and the results are presented as the NF-κB/TK luciferase activity. Data were analyzed employing one-way ANOVA and presented as the means ± standard error (n = 3/group).

REFERENCES

Al-Halabi, R., Bou, C. M., Abou, M. R., El-Hajj, H., Zahr, H., Schneider-Stock, R., et al. (2011). Gallotannin inhibits NFkB signaling and growth of human colon cancer xenografts. *Cancer Biol. Ther.* 12, 59–68. doi: 10.4161/cbt.12.1.15715

Borghi, A., Verstrepen, L., and Beyaert, R. (2016). TRAF2 multitasking in TNF receptor-induced signaling to NF-kappaB, MAP kinases and cell death. *Biochem. Pharmacol.* 116, 1–10. doi: 10.1016/j.bcp.2016.03.009

Choudhury, A., and Hoskin, P. J. (2019). Predictive biomarkers for muscle-invasive bladder cancer: the search for the holy grail continues. *Eur. Urol.* 76, 69–70. doi: 10.1016/j.eururo.2019.01.040

Cooper, E. M., Cutcliffe, C., Kristiansen, T. Z., Pandey, A., Pickart, C. M., and Cohen, R. E. (2009). K63-specific deubiquitination by two JAMM/MPN+ complexes: BRISC-associated Brcc36 and proteasomal Poh1. *EMBO J.* 28, 621–631. doi: 10.1038/emboj.2009.27

Cumberbatch, M., Jubber, I., Black, P. C., Esperto, F., Figueroa, J. D., Kamat, A. M., et al. (2018). Epidemiology of bladder cancer: a systematic review and contemporary update of risk factors in 2018. *Eur. Urol.* 74, 784–795. doi: 10.1016/j.eururo.2018.09.001

Dong, Y., Hakimi, M. A., Chen, X., Kumaraswamy, E., Cooch, N. S., Godwin, A. K., et al. (2003). Regulation of BRCC, a holoenzyme complex containing BRCA1 and BRCA2, by a signalosome-like subunit and its role in DNA repair. *Mol. Cell* 12, 1087–1099. doi: 10.1016/s1097-2765(03)00424-6

Dudley, J. C., Schroers-Martin, J., Lazzareschi, D. V., Shi, W. Y., Chen, S. B., Esfahani, M. S., et al. (2018). Detection and surveillance of bladder cancer using

urine tumor DNA. *Cancer Discov.* 9, 500–509. doi: 10.1158/2159-8290.cd-18-0825

Efstathiou, J. A., Mouw, K. W., Gibb, E. A., Liu, Y., Wu, C. L., Drumm, M. R., et al. (2019). Impact of immune and stromal infiltration on outcomes following bladder-sparing trimodality therapy for muscle-invasive bladder cancer. *Eur. Urol.* 76, 59–68. doi: 10.1016/j.eururo.2019.01.011

Etemadi, N., Chopin, M., Anderton, H., Tanzer, M. C., Rickard, J. A., Abeysekera, W., et al. (2015). TRAF2 regulates TNF and NF-kappaB signalling to suppress apoptosis and skin inflammation independently of Sphingosine kinase 1. *Elife* 4:e10592.

Habelhah, H., Frew, I. J., Laine, A., Janes, P. W., Relaix, F., Sassoon, D., et al. (2002). Stress-induced decrease in TRAF2 stability is mediated by Siah2. *EMBO J.* 21, 5756–5765. doi: 10.1093/emboj/cdf576

He, Y. T, Li, D, and Liang, D. (2018). Incidence and mortality of bladder cancer in China, 2014. *Zhonghua Zhong Liu Za Zhi.* 9, 647–652.

Hu, J., Wu, H., Wang, D., Yang, Z., and Dong, J. (2019). LncRNA ANRIL promotes NLRP3 inflammasome activation in uric acid nephropathy through miR-122-5p/BRCC3 axis. *Biochimie* 157, 102–110. doi: 10.1016/j.biochi.2018.10.011

Huang, D., Nagata, Y., Grossmann, V., Radivoyevitch, T., Okuno, Y., Nagae, G., et al. (2015). BRCC3 mutations in myeloid neoplasms. *Haematologica* 100, 1051–1057.

Kunnumakkara, A. B., Sailo, B. L., Banik, K., Harsha, C., Prasad, S., Gupta, S. C., et al. (2018). Chronic diseases, inflammation, and spices: how are they linked? *J. Transl. Med.* 16:14.

Li, L., Soetandyo, N., Wang, Q., and Ye, Y. (2009). The zinc finger protein A20 targets TRAF2 to the lysosomes for degradation. *Biochim. Biophys. Acta.* 1793, 346–353. doi: 10.1016/j.bbamcr.2008.09.013

Li, X., Stevens, P. D., Yang, H., Gulhati, P., Wang, W., Evers, B. M., et al. (2013). The deubiquitination enzyme USP46 functions as a tumor suppressor by controlling PHLPP-dependent attenuation of Akt signaling in colon cancer. *Oncogene* 32, 471–478. doi: 10.1038/onc.2012.66

Liu, Q., Wu, Y., Qin, Y., Hu, J., Xie, W., Qin, F. X., et al. (2018). Broad and diverse mechanisms used by deubiquitinase family members in regulating the type I interferon signaling pathway during antiviral responses. *Sci. Adv.* 4: r2824.

Massoumi, R. (2011). CYLD: a deubiquitination enzyme with multiple roles in cancer. *Future Oncol.* 7, 285–297. doi: 10.2217/fon.10.187

Py, B. F., Kim, M. S., Vakifahmetoglu-Norberg, H., and Yuan, J. (2013). Deubiquitination of NLRP3 by BRCC3 critically regulates inflammasome activity. *Mol. Cell* 49, 331–338. doi: 10.1016/j.molcel.2012.11.009

Rayet, B., and Gelinas, C. (1999). Aberrant rel/nfkb genes and activity in human cancer. *Oncogene* 18, 6938–6947. doi: 10.1038/sj.onc.1203221

Roos, P. H., Golka, K., and Hengstler, J. G. (2008). Predictive biomarkers and signatures in urinary bladder cancer. *Curr. Opin. Mol. Ther.* 10, 243–250.

Sun, Z. Z., Zhang, T., Ning, K., Zhu, R., Liu, F., Tang, S. C., et al. (2016). B7-H3 upregulates BRCC3 expression, antagonizing DNA damage caused by 5-Fu. *Oncol. Rep.* 36, 231–238. doi: 10.3892/or.2016.4808

Trompouki, E., Hatzivassiliou, E., Tsichritzis, T., Farmer, H., Ashworth, A., and Mosialos, G. (2003). CYLD is a deubiquitinating enzyme that negatively regulates NF-kappaB activation by TNFR family members. *Nature* 424, 793–796. doi: 10.1038/nature01803

Tu, Z., Xu, B., Qu, C., Tao, Y., Chen, C., Hua, W., et al. (2015). BRCC3 acts as a prognostic marker in nasopharyngeal carcinoma patients treated with radiotherapy and mediates radiation resistance in vitro. *Radiat. Oncol.* 10:123.

Wei, B., Liang, J., Hu, J., Mi, Y., Ruan, J., Zhang, J., et al. (2017). TRAF2 is a valuable prognostic biomarker in patients with prostate cancer. *Med. Sci. Monit.* 23, 4192–4204. doi: 10.12659/msm.903500

Wu, C. J., Conze, D. B., Li, X., Ying, S. X., Hanover, J. A., and Ashwell, J. D. (2005). TNF-alpha induced c-IAP1/TRAF2 complex translocation to a Ubc6-containing compartment and TRAF2 ubiquitination. *EMBO J.* 24, 1886–1898. doi: 10.1038/sj.emboj.7600649

Xiao, N., Li, H., Luo, J., Wang, R., Chen, H., Chen, J., et al. (2012). Ubiquitin-specific protease 4 (USP4) targets TRAF2 and TRAF6 for deubiquitination and inhibits TNFalpha-induced cancer cell migration. *Biochem. J.* 441, 979–986. doi: 10.1042/bj20111358

Zhang, F., and Zhou, Q. (2018). Knockdown of BRCC3 exerts an antitumor effect on cervical cancer in vitro. *Mol. Med. Rep.* 18, 4886–4894.

Zhong, H., Wang, D., Fang, L., Zhang, H., Luo, R., Shang, M., et al. (2013). Ubiquitin-specific proteases 25 negatively regulates virus-induced type I interferon signaling. *PLoS One* 8:e80976. doi: 10.1371/journal.pone.0080976

Conflict of Interest: The authors declare that the research was conducted in the absence of any commercial or financial relationships that could be construed as a potential conflict of interest.

Publisher's Note: All claims expressed in this article are solely those of the authors and do not necessarily represent those of their affiliated organizations, or those of the publisher, the editors and the reviewers. Any product that may be evaluated in this article, or claim that may be made by its manufacturer, is not guaranteed or endorsed by the publisher.

frontiers in Cell and Developmental Biology

ORIGINAL RESEARCH
published: 22 October 2021
doi: 10.3389/fcell.2021.738364

ID2 Inhibits Bladder Cancer Progression and Metastasis *via* PI3K/AKT Signaling Pathway

Weipu Mao[1,2,3†], Keyi Wang[4†], Si Sun[2†], Jianping Wu[2], Ming Chen[2,3], Jiang Geng[4*] and Ming Luo[4*]*

[1] Department of Urology, Shidong Hospital of Yangpu District, Shanghai, China, [2] Department of Urology, Affiliated Zhongda Hospital of Southeast University, Nanjing, China, [3] Surgical Research Center, Institute of Urology, Southeast University Medical School, Nanjing, China, [4] Department of Urology, School of Medicine, Shanghai Tenth People's Hospital, Tongji University, Shanghai, China

OPEN ACCESS

Edited by:
Yongwen Luo,
Wuhan University, China

Reviewed by:
Xiaolong Tang,
Shenzhen University Health Science Centre, China
Meser M. Ali,
Henry Ford Hospital, United States

****Correspondence:***
Ming Chen
mingchenseu@126.com
Jiang Geng
gengjiangsn@sina.com
Ming Luo
lm1191@126.com

† These authors have contributed equally to this work

Specialty section:
This article was submitted to Molecular and Cellular Pathology, a section of the journal Frontiers in Cell and Developmental Biology

Received: *08 July 2021*
Accepted: *06 October 2021*
Published: *22 October 2021*

Citation:
Mao W, Wang K, Sun S, Wu J, Chen M, Geng J and Luo M (2021) ID2 Inhibits Bladder Cancer Progression and Metastasis via PI3K/AKT Signaling Pathway. Front. Cell Dev. Biol. 9:738364. doi: 10.3389/fcell.2021.738364

Background: Inhibitors of DNA-binding (ID) proteins are important regulators of cell proliferation and differentiation. The aim of this study was to evaluated the role of ID proteins in bladder cancer (BCa) and related molecular mechanisms.

Methods: The TCGA database was analyzed for the expression and clinical significance of ID proteins. The expression of ID2 was determined by qRT-PCR, immunohistochemical staining and western blot. The role of ID2 was determined by CCK-8, colony formation, wound healing, transwell and xenograft tumor assays, and the potential mechanism of ID2 in BCa was investigated by RNA sequencing.

Results: ID2 expression was significantly downregulated in TCGA database and clinical samples, and high ID2 expression was associated with low-grade tumor staging and correlated with better overall survival, disease specific survival (DSS) and progress free interval (PFI). *In vivo* and *in vitro* experiments showed that knockdown of ID2 promoted proliferation, migration, invasion and metastasis of BCa cells, while overexpression of ID2 significantly inhibited cell proliferation, migration, invasion and metastasis. Mechanistically, ID2 acts as a tumor suppressor through PI3K/AKT signaling pathway to inhibit the progression and metastasis of BCa.

Conclusion: Our results suggest that ID2 exerts tumor suppressive effects in BCa through PI3K/AKT signaling pathway, and altered ID2 expression can be used as a biomarker of BCa progression and metastasis.

Keywords: bladder cancer, ID2, PI3K/AKT signaling pathway, progression, metastasis

BACKGROUND

Bladder cancer (BCa) is one of the tumors with high morbidity and mortality in the urinary system. In 2020, BCa ranked 12th in incidence and 13th in mortality among all malignant tumors (Sung et al., 2021). The latest statistical results from China Tumor Registry show that the incidence rate of BCa in China was 8.0/100,000 and the mortality rate was 3.3/100,000 in 2015 (Zhang et al., 2020).

BCa can be divided into non-muscle invasive bladder cancer (NMIBC) and muscle invasive bladder cancer (MIBC) based on muscle infiltration (Mao et al., 2019). NMIBC accounts for approximately more than 75% of BCa and the preferred treatment is transurethral resection of bladder tumour (TURBt) (Dy et al., 2017). Although NMIBC generally has a good prognosis, it has a high recurrence rate and about 10–15% of patients will progress to MIBC in the course of treatment (Ranzi et al., 2017). MIBC is highly aggressive and prone to metastasis, and patients have a poor prognosis (Robertson et al., 2017). After the progression of NMIBC to MIBC, radical cystectomy is generally chosen as the treatment modality (Witjes et al., 2021). However, the cost of surgery is significantly higher, the quality of life after surgery is significantly lower, and the burden on family and society is significantly higher (Garcia-Donas et al., 2017). Therefore, it is particularly important to explore the mechanisms of BCa progression, discover new biomarkers and identify effective therapeutic targets for BCa.

Inhibitors of DNA-binding (ID) proteins are important regulators of cell proliferation and differentiation. ID family proteins are a class of proteins that contain the basic Helix-Loop-Helix (bHLH) structural domain while lacking a DNA binding sites, which belong to the HLH family and are negative regulators of the basic HLH transcription factors (Benezra et al., 1990). ID proteins can inhibit cell differentiation and can induce cell proliferation by regulating different cell cycle regulators to enhance tissue invasiveness and angiogenesis of tumor cells (Perk et al., 2005). ID proteins are expressed in many tissues and organs, but their expression is somewhat variable in different developmental stages and tissues (Massari and Murre, 2000). An increasing number of studies have confirmed that abnormal expression of ID proteins is not only involved in tumor development, but also closely related to tumor invasion and metastasis formation (Volpert et al., 2002; Fong et al., 2004). However, the predictive value of ID proteins for BCa and their possible molecular mechanisms have not been elucidated.

In this study, we examined the expression of ID proteins (ID1, ID2, ID3, and ID4) in BCa tissues and found that ID2 expression was downregulated and associated with tumor stage and survival. Further analysis showed that ID2 inhibited BCa proliferation, migration, invasion and metastasis through the PI3K/AKT signaling pathway. Taken together, our study suggests that ID2 may be a potential therapeutic target for BCa.

MATERIALS AND METHODS

Clinical Specimens

Twenty-five pairs of BCa tumor tissues and corresponding adjacent normal tissues were collected from BCa patients who underwent radical cystectomy between January 2016 and December 2016 at Shanghai Tenth People's Hospital (Shanghai, China). None of the patients in this study received any radiotherapy or chemotherapy before the surgery. Pathology of all BCa patients was confirmed by hospital pathologists, and pathological staging was determined according to the American Joint Committee on Cancer TNM staging system (7th edition). The study was evaluated and approved by the Ethics Committee of the Shanghai Tenth People's Hospital (SHSY-IEC-4.1/19-120/01) and was conducted in accordance with the relevant regulations. All patients or their relatives had written informed consent.

The Cancer Genome Atlas Database

ID1, ID2, ID3, and ID4 expression in BCa and related clinical data are available from the Cancer Genomics Browser. In brief, we downloaded RNA-seq data and clinical information from the TCGA database for 433 BCa projects, including 19 cases with matched normal tissues. The downloaded data were used in transcripts per million (TPM) format for analysis. In addition, we downloaded RNA-seq data in TPM format from the TCGA and Genotype-Tissue Expression (GTEx) databases.

Cell Lines and Culture

The immortalized human normal bladder epithelial cell line SV-HUC-1 and human BCa cell lines UMUC3, 5637, T24, and EJ were purchased from the Cell Bank of the Chinese Academy of Sciences (Shanghai, China). UMUC3, 5637, T24, and EJ cells were cultured in RPMI-1640 medium (Gibco; Thermo Fisher Scientific, United States) and SV-HUC-1 cells were maintained in F12K medium (Sigma-Aldrich; Merck KGaA, Germany). All cell cultures were supplemented with 10% fetal bovine serum (FBS, Gibco; Thermo Fisher Scientific, United States) and 1% penicillin/streptomycin (Gibco; Thermo Fisher Scientific, United States) and cultured at 37°C in a humidified incubator containing 5% CO_2.

Cell Transfection

Small interfering RNAs specifically targeting ID2 (si-ID2: GGACTCGCATCCCACTATT) and negative control siRNA (Control) were purchased from RiboBio (Guangzhou, China). Transient transfection was performed at 30–50% cell confluence using Lipofectamine 3000 (Thermo Fisher Scientific, United States). ID2 knockdown lentivirus (sh-ID2) carrying si-ID2, Control lentivirus and ID2 overexpression lentivirus (OE-ID2) carrying si-ID2, Control, or ID2 sequences, respectively, and the lentivirus were constructed by BioLink (Shanghai, China). sh-ID2, Control, and OE-ID2 stable transfer cell lines were generated by lentivirus transfection.

RNA Sequencing Analysis

To find ID2-associated downstream pathways, we performed RNA sequencing analysis on EJ cell line transfected with OE-ID2, sh-ID2, and control lentivirus. mRNA expression analysis was performed on Agilent's whole human genome microarray 4 × 44 K v2 (026652) with monochrome hybridization, including probes for 34184 human mRNA transcripts. RNA sequencing was performed according to the previously described procedure (Luo et al., 2019). Sample preparation and microarray hybridization were performed according to the standard protocol of Arraystar (Majorbio, Shanghai, China). In addition, further Gene Ontology

(GO) and Kyoto Encyclopedia of Genes and Genomes (KEGG) enrichment analysis was used to screen for signaling pathways.

RNA Extraction and Quantitative Real-Time Polymerase Chain Reaction

Total RNA was extracted from cells or human tissue using Trizol reagent (TaKaRa, China) according to the manufacturer's instructions. Reverse transcription was performed using cDNA kits (R312, Vazyme Biotech, Nanjing, China) to synthesize cDNA. CT values were detected by qRT-PCR using SYBR Green PCR kit (Q141, Vazyme Biotech, Nanjing, China) and the ABI Prism 7500 sequence detection system (Applied Biosystems, United States). Primers for ID2 are listed below: ID2-F 5′ TCAGCACTTAAAAGATTCCGTG 3′; ID2-R 5′ GA CAGCAAAGCACTGTGTGG 3′; PI3K-F 5′ ATCAACAGCCAA

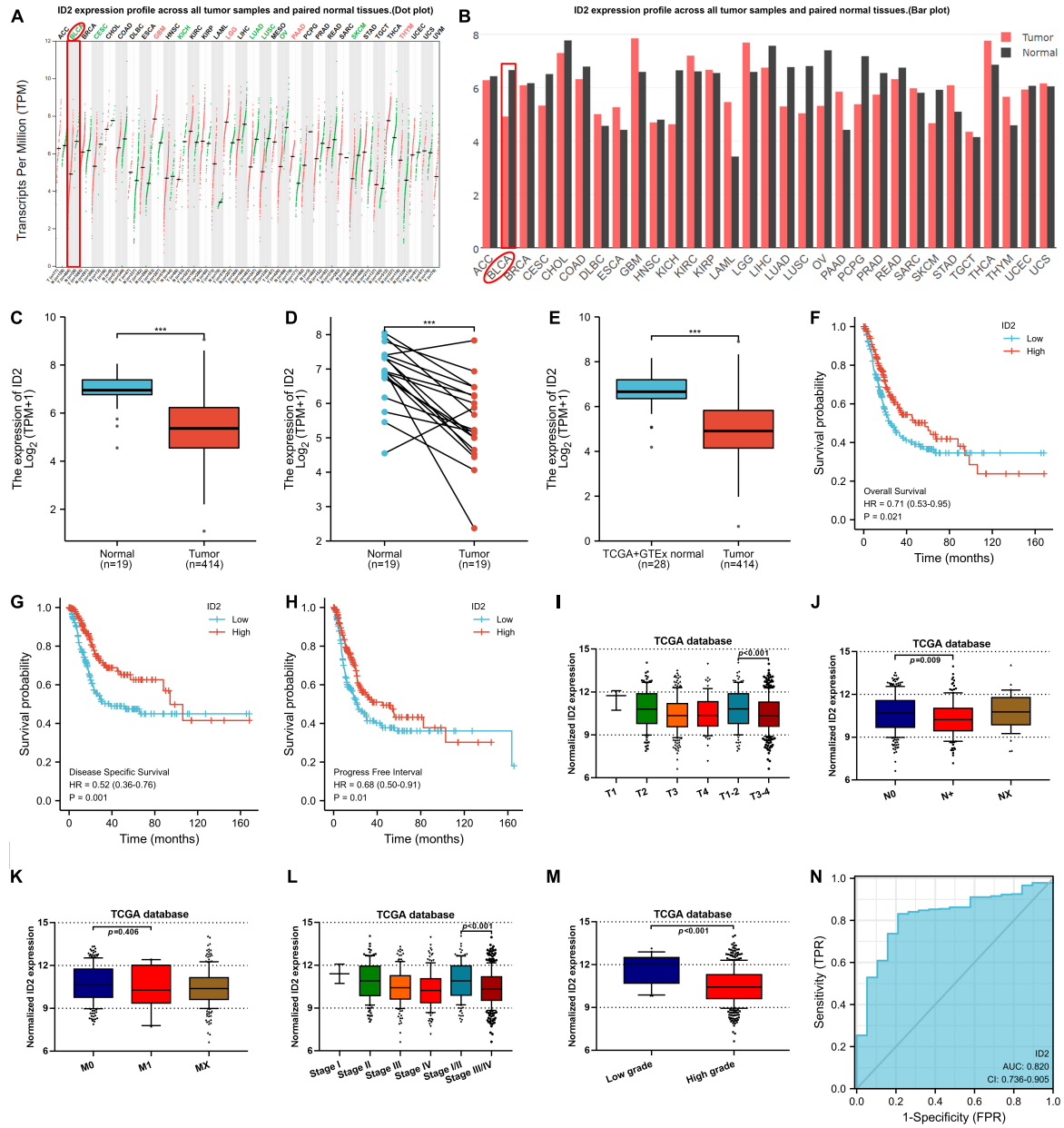

FIGURE 1 | ID2 expression correlates with clinical characteristics and survival rate in the TCGA database. **(A,B)** ID2 expression profile across all tumor samples and paired normal tissues. **(C)** The difference expression of ID2 in BCa tissues and adjacent normal tissues. **(D)** The difference expression of ID2 in BCa tissues and paired normal tissues. **(E)** The difference expression of ID2 in normal tissues of GTEx combined with TCGA and BCa tissues of TCGA. **(F–H)** Overall survival **(F)**, disease-specific survival **(G)**, and progress free interval **(H)** curve of BCa patients with low (n = 207) and high (n = 207) ID2 expression. **(I–M)** Relative expression levels of ID2 in TCGA database with T stage **(I)**, N stage **(J)**, M stage **(K)**, pathological stage **(L)**, tumor grade **(M)**. **(N)** ROC curve showed the efficiency of ID2 expression level to distinguishing BCa tissue from non-tumor tissue (***$p < 0.001$).

CAAATACC 3′; PI3K-R 5′ TTCTTATCACCGTCACCCT 3′; Akt-F 5′ ATCAACAGCCAACAAATACC 3′; Akt-R 5′ TTCTTA TCACCGTCACCCT 3′; SGK3-F 5′ TGGGGCTGTTCTGTA TGAAATGCTG 3′; SGK3-R 5′ TGGACCAGGCTGTAAGA CTCACTC 3′; GAPDH-F 5′ AACGGATTTGGTCGTATTG 3′; GAPDH-R 5′ GGAAGATGGTGATGGGATT 3′. The relative expression of ID2 was calculated using the $2^{-\Delta\Delta Ct}$ method and GAPDH was used as internal standards.

Cell Counting Kit-8 Assays

Transfected EJ and UNUC3 cells were seeded at a density of 2,000 cells per well into 96-well plates (Corning, United States). After seeding for 12, 24, 48, 72, and 96 h, 100 μl of serum-free medium and 10 μl of CCK8 solution (Yeasen, Shanghai, China) were added to each well and incubated at 37°C in the dark for 2 h, and optical density (OD) was detected at 450 nm.

Colony Formation Assays

Transfected cells were plated into 6-well plates (Corning, United States) at a density of 500 per well and cultured with complete medium for approximately 2 weeks. The culture was terminated when clones were visible to the naked eye in the culture dish. 2 weeks later, colonies were fixed using formaldehyde and then stained with 0.1% crystalline violet (Vicmed, China). These colonies were subsequently photographed and counted.

Wound Healing Assay

The transfected cells were seeded into 6-well plates (Corning, United States). When cells were reconnected and reached 80% confluence, cell monolayers were scratched with a 200 μL pipette. Subsequently, cells were washed with PBS to remove cell debris and medium containing 2% FBS was added. At 0, 12, and 24 h after injury, images were acquired at the same locations and wound area was calculated using ImageJ software (NIH, United States).

Cell Apoptosis Assay

Transfected cells were grown into 6-well plates (Corning, United States), and all cells in the medium and adherent to the wall were collected when the cells grew to 80% confluence. Cells were washed twice with cold 1 × PBS, Annexin V (BD Biosciences, United States) binding buffer was added, and then stained for 15 min at room temperature in the dark using fluorescein isothiocyanate (FITC) and propidium iodide (PI). Finally, the apoptosis rate was detected using BD FACS Calibur (Beckman Coulter, CA, United States).

Transwell Migration and Invasion Assays

Both cell migration and invasion ability assays were performed using Transwell chambers (8 μm pore size, Corning, United States). The upper chamber was not covered with Matrigel (BD Biosciences, United States) for the migration assay and 100 μl Matrigel for the invasion assay. Specifically, transfected cells (5×10^4) were inoculated in the upper chamber and culture medium containing 10% FBS was placed in the lower chamber. After 12–24 h incubation, the invading and migrating cells were fixed, stained with 0.1% crystalline violet (Vicmed, China), photographed and counted using an inverted microscope (Leica Microsystems, Germany).

Western Blot Analysis

Cells were lysed with RIPA buffer (Beyotime, China) containing protease inhibitors on ice and proteins were extracted, and protein concentrations were determined using BCA protein assay kit (Thermo Fisher Scientific, United States). Protein lysates (50 μg/lane) were separated by 10% sodium dodecyl sulfate-polyacrylamide gels (SDS-PAGE) electrophoresis and transferred to polyvinylidene fluoride membranes (Merck, United States). The membranes were subsequently blocked with 5% skim milk for 1 h and incubated with primary antibodies (**Supplementary Table 1**) overnight at 4°C. Subsequently, the membranes were incubated with secondary mouse or rabbit antibodies at room temperature for 1 h. After washing three times with PBST, the signals were observed

TABLE 1 | The relationship between the expression of ID2 and various clinicopathological variables in the TCGA database.

Characteristics	Total	ID2 expression		*P*-value
		Low	High	
Total	414	207	207	
Age (years)				0.921
≤70	234	116 (28.0%)	118 (28.5%)	
>70	180	91 (22.0%)	89 (21.5%)	
Sex				0.264
Female	109	60 (14.5%)	49 (11.8%)	
Male	305	147 (35.5%)	158 (38.2%)	
T-stage				**0.014**
T1	5	0 (0.0%)	5 (1.3%)	
T2	119	52 (13.7%)	67 (17.6%)	
T3	196	110 (28.9%)	86 (22.6%)	
T4	60	33 (8.7%)	27 (7.1%)	
N-stage				0.160
N0	239	112 (30.3%)	127 (34.3%)	
N1	46	27 (7.3%)	19 (5.1%)	
N2	77	46 (12.4%)	31 (8.4%)	
N3	8	4 (1.1%)	4 (1.1%)	
M-stage				0.657
M0	203	97 (45.5%)	105 (49.3%)	
M1	11	4 (1.9%)	7 (3.3%)	
Pathological stage				**0.004**
Stage I	4	0 (0.0%)	4 (1.0%)	
Stage II	130	53 (12.9%)	77 (18.7%)	
Stage III	142	74 (18.0%)	68 (16.5%)	
Stage IV	136	80 (19.4%)	56 (13.6%)	
Grade				**0.023**
High grade	390	202 (49.1%)	188 (45.7%)	
Low grade	21	5 (1.2%)	16 (3.9%)	

P < 0.05 are shown in bold.

using a Tanon (Shanghai, China) chemiluminescence image analysis system.

Xenograft Tumor Models

Forty 4-week male M-NSG mice were purchased from Model Biological Center Inc., (Shanghai, China), and the mice were randomly divided into 8 groups ($n = 5$ per group).

Subcutaneous xenograft tumor model: UMUC3 cells stably transfected with sh-ID2 or Control and EJ cells stably transfected with Control or OE-ID2 were collected and resuspended in saline. 100 μl of 5×10^7 density cells were mixed with 100 μl Matrigel (BD, United States) and injected subcutaneously into the mice. The length and width of the tumors were measured weekly and the tumor volume was calculated using the formula: volume (mm^3) = 0.5 × width^2 × length. Mice were sacrificed after 4 weeks, the subcutaneously transplanted tumors were excised, and the weight of each tumor was recorded. A portion of the tumor tissue was fixed in 10% buffered formalin and subjected to subsequent analysis.

In vivo lung metastasis model: Cell lines were constructed as described above in "Cell transfection." UMUC3 cells stably transfected with sh-ID2 or Control and EJ cells stably transfected

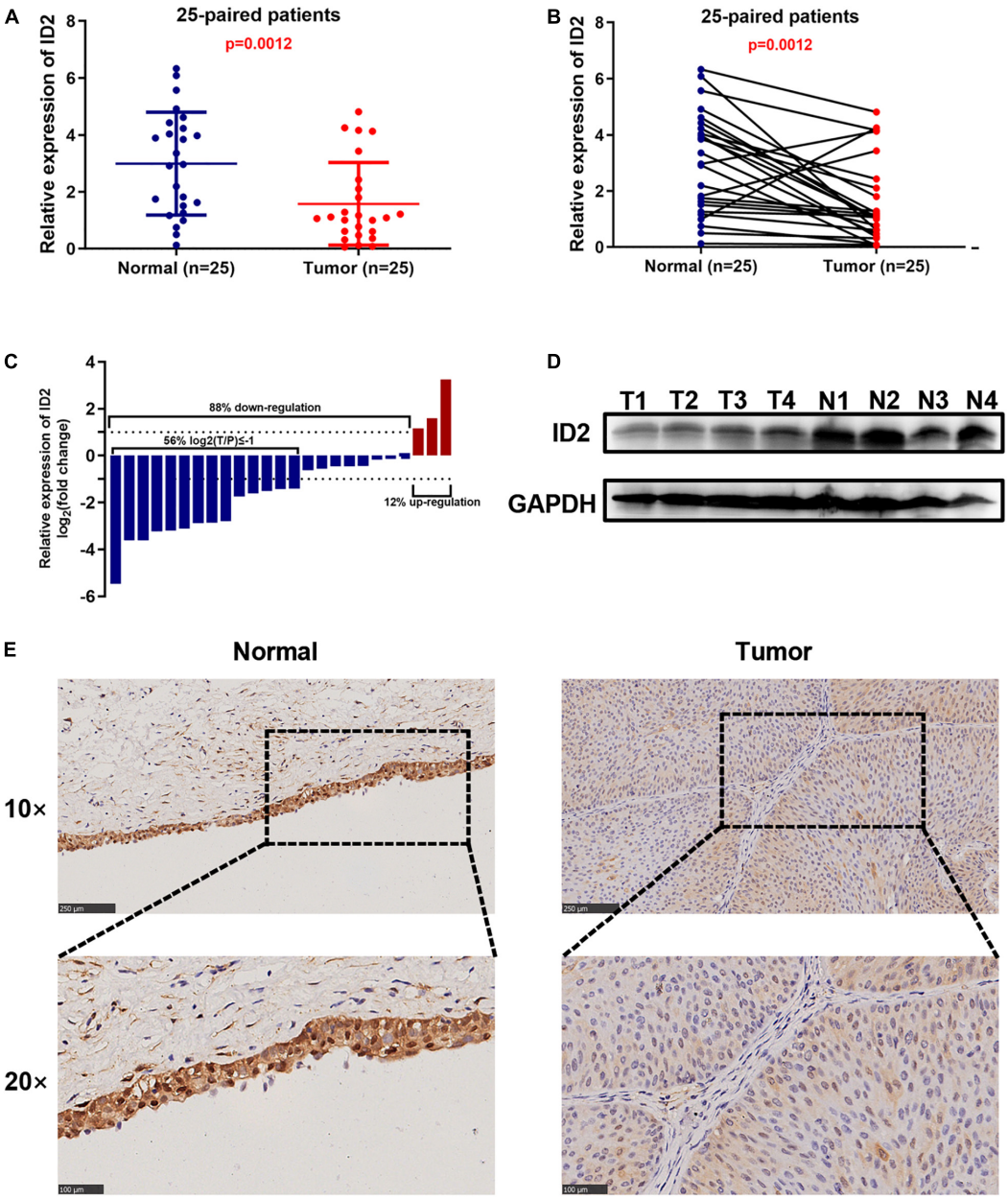

FIGURE 2 | ID2 is down-regulated in BCa clinical sample. **(A–D)** qRT-PCR **(A–C)** and western blot **(D)** analysis of ID2 expression levels in BCa tissues and paired normal tissues. **(E)** Representative IHC images showing ID2 staining in normal tissues (N) and BCa tumor (T) sections.

with Control or OE-ID2 were collected and resuspended in saline. 1×10^6 cells were injected from the tail vein of mice in a volume of 200 μl. Mice were executed after 4 weeks, lung tissue was excised, and fixed in 10% buffered formalin to observe the number of metastatic nodules in the lungs was observed using the *in vivo* imaging system (IVIS) imaging system (Calipers, Hopkinton, United States) for observation and subsequent analysis.

Haematoxylin and Eosin and Immunohistochemical Staining

Mice lung tissues were embedded in paraffin and sectioned at a thickness of 5μm, followed by H&E staining. Mice tumor tissues were fixed with 4% paraformaldehyde and embedded in paraffin after dehydration through ethanol solution. IHC was performed according to the previously described protocol (Mao et al., 2020), followed by recording images with a microscope (Leica Microsystems, Germany).

Statistical Analysis

The relationship between ID2 expression and various clinicopathological variables was examined using the chi-square test. SPSS 20.0 software (IBM, United States), GraphPad Prism 8.3 software (San Diego, United States), and R-Studio software (Boston, United States) were used for all statistical analyses. For all studies, $P < 0.05$ between groups were considered statistically significant.

RESULTS

ID2 Expression Correlates With Clinical Characteristics and Survival Rate in the Cancer Genome Atlas Database

To explore the expression of ID1, ID2, ID3, and ID4 in BCa, we first detected and analyzed their expression in the TCGA database. We analyzed their expression in 414 BCa tissues and 19 normal tissues, 19 BCa tissues and matched normal tissues, and found that ID2, ID3, and ID4 were downregulated in BCa tissues (**Figures 1A–D** and **Supplementary Figures 1H–J, O–Q**), while ID1 expression was not different (**Supplementary Figures 1A–C**). In addition, we also compared the expression of ID1, ID2, ID3, and ID4 in 28 normal samples from the GTEx combined TCGA database and 414 BCa samples from the TCGA database, and similarly found low expression of ID2, ID3 and ID4 (**Figure 1E** and **Supplementary Figures 1K,R**) and no difference in ID1 expression (**Supplementary Figure 1D**). Further survival analysis revealed that ID1 and ID2 expression were associated with overall survival (OS) (**Figure 1F** and **Supplementary Figure 1L**), disease specific survival (DSS) (**Figure 1G** and **Supplementary Figure 1M**), and progress free interval (PFI) (**Figure 1H** and **Supplementary Figure 1N**), while ID3 expression was not associated with survival (**Supplementary Figures 1E–G,S–U**). Subsequently, we examined the relationship between ID2 and clinical variables and found that ID2 expression correlated with TNM stage (**Figures 1I–K**), pathological stage (**Figure 1L**) and grade (**Figure 1M**) in TCGA patients. In addition, the chi-squared assay showed that ID2 expression correlated with T-stage, pathological stage and grade (**Table 1**). Moreover, receiver operating characteristic (ROC) curves were used to analyze the effectiveness of ID2 expression levels in distinguishing BCa tissue from normal tissue. The area under curve (AUC) of ID2 was 0.820 (**Figure 1N**), indicating that ID2 can be used as an ideal biomarker to distinguish BCa from normal tissue.

ID2 Is Down-Regulated in Bladder Cancer Clinical Sample

To further validate the conclusion that ID2 is downregulated expression in the TCGA database, we examined the ID2 mRNA expression levels in 25 paired BCa tissue samples by qRT-PCR. The results revealed that ID2 expression was low expression in tumor tissues (**Figures 2A–C**) and similar results were observed by western blotting (**Figure 2D**). The clinical and pathological characteristics of our patients are shown in **Table 2**, and we found that ID2 expression was associated with T-stage and M-stage. In addition, IHC results also showed that ID2 expression was significantly down-regulated in tumor tissues (**Figure 2E**).

ID2 Inhibits Proliferation, Migration, and Invasion of Bladder Cancer Cells *in vitro*

We first examined the expression of ID2 in BCa cell lines, and the results showed that ID2 was lowly expressed at both the mRNA level and protein level (**Figure 3A**). To investigate the biological role of ID2 in BCa cells, we designed siRNA against

TABLE 2 | The relationship between the expression of ID2 and various clinicopathological variables in our center.

Characteristics	Total	ID2 expression		*P*-value
		Low	High	
Total	25	12	13	
Age (years)				0.073
<70	13	4 (33.3)	9 (69.2)	
≥70	12	8 (66.7)	4 (30.8)	
Sex				0.035
Male	18	11 (91.7)	7 (53.8)	
Female	7	1 (8.3)	6 (46.2)	
T-stage				**0.019**
T1-T2	18	6 (50.0)	12 (92.3)	
T3-T4	7	6 (50.0)	1 (7.7)	
N-stage				0.114
N0	17	10 (83.3)	7 (53.8)	
N1/N2	8	2 (16.7)	6 (46.2)	
M-stage				**0.047**
M0	19	7 (58.3)	12 (92.3)	
M1	6	5 (41.7)	1 (7.7)	
Tumor size (cm)				0.543
<3	13	7 (58.3)	6 (46.2)	
≥3	12	5 (41.7)	7 (53.8)	

P < 0.05 are shown in bold.

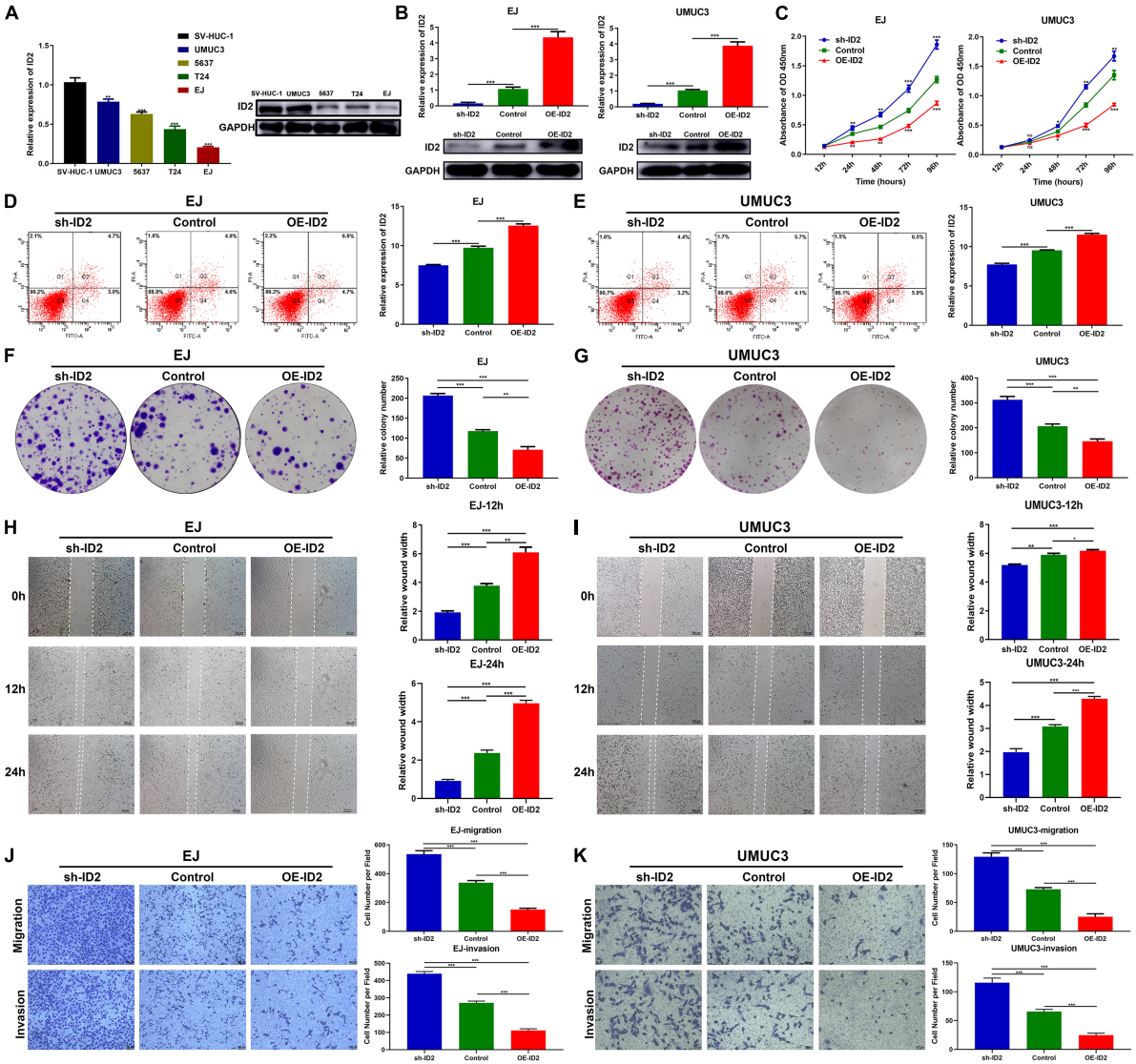

FIGURE 3 | ID2 inhibits proliferation, migration and invasion of BCa cells *in vitro*. **(A)** Relative expression of ID2 in SV-HUC-1 cell and BCa cell lines. **(B)** Expression of ID2 was confirmed by qRT-PCR in BCa cell lines EJ and UMUC3 transfected with sh-ID2, Control or OE-ID2. **(C)** CCK8 assay of cell proliferation capacity of EJ and UMUC3 cells after transfection with sh-ID2, Control, or OE-ID2. **(D,E)** Cell apoptosis assay were performed in EJ **(D)** and UMUC3 **(E)** cells after transfection with sh-ID2, Control or OE-ID2. **(F,G)** Colony formation assays were performed in EJ **(F)** and UMUC3 **(G)** cells after transfection with sh-ID2, Control, or OE-ID2. **(H,I)** Wound healing assays were performed in EJ **(H)** and UMUC3 **(I)** cells after transfection with sh-ID2, Control, or OE-ID2. **(J,K)** Transwell assays were performed in EJ **(J)** and UMUC3 **(K)** cells after transfection with sh-ID2, Control, or OE-ID2 (*$p < 0.05$, **$p < 0.01$, ***$p < 0.001$).

ID2 (si-ID2) and an overexpression plasmid (OE-ID2), which were transfected into EJ and UMUC3 cells. qRT-PCR showed that si-ID2 decreased ID2 expression, while transfection with OE-ID2 could upregulated ID2 expression levels (**Figure 3B**). Apoptosis assays showed that inhibition of ID2 expression inhibited apoptosis and overexpression promoted apoptosis in EJ and UMUC3 cells (**Figures 3D,E**). CCK-8 and colony formation assays showed that inhibition of ID2 significantly enhanced proliferation of EJ and UMUC3 cells, while overexpression of ID2 had the opposite effect (**Figures 3C,F,G**). In addition, wound healing and Transwell assays also showed that silencing ID2 enhanced the migration and invasion ability of EJ and UMUC3 cells, while overexpression of ID2 decreased the migration and invasion ability of the cells (**Figures 3H–K**).

ID2 Suppressed the Growth and Metastasis of Bladder Cancer Cells *in vivo*

To assess the effect of ID2 on BCa growth and metastasis *in vivo*, we designed subcutaneous xenograft tumor models and lung metastasis models. UMUC3 cells stably transfected with sh-ID2 and Control, and EJ cells stably transfected with Control and OE-ID2 were injected subcutaneously into M-NSG mice to

construct xenograft tumor models. As expected, after 4 weeks, the tumor volume and weight in the sh-ID2 group were higher than those in the control group, and the tumor volume and weight in the OE-ID2 group were smaller than those in the control group (**Figures 4A–C**). IHC assays showed that the expression of ID2 was significantly up-regulated in the OE-ID2 group and down-regulated in the sh-ID2 group compared to the Control group (**Figure 4D**).

In addition, the above-mentioned stable transfer cells were injected tail vein into mice. *In vitro* imaging and H&E staining results showed that the sh-ID2 group had more metastatic foci in the lungs of the mice, while the mice in the OE-ID2 group had essentially no metastatic foci (**Figures 4E,F**).

ID2 Regulated Bladder Cancer Progression via PI3K/AKT Signaling Pathway

To decipher the downstream-related pathways of ID2 in BCa progression, we constructed sh-ID2, NC-ID2, and OE-ID2 EJ stable transduction cell lines and sequenced the three cell lines at the transcriptional level (**Supplementary Table 2**). We first analyzed sh-ID2 and NC-ID2 and identified 18 down-regulated differentially expressed genes (DEGs) and 22 up-regulated DEGs (**Figures 5A–D**). Subsequent analysis of NC-ID2 and OE-ID2 revealed 22 genes with high expression and 27 genes with low expression (**Figures 5E–H**). Further analysis showed that 10 genes were co-variant (**Figures 5I,J**). We performed GO analysis and KEGG analysis on 10 genes and found that PI3K/AKT signaling pathway was significantly enriched (**Figures 5K,L** and **Supplementary Table 3**).

Subsequently, we examined the expression changes of PI3K/AKT signaling pathway related proteins (AKT and PI3K). Western blotting results showed that transfection of sh-ID2 could lead to decreased protein levels of ID2 and increased protein and mRNA levels of p-AKT and p-PI3K in EJ and UMUC3 cells (**Figures 6A–D**); transfection of OE-ID2 resulted in a significant increase in ID2 levels and decreased protein levels of p-AKT and p-PI3K in cells (**Figures 6A–D**). Through the above experiments, we demonstrated that ID2

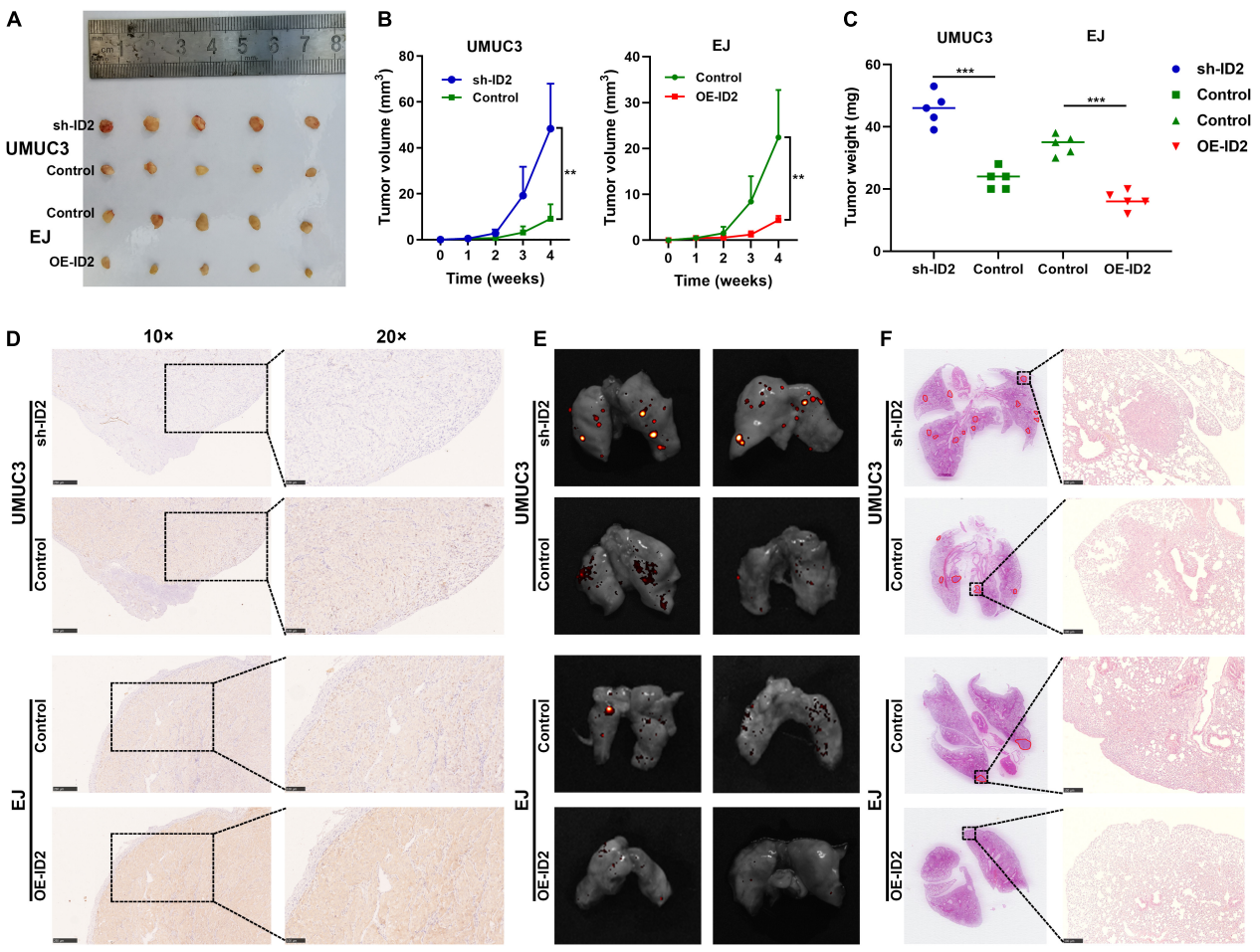

FIGURE 4 | ID2 suppressed the growth and metastasis of BCa cells *in vivo*. **(A)** Representative images of xenograft tumors in nude mice. **(B)** The growth curves of xenografts. **(C)** The tumor weight of xenografts. **(D)** IHC assay demonstrated the level of ID2 in pairs of tumors. **(E,F)** Representative *in vitro* imaging **(E)** and H&E images **(F)** of lung tissue sections (**$p < 0.01$, ***$p < 0.001$).

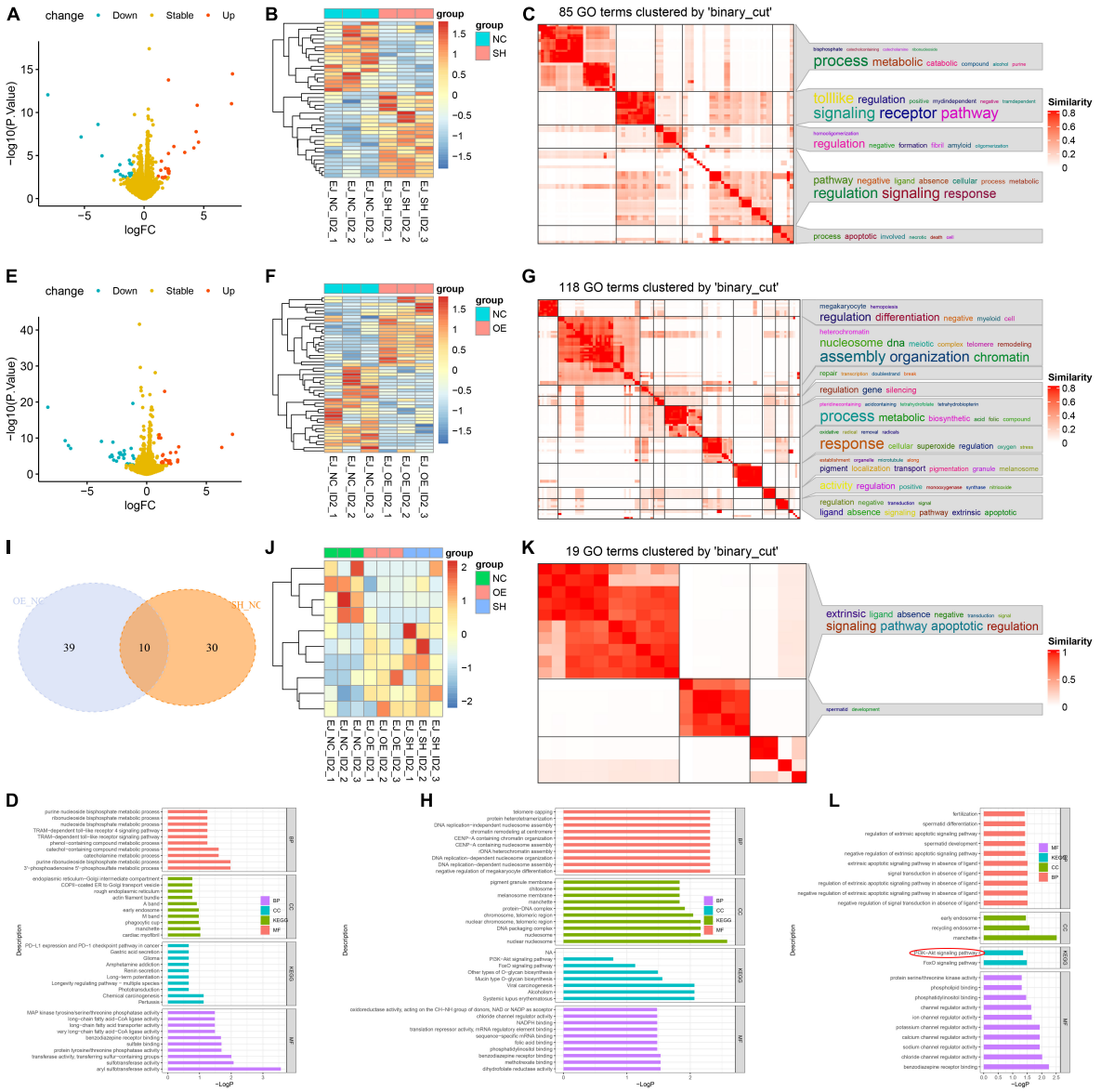

FIGURE 5 | ID2 regulated BCa progression via PI3K/AKT signaling pathway. **(A,B)** Volcano plot **(A)** and heatmap **(B)** of RNA-Seq analysis of NC-ID2 and sh-ID2 cells. **(C,D)** GO terms **(C)** and KEGG analysis **(D)** to detect differentially expressed genes. **(E,F)** Volcano plot **(E)** and heatmap **(F)** of RNA-Seq analysis of NC-ID2 and OE-ID2 cells. **(G,H)** GO terms **(G)** and KEGG analysis **(H)** to detect differentially expressed genes. **(I)** Venn diagrams show the number of genes with changes in NC-ID2 and sh-ID2, NC-ID2, and OE-ID2. **(J)** Heatmap of RNA-Seq analysis of sh-ID2, NC-ID2, and OE-ID2 cells. **(K,L)** GO terms **(K)** and KEGG analysis **(L)** to detect differentially expressed genes.

may be involved in BCa progression through PI3K/AKT signaling pathway.

DISCUSSION

In this study, we first examined the expression and prognostic value of four ID proteins in the TCGA BCa database. We found that ID2 was lowly expressed in BCa tumor tissues, ID2 expression correlated with TNM stage, grade and pathological stage, and that high ID2 expression was positively correlated with OS, DSS, and PFI. *In vivo* and *in vitro* functional experiments, we found that knockdown of ID2 promoted proliferation, migration, invasion and metastasis and inhibited apoptosis of BCa cells, while overexpression of ID2 significantly inhibited cell proliferation, migration, invasion and metastasis and promoted apoptosis. Mechanistically, we demonstrated that ID2 can be involved in BCa progression and metastasis through the PI3K/AKT signaling pathway.

Abnormal expression of many molecules or aberrant activation of signaling pathways can lead to the development, invasion and metastasis of BCa. Among them, PI3K/AKT

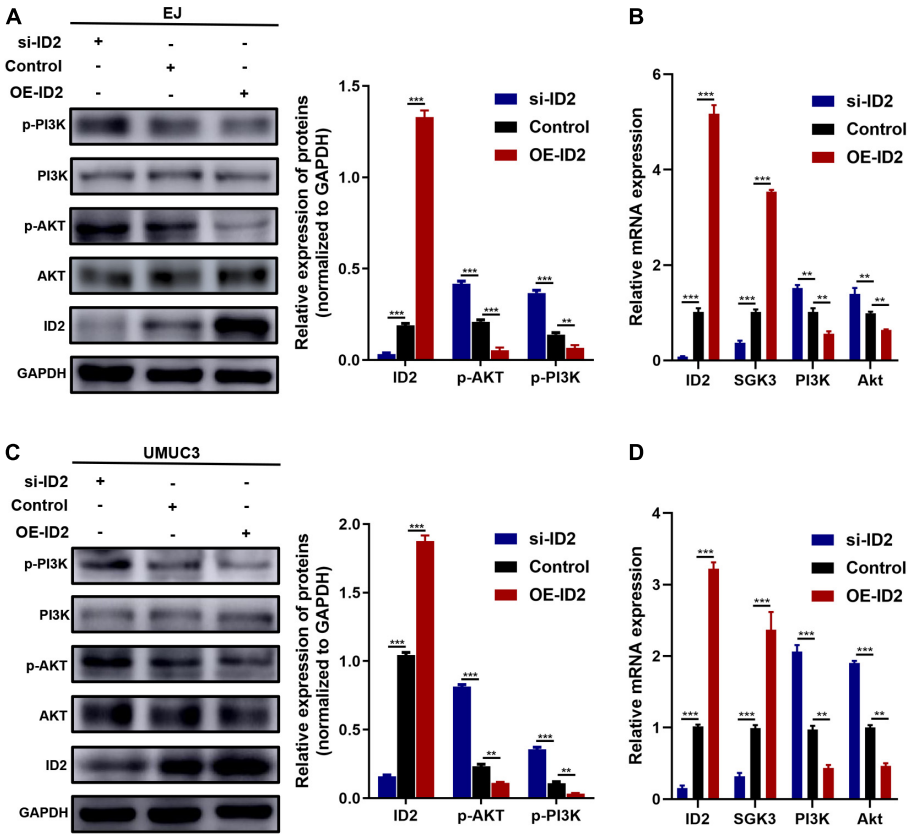

FIGURE 6 | Protein and mRNA changes in EJ and UMUC3 cells after transfection with si-ID2, NC-ID2 and OE-ID2. **(A,B)** Protein and mRNA changes in EJ cells. **(C,D)** Protein and mRNA changes in UMUC3 cell (**$p < 0.01$, ***$p < 0.001$).

signaling pathway is an important signaling pathway that is widely present in cells and can regulate cell growth, proliferation, apoptosis, metabolism, tumor invasion, and metastasis (Petrulea et al., 2015). This signaling pathway is abnormally activated in some BCa patients and is associated with the occurrence, development and prognosis of BCa (Sathe and Nawroth, 2018).

ID family proteins are members of the bHLH transcription factor family, and their negative regulatory role in the activation of bHLH transcription factors, which can inhibit cell differentiation by suppressing the binding of bHLH transcription factors to DNA and other tissue-specific bHLH (Kee, 2009). ID family proteins include ID1, ID2, ID3, and ID4, which are involved in the regulation of cell growth processes, including cell growth, differentiation, and death (Norton, 2000). ID family genes have been shown to be extensively involved in the development of a variety of cells and tissues in the body and have been associated with cancer (Ruzinova and Benezra, 2003; Wang and Baker, 2015).

Aberrant expression levels of ID2 protein have been reported in a variety of cancers, such as non-small cell lung cancer, breast cancer, esophageal squamous cell carcinoma (ESCC), and colorectal cancer (Yuen et al., 2007; Gray et al., 2008; Rollin et al., 2009; Liu et al., 2019). Yuen et al. (2007) found that ID1 and ID2 are highly expressed in ESCC and are markers of metastasis and prognosis in ESCC. Stighall et al. (2005) found that high ID2 protein expression was associated with a good prognosis in patients with primary breast cancer and reduced the invasiveness of breast cancer cells. In addition, Gray et al. (2008) found that ID2 protein was highly expressed in colorectal cancer samples and that intraperitoneal injection of ID2 small interfering RNA reduced the growth of colorectal cancer in mouse liver, suggesting that ID2 is a potential drug target for tumor therapy. A study of ID2 in bladder cancer found that ID2 was highly expressed in BCa and regulated by H19 (Luo et al., 2013). We speculate that there may be two reasons for the different findings in the present study and the study by Luo et al. (2013): first, it may be related to the tumor heterogeneity of bladder cancer (Chen et al., 2015; Warrick et al., 2019); second, patients who received preoperative chemotherapy or radiotherapy were excluded from the present study, and there were no relevant exclusion criteria for sample collection in the study by Luo et al. (2013). It has been found that treatment of human lung cancer NCI-H460 cells with an external drug (curcumin) can lead to high expression of ID1, ID2, and ID3 (Chiang et al., 2015). In the present study, we demonstrated that ID2 was significantly downregulated in BCa tissues at the mRNA level and protein level through the TCGA BCa database and clinical data from our center, high ID2 expression was negatively

associated with tumor stage and positively correlated with overall survival, DSS and PFI. Furthermore, ID2 mechanistically inhibits BCa progression and metastasis through the PI3K/AKT signaling pathway.

CONCLUSION

We found that ID2 expression was downregulated in BCa tissues and cell lines, and that low ID2 expression was associated with poor prognosis. ID2 could be a novel biomarker for BCa, and this signaling axis could be a potential therapeutic target for BCa.

DATA AVAILABILITY STATEMENT

The datasets presented in this study can be found in online repositories. The names of the repository/repositories and accession number(s) can be found in the article/ **Supplementary Material**.

ETHICS STATEMENT

This study was approved by the Ethics Committee of Shanghai Tenth People's Hospital of Tongji University (SHSY-IEC-4.1/19-120/01). The patients/participants provided their written informed consent to participate in this study. Written informed consent was obtained from the individual(s) for the publication of any potentially identifiable images or data included in this article.

AUTHOR CONTRIBUTIONS

WM, MC, JG, and ML designed the research. WM, KW, and SS performed the research, wrote the manuscript, and analyzed the results. WM, JW, MC, JG, and ML edited the manuscript and provided critical comments. All authors read and approved the final manuscript.

FUNDING

This work was supported by the Jiangsu Provincial Key Research and Development Program (BE2019751), the Natural Science Foundation of Shanghai (17ZR1421800), the Shanghai Chongming District Science and Technology Commission (CKY2019-21), the Scientific Research Foundation of Graduate School of Southeast University (YBPY2173), and the Postgraduate Research and Practice Innovation Program of Jiangsu Province (KYCX21_0156).

SUPPLEMENTARY MATERIAL

The Supplementary Material for this article can be found online at: https://www.frontiersin.org/articles/10.3389/fcell.2021.738364/full#supplementary-material

Supplementary Figure 1 | Expression of ID1, ID3, and ID4 in the TCGA database. **(A)** ID1 expression profile across all tumor samples and paired normal tissues. **(B)** The difference expression of ID1 in BCa tissues and adjacent normal tissues. **(C)** The difference expression of ID1 in BCa tissues and paired normal tissues. **(D)** The difference expression of ID1 in normal tissues of GTEx combined with TCGA and BCa tissues of TCGA. (**E–G**) Overall survival **(E)**, disease-specific survival **(F)**, and progress free interval **(G)** curve of BCa patients with low (n = 207) and high (n = 207) ID1 expression. **(H)** ID3 expression profile across all tumor samples and paired normal tissues. **(I)** The difference expression of ID3 in BCa tissues and adjacent normal tissues. **(J)** The difference expression of ID3 in BCa tissues and paired normal tissues. **(K)** The difference expression of ID3 in normal tissues of GTEx combined with TCGA and BCa tissues of TCGA. **(L–N)** Overall survival **(L)**, disease-specific survival **(M)** and progress free interval **(N)** curve of BCa patients with low (n = 207) and high (n = 207) ID3 expression. **(O)** ID4 expression profile across all tumor samples and paired normal tissues. **(P)** The difference expression of ID4 in BCa tissues and adjacent normal tissues. **(Q)** The difference expression of ID4 in BCa tissues and paired normal tissues. **(R)** The difference expression of ID4 in normal tissues of GTEx combined with TCGA and BCa tissues of TCGA. **(S–U)** Overall survival **(S)**, disease-specific survival **(T)**, and progress free interval **(U)** curve of BCa patients with low (n = 207) and high (n = 207) ID4 expression.

Supplementary Table 1 | Antibodies list.

Supplementary Table 2 | RNA sequencing data.

Supplementary Table 3 | GO analysis and KEGG analysis results.

REFERENCES

Benezra, R., Davis, R. L., Lockshon, D., Turner, D. L., and Weintraub, H. (1990). The protein Id: a negative regulator of helix-loop-helix DNA binding proteins. *Cell* 61, 49–59. doi: 10.1016/0092-8674(90)90214-y

Chen, C., Qi, X. J., Cao, Y. W., Wang, Y. H., Yang, X. C., Shao, S. X., et al. (2015). Bladder tumor heterogeneity: the impact on clinical treatment. *Urol. Int.* 95, 1–8. doi: 10.1159/000370165

Chiang, I. T., Wang, W. S., Liu, H. C., Yang, S. T., Tang, N. Y., and Chung, J. G. (2015). Curcumin alters gene expression-associated DNA damage, cell cycle, cell survival and cell migration and invasion in NCI-H460 human lung cancer cells in vitro. *Oncol. Rep.* 34, 1853–1874. doi: 10.3892/or.2015.4159

Dy, G. W., Gore, J. L., Forouzanfar, M. H., Naghavi, M., and Fitzmaurice, C. (2017). Global burden of urologic cancers, 1990-2013. *Eur. Urol.* 71, 437–446. doi: 10.1016/j.eururo.2016.10.008

Fong, S., Debs, R. J., and Desprez, P. Y. (2004). Id genes and proteins as promising targets in cancer therapy. *Trends Mol. Med.* 10, 387–392. doi: 10.1016/j.molmed.2004.06.008

Garcia-Donas, J., Font, A., Perez-Valderrama, B., Virizuela, J. A., Climent, M. A., Hernando-Polo, S., et al. (2017). Maintenance therapy with vinflunine plus best supportive care versus best supportive care alone in patients with advanced urothelial carcinoma with a response after first-line chemotherapy (MAJA; SOGUG 2011/02): a multicentre, randomised, controlled, open-label, phase 2 trial. *Lancet Oncol.* 18, 672–681a.

Gray, M. J., Dallas, N. A., Van Buren, G., Xia, L., Yang, A. D., Somcio, R. J., et al. (2008). Therapeutic targeting of Id2 reduces growth of human colorectal carcinoma in the murine liver. *Oncogene* 27, 7192–7200. doi: 10.1038/onc.2008.356

Kee, B. L. (2009). E and ID proteins branch out. *Nat. Rev. Immunol.* 9, 175–184. doi: 10.1038/nri2507

Liu, Y., Pandey, P. R., Sharma, S., Xing, F., Wu, K., Chittiboyina, A., et al. (2019). ID2 and GJB2 promote early-stage breast cancer progression by regulating cancer stemness. *Breast Cancer Res. Treat.* 175, 77–90. doi: 10.1007/s10549-018-05126-3

Luo, K., Geng, J., Zhang, Q., Xu, Y., Zhou, X., Huang, Z., et al. (2019). LncRNA CASC9 interacts with CPSF3 to regulate TGF-beta signaling in colorectal cancer. *J. Exp. Clin. Cancer Res.* 38:249.

Luo, M., Li, Z., Wang, W., Zeng, Y., Liu, Z., and Qiu, J. (2013). Upregulated H19 contributes to bladder cancer cell proliferation by regulating ID2 expression. *FEBS J.* 280, 1709–1716.

Mao, W., Huang, X., Wang, L., Zhang, Z., Liu, M., Li, Y., et al. (2019). Circular RNA hsa_circ_0068871 regulates FGFR3 expression and activates STAT3 by targeting miR-181a-5p to promote bladder cancer progression. *J. Exp. Clin. Cancer Res.* 38:169.

Mao, W., Liu, S., Wang, K., Wang, M., Shi, H., Liu, Q., et al. (2020). Cystatin C in evaluating renal function in ureteral calculi hydronephrosis in adults. *Kidney Blood Press. Res.* 45, 109–121. doi: 10.1159/000504441

Massari, M. E., and Murre, C. (2000). Helix-loop-helix proteins: regulators of transcription in eucaryotic organisms. *Mol. Cell Biol.* 20, 429–440. doi: 10.1128/mcb.20.2.429-440.2000

Norton, J. D. (2000). ID helix-loop-helix proteins in cell growth, differentiation and tumorigenesis. *J. Cell Sci.* 113(Pt 22), 3897–3905. doi: 10.1242/jcs.113.22.3897

Perk, J., Iavarone, A., and Benezra, R. (2005). Id family of helix-loop-helix proteins in cancer. *Nat. Rev. Cancer.* 5, 603–614. doi: 10.1038/nrc1673

Petrulea, M. S., Plantinga, T. S., Smit, J. W., Georgescu, C. E., and Netea-Maier, R. T. (2015). PI3K/Akt/mTOR: a promising therapeutic target for non-medullary thyroid carcinoma. *Cancer Treat. Rev.* 41, 707–713. doi: 10.1016/j.ctrv.2015.06.005

Ranzi, A. D., da Silva, J. N., Graziottin, T. M., Annels, N., and Bica, C. G. (2017). Immunohistochemistry biomarkers in nonmuscle invasive bladder cancer. *Appl. Immunohistochem. Mol. Morphol.* 25, 178–183. doi: 10.1097/pai.0000000000000280

Robertson, A. G., Kim, J., Al-Ahmadie, H., Bellmunt, J., Guo, G., Cherniack, A. D., et al. (2017). Comprehensive molecular characterization of muscle-invasive bladder cancer. *Cell* 171, 540–556.e25.

Rollin, J., Blechet, C., Regina, S., Tenenhaus, A., Guyetant, S., and Gidrol, X. (2009). The intracellular localization of ID2 expression has a predictive value in non small cell lung cancer. *PLos One* 4:e4158. doi: 10.1371/journal.pone.0004158

Ruzinova, M. B., and Benezra, R. (2003). Id proteins in development, cell cycle and cancer. *Trends Cell Biol.* 13, 410–418. doi: 10.1016/s0962-8924(03)00147-8

Sathe, A., and Nawroth, R. (2018). Targeting the PI3K/AKT/mTOR pathway in bladder cancer. *Methods Mol. Biol.* 1655, 335–350. doi: 10.1007/978-1-4939-7234-0_23

Stighall, M., Manetopoulos, C., Axelson, H., and Landberg, G. (2005). High ID2 protein expression correlates with a favourable prognosis in patients with primary breast cancer and reduces cellular invasiveness of breast cancer cells. *Int. J. Cancer* 115, 403–411. doi: 10.1002/ijc.20875

Sung, H., Ferlay, J., Siegel, R. L., Laversanne, M., Soerjomataram, I., Jemal, A., et al. (2021). Global cancer statistics 2020: GLOBOCAN Estimates of incidence and mortality worldwide for 36 cancers in 185 countries. *CA Cancer J. Clin.* 71, 209–249. doi: 10.3322/caac.21660

Volpert, O. V., Pili, R., Sikder, H. A., Nelius, T., Zaichuk, T., Morris, C., et al. (2002). Id1 regulates angiogenesis through transcriptional repression of thrombospondin-1. *Cancer Cell* 2, 473–483. doi: 10.1016/s1535-6108(02)00209-x

Wang, L. H., and Baker, N. E. E. (2015). Proteins and ID proteins: helix-loop-helix partners in development and disease. *Dev. Cell* 35, 269–280. doi: 10.1016/j.devcel.2015.10.019

Warrick, J. I., Sjodahl, G., Kaag, M., Raman, J. D., Merrill, S., Shuman, L., et al. (2019). Intratumoral heterogeneity of bladder cancer by molecular subtypes and histologic variants. *Eur. Urol.* 75, 18–22. doi: 10.1016/j.eururo.2018.09.003

Witjes, J. A., Bruins, H. M., Cathomas, R., Comperat, E. M., Cowan, N. C., Gakis, G., et al. (2021). European association of urology guidelines on muscle-invasive and metastatic bladder cancer: summary of the 2020 guidelines. *Eur. Urol.* 79, 82–104. doi: 10.1016/j.eururo.2020.03.055

Yuen, H. F., Chan, Y. P., Chan, K. K., Chu, Y. Y., Wong, M. L., Law, S. Y., et al. (2007). Id-1 and Id-2 are markers for metastasis and prognosis in oesophageal squamous cell carcinoma. *Br. J. Cancer* 97, 1409–1415. doi: 10.1038/sj.bjc.6604035

Zhang, S., Sun, K., Zheng, R., Zeng, H., and He, J. (2020). Cancer incidence and mortality in China, 2015. *J. Natl. Cancer Center* 1, 2–11.

Conflict of Interest: The authors declare that the research was conducted in the absence of any commercial or financial relationships that could be construed as a potential conflict of interest.

Publisher's Note: All claims expressed in this article are solely those of the authors and do not necessarily represent those of their affiliated organizations, or those of the publisher, the editors and the reviewers. Any product that may be evaluated in this article, or claim that may be made by its manufacturer, is not guaranteed or endorsed by the publisher.

frontiers in Cell and Developmental Biology

ORIGINAL RESEARCH
published: 03 December 2021
doi: 10.3389/fcell.2021.764125

Multi-Omics Analysis of Novel Signature for Immunotherapy Response and Tumor Microenvironment Regulation Patterns in Urothelial Cancer

Guangdi Chu[1†], *Wenhong Shan*[2†], *Xiaoyu Ji*[3], *Yonghua Wang*[1*] *and Haitao Niu*[1*]

[1]*Department of Urology, The Affiliated Hospital of Qingdao University, Qingdao, China,* [2]*Department of Nephrology, Qingdao Central Hospital, The Second Clinical Medical College of Qingdao University, Qingdao, China,* [3]*Department of Obstetrics and Gynecology, The Affiliated Hospital of Qingdao University, Qingdao, China*

OPEN ACCESS

Edited by:
Yongwen Luo,
Wuhan University, China

Reviewed by:
Benyi Li,
University of Kansas Medical Center, United States
Jinhui Liu,
Nanjing Medical University, China

***Correspondence:**
Haitao Niu
niuht0532@126.com
Yonghua Wang
doctorwangyonghua@163.com

[†]*These authors have contributed equally to this work*

Specialty section:
This article was submitted to Molecular and Cellular Pathology, a section of the journal Frontiers in Cell and Developmental Biology

Received: *25 August 2021*
Accepted: *17 November 2021*
Published: *03 December 2021*

Citation:
Chu G, Shan W, Ji X, Wang Y and Niu H (2021) Multi-Omics Analysis of Novel Signature for Immunotherapy Response and Tumor Microenvironment Regulation Patterns in Urothelial Cancer. Front. Cell Dev. Biol. 9:764125. doi: 10.3389/fcell.2021.764125

The tumor microenvironment (TME) is mainly composed of tumor cells, tumor-infiltrating immune cells, and stromal components. It plays an essential role in the prognosis and therapeutic response of patients. Nonetheless, the TME landscape of urothelial cancer (UC) has not been fully elucidated. In this study, we systematically analyzed several UC cohorts, and three types of TME patterns (stromal-activation subtype, immune-enriched subtype and immune-suppressive subtype) were defined. The tumor microenvironment signature (TMSig) was constructed by modified Lasso penalized regression. Patients were stratified into high- and low-TMSig score groups. The low-score group had a better prognosis ($p < 0.0001$), higher M1 macrophage infiltration ($p < 0.01$), better response to immunotherapy ($p < 0.05$), and more similar molecular characteristics to the luminal (differentiated) subtype. The accuracy of the TMSig for predicting the immunotherapy response was also verified in three independent cohorts. We highlighted that the TMSig is an effective predictor of patient prognosis and immunotherapy response. Quantitative evaluation of a single sample is valuable for us to combine histopathological and molecular characteristics to comprehensively evaluate the status of the patient. Targeted macrophage treatment has great potential for the individualized precision therapy of UC patients.

Keywords: tumor microenvironment, immunotherapy, urothelial cancer, macrophage, immune checkpoint

INTRODUCTION

Urothelial carcinoma of the bladder comprises two disease entities with different molecular characteristics and clinical outcomes (Knowles and Hurst, 2015). It is one of the most common malignant tumors of the genitourinary system, and it was estimated that there will be 83,730 new cases and 17,200 deaths worldwide in 2021 (Siegel et al., 2021). Non-muscle invasive bladder cancer (NMIBC) accounts for approximately 70% of newly diagnosed bladder cancers and comprises different entities, including carcinoma *in situ* (CIS), noninvasive nipple tumors, and papillary tumors invading the lamina propria. The overall survival (OS) rate of patients with NMIBC has been approximately 90% for 5 years. However, approximately 15 to 20% of NMIBC progresses to muscle

invasive bladder cancer (MIBC), and CIS and advanced papillomas are more likely to progress to MIBC than low-grade papillomas. MIBC refers to tumor invasion of the detrusor, the prognosis of it is poor. It easily metastasizes and the determination of treatment is complex and difficult (Knowles and Hurst, 2015; Dinney et al., 2004; Kamat et al., 2016; Siegel et al., 2018; Magers et al., 2019; Patel et al., 2020).

Over the past few decades, cancer treatment has undergone revolutionary changes, from traditional chemotherapy and radiation-targeting of tumors to antibody-based immunotherapy. This antibody-based therapy can more accurately regulate the immune response to tumors. The clinical treatment for metastatic urothelial carcinoma has also changed dramatically due to recent immunotherapy developments (Li et al., 2019a; Powles et al., 2020). Immunotherapy with immune checkpoint blockades, such as those targeting PD-1/PD-L1 and CTLA-4, has shown amazing clinical benefit in a small number of patients who achieve a persistent response. However, the clinical efficacy in most patients is small or nonexistent, far from meeting clinical needs (Topalian et al., 2012).

Traditional cognition holds that tumor progression is caused only by alterations in the genetic or epigenetic characteristics of tumor cells. However, with the gradual deepening of research, it has become clear that the TME also plays a key role in the growth and survival of tumor cells (Zhang et al., 2020a). Tumor cells can not only adapt and survive in such environments but also evade the detection and elimination by the host immune surveillance system by disguising themselves as normal cells. It can also induce various biological behavior changes by directly and indirectly interacting with other TME components, inducing processes such as cell proliferation, immune tolerance, and angiogenesis (Zhang et al., 2020a; Zhang et al., 2020b). Determining the status of TME at the time of diagnosis can help determine their response to immunotherapy (Rosenberg et al., 2016) and provide information on the benefit of chemotherapy (Jiang et al., 2018). The changes in the infiltration levels of $CD8^+$ T cells, $CD4^+$ T cells and tumor-associated macrophages in the TME are related to the prognosis of a variety of malignant tumors, including urothelial carcinoma, melanoma, lung cancer, breast cancer and gastric cancer (Turley et al., 2015; Nishino et al., 2017; Mariathasan et al., 2018; Zeng et al., 2019). Increasing evidence has confirmed the clinicopathological significance of TME infiltration for predicting patient prognosis and therapeutic responses. However, the comprehensive landscape of the TME in UC has not been fully elucidated up to now.

In this study, we comprehensively evaluated the TME pattern by integrating multi-omics data from multiple cohorts. The TME phenotype was associated with the genomic, clinical, and pathological features of UC and a scoring scheme was established to quantify the immune status of a single sample. The TMSig was constructed by modified Lasso penalized regression and could serve as a robust predictor of patient prognosis and immunotherapy response.

MATERIALS AND METHODS

We used five urothelial cancer cohorts were used in this study, including the IMvigor210 cohort (Balar et al., 2017), the TCGA-BLCA cohort (Robertson et al., 2017), the GSE32548 cohort (Lindgren et al., 2012), the GSE48075 cohort (Choi et al., 2014), and the UTUC cohort (Su et al., 2021). The TMSig constructed in the current study was assessed for prognostic ability in all five independent cohorts and the combined cohort. We also obtained pretreatment tumor expression profiles from three cohorts receiving immunotherapy to examine the response to immunotherapy in high- and low-scoring populations. Expression profile data for human cancer cell lines (CCL) data was from the Broad Institute Cancer Cell Line Encyclopedia (CCLE) (Ghandi et al., 2019). In addition, molecular and drug sensitivity data from two pharmacogenomic datasets (CTRP and PRISM) (Basu et al., 2013; Yu et al., 2016) of hundreds of CCLs were used to estimate drug response in clinical samples.

Additional detailed methodological descriptions, including the data preprocessing process, assessment of immune cell infiltration levels, identification of TME regulatory patterns, biofunctional analysis, TMSig construction process and evaluation of clinical applicability, clinical cohort drug sensitivity assessment, and statistical analysis were described in detail in **Supplementary Materials and Methods**.

RESULTS

The Landscape of TME Immune Cell Infiltration of Urothelial Cancer and the Identification of TME Patterns

An overview of our research is shown in **Figure 1A**. First, we systematically constructed a landscape of the TME immune cell network that comprehensively demonstrated the interactions between immune cells (**Supplementary Figure S1A**). Then, CIBERSORT algorithms were performed to quantify the infiltration levels of immune cells in UC tissues (**Supplementary Table S1**). According to the immune cell infiltration data and clinical information of 348 patients (**Supplementary Table S2**), we performed unsupervised clustering to classify the UC patients into three distinct subtypes (**Figure 1B**), including 62 patients in TME-ClusterA, 137 patients in TME-ClusterB, and 149 patients in TME-ClusterC (**Supplementary Figure S1B**). And there were significant differences in prognosis outcomes among these clusters. The TME-ClusterB exhibited a prominent survival advantage, while the prognosis of patients in TME-ClusterA was the worst (log-rank test, $p = 0.01$, **Figure 1C**). And the distribution of immune cell infiltration in the IMvigor210 cohort was shown in **Figure 1D**. In addition, we also performed CIBERSORT analysis in The Cancer Genome Atlas (TCGA) cohort and used the same parameters for consistent clustering. We found that the TCGA cohort could also be divided into three categories, and also had a significant difference in prognosis among three categories (log-rank test, $p = 0.00052$,

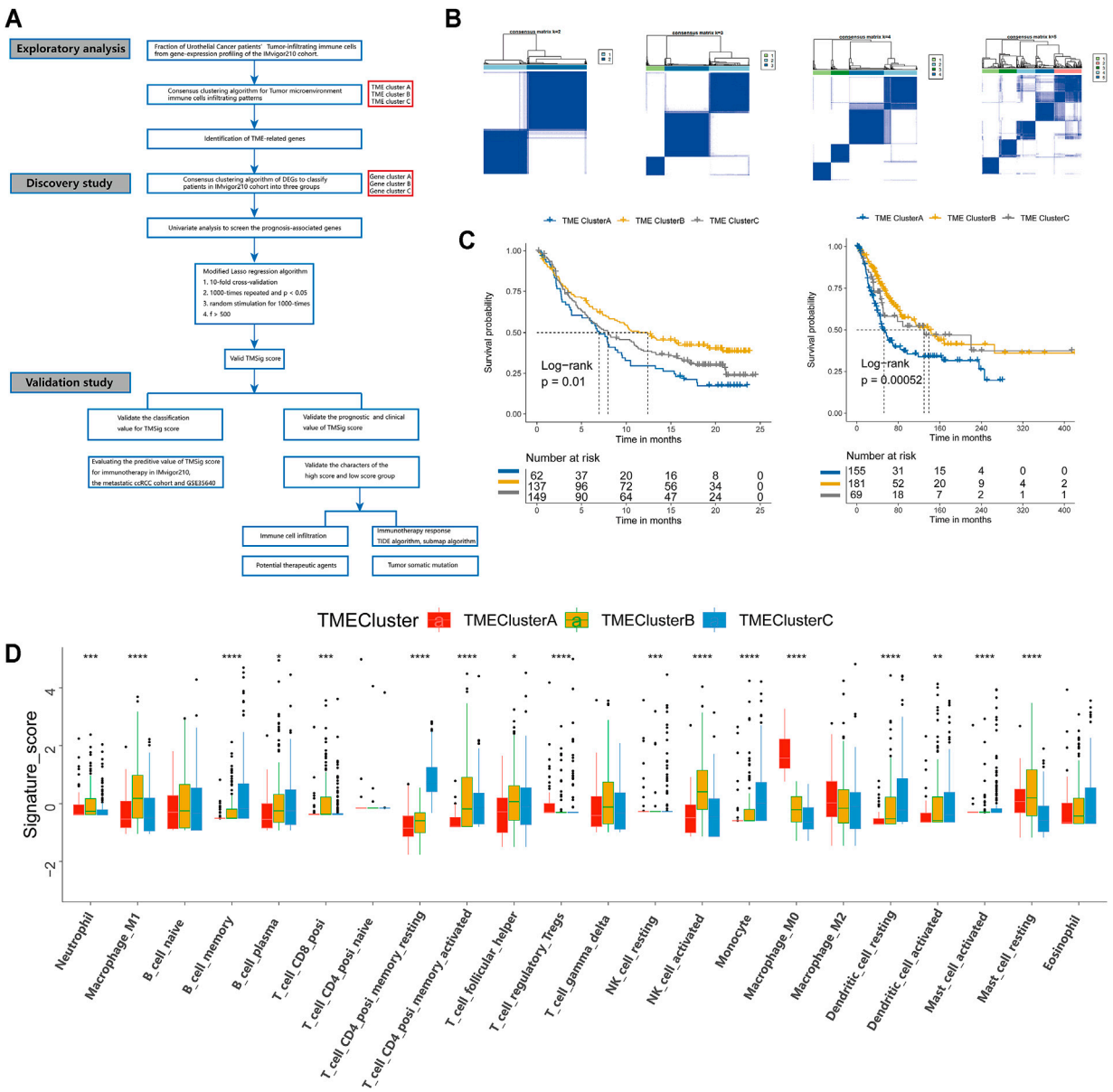

FIGURE 1 | Landscape of the TME in urothelial cancer and characteristics of TME subtypes. **(A)** The overview of study design. **(B)** Consensus matrixes of all patients with urothelial cancer for each k (k = 2–5), displaying the clustering stability using 1,000 iterations of hierarchical clustering. **(C)** Kaplan-Meier curves for overall survival (OS) of urothelial cancer patients from the IMvigor210 cohort with the TME patterns. **(D)** Immune infiltration cells expressed in TMEclusters. The range of *p* values are labeled above each boxplot with asterisks (**p* < 0.05, ***p* < 0.01, ****p* < 0.001, *****p* < 0.0001). **(E)** Kaplan Meier curves for overall survival (OS) of urothelial cancer patients from the TCGA cohort with the TME patterns.

Figure 1E), which further indicates the rationality of stratifying urothelial cancer patients according to TME characteristics. Interestingly, we found that in the TCGA cohort, there was a partial overlap in the survival curves between ClusterB and ClusterC, which is most likely due to a batch effect between these two cohorts. And the main conclusion that ClusterB has the best prognosis and ClusterA has the worst prognosis obtained by clustering is not affected.

Immune-associated cells could reflect the characteristics of individual immune microenvironment to a certain extent, and the immune checkpoint is also considered to be an important factor in predicting the response to immunotherapy. The Kaplan-Meier analysis we performed also showed that patients with different levels of immune cell infiltration and immune checkpoint expression had significant difference in clinical prognosis (**Supplementary Figure S2**). In order to explore the characteristics of patients in different patterns, we carried out a detailed comparison of them. The expression levels of $CD8^+$ effector T cells and immune checkpoints in patients of TME-ClusterB were higher than those in patients in the other clusters

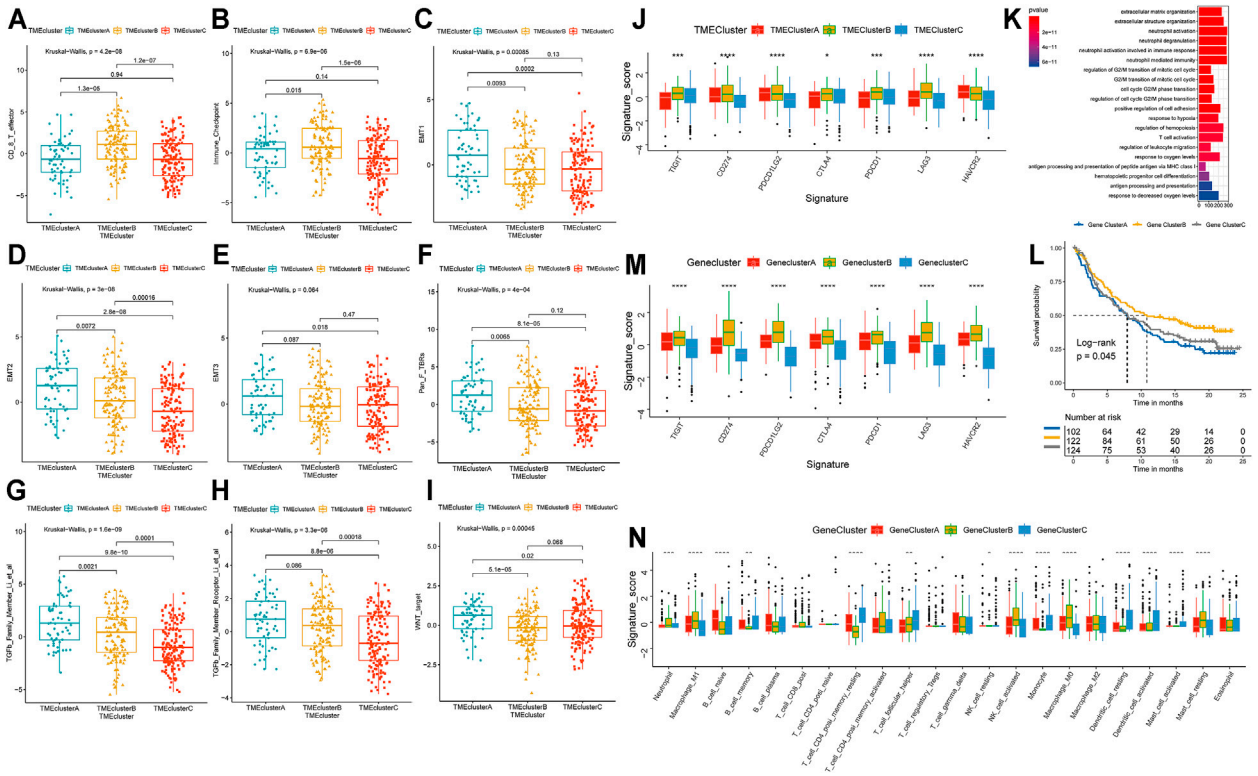

FIGURE 2 | Molecular characterization of TME-Clusters and identification of Gene-Cluster. **(A)** $CD8^+$T cell effector, **(B)** Immune checkpoint signature, **(C–E)** EMT-related signature, **(F)**. Pan_F_TBRs signature, **(G)** TGFb Family Member signature, **(H)** TGFb Family Member Receptor signature, **(I)** WNT target signature. **(J)** Immune checkpoints expression in TME-Clusters. **(K)** GO enrichment analysis of the TME-related genes. **(L)** Kaplan–Meier curves for Gene-Clusters. **(M)** Immune checkpoints expression in Gene-Clusters. **(N)** Immune infiltration cells expressed in Gene-Clusters. The range of *p* values are labeled above each boxplot with asterisks (*p < 0.05, **p < 0.01, ***p < 0.001, ****p < 0.0001).

(p < 0.05) (**Figures 2A,B**). These results strongly imply that patients in TME-ClusterB may be more likely to benefit from immunotherapy, which is consistent with the favorable prognosis in TME-ClusterB patients. The high level of immune-associated cell infiltration level also indicated that this cluster may be associated with multiple immune-related responses or activities and could be identified as immune-enriched subtype. TME-ClusterA was associated with the activation of epithelial-mesenchymal transition (EMT), the transforming growth factor-β (TGF-β), and Wnt signaling pathways (**Figures 2C–I**). The expression of specific immune checkpoints was also lower in this cluster (**Figure 2J**). The patients in this cluster had the worst prognosis, and the infiltration levels of T regulatory cells and M0 and M2 macrophages in this cluster were significantly higher than those in other clusters. Based on these characteristics, this cluster could be identified as the stromal-activation subtype. Interestingly, we also observed abundant immune cell infiltration in TME-ClusterC, such as memory B cells, plasma cells, $CD4^+$ memory resting T cells, monocytes, resting dendritic cells, activated dendritic cells, activated mast cells, and eosinophils, but the relative abundance of immune cells did not significantly change the prognosis of these patients, and their powerful antitumor effect was suppressed. So, we defined this group as the immune-suppressive subtype.

Identification of TME-Cluster Related Differentially Expressed Genes (DEGs) and Functional Analysis

To clarify the unique biological role of each cluster in the TME, we performed a differential expression analysis with the limma package. Each cluster was compared with the other clusters in the cohort, and a total of 7,996 DEGs were identified (**Supplementary Figure S3A and Supplementary Table S3**). Based on these DEGs, the GSVA package was used to analyze the specific enrichment pathways of each cluster (**Supplementary Table S4**). We found that TME-ClusterA was significantly enriched in HALLMARK EPITHELIAL MESENCHYMAL TRANSITION, HALLMARK COAGULATION, and HALLMARK ANGIOGENESIS, which may be related to the poor prognosis outcome (**Supplementary Figure S3B**). We conducted a functional enrichment analysis by the clusterProfiler R package (**Supplementary Table S5**) and found enrichment mainly in neutrophil activation, neutrophil-mediated immunity, T cell activation, regulation of innate immune response, and other immune-related Gene Ontology (GO) terms (**Figure 2K**). This once again proved the close relationship between the DEGs and immune-related functions.

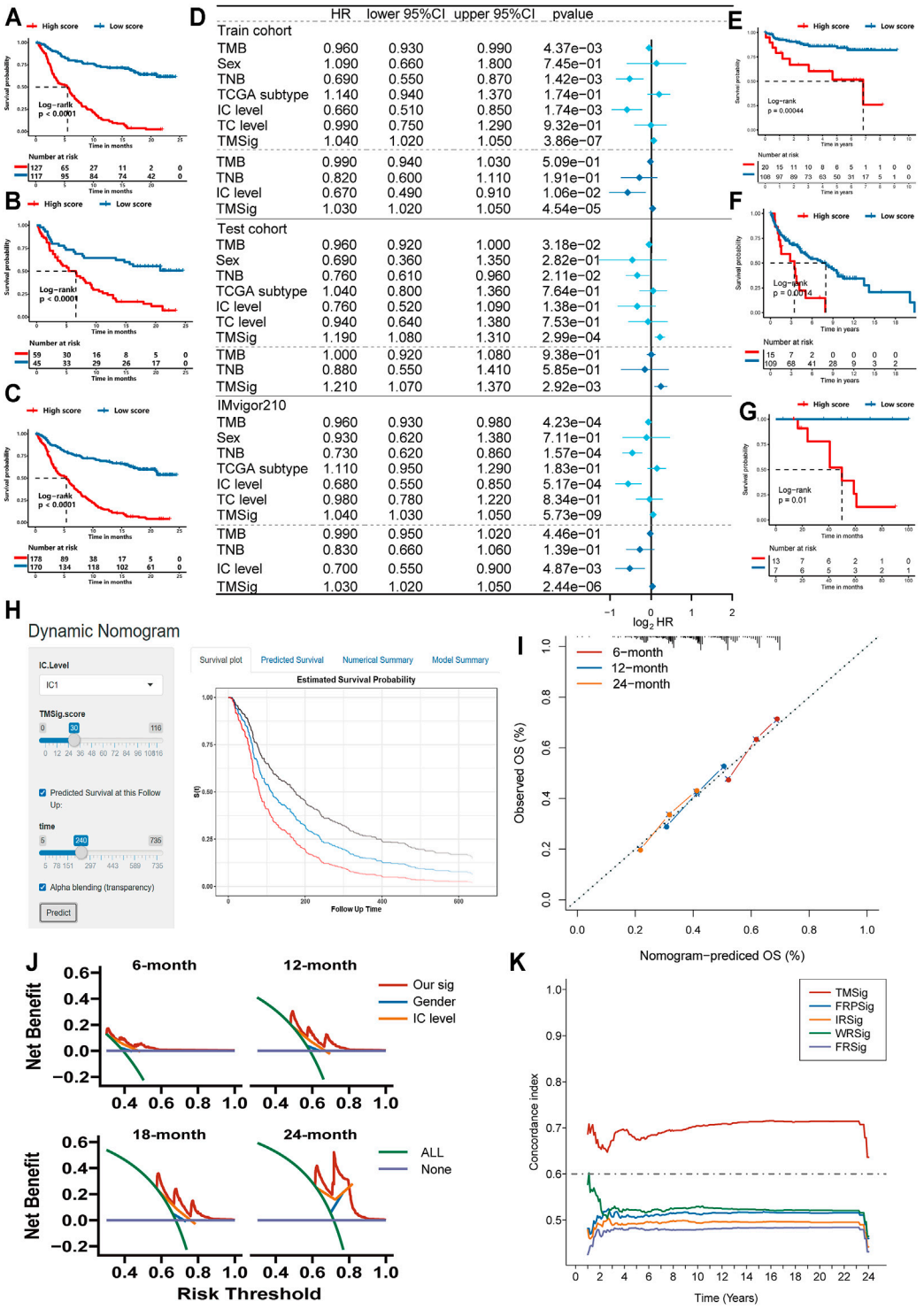

FIGURE 3 | Exploring the clinical practice value of TMSig. **(A)** Kaplan-Meier curves for overall survival (OS) of patients from the train cohort. **(B)** Kaplan-Meier curves for OS of patients from the test cohort. **(C)** Kaplan-Meier curves for OS of patients from the IMvigor210 cohort. **(D)** Independent prognostic analysis of TMSig. **(E)** Kaplan-Meier curves for OS of patients from the GSE32548 cohort. **(F)** Kaplan-Meier curves for OS of patients from the GSE48075 cohort. **(G)** Kaplan-Meier curves for OS of patients from the UTUC cohort. **(H)** Dynamic nomogram for clinical practice. **(I)** Calibration curve analysis. **(J)** The decision curves analysis. **(K)** The c-index of TMSig compared with other signatures.

To further explore the association between the DEGs and phenotypes, we conducted another unsupervised clustering analysis (**Supplementary Figure S3C**) and found that the cohort could also be divided into three cohorts with significant prognosis differences (log-rank $p = 0.045$) (**Figure 2L**). We referred to these as Gene-Clusters A, B, and C. Patients in Gene-ClusterB had the best prognostic outcomes, while patients in Gene-ClusterA had the worst. Using a chi-square analysis to compare the gene clusters and TME patterns, we found good consistency between these two grouping methods (χ^2 contingency tests, $p < 2.2e\text{-}16$). The distribution of patients by TME patterns and TME gene clusters are shown and specific information can be found in **Supplementary Table S6**. There were also significant differences in the level of immune checkpoint expression (**Figure 2M**) and immune cell infiltration (**Figure 2N**) among these gene clusters, indicating that these gene clusters could also represent the TME characteristics of the patients.

Construction of the TMSig

For the TME-related DEGs, we first matched expression data with clinical information, then reduced the dimension by using the univariate Cox regression model and used the more stringent $p < 0.01$ as the screening criterion to select 318 prognosis-related genes for further analysis (**Supplementary Table S7**). Next, we divided the IMvigor210 cohort into a training set and testing set at a ratio of 7:3. In the training set ($n = 244$), we performed modified Lasso regression analysis to construct the TMSig. In the process of cyclic calculation, we found that the maximum AUC value of the TMSig at 2 years was 0.906 (**Supplementary Figure S4A**). We defined the gene signature present at this time as the best candidate model. The prognosis of the low-score group was significantly better than that of the high-score group in the training set (log-rank $p < 0.0001$) (**Figure 3A**). Similar to the results obtained with the training set, the low-score group had a better prognosis in the internal testing set (log-rank $p < 0.0001$) (**Figure 3B**) and in the entire IMvigor210 cohort (log-rank $p < 0.0001$) (**Figure 3C**). The ROC curves proved the robust predictive ability of the TMSig, and the AUC at 1 year was 0.88 and 0.906 at 2 years in the training set. The AUC at 1 year was 0.747, and that at 2 years was 0.805 in the testing cohort. In the whole cohort, the AUC was 0.840 at 1 year and 0.876 at 2 years (**Supplementary Figures S4B–D**). Then we performed the univariate Cox regression algorithm to analyze TMSig together with other clinical characteristics of the patients in the training set. And further included them in the multivariate Cox regression algorithm after screening out the features with $p < 0.05$. And the same analysis was performed not only in the train cohort, but also in the test cohort and the entire IMvigor210 cohort. The p-value of TMSig < 0.05 in each time of analysis, proving that it can be served as an independent prognostic factor for patients (**Figure 3D**). And the TMSig also showed better prognostic predictive power in three independent cohorts (**Figures 3E–G**).

The TMSig score had a significantly different distribution in BOR, immune phenotype, IC level and other subgroups (Kruskal–Wallis, $p < 0.05$) and had a difference in TC level, but it was not significant (**Supplementary Figures S4E–H**). To further verify the reliability of the TMSig for predicting the prognostic outcomes, we performed a stratified analysis based on the clinical information of the IMvigor210 cohort. Through the Kaplan-Meier analysis, we found the TMSig has a great performance in several clinical subgroups (Immune phenotype: immune desert type, immune excluded type, immune inflamed type, IC level: IC0, IC1, IC2, Sex: Male, Female, BOR: SD/PD, CR/PR, TC level: TC0, TC1, TC2, Tobacco history: NEVER, PREVIOUS OR CURRENT, **Supplementary Figures S4I–W**). We also conducted an external verification of the prognostic value of the TMSig in the independent TCGA-BLCA cohort and found that it was of great significance for predicting both the overall survival (OS) and disease-specific survival (DSS) rates of these patients (**Supplementary Figures S5A,B**). In addition, stratified analysis of the TCGA cohort showed that the TMSig had significant prognostic significance in patients with higher disease stages (**Supplementary Figures S5C,D**), which inspired us to conclude that the TMSig may play a unique role in predicting the prognosis of patients with advanced neoplasia.

To improve the clinical application of TMSig, we constructed dynamic nomogram (TMSigDynNomapp: https://the-nomogram.shinyapps.io/TMSigDynNomapp/, **Figure 3H**), while calibration plots showed that comprehensive signature has accurate predictive power at different time points (**Figure 3I**). Decision curve analysis also showed that comprehensive signature can provide better clinical benefit to patients compared to applying gender, IC level, and other indicators for prediction (**Figure 3J**). Compared with other previously reported bladder cancer-related signatures, TMSig also has more robust predictive power (**Figure 3K**).

The TMSig Could Effectively Predict Patient Response to Immunotherapy and Correlates With Immune Cell Infiltration, Tumor Mutation Load (TMB), and Tumor Neoantigen Burden (TNB)

We used ROC curves to evaluate the ability of the TMSig score to predict the efficacy of immunotherapy among patients in the IMvigor210 cohort and compared the score with known effective predictors such as TMB (Samstein et al., 2019), TNB (Wolf et al., 2019), and M1 macrophages (Zeng et al., 2020). It was found that the accuracy of the TMSig in effectively predicting the response to immunotherapy was not inferior to that of other biomarkers. (TMSig score AUC: 0.826, TMB AUC: 0.728, TNB AUC: 0.767, M1 macrophage AUC: 0.702) (**Supplementary Figure S5E**). To fully demonstrate the robustness of the TMSig for predicting immunotherapy response, we included two independent data sets for external validation. The AUC predicted by the TMSig score in the data from Miao et al. was 0.75 (**Supplementary**

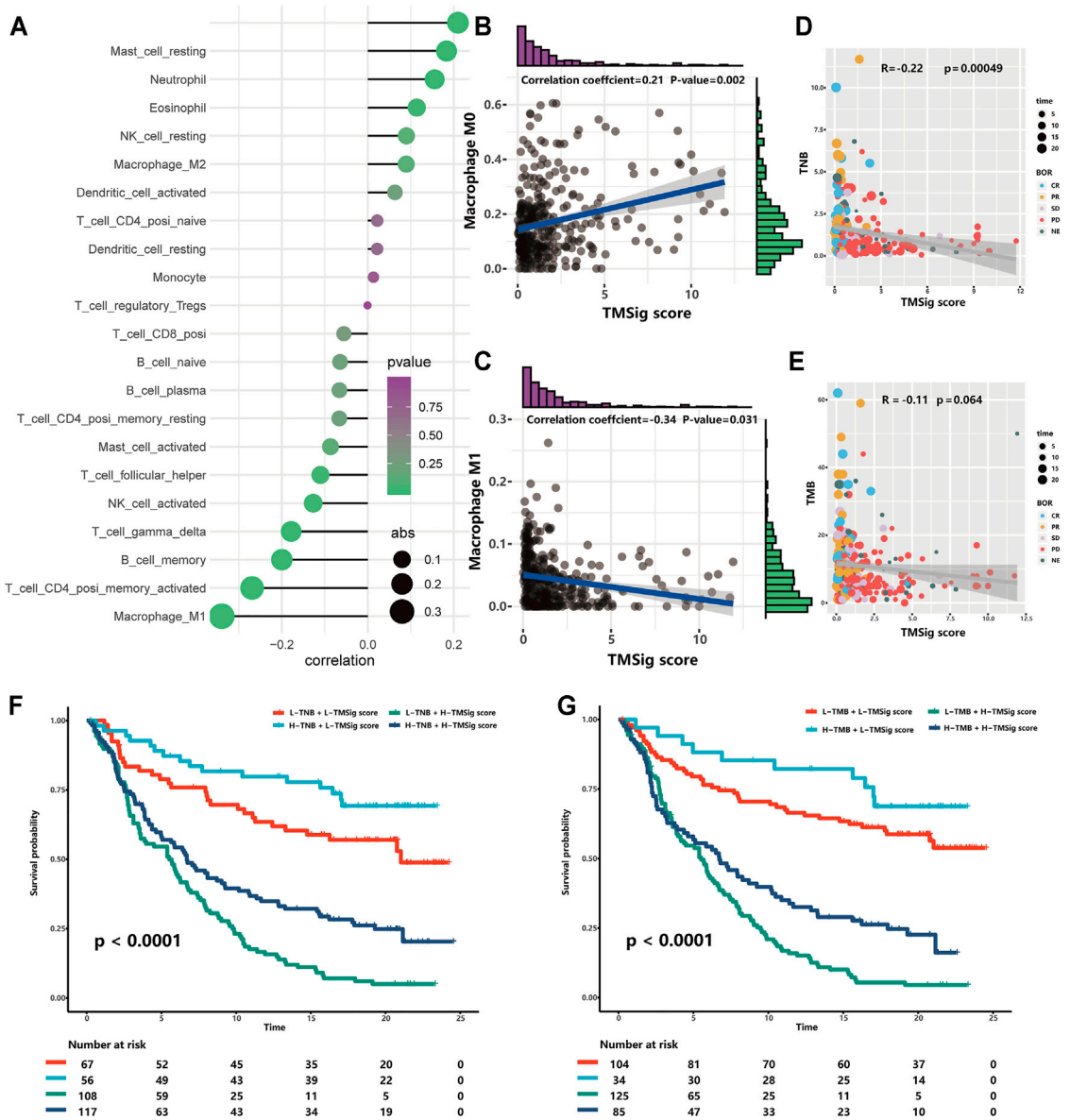

FIGURE 4 | The association of TMSig score with immune-associated cells, TMB and TNB. **(A)** The correlation of TMSig score with immune cell infiltration level. The depth of the color represents the *p*-value and the size of the dot represents the absolute value of the correlation coefficient. **(B)** The correlation of TMSig score with M0 Macrophage. **(C)** The correlation of TMSig score with M1 Macrophage. **(D)** Modest but significant correlation of TMSig score with TNB. **(E)** The correlations of TMSig score with TMB. **(F)** Kaplan-Meier curves for patients stratified by both TNB and TMSig score. **(G)** Kaplan-Meier curves for patients stratified by both TMB and TMSig score.

Figure S5F), and the AUC predicted by the TMSig score in the GSE35640 dataset was 0.687 (**Supplementary Figure S5G**). All these results indicate the great potential of the TMSig for discriminating patients who may benefit from immunotherapy.

It is well known that patients with different infiltration levels of immune cells have different prognostic outcomes or treatment responses. Therefore, we performed a Spearman correlation analysis to explore the relationship between the TMSig score and the infiltration level of various immune cells and found that there was a significant positive correlation between the TMSig score and M0 macrophages, resting mast cells, neutrophils, and eosinophils ($p < 0.05$, cor > 0) and a significant negative correlation with the infiltration level of follicular helper T cells, activated NK cells, gamma delta T cells, memory B cells, $CD4^+$ memory-activated T cells, and M1 macrophages ($p < 0.05$, cor < 0) (**Figure 4A**). The strongest positive correlation was between the TMSig score and M0 macrophages (**Figure 4B**), and the strongest negative correlation was between the TMSig score and M1 macrophages

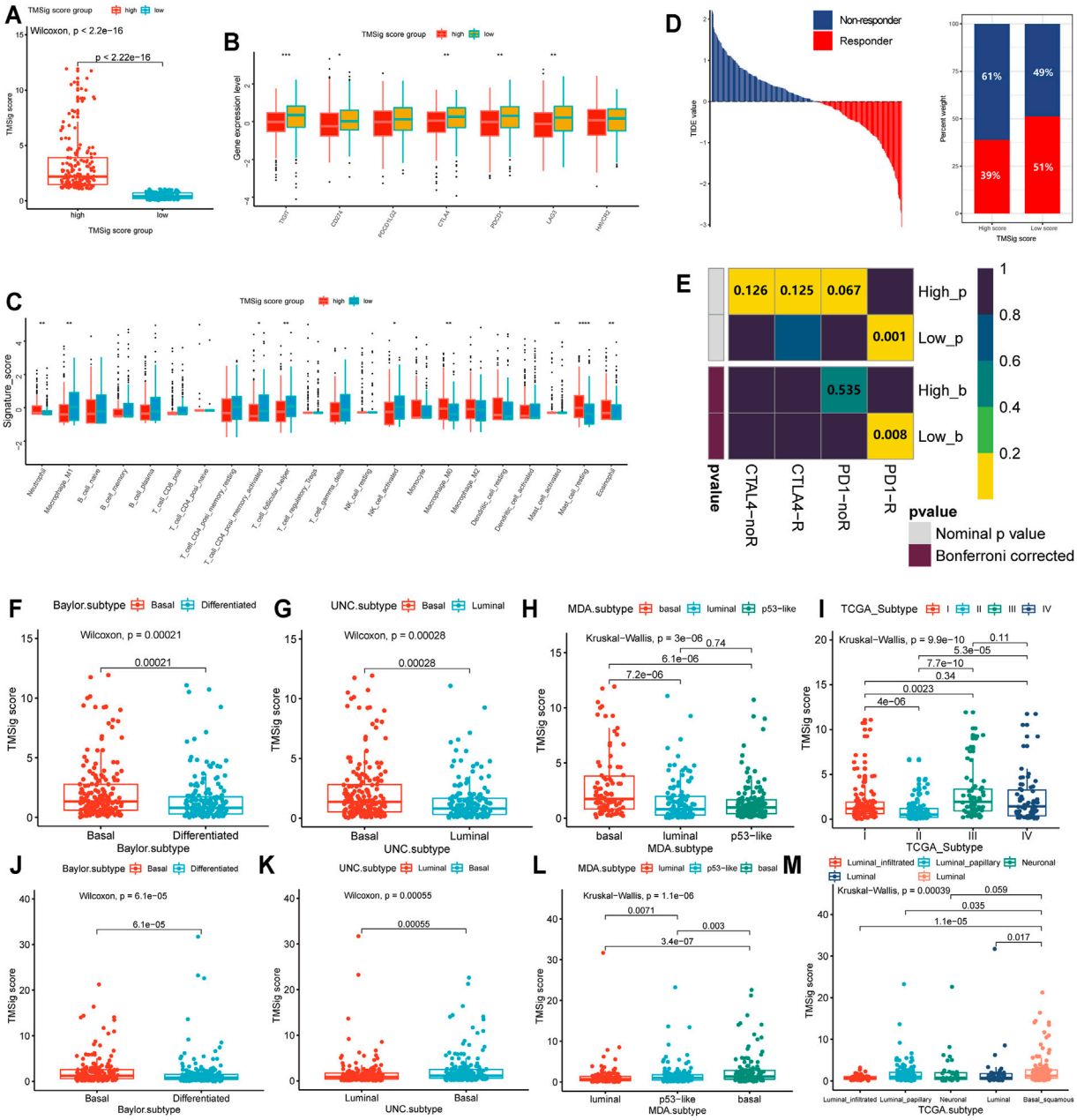

FIGURE 5 | Molecular differences between high- and low-score subgroups and distribution among previous subtypes. **(A)** The TMSig score in the high score group was significantly higher than that in the low score group. **(B)** The expression level of immune checkpoints in the high score and low score groups. **(C)** Immune infiltration cells are expressed in the high score and low score groups (*$p < 0.05$, **$p < 0.01$, ***$p < 0.001$, ****$p < 0.0001$). **(D)** The immune therapy response and TIDE value of patients with urothelial cancer. **(E)** The subclass mapping analysis showed a significant difference in response to anti-PD-1 therapy among these two groups. The distribution of TMSig score of the IMvigor210 cohort in molecular subtypes. **(F)** Baylor subtype, **(G)** UNC subtype, **(H)** MDA subtype, **(I)** TCGA subtypes. The distribution of TMSig score of the TCGA cohort in molecular subtypes. **(J)** Baylor subtype, **(K)** UNC subtype, **(L)** MDA subtype, **(M)** TCGA subtypes.

(**Figure 4C**). There was a moderate but significant negative correlation between the TMSig score and TNB (Kruskal-Wallis, $p = 0.00049$) (**Figure 4D**), and the correlation between the TMSig score and TMB also demonstrated the same trend (**Figure 4E**). Intriguingly, combining the TMSig score with TMB or TNB contributed to the survival assessment (Kaplan-Meier analysis, TMSig score +TNB binary: $p < 0.0001$; TMSig score +TMB binary: $p < 0.0001$) (**Figures 4F,G**). We should clear that the correlation between TMSig and M1 macrophages is strong and deserves focused attention. But its correlation with TMB or TNB is moderate, which could provide direction for our study, but the exact relationship needs to be verified by further studies.

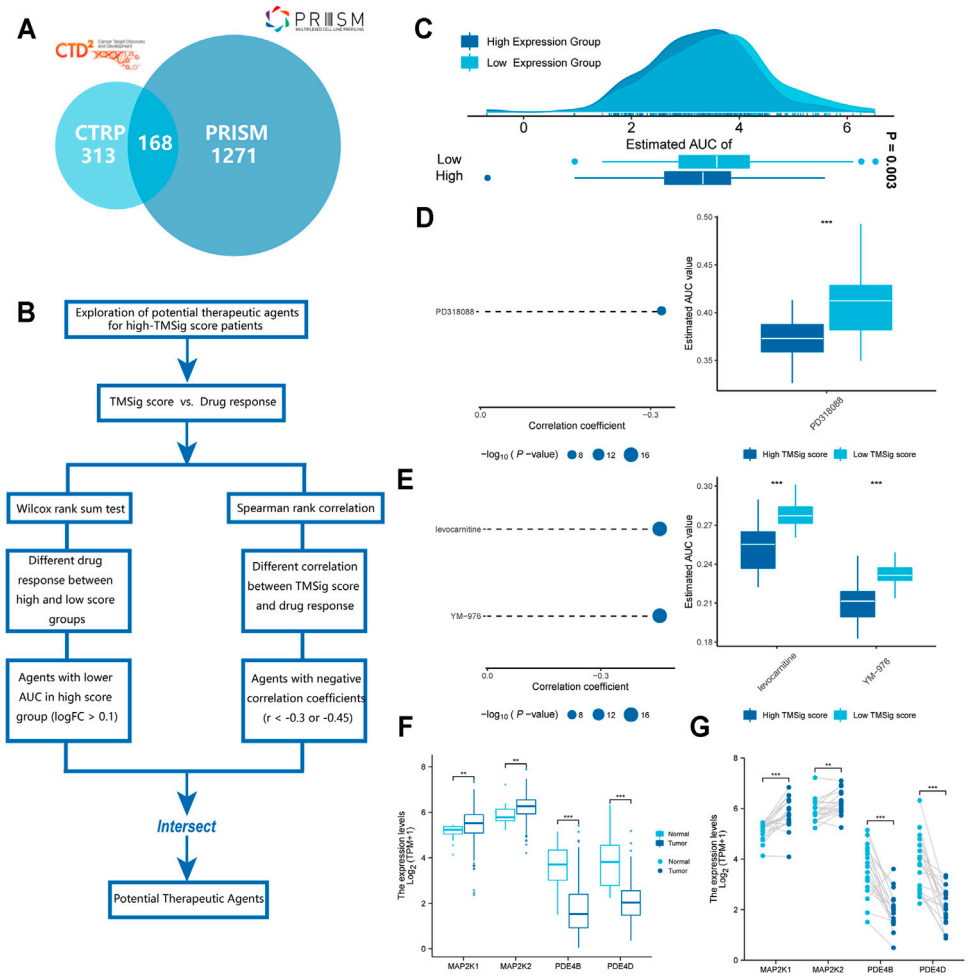

FIGURE 6 | Identification of candidate agents with higher drug sensitivity in high-TMSig score patients. **(A)** A venn diagram of compounds from the CTRP and the PRISM datasets. **(B)** Schematic outlining the strategy for identification of potential therapeutic agents. **(C)** Comparison of estimated cisplatin's sensitivity (logAUC) between high GULP1 expression and low GULP1 expression groups. **(D)** The results of differential drug response analysis and Spearman's correlation analysis of compounds from CTRP datasets. **(E)** The results of differential drug response analysis and Spearman's correlation analysis of compounds from PRISM datasets. **(F)** Unpaired comparative analysis of target genes for potential drugs. **(G)** Paired comparative analysis of target genes for potential drugs.

Characteristic Differences Between the High and Low TMSig Score Groups

The high-score group had a higher TMSig score (Wilcoxon, $p <$ 2.2e−16) (**Figure 5A**), indicating that the two groups have unique features not only in prognosis but also in immune-related characteristics. TIGIT, CD274, CTLA4, PDCD1, and LAG3 presented higher expression levels in the low score group ($p <$ 0.05) (**Figure 5B**), which suggests that people with low TMSig scores might have a better response to immunotherapies targeting immune checkpoints. The immune infiltration cell analysis also showed that these two groups had significantly different marker immune cells (**Figure 5C**). Then, we used the Tumor Immune Dysfunction and Exclusion (TIDE) algorithm to evaluate each patient's potential response to immunotherapy and observed that the responsiveness of immunotherapy in the low-score group was higher than that in the high-score group ($p = 0.02$) (**Figure 5D**). Moreover, subclass mapping was performed with another group of 47 melanoma patients who responded to immunotherapy (Roh et al., 2017). We were encouraged by the observation that a low score indicated potential patient response to PD-1 treatment. (Bonferroni corrected $p =$ 0.008) (**Figure 5E**). These results reconfirmed the application value of the TMSig. To further explore the significantly enriched pathways of the DEGs between the two groups, we carried out GSEA using the clusterProfiler and fgsea R packages. It was found that HALLMARK ANGIOGENESIS, HALLMARK TGF-ß_ SIGNALING, HALLMARK APOPTOSIS, HALLMARK HYPOXIA, and HALLMARK P53 PATHWAY were significantly enriched in the upregulated genes (**Supplementary Table S8**), which may be related to poor prognosis.

In addition, we found that the high-score samples of the Baylor subtype and UNC subtype were mainly concentrated in the basal type (Wilcoxon, Baylor subtype, p = 2.1e-04; UNC

subtype, p = 2.8e-04) (**Figures 5F,G**), and the TMSig score in the basal MDA subtype was also significantly higher than that in the luminal type and p53-like type (Kruskal–Wallis, p = 3e−06) (**Figure 5H**). In the TCGA subtypes, high scores were mainly distributed in clusters III and IV (**Figure 5I**), and it is generally believed that clusters I/II and III/IV in the molecular subtypes officially obtained by the TCGA are similar to differentiated (or luminal) and basal tumors, respectively (Mo et al., 2018). We also verified the distribution of TMSig scores among the four classification methods in the independent TCGA-BLCA dataset, and the results were consistent with those of the IMvigor210 cohort (**Figures 5J–M**). Therefore, we inferred that the TMSig is closely related to molecular subtypes of bladder cancer, and different scores may indicate different molecular characteristics, which is of great significance for further understanding the characteristics of these two groups.

Identification of Potential Therapeutic Agents for High TMSig Score Patients

The CTRP and PRISM datasets contain gene expression profiles and drug sensitivity profiles for hundreds of CCLs and can be used to construct predictive models of drug response. After removing duplicate drugs, these two datasets share 168 compounds, for a total of 1752 compounds (**Figure 6A**). We removed drugs with deletion values greater than 20% and cell lines derived from haematopoietic and lymphoid tissue. Finally, 680 CCLs for 354 compounds in the CTRP dataset and 480 CCLs for 1285 compounds in the PRISM dataset were used for subsequent analyses. The specific screening process is shown in **Figure 6B**. Before proceeding further, we first demonstrated that the results of drug response estimation are reliable. Cisplatin is a common therapeutic agent for bladder cancer patients, and a recent study showed that high GULP1 expression enhanced the sensitivity of patients to cisplatin (Teramoto et al., 2021). We divided the patients into high and low expression groups according to the expression level of GULP1. The Wilcoxon rank sum test was used to compare the difference in AUC estimates of cisplatin between the two groups, and the results showed that the AUC estimates were significantly higher (p = 0.003) in patients with high GULP1 expression (**Figure 6C**), consistent with the clinical presentation of cisplatin. After verifying the reliability of the calculation method, we adopted a similar analysis method to Yang et al. (2021). First, differential drug response analysis was performed between the group with high TMSig score (upper decile) and the group with low TMSig score (lower decile) to identify the group with high TMSig score (log2FC > 0.10) with low estimated AUC values. Then, by Spearman correlation analysis between AUC value and TMSig score, compounds with negative correlation coefficients (Spearman's r < −0.30 for CTRP or <0.45 for PRISM). These analyses yielded one CTRP-derived compound (PD318088) and two Prism-derived compounds (Levocarnitine, YM−976) (**Figures 6D,E**). Secondly, the fold-change difference of the expression level of candidate drug target genes between tumor tissues and normal tissues (including paired analysis and unpaired analysis) was calculated. A higher fold change value indicated a greater potential of candidate agent for UC treatment (PD318088: MAP2K1, MAP2K2; YM−976: PDE4B, PDE4D) (**Figures 6F,G**). Finally, we searched at PubMed (https://www.ncbi.nlm.nih.gov/PubMed/) to find evidence of candidate compounds for UC treatment. Overall, PD318088 and YM−976, with relatively sufficient evidence, are considered to be the most promising potential treatment drugs for people with high TMSig score.

DISCUSSION

Mounting evidence has identified the essential role of the TME in the occurrence and development of UC and the prognosis of patients. However, there is still a lack of comprehensive understanding of the tumor microenvironment of UC. So, we comprehensively analyzed a large cohort of UC patients and constructed the TMSig to comprehensively analyze the tumor microenvironment pattern and predict the survival rate of UC patients and guide more accurate and effective applications of immunotherapy and chemotherapy strategies.

Compared with previous published articles, our study has significant innovation and advantages. Our study not only identified TME patterns in patients with urothelial cancer and established TMSig as a metric to quantify individual patients, but also developed a convenient and practical webpage nomogram, which is more clinically useful than the study by Meng et al. (2021). Meanwhile, the predictive power of TMSig for immunotherapy response has been fully validated by the TIDE algorithm, Submap algorithm, and multiple clinical cohorts receiving immunotherapy. Moreover, potential sensitive drugs have been fully explored with the help of the robust approach. Compared with the study of Meireson et al. (2021), it is a greater improvement in the depth and breadth. In addition, we performed the improved lasso algorithm, which is more advanced in its selection compared to the study of Zhang et al. (2021). Besides, we used multiple omics data such as genomics, transcriptomics to make the analysis more in-depth and complete. Compared with many previous reported signatures (Sun et al., 2021a; Sun et al., 2021b; He et al., 2021; Yan et al., 2021), the predictive power of TMsig is more outstanding. Besides, the TMSig scoring system we constructed can effectively assess the immune profile of patients with urothelial cancer and predict patient prognosis, which we have validated with a sample of 1025 cases. To make the TMSig score better applicable to clinical practice, we included TMSig and IC level in the follow-up analysis and constructed a web-based dynamic nomogram. And the high accuracy and better clinical benefit results of this nomogram was well demonstrated by calibration plots and decision curves. In addition, TMSig can identify potential therapeutic agents for high-risk populations and fully validate them with robust methods to guide clinical precision treatment.

In this study, we identified a TME pattern with a stromal-activation subtype, immune-enriched subtype and immune-suppressive subtype based on unsupervised consensus clustering of immune cell infiltration in the TME. These

subtypes are characterized by different immunophenotypes and immune states, which are related to different prognostic outcomes and antitumor immunity levels. Mariathasan et al. found that TGF-β inhibits antitumor immunity by limiting T cell infiltration to shape the tumor microenvironment (Tauriello et al., 2018). Blockade of TGF β signal transduction makes it easy to target tumors with anti-PD-1/PD-L1 checkpoint therapy (Panagi et al., 2020). They also found that TGF-β-blocking antibodies and anti-PD-L1 therapy reduced the transduction of TGF-β signaling in stromal cells and improved the infiltration level of T cells into the center of the tumor, thereby stimulating a strong antitumor immune response and causing tumor regression (Tauriello et al., 2018). Based on these findings, we speculate that the stromal-activation subtype may benefit from a combination of immune checkpoint block drugs and TGF-β blockers (Lan et al., 2018; Ravi et al., 2018). The immune-enriched subtype is similar to the known immunoinflammatory phenotype. This finding supports the potential predictive value of the benefits of immunotherapy. Zhao et al. demonstrated that the immunoinflammatory phenotype of triple-negative breast cancer is characterized by the infiltration of $CD8^+$ T cells into the tumor parenchyma (Mariathasan et al., 2018). Job et al. reported that the immune-inflammatory type is characterized by a large level of T lymphocyte infiltration and the activation and upregulation of inflammatory and immune checkpoint pathways. This phenotype is associated with better patient prognosis (Zhao et al., 2020). Our study also revealed that the patients in this subtype had the best prognosis outcomes, which is similar to the results of previous studies.

The TMSig score had the strongest significant negative correlation with M1 macrophages and the strongest significant positive correlation with M0 macrophages. Regarding the low-score group, M1 macrophage infiltration was significant, and the prognosis was good, while in the high-score group, M0 macrophage infiltration was significant, and the prognosis was poor. This suggests that the different states of macrophages may be an important reason for the difference in prognosis among patients with different scores. Tumor-associated macrophages (TAMs) are one of the most abundant matrix components in the tumor microenvironment (Mantovani et al., 2008; Hanahan and Weinberg, 2011; Li et al., 2019b). Previous studies have mainly focused on M2 macrophages because they account for the vast majority of TAMs and have the potential for transformation (Ge et al., 2019). However, M0 and M1 macrophages have attracted increasing attention. M2 macrophages differentiated from M0 macrophages were also highly infiltrated in the population with high infiltration of M0 macrophages, which inhibited inflammation, T cell proliferation and differentiation and promoted angiogenesis of the tumor matrix and tumor cell proliferation (Bingle et al., 2002; Gordon, 2003; Pollard, 2004; Mantovani et al., 2005; Hume, 2015). These mechanisms cannot be ignored due to the poor prognosis of this population. In addition, M1 macrophages have been proven by a previous study to be an important marker for predicting patient prognosis outcomes and the immunotherapy response of patients with mUC (Zeng et al., 2020; Mantovani et al., 2017), and their anticancer ability, such as activating the inflammatory response, participating in host innate immunity and inhibiting tumor cells in the TME, has also been widely recognized (Bingle et al., 2002; Gordon, 2003; Pollard, 2004; Mantovani et al., 2005; Hume, 2015). Samples with high M1 infiltration levels often show immune activation, while those with low M1 infiltration may show an activation of steroid hormone metabolism, which may promote the exclusion of $CD8^+$ T cells from the TME (Zeng et al., 2020; Ma et al., 2019). Therefore, the different states of macrophages between the high- and low-score groups worth investigating further and may contribute to the accurate application of treatments (Li et al., 2019b; Tang et al., 2013).

In this study, we found that the high TMSig score group was mainly distributed in the basal subtype, with poor prognosis and significantly lower expression levels of immune checkpoints, which was consistent with previously reported characteristics of the basal subtype (Mo et al., 2018), and the low-score group presented similar characteristics to the differentiated (or luminal) subtype. This indicates that the TMSig score could effectively represent the tumor differentiation status of the samples. In addition, the TMSig score verified the robustness of the prediction of patient immunotherapy response in multiple independent cohorts and was not limited to the comparison of the expression levels of relevant genes, which also demonstrates the superiority of our approach in comparison with signatures reported in previous studies. EGFR pathways are specifically activated in basal-like MIBC. *In vitro* and *in vivo* experiments have also proven that basal-like MIBC cell lines are sensitive to EGFR inhibitors, suggesting that EGFR has great potential as a basal-like MIBC treatment target (Rebouissou et al., 2014). Due to the close correlation between the high-score group and basal-like MIBC, EGFR is worth further investigations in this group. In addition, because of the remarkable tumor heterogeneity in bladder cancer, research on the subtype-specific targets and treatment therapies of bladder cancer is important and urgent.

High TNB and TMB in tumors are related to enhanced responses to immunotherapy (Samstein et al., 2019; Zeng et al., 2020). The new antigens generated by somatic cell mutations in tumors represent a promising method to promote tumor immune recognition. The main hypothesis of immunotherapy is that tumors with elevated TMB will have more new antigens and therefore have higher immunogenicity (Wolf et al., 2019). The TMSig score was closely related to immune response predictors, suggesting that it may be related to different immunotherapy responses. Independent prognostic analysis showed that the TMSig score is an independent prognostic factor for UC patients and is not affected by other factors. The correlation coefficient between them was relatively low, indicating that the TMSig score, TMB, and TNB represent different aspects of tumor immune features. In addition, the high- and low-score groups not only had significant differences in survival and prognosis outcomes but also had significant differences in responses to immunotherapy. GSEA also showed that many carcinogenic pathways were significantly activated in high-score patients. The sensitivity of patients with high and low scores to different chemotherapeutic drugs has also been explored, which will provide new clinical treatment ideas for patients with urothelial carcinoma.

In the current study, we combined multicohort and multigroup data to comprehensively evaluate multidimensional features associated with TME infiltration patterns. We constructed the TMSig, an effective predictor of prognosis, immunotherapy response by scoring patients, which provides new insights into the identification of subtype-specific populations and markers. The low-score group had a better prognosis, better response to immunotherapy, stronger infiltration of M1 macrophages and was more inclined to be in the luminal (differentiated) molecular subtypes. In addition, macrophage-targeted therapy should be considered. Giving full consideration to the antitumor effect of M1 macrophages may have an essential impact on the prognosis of UC patients. Although there is significantly difference of the immune checkpoint distribution between high and low score groups, they had some overlap. So, its clinical application should be more cautious in predicting immune checkpoints. Besides, our findings should be further verified in more prospective cohorts to define the clinical application value more accurately. The important role of macrophages in UC patients should be further explored at the single-cell level. Since not all patients with higher TMSig scores benefit from immunotherapy, more meaningful clinical features should be included in the predictive model to improve its accuracy.

CONCLUSION

Through a comprehensive and systematic analysis of the TME characteristics of UC patients, we identified the TMSig score as an independent prognostic factor. The TMSig score can not only accurately predict the prognosis outcomes of patients with UC but also robustly predict patient immunotherapy response in multiple independent cohorts. Interestingly, we found that the TMSig score may play a unique role in high-grade and advanced-stage UC. The high- and low-risk TMSig score groups are in good agreement with the previously recognized molecular subtypes. This enables us to combine histopathological staging with molecular subtypes, comprehensively evaluate the samples, and inspire new ideas for subtype-specific precision therapy. We also found that the difference in the state of macrophages may be the essential factor underlying the difference in patient prognoses. The in-depth study of macrophage-targeted therapy would have great value in advancing the individualized therapy approach for patients with urothelial cancer.

DATA AVAILABILITY STATEMENT

The original contributions presented in the study are included in the article/**Supplementary Material**, further inquiries can be directed to the corresponding authors.

ETHICS STATEMENT

The authors are accountable for all aspects of the work in ensuring that questions related to the accuracy or integrity of any part of the work are appropriately investigated and resolved.

AUTHOR CONTRIBUTIONS

GC and WS designed the whole study and drafted the manuscript. XJ analyzed the data. HN and YW revised the manuscript. All authors read and approved the final manuscript.

FUNDING

This work was supported by the National Natural Science Foundation of China under grant numbers 81772713, 81472411, 81981260351, and 81972378; Taishan Scholar Program of Shandong Province under grant number tsqn20161077; Natural Science Foundation of Shandong Province under grant number ZR2016HQ18; and Key Research and Development Program of Shandong Province under grant number 2018GSF118197.

ACKNOWLEDGMENTS

We thank Jianming Zeng (University of Macau), and all the members of his bioinformatics team, biotrainee, for generously sharing their experience and codes.

SUPPLEMENTARY MATERIAL

The Supplementary Material for this article can be found online at: https://www.frontiersin.org/articles/10.3389/fcell.2021.764125/full#supplementary-material

REFERENCES

Balar, A. V., Galsky, M. D., Rosenberg, J. E., Powles, T., Petrylak, D. P., Bellmunt, J., et al. (2017). Atezolizumab as First-Line Treatment in Cisplatin-Ineligible Patients with Locally Advanced and Metastatic Urothelial Carcinoma: a Single-Arm, Multicentre, Phase 2 Trial. *The Lancet* 389 (10064), 67–76. doi:10.1016/S0140-6736(16)32455-2

Basu, A., Bodycombe, N. E., Cheah, J. H., Price, E. V., Liu, K., Schaefer, G. I., et al. (2013). An Interactive Resource to Identify Cancer Genetic and Lineage Dependencies Targeted by Small Molecules. *Cell* 154 (5), 1151–1161. doi:10.1016/j.cell.2013.08.003

Bingle, L., Brown, N. J., and Lewis, C. E. (2002). The Role of Tumour-Associated Macrophages in Tumour Progression: Implications for New Anticancer Therapies. *J. Pathol.* 196 (3), 254–265. doi:10.1002/path.1027

Choi, W., Porten, S., Kim, S., Willis, D., Plimack, E. R., Hoffman-Censits, J., et al. (2014). Identification of Distinct Basal and Luminal Subtypes of Muscle-Invasive Bladder Cancer with Different Sensitivities to Frontline Chemotherapy. *Cancer Cell* 25 (2), 152–165. doi:10.1016/j.ccr.2014.01.009

Dinney, C. P. N., McConkey, D. J., Millikan, R. E., Wu, X., Bar-Eli, M., Adam, L., et al. (2004). Focus on Bladder Cancer. *Cancer Cell* 6 (2), 111–116. doi:10.1016/j.ccr.2004.08.002

Ge, P., Wang, W., Li, L., Zhang, G., Gao, Z., Tang, Z., et al. (2019). Profiles of Immune Cell Infiltration and Immune-Related Genes in the Tumor Microenvironment of Colorectal Cancer. *Biomed. Pharmacother.* 118, 109228. doi:10.1016/j.biopha.2019.109228

Ghandi, M., Huang, F. W., Jané-Valbuena, J., Kryukov, G. V., Lo, C. C., McDonald, E. R., et al. (2019). Next-generation Characterization of the Cancer Cell Line Encyclopedia. *Nature* 569 (7757), 503–508. doi:10.1038/s41586-019-1186-3

Gordon, S. (2003). Alternative Activation of Macrophages. *Nat. Rev. Immunol.* 3 (1), 23–35. doi:10.1038/nri978

Hanahan, D., and Weinberg, R. A. (2011). Hallmarks of Cancer: the Next Generation. *Cell* 144 (5), 646–674. doi:10.1016/j.cell.2011.02.013

He, Y., Wu, Y., Liu, Z., Li, B., Jiang, N., Xu, P., et al. (2021). Identification of Signature Genes Associated with Invasiveness and the Construction of a Prognostic Model that Predicts the Overall Survival of Bladder Cancer. *Front. Genet.* 12, 694777. doi:10.3389/fgene.2021.694777

Hume, D. A. (2015). The Many Alternative Faces of Macrophage Activation. *Front. Immunol.* 6, 370. doi:10.3389/fimmu.2015.00370

Jiang, Y., Zhang, Q., Hu, Y., Li, T., Yu, J., Zhao, L., et al. (2018). ImmunoScore Signature. *Ann. Surg.* 267 (3), 504–513. doi:10.1097/SLA.0000000000002116

Kamat, A. M., Hahn, N. M., Efstathiou, J. A., Lerner, S. P., Malmström, P.-U., Choi, W., et al. (2016). Bladder Cancer. *The Lancet* 388 (10061), 2796–2810. doi:10.1016/S0140-6736(16)30512-8

Knowles, M. A., and Hurst, C. D. (2015). Molecular Biology of Bladder Cancer: New Insights into Pathogenesis and Clinical Diversity. *Nat. Rev. Cancer* 15 (1), 25–41. doi:10.1038/nrc3817

Lan, Y., Zhang, D., Xu, C., Hance, K. W., Marelli, B., Qi, J., et al. (2018). Enhanced Preclinical Antitumor Activity of M7824, a Bifunctional Fusion Protein Simultaneously Targeting PD-L1 and TGF-β. *Sci. Transl. Med.* 10 (424), 10. doi:10.1126/scitranslmed.aan5488

Li, R., Spiess, P. E., Gilbert, S. M., and Necchi, A. (2019). Towards Personalized Neoadjuvant Therapy for Muscle-Invasive Bladder Cancer. *Eur. Urol.* 76 (1), 4–6. doi:10.1016/j.eururo.2019.02.027

Li, X., Liu, R., Su, X., Pan, Y., Han, X., Shao, C., et al. (2019). Harnessing Tumor-Associated Macrophages as Aids for Cancer Immunotherapy. *Mol. Cancer* 18 (1), 177. doi:10.1186/s12943-019-1102-3

Lindgren, D., Sjödahl, G., Lauss, M., Staaf, J., Chebil, G., Lövgren, K., et al. (2012). Integrated Genomic and Gene Expression Profiling Identifies Two Major Genomic Circuits in Urothelial Carcinoma. *PLoS One* 7 (6), e38863. doi:10.1371/journal.pone.0038863

Ma, X., Bi, E., Lu, Y., Su, P., Huang, C., Liu, L., et al. (2019). Cholesterol Induces CD8+ T Cell Exhaustion in the Tumor Microenvironment. *Cell Metab.* 30 (1), 143–156. doi:10.1016/j.cmet.2019.04.002

Magers, M. J., Lopez-Beltran, A., Montironi, R., Williamson, S. R., Kaimakliotis, H. Z., and Cheng, L. (2019). Staging of Bladder Cancer. *Histopathology* 74 (1), 112–134. doi:10.1111/his.13734

Mantovani, A., Allavena, P., Sica, A., and Balkwill, F. (2008). Cancer-related Inflammation. *Nature* 454 (7203), 436–444. doi:10.1038/nature07205

Mantovani, A., Marchesi, F., Malesci, A., Laghi, L., and Allavena, P. (2017). Tumour-associated Macrophages as Treatment Targets in Oncology. *Nat. Rev. Clin. Oncol.* 14 (7), 399–416. doi:10.1038/nrclinonc.2016.217

Mantovani, A., Sica, A., and Locati, M. (2005). Macrophage Polarization Comes of Age. *Immunity* 23 (4), 344–346. doi:10.1016/j.immuni.2005.10.001

Mariathasan, S., Turley, S. J., Nickles, D., Castiglioni, A., Yuen, K., Wang, Y., et al. (2018). TGFβ Attenuates Tumour Response to PD-L1 Blockade by Contributing to Exclusion of T Cells. *Nature* 554 (7693), 544–548. doi:10.1038/nature25501

Meireson, A., Tavernier, S. J., Van Gassen, S., Sundahl, N., Demeyer, A., Spaas, M., et al. (2021). Immune Monitoring in Melanoma and Urothelial Cancer Patients Treated with Anti-PD-1 Immunotherapy and SBRT Discloses Tumor Specific Immune Signatures. *Cancers* 13 (11), 2630. doi:10.3390/cancers13112630

Meng, J., Lu, X., Zhou, Y., Zhang, M., Ge, Q., Zhou, J., et al. (2021). Tumor Immune Microenvironment-Based Classifications of Bladder Cancer for Enhancing the Response Rate of Immunotherapy. *Mol. Ther. - Oncolytics* 20, 410–421. doi:10.1016/j.omto.2021.02.001

Mo, Q., Nikolos, F., Chen, F., Tramel, Z., Lee, Y.-C., Hayashi, K., et al. (2018). Prognostic Power of a Tumor Differentiation Gene Signature for Bladder Urothelial Carcinomas. *J. Natl. Cancer Inst.* 110 (5), 448–459. doi:10.1093/jnci/djx243

Nishino, M., Ramaiya, N. H., Hatabu, H., and Hodi, F. S. (2017). Monitoring Immune-Checkpoint Blockade: Response Evaluation and Biomarker Development. *Nat. Rev. Clin. Oncol.* 14 (11), 655–668. doi:10.1038/nrclinonc.2017.88

Panagi, M., Voutouri, C., Mpekris, F., Papageorgis, P., Martin, M. R., Martin, J. D., et al. (2020). TGF-β Inhibition Combined with Cytotoxic Nanomedicine Normalizes Triple Negative Breast Cancer Microenvironment towards Anti-tumor Immunity. *Theranostics* 10 (4), 1910–1922. doi:10.7150/thno.36936

Patel, V. G., Oh, W. K., and Galsky, M. D. (2020). Treatment of Muscle-invasive and Advanced Bladder Cancer in 2020. *CA A. Cancer J. Clin.* 70 (5), 404–423. doi:10.3322/caac.21631

Pollard, J. W. (2004). Tumour-educated Macrophages Promote Tumour Progression and Metastasis. *Nat. Rev. Cancer* 4 (1), 71–78. doi:10.1038/nrc1256

Powles, T., Park, S. H., Voog, E., Caserta, C., Valderrama, B. P., Gurney, H., et al. (2020). Avelumab Maintenance Therapy for Advanced or Metastatic Urothelial Carcinoma. *N. Engl. J. Med.* 383 (13), 1218–1230. doi:10.1056/NEJMoa2002788

Ravi, R., Noonan, K. A., Pham, V., Bedi, R., Zhavoronkov, A., Ozerov, I. V., et al. (2018). Bifunctional Immune Checkpoint-Targeted Antibody-Ligand Traps that Simultaneously Disable TGFβ Enhance the Efficacy of Cancer Immunotherapy. *Nat. Commun.* 9 (1), 741. doi:10.1038/s41467-017-02696-6

Rebouissou, S., Bernard-Pierrot, I., de Reyniès, A., Lepage, M.-L., Krucker, C., Chapeaublanc, E., et al. (2014). EGFR as a Potential Therapeutic Target for a Subset of Muscle-Invasive Bladder Cancers Presenting a Basal-like Phenotype. *Sci. Transl. Med.* 6 (244), 244ra91. doi:10.1126/scitranslmed.3008970

Robertson, A. G., Kim, J., Al-Ahmadie, H., Bellmunt, J., Guo, G., Cherniack, A. D., et al. (2017). Comprehensive Molecular Characterization of Muscle-Invasive Bladder Cancer. *Cell* 171 (3), 540–e25. doi:10.1016/j.cell.2017.09.007

Roh, W., Chen, P.-L., Reuben, A., Spencer, C. N., Prieto, P. A., Miller, J. P., et al. (2017). Integrated Molecular Analysis of Tumor Biopsies on Sequential CTLA-4 and PD-1 Blockade Reveals Markers of Response and Resistance. *Sci. Transl. Med.* 9 (379), 9. doi:10.1126/scitranslmed.aah3560

Rosenberg, J. E., Hoffman-Censits, J., Powles, T., van der Heijden, M. S., Balar, A. V., Necchi, A., et al. (2016). Atezolizumab in Patients with Locally Advanced and Metastatic Urothelial Carcinoma Who Have Progressed Following Treatment with Platinum-Based Chemotherapy: a Single-Arm, Multicentre, Phase 2 Trial. *The Lancet* 387 (10031), 1909–1920. doi:10.1016/S0140-6736(16)00561-4

Samstein, R. M., Lee, C.-H., Shoushtari, A. N., Hellmann, M. D., Shen, R., Janjigian, Y. Y., et al. (2019). Tumor Mutational Load Predicts Survival after Immunotherapy across Multiple Cancer Types. *Nat. Genet.* 51 (2), 202–206. doi:10.1038/s41588-018-0312-8

Siegel, R. L., Miller, K. D., Fuchs, H. E., and Jemal, A. (2021). Cancer Statistics, 2021. *CA A. Cancer J. Clin.* 71 (1), 7–33. doi:10.3322/caac.21654

Siegel, R. L., Miller, K. D., and Jemal, A. (2018). Cancer Statistics, 2018. *CA: A Cancer J. Clinicians* 68 (1), 7–30. doi:10.3322/caac.21442

Su, X., Lu, X., Bazai, S. K., Compérat, E., Mouawad, R., Yao, H., et al. (2021). Comprehensive Integrative Profiling of Upper Tract Urothelial Carcinomas. *Genome Biol.* 22 (1), 7. doi:10.1186/s13059-020-02230-w

Sun, J., Yue, W., You, J., Wei, X., Huang, Y., Ling, Z., et al. (2021). Identification of a Novel Ferroptosis-Related Gene Prognostic Signature in Bladder Cancer. *Front. Oncol.* 11, 730716. doi:10.3389/fonc.2021.730716

Sun, S., Wang, Y., Wang, J., and Bi, J. (2021). Wnt Pathway-Related Three-mRNA Clinical Outcome Signature in Bladder Urothelial Carcinoma: Computational Biology and Experimental Analyses. *J. Transl Med.* 19 (1), 409. doi:10.1186/s12967-021-03061-4

Tang, X., Mo, C., Wang, Y., Wei, D., and Xiao, H. (2013). Anti-tumour Strategies Aiming to Target Tumour-Associated Macrophages. *Immunology* 138 (2), 93–104. doi:10.1111/imm.12023

Tauriello, D. V. F., Palomo-Ponce, S., Stork, D., Berenguer-Llergo, A., Badia-Ramentol, J., Iglesias, M., et al. (2018). TGFβ Drives Immune Evasion in Genetically Reconstituted colon Cancer Metastasis. *Nature* 554 (7693), 538–543. doi:10.1038/nature25492

Teramoto, Y., Jiang, G., Goto, T., Mizushima, T., Nagata, Y., Netto, G. J., et al. (2021). Androgen Receptor Signaling Induces Cisplatin Resistance via Down-Regulating GULP1 Expression in Bladder Cancer. *Ijms* 22 (18), 10030. doi:10.3390/ijms221810030

Topalian, S. L., Hodi, F. S., Brahmer, J. R., Gettinger, S. N., Smith, D. C., McDermott, D. F., et al. (2012). Safety, Activity, and Immune Correlates of

Anti-PD-1 Antibody in Cancer. *N. Engl. J. Med.* 366 (26), 2443–2454. doi:10.1056/NEJMoa1200690

Turley, S. J., Cremasco, V., and Astarita, J. L. (2015). Immunological Hallmarks of Stromal Cells in the Tumour Microenvironment. *Nat. Rev. Immunol.* 15 (11), 669–682. doi:10.1038/nri3902

Wolf, Y., Bartok, O., Patkar, S., Eli, G. B., Cohen, S., Litchfield, K., et al. (2019). UVB-induced Tumor Heterogeneity Diminishes Immune Response in Melanoma. *Cell* 179 (1), 219–235. doi:10.1016/j.cell.2019.08.032

Yan, Y., Cai, J., Huang, Z., Cao, X., Tang, P., Wang, Z., et al. (2021). A Novel Ferroptosis-Related Prognostic Signature Reveals Macrophage Infiltration and EMT Status in Bladder Cancer. *Front. Cell Dev. Biol.* 9, 712230. doi:10.3389/fcell.2021.712230

Yang, C., Huang, X., Li, Y., Chen, J., Lv, Y., and Dai, S. (2021). Prognosis and Personalized Treatment Prediction in TP53-Mutant Hepatocellular Carcinoma: an In Silico Strategy towards Precision Oncology. *Brief. Bioinformatics* 22 (3). doi:10.1093/bib/bbaa164

Yu, C., Mannan, A. M., Yvone, G. M., Ross, K. N., Zhang, Y.-L., Marton, M. A., et al. (2016). High-throughput Identification of Genotype-specific Cancer Vulnerabilities in Mixtures of Barcoded Tumor Cell Lines. *Nat. Biotechnol.* 34 (4), 419–423. doi:10.1038/nbt.3460

Zeng, D., Li, M., Zhou, R., Zhang, J., Sun, H., Shi, M., et al. (2019). Tumor Microenvironment Characterization in Gastric Cancer Identifies Prognostic and Immunotherapeutically Relevant Gene Signatures. *Cancer Immunol. Res.* 7 (5), 737–750. doi:10.1158/2326-6066.CIR-18-0436

Zeng, D., Ye, Z., Wu, J., Zhou, R., Fan, X., Wang, G., et al. (2020). Macrophage Correlates with Immunophenotype and Predicts Anti-PD-L1 Response of Urothelial Cancer. *Theranostics* 10 (15), 7002–7014. doi:10.7150/thno.46176

Zhang, B., Wu, Q., Li, B., Wang, D., Wang, L., and Zhou, Y. L. (2020). m6A Regulator-Mediated Methylation Modification Patterns and Tumor Microenvironment Infiltration Characterization in Gastric Cancer. *Mol. Cancer* 19 (1), 53. doi:10.1186/s12943-020-01170-0

Zhang, H., Song, J., Dong, J., Liu, Z., Lin, L., Wang, B., et al. (2021). Tumor Microenvironment Analysis Identified Subtypes Associated with the Prognosis and the Tumor Response to Immunotherapy in Bladder Cancer. *Front. Genet.* 12, 551605. doi:10.3389/fgene.2021.551605

Zhang, X., Shi, M., Chen, T., and Zhang, B. (2020). Characterization of the Immune Cell Infiltration Landscape in Head and Neck Squamous Cell Carcinoma to Aid Immunotherapy. *Mol. Ther. - Nucleic Acids* 22, 298–309. doi:10.1016/j.omtn.2020.08.030

Zhao, S., Ma, D., Xiao, Y., Li, X. M., Ma, J. L., Zhang, H., et al. (2020). Molecular Subtyping of Triple-Negative Breast Cancers by Immunohistochemistry: Molecular Basis and Clinical Relevance. *Oncol.* 25 (10), e1481–e91. doi:10.1634/theoncologist.2019-0982

Conflict of Interest: The authors declare that the research was conducted in the absence of any commercial or financial relationships that could be construed as a potential conflict of interest.

Publisher's Note: All claims expressed in this article are solely those of the authors and do not necessarily represent those of their affiliated organizations, or those of the publisher, the editors and the reviewers. Any product that may be evaluated in this article, or claim that may be made by its manufacturer, is not guaranteed or endorsed by the publisher.

frontiers in Cell and Developmental Biology

ORIGINAL RESEARCH
published: 03 December 2021
doi: 10.3389/fcell.2021.760369

DNA Methylation Modification Map to Predict Tumor Molecular Subtypes and Efficacy of Immunotherapy in Bladder Cancer

Fangdie Ye[1,2†], Yingchun Liang[1,2†], Jimeng Hu[1,2†], Yun Hu[1,2], Yufei Liu[1,2], Zhang Cheng[1,2], Yuxi Ou[1,2], Chenyang Xu[1,2] and Haowen Jiang[1,2,3*]*

[1]Department of Urology, Huashan Hospital, Fudan University, Shanghai, China, [2]Fudan Institute of Urology, Huashan Hospital, Fudan University, Shanghai, China, [3]National Clinical Research Center for Aging and Medicine, Huashan Hospital, Fudan University, Fudan, China

OPEN ACCESS

Edited by:
Yi Zhang,
Euler Technology, China

Reviewed by:
Yu Zhao,
Capital Medical University, China
Kaijie Wu,
The First Affiliated Hospital of Xi'an Jiaotong University, China

***Correspondence:**
Chenyang Xu
cyxu_huashan@163.com
Haowen Jiang
urology_hs@163.com

[†]*These authors have contributed equally to this work*

Specialty section:
This article was submitted to Molecular and Cellular Pathology, a section of the journal Frontiers in Cell and Developmental Biology

Received: *18 August 2021*
Accepted: *10 November 2021*
Published: *03 December 2021*

Citation:
Ye F, Liang Y, Hu J, Hu Y, Liu Y, Cheng Z, Ou Y, Xu C and Jiang H (2021) DNA Methylation Modification Map to Predict Tumor Molecular Subtypes and Efficacy of Immunotherapy in Bladder Cancer. Front. Cell Dev. Biol. 9:760369. doi: 10.3389/fcell.2021.760369

Background: Considering the heterogeneity and complexity of epigenetic regulation in bladder cancer, the underlying mechanisms of global DNA methylation modification in the immune microenvironment must be investigated to predict the prognosis outcomes and clinical response to immunotherapy.

Methods: We systematically assessed the DNA methylation modes of 985 integrated bladder cancer samples with the unsupervised clustering algorithm. Subsequently, these DNA methylation modes were analyzed for their correlations with features of the immune microenvironment. The principal analysis algorithm was performed to calculate the DMRscores of each samples for qualification analysis.

Findings: Three DNA methylation modes were revealed among 985 bladder cancer samples, and these modes are related to diverse clinical outcomes and several immune microenvironment phenotypes, e.g., immune-desert, immune-inflamed, and immune-excluded ones. Then patients were classified into high- and low-DMRscore subgroups according to the DMRscore, which was calculated based on the expression of DNA methylation related genes (DMRGs). Patients with the low-DMRscore subgroup presented a prominent survival advantage that was significantly correlated to the immune-inflamed phenotype. Further analysis revealed that patients with low DMRscores exhibited less TP53 wild mutation, lower cancer stage and molecular subtypes were mainly papillary subtypes. In addition, an independent immunotherapy cohort confirmed that DMRscore could serve as a signature to predict prognosis outcomes and immune responses.

Conclusion: Global DNA methylation modes can be used to predict the immunophenotypes, aggressiveness, and immune responses of bladder cancer. DNA methylation status assessments will strengthen our insights into the features of the immune microenvironment and promote the development of more effective treatment strategies.

Keywords: bladder cancer, DNA methylation regulators, immunotherapy, prognostic model, tumor microenvironment

INTRODUCTION

DNA methylation modification is one of the most representative epigenetic modifications, which is indispensable in vertebrate development and illnesses (Ortega-Recalde and Hore, 2019; da Rocha and Gendrel, 2019). Besides, it has been demonstrated to associate with multiple biological functions in cancer, e.g., the formation and evolution of tumor microenvironment, as well as impairment restoration in the immune cycle (Chen et al., 2020; Zhang et al., 2020a). On the other hand, abnormal DNA methylation is also significantly related to the occurrence of multiple cancer types, such as sarcoma (Koelsche et al., 2021), bladder cancer (Liu et al., 2021a), and vulvar intraepithelial neoplasia (Thuijs et al., 2021).

Bladder cancer is an extremely malignant urogenital neoplasm (Siegel et al., 2021). Heterogeneous distributions of genome clusters lead to molecular and cellular heterogeneity in tumors, which affect clinical outcomes and treatment responses (Qiu et al., 2019; Craig et al., 2020). Despite pronounced progress in the treatment of bladder cancer, more effective therapeutic strategies are still in demand. Studies have demonstrated that several genes involved in the occurrence and progression of bladder cancer are regulated by promoter methylation. For example, Chen X et al. built a diagnostic model based on 2 DNA methylation markers for early detection and recurrent monitoring of bladder cancer. Wilhelm CS et al. discovered that LINE1 hypomethylation may contribute to bladder cancer tumorigenesis, especially in women (Wilhelm et al., 2010). Kandimalla R et al. summarized the biomarkers of DNA methylation and identified that methylated genes, including SFRP1, SOX9, FHIT, CDH1, PMF1, RUNX3, LAMC2, and RASSF1A, are related to the poor clinical outcomes in bladder cancer patients (Kandimalla et al., 2013). In short, DNA methylation is involved in carcinogenesis or tumor inhibition across varying scenarios.

In recent years, immune checkpoint blockade therapy has emerged as a promising therapeutic strategy. It aims to enhance the immune activity of T lymphocytes to kill tumor cells by inhibiting immune checkpoints, such as PD-1 and its ligand PD-L1 (Yi et al., 2018). Studies have shown that immunotherapy could improve clinical outcomes of numerous tumors, such as ovarian cancer (Wan et al., 2021), bladder cancer (Han et al., 2021), and colorectal cancer (Liu et al., 2021b). However, patients respond to immunotherapy differently, and the effective rate of immune checkpoint blockade therapy has been less than 20%. The expression level of PD-L1, tumor microenvironment (TME), and tumor mutation burden (TMB) have been reported as signatures to evaluate the clinical responses to immunotherapy (Samstein et al., 2019). Previous studies demonstrated that DNA methylation may contribute to the alteration of TME. For instance, Sasidharan Nair V et al. discovered that DNA hypomethylation shall alter the expression of CTLA-4, TIGIT, and PD-1 genes (Sasidharan Nair et al., 2018). Elashi AA et al. also revealed that an abnormal promoter methylation profile is correlated to the peripheral upregulation of TIGIT and PD-1 in many cancers. They speculated that a combined administration of anti-PD-1 agents and demethylation inhibitors could be a more effective immunotherapeutic strategy than the current ones (Elashi et al., 2019). However, the regulatory mechanisms of global DNA methylation on tumor microenvironment and immune response in bladder cancer remain unclear.

In this study, genomic data and clinical information of 985 samples from six independent bladder cancer cohorts were included. DNA methylation modes were clarified by analyzing the expression of fifteen DNA methylation regulators in these samples We investigate the DNA methylation regulators rather than DNA methylation itself, because the biology function of DNA methylation would be altered according to the genomic environment. Specifically, three DNA methylation modes were identified to meet the criteria of immune-desert, immune-inflamed, and immune-excluded immunophenotypes, respectively. Moreover, an evaluation system was built to qualify the DNA methylation modes in individual patients, and the patients' clinical responses to immunotherapy were assessed based on their DMRscore. Our study provides a new perspective to observe the global DNA methylation status and the immunophenotype of individual tumors in bladder cancer so that more specified precision medicine could be achieved.

RESULTS

The Landscape of DNA Methylation Regulators in Bladder Cancer

We executed systematic research that included 15 DNA methylation regulators and summarizes the mutation rates of all these regulators in bladder cancer. Among 412 samples, 52 samples experienced alteration of DNA methylation regulators, with frequency 12.62%. According to the waterfall diagram, alterations of the MBD1 gene were the most frequent, and these alterations have been reported to participate in tumorigenesis. Besides, DNMT1, DNMT3A, and DNMT3B genes also exhibited an alteration frequency of 2% (**Figure 1A**). Furthermore, co-occurrence mutation was observed in several DNA methylation regulators despite their functional differences, including NTHL1, MBD3, MECP2, UHRF2, and ZBTB33 (**Supplementary Figure S1C**).

In addition, a prevalent CNV alteration was observed in the fifteen regulators (**Figure 1D**). Specifically, DNMT3B, UHRF2, and MECP2 demonstrated a widespread frequency of amplification in samples while MBD3, UHRF1, and NTHL1 were frequently detected. The locations and circle sequences of the DNA methylation regulators along the chromosomes are depicted in **Figure 1B**. Moreover, the principal component analysis revealed that the bladder cancer can be distinguished from normal samples by observing the expression levels of the 15 regulators (**Figure 1C**). In addition, the mRNA expressions of the 15 DNA methylation regulators are also significantly different between BLCA tumors and normal tissues (**Figure 1E**). In a word, the genomic imbalance of DNA methylation regulators is vital for bladder cancer tumorigenesis and development.

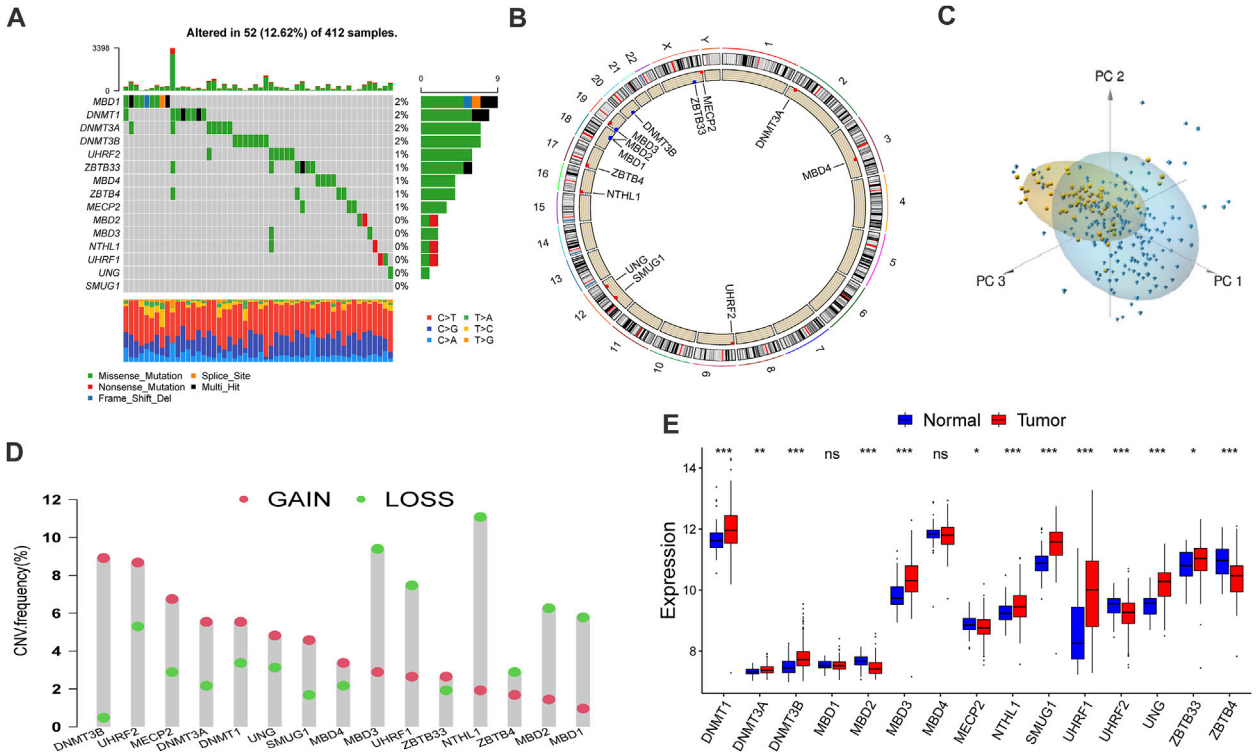

FIGURE 1 | Landscape of genetic alteration and transcriptome variation of DNA methylation regulators in bladder cancer. **(A)** The alteration frequency of 15 DNA methylation regulators in 412 bladder cancer samples (TCGA-BLCA). the annotation of each variant types was displayed by the bagplots right barplots. Each cohort represented an individual sample. The stacked barplot below displayed conversion ratio for each sample. **(B)** The location of CNV alteration of DNA methylation regulators on 23 chromosomes was displayed by circular plot. **(C)** Principal component analysis (PCA) for the transcriptome characteristics of 15 DNA methylation regulators to distinguish tumors from normal samples in GSE13507 cohort. Tumor samples were labeled with blue color and normal samples were labeled with yellow. **(D)** The frequency of copy number variation in TCGA-BLCA cohort. Deletion frequency: the green dot and amplification frequency: red dot. The number represented the variation frequency. **(E)** The transcriptome characteristics of 15 DNA methylation regulators between normal and bladder cancer tissues. Tumor: red box; Normal: blue box. The median value: black lines in boxes, the outliers: black dots out boxes. The asterisks represented the statistical *p* value (*$p < 0.05$; **$p < 0.01$; ***$p < 0.001$).

DNA Methylation Regulator Clusters

The complete clinical information and transcriptome data of six GEO datasets (GSE13507, GSE31684, GSE32548, GSE48075, GSE48476, GSE80691) and TCGA-BLCA were enrolled into one cohort for further exploration. A univariate Cox regression analysis was performed to find the prognostic value of the 15 DNA methylation regulators in bladder cancer patients (**Supplementary Figure S1B**). Following that, the comprehensive landscape of the regulators' intercorrelation and their prognostic attributes for bladder cancer were calculated by network planning (**Figure 2B**). From these results, we speculated that DNA methylation regulators may be related to the heterogeneity of bladder cancer. Therefore, unsupervised clustering was performed to explore ultramodern DNA methylation regulator clusters (DMRclusters) based on the expression levels of the regulators in the meta-cohort. Three DMRclusters were classified, including 306, 348, and 331 sample patients in DMRcluster A, B, and C, respectively, and these distinct DMRclusters could be distinguished via the principal component analysis (**Figure 2D**). Specifically, DMRcluster A presented a particularly prominent survival advantage, but DMRCluster B exhibited the worst clinical outcome in the integrated cohort (**Figure 2A**).

The Immune Features of Distinct DMRclusters

The GSVA enrichment analysis was performed to identify the biological processes in the DMRclusters. Judging from the results, DMRcluster A was enriched in immune activation pathways, such as the T/B cell receptor signaling pathway, toll-like receptor signature, as well as complement and coagulation cascades. On the other hand, DMRcluster B was prominently associated with immune suppression, and DMRcluster C was even more prominent in carcinogenic pathways, including the P53 signature pathway and the ERBB signature pathway (**Figures 2E,F**). As expected, subsequent analyses revealed that DMRcluster A was significantly enriched in cells related to acquired immunity, including activated B cells, central memory CD4/CD8 T cells, and activated dendritic cells (**Figure 3B**). Such a finding could well explain the results of the survival analysis. Meanwhile, stromal activity (e.g., epithelial-mesenchymal transition &, EMT) was remarkably enriched in

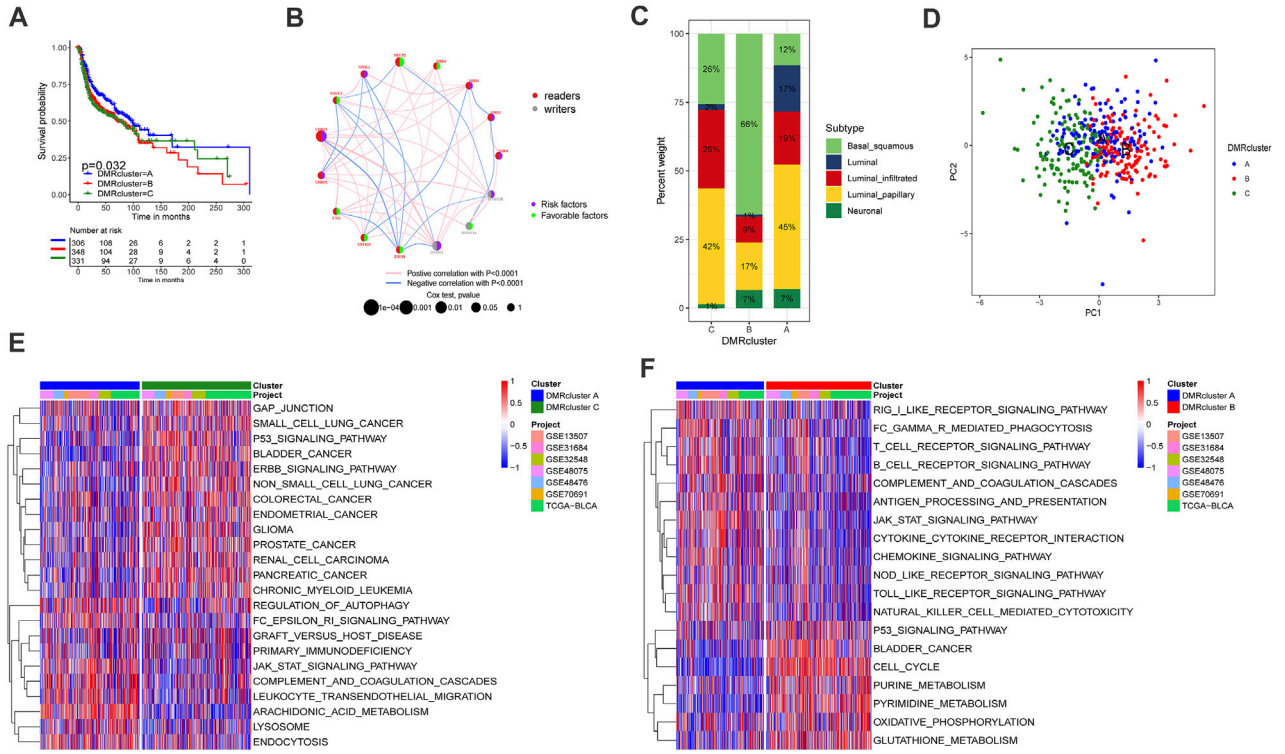

FIGURE 2 | Clusters of DNA methylation modes and biological profiles of each cluster. A Kaplan-Meier curve with *p* value 0.032 displayed a remarkable difference among three DNA methylation modes, the DMRcluster B presented a remarkable poor clinical outcome. DMRcluster **(A)**: 306 samples, DMRcluster **(B)**: 348 samples and DMRcluster **(C)**: 331 samples. The meta cohort including 985 samples (GSE13507, GSE31684, GSE32548, GSE48075, GSE48476, GSE80691 and TCGA-BLCA). **(B)** The interplay among DNA methylation regulators in bladder cancer. Red and gary represented readers and writers respectively. The size of circles displayed the influence of each regulator on clinical outcomes. The lines connecting regulators represented their interactions, and thickness represented the correlation strength. Negative correlation was labeled with blue and positive correlation was labeled with red. Risk factor: purple, favorable factor: green. **(C)** The proportion of molecular subtypes in the three DNA methylation modes (TCGA-BLCA). Basal squamous subtype, green; Luminal subtype, blue; luminal infiltrated subtype, red; luminal papillary subtype, yellow; and Neuronal subtype, olivedrab. **(D)** Principal component analysis (PCA) for the transcriptome characteristics of three DMRclusters. DMRcluster A was labeled with blue color, DMRcluster **(B)** was labeled with red color and DMRcluster **(C)** was labeled with green. **(E,F)** Gene set variant analysis displayed the activation status of biological pathways in diverse DMRclusters. The heatmap help us to observe the difference of biology pathway activity among three DMRclusters. Blue represented inhibited pathways and red represented activated pathway. **(E)** DMRcluster **(A)** vs. DMRcluster **(B)**; F DMRcluster **(B)** vs. DMRcluster **(C)**.

DMRcluster C (**Figure 3A**). Based on all the previous results, we speculated that these DMRclusters had remarkably diverse features in terms of immune cell infiltration into the tumor microenvironment. Specifically, DMRclusters A, B, C were featured by immune-inflamed, immune-desert, and immune-excluded phenotypes, respectively.

The Transcriptome Data and Clinical Features of DMRclusters

To further investigate these DMRclusters in diverse biological processes and clinical features, we focused on the TCGA-BLCA cohort containing 407 bladder cancer patients and their exhaustive clinical information. Similarly, the patients were classified into three clusters with unsupervised clustering (**Supplementary Figures S2A–D**). Judging from the results DNA methylation regulators' transcriptional profiles among the three DMRclusters demonstrated significant difference, which was validated by one-way ANOVA analysis (**Supplementary Figure S2E**). Specifically, DMRcluster A revealed high expression of DNMT3B and DNMT3A, DMRcluster B was characterized by higher DNMT1 and UHRF1 expressions, and DMRcluster C exhibited lower contents of DNMT1, DNMT3A, DNMT3B, and UHRF1 at various extents (**Figure 3C**). Patients with the luminal infiltrated subtype were characterized by DMRcluster A, while the basal squamous subtype was featured by DMRcluster B (**Figure 2C**); besides, both DMRclusters B and C were enriched in the neuronal subtype (**Figure 4D**). In bladder cancer treatments, the neuronal subtype is particularly difficult because of its poor clinical outcome, while the luminal papillary subtype is prone to better survival. Thus, we performed the K-M analysis, and the results also validated our conjecture that patients characterized by DMRclusters B and C exhibited significantly more rapid disease progression and poorer clinical outcomes, while DMRcluster A presented a remarkable survival advantage (**Supplementary Figure S2F**). In addition, the luminal infiltration subtype in bladder cancer is characterized by low

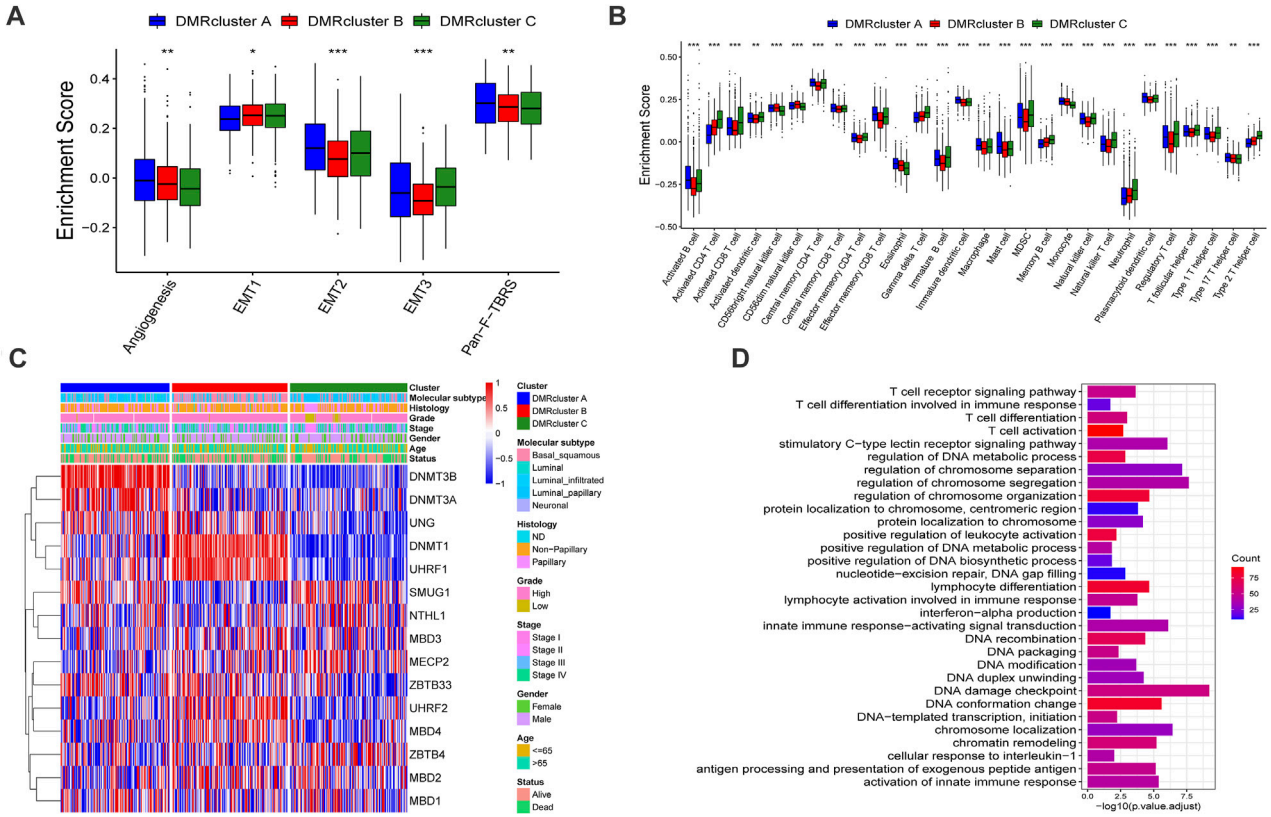

FIGURE 3 | Tumor microenvironment characteristics and transcriptome profile in three DNA methylation modification modes. **(A)** stromal activation pathways among three different DNA methylation modification modes include EMT, angiogenesis and Pan-F-TBRS. **(B)** The content of each tumor microenvironment immune infiltrating cells in three DNA methylation modification modes. The median value: black lines in boxes, the outliers: black dots out boxes. **(C)** The heatmap help us to observe the expression level of DNA methylation regulators among different DMRclusters (TCGA-BLCA cohort). DMRcluster subtypes, Molecular subtypes, Histology, Grade, Stage, Gender, Age and Survival status were used as patient annotations. Red represented high expression level of DNA methylation regulators and blue represented low expression level. **(D)** Functional annotation for DNA methylation-related genes. Red represented more enriched genes and blue represented a small number of enriched genes.

tumor cell purity and high lymphocytic infiltration. Most patients with the luminal infiltration subtype were categorized into DMRcluster A, and only a small amount of luminal infiltration was observed in DMRcluster B (**Figure 4D**), suggesting that DMRcluster A is related to immune activation and DMRcluster B is associated with the immune-desert phenotype.

Functional Annotations of DMRGs

To further explore the potential biological processes in each DMRcluster, the R package named "limma" was performed to find DMRGs, and a total of 832 genes were selected (**Supplementary Figure S2G**). GO analysis was executed on the DMRGs using the R package "clusterProfiler." DMRGs were prominently enriched in immunity activation pathways, DNA methylation, and cell proliferation, which verified that DNA methylation is vital in the immune regulation of tumor progression (**Figure 3D**).

To further investigate the mechanisms of DNA regulation, the patients were classified into three genomic subtypes based on the expression of the 832 DMRGs. Similarly, the genomic subtypes were identified via the unsupervised clustering algorithm. They were termed Gene cluster A, B, and C, respectively (**Supplementary Figures S3A–D**), and they were all related to DNA methylation in bladder cancer. A heat map also demonstrated that the three Gene clusters can be distinguished by their signature transcriptomes (**Figure 4A**). According to the K-M survival method, Gene cluster A presented a remarkable survival advantage, while Gene cluster B was proved to be associated with a poorer prognosis (**Figure 4D**). Moreover, the three Gene clusters revealed significant differences in the expression of DNA methylation regulators (**Figure 4G**).

TME Characteristics in the Three Gene.clusters

To identify the role of Gene clusters in the immune regulation of TME, we investigated the expression of cytokines and chemokines in Gene clusters. The targets of identification were chosen from the literature, among which ZEB1, TGFB2, PDGFRA, VIM, COL4A1, TGFBR2, TWIST1, ACTA2, and SMAD9 are related to transcripts of the transforming growth

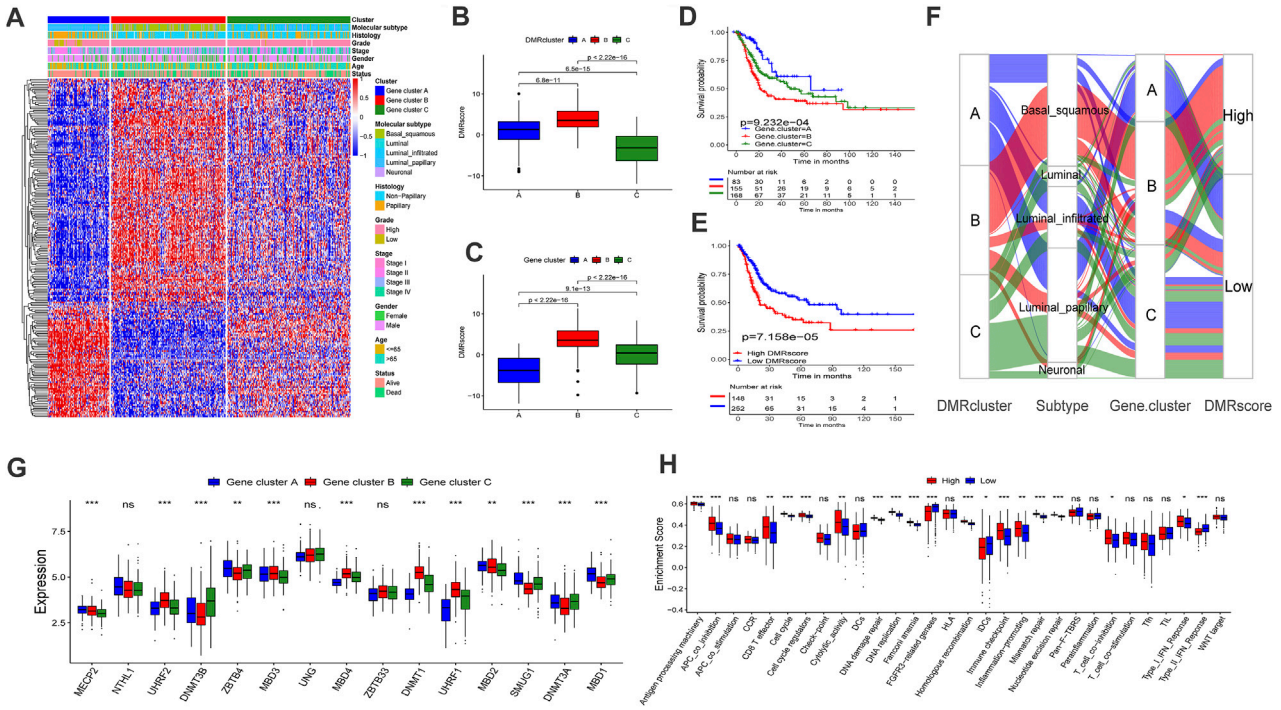

FIGURE 4 | Construction of DNA methylation signatures for individual sample. **(A)** The heatmap help us to observe the transcriptome landscape among different Gene.clusters (TCGA-BLCA cohort). Gene.cluster subtypes, Molecular subtypes, Histology, Grade, Stage, Gender, Age and Survival status were used as patient annotations. Red represented high expression level and blue represented low expression level. B-C Differences in DMRscore among three DMRclusters **(B)** or Gene.clusters **(C)** in TCGA-BLCA cohort (Kruskal-Wallis test, $p < 0.001$). D-E Kaplan-Meier curve displayed a remarkable difference among three Gene. clusters (**(D)**, $p < 0.001$) or DMRscore subgroups (**(E)**, $p < 0.001$) in TCGA-BLCA cohort. **(F)** Sankey diagram displayed the alteration of DMRclusters, molecular subtypes, Gene.cluster and DMRscore. **(G)** The transcriptome characteristics of 15 DNA methylation regulators among Gene.clusters. Gene.cluster **(A)**: blue box; Gene.cluster **(B)**: red box. Gene.cluster C: green box. The median value: black lines in boxes, the outliers: black dots out boxes. **(H)** Differences in the known gene signatures between high DMRscore and low DMRscore subgroups. APC: antigen-presenting cells. The asterisks represented the statistical p value (*$p < 0.05$; **$p < 0.01$; ***$p < 0.001$).

factor (TGF) b/EMT pathway. Besides, HAVCR2, CD80, LAG3, CD86, TIGIT, PDCD1, TNFRSF9, PD-L1, IDO1, CTLA4, and PD-L2 are associated with the transcripts of immune checkpoints, and CXCL10, PRF1, CD8A, CXCL9, GZMB, GZMA, TNF, IFNG, and TBX2 are associated with immune-activated transcripts (Sotiriou et al., 2006; Barbie et al., 2009; Ritchie et al., 2015; Zeng et al., 2019).

We found that the transcripts related to immune activation pathways were significantly up-regulated in Gene cluster B, but the patients in this cluster did not show an expected survival advantage. Previous studies revealed that high stromal activation was associated with limited immune activation (MacGregor et al., 2019). Therefore, we investigated the transcripts related to the (TGF)b/EMT pathway in this cluster and demonstrated stromal activation within. Based on these findings, we assumed that anti-tumor effects of immune cells in Gene cluster B are limited by stromal activation, indicating that Gene cluster B is the immune-excluded subtype. Besides, the transcripts of immune checkpoints were examined as highly expressed in Gene cluster B, suggesting that immunotherapy may bring unexpected outcomes (**Supplementary Figures S3F–H**).

To further investigate the functions of DMRGs, we examined the identified pathways in bladder cancer patients. Gene cluster A was found to enrich in CD8 T effector, DNA replication, mismatch repair, and antigen processing machinery pathways (**Supplementary Figure S3E**). Previous studies demonstrated that bladder cancer can be classified into five subtypes according to the molecular phenotype. Among them, the luminal-papillary subtype exhibits the best prognosis with a five-year survival rate of 60%. On the other hand, the five-year survival rate of neuronal bladder cancer is only 17% (Robertson et al., 2017). Our findings suggested that Gene cluster A was almost fully composed of the luminal-papillary subtype, which was relevant to survival advantage (**Figure 4F**).

Individual Modification Patterns of DNA Methylation

By now, the experimental results have confirmed that DNA methylation is irreplaceable in the formation of distinct TME landscapes. However, investigations above were not helpful to predict the DNA methylation status of an individual sample as they were conducted on a population. Since tumors are heterogeneous and complex, we built the DMRscore model to qualify the DNA methylation status based on the expression of DMRGs.

In this section, we attempted to assess whether DMRscore is effective in predicting clinical outcomes. Patients were classified

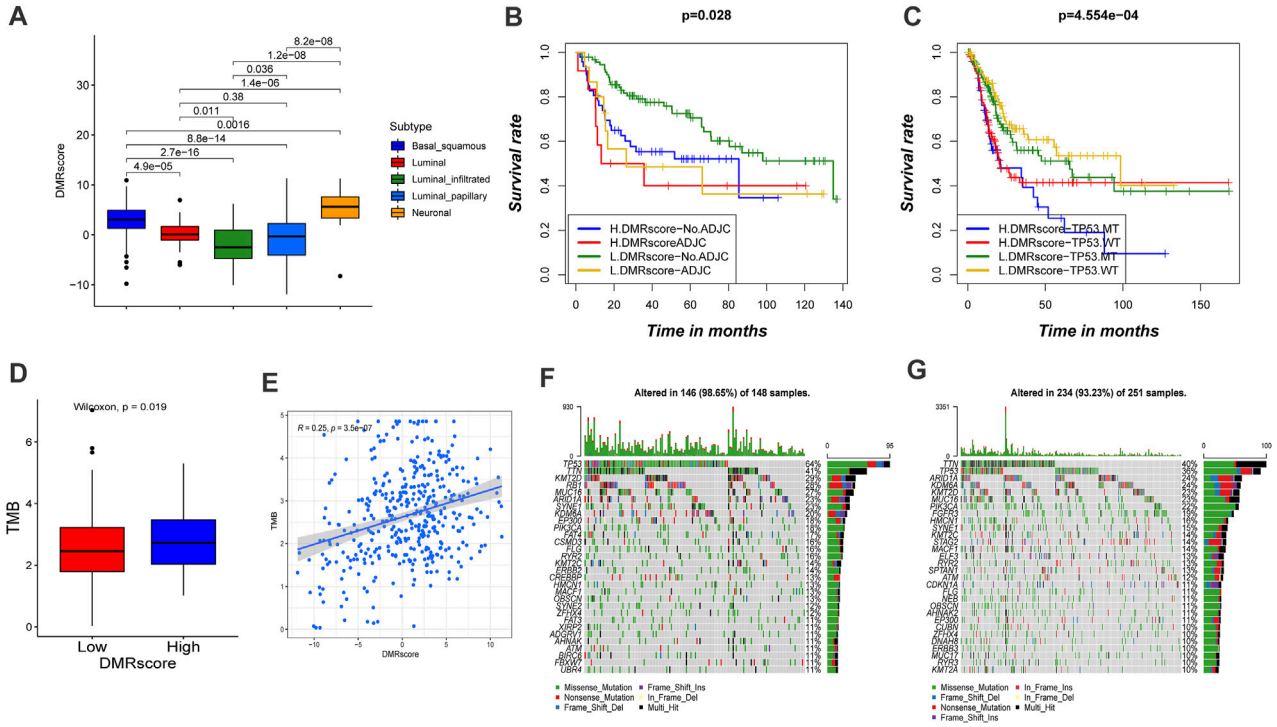

FIGURE5 | Characteristics of DMRscore in TCGA molecular subtypes and tumor mutation burden. **(A)** Differences in DMRscore among diverse bladder cancer molecular subtypes. Basal squamous subtype, blue; Luminal subtype, red; luminal infiltrated subtype, green; luminal papillary subtype, sapphire; and Neuronal subtype, yellow. **(B)** Kaplan-Meier curve showed the clinical prognosis of patients with combination of DMRscore and adjuvant chemotherapy stratification. H, high. L, low. ADJC, adjuvant chemotherapy (p = 0.028). **(C)** Kaplan-Meier curve showed the clinical prognosis of patients with combination of DMRscore and TP53 stratification. H, high. L, low. MT, mutation type; WT, wild type (p < 0.001). **(D)** Difference in tumor mutation burden between high DMRscore and low DMRscore (p = 0.019). **(E)** Correlation between DMRscore and tumor mutation burden. (R = 0.25, p < 0.001) **(F,G)** The landscape of tumor somatic mutation in TCGA-BLCA established by high **(F)** and low DMRscore **(G)**. Each column represented individual patients. The upper barplot displayed tumor mutation burden.

into groups of high and low DMRscores according to the best cutoff value. The correlation results between DMRscores and clinical outcomes showed that patients in the low DMRscore group exhibited a remarkable clinical advantage, while those in the other group demonstrated less satisfactory clinical outcomes (TCGA-BLCA cohort) (**Figure 4E**, p = 7.158e-05). The **Figure 4H** shown that patients with high DMRscore were enriched in APC_co_inhibition, T_cell_coinhibition, which revealed that this subgroup presented immunosuppression. Subsequently, we examined whether the DMRscore can serve as an independent index to evaluate the clinical outcomes of bladder cancer. Multivariate Cox regression analysis was used to take the independent indices, including age and DMRscore, into the calculation, and the results confirmed DMRscore as an independent and robust prognostic index (HR = 1.05; **Supplementary Figure S4A**). Variations of individual patients are displayed by the Sankey diagram (**Figure 4F**).

To reassure the predictive effects of DMRscore, we examined its relationship with the identified clusters by Kruskal-Wallis tests. The test results suggested that DMRscore could be used to predict DNA methylation clusters. Specifically, both DMRcluster B and Gene cluster B showed the highest median DMRscore (**Figures 4B,C**). In addition, patients suffering from neuronal bladder cancer also exhibited the highest median DMRscore among five molecular subtypes (**Figure 5A**). In a word, DMRscore has been proved as an effective index to assess the DNA methylation status of individual samples and predict clinical outcomes. In order to develop the accuracy of predictive performance, the prognostic nomogram included a DMRscore, and other clinical variables was constructed to evaluate the 1-, 3-, and 5-year overall survival probabilities (**Supplementary Figure S6**).

Particularly, the capability of DMRscore to assess the efficacy of adjuvant chemotherapy (ADJC) in bladder cancer patients was evaluated. DMRscore prediction results were not disturbed by ADJC: whether receiving ADJC or not, the low-DMRscore group always presented significant survival advantages. However, DMRscore cannot be utilized to judge whether ADJC can be applied on a bladder cancer patient, and patients with low DMRscores had shorter survival after ADJC. (**Figure 5B**). In addition, patients with high grade, TP53MT, and non-papillary subtypes of the cancer showed significantly higher DMRscores, with a poorer survival prognosis (**Figure 6A**). This also validated in E-MTAB-4321 cohort (**Supplementary Figure S4C**). Furthermore, the capability of DMRscore to assess the efficacy of TP53 mutation in bladder cancer patients was examined as well. We found that the L. DMRscore-TP53. WT group exhibited a remarkably advantageous survival, while the H. DMRscore-TP53. MT group demonstrated the worst clinical outcome

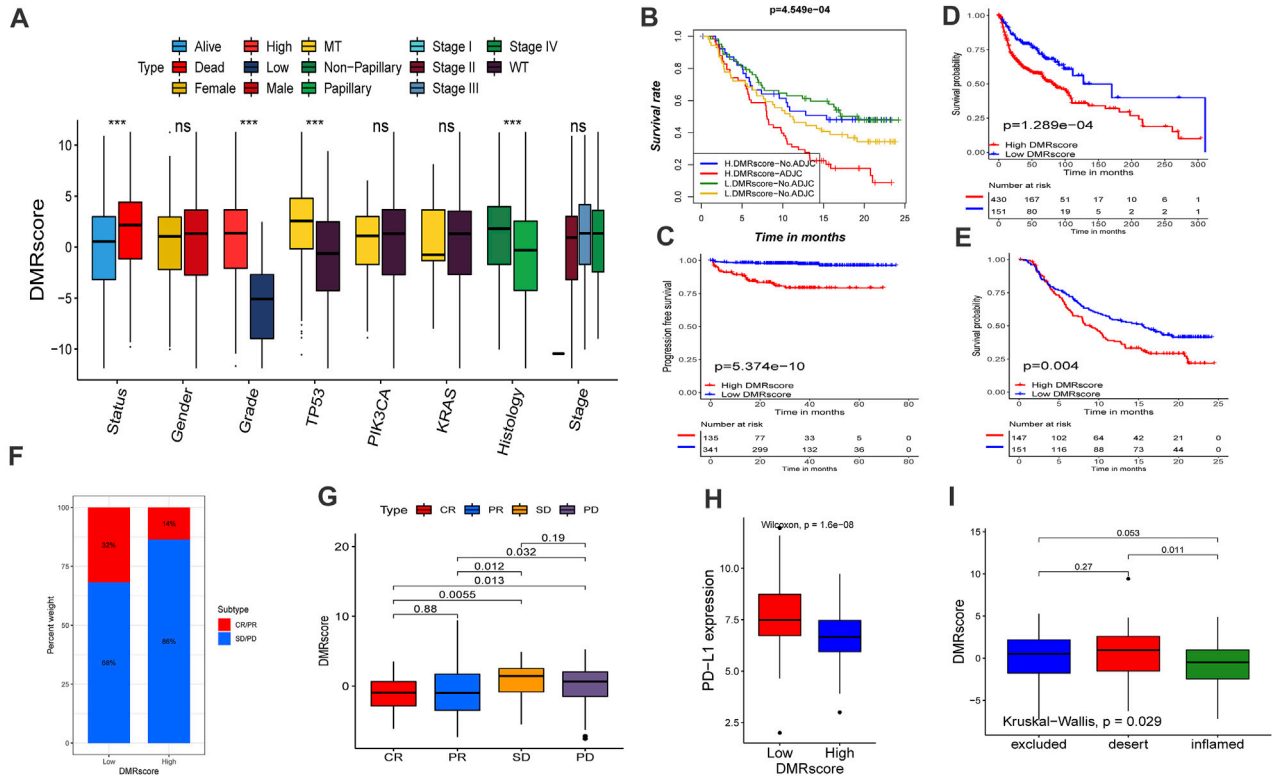

FIGURE 6 | Role of DNA methylation modification in clinical prediction. **(A)** Differences in DMRscore among different clinical status. The median value: black lines in boxes, the outliers: black dots out boxes. MT, mutation type; WT, wild type. **(B)** Kaplan-Meier curve showed the clinical prognosis of patients with combination of DMRscore and NEO stratification. H, high. L, low. NEO, Newantigen burden ($p < 0.001$). **(C)** Survival analyses for high (135 samples) and low (341 samples) DMRscore subgroups in the E-MTAB-4321 cohort using Kaplan-Meier curves ($p < 0.001$). **(D)** Survival analyses for high (430 samples) and low (151 samples) DMRscore subgroups in the GEO-metacohort cohort using Kaplan-Meier curves ($p < 0.001$). **(E)** Survival analyses for high (147 samples) and low (151 samples) DMRscore subgroups in the anti-PD-L1 cohort (IMvigor210 cohort) using Kaplan-Meier curves ($p = 0.004$). **(F,G)** The proportion of patients with response to PD-L1 blockade immunotherapy in low or high DMRscore subgroups. SD, stable disease; PD, progressive disease; CR, complete response; PR, partial response. Responser/Nonresponer: 32%/68% in the low m6Ascore groups and 14%/86% in the high m6Ascore groups. H Differences in PD-L1 expression between low and high m6Ascore groups ($p < 0.0001$). L Differences in DMRscore among distinct tumor immune phenotypes in IMvigor210 cohort. ($p = 0.029$).

(**Figure 5C**). K-M survival analysis and multivariate Cox regression analysis for the E-MTAB-4321 cohort also verified that DMRscore can serve as an independent prognostic index in bladder cancer (**Figure 6C**; **Supplementary Figure S4B**).

The Role of DNA Methylation Mode in anti-PD-1/PD-L1 Immunotherapy

Studies have verified that patients' response to immunotherapy is related to the TMB frequency, and higher TMB statuses lead to a persistent response to anti-PD-1/PD-L1 immunotherapy. We investigated the somatic mutation frequencies between high- and low-DMRscore groups in the TCGA-BLCA cohort. However, TMB quantification analysis verified that DMRscore is significantly and positively correlated to TMB (**Figures 5D,E**). Besides, the waterfall diagram showed that the high-DMRscore group was more susceptible to somatic mutations than the other group, with somatic mutation frequencies of 146/148 (98.65%) and 234/251 (93.23%), respectively (**Figures 5F,G**). Thus, our experimental results indicated that patients with a high DMRscore exhibit good response to anti-PD-1/PD-L1 immunotherapy, which is contradictory to previous findings. Consequently, we speculated that TMB frequency cannot be utilized to predict the effect of immunotherapy in this model.

In order to further examine the prediction performance of the DMRscore model, we applied the established DMRscore signature to other independent bladder cancer cohorts. Almost all cohorts presented survival differences as revealed by the DMRscore model except for two GEO datasets with few samples (**Supplementary Figures S5A–E**). The prediction performance of the DMRscore model for tumor stages was assessed by the receiver operating characteristic (ROC) curves, and the area under the curve (AUC) was 0.699 and 0.721at 3 and 5 years, respectively (**Supplementary Figures S5F,G**). These data indicated that the DMRscore signature could serve as a new biomarker to predict clinical outcomes.

Immune checkpoint blockade therapy has undoubtedly produced significant therapeutic benefits for many cancer patients. Based on the collected immunotherapy cohorts, we explored whether DMRscore can serve as a signature to

predict patients ' response to immunotherapy. Remarkable survival advantages are seen in patients with low DMRscores in the GEO-metacohort and anti-PD-L1 cohorts (IMvigor210, advantaged urothelial cancer) (**Figures 6D,E**). In addition, these patients also exhibited much better clinical outcomes when receiving anti-PD-L1 immune checkpoint blockade therapy (**Figure 6F**), and they were characterized by a significantly higher expression of PD-L1, a potential clinical response to immunotherapy (**Figure 6H**). Besides, we evaluated the tumor neoantigen burden in bladder cancer patients, and those with high neoantigen burden and low DMRscore signatures presented a significant survival advantage. (**Figure 6B**). Judging from **Figure 6G**, the DMRscore signature was a robust and potential biomarker to estimate patient response and clinical outcomes in immunotherapy. The immunophenotypes of metastatic urothelial cancer have been distinguished in the IMvigor210 cohort, so we studied the differences of DMRscore among them (**Figure 6I**). Most patients with low DMRscores exhibited the inflamed immunophenotype, to which individualized immunotherapy is crucial in treatment. In a word, DNA methylation modes are significantly related to tumor immunophenotypes and patients' clinical responses to immunotherapy.

DISCUSSION

DNA methylation is closely related to tumorigenesis and tumor progression. The extent of DNA methylation varies among cancer types and different stages of cancer progression. For example, the progression of prostate cancer has been related to DNA hypomethylation (Fraser et al., 2017; Wu et al., 2020), while bladder cancer pathology was characterized by global DNA hypermethylation (Osei-Amponsa et al., 2020). Thus, this observation revealed that DNA methylation may occur in a cancer-specific manner and alter the tumor microenvironment. Liu P et al. demonstrated that DNMT1 regulated the tumor growth in bladder cancer via modulating the status of DNA methylation in the promoter of PTEN (Liu et al., 2020). Zhu Y et al. demonstrated that MBD2 was a protective signature against bladder carcinoma according to the RNA data from the peripheral blood lymphocytes of 98 bladder cancer patients and 135 frequency-matched control patients (Zhu et al., 2004). Ying L et al. confirmed that epigenetic repression of RGS2 by UHRF1 contributes to bladder cancer progression (Ying et al., 2015). However, most researches only focused on the effect of a single DNA methylation regulator on the alteration of TME and tumor progression. As a result, the landscape of immune cell infiltration characteristics, which is mediated by the synergistic effect of multiple DNA methylation regulators, remained less understood. By clarifying the roles of diverse DNA methylation modes in immune cell infiltration, our knowledge about TME and anti-tumor response could advance, and foundations of more efficient immunotherapy strategies could be established.

In this study, we identified three DNA methylation modes based on expression level 15 DNA methylation regulators, and each DMRcluster was found to correlate with significantly different TMEs. Specifically, DMRclusters A, B, and C are characterized by immune-inflamed, immune-desert, and immune-excluded phenotypes, respectively. The immune-inflamed phenotype, or "hot tumor," is characterized by the existence of a large number of immune cells in the TME (Zhang et al., 2020b; Gruber et al., 2020; Yu et al., 2021). The other two phenotypes, or "cold tumor," show non-inflammatory infiltration. Despite the immune-excluded phenotype exhibits considerable immune cell infiltration, the immune cells are constrained by the stromal component that can be present either in the tumor capsule or throughout the whole tumor tissue to prevent the immune cells from exerting anti-tumor effects (Lambrechts et al., 2018; Kaymak et al., 2021). Such an idea is verified by the strong stromal activation in DMRcluster C, where the EMT pathway inhibited the activity of immune cells. Thus, our classifications of different DNA methylation modes were confirmed feasible and effective.

In addition, we confirmed that the transcriptomes in distinct DNA methylation modes are different, and obtained differentially expressed genes among thses DNA methylation patterns. Their actual compositions are related to DNA methylation and immune-related biological pathways. Therefore, we termed these differentially expressed genes as DMRGs. Three genomic subtypes were divided from the samples based on the expression of DMRGs, and these subtypes were also significantly related to distinct immunophenotypes. Therefore, DNA methylation is indeed irreplaceable in shaping the TME, and a systematic assessment of DNA methylation modes will contribute to understanding the mechanisms of tumorigenesis and to the advancements of personal medicine.

Since tumors are heterogeneous, we built a DMRscore model to evaluate DNA methylation features in individual tumors. The patients with high DMRscores were characterized as the immune-desert phenotype, while the patients with low DMRscores were characterized as the immune-inflamed phenotype. These results were further verified in the IMvigor210 cohort whose immunophenotypes have been identified (Necchi et al., 2017). Comprehensive analyses suggest that DMRscore signature is a robust and potential biomarker to assess patients' response to immunotherapy, Patients with low DMRscore displayed higher expression of PD-L1 compared to patients with higher DMRscore, and had a better response to Atezolizumab. In addition, patients with low DMRscores exhibited less TP53 wild mutation, lower cancer grade, low tumor mutation burden, and molecular subtypes were mainly papillary subtypes.

In summary, DMRscore can systematically assess the DNA methylation landscape and detect the TME characteristics, thereby identifying the immunophenotypes of individual patients for more efficient immunotherapeutic strategies. Besides, DMRscore can be used to evaluate other features of bladder cancer patients, including molecular subtypes, genetic mutation, tumor stage, and clinical histology. Moreover, DMRscore could serve as an independent prognostic indicator for effective prediction of clinical outcomes, as well as a factor that reflects the efficacy of and clinical responses to immunotherapy. Our research uncovers that DNA methylation can alter the immune microenvironment, resulting in the emergence of a "cold tumor." Herein, we propose a new hypothesis:

TABLE 1 | The gene expression profiles of bladder cancer included in this study.

Accession number	Source	Number of patients	Survival
TCGA: BLCA	Illumina RNAseq	432	OS
GEO: GSE13507	Illumina human-6 v2.0 expression beadchip	256	OS
GEO: GSE31684	Affymetrix Human Genome U133 Plus 2.0 Array	93	OS
GEO: GSE32548	Illumina HumanHT-12 V3.0 expression beadchip	131	OS
GEO: GSE48075	Illumina HumanHT-12 V3.0 expression beadchip	142	OS
GEO: GSE48276	Illumina HumanHT-12 WG-DASL V4.0 R2 expression beadchip	116	OS
GEO: GSE70691	Illumina HumanHT-12 WG-DASL V4.0 R2 expression beadchip	49	OS
ArrayExpress: E-MTAB-4321	Illumina HiSeq 2000	476	PFS
IMvigor210	Illumina RNAseq	348	OS

targeting DNA methylation regulators or DMR-related biological pathways could be effective to alter the DNA methylation status so that the unfavorable factors could be removed, and "cold tumors" could transform into "hot" ones. If proved correct, this hypothesis may promote the development of immunotherapeutic agents and drug combinations. Our study provided a new perspective to reveal the global DNA methylation status in bladder cancer patients, to predict the immunophenotype of individual tumors, and to promote individualized medicine.

Compared with existing investigations on prognostic signatures of bladder cancer, this study has some noteworthy advantages and shortcomings. Firstly, our investigation contributed to demonstrate the effect of DNA methylation modification in shaping of tumor microenvironment complexity and diversity, and explored the potential role of DNA methylation status to predict the clinical response to Atezolizumab therapy in urothelial carcinoma. The global DNA methylation landscape was constructed as the observation object to systematically investigate the effect of DNA methylation modification on tumor microenvironment, which has not been clarified before this study. Our study is mainly based on bioinformatics analysis and requires further clinical verification. Basic experiments are needed to verify the relationship between prognostic characteristics and immune infiltration; In the future we will conduct multicenter, large sample size studies to prospectively validate the model in order to further test the predictive potential and clinical ability of our model.

METHODS

Data Acquisition and Processing

The workflow in our study is displayed in **Supplementary Figure S1A**. 7 sets of transcriptome data and their corresponding clinical annotations were obtained from The Cancer Genome Alta (TCGA) and Gene-expression omnibus (GEO) databases, in which patients without complete clinical annotation were excluded. The "ComBat" algorithm in the R package "sva" was used to correct the batch effect of non-biological technical deviations. The comprehensive information of all alternative bladder cancer datasets is summarized in **Table 1**. The transcriptome data were downloaded from UCSC Xena database, and the somatic mutation information was obtained from TCGA database. We investigated numerous DNA methylation regulators, including the DNA methyltransferase family (DNMT1, DNMT3A, DNMT3B), the methyl-CpG-binding domain proteins (MeCP2, MBD1, MBD2, MBD3, MBD4), the ubiquitin-like proteins containing PHD and RING finger domains (UHRF1, UHRF2), zinc-finger domain proteins (ZBTB33, ZBTB4), NTHL1, SMUG1, and UNG (Jones, 2012; Moore et al., 2013; Koch et al., 2018). All the data were processed with the R package "Bioconductor" in R software (version 4.0.3).

Unsupervised Clustering of the Fifteen DNA Methylation Regulators

The unsupervised clustering algorithm was utilized to find out the distinct DNA methylation patterns based on the expression of the fifteen alternative DNA methylation regulators. The R package "ConsensuClsterPlus" was run 1,000 repetitive times to ensure the stability of classification, and the clustering number was assigned according to the K value. Subsequently, to verify the differences in biological functions among the three DNA methylation patterns, we ran the R package "GSVA." GSVA (gene set variation analysis) is an unsupervised method to evaluate variations of biological pathways in a sample population (Hänzelmann et al., 2013). The gene sets identified from GSVA were named "c2.cp.kegg.v6.2.-symbols."

Estimation of Tumor Microenvironment Cell Infiltration

The ssGSEA (single-sample gene set enrichment analysis) was utilized to calculate the relative amounts of gene components in each TME cell infiltration. A gene set that labels each immune cell type was adopted from the published studies (Charoentong et al., 2017). We investigated several immune cell types, including activated B cells, activated CD4 T cells, macrophages, eosinophils, CD56dim natural killer cells, and neutrophils. Each type of immune cell was counted for its enrichment score, and a box diagram was used to compare the scores in different DNA methylation patterns.

Identification of DNA Methylation Related Genes Among Distinct DNA Methylation Modes

To reveal which genes are DMRGs, we classified the samples into three DNA methylation clusters based on the expression levels of

fifteen DNA methylation regulators. The differentially expressed genes (DEGs) among the clusters were picked out by an R package named "limma" with the adjusted *p*-value <0.001.

Construction of DNA Methylation Regulator Score Groups

To qualify the DNA methylation status of individual samples from bladder cancer patients, we designed a DNA methylation signature termed DMRscore for assessments. The DNA methylation score groups were designed as follows: After identifying the DMRGs, we extracted the overlapping genes in them. Patients were divided into groups with distinct immune subtypes for further analysis, which was performed by an unsupervised clustering approach on the overlapping DMRGs. The number of gene clusters and model stability were validated by the consensus clustering algorithm. Furthermore, the univariate Cox regression analysis was executed for each overlapping DMRG to find out the ones related to prognosis. Subsequently, the established DMRscore model was subject to the principal component analysis (PCA) that combines the linear high-dimension indicators into their linear independent low-dimension counterparts. Moreover, in PCA, both types of indicators retain their original information, and the speed of data processing is accelerated. Both principal components (i.e., the two types of indicators) were extracted to calculate the DMRscore as DMRscore = $\sum$(PC1i + PC2i), where i is the expression level of the prognostic-related DMRGs.

To comprehensively evaluate the clinical outcome of each patient, a prognostic nomogram that contained the T stage, M stage, N stage, Gender, Age, clinical Stage and DMRscore was constructed. Subsequently, the 1-, 3-, 5- year overall survival probabilities were assessed by the calibration curve. A calibration curve close to 45° indicated the prominent prediction ability of the constructed model.

The Relationship Between DNA Methylation Features and Other Relevant Biological Functions

We obtained several gene sets that are involved in certain biological processes, e.g., DNA damage repair, homologous recombination, cell cycle, mismatch repair, DNA replication, nucleotide excision, carcinogenesis, Pan-F-TBRS, EMT, angiogenesis, immune checkpoint, actions of CD8 T effector cells, and antigen processing (Rosenberg et al., 2016; Şenbabaoğlu et al., 2016; Mariathasan et al., 2018). The correlations between DNA methylation features and these processes were further identified via correlation analysis.

The Genomic Profiles of Immune Checkpoint Blockage Effects and Corresponding Clinical Information

In order to explore the predictive effect of DNA methylation statuses in immunotherapy, we included an immunotherapeutic cohort in this study, advanced urothelial cancer treated with atezolizumab (IMvigor210 cohort) (Rosenberg et al., 2016). Atezolizumab is anti-PD-1 monoclonal antibody. The transcriptome profiles of immune checkpoint blockage effects and their corresponding clinical information were obtained from the public dataset.

Statistical Analysis

Data processing was conducted solely on R software (version 4.0.3). The R package named "limma" was run to analyze differential gene expressions among distinct subtypes. The Spearman analysis and distance correlation analysis were performed to calculate correlation coefficients between the DNA methylation regulators and the infiltration of immune cells. The survival curves of bladder cancer patients were plotted via the Kaplan-Meier method, and the curves' area under the curve (AUC) was calculated to evaluate the specificity and sensitivity of DMRscores obtained by the R package "pROC". The location and circle sequence of the DNA methylation regulators along the chromosomes were depicted by the R package "RCircos". Moreover, the R package "DEseq2" was run to normalize the raw data and convert the normalized cell count to TPM in the "IMvigor 210" cohort. Finally, the mutation landscape was drawn and presented via the R package "maftools." All statistic p numbers were bilateral, and $p < 0.05$ was considered statistically significant.

DATA AVAILABILITY STATEMENT

All datasets generated for this study are included in the article material, including the TCGA. database (https://portal.gdc.cancer.gov/), and GEO dataset (https://www.ncbi.nlm.nih.gov/gds/).

AUTHOR CONTRIBUTIONS

Study design and concept, FY. Supervision, HJ. Adviser, CX. All authors contributed towards data collection and analysis.

FUNDING

This study was supported by the National Natural Science Foundation of China (Grant Numbers: 81872102 and 81803900).

ACKNOWLEDGMENTS

We sincerely appreciate all members who participated in the data collection and analysis.

SUPPLEMENTARY MATERIAL

The Supplementary Material for this article can be found online at: https://www.frontiersin.org/articles/10.3389/fcell.2021.760369/full#supplementary-material

REFERENCES

Barbie, D. A., Tamayo, P., Boehm, J. S., Kim, S. Y., Moody, S. E., Dunn, I. F., et al. (2009). Systematic RNA Interference Reveals that Oncogenic KRAS-Driven Cancers Require TBK1. *Nature* 462 (7269), 108–112. doi:10.1038/nature08460

Charoentong, P., Finotello, F., Angelova, M., Mayer, C., Efremova, M., Rieder, D., et al. (2017). Pan-cancer Immunogenomic Analyses Reveal Genotype-Immunophenotype Relationships and Predictors of Response to Checkpoint Blockade. *Cel Rep.* 18 (1), 248–262. doi:10.1016/j.celrep.2016.12.019

Chen, X., Pan, X., Zhang, W., Guo, H., Cheng, S., He, Q., et al. (2020). Epigenetic Strategies Synergize with PD-L1/pd-1 Targeted Cancer Immunotherapies to Enhance Antitumor Responses. *Acta pharmaceutica Sinica B* 10 (5), 723–733. doi:10.1016/j.apsb.2019.09.006

Craig, A. J., von Felden, J., Garcia-Lezana, T., Sarcognato, S., and Villanueva, A. (2020). Tumour Evolution in Hepatocellular Carcinoma. *Nat. Rev. Gastroenterol. Hepatol.* 17 (3), 139–152. doi:10.1038/s41575-019-0229-4

da Rocha, S. T., and Gendrel, A.-V. (2019). The Influence of DNA Methylation on Monoallelic Expression. *Essays Biochem.* 63 (6), 663–676. doi:10.1042/ebc20190034

Elashi, A. A., Sasidharan Nair, V., Taha, R. Z., Shaath, H., and Elkord, E. (2019). DNA Methylation of Immune Checkpoints in the Peripheral Blood of Breast and Colorectal Cancer Patients. *Oncoimmunology* 8 (2), e1542918. doi:10.1080/2162402x.2018.1542918

Fraser, M., Sabelnykova, V. Y., Yamaguchi, T. N., Heisler, L. E., Livingstone, J., Huang, V., et al. (2017). Genomic Hallmarks of Localized, Non-indolent Prostate Cancer. *Nature* 541 (7637), 359–364. doi:10.1038/nature20788

Gruber, T., Kremenovic, M., Sadozai, H., Rombini, N., Baeriswyl, L., Maibach, F., et al. (2020). IL-32γ Potentiates Tumor Immunity in Melanoma. *JCI insight* 5 (18). doi:10.1172/jci.insight.138772

Han, H. S., Jeong, S., Kim, H., Kim, H.-D., Kim, A. R., Kwon, M., et al. (2021). TOX-expressing Terminally Exhausted Tumor-Infiltrating CD8+ T Cells Are Reinvigorated by Co-blockade of PD-1 and TIGIT in Bladder Cancer. *Cancer Lett.* 499, 137–147. doi:10.1016/j.canlet.2020.11.035

Hänzelmann, S., Castelo, R., and Guinney, J. (2013). GSVA: Gene Set Variation Analysis for Microarray and RNA-Seq Data. *BMC Bioinformatics* 14, 7. doi:10.1186/1471-2105-14-7

Jones, P. A. (2012). Functions of DNA Methylation: Islands, Start Sites, Gene Bodies and beyond. *Nat. Rev. Genet.* 13 (7), 484–492. doi:10.1038/nrg3230

Kandimalla, R., van Tilborg, A. A., and Zwarthoff, E. C. (2013). DNA Methylation-Based Biomarkers in Bladder Cancer. *Nat. Rev. Urol.* 10 (6), 327–335. doi:10.1038/nrurol.2013.89

Kaymak, I., Williams, K. S., Cantor, J. R., and Jones, R. G. (2021). Immunometabolic Interplay in the Tumor Microenvironment. *Cancer Cell* 39 (1), 28–37. doi:10.1016/j.ccell.2020.09.004

Koch, A., Joosten, S. C., Feng, Z., de Ruijter, T. C., Draht, M. X., Melotte, V., et al. (2018). Analysis of DNA Methylation in Cancer: Location Revisited. *Nat. Rev. Clin. Oncol.* 15 (7), 459–466. doi:10.1038/s41571-018-0004-4

Koelsche, C., Schrimpf, D., Stichel, D., Sill, M., Sahm, F., Reuss, D. E., et al. (2021). Sarcoma Classification by DNA Methylation Profiling. *Nat. Commun.* 12 (1), 498. doi:10.1038/s41467-020-20603-4

Lambrechts, D., Wauters, E., Boeckx, B., Aibar, S., Nittner, D., Burton, O., et al. (2018). Phenotype Molding of Stromal Cells in the Lung Tumor Microenvironment. *Nat. Med.* 24 (8), 1277–1289. doi:10.1038/s41591-018-0096-5

Liu, C., Liu, R., Wang, B., Lian, J., Yao, Y., Sun, H., et al. (2021). Blocking IL-17A Enhances Tumor Response to Anti-PD-1 Immunotherapy in Microsatellite Stable Colorectal Cancer. *J. Immunother. Cancer* 9 (1). doi:10.1136/jitc-2020-001895

Liu, P., Wu, L., Chand, H., Li, C., Hu, X., and Li, Y. (2020). Silencing of miR-152 Contributes to DNMT1-Mediated CpG Methylation of the PTEN Promoter in Bladder Cancer. *Life Sci.* 261, 118311. doi:10.1016/j.lfs.2020.118311

Liu, Z., Sun, T., Zhang, Z., Bi, J., and Kong, C. (2021). An 18-gene Signature Based on Glucose Metabolism and DNA Methylation Improves Prognostic Prediction for Urinary Bladder Cancer. *Genomics* 113 (1 Pt 2), 896–907. doi:10.1016/j.ygeno.2020.10.022

MacGregor, H. L., Sayad, A., Elia, A., Wang, B. X., Katz, S. R., Shaw, P. A., et al. (2019). High Expression of B7-H3 on Stromal Cells Defines Tumor and Stromal Compartments in Epithelial Ovarian Cancer and Is Associated with Limited Immune Activation. *J. Immunotherapy Cancer* 7 (1), 357. doi:10.1186/s40425-019-0816-5

Mariathasan, S., Turley, S. J., Nickles, D., Castiglioni, A., Yuen, K., Wang, Y., et al. (2018). TGFβ Attenuates Tumour Response to PD-L1 Blockade by Contributing to Exclusion of T Cells. *Nature* 554 (7693), 544–548. doi:10.1038/nature25501

Moore, L. D., Le, T., and Fan, G. (2013). DNA Methylation and its Basic Function. *Neuropsychopharmacol* 38 (1), 23–38. doi:10.1038/npp.2012.112

Necchi, A., Joseph, R. W., Loriot, Y., Hoffman-Censits, J., Perez-Gracia, J. L., Petrylak, D. P., et al. (2017). Atezolizumab in Platinum-Treated Locally Advanced or Metastatic Urothelial Carcinoma: post-progression Outcomes from the Phase II IMvigor210 Study. *Ann. Oncol.* 28 (12), 3044–3050. doi:10.1093/annonc/mdx518

Ortega-Recalde, O., and Hore, T. A. (2019). DNA Methylation in the Vertebrate Germline: Balancing Memory and Erasure. *Essays Biochem.* 63 (6), 649–661. doi:10.1042/ebc20190038

Osei-Amponsa, V., Buckwalter, J. M., Shuman, L., Zheng, Z., Yamashita, H., Walter, V., et al. (2020). Hypermethylation of FOXA1 and Allelic Loss of PTEN Drive Squamous Differentiation and Promote Heterogeneity in Bladder Cancer. *Oncogene* 39 (6), 1302–1317. doi:10.1038/s41388-019-1063-4

Qiu, Z., Li, H., Zhang, Z., Zhu, Z., He, S., Wang, X., et al. (2019). A Pharmacogenomic Landscape in Human Liver Cancers. *Cancer Cell* 36 (2), 179–193. e11. doi:10.1016/j.ccell.2019.07.001

Ritchie, M. E., Phipson, B., Wu, D., Hu, Y., Law, C. W., Shi, W., et al. (2015). Limma powers Differential Expression Analyses for RNA-Sequencing and Microarray Studies. *Nucleic Acids Res.* 43 (7), e47. doi:10.1093/nar/gkv007

Robertson, A. G., Kim, J., Al-Ahmadie, H., Bellmunt, J., Guo, G., Cherniack, A. D., et al. (2017). Comprehensive Molecular Characterization of Muscle-Invasive Bladder Cancer. *Cell* 171 (3), 540–e25. doi:10.1016/j.cell.2017.09.007

Rosenberg, J. E., Hoffman-Censits, J., Powles, T., van der Heijden, M. S., Balar, A. V., Necchi, A., et al. (2016). Atezolizumab in Patients with Locally Advanced and Metastatic Urothelial Carcinoma Who Have Progressed Following Treatment with Platinum-Based Chemotherapy: a Single-Arm, Multicentre, Phase 2 Trial. *The Lancet* 387 (10031), 1909–1920. doi:10.1016/s0140-6736(16)00561-4

Samstein, R. M., Lee, C.-H., Shoushtari, A. N., Hellmann, M. D., Shen, R., Janjigian, Y. Y., et al. (2019). Tumor Mutational Load Predicts Survival after Immunotherapy across Multiple Cancer Types. *Nat. Genet.* 51 (2), 202–206. doi:10.1038/s41588-018-0312-8

Sasidharan Nair, V., Toor, S. M., Taha, R. Z., Shaath, H., and Elkord, E. (2018). DNA Methylation and Repressive Histones in the Promoters of PD-1, CTLA-4, TIM-3, LAG-3, TIGIT, PD-L1, and Galectin-9 Genes in Human Colorectal Cancer. *Clin. Epigenet* 10 (1), 104. doi:10.1186/s13148-018-0539-3

Şenbabaoğlu, Y., Gejman, R. S., Winer, A. G., Liu, M., Van Allen, E. M., de Velasco, G., et al. (2016). Tumor Immune Microenvironment Characterization in clear Cell Renal Cell Carcinoma Identifies Prognostic and Immunotherapeutically Relevant Messenger RNA Signatures. *Genome Biol.* 17 (1), 231. doi:10.1186/s13059-016-1092-z

Siegel, R. L., Miller, K. D., Fuchs, H. E., and Jemal, A. (2021). Cancer Statistics, 2021. *CA A. Cancer J. Clin.* 71 (1), 7–33. doi:10.3322/caac.21654

Sotiriou, C., Wirapati, P., Loi, S., Harris, A., Fox, S., Smeds, J., et al. (2006). Gene Expression Profiling in Breast Cancer: Understanding the Molecular Basis of Histologic Grade to Improve Prognosis. *J. Natl. Cancer Inst.* 98 (4), 262–272. doi:10.1093/jnci/djj052

Thuijs, N. B., Berkhof, J., Özer, M., Duin, S., Splunter, A. P., Snoek, B. C., et al. (2021). DNA Methylation Markers for Cancer Risk Prediction of Vulvar Intraepithelial Neoplasia. *Int. J. Cancer* 148 (10), 2481–2488. doi:10.1002/ijc.33459

Wan, C., Keany, M. P., Dong, H., Al-Alem, L. F., Pandya, U. M., Lazo, S., et al. (2021). Enhanced Efficacy of Simultaneous PD-1 and PD-L1 Immune Checkpoint Blockade in High-Grade Serous Ovarian Cancer. *Cancer Res.* 81 (1), 158–173. doi:10.1158/0008-5472.CAN-20-1674

Wilhelm, C. S., Kelsey, K. T., Butler, R., Plaza, S., Gagne, L., Zens, M. S., et al. (2010). Implications of LINE1 Methylation for Bladder Cancer Risk in Women. *Clin. Cancer Res.* 16 (5), 1682–1689. doi:10.1158/1078-0432.ccr-09-2983

Wu, A., Cremaschi, P., Wetterskog, D., Conteduca, V., Franceschini, G. M., Kleftogiannis, D., et al. (2020). Genome-wide Plasma DNA Methylation Features of Metastatic Prostate Cancer. *J. Clin. Invest.* 130 (4), 1991–2000. doi:10.1172/jci130887

Yi, M., Jiao, D., Xu, H., Liu, Q., Zhao, W., Han, X., et al. (2018). Biomarkers for Predicting Efficacy of PD-1/pd-L1 Inhibitors. *Mol. Cancer* 17 (1), 129. doi:10.1186/s12943-018-0864-3

Ying, L., Lin, J., Qiu, F., Cao, M., Chen, H., Liu, Z., et al. (2015). Epigenetic Repression of Regulator of G-Protein Signaling 2 by Ubiquitin-like with PHD and Ring-finger Domain 1 Promotes Bladder Cancer Progression. *Febs J.* 282 (1), 174–182. doi:10.1111/febs.13116

Yu, X., Liu, W., Chen, S., Cheng, X., Paez, P. A., Sun, T., et al. (2021). Immunologically Programming the Tumor Microenvironment Induces the Pattern Recognition Receptor NLRC4-dependent Antitumor Immunity. *J. Immunother. Cancer* 9 (1). doi:10.1136/jitc-2020-001595

Zeng, D., Li, M., Zhou, R., Zhang, J., Sun, H., Shi, M., et al. (2019). Tumor Microenvironment Characterization in Gastric Cancer Identifies Prognostic and Immunotherapeutically Relevant Gene Signatures. *Cancer Immunol. Res.* 7 (5), 737–750. doi:10.1158/2326-6066.cir-18-0436

Zhang, B., Wu, Q., Li, B., Wang, D., Wang, L., and Zhou, Y. L. (2020). m6A Regulator-Mediated Methylation Modification Patterns and Tumor Microenvironment Infiltration Characterization in Gastric cancerA Regulator-Mediated Methylation Modification Patterns and Tumor Microenvironment Infiltration Characterization in Gastric Cancer. *Mol. Cancer* 19 (1), 53. doi:10.1186/s12943-020-01170-0

Zhang, Y., Yang, M., Ng, D. M., Haleem, M., Yi, T., Hu, S., et al. (2020). Multi-omics Data Analyses Construct TME and Identify the Immune-Related Prognosis Signatures in Human LUAD. *Mol. Ther. - Nucleic Acids* 21, 860–873. doi:10.1016/j.omtn.2020.07.024

Zhu, Y., Spitz, M. R., Zhang, H., Grossman, H. B., Frazier, M. L., and Wu, X. (2004). Methyl-CpG-binding Domain 2. *Cancer* 100 (9), 1853–1858. doi:10.1002/cncr.20199

Conflict of Interest: The authors declare that the research was conducted in the absence of any commercial or financial relationships that could be construed as a potential conflict of interest.

Publisher's Note: All claims expressed in this article are solely those of the authors and do not necessarily represent those of their affiliated organizations, or those of the publisher, the editors and the reviewers. Any product that may be evaluated in this article, or claim that may be made by its manufacturer, is not guaranteed or endorsed by the publisher.

frontiers in Cell and Developmental Biology

ORIGINAL RESEARCH
published: 24 December 2021
doi: 10.3389/fcell.2021.748280

LCK and CD3E Orchestrate the Tumor Microenvironment and Promote Immunotherapy Response and Survival of Muscle-Invasive Bladder Cancer Patients

Xiaonan Zheng[1,2†], Xinyang Liao[1†], Ling Nie[3†], Tianhai Lin[1], Hang Xu[1], Lu Yang[1], Bairong Shen[2], Shi Qiu[1], Jianzhong Ai[1]* and Qiang Wei[1]**

[1]Department of Urology, Institute of Urology, West China Hospital, Sichuan University, Chengdu, China, [2]Institute of Systems Genetics, West China Hospital, Sichuan University, Chengdu, China, [3]Department of Pathology, West China Hospital, Sichuan University, Chengdu, China

OPEN ACCESS

Edited by:
Yongwen Luo,
Wuhan University, China

Reviewed by:
Kai Kang,
Peking Union Medical College Hospital (CAMS), China
Xinwei Han,
Zhengzhou University, China

***Correspondence:**
Shi Qiu
qiushi@scu.edu.cn
Jianzhong Ai
Jianzhong.Ai@scu.edu.cn
Qiang Wei
weiqiang933@126.com

†These authors have contributed equally to this work and share first authorship

Specialty section:
This article was submitted to Molecular and Cellular Pathology, a section of the journal Frontiers in Cell and Developmental Biology

Received: 27 July 2021
Accepted: 08 December 2021
Published: 24 December 2021

Citation:
Zheng X, Liao X, Nie L, Lin T, Xu H, Yang L, Shen B, Qiu S, Ai J and Wei Q (2021) LCK and CD3E Orchestrate the Tumor Microenvironment and Promote Immunotherapy Response and Survival of Muscle-Invasive Bladder Cancer Patients. Front. Cell Dev. Biol. 9:748280. doi: 10.3389/fcell.2021.748280

Background: Studies have demonstrated the significance of multiple biomarkers for bladder cancer. Here, we attempt to present biomarkers potentially predictive of the prognosis and immunotherapy response of muscle-invasive bladder cancer (MIBC).

Method: Immune and stromal scores were calculated for MIBC patients from The Cancer Genome Atlas (TCGA). Core differential expression genes (DEGs) with prognostic value were identified and validated using an independent dataset GSE31684. The clinical implications of prognostic genes and the inter-gene correlation were presented. The distribution of tumor-infiltrating immune cells (TICs), the correlation with tumor mutation burden (TMB), and the expression of eight immune checkpoint–relevant genes and CD39 were accordingly compared. Two bladder cancer cohorts (GSE176307 and IMvigor210) receiving immunotherapy were recruited to validate the prognostic value of LCK and CD3E for immunotherapy.

Results: 361 MIBC samples from TCGA revealed a worse overall survival for higher stromal infiltration ($p = 0.009$) but a better overall survival for higher immune infiltration ($p = 0.042$). CD3E and LCK were independently validated by TCGA and GSE31684 to be prognostic for MIBC. CD3E was the most correlative gene of LCK, with a coefficient of $r = 0.86$ ($p < 0.001$). $CD8^+$ T cells and macrophage M1 are more abundant in favor of a higher expression of CD3E and LCK in MIBC and across pan-cancers. Immune checkpoints like CTLA4, CD274 (PD-1), and PDCD1 (PD-L1) were highly expressed in high-CD3E and high-LCK groups for MIBC and also for pan-cancers, except for thymoma. LCK and CD3E had a moderate positive correlation with CD39 expression. Importantly, high-LCK and high-CD3E groups had a higher percentage of responders than the low-expression groups both in GSE176307 (LCK: 22.73*vs.* 13.64%, CD3E: 22.00 *vs.* 13.16%) and IMvigor210 cohorts (LCK: 28.19 *vs.* 17.45%, CD3E: 25.50 *vs.* 20.13%).

Conclusion: CD3E and LCK were potential biomarkers of MIBC. CD3E and LCK were positively correlated with several regular immunotherapy biomarkers, which is supported by real-world outcomes from two immunotherapy cohorts.

Keywords: muscle-invasive bladder cancer, LCK, CD3e, tumor microenvironment, immunotherapy

INTRODUCTION

As one of the most common malignant solid tumors, bladder cancer (BC) causes 573,278 incidents and 212,536 deaths in 2020 (Sung et al., 2021). Muscle-invasive bladder cancer (MIBC), the advanced stage of BC, makes up 20–30% of BC at the initial diagnosis, and the five-year overall survival is maintained less than 50% (Lenis et al., 2020). Although radical cystectomy still remains a common approach, immunotherapy has rapidly progressed, with five immune checkpoint inhibitors approved to treat advanced BC. However, it is noticeable that the response rate to those immunotherapy drugs reaches only 20–40%, which greatly restricts the clinical management of MIBC (Doroshow et al., 2021).

Studies have demonstrated the positive role of multiple biomarkers such as tumor mutation burden (TMB) (Goodman et al., 2017), the abundance of tumor-infiltrating immune cells (TICs) (Petitprez et al., 2020), and the expression level of PD-L1 (Jia et al., 2018) and CD39 (also known as ENTPD1) (Allard et al., 2017; Moesta et al., 2020) in predicting the response rate to immune checkpoint inhibitors (ICIs). However, the limited accuracy of those biomarkers should still be noted. In recent years, immune cells have been recognized as a key component of the tumor microenvironment. Immune cells are essentially involved in tumorigenesis and tumor progression and thus influence the survival outcomes (Fu et al., 2018; Hinshaw and Shevde, 2019; Jiang et al., 2019). Based on this concept, it appears reasonable to identify prognostic biomarkers for MIBC by predicting the level of TICs (Yoshihara et al., 2013). With these immune-based prognostic genes, we can further estimate their correlation with immune checkpoint genes, tumor mutation burden, TICs, and certain predictors such as CD39, which may hopefully provide us new insights into the precise immunotherapy of MIBC. Therefore, this study aims to identify new immune-based prognostic genes of MIBC and validate them in clinical cohorts receiving immunotherapy.

METHODS

Data Collection and Immune and Stromal Score Calculation

Gene expression data of bladder cancer with clinical variables were obtained from The Cancer Genome Atlas (TCGA) database, and patients with MIBC (T2 to T4) were selected for subsequent analysis. Another independent dataset was downloaded from Gene Expression Omnibus (GEO) for external validation. The ESTIMATE algorithm was used to calculate scores to predict the level of immune and stromal cell infiltration for each patient (Yoshihara et al., 2013). The R package "ESTIMATE" has been widely utilized in cancer-related studies (Liu et al., 2021a; Liu et al., 2021b; Liu et al., 2021c). The optimal cutoff values of immune and stromal scores were determined with maximally selected log-rank using the R package "survminer" (Li et al., 2020), and patients were then divided into immune-high/-low and stromal-high/-low groups. Kaplan–Meier curves were utilized to evaluate the association of immune and stromal scores with survival outcomes.

Identification of Prognostic Genes

Differential expression genes (DEGs) between immune-high versus immune-low and stromal-high versus stromal-low subgroups were identified using the "limma" R package with a setting of $|\text{fold change}| > 2$ and a p value < 0.05, visualized with a heatmap and intersected with a Venn plot. Enrichment analyses of gene ontology (GO) and the Kyoto Encyclopedia of Genes and Genomes (KEGG) pathway were performed to reveal the biological process, cellular component, molecular function, and molecular pathways that the intersected DEGs were associated with.

The protein–protein interaction (PPI) network of the DEGs was constructed with the STRING database (https://string-db.org/), with an interaction confidence of 0.99, and the core modules of the network were identified, defined as a collection of genes with no less than three nodes within the network. The prognostic value of the genes present in the core modules of the PPI network was evaluated with Kaplan–Meier curves. Then an independent GEO dataset GSE31684 was used for the external validation of the prognostic genes. A p value < 0.05 indicates that the correlation is significant.

Clinical and Immune Implications of the Prognostic Genes

The first 100 most correlative genes of each prognostic gene were identified and then intersected. Subsequent enrichment analyses and network construction were performed. The expression of the

TABLE 1 | Characteristics of included patients from TCGA and GSE31684 datasets.

	TCGA MIBC	GEO GSE31684
Age (years)		
<65	129 (35.73%)	24 (30.77%)
≥65	232 (64.27%)	54 (69.23%)
Sex		
Female	95 (26.32%)	21 (26.92%)
Male	266 (73.68%)	57 (73.08%)
T stage		
T2	114 (31.58%)	17 (21.79%)
T3	190 (52.63%)	42 (53.85%)
T4	57 (15.79%)	19 (24.36%)
Mean follow-up (days)	785.07	1209.45

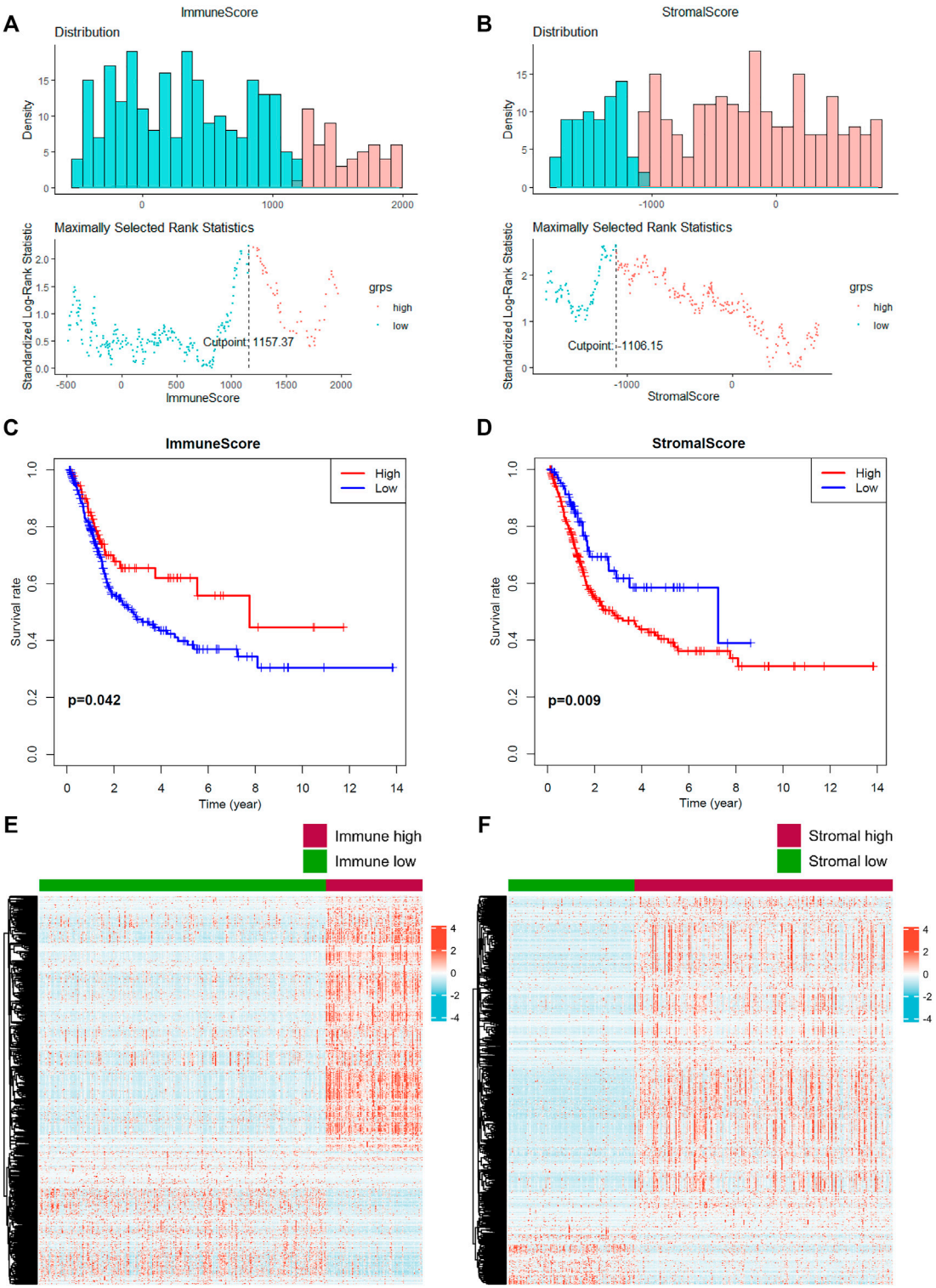

FIGURE 1 | Prediction of the level of tumor-infiltrating immune cells and stromal cells. **(A–B)** The optimal cutoff value of the immune score and stromal score was calculated. **(C–D)** Prognostic value of the immune score and stromal score. **(E–F)** Identification of differential expressed genes according to the immune and stromal scores. A p value < 0.05 indicates statistical significance.

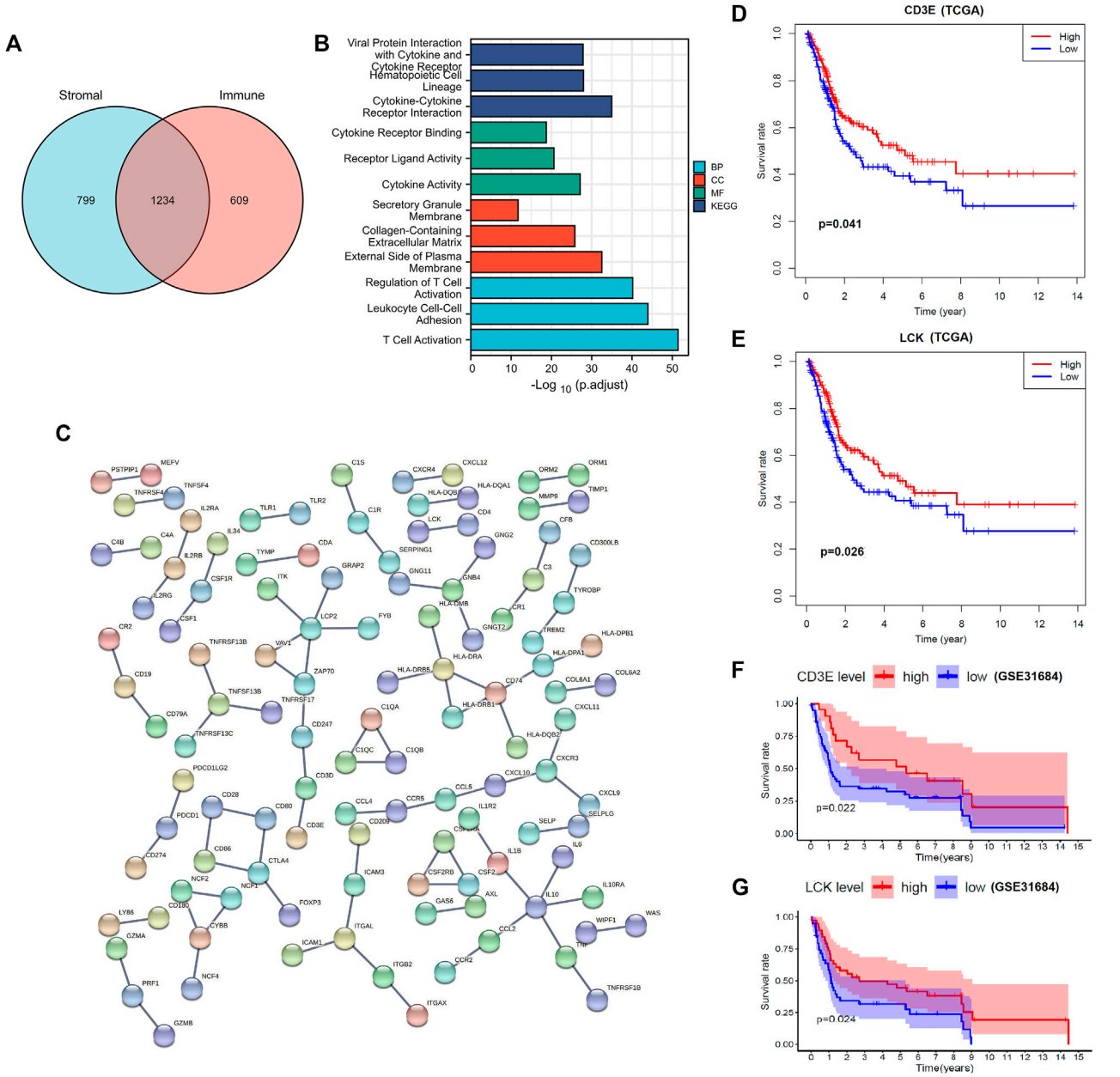

FIGURE 2 | Identification and validation of prognostic genes of muscle-invasive bladder cancer. **(A)** Intersection of differential expressed genes. **(B–C)** Enrichment analyses and the protein–protein network construction of the intersected differential expressed genes. **(D–E)** Partial presentation of the prognostic genes with the core module of the protein–protein network found through TCGA samples. **(F–G)** External validation with the GSE31684 dataset identifies that LCK and CD3E were the prognostic genes of muscle-invasive bladder cancer. A p value < 0.05 indicates statistical significance.

prognostic genes was compared between tumor and normal samples with data downloaded from the UALCAN cancer database (Chandrashekar et al., 2017) and the Human Protein Atlas (Uhlén et al., 2015). The connection between the prognostic genes and clinical variables was presented in a Sanguini diagram using the R package "ggalluval." The percentage abundance of TICs was predicted and displayed using the R package "pheatmap," and the CIBERSORT algorithm was utilized to compare the distribution of TICs according to the expression level of prognostic genes with the R package "ggplot." We further evaluated the expression of eight immune checkpoint–relevant genes to reveal a potential role of the prognostic genes in immunotherapy. Correlation between TICs, immune checkpoint–relevant genes expression levels, and TMB with LCK and CD3E was further performed for pan-cancers, including 32 kinds of tumors. Another two independent bladder cancer cohorts receiving anti-PD1/PD-L1 inhibitor immunotherapy (GSE176307 (Rose et al., 2021) and IMvigor210 (Mariathasan et al., 2018)) were recruited to validate the predictive value of LCK and

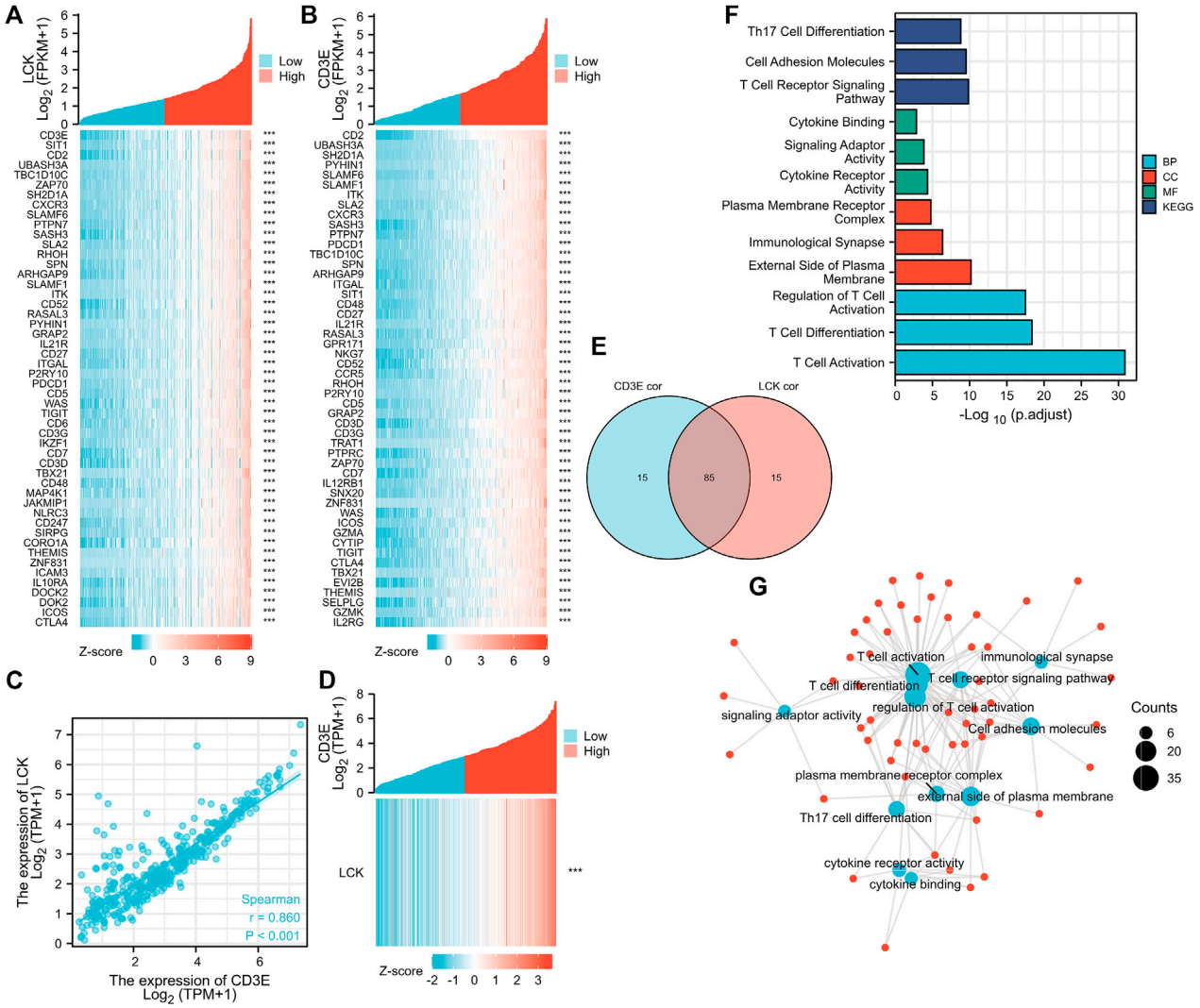

FIGURE 3 | Correlation between LCK and CD3E. **(A–B)** co-expressed genes of LCK and CD3E. **(C–D)** Spearman correlation and co-expression analysis between LCK and CD3E. **(E)** Intersection of the first 100 genes co-expressed with LCK and CD3E. **(F–G)** Enrichment analyses and the network pathway of the 85 intersected genes.

CD3E for immune response (responder: partial response [PR] or complete response [CR]; non-responder: stable disease [SD]; or progressed disease [PD]). The R package "Maxstat," "Survminer," "Survival," and "ggplot2" were used to assess the prognostic significance of LCK and CD3E. The correlation of LCK and CD3E with immune phenotypes (inflamed, excluded, and desert) in the IMvigor210 cohort was also analyzed.

RESULT

CD3E and LCK Are the Prognostic Genes of MIBC

A total of 361 and 78 MIBC patients were identified from TCGA and GSE31684 (**Table 1**), respectively. The optimal cutoff values were 1157.37 for the immune score and -1106.15 for the stromal score (**Figures 1A, B**). In total, 92 patients from TCGA were assigned to the immune-high group and 269 to the immune-low group, while 253 patients were classified as stromal-high and 108 stromal-low. Higher immune infiltration was associated with improved overall survival (p = 0.042), while increased stromal infiltration was associated with worse overall survival (p = 0.009) (**Figures 1C, D**).

In total, 2033 DEGs were identified in stromal-high/low groups and 1843 DEGs in the immune-high/low groups (**Figures 1E, F**). Then 1234 DEGs were eventually intersected (**Figure 2A**), and the enrichment analyses indicated a role in cytokine–cytokine receptor interaction and T-cell activation (**Figure 2B**). Network construction identified a core module of 173 genes (**Figure 2C**). Survival curves demonstrated that CD3E (TCGA: p = 0.041, GEO: p = 0.022) and LCK (TCGA: p = 0.026, GEO: p = 0.024) were the prognostic genes of MIBC after external validation with GSE31684 (**Figures 2D–G**).

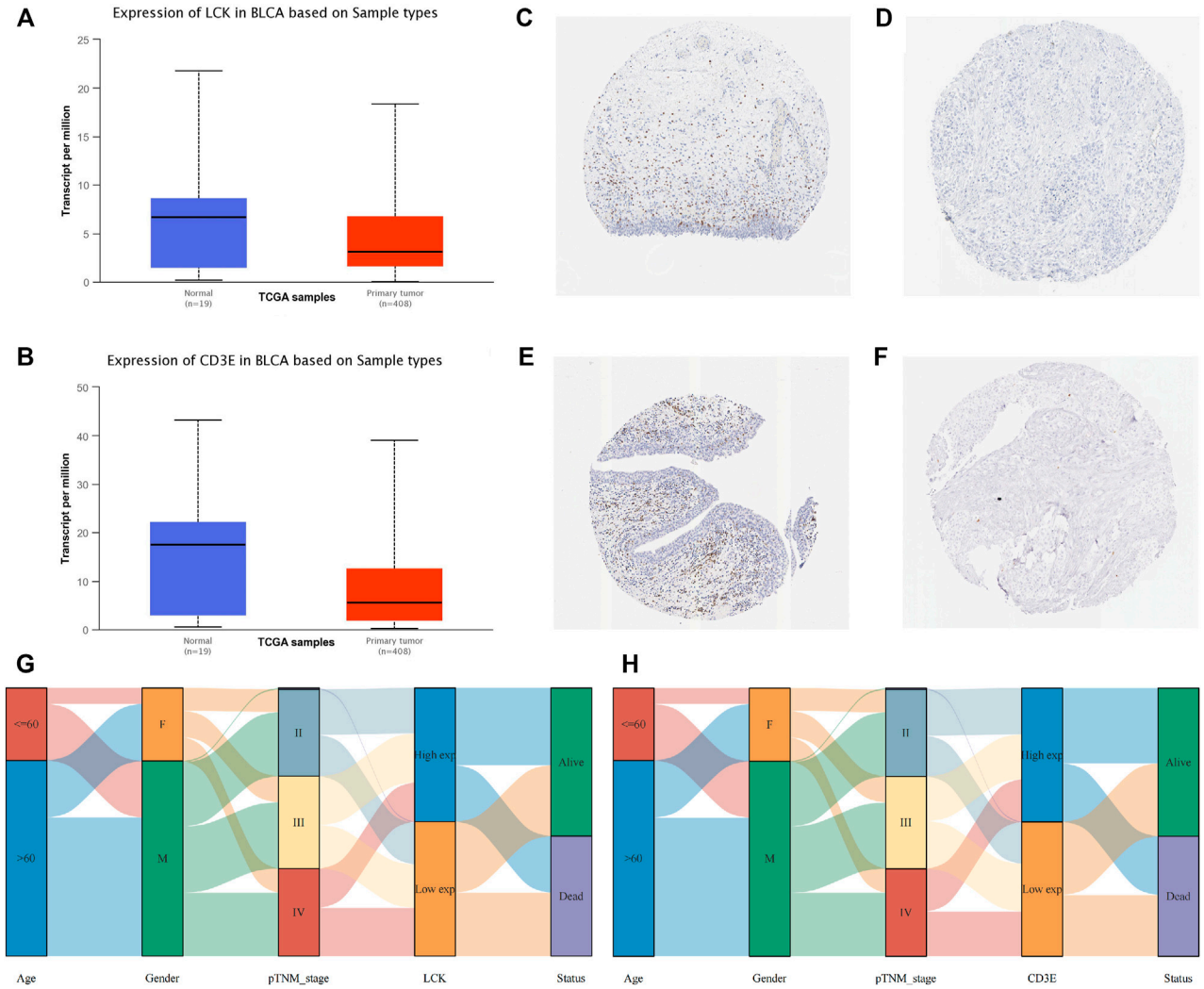

FIGURE 4 | Clinical implication of LCK and CD3E. **(A)** Comparison of the expression value of LCK between normal tissue and bladder cancer tissue from TCGA; immunohistochemical staining of LCK in normal tissue **(C)**and bladder tumor tissue **(D)**. **(B)** Comparison of the expression value of CD3E between normal tissue and bladder cancer tissue from TCGA. Immunohistochemical staining of LCK in normal tissue **(E)** and bladder tumor tissue **(F)**. **(G–H)** Correlation of LCK and CD3E with clinical information of muscle-invasive bladder cancer.

CD3E Is the Most Correlative Gene of LCK in MBC

The top 100 genes that co-express with LCK and CD3E are partially presented in **Figures 3A, B**. Interestingly, CD3E was the most correlative gene of LCK, with a Spearman coefficient r = 0.86 ($p < 0.001$) (**Figures 3C, D**). The intersection of the top 100 co-expressed genes of LCK and CD3E were found to be associated with T-cell activation and differentiation and the T-cell receptor signaling pathway (**Figures 3E–G**).

Correlation of LCK/CD3E with Clinical Characteristics of MIBC

The expression of LCK and CD3E was found to be much lower in tumor samples than in normal samples, with a median expression value (transcript per million) of 6.685 vs 3.116 for LCK (**Figure 4A**) and 17.484 vs 5.58 for CD3E (**Figure 4B**). Immunohistochemical staining showed a consistent expression trend of LCK (**Figures 4C, D**) and CD3E (**Figures 4E, F**) between normal tissue and bladder cancer samples. The association between clinical variables, including age, gender, and pathological stage, with the expression of LCK and CD3E, was also displayed, from which we could observe that there was a tendency of the distribution of high/low LCK/CD3E across different pathologic stages of MIBC (**Figures 4G, H**). **Supplementary Figure S1** more quantitatively shows that MIBC patients in earlier stages (stages II and III vs stage IV) had a slightly higher percentage of high-LCK and high-CD3E expression (high-LCK: 53.11 *vs.* 44.19%; high-CD3E: 51.55*vs.*vs 48.06%; **Supplementary Figure S1A**). Further subgroup analyses consistently indicated that higher expressions of LCK and CD3E were found in MIBC patients diagnosed with earlier T stage

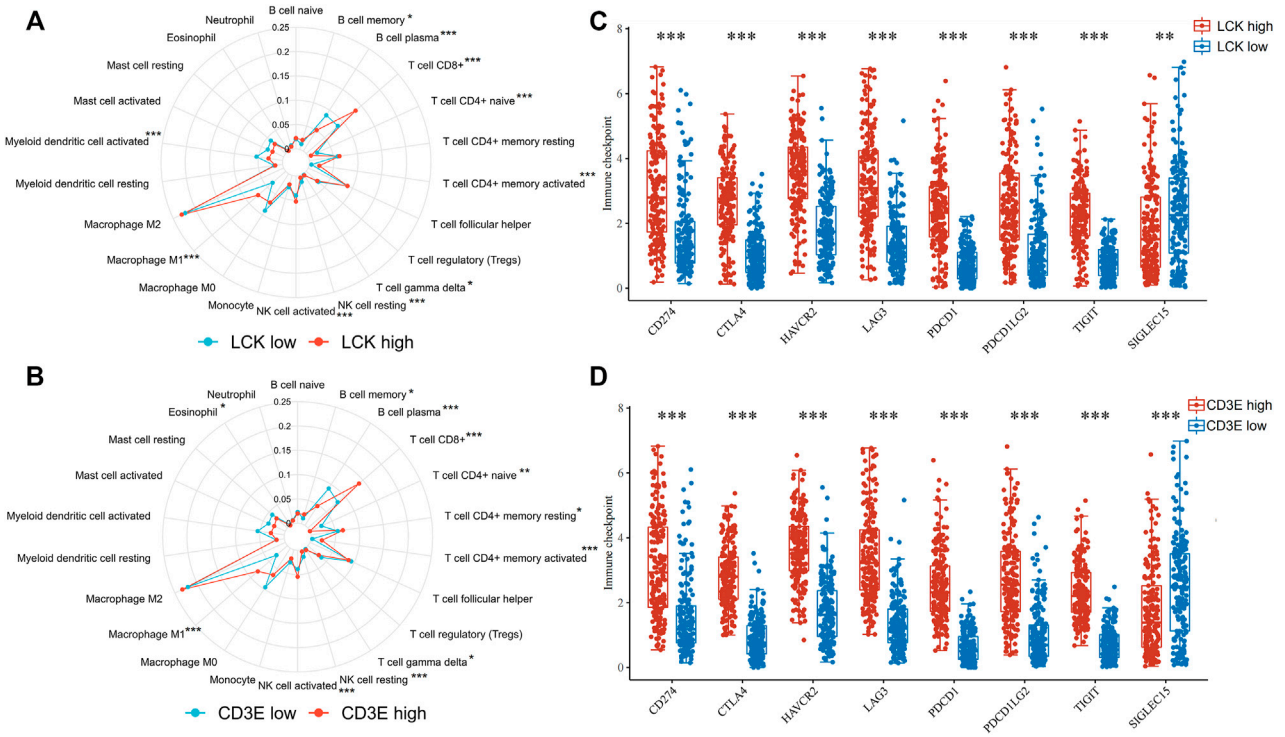

FIGURE 5 | Association of LCK and CD3E with the distribution of tumor-infiltrating immune cells and with the expression of immune checkpoint genes in muscle-invasive bladder cancer. **(A–B)** Distribution of tumor-infiltrating immune cells based on the expression level of LCK and CD3E. **(C–D)** Expression level of immune checkpoint genes based on the expression level of LCK and CD3E. * $p < 0.05$, ** $p < 0.01$, *** $p < 0.001$.

(T2&T3 *vs.* T4: high-LCK: 50.16*vs.*vs 48.28%; high-CD3E: 50.32 vs 46.55%; **Supplementary Figure S1B**), and in particular earlier N stage (N0 *vs.* N1 and N2 *vs.* N3: high-LCK: 52.04 *vs.* 46.22*vs.*vs 28.57%; high-CD3E: 51.58 vs 49.58% *vs.* 28.57%; **Supplementary Figure S1C**) and earlier M stage (M0 *vs.* M1: high-LCK: 45.76 *vs.* 0%; high-CD3E: 42.94 *vs.* 12.50%; **Supplementary Figure S1D**).

Correlation of LCK/CD3E with Tumor-Infiltrating Lymphocytes, Immune Checkpoint, Tumor Mutation Burden, and ENTPD1 (CD39)

The percentage abundance of TICs in MIBC patients is shown in **Supplementary Figure S2** and **Supplementary Table S1**, from which we have a general view of the percentage of different TICs in MIBC samples. The CIBERSORT algorithm revealed the significantly different distribution of TICs between LCK-high/low and CD3E-high/low subgroups; for instance, the infiltration of memory B cells, $CD8^+$ T cells, $CD4^+$memory activated, and macrophage M1 was higher in the LCK-high and CD3E-high subgroups (**Figures 5A, B**). Further analysis indicated a higher expression of several key immune checkpoint–relevant genes such as PD-1, PD-L1, PD-L2, and CTLA4 in LCK-high and CD3E-high subgroups (**Figures 5C, D**). Moreover, this positive correlation between memory B cell, $CD8^+$ T cell, $CD4^+$ memory activated, and macrophage M1 with LCK and CD3E was also consistent across different cancer types (**Figures 6A,B**).

Interestingly, LCK and CD3E had a generally positive correlation with those eight immune checkpoint genes for pan-cancers, except for thymoma (**Figures 7A, B**). Pan-cancer analysis also revealed a positive correlation between LCK/CD3E and TMB in several types of cancers, despite the coefficients being small (**Figures 7C, D**). Further analyses showed that the correlation of LCK and CD3E with TMB in bladder cancer was weak, although a statistical significance was reached (**Figures 7E, F**). Last but not least, there was a moderate correlation between CD39, a previously reported gene predictive of response rate to PD-1 inhibitors, with LCK ($r = 0.48$, $p < 0.001$) and CD3E ($r = 0.52$, $p < 0.001$) (**Figures 7G, H**).

Prognostic Value of LCK and CD3E for MIBC in Predicting Immune Response and Survival After Immunotherapy Among Two Independent Validation Cohorts

Figures 8A, B show a greater percentage of high LCK (62.50 *vs.* 47.22%) and high CD3E (68.75% *vs.* 54.17%) in MIBC patients defined as immunotherapy responders in GSE176307 dataset, which was consistent with the tendency in the IMvigor210 cohort (LCK: 61.76 *vs.* 46.52%, CD3E: 55.88 *vs.* 48.26%, **Figures 8C, D**). More importantly, the percentage of responders distributed in high-LCK and high-CD3E groups was obviously higher, considering the generally relatively limited response rate of immunotherapy, than the low-expression groups, both in

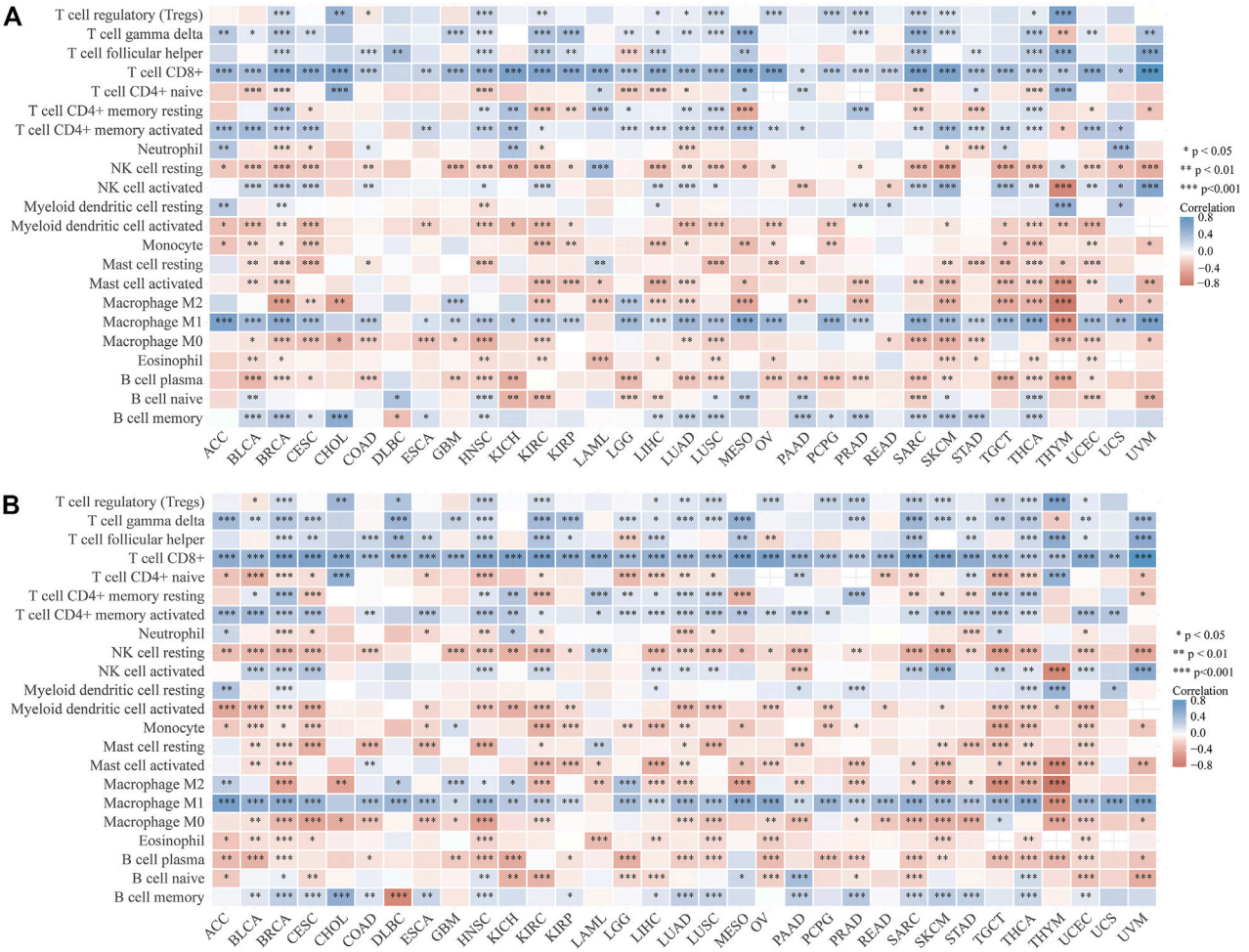

FIGURE 6 | Correlation between tumor-infiltrating immune cells with the expression of LCK **(A)** and CD3E **(B)** across pan-cancers.

GSE176307 (LCK: 22.73 *vs.* 13.64%, CD3E: 22.00 *vs.* 13.16%, **Figures 8E,F**) and IMvigor210 cohorts (LCK: 28.19*vs.*vs 17.45%, CD3E: 25.50 *vs.* 20.13%, immune cells), excluded (immune cells accumulated but not efficiently infiltrated) and desert phenotypes (absence of $CD8^+$ T cells) (**Figures 8I,J**). Similarly, high-LCK and high-CD3E group also had more inflamed phenotypes (LCK: 42.28*vs.*vs 8.26%, CD3E: 42.74*vs.*vs 7.50%, **Figures 8K, 8L**). **Supplementary Figure S3** presents a tendency of higher expression of LCK and CD3E in the responder group versus the non-responders (**Supplementary Figures S3A–S3D**), but statistical significance was not reached. However, a significant trend of LCK/CD3E expression was observed across the immune phenotypes (**Supplementary Figure S3E–S3F**). Last, the prognostic value of LCK and CD3E was validated by indicating higher expression of LCK (GSE176307: HR 0.44, 95% CI 0.26–0.75, p = 0.003; IMvigor210: HR 0.45, 95% CI 0.26–0.76, p = 0.003, **Figures 8M,N**) or CD3E (GSE176307: HR 0.64, 95% CI 0.48–0.86, p = 0.003; IMvigor210: HR 0.58, 95% CI 0.39–0.87, p = 0.008, **Figures 8O,P**) and was associated with an improved overall survival for bladder cancer patients receiving immunotherapy.

DISCUSSION

The current study found the prognostic value of LCK and CD3E for MIBC. A higher expression of LCK/CD3E was indicative of improved survival of MIBC patients. LCK is the major T-cell receptor (TCR) kinase and has selectivity on the four CD3-signaling proteins of TCR (Marth et al., 1985). Early studies demonstrated that LCK was widely expressed in immune cells and was a potential biomarker of malignant tumors (Harr et al., 2010; Till et al., 2017; Zeng et al., 2020). Importantly, through an ionic interaction between basic residue-rich sequences and acidic residues, CD3E is the only CD3 chain that can efficiently interact with LCK (Li et al., 2017). The ionic interaction between LCK and CD3E controls the TCR phosphorylation, which is considered as the initial step in T-cell signaling to trigger adaptive immunity

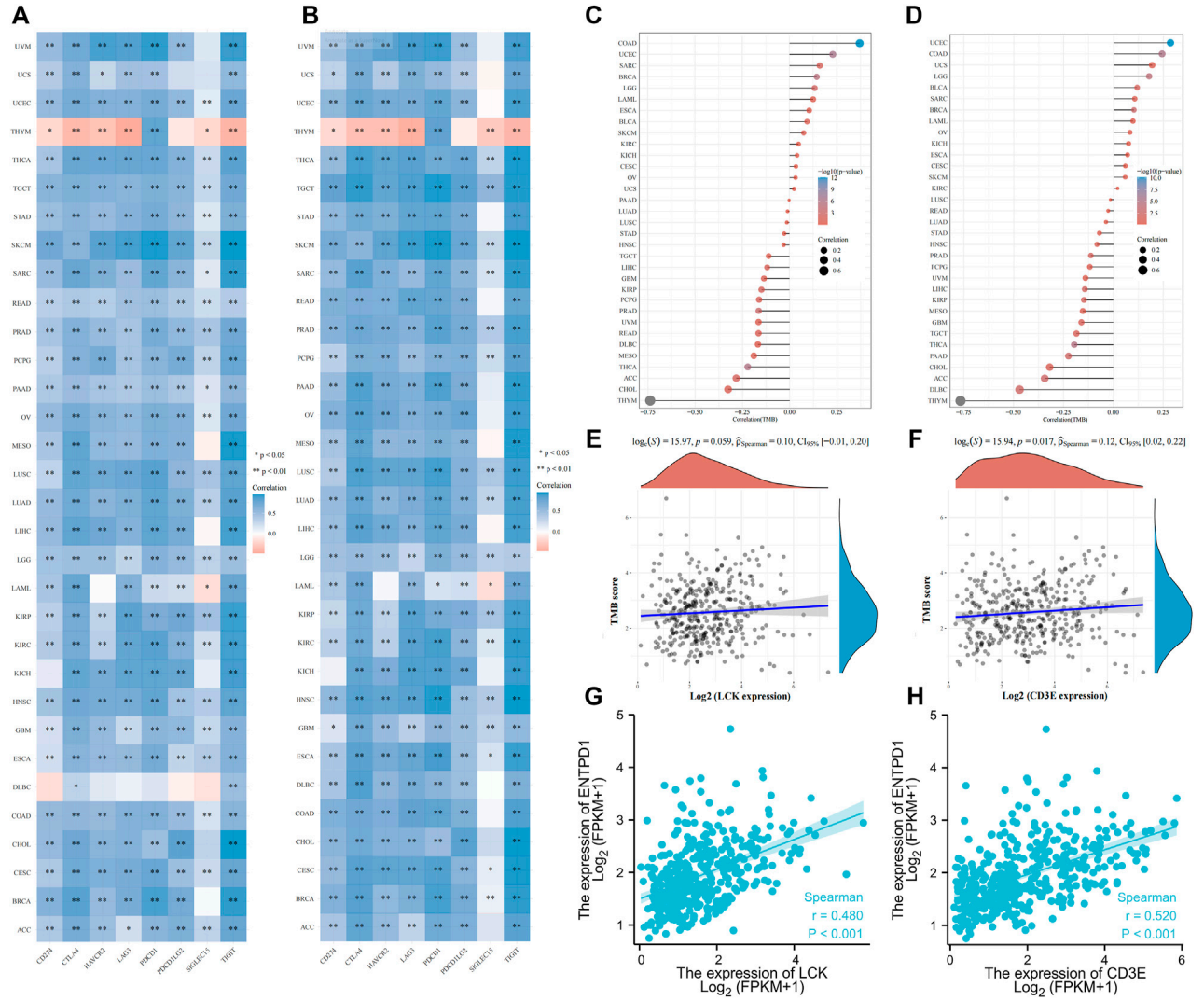

FIGURE 7 | Correlation of LCK/CD3E with immune checkpoint genes and tumor mutation burden across pan-cancers. **(A–B)** Correlation of LCK/CD3E with immune checkpoint genes across pan-cancers. **(C–D)** Correlation of LCK/CD3E with tumor mutation burden across pan-cancers. **(E–F)** Spearman correlation between LCK/CD3E and tumor mutation burden in bladder cancer. **(G–H)** Spearman correlation between ENTPD1 (CD39) with LCK/CD3E in bladder cancer.

against tumor cells (Li et al., 2017; Hartl et al., 2020). This might also explain our findings of the richer abundance of $CD8^+$ T cells in the high-LCK and high-CD3E groups. The $CD8^+$ T cell, also known as the cytotoxic T cell, is one of the dominant differentiated T cells. $CD8^+$ T cells have been well proved to be the main effector of eliminating tumor cells through the recognition of MHC I molecules binding to the antigen on the surface of tumor cells (Vesely et al., 2011). However, increasing evidence has revealed the shift of $CD8^+$ T cells from a functional state to an exhausted state, indicating the high heterogeneity of $CD8^+$ T cells (Simoni et al., 2018; Thommen and Schumacher, 2018) and also demanding the combination of CD8 with other biomarkers in predicting prognosis. An early study demonstrated high-affinity neoantigens correlated with better prognosis of hepatocellular carcinoma by activating CD39 $^+$ $CD8^+$ T cells (Liu et al., 2020). Therefore, our study assessed the correlation of CD39 with LCK and CD3E, and a positive correlation was found. Altogether, these findings explained, to an extent, the prognostic value of LCK and CD3E for MIBC diagnosis.

Immunotherapy of ICIs has become a common choice for treating advanced cancer worldwide. However, the response rate to ICIs remains low (Doroshow et al., 2021). To provide better guidance of administrating ICIs to patients who are potentially responsive, researchers have longed to explore biomarkers that can predict the benefit of ICI treatment. TMB, the expression level of PD-L1, and the abundance of TICs have been proposed in this context (Goodman et al., 2017; Jia et al., 2018). Nevertheless, controversies still remain in terms of predicting accuracy. For instance, the higher expression of PD-L1 was reported to be predictive of improved survival after ICI immunotherapy, but a small part of patients lacking PD-L1 expression would still benefit from ICIs (Patel and Kurzrock, 2015). The abundance of tumor-

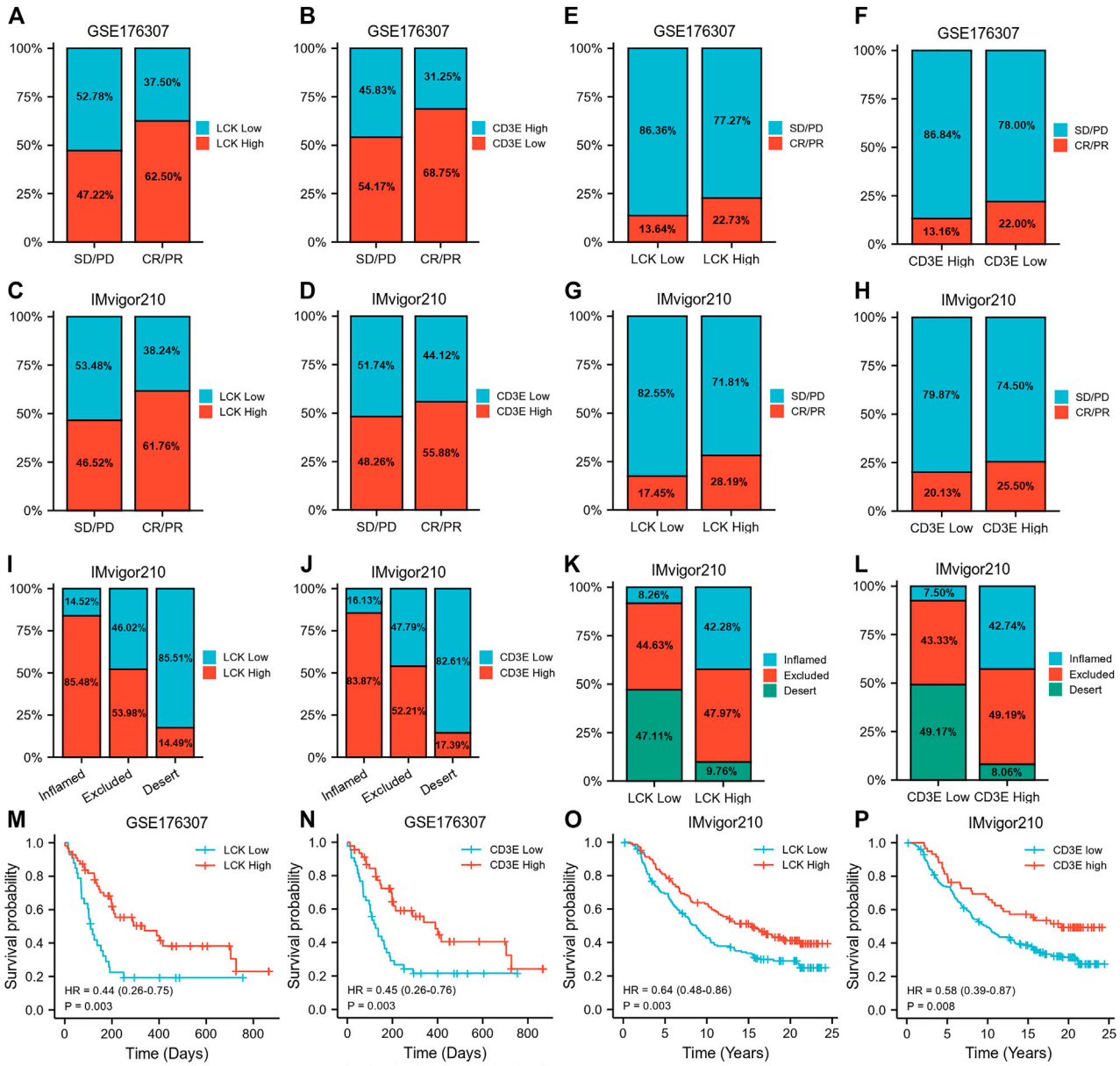

FIGURE 8 | Prognostic value of LCK and CD3E for MIBC in predicting immune response and survival after immunotherapy among two independent validation cohorts. **(A–D)** Percentage of high/low LCK/CD3E expression in responders and non-responders. **(E–H)** Proportion of responder and non-responder in high/low-LCK/CD3E groups. **(I–J)** Percentage of high/low-LCK/CD3E expression in different immune phenotypes. **(K–L)** Proportion of different immune phenotypes in high/low-LCK/CD3E groups. **(M–P)** Kaplan–Meier curves showing the prognostic value of LCK and CD3E for MIBC overall survival in GSE176306 and IMvior210.

infiltrating $CD8^+$ T cells also demonstrated to mediate response to immunotherapy. However, $CD8^+$ T-cell persistence was observed when it was associated with a CD39-negative state, and a higher proportion of $CD39^+$ $CD8^+$ T cells was correlated with an improved response rate to ICIs (Krishna and Lowery, 2020). Therefore, it looks unreasonable for a single biomarker to predict the survival benefits of ICIs and prognosis for MIBC, which necessitates the inter-biomarker correlation analyses and the integration of different biomarkers. In this context, our study did not only reveal a positive correlation of LCK and CD3E with $CD8^+$ T-cell abundance and CD39 expression level but also report a higher expression of several typical immune checkpoint–relevant genes such as PD-1, PD-L1, and CTLA4 in the LCK-high and CD3E-high groups. Notably, LCK- and CD3E-related TMBs were low in our study. These findings taken together suggested the potential of LCK and CD3E in predicting the effect of ICI therapy.

To our knowledge, this is the first study reporting the potential prognostic value of LCK and CD3E in MIBC. However, our findings should not be interpreted without limitations. The first limitation is the retrospective nature of our study. Given that two

independent public datasets were employed for validation, multicenter samples would make the findings more convincing. Furthermore, samples used in this study were from the core region of the tumor tissue, making us unable to take different parts of the tumor into the analysis. All those limitations imply well-designed prospective research to validate the prognostic value of LCK and CD3E in clinical practice. Moreover, experiments exploring the potential signaling pathway of LCK/CD3E/TCR, $CD8^+$ T cells, CD39, and PD-1/PD-L1 are required.

CONCLUSION

CD3E and LCK, two tightly correlated genes in T-cell receptor phosphorylation, were found to be potential biomarkers of MIBC prognosis. Importantly, CD3E and LCK were positively correlated with several regular immunotherapy biomarkers such as TIC infiltration (memory B cells, $CD8^+$ T cells, $CD4^+$ memory activated, and macrophage M1) and the expression of PD-1, PD-L1, CTLA4, and CD39, which was supported by real-world data from two independent MIBC immunotherapy cohorts.

DATA AVAILABILITY STATEMENT

The datasets presented in this study can be found in online repositories. The names of the repository/repositories and accession number(s) can be found in the article/**Supplementary Material**.

AUTHOR CONTRIBUTIONS

SQ, QW, and JA contributed to study design and protocol. XZ, XL, LN, TL, HX, and LY helped with data acquirement, analysis, and interpretation. XZ, XL, LN, SQ, and JA assisted with manuscript draft and revision. XZ and JA contributed to funding. All the authors have reviewed the manuscript and approved the submission.

FUNDING

This study was supported by the grants from the China Postdoctoral Science Foundation (No. 2021M692306), the Post-Doctor Research Project of West China Hospital of Sichuan University (2021HXBH025), and the National Natural Science Foundation of China (82070784, 81702536).

SUPPLEMENTARY MATERIAL

The Supplementary Material for this article can be found online at https://www.frontiersin.org/articles/10.3389/fcell.2021.748280/full#supplementary-material

REFERENCES

Allard, B., Longhi, M. S., Robson, S. C., and Stagg, J. (2017). The Ectonucleotidases CD39 and CD73: Novel Checkpoint Inhibitor Targets. *Immunol. Rev.* 276, 121–144. doi:10.1111/imr.12528

Chandrashekar, D. S., Bashel, B., Balasubramanya, S. A. H., Creighton, C. J., Ponce-Rodriguez, I., Chakravarthi, B. V. S. K., et al. (2017). UALCAN: A Portal for Facilitating Tumor Subgroup Gene Expression and Survival Analyses. *Neoplasia* 19, 649–658. doi:10.1016/j.neo.2017.05.002

Doroshow, D. B., Bhalla, S., Beasley, M. B., Sholl, L. M., Kerr, K. M., and Gnjatic, S. (2021). PD-L1 as a Biomarker of Response to Immune-Checkpoint Inhibitors. *Nat. Rev. Clin. Oncol.* 18, 345–362. doi:10.1038/s41571-021-00473-5

Fu, H., Zhu, Y., Wang, Y., Liu, Z., Zhang, J., Xie, H., et al. (2018). Identification and Validation of Stromal Immunotype Predict Survival and Benefit from Adjuvant Chemotherapy in Patients with Muscle-Invasive Bladder Cancer. *Clin. Cancer Res.* 24, 3069–3078. doi:10.1158/1078-0432.ccr-17-2687

Goodman, A. M., Kato, S., Bazhenova, L., Patel, S. P., Frampton, G. M., Miller, V., et al. (2017). Tumor Mutational Burden as an Independent Predictor of Response to Immunotherapy in Diverse Cancers. *Mol. Cancer Ther.* 16, 2598–2608. doi:10.1158/1535-7163.mct-17-0386

Harr, M. W., Caimi, P. F., Mccoll, K. S., Zhong, F., Patel, S. N., Barr, P. M., et al. (2010). Inhibition of Lck Enhances Glucocorticoid Sensitivity and Apoptosis in Lymphoid Cell Lines and in Chronic Lymphocytic Leukemia. *Cell Death Differ.* 17, 1381–1391. doi:10.1038/cdd.2010.25

Hartl, F. A., Beck-Garcìa, E., Woessner, N. M., Flachsmann, L. J., Cárdenas, R. M.-H. V., Brandl, S. M., et al. (2020). Noncanonical Binding of Lck to CD3ε Promotes TCR Signaling and CAR Function. *Nat. Immunol.* 21, 902–913. doi:10.1038/s41590-020-0732-3

Hinshaw, D. C., and Shevde, L. A. (2019). The Tumor Microenvironment Innately Modulates Cancer Progression. *Cancer Res.* 79, 4557–4566. doi:10.1158/0008-5472.can-18-3962

Jia, L., Zhang, Q., and Zhang, R. (2018). PD-1/PD-L1 Pathway Blockade Works as an Effective and Practical Therapy for Cancer Immunotherapy. *Cancer Biol. Med.* 15, 116–123. doi:10.20892/j.issn.2095-3941.2017.0086

Jiang, Q., Fu, Q., Chang, Y., Liu, Z., Zhang, J., Xu, L., et al. (2019). CD19+ Tumor-Infiltrating B-Cells Prime CD4+ T-Cell Immunity and Predict Platinum-Based Chemotherapy Efficacy in Muscle-Invasive Bladder Cancer. *Cancer Immunol. Immunother.* 68, 45–56. doi:10.1007/s00262-018-2250-9

Krishna, S., Lowery, F. J., Copeland, A. R., Bahadiroglu, E., Mukherjee, R., Jia, L., et al. (2020). Stem-like CD8 T Cells Mediate Response of Adoptive Cell Immunotherapy Against Human Cancer. *Science* 370, 1328–1334. doi:10.1126/science.abb9847

Lenis, A. T., Lec, P. M., Chamie, K., and Mshs, M. (2020). Bladder Cancer. *JAMA* 324, 1980–1991. doi:10.1001/jama.2020.17598

Li, L., Guo, X., Shi, X., Li, C., Wu, W., Yan, C., et al. (2017). Ionic CD3–Lck Interaction Regulates the Initiation of T-Cell Receptor Signaling. *Proc. Natl. Acad. Sci. USA* 114, E5891–e5899. doi:10.1073/pnas.1701990114

Li, S., Chen, S., Wang, B., Zhang, L., Su, Y., and Zhang, X. (2020). A Robust 6-lncRNA Prognostic Signature for Predicting the Prognosis of Patients with Colorectal Cancer Metastasis. *Front. Med.* 7, 56. doi:10.3389/fmed.2020.00056

Liu, T., Tan, J., Wu, M., Fan, W., Wei, J., Zhu, B., et al. (2020). High-affinity Neoantigens Correlate with Better Prognosis and Trigger Potent Antihepatocellular Carcinoma (HCC) Activity by Activating CD39(+) CD8(+) T Cells. *Hepatology* 70. doi:10.1136/gutjnl-2020-322196

Liu, Z., Liu, L., Jiao, D., Guo, C., Wang, L., Li, Z., et al. (2021a). Association of RYR2 Mutation with Tumor Mutation Burden, Prognosis, and Antitumor Immunity in Patients with Esophageal Adenocarcinoma. *Front. Genet.* 12, 669694. doi:10.3389/fgene.2021.669694

Liu, Z., Lu, T., Wang, L., Liu, L., Li, L., and Han, X. (2021b). Comprehensive Molecular Analyses of a Novel Mutational Signature Classification System with Regard to Prognosis, Genomic Alterations, and Immune Landscape in Glioma. *Front. Mol. Biosci.* 8, 682084. doi:10.3389/fmolb.2021.682084

Liu, Z., Wang, L., Liu, L., Lu, T., Jiao, D., Sun, Y., et al. (2021c). The Identification and Validation of Two Heterogenous Subtypes and a Risk Signature Based on Ferroptosis in Hepatocellular Carcinoma. *Front. Oncol.* 11, 619242. doi:10.3389/fonc.2021.619242

Mariathasan, S., Turley, S. J., Nickles, D., Castiglioni, A., Yuen, K., Wang, Y., et al. (2018). TGFβ Attenuates Tumour Response to PD-L1 Blockade by Contributing to Exclusion of T Cells. *Nature* 554, 544–548. doi:10.1038/nature25501

Marth, J. D., Peet, R., Krebs, E. G., and Perlmutter, R. M. (1985). A Lymphocyte-specific Protein-Tyrosine Kinase Gene Is Rearranged and Overexpressed in the Murine T Cell Lymphoma LSTRA. *Cell* 43, 393–404. doi:10.1016/0092-8674(85)90169-2

Moesta, A. K., Li, X.-Y., and Smyth, M. J. (2020). Targeting CD39 in Cancer. *Nat. Rev. Immunol.* 20, 739–755. doi:10.1038/s41577-020-0376-4

Patel, S. P., and Kurzrock, R. (2015). PD-L1 Expression as a Predictive Biomarker in Cancer Immunotherapy. *Mol. Cancer Ther.* 14, 847–856. doi:10.1158/1535-7163.mct-14-0983

Petitprez, F., Meylan, M., de Reyniès, A., Sautès-Fridman, C., and Fridman, W. H. (2020). The Tumor Microenvironment in the Response to Immune Checkpoint Blockade Therapies. *Front. Immunol.* 11, 784. doi:10.3389/fimmu.2020.00784

Rose, T. L., Weir, W. H., Mayhew, G. M., Shibata, Y., Eulitt, P., Uronis, J. M., et al. (2021). Fibroblast Growth Factor Receptor 3 Alterations and Response to Immune Checkpoint Inhibition in Metastatic Urothelial Cancer: a Real World Experience. *Br. J. Cancer* 125, 1251–1260. doi:10.1038/s41416-021-01488-6

Simoni, Y., Becht, E., Fehlings, M., Loh, C. Y., Koo, S.-L., Teng, K. W. W., et al. (2018). Bystander CD8+ T Cells Are Abundant and Phenotypically Distinct in Human Tumour Infiltrates. *Nature* 557, 575–579. doi:10.1038/s41586-018-0130-2

Sung, H., Ferlay, J., and Siegel, R. L. (2021). Global Cancer Statistics 2020: GLOBOCAN Estimates of Incidence and Mortality Worldwide for 36 Cancers in 185 Countries. *CA Cancer J. Clin.* 71, 209–249. doi:10.3322/caac.21660

Thommen, D. S., and Schumacher, T. N. (2018). T Cell Dysfunction in Cancer. *Cancer Cell* 33, 547–562. doi:10.1016/j.ccell.2018.03.012

Till, K. J., Allen, J. C., Talab, F., Lin, K., Allsup, D., Cawkwell, L., et al. (2017). Lck Is a Relevant Target in Chronic Lymphocytic Leukaemia Cells Whose Expression Variance Is Unrelated to Disease Outcome. *Sci. Rep.* 7, 16784. doi:10.1038/s41598-017-17021-w

Uhlén, M., Fagerberg, L., Hallström, B. M., Lindskog, C., Oksvold, P., Mardinoglu, A., et al. (2015). Proteomics. Tissue-Based Map of the Human Proteome. *Science* 347, 1260419. doi:10.1126/science.1260419

Vesely, M. D., Kershaw, M. H., Schreiber, R. D., and Smyth, M. J. (2011). Natural Innate and Adaptive Immunity to Cancer. *Annu. Rev. Immunol.* 29, 235–271. doi:10.1146/annurev-immunol-031210-101324

Yoshihara, K., Shahmoradgoli, M., Martínez, E., Vegesna, R., Kim, H., Torres-Garcia, W., et al. (2013). Inferring Tumour Purity and Stromal and Immune Cell Admixture from Expression Data. *Nat. Commun.* 4, 2612. doi:10.1038/ncomms3612

Zeng, H., Liu, Z., Wang, Z., Zhou, Q., Qi, Y., Chen, Y., et al. (2020). Intratumoral IL22-producing Cells Define Immunoevasive Subtype Muscle-invasive Bladder Cancer with Poor Prognosis and superior Nivolumab Responses. *Int. J. Cancer* 146, 542–552. doi:10.1002/ijc.32715

Conflict of Interest: The authors declare that the research was conducted in the absence of any commercial or financial relationships that could be construed as a potential conflict of interest.

Publisher's Note: All claims expressed in this article are solely those of the authors and do not necessarily represent those of their affiliated organizations, or those of the publisher, the editors, and the reviewers. Any product that may be evaluated in this article, or claim that may be made by its manufacturer, is not guaranteed or endorsed by the publisher.

GLOSSARY

ACC adrenocortical carcinoma
BC bladder cancer
BLCA bladder urothelial carcinoma
BRCA breast invasive carcinoma
CESC cervical squamous cell carcinoma and endocervical adenocarcinoma
CHOL cholangiocarcinoma
COAD colon adenocarcinoma
DEGs differential expression genes
DLBC lymphoid neoplasm diffuse large B-cell lymphoma
ESCA esophageal carcinoma
GBM glioblastoma multiforme
GEO Gene Expression Omnibus
GO gene ontology
HNSC head and neck squamous cell carcinoma
ICIs immune checkpoint inhibitors
KEGG Kyoto Encyclopedia of Genes and Genomes
KICH kidney chromophobe
KIRC kidney renal clear cell carcinoma
KIRP kidney renal papillary cell carcinoma
LAML acute myeloid leukemia
LGG brain lower grade glioma
LIHC liver hepatocellular carcinoma
LUAD lung adenocarcinoma
LUSC lung squamous cell carcinoma
MESO mesothelioma
MIBC muscle-invasive bladder cancer
OV ovarian serous cystadenocarcinoma
PAAD pancreatic adenocarcinoma
PCPG pheochromocytoma and paraganglioma
PRAD prostate adenocarcinoma
PPI protein–protein interaction
READ rectum adenocarcinoma
SARC sarcoma
SKCM skin cutaneous melanoma
STAD stomach adenocarcinoma
TCGA The Cancer Genome Atlas
TCR T-cell receptor
TGCT testicular germ cell tumors
THCA thyroid carcinoma
THYM thymoma
TICs tumor-infiltrating immune cells
TMB tumor mutation burden
UCS uterine carcinosarcoma
UVM uveal melanoma.

frontiers in Cell and Developmental Biology

ORIGINAL RESEARCH
published: 21 January 2022
doi: 10.3389/fcell.2021.809620

Gemcitabine-Resistant Biomarkers in Bladder Cancer are Associated with Tumor-Immune Microenvironment

*Yuxuan Song[1,2], Yiqing Du[1], Caipeng Qin[1], Haohong Liang[2], Wenbo Yang[1], Jiaxing Lin[1], Mengting Ding[1], Jingli Han[1] and Tao Xu[1]**

[1]Department of Urology, Peking University People's Hospital, Beijing, China, [2]Biomedical Pioneering Innovation Center (BIOPIC), School of Life Sciences, Peking University, Beijing, China

To identify key biomarkers in gemcitabine (GEM)-resistant bladder cancer (BCa) and investigate their associations with tumor-infiltrating immune cells in a tumor immune microenvironment, we performed the present study on the basis of large-scale sequencing data. Expression profiles from the Gene Expression Omnibus GSE77883 dataset and The Cancer Genome Atlas BLCA dataset were analyzed. Both BCa development and GEM-resistance were identified to be immune-related through evaluating tumor-infiltrating immune cells. Eighty-two DEGs were obtained to be related to GEM-resistance. Functional enrichment analysis demonstrated they were related to regulation of immune cells proliferation. Protein–protein interaction network selected six key genes (CAV1, COL6A2, FABP4, FBLN1, PCOLCE, and CSPG4). Immunohistochemistry confirmed the down-regulation of the six key genes in BCa. Survival analyses revealed the six key genes were significantly associated with BCa overall survival. Correlation analyses revealed the six key genes had high infiltration of most immune cells. Gene set enrichment analysis further detected the key genes might regulate GEM-resistance through immune response and drug metabolism of cytochrome P450. Next, microRNA-gene regulatory network identified three key microRNAs (hsa-miR-124-3p, hsa-miR-26b-5p, and hsa-miR-192-5p) involved in GEM-resistant BCa. Connectivity Map analysis identified histone deacetylase inhibitors might circumvent GEM-resistance. In conclusion, CAV1, COL6A2, FABP4, FBLN1, PCOLCE, and CSPG4 were identified to be critical biomarkers through regulating the immune cell infiltration in an immune microenvironment of GEM-resistance and could act as promising treatment targets for GEM-resistant muscle-invasive BCa.

Keywords: bladder cancer, gemcitabine, tumor immune microenvironment, GEO, TCGA

OPEN ACCESS

Edited by:
Yongwen Luo,
Wuhan University, China

Reviewed by:
Xiongbing Zu,
Central South University, China
Yu-Zheng Ge,
Nanjing Medical University, China

****Correspondence:***
Tao Xu
xutao@pkuph.edu.cn

Specialty section:
This article was submitted to Molecular and Cellular Pathology, a section of the journal Frontiers in Cell and Developmental Biology

Received: *05 November 2021*
Accepted: *13 December 2021*
Published: *21 January 2022*

Citation:
Song Y, Du Y, Qin C, Liang H, Yang W, Lin J, Ding M, Han J and Xu T (2022) Gemcitabine-Resistant Biomarkers in Bladder Cancer are Associated with Tumor-Immune Microenvironment. Front. Cell Dev. Biol. 9:809620. doi: 10.3389/fcell.2021.809620

INTRODUCTION

Bladder cancer (BCa) is the ninth most prevalent cancer globally (Antoni et al., 2017; Bray et al., 2018). Approximately 540,000 new cases have been diagnosed and 195,000 patients die of BCa each year (Antoni et al., 2017; Bray et al., 2018). The BCa incidence is elevated worldwide and the tumor burden increases due to population aging and environmental pollution during the past 2 decades (Ebrahimi et al., 2019; Yang et al., 2019).

Although surgical operation has been utilized in BCa treatment, the prognosis is still poor (Kirkali et al., 2005; Goebell et al., 2008; Humphrey et al., 2016). The 5-year relapse rate after initial treatment is from 55% to 85% in non-muscle-invasive BCa (NMIBC) and the 5-year survival rate is from 30% to 45% in muscle-invasive BCa (MIBC) (Choueiri and Raghavan, 2008; Lightfoot et al., 2014; Antoni et al., 2017). Chemotherapy is a promising treatment for reducing the recurrence rate and improving the survival rate of BCa patients (Coen et al., 2019). Gemcitabine (GEM) is a kind of cytosine analogue that inhibits DNA synthesis. Combination therapy of GEM and other chemotherapeutic drugs has been widely utilized in the treatment of MIBC (Oh et al., 2009).

However, GEM-resistance causes a severe challenge in the treatment of MIBC. It is reported that the response rate of advanced MIBC with GEM treatment is less than 40%, which indicates a limited efficacy of GEM treatment (Kaufman et al., 2009; Sternberg et al., 2013). The long-term curative effects of GEM declined sharply with the extension of treatment time (Cao et al., 2018). In addition, inherent or acquired drug resistance is usually observed in clinical practice (Bergman et al., 2002; Wang and Lippard, 2005). As a consequence, it is necessary and vital to explore potential mechanisms of GEM-resistance. On the one hand, MIBC has the nature of high somatic-mutation frequency and molecular heterogeneity, which exerts a critical role in drug resistance (Giannopoulou et al., 2019). On the other hand, dysfunction of immune system exerts a crucial role in tumor resistance (Yu et al., 2018). Co-delivery of GEM and small interfering RNA targeting IDO1 could relieve the immune brakes and further alleviate the immune inhibition of M2 macrophages, which indicates that these immune cells are associated with regulation of immune response to GEM (Chen et al., 2020). In addition, bioinformatics analyses constructs a microRNA (miRNA)-gene regulatory network associated with alteration of memory $CD4^+$ T cells in GEM-resistant pancreatic cancer cells, which suggests the immune system is implicated in the microenvironment of GEM-resistance (Gu et al., 2020).

The present study focused on the key genes, miRNA-gene regulatory network, and their immune microenvironment based on GEM-resistant BCa in order to explore reliable prognostic indicators and provide treatment targets for GEM-resistant BCa.

MATERIALS AND METHODS

The Cancer Genome Atlas (TCGA) Bladder Urothelial Carcinoma (BLCA) dataset

The gene expression profiling dataset and clinical data of TCGA BLCA (accessed September 1, 2021) were downloaded from the TCGA website (http://portal.gdc.cancer.gov/). TCGA BLCA comprised BCa tissues (n = 404) and adjacent normal tissues (n = 18). Among all samples, there were 18 pairs of BCa tissues (n = 18) and matched adjacent normal tissues (n = 18).

GSE77883 dataset from Gene Expression Omnibus (GEO) database

Gene expression profiles of GSE77883 (accessed September 1st, 2021) were downloaded from GEO (http://www.ncbi.nlm.nih.gov/geo/). Six cells containing untreated T24 cells (n = 3) and GEM-resistant T24 cells (n = 3) were enrolled. RNA was extracted and measured through microarray (Platform: GPL17077 Agilent-039494 SurePrint G3 Human GE v2 8 × 60 K Microarray 039381).

Gene Set Variation Analysis (GSVA)

We downloaded the gene set of TOOKER_GEMCITABINE_RESISTANCE_UP (M19654) (Tooker et al., 2007) from the Molecular Signatures Database (MSigDB: http://www.gsea-msigdb.org/gsea/index.jsp) (Liberzon et al., 2015), and M19654 is the key GEM-related gene set from chemical and genetic perturbations of MSigDB. The normalized GEM-resistance GSVA score of the gene set was measured for each BCa tissue from TCGA BLCA using the GSVA algorithm with the GSVA R package (Hänzelmann et al., 2013). The median value of the GEM-resistance score was used to divide all TCGA BCa tissues into high score of the GEM-resistance group (n = 202) and low score of the GEM-resistance group (n = 202).

Immune cells analysis in tumor-immune microenvironment

Tumor-infiltrating immune cells were measured and analyzed with the MCPcounter (Microenvironment Cell Populations-counter) R package (Becht et al., 2016). In order to explore whether GEM-resistance is immune-related, we compared the immune cells between the high score of the GEM-resistance group (n = 202) and low score of the GEM-resistance group (n = 202) in TCGA BCa tissues. The Pearson method was adopted to assess the correlation between the normalized GEM-resistance GSVA score and immune cells. To further clarify the correlation between immune system and BCa development, we compared the immune cells between 18 pairs of BCa tissues (n = 18) and matched adjacent normal tissues (n = 18) in TCGA BLCA.

Identification of differentially expressed genes (DEGs) in GSE77883 and TCGA BLCA datasets

Limma R package was adopted to detect DEGs between GEM-resistant T24 cells and untreated T24 cells in the GSE77883 dataset (Ritchie et al., 2015). In addition, we also identified DEGs between 18 pairs of BCa tissues and adjacent tissues in TCGA BLCA. Benjamini-Hochberg method (Benjamini and Hochberg, 1995; Benjamini and Hochberg, 2000) was used to adjust the p-values for multiplicity and control false discovery rate. The thresholds were $|\log FC| \geq 1$ and adjusted p-value (adj. p-value) < 0.05. Venn diagram was adopted to find overlapped DEGs in the GSE77883 and TCGA BLCA datasets. These overlapped DEGs were considered as GEM-resistant genes in BCa.

Functional enrichment analysis

ClusterProfiler R package (Yu et al., 2012) was applied to identify the biological functions of overlapped DEGs through Gene Ontology (GO) and Kyoto Encyclopedia of Genes and Genomes (KEGG) pathway collections. Metascape (http://metascape.org) was utilized to identify the most closely enriched clusters (Zhou et al., 2019).

Protein–protein interaction (PPI) network and selection of hub genes

We applied String (version 11.0: http://string-db.org/) (Szklarczyk et al., 2017) to construct interactions among proteins on the basis of the overlapped DEGs with the interaction score of 0.400 was set as threshold. In addition, cytoHubba in Cytoscape software screened 10 genes with highest connection degrees. Univariate Cox regression analysis further detected prognosis-related genes among the top 10 genes based on BCa patients (n = 404) from the TCGA BLCA dataset.

Immunohistochemistry and validation by TCGA BLCA and Genotype-Tissue Expression (GTEx) datasets

Immunohistochemistry was extracted and analyzed from The Human Protein Atlas (THPA) database (http://www.proteinatlas.org/) (Uhlen et al., 2010). We evaluated expression levels of the identified six prognosis-related genes (CAV1, CSPG4, FBLN1, COL6A2, FABP4, and PCOLCE) between tumor and normal tissues at protein level.

To confirm the differential expression of the six prognosis-related genes in a larger sample size, box plots were adopted to compare the expression of CAV1, CSPG4, FBLN1, COL6A2, FABP4, and PCOLCE between BCa tissues and normal tissues from the TCGA BLCA dataset and the GTEx dataset through Gene Expression Profiling Interactive Analysis (GEPIA) (http://gepia.cancer-pku.cn/) (Tang et al., 2017).

Survival analysis

Based on the TCGA BLCA dataset, we analyzed the six selected genes (CAV1, CSPG4, FBLN1, COL6A2, FABP4, and PCOLCE) with overall survival (OS) and disease-free survival (DFS) through the Kaplan–Meier (KM) Plotter (http://kmplot.com/analysis/) (Nagy et al., 2018).

Predictive value of the six hub genes in immunotherapy

CAMOIP (Comprehensive Analysis on Multi-Omics of Immunotherapy in Pan-cancer) is a tool for analyzing the expression data and mutation data from the immunotherapy-treated projects, using a standard processing pipeline (Lin et al., 2021). The IMvigor210 cohort to investigate the clinical activity of immunotherapy with atezolizumab in metastatic BCa was used for an integrated biomarker evaluation (Mariathasan et al., 2018). We used gene expression profiling from the IMvigor210 cohort to evaluate the predictive value of the six key genes (CAV1, COL6A2, FABP4, FBLN1, PCOLCE, and CSPG4) in OS after immunotherapy through CAMOIP.

Pearson correlation analysis explored the six hub genes with tumor-infiltrating immune cells

TIMER (Tumor Immune Estimation Resource) (http://timer.cistrome.org/) (Li et al., 2016; Li et al., 2017) was adopted to measure the impacts of immune cells on BCa OS through separating all BCa samples (n = 404) into high and low abundance groups based on median value of each immune cell abundance. In addition, Pearson method measured correlations between immune cells and expression levels of the six genes (CAV1, CSPG4, FBLN1, COL6A2, FABP4, and PCOLCE) in BCa patients (n = 404) from the TCGA BLCA dataset through Pearson correlation analysis.

Genetic mutation analysis

The cBioPortal database (http://www.cbioportal.org/) was utilized to investigate mutations of the six hub genes (CAV1, CSPG4, FBLN1, COL6A2, FABP4, and PCOLCE) in BCa patients (n = 404) from the TCGA BLCA dataset. Survival analysis and immune cells were also explored based on genetic mutations.

miRNA-Gene regulatory network

Two databases including miRTarbase (http://mirtarbase.mbc.nctu.edu.tw/php/) (Chou et al., 2018) and Targetscan (http://www.targetscan.org/vert_72/) (Agarwal et al., 2015) were experimentally validated miRNA-target gene interaction databases and they were adopted to predict upstream miRNAs and to build the miRNA-gene regulatory network. Venn diagram was used to identify overlapped miRNAs as key miRNAs and KM Plotter was utilized to evaluate the effects of key miRNAs on BCa OS based on BCa patients from the TCGA BLCA dataset as mentioned before. Pearson method was performed to evaluate the pairwise gene correlation in BCa samples from the TCGA BLCA dataset.

Gene set enrichment analysis (GSEA)

To clarify the roles of the six hub genes (CAV1, CSPG4, FBLN1, COL6A2, FABP4, and PCOLCE), we applied GSEA to analyze the enrichment of BCa samples (n = 404) in the TCGA BLCA dataset by assessing the normalized enrichment score (NES) (Subramanian et al., 2007).

Screening of potential targeted drugs in GEM-resistant BCa

The Connectivity Map (CMAP) database (http://portals.broadinstitute.org/cmap) (Lamb et al., 2006; Lamb, 2007) was utilized to explore the potential drugs with antagonism or synergism to GEM-resistance. This database used details of DEGs to identify potential targeted drugs. Eighty-two key DEGs in GEM-resistant BCa were uploaded to the CMAP database. Next, the 82 key DEGs were compared to expression profiles stored in CMAP in order to select potential drugs. Drugs

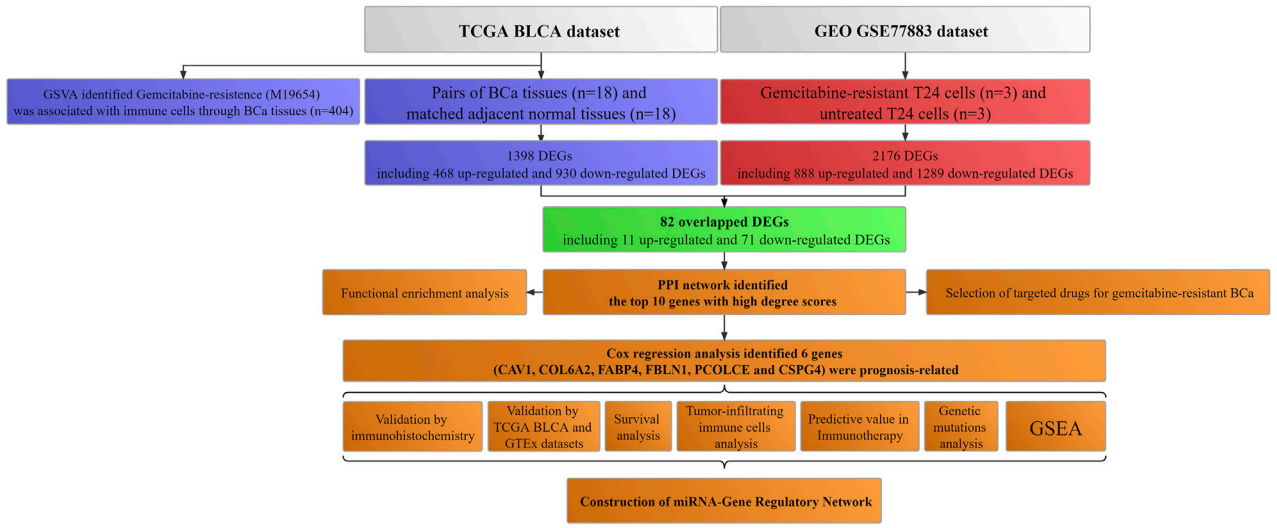

FIGURE 1 | Workflow of this study. TCGA: The Cancer Genome Atlas; BLCA: Bladder urothelial carcinoma; GEO: Gene Expression Omnibus; BCa: Bladder cancer; GSVA: Gene set variation analysis; GTEx: Genotype-tissue expression; DEGs: Differentially expressed genes; PPI: Protein–protein interaction; miRNA: microRNA; GSEA: Gene set enrichment analysis.

with p-value <0.05 were considered as significant targeted drugs to GEM-resistance.

Statistical analysis

Statistical analyses were performed by R software (v3.6.1: http://www.r-project.org), GraphPad Prism 7.0, Metascape, GEPIA, KM Plotter, TIMER, and cBioPortal. Univariate Cox regression, KM method, and log-rank test were adopted for survival analysis by calculating hazard ratio (HR) and 95% confidence interval (CI). Student's *t* test was applied to evaluate quantitative variables. The correlation coefficient, *R*-value, was used to estimate the strength of Pearson correlation analysis. The two-sided p-value <0.05 was set as the threshold. Cytoscape software (v.3.6.1) was adopted for visualization of networks.

RESULTS

Figure 1 showed the workflow.

Tumor immune microenvironment in GEM-resistance

Based on 404 BCa tissues from the TCGA BLCA dataset, GSVA analysis indicated that BCa patients with high score of GEM-resistance had worse OS compared with those with low score (HR = 1.57, 95%CI = 1.14–2.16) (p = 0.006) (**Figure 2A**). Furthermore, correlation analysis revealed GEM-resistance score was positively associated with cytotoxicity scores (R = 0.376, p < 0.001), macrophages/monocytes (R = 0.317, p < 0.001), NK cells, and cancer-associated fibroblasts. GEM-resistance score was negatively associated with myeloid dendritic cells (**Figures 2B,C**). In addition, BCa patients with high score of GEM-resistance had higher abundance of the cytotoxicity scores, macrophages/monocytes, NK cells, and cancer-associated fibroblasts as well as lower abundance of myeloid dendritic cells in comparison with those with low score, which confirmed the results of correlation analysis (**Figures 2D,E**). From the above results, we identified that GEM-resistance score in BCa is closely related to immune microenvironment. In addition, GSVA analysis based on the GSE77883 dataset indicated that GEM-resistant T24 cells had higher score of GEM-resistance than untreated T24 cells (p = 0.03) (**Supplementary Figure S1**).

Tumor-immune microenvironment in BCa development

Based on 18 pairs of BCa tissues and matched adjacent normal tissues, immune cells infiltration analysis suggested that the abundance of B cells, myeloid dendritic cells, endothelial cells, and cancer associated fibroblast cells was obviously down-regulated in BCa tissues compared with matched adjacent normal tissues (p < 0.05). However, for other immune cells, no change was observed (p > 0.05) (**Supplementary Figure S2**). From the above results, we identified that BCa development is closely related to an immune microenvironment.

Identification of key genes in GSE77883 and TCGA BLCA datasets

We firstly compared GEM-resistant T24 cells with untreated T24 cells in the GSE77883 dataset; 2,176 DEGs containing 888 up-regulated and 1,289 down-regulated genes were obtained in GEM-resistant BCa cells (**Figure 3A** and **Figure 3C**).

In addition, we compared 18 pairs of BCa tissues and matched adjacent normal tissues in the TCGA BLCA dataset. We obtained 1,398 DEGs containing 468 up-regulated and 930 down-regulated genes in BCa tissues (**Figure 3B** and **Figure 3D**).

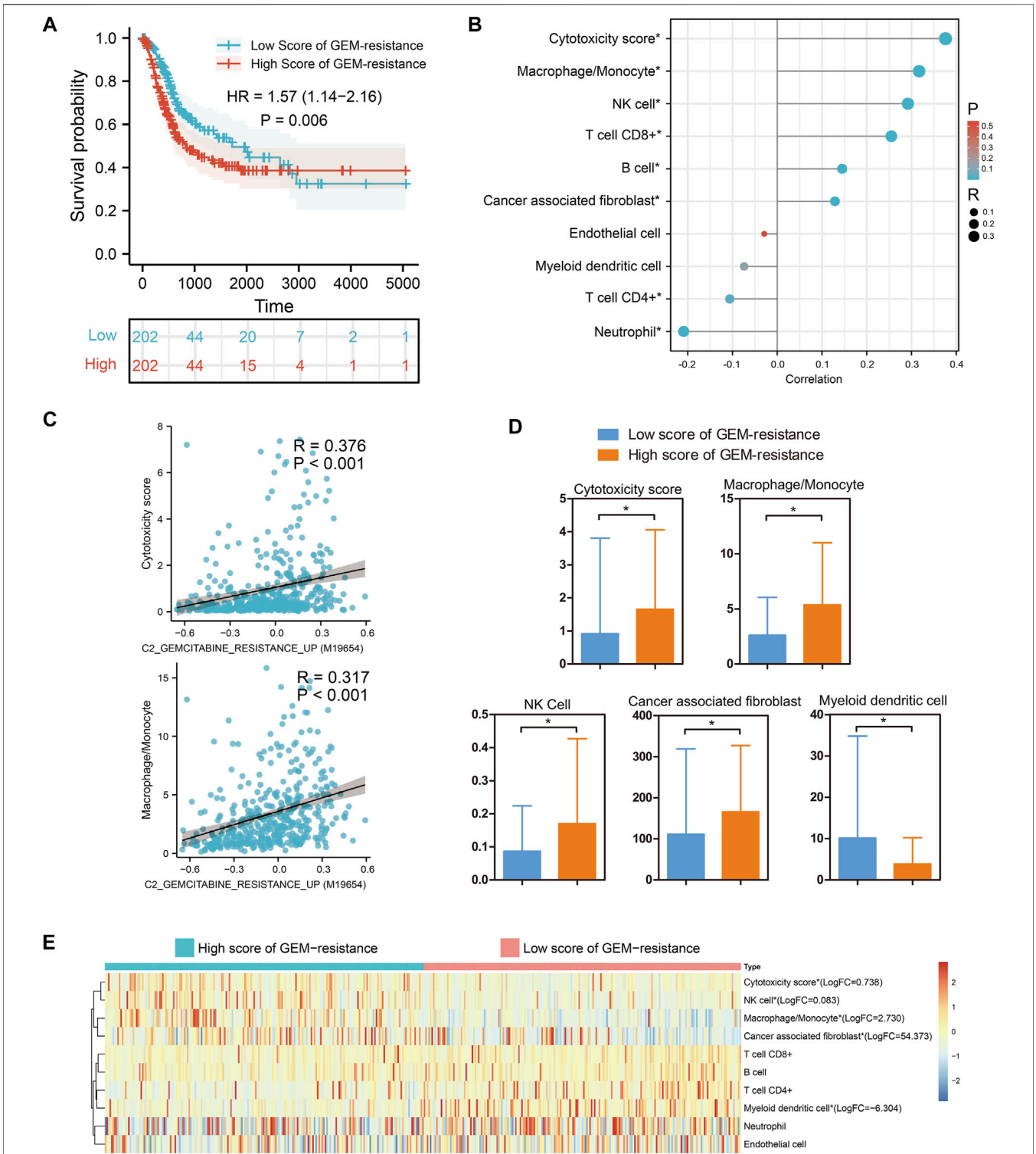

FIGURE 2 | Gene set variation analysis identified that gemcitabine (GEM)-resistance was associated with prognosis and immune microenvironment in 404 bladder cancer (BCa) patients from the TCGA BLCA dataset. **(A)** Kaplan–Meier survival indicated BCa patients with high score of GEM-resistance had poor overall survival; **(B,C)** Correlations between GEM-resistance score and immune cells; **(D,E)** Differences in abundance of immune cells between high score and low score of GEM-resistance. *$p < 0.05$.

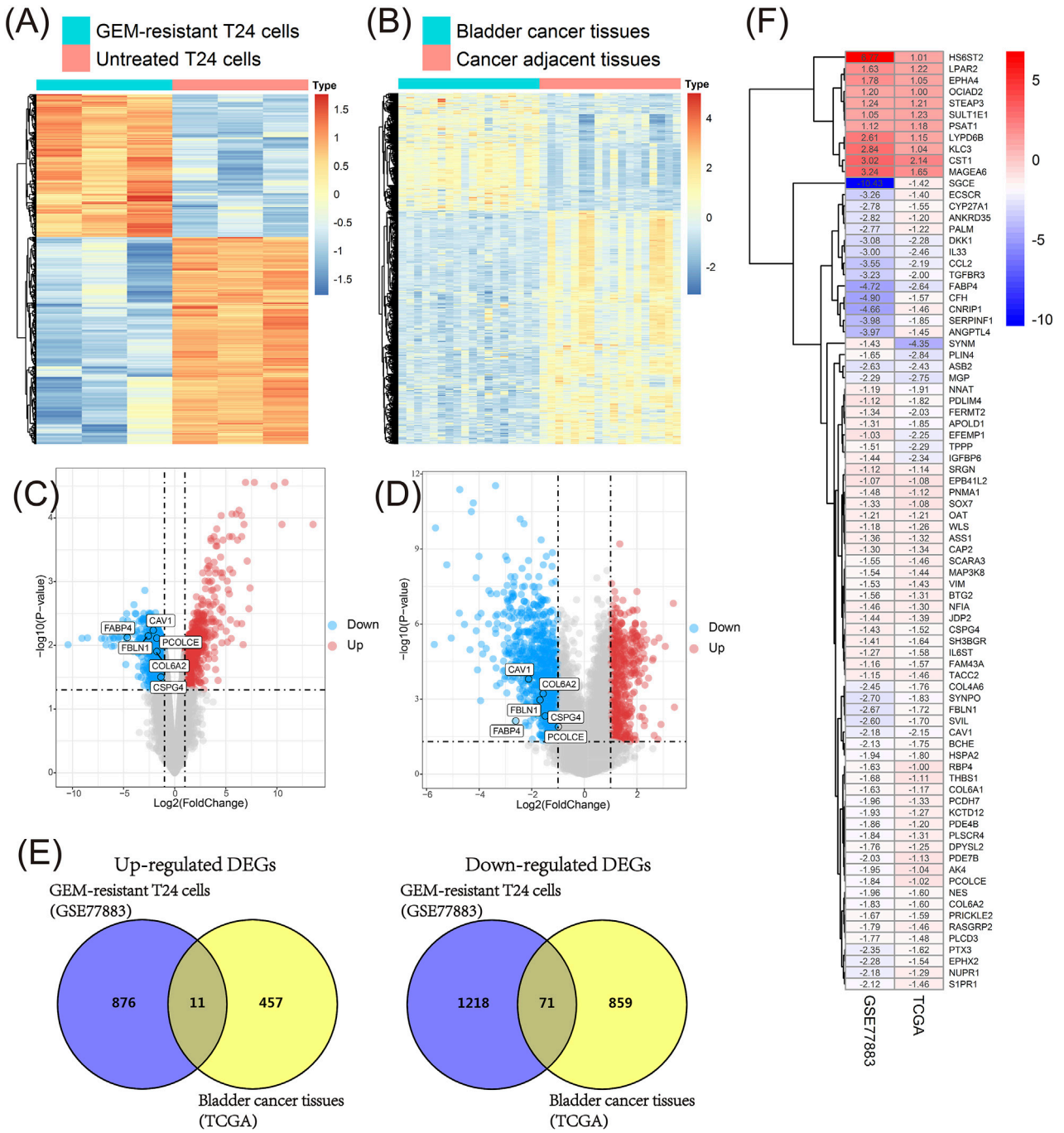

FIGURE 3 | Identification of key genes in the GSE77883 and TCGA BLCA datasets. **(A)** Heat map of differentially expressed genes (DEGs) between gemcitabine (GEM)-resistant T24 cells and untreated T24 cells based on the GSE77883 dataset; **(B)** Heat map of DEGs between bladder cancer (BCa) tissues and matched adjacent normal tissues based on the TCGA BLCA dataset; **(C)** Volcano plot of DEGs between GEM-resistant T24 cells and untreated T24 cells based on the GSE77883 dataset; **(D)** Volcano plot of DEGs between BCa tissues and matched adjacent normal tissues based on the TCGA BLCA dataset; **(E)** Venn diagram identified overlapped DEGs in both GSE77883 and TCGA BLCA datasets; **(F)** Heat map of 82 overlapped DEGs and they were key genes in both GEM-resistance and BCa development. adj.P.-value was adjusted p-value for Benjamini-Hochberg (BH) method.

In order to investigate which genes were associated with both GEM-resistance and BCa development, Venn diagram combined the DEGs from two datasets and identified the overlapped DEGs obtained in both datasets. Ultimately, 82 overlapped DEGs (11 overlapped up-regulated and 71 overlapped down-regulated genes) were obtained and were considered as GEM-resistant genes in BCa (**Figures 3E,F**) (**Supplementary Table S1**).

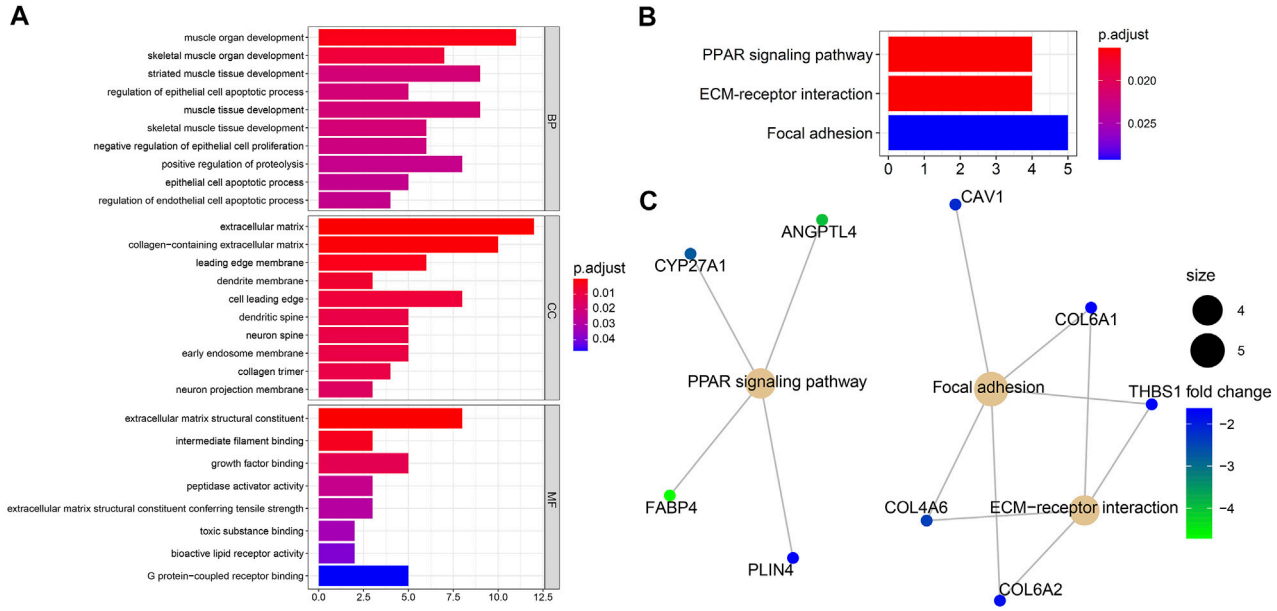

FIGURE 4 | Enrichment analyses through 82 overlapped differentially expressed genes. **(A)** Gene ontology enrichment analysis. Biological process (BP) indicated they were enriched in regulation of epithelial cell apoptotic process (GO:1904035) and muscle tissue development (GO:0060537); cell component (CC) indicated they were enriched in extracellular matrix (GO:0031012) and cell leading edge (GO:0031252); molecular function (MF) indicated they were enriched in growth factor binding (GO:0019838) and toxic substance binding (GO:0015643); **(B,C)** Kyoto Encyclopedia of Genes and Genomes (KEGG) pathway and gene-concept network analysis. They were enriched in the peroxisome proliferator-activated receptor (PPAR) signaling pathway (hsa03320), extracellular matrix (ECM)-receptor interaction (hsa04512), and focal adhesion (hsa04510).

Functional enrichment analysis

Biological process analysis indicated that the 82 overlapped DEGs were enriched in regulation of the epithelial cell apoptotic process (GO:1904035) and muscle tissue development (GO:0060537). Component analysis detected that they were mainly located at the extracellular matrix (GO:0031012) and cell leading edge (GO:0031252). Molecular function analysis demonstrated that they participated in growth factor binding (GO:0019838) and toxic substance binding (GO:0015643) (**Figure 4A** and **Table 1**). Pathway analyses identified GEM-resistance was associated with the peroxisome proliferator-activated receptor (PPAR) signaling pathway (hsa03320), extracellular matrix (ECM)-receptor interaction (hsa04512), and focal adhesion (hsa04510) (**Figures 4B,C** and **Table 1**).

Metascape identified the interactions of the main 19 clustered enrichment terms (**Supplementary Figure S3** and **Supplementary Table S2**). **Table 2** shows that negative regulation of cell proliferation (GO:0008285) and its relevant enrichment terms were significantly associated with immune cells including endothelial cells (GO:2000351), T cells (GO:0050870), and granulocytes (GO:0071621), which confirmed the close relationship between GEM-resistance and immune system.

PPI network and selection of hub genes

Finally, PPI network enrolled 37 nodes and 49 edges (**Figure 5A**). Among the interactions,CAV1, COL6A2, FABP4, FBLN1, PCOLCE, CSPG4, CCL2, THBS1, CFH, and COL6A1 with the highest degree scores were considered as the top 10 genes. **Figure 5B** showed the key module constituted by the 10 genes.

Ultimately, univariate Cox regression analysis detected that six genes (CAV1, COL6A2, FABP4, FBLN1, PCOLCE, and CSPG4) were identified to be prognosis-related ($p < 0.05$) (**Table 3**) (**Figure 5C**).

Immunohistochemistry and validation of hub genes by TCGA and GTEx datasets

We collected and analyzed immunohistochemistry of BCa tissues and normal bladder tissues from THPA. Expression levels of the six hub genes (CAV1, COL6A2, FABP4, FBLN1, PCOLCE, and CSPG4) were evaluated at protein level. **Figure 6** reveals the six hub genes were down-regulated in BCa tissues.

In addition, we also validated the six hub genes between 404 BCa tissues and 28 normal bladder tissues from the TCGA BLCA and GTEx datasets. Box plots indicated that they were all down-regulated in BCa samples ($p < 0.05$), which was in accord with the results of immunohistochemistry (**Figure 6**).

Survival analysis and predictive value of the six hub genes in immunotherapy

KM curves suggested that the six hub genes could influence the OS time (**Supplementary Figure S4**). Lower expression levels

TABLE 1 | Functional enrichment analysis results

Term	Description	Category	Adjusted p-value
GO:0007517	Muscle organ development	GO (BP)	2.59E-03
GO:0060538	Skeletal muscle organ development	GO (BP)	7.46E-03
GO:0014706	Striated muscle tissue development	GO (BP)	1.99E-02
GO:1904035	Regulation of epithelial cell apoptotic process	GO (BP)	1.99E-02
GO:0060537	Muscle tissue development	GO (BP)	1.99E-02
GO:0007519	Skeletal muscle tissue development	GO (BP)	2.00E-02
GO:0050680	Negative regulation of epithelial cell proliferation	GO (BP)	2.18E-02
GO:0045862	Positive regulation of proteolysis	GO (BP)	2`.45E-02
GO:1904019	Epithelial cell apoptotic process	GO (BP)	2.49E-02
GO:2000351	Regulation of endothelial cell apoptotic process	GO (BP)	2.49E-02
GO:0031012	Extracellular matrix	GO (CC)	1.04E-04
GO:0062023	Collagen-containing extracellular matrix	GO (CC)	6.16E-04
GO:0031256	Leading edge membrane	GO (CC)	2.91E-03
GO:0032590	Dendrite membrane	GO (CC)	5.90E-03
GO:0031252	Cell leading edge	GO (CC)	8.01E-03
GO:0043197	Dendritic spine	GO (CC)	9.77E-03
GO:0044309	Neuron spine	GO (CC)	9.77E-03
GO:0031901	Early endosome membrane	GO (CC)	9.77E-03
GO:0005581	Collagen trimer	GO (CC)	1.03E-02
GO:0032589	Neuron projection membrane	GO (CC)	1.55E-02
GO:0005201	Extracellular matrix structural constituent	GO (MF)	7.61E-05
GO:0019215	Intermediate filament binding	GO (MF)	3.35E-03
GO:0019838	Growth factor binding	GO (MF)	1.15E-02
GO:0016504	Peptidase activator activity	GO (MF)	2.46E-02
GO:0030020	Extracellular matrix structural constituent conferring tensile strength	GO (MF)	2.90E-02
GO:0015643	Toxic substance binding	GO (MF)	3.26E-02
GO:0045125	Bioactive lipid receptor activity	GO (MF)	3.95E-02
GO:0001664	G protein-coupled receptor binding	GO (MF)	4.73E-02
hsa03320	Peroxisome proliferators-activated receptor (PPAR) signaling pathway	KEGG pathway	1.62E-02
hsa04512	Extracellular matrix (ECM)-receptor interaction	KEGG pathway	1.62E-02
hsa04510	Focal adhesion	KEGG pathway	2.93E-02

GO: Gene Ontology; KEGG: Kyoto Encyclopedia of Genes and Genomes; BP: biological process; CC: cell component; MF: molecular function.

TABLE 2 | Immune-related enrichment terms associated with immune cells proliferation

Term	Description	Category	Adjusted p-value
GO:0008285	Negative regulation of cell proliferation	GO (BP)	1.13E-05
GO:2000351	Regulation of endothelial cell apoptotic process	GO (BP)	5.92E-05
GO:0072577	Endothelial cell apoptotic process	GO (BP)	8.03E-05
GO:2000353	Positive regulation of endothelial cell apoptotic process	GO (BP)	8.22E-05
GO:0002696	Positive regulation of leukocyte activation	GO (BP)	2.15E-03
GO:0001937	Negative regulation of endothelial cell proliferation	GO (BP)	2.48E-03
GO:1903037	Regulation of leukocyte cell-cell adhesion	GO (BP)	4.40E-03
GO:0050870	Positive regulation of T cell activation	GO (BP)	5.35E-03
GO:0007159	Leukocyte cell-cell adhesion	GO (BP)	6.74E-03
GO:0030595	Leukocyte chemotaxis	GO (BP)	7.05E-03
GO:0050900	Leukocyte migration	GO (BP)	7.37E-03
GO:1903039	Positive regulation of leukocyte cell-cell adhesion	GO (BP)	7.39E-03
GO:0071621	Granulocyte chemotaxis	GO (BP)	7.78E-03

GO: Gene Ontology; BP: biological process.

of FABP4, FBLN1, and COL6A2 indicated worse OS time ($p < 0.05$). However, higher expression levels of CSPG4, CAV1, and PCOLCE might be indicators for worse OS time ($p < 0.05$) for BCa patients. In addition, we identified that FABP4, CSPG4, COL6A2, and PCOLCE were related to DFS time of BCa ($p < 0.05$) (**Supplementary Figure S4**).

IMvigor210 cohort indicated that COL6A2 (HR > 1), FABP4 (HR > 1), and FBLN1 (HR < 1) could predict the

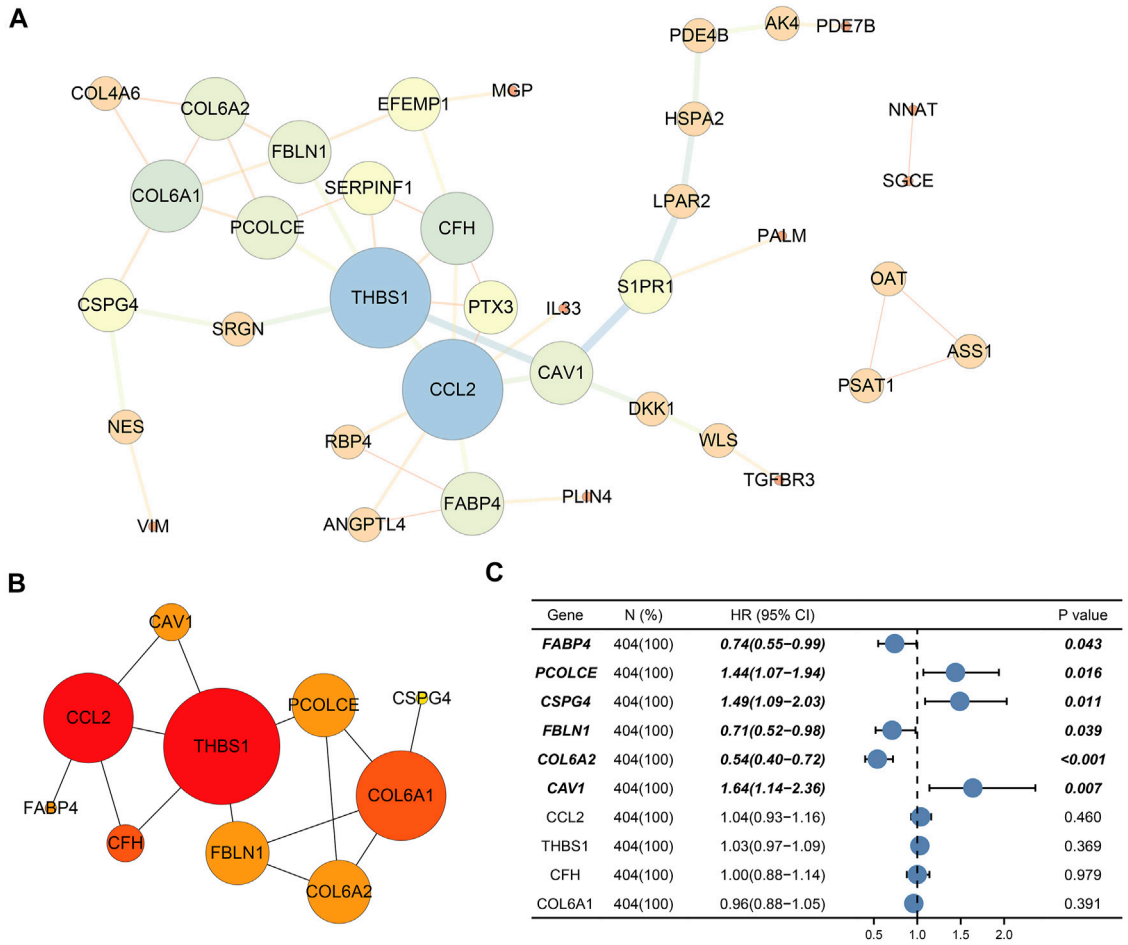

FIGURE 5 | Protein–protein interaction (PPI) network and selection of hub genes. **(A)** PPI network of DEGs; **(B)** Hub module; **(C)** Six prognostic genes (CAV1, COL6A2, FABP4, FBLN1, PCOLCE, and CSPG4) through univariate Cox regression. Bold genes meant prognosis-related genes.

TABLE 3 | The six hub genes with high degree scores

Gene symbol	Ensembel ID	Description	Type	Hazard ratio (95% confidence interval)	p-Value
CAV1	ENSG00000105974	Caveolin 1	Down-regulated	1.64 (1.14–2.36)	0.007
COL6A2	ENSG00000142173	Collagen type VI alpha 2 chain	Down-regulated	0.54 (0.40–0.72)	<0.001
FABP4	ENSG00000170323	Fatty acid binding protein 4	Down-regulated	0.74 (0.55–0.99)	0.043
FBLN1	ENSG00000077942	Fibulin 1	Down-regulated	0.71 (0.52–0.98)	0.039
PCOLCE	ENSG00000106333	Procollagen C-endopeptidase enhancer	Down-regulated	1.44 (1.07–1.94)	0.016
CSPG4	ENSG00000173546	Chondroitin sulfate proteoglycan 4	Down-regulated	1.49 (1.09–2.03)	0.011

OS after immunotherapy with atezolizumab ($p < 0.05$) (**Figure 7**).

Tumor-infiltrating immune cells with hub genes in TCGA BLCA dataset

We used TIMER to clarify the effects of immune cells on OS of BCa patients in the TCGA BLCA dataset. We found that five immune cells ($CD4^+$ T cells, $CD8^+$ T cells, neutrophils, endothelial cells, and cancer associated fibroblast cells) were associated with OS of BCa. Patients with high abundance of $CD4^+$ T cells and $CD8^+$ T cells had longer OS time than those with low infiltration levels. However, patients with low infiltration levels of neutrophils, endothelial cells, and cancer-associated fibroblast cells had longer OS time compared with those with high infiltration levels of these immune cells (**Supplementary Figure S5**).

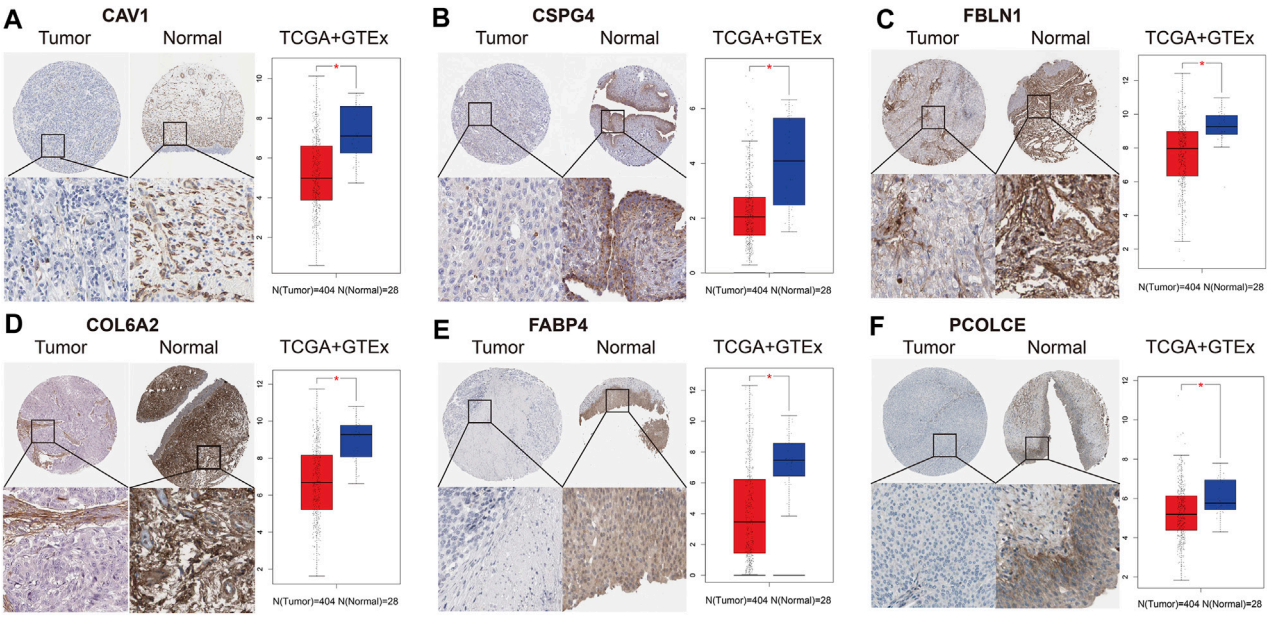

FIGURE 6 | Immunohistochemistry and validation of six hub genes by the TCGA BLCA and GTEx datasets. Immunohistochemistry from THPA (left part in each subfigure) and bladder cancer (BCa) tissues ($n = 404$) and normal tissues ($n = 28$) from the TCGA BLCA and GTEx datasets (right part in each subfigure) indicated that the six selected genes (CAV1, COL6A2, FABP4, FBLN1, PCOLCE, and CSPG4) were down-regulated in BCa. **(A)** CAV1; **(B)** CSPG4; **(C)** FBLN1; **(D)** COL6A2; **(E)** FABP4; **(F)** PCOLCE.

Pearson correlation analysis evaluated the correlations between the six hub genes (CAV1, COL6A2, FABP4, FBLN1, PCOLCE, and CSPG4) and abundance of main immune cells (**Table 4** and **Figure 8A**) (**Supplementary Figure S6**). When we restricted the robust R-value to more than 0.400, we found CAV1 had strong correlation with dendritic cells. COL6A2 and PCOLCE had strong correlations with macrophages (**Figure 8B**).

In addition, GSVA and Pearson correlation analysis identified PCOLCE, CSPG4, COL6A2, and CAV1 were positively correlated with the score of GEM-resistance (R-value >0, $p < 0.05$) (**Figures 9A–D**). However, FBLN1 and FABP4 were negatively correlated with GEM-resistance (R-value <0, $p < 0.05$) (**Figures 9E,F**).

Genetic mutations of hub genes in TCGA BLCA dataset

Figure 9G illustrated the mutation frequencies of the six hub genes (CAV1, COL6A2, FABP4, FBLN1, PCOLCE, and CSPG4) in 404 BCa patients from the TCGA BLCA dataset. Among the six hub genes, the top three most frequently mutated genes were FBLN1 (5.0%), FABP4 (4.0%), and CSPG4 (4.0%). FBLN1 mutations included fusion mutation, amplification mutation, and deletion mutation. Most of FABP4 mutations were amplification mutations and most of CSPG4 mutations were missense mutations.

Furthermore, mutations of all the six hub genes didn't influence the OS time in comparison with the wild-type group ($p > 0.05$) (**Figure 9H**). TIMER identified that CSPG4 mutations could elevate the abundance of $CD4^+$ T cells ($p = 0.009$) and NK cells ($p = 0.021$) (**Figure 9I**), while the genetic mutations of the other five hub genes were not associated with abundance of immune cells.

Construction of miRNA-gene regulatory network

A total of 72 miRNAs might regulate the expression levels of six hub genes through the miRTarBase and Targetscan databases (**Table 5**). The miRNA-gene regulatory network is displayed in **Figure 10**.

As we could see in **Figure 11A**, hsa-miR-124-3p was the overlapped upstream miRNA of CAV1, COL6A2, and CSPG4; hsa-miR-26b-5p and hsa-miR-192-5p were overlapped upstream miRNAs of CAV1 and PCOLCE, which indicated the three miRNAs might be key miRNAs in regulating the hub genes. Survival analysis demonstrated that higher expression levels of hsa-miR-124-3p and hsa-miR-192-5p were significantly related to better prognosis in BCa patients from the TCGA BLCA dataset.

Furthermore, a pairwise correlation analysis of CAV1, COL6A2, CSPG4, and PCOLCE was carried out. Expression of the four genes demonstrated a significant positive correlation ($p < 0.05$). The increase of one hub gene was strongly correlated with the increase of another one (**Figure 11B**). Hence, based on the overlapped upstream miRNAs and correlation analysis, we confirmed that the

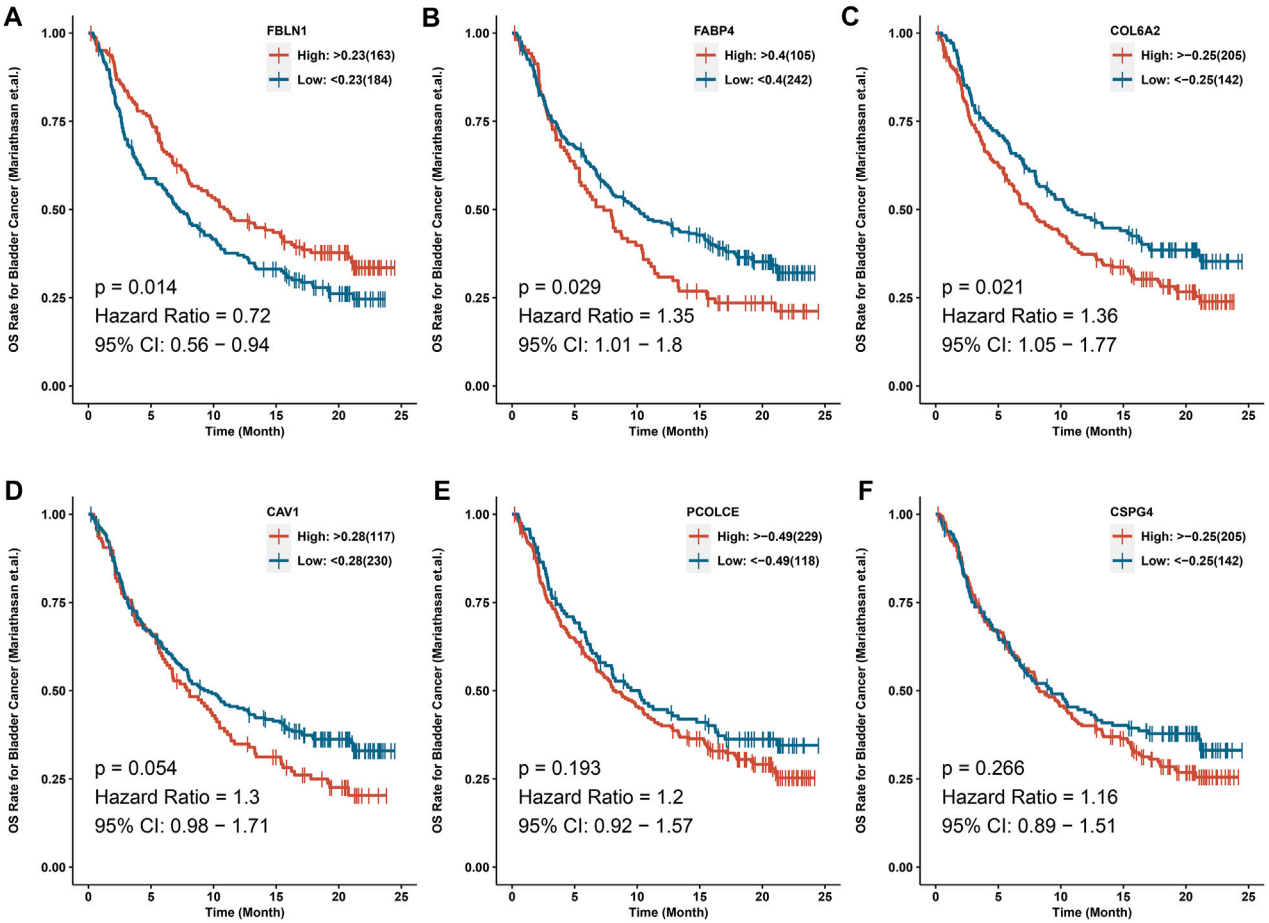

FIGURE 7 | IMvigor210 cohort indicated that COL6A2, FABP4 and FBLN1 could predict the OS after immunotherapy with atezolizumab. **(A)** FBLN1; **(B)** FABP4; **(C)** COL6A2; **(D)** CAV1; **(E)** PCOLCE; **(F)** CSPG4.

three key miRNAs (hsa-miR-124-3p, hsa-miR-26b-5p, and hsa-miR-192-5p) could regulate the four hub genes (CAV1, COL6A2, CSPG4, and PCOLCE) in GEM-resistance and tumor immune microenvironment. We also plotted the key regulatory network in **Figure 11C**. In addition, we detected DEGs between high score of GEM-resistance and low score of GEM-resistance. We found PCOLCE, CSPG4, COL6A2, and CAV1 were up-regulated in patients with high GEM-resistance scores, which further confirmed their key roles in GEM-resistance (**Supplementary Figure S7**).

Gene set enrichment analysis

GSEA was conducted to investigate the possible role of the six hub genes (CAV1, COL6A2, FABP4, FBLN1, PCOLCE, and CSPG4) involved in GEM-resistance. We identified CSPG4 (**Figure 12**) was obviously enriched in cancer-related pathways and functions including the bladder cancer pathway (hsa05219) and TGF-β signaling pathway (hsa04350). In addition, CSPG4 exerted a vital role in chemotherapy-related functions including drug metabolism of cytochrome P450 (hsa00982), drug metabolism of other enzymes (hsa00983), cellular response to drug (GO:0035690), and response to drug (GO:0042493). Further, CSPG4 was also enriched in pathways of immune response and immune cells including the B cell receptor signaling pathway (hsa04662), NK cell-mediated cytotoxicity pathway (hsa04650), and T cell receptor signaling pathway (hsa04660) (**Supplementary Tables S3, S4**). In addition, the other five genes were also enriched in cancer-related (hsa05200 and hsa05219), immune-related (hsa04660, hsa4650, and hsa04662), and chemotherapy-related (hsa00982 and hsa00983) pathways (**Supplementary Table S5**).

Selection of targeted drugs for GEM-resistant BCa

CMAP analysis indicated 75 drugs might have antagonistic or synergistic effects on GEM-resistance. According to the enrichment score, **Table 6** displayed the top 10 drugs with antagonism and the top 10 drugs with synergism, respectively.

TABLE 4 | Pearson correlation analysis indicated the six hub genes (CAV1, COL6A2, FABP4, FBLN1, PCOLCE and CSPG4) were associated with immune cells infiltration

Immune cells	Hub gene	R-value	p-Value
B cell	CAV1	–0.193	**2.22E–04**
—	COL6A2	–0.18	**5.87E–04**
—	FABP4	0.053	3.09E–01
—	FBLN1	0.224	**1.58E–05**
—	PCOLCE	–0.146	**5.34E–03**
—	CSPG4	–0.087	9.81E–02
CD8+ T cell	CAV1	0.356	**2.24E–12**
—	COL6A2	0.198	**1.35E–04**
—	FABP4	–0.065	2.18E–01
—	FBLN1	–0.133	**1.09E–02**
—	PCOLCE	0.062	2.37E–01
—	CSPG4	0.198	**1.35E–04**
CD4+ T cell	CAV1	0.127	**1.55E–02**
—	COL6A2	0.303	**3.48E–09**
—	FABP4	0.054	3.04E–01
—	FBLN1	–0.188	**3.13E–04**
—	PCOLCE	0.215	**3.42E–05**
—	CSPG4	0.16	**2.21E–03**
Macrophage	CAV1	0.217	**2.99E–05**
—	COL6A2	**0.443**	**5.44E–19**
—	FABP4	0.008	8.75E–01
—	FBLN1	0.305	**2.61E–09**
—	PCOLCE	**0.411**	**2.79E–16**
—	CSPG4	0.24	**3.39E–06**
Neutrophil	CAV1	0.348	**9.07E–12**
—	COL6A2	0.271	**1.52E–07**
—	FABP4	–0.159	**2.40E–03**
—	FBLN1	–0.141	**6.94E–03**
—	PCOLCE	0.102	5.28E–02
—	CSPG4	0.21	**5.62E–05**
Dendritic cell	CAV1	**0.417**	**8.02E–17**
—	COL6A2	0.368	**3.71E–13**
—	FABP4	–0.127	**1.50E–02**
—	FBLN1	–0.262	**3.92E–07**
—	PCOLCE	0.156	**2.82E–03**
—	CSPG4	0.235	**5.85E–06**

The bold values indicated statistical significance.

The top 10 antagonistic drugs for GEM-resistant BCa were lisinopril, rifabutin, clonidine, prasterone, vorinostat, prednisone, nifenazone, alvespimycin, trichostatin A, and tanespimycin.

DISCUSSION

Accumulating evidence indicates that aberrantly expressed genes are significantly associated with GEM-resistance in BCa. It is reported that CSNK1D played a key role in the metabolism of GEM, and inhibition of CSNK1D could sensitize BCa cells to GEM treatment, which might be utilized as a therapeutic target for metastatic BCa (Udhaya Kumar et al., 2020; Vena et al., 2020). Xie et al. identified that circular RNA (circRNA) circHIPK3 was an independent prognostic predictor, and up-regulation of circHIPK3 promoted GEM-sensitivity in BCa (Xie et al., 2020). Another study based on BCa cells indicated that inhibition of GP130 could enhance the sensitivity to GEM and reduce viability and migration of tumor cells through regulating the PI3K/AKT/mTOR signaling pathways (Li X. et al., 2019). This study analyzed the GSE77883 dataset from the GEO and TCGA BLCA datasets to identify promising biomarkers for GEM-resistant BCa through high-throughput sequencing data and bioinformatics analyses.

We assessed immune cells and identified that both BCa development and GEM-resistance were immune-related. We found that 82 key DEGs were significantly related to both BCa development and GEM-resistance. Functional enrichment analyses found these key DEGs were enriched in immune-related items, especially in the regulation of immune cell proliferation. After construction of the PPI network and Cox regression analysis, we selected six hub genes (CAV1, COL6A2, FABP4, FBLN1, PCOLCE, and CSPG4) with the highest connectivity degrees and prognostic values for further analyses. We used immunohistochemistry from THPA and expression profiles from larger samples to confirm the down-regulation of six hub genes in BCa at protein and mRNA level, respectively. Survival analyses demonstrated that they were related to OS time. Down-regulation of CSPG4, CAV1, and PCOLCE might be related to elevated chemotherapy sensitivity and thus lower expression levels of them were associated with better OS. IMvigor210 cohort validated that COL6A2, FABP4, and FBLN1 could predict the OS after immunotherapy with atezolizumab. Pearson correlation analysis revealed CAV1, COL6A2, and PCOLCE had strong correlations with immune cells, such as dendritic cells and macrophages. Next, we constructed the key miRNA-gene regulatory network based on four key genes (CAV1, COL6A2, PCOLCE, and CSPG4) and three key miRNAs (hsa-miR-124-3p, hsa-miR-26b-5p, and hsa-miR-192-5p).

CAV1 is the chief component of the caveolae plasma membranes in most human cells and participates in immune response and cancer progression (Shi et al., 2020). CAV1 in prostate cancer could induce epithelial–mesenchymal transition through activating cancer immune evasion, and CAV1 in cancer-derived exosomes was able to induce chemoresistance in recipient cells (Lin et al., 2019), which conformed to our results revealed in GEM-resistant BCa. In addition, CAV1 might also promote systemic lupus erythematosus through regulating pathways of T cell costimulation, lymphocyte costimulation, and B cell receptor signaling (Udhaya Kumar et al., 2020). CAV1 was pivotal in acute immune-mediated hepatic damage through driving RNS-mediated ferroptosis (Deng et al., 2020). The presently found CAV1 was the key gene regulated by three upstream miRNAs in the miRNA-gene regulatory network. Zhou et al. found that hsa-miR-124-3p and hsa-miR-192-5p suppressed the proliferation and invasion of tumor cells by targeting CAV1 (Zhou et al., 2018; Chen et al., 2019). Therefore, we hypothesized that CAV1 could facilitate tumor development and GEM-resistance via immune escape mechanism.

COL6A2 is one of the collagen family members and encodes one alpha chain of type VI collagen identified in most

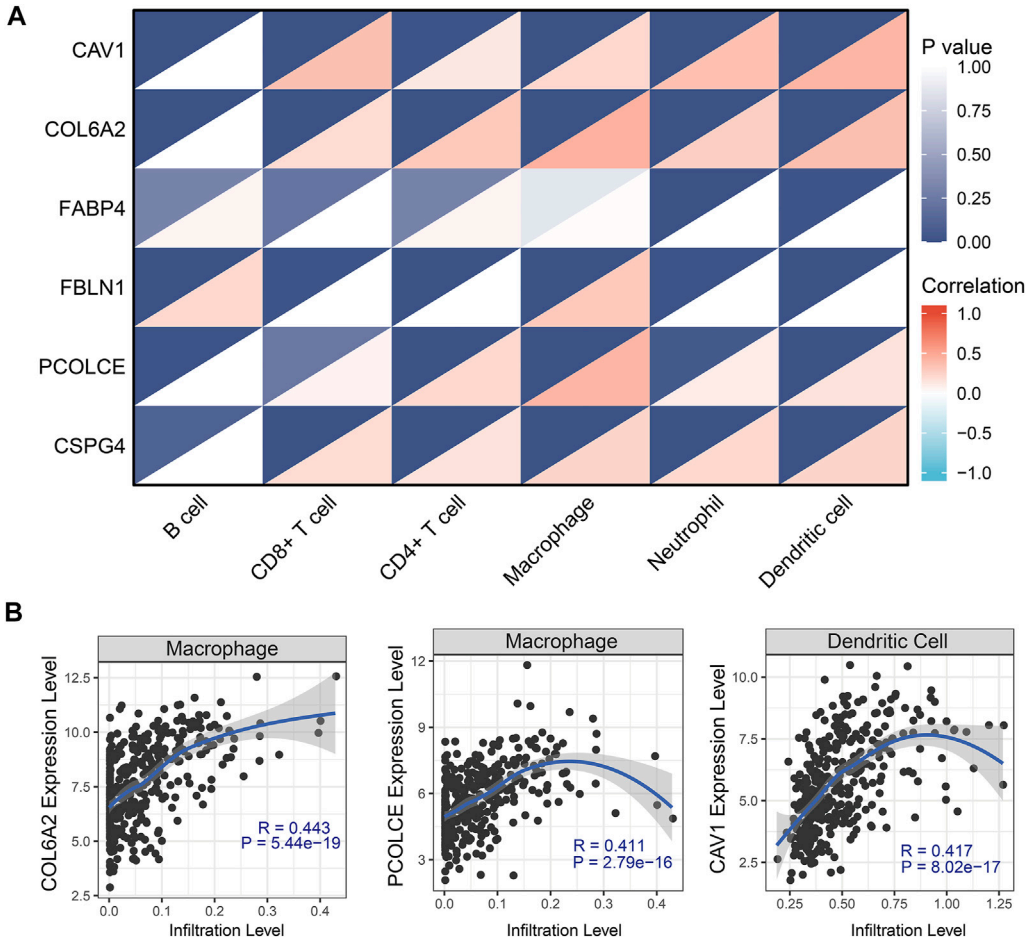

FIGURE 8 | Tumor-infiltrating immune cell analysis with the six hub genes (CAV1, COL6A2, FABP4, FBLN1, PCOLCE, and CSPG4) through Pearson correlation method. **(A)** Heat map showed correlations between immune cells and six hub genes; **(B)** Robust correlations (R-value more than 0.400) was identified between CAV1, COL6A2, and PCOLCE and immune cells.

connective tissues (Hou et al., 2016). COL6A2 was reported to be up-regulated and to gather in the ECM-receptor interaction signaling pathway, which promoted the BCa progression (Zhu et al., 2019). Down-regulation of COL6A2 induced by decreased IDO1 could suppress host anti-tumor immune response through inhibiting immune-related pathways (Xiang et al., 2019). We found COL6A2 was positively correlated with most immune cells in a tumor-immune microenvironment, which could support the highly immunogenic nature of COL6A2 in BCa.

CSPG4 is a kind of transmembrane proteoglycan, considered as a promising tumor-associated antigen (Cavallo et al., 2007). Previous investigations have identified CSPG4 as a key gene in soft-tissue sarcoma, melanoma, and glioblastoma (Benassi et al., 2009; Wang et al., 2011). We found CSPG4 exerted a vital role in BCa prognosis, and both the expression and mutation of CSPG4 might influence the immune cells in BCa. In addition, Rolih et al. systematically summarized the evidence of CSPG4 in tumor biology and suggested that CSPG4 and anti-CSPG4 vaccination strategy had the potential to be an attractive target for anti-tumor immunotherapy (Rolih et al., 2017). GSEA detected that CSPG4 contributed to cancer-related pathways, immune system process, and drug metabolism, which further confirmed its value in drug-resistance and immunotherapy of BCa (Song et al., 2020). Nevertheless, further investigations are demanded to verify its mechanisms in BCa.

PCOLCE is a glycoprotein that elevates the activity of procollagen C-proteinase (Pulido et al., 2018). PCOLCE was up-regulated in osteosarcoma and promotes the distant metastasis (Wang et al., 2019). We found PCOLCE was down-regulated and was also associated with prognosis in BCa. The difference of PCOLCE expression between the two tumors could be explained by the miRNA-gene regulatory network; hsa-miR-26b-5p and hsa-miR-192-5p regulated the co-expression of PCOLCE and CAV1 in the network of BCa. Besides, PCOLCE was revealed to be involved

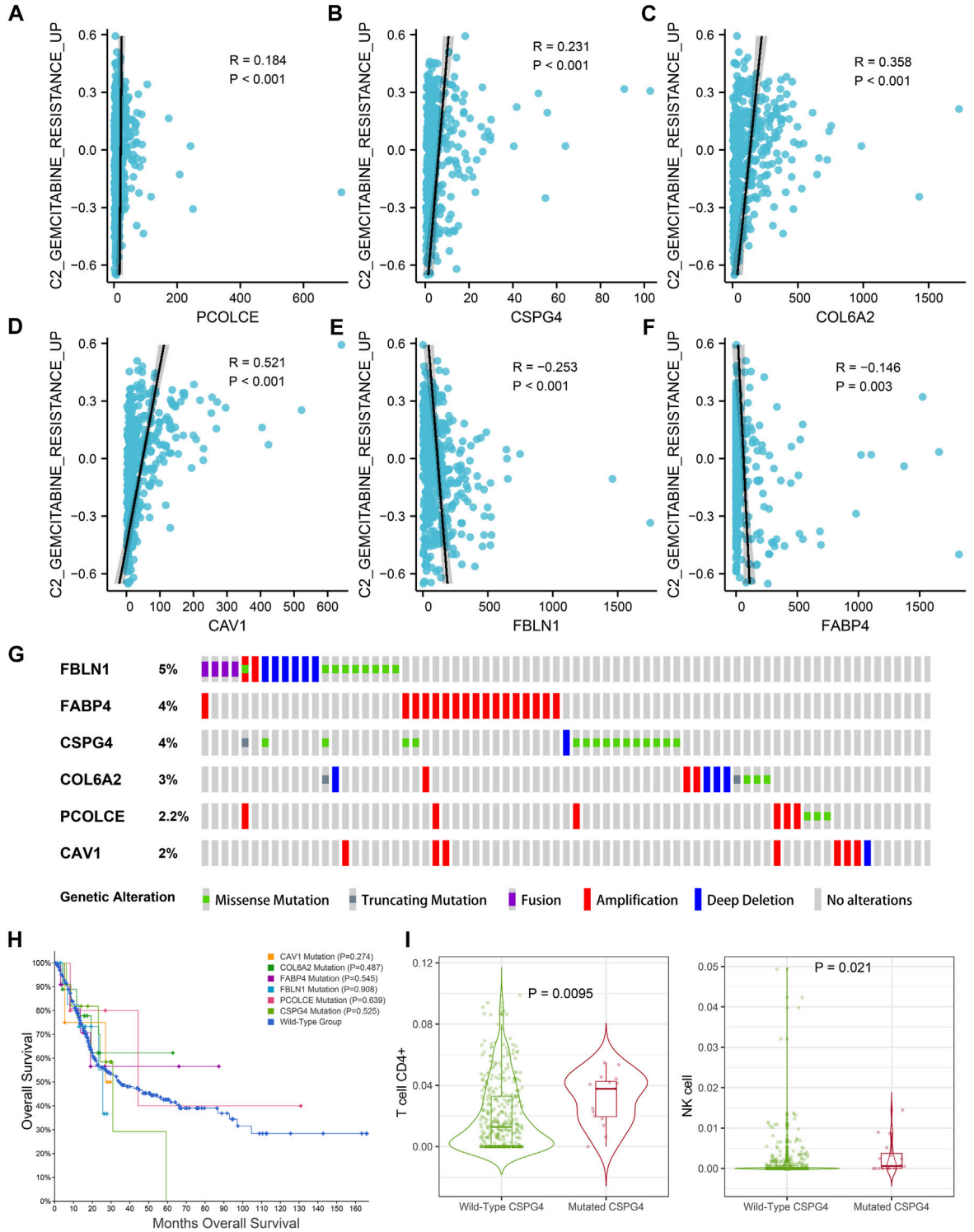

FIGURE 9 | Genetic mutations analysis of the six hub genes (CAV1, COL6A2, FABP4, FBLN1, PCOLCE, and CSPG4) in the TCGA BLCA dataset. **(A–F)** Correlations between GEM-resistance score and the six hub genes; **(G)** Mutation frequencies of CAV1, COL6A2, FABP4, FBLN1, PCOLCE, and CSPG4 in the TCGA BLCA dataset; **(H)** Kaplan–Meier survival curves showed that genetic mutations of six selected genes (CAV1, COL6A2, FABP4, FBLN1, PCOLCE, and CSPG4) were not associated with overall survival (OS) based on the TCGA BLCA dataset; **(I)** CSPG4 mutation was associated with infiltration levels of $CD4^+$ T cells and natural killer (NK) cells.

TABLE 5 | Upstream microRNAs (miRNAs) of the six hub genes (CAV1, COL6A2, FABP4, FBLN1, PCOLCE and CSPG4)

Hub gene	Upstream miRNAs
CAV1	**hsa-miR-124-3p**, **hsa-miR-26b-5p**, **hsa-miR-192-5p**, hsa-miR-34c-5p, hsa-miR-34b-5p, hsa-miR-103a-3p, hsa-miR-7-5p, hsa-miR-199a-5p, hsa-miR-203a-3p, hsa-miR-107, hsa-miR-17-5p, hsa-miR-20a-5p, hsa-miR-93-5p, hsa-miR-106a-5p, hsa-miR-194-5p, hsa-miR-106b-5p, hsa-miR-20b-5p, hsa-miR-526b-3p, hsa-miR-519d-3p, hsa-miR-3609, hsa-miR-548ah-5p, hsa-miR-4796-3p, hsa-miR-3973, hsa-miR-873-5p, hsa-miR-520h, hsa-miR-520g-3p, hsa-miR-4463, hsa-miR-1238-3p, hsa-miR-6749-3p, hsa-miR-6792-3p, hsa-miR-4691-5p, hsa-miR-627-3p, hsa-miR-660-3p, hsa-miR-5193, hsa-miR-670-3p, hsa-miR-4277, hsa-miR-584-3p, hsa-miR-5004-3p, hsa-miR-1261, hsa-miR-4791, hsa-miR-3201, hsa-miR-766-5p, hsa-miR-3140-3p, hsa-miR-4722-5p, hsa-miR-4468, hsa-miR-4673, hsa-miR-4645-5p, hsa-miR-4692, hsa-miR-4514, hsa-miR-4459, hsa-miR-556-5p, hsa-miR-208b-5p, hsa-miR-208a-5p, hsa-miR-6165, hsa-miR-6753-5p, hsa-miR-1911-3p, hsa-miR-338-5p, hsa-miR-4517
COL6A2	**hsa-miR-124-3p**, hsa-miR-10b-5p, hsa-miR-10a-5p, hsa-miR-3928-3p, hsa-miR-29c-3p
PCOLCE	**hsa-miR-192-5p**, **hsa-miR-26b-5p**, hsa-miR-215-5p, hsa-miR-182-5p
FABP4	hsa-miR-138-5p, hsa-miR-369-5p, hsa-miR-335-5p
FBLN1	hsa-miR-30a-3p
CSPG4	**hsa-miR-124-3p**

Bold miRNAs meant key miRNAs regulating ≥2 hub genes.

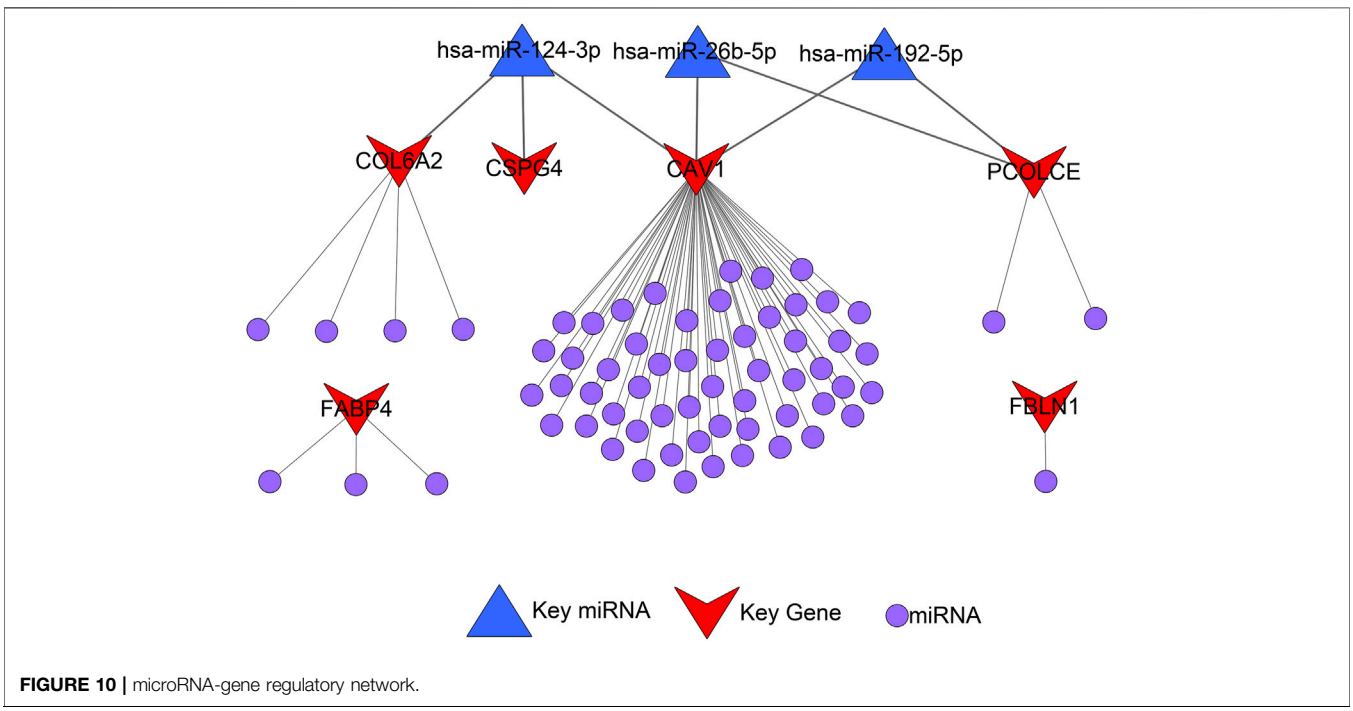

FIGURE 10 | microRNA-gene regulatory network.

in platelet and endothelial function and immune activation in human immunodeficiency virus (HIV) patients after pitavastatin treatment, which bound PCOLCE to immune related functions (DeFilippi et al., 2020).

The identified key miRNA-gene regulatory network indicated that hsa-miR-124-3p, hsa-miR-192-5p, and hsa-miR-26b-5p were key miRNAs in regulating the above genes. It is reported that higher expression level of hsa-miR-124-3p suppressed tumor proliferation and indicated better BCa prognosis in BCa through targeting downstream genes (Wang et al., 2015; Zhou et al., 2018; Zo and Long, 2019). Besides, hsa-miR-124-3p was frequently and tumor-specifically methylated in primary BCa, indicating that epigenetic silencing of hsa-miR-124-3p may also participate in BCa development (Shimizu et al., 2013). *In vitro* studies demonstrated that hsa-miR-192-5p was a suppressor for BCa cells by cell cycle regulation and clinical studies identified hsa-miR-192-5p as an independent prognostic marker based on multivariate COX regression (Jin et al., 2015; Hu et al., 2017). Bioinformatics analysis combined with *in vitro* experiments demonstrated that hsa-miR-26b-5p was a critical regulator in BCa progression by targeting the proliferation-related gene

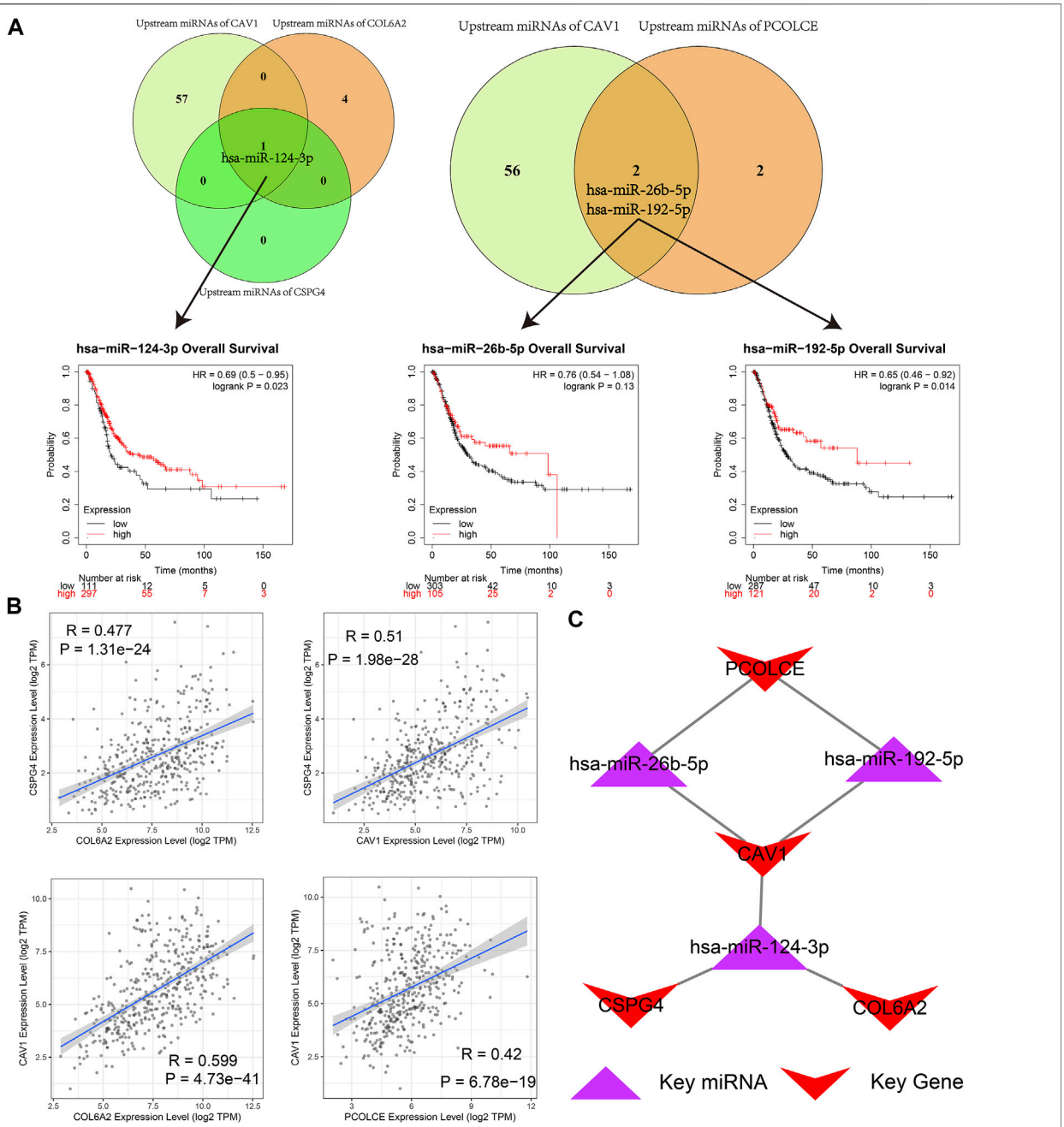

FIGURE 11 | Identification of hub microRNAs (miRNAs) and the key miRNA-gene regulatory network. **(A)** hsa-miR-124-3p, hsa-miR-26b-5p, and hsa-miR-192-5p were overlapped upstream miRNAs of four hub genes (CAV1, COL6A2, PCOLCE, and CSPG4) and their survival analyses; **(B)** Pairwise correlation analyses of four hub genes (CAV1, COL6A2, PCOLCE, and CSPG4); **(C)** Key miRNA-gene regulatory network formed by the three overlapped miRNAs and the four hub genes.

PDCD10 (Wu et al., 2018). With regard to the relationship between the three miRNAs and immune system, there is evidence that they played roles in modulating immune escape and immune cells (Li K. et al., 2019; Ji et al., 2019; Amoruso et al., 2020).

The CMAP database analysis identified the potential drugs with synergism or antagonism to GEM-resistance. We identified that two histone deacetylase inhibitors (HDACIs), trichostatin A and vorinostat, had antagonistic effects on GEM-resistance, indicating that the two drugs

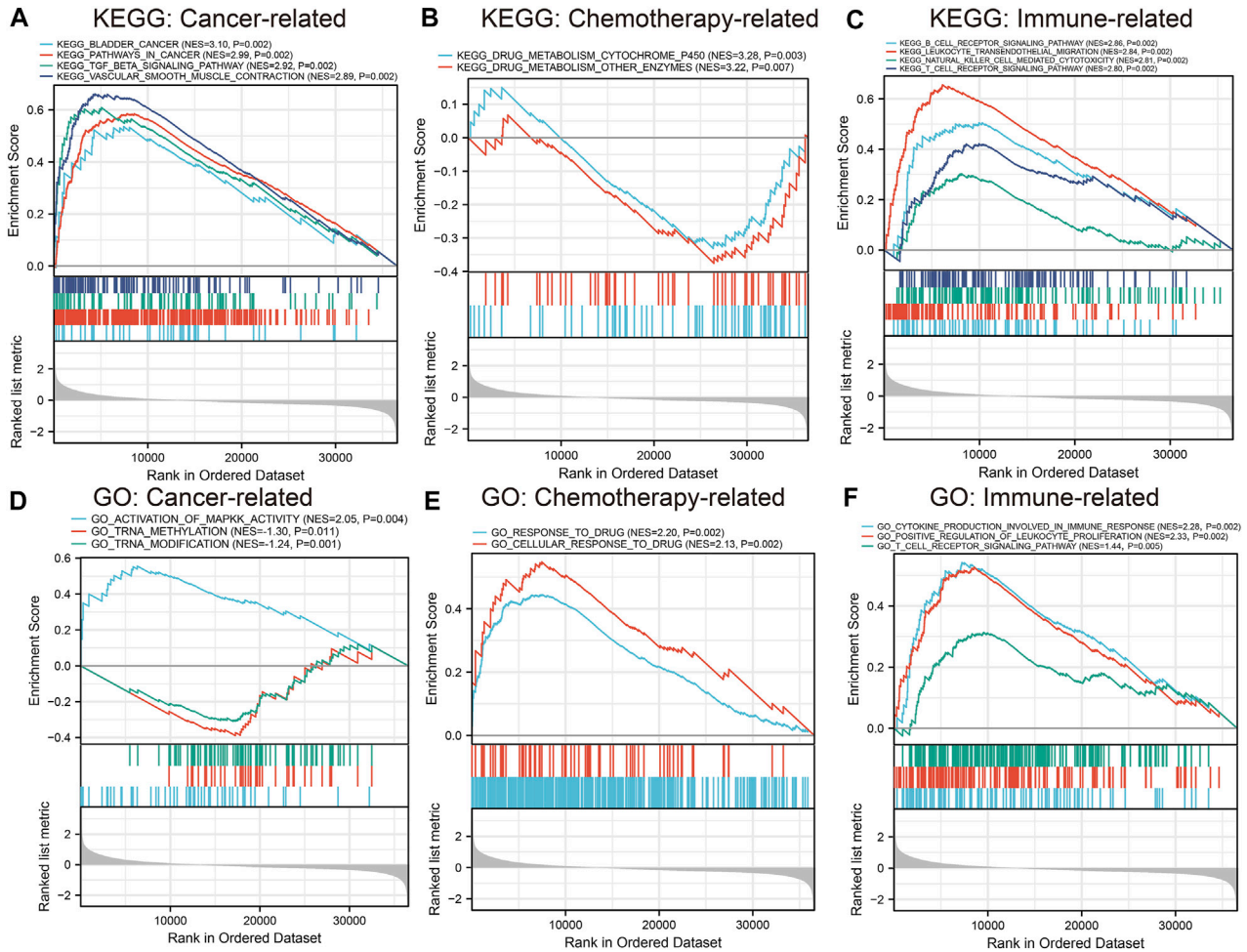

FIGURE 12 | Gene set enrichment analysis of CSPG4. Kyoto Encyclopedia of Genes and Genomes (KEGG) pathway analysis and Gene Ontology (GO) functional analysis identified that CSPG4 was enriched in cancer-related, chemotherapy-related, and immune-related functions. **(A)** Cancer-related KEGG pathway analysis; **(B)** Chemotherapy-related KEGG pathway analysis; **(C)** Immune-related KEGG pathway analysis; **(D)** Cancer-related GO enrichment analysis; **(E)** Chemotherapy-related GO enrichment analysis; **(F)** Immune-related GO enrichment analysis.

might circumvent the GEM-resistance and enhance the sensitivity to GEM. *In vivo* studies based on BCa cells revealed that trichostatin A may synergistically enhance GEM-mediated cell cycle arrest and apoptosis through inhibiting the Raf/MEK/ERK pathway (Jeon et al., 2011; Lin et al., 2018), which provided HDACIs as promising treatment methods to improve GEM-resistant BCa patients in future clinical practice. It is also worth noticing that oxybuprocaine and benzocaine had the synergistic effects to GEM-resistance and the two anesthetics might aggravate GEM-resistance in BCa. Furthermore, ascorbic acid, also called vitamin C, was identified to be associated with aggravate GEM-resistance. However, a phase I clinical trial based on pancreatic cancer patients indicated that ascorbic acid combined concurrently with GEM was well tolerated and could reduce adverse events, which is inconsistent with our results (Welsh et al., 2013).

In order to reduce the potential bias caused by one single method and to verify the relationship between key biomarkers in GEM-resistant BCa and tumor immune microenvironment, the present study used two methods including MCPcounter (Becht et al., 2016) and TIMER (Li et al., 2016; Li et al., 2017) for the calculating of the immune cells. By using these two methods separately, the results indicated that GEM-resistance and the key genes were closely related to immune cells, which further verified that the results were stable and convincing. However, several limitations existed. Even if immunohistochemistry was used to confirm the down-regulation of hub genes, and cell lines instead of *in vivo* models were used to perform CMAP analysis, we didn't verify their actual molecular mechanisms. Therefore, the above hypotheses should be verified through experimental methods in future studies. Since most BCa tissues from the TCGA BLCA dataset were MIBC tissues, our findings were more applicable to GEM-resistant MIBC patients.

TABLE 6 | Connectivity map (CMAP) database analysis

Type	Rank	CMAP name	Enrichment	p-Value
Antagonistic drugs	1	Lisinopril	−0.898	0.002
	2	Rifabutin	−0.882	0.003
	3	Clonidine	−0.819	0.002
	4	Prasterone	−0.787	0.004
	5	Vorinostat	−0.752	<0.001
	6	Prednisone	−0.685	0.007
	7	Nifenazone	−0.675	0.008
	8	Alvespimycin	−0.532	0.001
	9	Trichostatin A	−0.460	<0.001
	10	Tanespimycin	−0.421	<0.001
Synergistic drugs	1	Oxybuprocaine	0.874	<0.001
	2	Ascorbic acid	0.870	<0.001
	3	Disopyramide	0.790	0.004
	4	Benzocaine	0.788	0.004
	5	Eticlopride	0.782	0.004
	6	Sisomicin	0.770	0.005
	7	Viomycin	0.748	0.008
	8	Midodrine	0.726	0.004
	9	6-Bromoindirubin-3′-oxime	0.677	0.001
	10	Fludrocortisone	0.541	0.010

CONCLUSION

We identified both BCa development and GEM-resistance were immune-related. CAV1, COL6A2, FABP4, FBLN1, PCOLCE, and CSPG4 are hub genes in GEM-resistant MIBC. They could serve as potential prognostic predictors and immunotherapy targets for MIBC. In addition, the key miRNA-gene regulatory network suggested three key miRNAs (hsa-miR-124-3p, hsa-miR-26b-5p, and hsa-miR-192-5p) might also be implicated in GEM-resistance. Ultimately, CMAP analysis identified HDACIs (trichostatin A and vorinostat) might circumvent the GEM-resistance and enhance the sensitivity to GEM.

DATA AVAILABILITY STATEMENT

The datasets presented in this study can be found in online repositories. The names of the repository/repositories and accession number(s) can be found in the article/ **Supplementary Material**.

AUTHOR CONTRIBUTIONS

YS, TX, YD, CQ, and HL: conception and design. YS, WY, and YD: collection and analysis of data. YS, TX, JL, MD, and JH: interpretation and manuscript writing.

FUNDING

This work was supported by National Key Research and Development Program of China (2018YFA0902802), Natural Science Foundation of Beijing, China (7202219), National Natural Science Foundation of China (81802533), and Beijing Municipal Science and Technology Commission (Z191100006619010).

SUPPLEMENTARY MATERIAL

The Supplementary Material for this article can be found online at: https://www.frontiersin.org/articles/10.3389/fcell.2021.809620/full#supplementary-material

REFERENCES

Agarwal, V., Bell, G. W., Nam, J.-W., and Bartel, D. P. (2015). Predicting Effective microRNA Target Sites in Mammalian mRNAs. *Elife* 4, e05005. doi:10.7554/eLife.05005

Amoruso, A., Blonda, M., Gironi, M., Grasso, R., Di Francescantonio, V., Scaroni, F., et al. (2020). Immune and central Nervous System-Related miRNAs Expression Profiling in Monocytes of Multiple Sclerosis Patients. *Sci. Rep.* 10 (1), 6125. doi:10.1038/s41598-020-63282-3

Antoni, S., Ferlay, J., Soerjomataram, I., Znaor, A., Jemal, A., and Bray, F. (2017). Bladder Cancer Incidence and Mortality: A Global Overview and Recent Trends. *Eur. Urol.* 71 (1), 96–108. doi:10.1016/j.eururo.2016.06.010

Becht, E., Giraldo, N. A., Lacroix, L., Buttard, B., Elarouci, N., Petitprez, F., et al. (2016). Estimating the Population Abundance of Tissue-Infiltrating Immune and Stromal Cell Populations Using Gene Expression. *Genome Biol.* 17 (1), 218. doi:10.1186/s13059-016-1070-5

Benassi, M. S., Pazzaglia, L., Chiechi, A., Alberghini, M., Conti, A., Cattaruzza, S., et al. (2009). NG2 Expression Predicts the Metastasis Formation in Soft-Tissue Sarcoma Patients. *J. Orthop. Res.* 27 (1), 135–140. doi:10.1002/jor.20694

Benjamini, Y., and Hochberg, Y. (1995). Controlling the False Discovery Rate: A Practical and Powerful Approach to Multiple Testing. *J. R. Stat. Soc. Ser. B (Methodological)* 57 (1), 289–300. doi:10.1111/j.2517-6161.1995.tb02031.x

Benjamini, Y., and Hochberg, Y. (2000). On the Adaptive Control of the False Discovery Rate in Multiple Testing with Independent Statistics. *J. Educ. Behav. Stat.* 25 (1), 60–83. doi:10.3102/10769986025001060

Bergman, A. M., Pinedo, H. M., and Peters, G. J. (2002). Determinants of Resistance to 2′,2′-difluorodeoxycytidine (Gemcitabine). *Drug Resist. Updates* 5 (1), 19–33. doi:10.1016/s1368-7646(02)00002-x

Bray, F., Ferlay, J., Soerjomataram, I., Siegel, R. L., Torre, L. A., and Jemal, A. (2018). Global Cancer Statistics 2018: GLOBOCAN Estimates of Incidence and Mortality Worldwide for 36 Cancers in 185 Countries. *CA: A Cancer J. Clinicians* 68 (6), 394–424. doi:10.3322/caac.21492

Cao, J., Wang, Q., Wu, G., Li, S., and Wang, Q. (2018). miR-129-5p Inhibits Gemcitabine Resistance and Promotes Cell Apoptosis of Bladder Cancer Cells by Targeting Wnt5a. *Int. Urol. Nephrol.* 50 (10), 1811–1819. doi:10.1007/s11255-018-1959-x

Cavallo, F., Calogero, R. A., and Forni, G. (2007). Are Oncoantigens Suitable Targets for Anti-tumour Therapy? *Nat. Rev. Cancer* 7 (9), 707–713. doi:10.1038/nrc2208

Chen, C., Li, A., Sun, P., Xu, J., Du, W., Zhang, J., et al. (2020). Efficiently Restoring the Tumoricidal Immunity against Resistant Malignancies via an Immune Nanomodulator. *J. Controlled Release* 324, 574–585. doi:10.1016/j.jconrel.2020.05.039

Chen, P., Feng, Y., Zhang, H., Shi, X., Li, B., Ju, W., et al. (2019). MicroRNA-192 I-nhibits C-ell P-roliferation and I-nduces A-poptosis in H-uman B-reast C-ancer by T-argeting C-aveolin 1. *Oncol. Rep.* 42 (5), 1667–1676. doi:10.3892/or.2019.7298

Chou, C.-H., Shrestha, S., Yang, C.-D., Chang, N.-W., Lin, Y.-L., Liao, K.-W., et al. (2018). miRTarBase Update 2018: a Resource for Experimentally Validated microRNA-Target Interactions. *Nucleic Acids Res.* 46 (D1), D296–D302. doi:10.1093/nar/gkx1067

Choueiri, T. K., and Raghavan, D. (2008). Chemotherapy for Muscle-Invasive Bladder Cancer Treated with Definitive Radiotherapy: Persisting Uncertainties. *Nat. Rev. Clin. Oncol.* 5 (8), 444–454. doi:10.1038/ncponc1159

Coen, J. J., Zhang, P., Saylor, P. J., Lee, C. T., Wu, C.-L., Parker, W., et al. (2019). Bladder Preservation with Twice-A-Day Radiation Plus Fluorouracil/Cisplatin or once Daily Radiation Plus Gemcitabine for Muscle-Invasive Bladder Cancer: NRG/RTOG 0712-A Randomized Phase II Trial. *Jco* 37 (1), 44–51. doi:10.1200/JCO.18.00537

DeFilippi, C., Toribio, M., Wong, L. P., Sadreyev, R., Grundberg, I., Fitch, K. V., et al. (2020). Differential Plasma Protein Regulation and Statin Effects in Human Immunodeficiency Virus (HIV)-Infected and Non-HIV-infected Patients Utilizing a Proteomics Approach. *J. Infect. Dis.* 222 (6), 929–939. doi:10.1093/infdis/jiaa196

Deng, G., Li, Y., Ma, S., Gao, Z., Zeng, T., Chen, L., et al. (2020). Caveolin-1 Dictates Ferroptosis in the Execution of Acute Immune-Mediated Hepatic Damage by Attenuating Nitrogen Stress. *Free Radic. Biol. Med.* 148, 151–161. doi:10.1016/j.freeradbiomed.2019.12.026

Ebrahimi, H., Amini, E., Pishgar, F., Moghaddam, S. S., Nabavizadeh, B., Rostamabadi, Y., et al. (2019). Global, Regional and National Burden of Bladder Cancer, 1990 to 2016: Results from the GBD Study 2016. *J. Urol.* 201 (5), 893–901. doi:10.1097/JU.0000000000000025

Giannopoulou, A., Velentzas, A., Konstantakou, E., Avgeris, M., Katarachia, S., Papandreou, N., et al. (2019). Revisiting Histone Deacetylases in Human Tumorigenesis: The Paradigm of Urothelial Bladder Cancer. *Ijms* 20 (6), 1291. doi:10.3390/ijms20061291

Goebell, P. J., Legal, W., Weiss, C., Fietkau, R., Wullich, B., and Krause, S. (2008). Multimodale Therapien zum Blasenerhalt bei High-grade-Blasentumoren. *Urologe* 47 (7), 838–845. doi:10.1007/s00120-008-1715-4

Gu, J., Zhang, J., Huang, W., Tao, T., Huang, Y., Yang, L., et al. (2020). Activating miRNA-mRNA Network in Gemcitabine-Resistant Pancreatic Cancer Cell Associates with Alteration of Memory CD4+ T Cells. *Ann. Transl Med.* 8 (6), 279. doi:10.21037/atm.2020.03.53

Hänzelmann, S., Castelo, R., and Guinney, J. (2013). GSVA: Gene Set Variation Analysis for Microarray and RNA-Seq Data. *BMC bioinformatics* 14, 7. doi:10.1186/1471-2105-14-7

Hou, T., Tong, C., Kazobinka, G., Zhang, W., Huang, X., Huang, Y., et al. (2016). Expression of COL6A1 Predicts Prognosis in Cervical Cancer Patients. *Am. J. Transl Res.* 8 (6), 2838–2844.

Hu, Y., Cheng, C., Hong, Z., and Shi, Z. (2017). Independent Prognostic miRNAs for Bladder Urothelial Carcinoma. *Oncol. Lett.* 14 (3), 3001–3005. doi:10.3892/ol.2017.6471

Humphrey, P. A., Moch, H., Cubilla, A. L., Ulbright, T. M., and Reuter, V. E. (2016). The 2016 WHO Classification of Tumours of the Urinary System and Male Genital Organs-Part B: Prostate and Bladder Tumours. *Eur. Urol.* 70 (1), 106–119. doi:10.1016/j.eururo.2016.02.028

Jeon, H. G., Yoon, C. Y., Yu, J. H., Park, M. J., Lee, J. E., Jeong, S. J., et al. (2011). Induction of Caspase Mediated Apoptosis and Down-Regulation of Nuclear Factor-Kb and Akt Signaling Are Involved in the Synergistic Antitumor Effect of Gemcitabine and the Histone Deacetylase Inhibitor Trichostatin A in Human Bladder Cancer Cells. *J. Urol.* 186 (5), 2084–2093. doi:10.1016/j.juro.2011.06.053

Ji, C., Guo, X., Ren, J., Zu, Y., Li, W., and Zhang, Q. (2019). Transcriptomic Analysis of microRNAs-mRNAs Regulating Innate Immune Response of Zebrafish Larvae against Vibrio Parahaemolyticus Infection. *Fish Shellfish Immunol.* 91, 333–342. doi:10.1016/j.fsi.2019.05.050

Jin, Y., Lu, J., Wen, J., Shen, Y., and Wen, X. (2015). Regulation of Growth of Human Bladder Cancer by miR-192. *Tumor Biol.* 36 (5), 3791–3797. doi:10.1007/s13277-014-3020-8

Kaufman, D. S., Shipley, W. U., and Feldman, A. S. (2009). Bladder Cancer. *The Lancet* 374 (9685), 239–249. doi:10.1016/S0140-6736(09)60491-8

Kirkali, Z., Chan, T., Manoharan, M., Algaba, F., Busch, C., Cheng, L., et al. (2005). Bladder Cancer: Epidemiology, Staging and Grading, and Diagnosis. *Urology* 66 (6), 4–34. doi:10.1016/j.urology.2005.07.062

Lamb, J., Crawford, E. D., Peck, D., Modell, J. W., Blat, I. C., Wrobel, M. J., et al. (2006). The Connectivity Map: Using Gene-Expression Signatures to Connect Small Molecules, Genes, and Disease. *Science* 313 (5795), 1929–1935. doi:10.1126/science.1132939

Lamb, J. (2007). The Connectivity Map: a New Tool for Biomedical Research. *Nat. Rev. Cancer* 7 (1), 54–60. doi:10.1038/nrc2044

Li, B., Severson, E., Pignon, J.-C., Zhao, H., Li, T., Novak, J., et al. (2016). Comprehensive Analyses of Tumor Immunity: Implications for Cancer Immunotherapy. *Genome Biol.* 17 (1), 174. doi:10.1186/s13059-016-1028-7

Li, K., Chen, Y., Li, A., Tan, C., and Liu, X. (2019a). Exosomes Play Roles in Sequential Processes of Tumor Metastasis. *Int. J. Cancer* 144 (7), 1486–1495. doi:10.1002/ijc.31774

Li, T., Fan, J., Wang, B., Traugh, N., Chen, Q., Liu, J. S., et al. (2017). TIMER: A Web Server for Comprehensive Analysis of Tumor-Infiltrating Immune Cells. *Cancer Res.* 77 (21), e108–e110. doi:10.1158/0008-5472.CAN-17-0307

Li, X., He, S., Tian, Y., Weiss, R. M., and Martin, D. T. (2019b). Synergistic Inhibition of GP130 and ERK Signaling Blocks Chemoresistant Bladder Cancer Cell Growth. *Cell Signal.* 63, 109381. doi:10.1016/j.cellsig.2019.109381

Liberzon, A., Birger, C., Thorvaldsdóttir, H., Ghandi, M., Mesirov, J. P., and Tamayo, P. (2015). The Molecular Signatures Database Hallmark Gene Set Collection. *Cell Syst.* 1 (6), 417–425. doi:10.1016/j.cels.2015.12.004

Lightfoot, A. J., Breyer, B. N., Rosevear, H. M., Erickson, B. A., Konety, B. R., and O'Donnell, M. A. (2014). Multi-institutional Analysis of Sequential Intravesical Gemcitabine and Mitomycin C Chemotherapy for Non-muscle Invasive Bladder Cancer. *Urol. Oncol. Semin. Original Invest.* 32 (1), e15–35. doi:10.1016/j.urolonc.2013.01.009

Lin, A., Wei, T., Liang, J., Qi, C., Li, M., Luo, P., et al. (2021). CAMOIP: A Web Server for Comprehensive Analysis on Multi-Omics of Immunotherapy in Pan-Cancer. *bioRxiv*. doi:10.1101/2021.09.10.459722

Lin, C.-J., Yun, E.-J., Lo, U.-G., Tai, Y.-L., Deng, S., Hernandez, E., et al. (2019). The Paracrine Induction of Prostate Cancer Progression by Caveolin-1. *Cell Death Dis* 10 (11), 834. doi:10.1038/s41419-019-2066-3

Lin, W.-C., Hsu, F.-S., Kuo, K.-L., Liu, S.-H., Shun, C.-T., Shi, C.-S., et al. (2018). Trichostatin A, a Histone Deacetylase Inhibitor, Induces Synergistic Cytotoxicity with Chemotherapy via Suppression of Raf/MEK/ERK Pathway in Urothelial Carcinoma. *J. Mol. Med.* 96 (12), 1307–1318. doi:10.1007/s00109-018-1697-7

Mariathasan, S., Turley, S. J., Nickles, D., Castiglioni, A., Yuen, K., Wang, Y., et al. (2018). TGFβ Attenuates Tumour Response to PD-L1 Blockade by Contributing to Exclusion of T Cells. *Nature* 554 (7693), 544–548. doi:10.1038/nature25501

Nagy, Á., Lánczky, A., Menyhárt, O., and Győrffy, B. (2018). Validation of miRNA Prognostic Power in Hepatocellular Carcinoma Using Expression Data of Independent Datasets. *Sci. Rep.* 8 (1), 9227. doi:10.1038/s41598-018-27521-y

Oh, K. S., Soto, D. E., Smith, D. C., Montie, J. E., Lee, C. T., and Sandler, H. M. (2009). Combined-Modality Therapy with Gemcitabine and Radiation Therapy as a Bladder Preservation Strategy: Long-Term Results of a Phase I Trial. *Int.*

*J. Radiat. Oncology*Biology*Physics* 74 (2), 511–517. doi:10.1016/j.ijrobp.2008.08.021

Pulido, D., Sharma, U., Vadon-Le Goff, S., Hussain, S.-A., Cordes, S., Mariano, N., et al. (2018). Structural Basis for the Acceleration of Procollagen Processing by Procollagen C-Proteinase Enhancer-1. *Structure* 26 (10), 1384–1392. doi:10.1016/j.str.2018.06.011

Ritchie, M. E., Phipson, B., Wu, D., Hu, Y., Law, C. W., Shi, W., et al. (2015). Limma powers Differential Expression Analyses for RNA-Sequencing and Microarray Studies. *Nucleic Acids Res.* 43 (7), e47. doi:10.1093/nar/gkv007

Rolih, V., Barutello, G., Iussich, S., De Maria, R., Quaglino, E., Buracco, P., et al. (2017). CSPG4: a Prototype Oncoantigen for Translational Immunotherapy Studies. *J. Transl Med.* 15 (1), 151. doi:10.1186/s12967-017-1250-4

Shi, Y.-B., Li, J., Lai, X.-N., Jiang, R., Zhao, R.-C., and Xiong, L.-X. (2020). Multifaceted Roles of Caveolin-1 in Lung Cancer: A New Investigation Focused on Tumor Occurrence, Development and Therapy. *Cancers* 12 (2), 291. doi:10.3390/cancers12020291

Shimizu, T., Suzuki, H., Nojima, M., Kitamura, H., Yamamoto, E., Maruyama, R., et al. (2013). Methylation of a Panel of MicroRNA Genes Is a Novel Biomarker for Detection of Bladder Cancer. *Eur. Urol.* 63 (6), 1091–1100. doi:10.1016/j.eururo.2012.11.030

Song, Y., Jin, D., Chen, J., Liang, W., and Liu, X. (2020). Effects of Arsenic (+3 Oxidation State) Methyltransferase Gene Polymorphisms and Expression on Bladder Cancer: Evidence from a Systematic Review, Meta-Analysis and TCGA Dataset. *Toxicol. Sci.* 177 (1), 27–40. doi:10.1093/toxsci/kfaa087

Sternberg, C. N., Bellmunt, J., Sonpavde, G., Siefker-Radtke, A. O., Stadler, W. M., Bajorin, D. F., et al. (2013). ICUD-EAU International Consultation on Bladder Cancer 2012: Chemotherapy for Urothelial Carcinoma-Neoadjuvant and Adjuvant Settings. *Eur. Urol.* 63 (1), 58–66. doi:10.1016/j.eururo.2012.08.010

Subramanian, A., Kuehn, H., Gould, J., Tamayo, P., and Mesirov, J. P. (2007). GSEA-P: a Desktop Application for Gene Set Enrichment Analysis. *Bioinformatics* 23 (23), 3251–3253. doi:10.1093/bioinformatics/btm369

Szklarczyk, D., Morris, J. H., Cook, H., Kuhn, M., Wyder, S., Simonovic, M., et al. (2017). The STRING Database in 2017: Quality-Controlled Protein-Protein Association Networks, Made Broadly Accessible. *Nucleic Acids Res.* 45 (D1), D362–D368. doi:10.1093/nar/gkw937

Tang, Z., Li, C., Zhang, K., Yang, M., and Hu, X. (2017). GE-mini: a mobile APP for Large-Scale Gene Expression Visualization. *Bioinformatics* w775, btw775. doi:10.1093/bioinformatics/btw775

Tooker, P., Yen, W.-C., Ng, S.-C., Negro-Vilar, A., and Hermann, T. W. (2007). Bexarotene (LGD1069, Targretin), a Selective Retinoid X Receptor Agonist, Prevents and Reverses Gemcitabine Resistance in NSCLC Cells by Modulating Gene Amplification. *Cancer Res.* 67 (9), 4425–4433. doi:10.1158/0008-5472.can-06-4495

Udhaya Kumar, S., Thirumal Kumar, D., Siva, R., George Priya Doss, C., Younes, S., Younes, N., et al. (2020). Dysregulation of Signaling Pathways Due to Differentially Expressed Genes from the B-Cell Transcriptomes of Systemic Lupus Erythematosus Patients - A Bioinformatics Approach. *Front. Bioeng. Biotechnol.* 8, 276. doi:10.3389/fbioe.2020.00276

Uhlen, M., Oksvold, P., Fagerberg, L., Lundberg, E., Jonasson, K., Forsberg, M., et al. (2010). Towards a Knowledge-Based Human Protein Atlas. *Nat. Biotechnol.* 28 (12), 1248–1250. doi:10.1038/nbt1210-1248

Vena, F., Bayle, S., Nieto, A., Quereda, V., Aceti, M., Frydman, S. M., et al. (2020). Targeting Casein Kinase 1 Delta Sensitizes Pancreatic and Bladder Cancer Cells to Gemcitabine Treatment by Upregulating Deoxycytidine Kinase. *Mol. Cancer Ther.* 19 (8), 1623–1635. doi:10.1158/1535-7163.MCT-19-0997

Wang, D., and Lippard, S. J. (2005). Cellular Processing of Platinum Anticancer Drugs. *Nat. Rev. Drug Discov.* 4 (4), 307–320. doi:10.1038/nrd1691

Wang, J., Svendsen, A., Kmiecik, J., Immervoll, H., Skaftnesmo, K. O., Planagumà, J., et al. (2011). Targeting the NG2/CSPG4 Proteoglycan Retards Tumour Growth and Angiogenesis in Preclinical Models of GBM and Melanoma. *PLoS ONE* 6 (7), e23062. doi:10.1371/journal.pone.0023062

Wang, S., Zhong, L., Li, Y., Xiao, D., Zhang, R., Liao, D., et al. (2019). Up-regulation of PCOLCE by TWIST1 Promotes Metastasis in Osteosarcoma. *Theranostics* 9 (15), 4342–4353. doi:10.7150/thno.34090

Wang, X., Wu, Q., Xu, B., Wang, P., Fan, W., Cai, Y., et al. (2015). miR-124 Exerts Tumor Suppressive Functions on the Cell Proliferation, Motility and Angiogenesis of Bladder Cancer by fine-tuning UHRF1. *Febs J.* 282 (22), 4376–4388. doi:10.1111/febs.13502

Welsh, J. L., Wagner, B. A., van't Erve, T. J., Zehr, P. S., Berg, D. J., Halfdanarson, T. R., et al. (2013). Pharmacological Ascorbate with Gemcitabine for the Control of Metastatic and Node-Positive Pancreatic Cancer (PACMAN): Results from a Phase I Clinical Trial. *Cancer Chemother. Pharmacol.* 71 (3), 765–775. doi:10.1007/s00280-013-2070-8

Wu, K., Mu, X. Y., Jiang, J. T., Tan, M. Y., Wang, R. J., Zhou, W. J., et al. (2018). miRNA-26a-5p and miR-26b-5p I-nhibit the P-roliferation of B-ladder C-ancer C-ells by R-egulating PDCD10. *Oncol. Rep.* 40 (6), 3523–3532. doi:10.3892/or.2018.6734

Xiang, Z., Li, J., Song, S., Wang, J., Cai, W., Hu, W., et al. (2019). A Positive Feedback between Ido1 Metabolite and COL12A1 via MAPK Pathway to Promote Gastric Cancer Metastasis. *J. Exp. Clin. Cancer Res.* 38 (1), 314. doi:10.1186/s13046-019-1318-5

Xie, F., Zhao, N., Zhang, H., and Xie, D. (2020). Circular RNA CircHIPK3 Promotes Gemcitabine Sensitivity in Bladder Cancer. *J. Cancer* 11 (7), 1907–1912. doi:10.7150/jca.39722

Yang, Y., Cheng, Z., Jia, X., Shi, N., Xia, Z., Zhang, W., et al. (2019). Mortality Trends of Bladder Cancer in China from 1991 to 2015: an Age-Period-Cohort Analysis. *Cmar* 11, 3043–3051. doi:10.2147/CMAR.S189220

Yu, G., Wang, L.-G., Han, Y., and He, Q.-Y. (2012). clusterProfiler: an R Package for Comparing Biological Themes Among Gene Clusters. *OMICS: A J. Integr. Biol.* 16 (5), 284–287. doi:10.1089/omi.2011.0118

Yu, W. D., Wang, H., He, Q. F., Xu, Y., and Wang, X. C. (2018). Long Noncoding RNAs in Cancer-immunity Cycle. *J. Cell Physiol* 233 (9), 6518–6523. doi:10.1002/jcp.26568

Zhou, W., He, L., Dai, Y., Zhang, Y., Wang, J., and Liu, B. (2018). MicroRNA-124 I-nhibits C-ell P-roliferation, I-nvasion and M-igration by T-argeting CAV1 in B-ladder C-ancer. *Exp. Ther. Med.* 16 (4), 2811–2820. doi:10.3892/etm.2018.6537

Zhou, Y., Zhou, B., Pache, L., Chang, M., Khodabakhshi, A. H., Tanaseichuk, O., et al. (2019). Metascape Provides a Biologist-Oriented Resource for the Analysis of Systems-Level Datasets. *Nat. Commun.* 10 (1), 1523. doi:10.1038/s41467-019-09234-6

Zhu, H., Chen, H., Wang, J., Zhou, L., and Liu, S. (2019). Collagen Stiffness Promoted Non-muscle-invasive Bladder Cancer Progression to Muscle-Invasive Bladder Cancer. *Ott* 12, 3441–3457. doi:10.2147/OTT.S194568

Zo, R. B., and Long, Z. (2019). MiR-124-3p Suppresses Bladder Cancer by Targeting DNA Methyltransferase 3B. *J. Cell Physiol* 234 (1), 464–474. doi:10.1002/jcp.26591

Conflict of Interest: The authors declare that the research was conducted in the absence of any commercial or financial relationships that could be construed as a potential conflict of interest.

Publisher's Note: All claims expressed in this article are solely those of the authors and do not necessarily represent those of their affiliated organizations, or those of the publisher, the editors and the reviewers. Any product that may be evaluated in this article, or claim that may be made by its manufacturer, is not guaranteed or endorsed by the publisher.

frontiers in Cell and Developmental Biology

ORIGINAL RESEARCH
published: 31 January 2022
doi: 10.3389/fcell.2021.813420

Novel Non-Invasive Diagnosis of Bladder Cancer in Urine Based on Multifunctional Nanoparticles

Jinshan Xu[1†], Shuxiong Zeng[1†], Jun Li[2†], Li Gao[3], Wenjun Le[2], Xin Huang[2], Guandan Wang[4], Bingdi Chen[2], Zhensheng Zhang[1]* and Chuanliang Xu[1]**

[1]Department of Urology, Changhai Hospital, Naval Medical University, Shanghai, China, [2]Institute for Regenerative Medicine, Shanghai East Hospital, The Institute for Biomedical Engineering & Nano Science, Tongji University School of Medicine, Shanghai, China, [3]Department of Pathology, Changhai Hospital, Naval Medical University, Shanghai, China, [4]Department of Nutrition, Changhai Hospital, Naval Medical University, Shanghai, China

OPEN ACCESS

Edited by:
Yu Xiao,
Zhongnan Hospital, Wuhan University, China

Reviewed by:
Tianxin Lin,
Sun Yat-sen Memorial Hospital, China
Song Wu,
Shenzhen University, China
Hui Gan,
Guangzhou Medical University, China
Wan Jin,
Euler Technology, China

***Correspondence:**
Bingdi Chen
inanochen@tongji.edu.cn
Zhensheng Zhang
13761178177@163.com
Chuanliang Xu
chuanliang_xu@126.com

†These authors have contributed equally to this work and share first authorship

Specialty section:
This article was submitted to Molecular and Cellular Pathology, a section of the journal Frontiers in Cell and Developmental Biology

Received: 11 November 2021
Accepted: 27 December 2021
Published: 31 January 2022

Citation:
Xu J, Zeng S, Li J, Gao L, Le W, Huang X, Wang G, Chen B, Zhang Z and Xu C (2022) Novel Non-Invasive Diagnosis of Bladder Cancer in Urine Based on Multifunctional Nanoparticles. Front. Cell Dev. Biol. 9:813420. doi: 10.3389/fcell.2021.813420

Objectives: Tumor cells were reported to have perpetual negative surface charges due to elevated glycolysis, and multifunctional nanoprobes (Fe_3O_4@SiO_2, mNPs) could attach onto tumor cells *via* opposite surface charges. We thus evaluated whether mixing mNPs with urine could improve the sensitivity of urine cytology test (UCT).

Methods: We developed a novel UCT method by mixing urine with mNPs (Nano-cytology) to harvest more tumor cells during UCT procedures. The same voided urine sample was divided equally for the Nano-cytology and UCT assay, and evaluated by cytopathologists in a blinded way. The accuracy of UCT, Nano-cytology, and the combination of the two approaches (Nano-UCT) for detecting bladder cancer were determined.

Results: Urine samples were prospectively collected from 102 bladder cancer patients and 49 non-cancer participants from June 2020 to February 2021 in Changhai Hospital. Overall sensitivity of the Nano-cytology assay was significantly higher than that of the UCT assay (82.4 vs. 59.8%, $p < .01$). Sensitivity for low- and high-grade tumors was 79.1% and 39.5% ($p < .01$) and 84.7% and 74.6% ($p = .25$) for Nano-cytology and UCT, respectively. Specificity of Nano-cytology was slightly lower than that of UCT (89.8% vs. 100%, $p = .022$), which is mainly caused by severe urinary tract infection. In addition, Nano-UCT showed increased sensitivity with 90.2% for overall patients, and 83.7% and 94.9% for low- and high-grade tumor, respectively.

Conclusion: The Nano-cytology assay had a significantly improved sensitivity compared with UCT for detecting bladder cancer patients. It represents a promising tool for diagnosis of bladder cancer in clinical practice.

Keywords: bladder cancer, diagnosis, nanoparticles, urine cytology, nano

INTRODUCTION

Bladder cancer (BC) is the 10th most commonly diagnosed cancer worldwide (International Agency for Research on Cancer, 2021). Approximately 75% of patients with BC present with non-muscle-invasive bladder cancer (NMIBC) (Compérat et al., 2015). Patients with NMIBC have a significant risk of recurrence and progression after transurethral resection of bladder tumor (TURBT) (Babjuk

et al., 2019). As a result, patients with NMIBC need lifelong surveillance after therapy. Cystoscopy and urine cytology are the most important examinations for both diagnosis and surveillance of BC. However, cystoscopy is invasive and costly, and may miss flat lesions and carcinoma *in situ* (CIS) with a false-negative outcome ranging from 10% to 40% (Grossman et al., 2005). Currently, although numerous non-invasive urine biomarkers have been developed for diagnosis of UC, urine cytology test (UCT) is the only recommended liquid biopsy for surveillance of BC in different treatment guidelines for BC (Witjes et al., 2021). LCT (liquid-based cytology test) is commonly used in UCT daily practice with the advantages of being specific and non-invasive, but LCT depends on the experience of cytopathologists and the sensitivity is unsatisfactory, varying from 29% to 84% for different grades of BC, especially lower for low-grade BC (Yafi et al., 2015; Babjuk et al., 2022). Therefore, there is a clinical need to decrease the technique difficulty of LCT and improve its sensitivity.

With the rapid development of nanoscience and nanotechnology, numerous studies have focused on exploring nanomaterials for diagnosis and treatment of a myriad of cancers (Sahoo et al., 2007). Although glutamine, sialic acid, etc. can affect the surface charge of tumor cells, the most important effect is the that of glucose metabolism. Elevated glycolysis in tumor cells usually led to a higher-level secretion of lactate, which caused negative charges on the cell surfaces, while the surfaces of normal cells remain charge-neutral or slightly positive due to normal glycolysis (Chen et al., 2016). Taking advantage of the unique biophysical property of tumor cells, novel multifunctional nanoprobes (Fe_3O_4@SiO_2, mNPs) with positive charges were developed to capture tumor cells specifically without using any specific molecular marker (Chen et al., 2016).

In the present study, we aimed to evaluate whether mixing mNPs with urine (Nano-cytology) could help to identify tumor cells in patients with hematuria, and to compare the diagnostic accuracy of Nano-cytology with traditional UCT in a prospective, blinded, single-center clinical trial.

MATERIALS AND METHODS

Construction of Electrically Charged mNPs

The mNPs are composed of the positively charged mNPs and the negatively charged mNPs. Detailed procedures to construct mNPs were described in a previous study, and all the mNPs used in the present study were synthesized by The Institute for Biomedical Engineering & Nano Science, Tongji University School of Medicine (Chen et al., 2016).

Cell Culture

T921, 5637, EJ, RT-4, Biu-87, and T-24 cells were grown in RPMI 1640 medium supplemented with 10% (v/v) heat-inactivated fetal bovine serum (FBS) and 1% (v/v) penicillin–streptomycin (PS) at 37°C in a 5% CO_2 humidified atmosphere. Hela cells were cultured at 37°C in DMEM supplemented with 10% FBS and 1% (v/v) PS in a humidified atmosphere in the presence of 5% CO_2. Non-cancerous bladder epithelial cells SVHUC were grown in F12K supplemented with the 10% (v/v) heat-inactivated fetal bovine serum (FBS) and 1% (v/v) penicillin–streptomycin (PS) at 37°C in a 5% CO_2 humidified atmosphere. Typically, cells were passaged by trypsinization and maintained in medium accordingly.

Preparation of Primary Cells

Primary bladder tumor cells were isolated from rates of xenograft bladder cancer models and bladder cancer patients' tissue who underwent radical cystectomy in our hospital as previously reported (Xu et al., 2013). A total of six cases of tumor tissue and corresponding normal urothelial tissue (adjacent to cancer) were collected from patients. Primary cells were cultured in 24-well plates with 1×10^5 cells per well. Cells were incubated in RPMI 1640 medium containing 10% FBS, 100 U/ml penicillin, and 100 μg/ml streptomycin. The research was approved and performed under the ethical and legal standards of the Ethics Committee of Shanghai Changhai Hospital (CHEC2019082).

Fluorescence Microscopy Analysis

Bladder tumor cells and Hela cells were grown at 37°C under normal cell culture conditions to 70%–80% confluency. The culture wells were washed thoroughly with PBS, trypsin, and resuspended in PBS. mNPs were added at the indicated concentrations to the cell suspensions and incubated on ice for 5 min with gentle agitation. After incubation, the NP-bound cells were captured by a permanent magnet placed against the side wall of the tube and free cells were removed by washing three times with PBS. The captured cells were released by removing the magnet and resuspended in PBS. Then, the captured cells were imaged using fluorescence microscopy (DMIL, Leica, Germany) and counted by a hemocytometer.

Patients and Samples

During June 2020 to February 2021, participants were prospectively recruited from Changhai Hospital. The inclusion criteria for patients with bladder cancer were as follows: patients diagnosed with bladder cancer and underwent TURBT or cystectomy for treatment; male or female ages >18 years; patients without any other tumor history; and patients who signed the informed consent form. The inclusion criteria for participants in the control group were as follows: participants without any tumor disease and willing to provide urine samples, participants who signed the informed consent, and participants with any benign urinary diseases, such as urinary stones, cystitis glandularis, interstitial cystitis, and cystitis. Exclusion criteria included patients unwilling to sign the consent form or unwilling to provide urine sample for analysis; patients who already had an indwelling catheter; and patients with incidental prostate cancer by prostate biopsy, transurethral resection of prostate, or cystectomy. Urine samples of approximately 100 ml were collected from participants at the time of hospital admission. Urine samples were divided equally for UCT and nano-cytology analysis.

Urine Cytology Test

Approximately 50 ml of urine was used for UCT analysis. We used the BD-TriPath Preparatory (BD-TriPath Imaging, Burlington, NC), a liquid-based sampling technique, for the

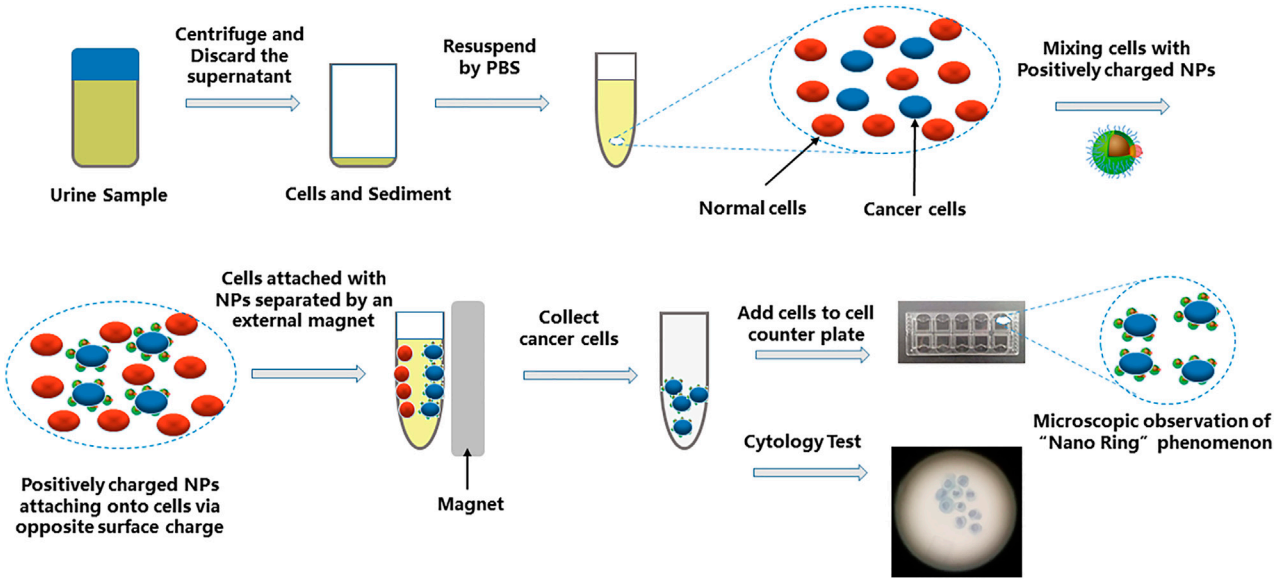

FIGURE 1 | Schematic diagram showing the procedure of Nano-cytology. The cells in suspension are mixed with positively charged NPs. Cell/NP bindings take place due to the opposite charges. The captured cells are magnetically attracted to the side of the tube by a permanent magnet. The "Nano-ring" phenomenon can be observed by a microscope. The collected cells also need a cytology test.

preparation of urine cytologic samples. Slides were prepared and processed according to the manufacturer's protocol, and were evaluated by experienced cytopathologists blinded to the patients' clinical information. The UCT assay was given as negative (normal cells and atypical cells were regarded as negative) and positive (suspicious tumor cells and tumor cells were regarded as positive).

Nano-Cytology Assay

Urine samples (50 ml) were processed for the Nano-cytology assay as soon as they were obtained. Urine was centrifuged at 600 *g* for 5 min. The cell pellet was resuspended in phosphate-buffered saline (×1) and centrifuged at 600 *g* for 5 min. Cells seeded in a 5-ml centrifuge tube were incubated with the positively or negatively charged mNPs at 4°C for 15 min. After incubation, the magnet was used to capture the cells surrounded by mNPs. All cell-mNPs incubations were performed on ice to avoid endocytic events. The captured cells were resuspended in 200 µl of phosphate-buffered saline (×1), and 20 µl of the remixed samples was placed in the cell counting plate and imaged using microscopy (Cellometer Auto 1000, Nexcelom Bioscience, United States) to look for suspicious tumor cells. If suspicious tumor cell was found, the result score value = 1; otherwise, value = 0. The rest of the captured cells were prepared and processed according to the UCT protocol (**Figure 1**). Cytology was evaluated by experienced cytopathologists blinded to the patients' clinical information. The results were given as negative (N) or positive (P). Finally, a Nano-cytology modality was developed combining the value and the cytology result. The protocol could be made as follows: positive results include P1, P0, and N1; a negative result is N0.

Statistical Analysis

Sensitivity, specificity, negative predictive value (NPV), and positive predictive value (PPV) were calculated for Nano-cytology, UCT, and a combination of these two methods (Nano-UCT). Subgroup analyses were performed for different tumor grades and stages. The Fisher's test (by SPSS Statistics software, v22.0, IBM Institute) was used to determine the statistical difference for categorical variables. A p-value <.05 was considered statistically significant.

RESULTS

Interaction of the mNPs With Bladder Cancer Cell

To determine whether positively charged mNPs could bind bladder tumor cells specifically, six different bladder cancer cell lines and the Hela cell line (positive control) were incubated with positively and negatively charged mNPs, respectively. Upon electrostatic interaction with enough mNPs, the captured cells were "pulled" to the side of the tube by a magnet. **Figure 2A** shows that positively and negatively charged mNPs had a completely different pattern of interaction with tumor cells, and positively charged mNPs had a significantly higher ability to capture tumor cells, which was in line with our previous study (Chen et al., 2016). Furthermore, we tried to characterize the interaction of the bladder cancer cell and mNPs; a constant number of three different bladder cancer cells were incubated with various concentrations of positively charged mNPs ranging from 5 to 150 µg/ml, and with 50 µg/ml mNPs at different pH. The efficiency of the magnetic capture ability for bladder tumor cells by mNPs is shown in **Figures 2B,C**; 50 µg/ml positive NPs were enough to capture most of the 5×10^5 bladder cancer cells, and the mNPs

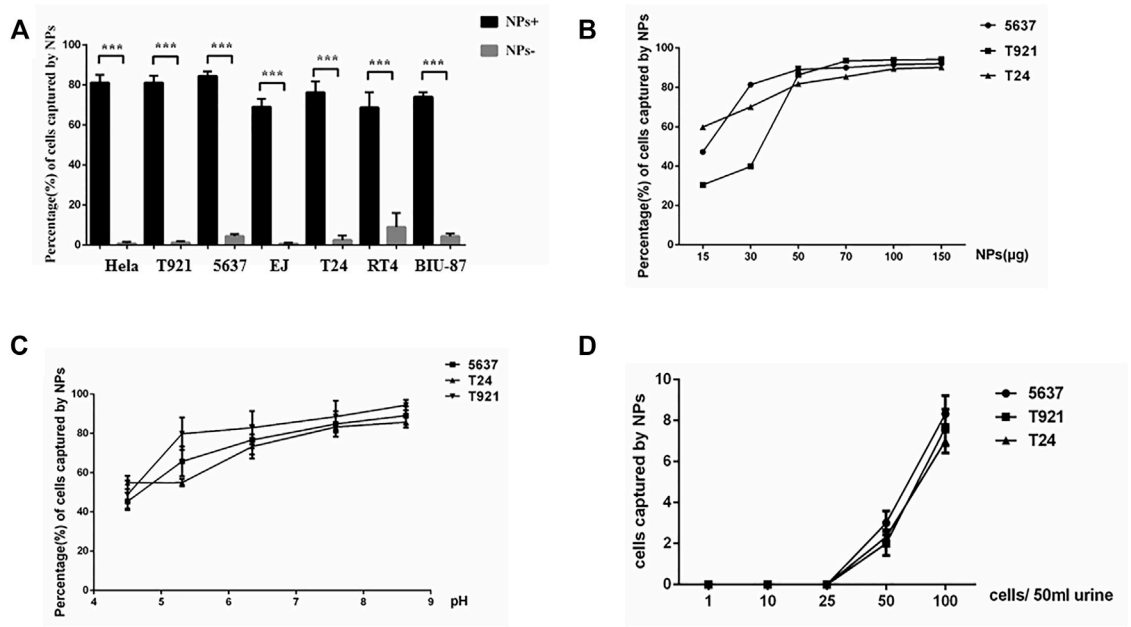

FIGURE 2 | Interaction of the mNPs with bladder tumor cells. **(A)** Positive mNPs and negative mNPs have completely different patterns of interaction with bladder tumor cells. ***$p < .001$. **(B)** The magnetic capture efficiencies of bladder tumor cells by NPs of positive charges are plotted at various mNP concentrations. **(C)** The magnetic capture efficiencies of bladder tumor cells by mNPs of positive charges are plotted at various pH value. **(D)** Positive mNPs can capture cancer cell if more than 50 cells in 50-ml samples were given.

showed stable capture efficiency with pH ranging from 6 to 9. Moreover, we demonstrated that 50 μg/ml positively charged mNPs could capture 50 tumor cells per 50 ml of urine (**Figure 2D**).

mNPs Formed Nano-Ring Around Bladder Tumor Cells

We transfected green fluorescent labeled lentivirus into Biu-87 cells (**Figure 3A**) and incubated with mNPs. As shown in **Figure 3B**, we found positively charged mNPs binding to and covering the surface of Biu-87 cells. The phenomenon looked like rings (nano-ring) under a microscope (**Figure 3A**). We further performed an experiment to validate the positively charged mNPs specifically capturing tumor cells. Labeled Biu-87 cells were mixed with the non-cancerous SVHUC cells in a ratio of 1:1 and incubated with positively charged mNPs. As displayed, nano-ring was found around Biu-87 cells, but not detected around SVHUC cells, which showed no fluorescence (**Figure 3C**).

The Ability of mNPs to Differentiate Tumor Cells in Primary Cultured Cells

To determine whether the nano-ring phenomenon also existed in primary cultured cells, different types of primary cells were harvested from SCID, FVB, C57, nude mice's bladder, bladder cancer patients' tissue, and subcutaneous xenograft tumor by T24 cells on nude mice and incubated with positively charged mNPs. No nano-ring phenomenon was found in the normal mice cells. Cells from subcutaneous xenograft tumor and patients' tumor tissue, the nano-ring phenomena were obvious (**Figures 4A–C**). The mNPs bond cells were then magnetically captured and separated. Slides contained separated cells that were confirmed to be tumor cells by cytopathologists blinded to the information of cells (**Figure 4D**).

The Ability of mNPs to Differentiate Tumor Cells in Urine

We further investigated whether mNPs could identify tumor cells from urine and avoid the influence of red blood cells and white blood cells in urine. Urine exfoliated cells from bladder cancer patients were used to incubate with positively charged mNPs. Many cells showed the nano-ring phenomenon (**Figure 4E**). In **Figure 4E**, white blood cells were smaller than bladder cancer cells, and nano-ring was not seen. While red blood cells were found in hematuria cases due to its properties, which adheres to the tube and is hard to wipe off. However, this could be distinguished by the feature of round cake with concave center on both sides. As shown in **Figure 4F**, tumor cells with nano-ring were detected and confirmed by cytopathologists.

Nano-Cytology Showed Improved Sensitivity Compared With Urine Cytology Test

One hundred and six patients and 49 controls were enrolled to compare the sensitivity between nano-cytology and traditional UCT assays. Four participants were excluded due to the incidental prostate cancer found after cystectomy. Detailed information of

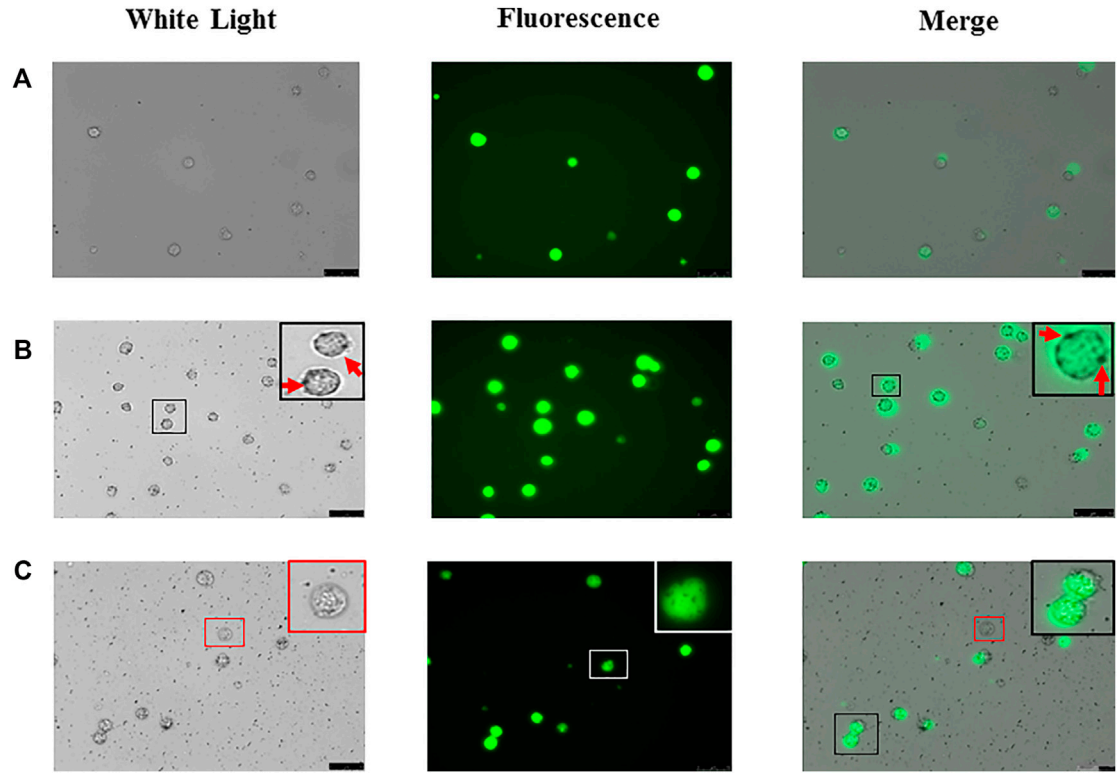

FIGURE 3 | Foundation of "nano ring" in bladder tumor cells. **(A)** Biu-87 cells show green fluorescence. **(B)** Incubate fluorescent Biu-87 cells with positive mNPs, cells were surrounded by the mNPs (red arrows). **(C)** Mix the same number of fluorescent Biu-87 cells, SVHUC cells, and positive mNPs; mNPs only surround green fluorescent Biu-87 cells (black frame), and no NPs surround the only cell without fluorescence (red frame).

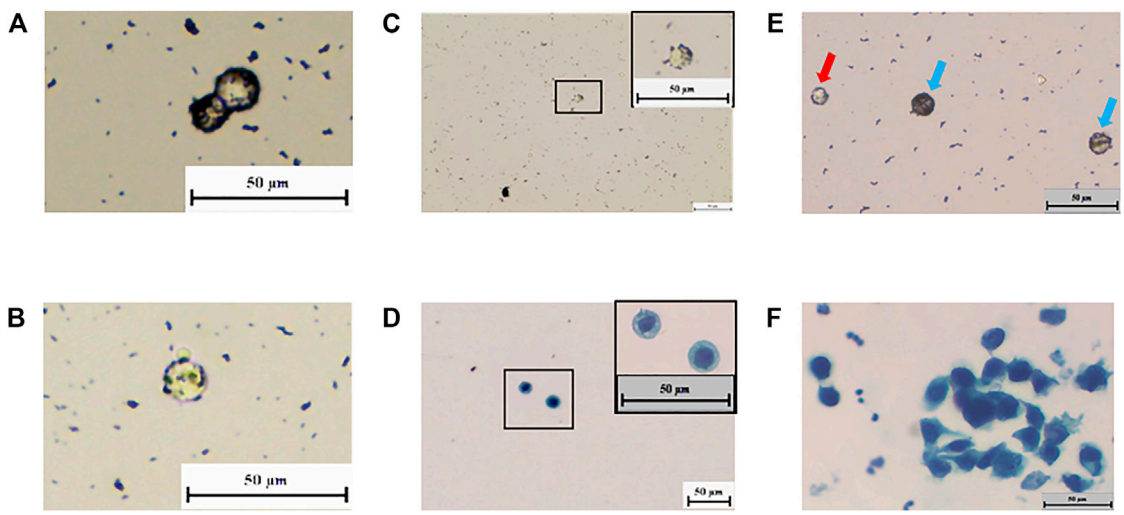

FIGURE 4 | "Nano ring" in living organisms' bladder tumor cells. **(A–C)** In subcutaneous tumorigenic mice's cells and patients' tissue, the "nano ring" phenomenon is obvious. **(D)** Cytology test proves the NP-bound patient's tissue cells were tumor cells. **(E)** Incubate positive mNPs with Bladder cancer patients' urine exfoliated cells. "Nano ring" phenomenon is obvious. White blood cell (red arrow) is smaller than the bladder cancer cell (blue arrow). **(F)** Cytology test proves that the NP-bound patients' exfoliated cells were tumor cells.

included participants is shown in **Table 1**. Compared with UCT, nano-cytology identified BC with significantly improved overall sensitivity (82.4% vs. 59.8%, $p < .01$), but slightly lower specificity (89.8% vs. 100%, $p = .022$, **Table 2**). Nano-cytology resulted in higher sensitivity for identifying low-grade (79.1% vs. 39.5%, $p < .01$) and high-grade BC (84.7% vs. 74.6%, $p = .25$) compared with UCT.

TABLE 1 | Patient baseline characteristics.

Urine samples	Tumor	Control	*p*-value
Participants included	102	49	
Participants excluded	4		
Gender			.601
Male	87	41	
Female	15	8	
Age			
Mean (SD)	66.51 (12.31)	66.24 (13.55)	.354
Tumor stage			
<pT2	85		
≥pT2	17		
Tumor grade			
Low grade	43		
High grade	59		
Benign urinary diseases in control			
Urinary stones		13	
Benign prostate hyperplasia		21	
Incontinence		4	
Others		11	

Moreover, the advantage of nano-cytology was maintained in the detection of NMIBC (82.4 vs. 56.5%, $p < .01$), but there was no difference between muscle-invasive BC (82.4% vs. 76.5%, $p = 1$). When combining these two methods together, nano-UCT resulted in a sensitivity of 90.2%, a specificity of 89.8%, a PPV of 94.8%, and an NPV of 81.5% (**Table 3**).

DISCUSSION

In the present study, we found that positively charged mNPs could specifically capture bladder tumor cells in urine, and tumor cells that bond with mNPs could be enriched under the influence of a magnet. The patient exfoliated cells that showed the nano-ring phenomenon should be regarded as suspicious tumor cells and tumor cells. The sensitivity of standard UCT for detecting urothelial carcinoma is low, largely due to its inability to process the entire sample, paucicellularity, and the presence of background cells (Miyake et al., 2021). Our novel approach could help to reduce the confounding background cells such as normal urothelial cells, apoptotic cells, and red and white blood cells in urine. Cytopathologists thus could focus on evaluating suspicious cells captured by mNPs. As a result, our study showed that nano-cytology had a significantly higher sensitivity (82.4% vs. 59.8%), especially for low-grade tumor cells (79.1% vs. 39.5%), and comparable specificity compared with traditional UCT. In addition, the mNPs are cost-effective, which can be synthesized at a cost of $100 and test tens of thousands of samples. So there is not much difference between nano-cytology and UCT in terms of cost.

Urine cytology is a commonly used noninvasive approach for detecting tumor cells in the urinary tract with high specificity. Currently, UCT is recommended in the surveillance of high-risk NMIBC in clinical guidelines at certain intervals (Babjuk et al., 2019). However, the sensitivity of UCT varied from 29% to 84% for tumors of different grades and stages (Dimashkieh et al., 2013), and the sensitivity for detecting CIS was 28%–100% (Babjuk et al., 2022). Meanwhile, the accuracy of UCT largely depends on the experience and skill of the technicians and cytopathologists. The Paris System for Reporting Urinary Cytology have been put forward to standardize the reporting system of UCT (Babjuk et al., 2022). Meilleroux et al. (2018) reported that the Paris System helped to characterize the atypical

TABLE 2 | Detailed comparison of sensitivity obtained by Nano-cytology and UCT for BCa detection in relation to tumor stages and grades.

Tumors	Nano-cytology		UCT		*p*-value
	n Positive/*n* Total	Sensitivity (%)	*n* Positive/*n* Total	Sensitivity (%)	
BC	84/102	82.4	61/102	59.8	.001*
BC by grade					
Low	34/43	79.1	17/43	39.5	.000*
TaLG	27/34	79.4	9/34	26.5	.000*
T1LG	6/7	85.7	6/7	85.7	1
T2–4LG	1/2	50.0	2/2	100.0	.248
High	50/59	84.7	44/59	74.6	.253
TaHG	9/12	75.0	8/12	66.7	.653
T1HG	28/32	87.5	25/32	78.1	.320
T2–4HG	13/15	86.7	11/15	73.3	.361
BC by stage					
<pT2	70/85	82.4	48/85	56.5	.000*
Ta	36/46	78.3	17/46	37.0	.000*
T1	34/39	87.2	31/39	79.5	.362
≥pT2	14/17	82.4	13/17	76.5	1.000
Control	*n* Negative/*n* Total	Specificity (%)	*n* Negative/*n* Total	Specificity (%)	
All	44/49	89.8	49/49	100.0	.022*
Normal	32/32	100.0	32/32	100.0	1
Infection	12/17	70.6	17/17	100.0	.003*
PPV	94.3%		100%		
NPV	71.0%		54.4%		

NPV, negative predictive value; PPV, positive predictive value.
**Significant,* $p < .05$.

TABLE 3 | Detailed comparison of sensitivity obtained by Nano-UCT for BCa detection in relation to tumor stages and grades.

Tumors	Combination of Nano-cytology and UCT	
	n Positive/*n* Total	Sensitivity (%)
BC	92/102	90.2
BC by grade		
Low	36/43	83.7
TaLG	27/34	79.4
T1LG	7/7	100.0
T2–4LG	2/2	100.0
High	56/59	94.9
TaHG	12/12	100.0
T1HG	30/32	93.8
T2–4HG	14/15	93.3
BC by stage		
<pT2	76/85	89.4
Ta	39/46	84.8
T1	37/39	94.9
≥pT2	16/17	94.1
Control	*n* Negative/*n* Total	Specificity (%)
All	44/49	89.8
Normal	32/32	100.0
Infection	12/17	70.6
PPV	94.8%	
NPV	81.5%	

NPV, negative predictive value; PPV, positive predictive value.

urothelial cells and low-grade urothelial neoplasm. Several novel approaches have been explored to improve the sensitivity of UCT. Birkhahn et al. (2013) invented a novel portable microfiltration device for the capture, enumeration, and characterization of exfoliated tumor cells in urine. Sensitivity (53.3% vs. 40.0%) and specificity (100% vs. 95.8%) of microfilter cytology were higher than standard cytology. Miyake et al. (2021) created a high-throughput detection device for hexylaminolevulinate-mediated fluorescent voided urine cytology, and this novel approach was found to have significantly higher sensitivity compared with standard cytology (63% vs. 29%).

Over the last few decades, numerous studies have tried to explore novel techniques to detect urothelial carcinoma by analyzing protein and nucleic acid in urine. Several methods such as bladder tumor antigen, FISH, and NMP22 have been approved by the FDA. However, clinical application of these markers is still rare due to the lower specificity compared with UCT and the low reproducibility. None of these markers have been accepted for diagnosis or follow-up in daily practice or clinical guidelines (Babjuk et al., 2022). More recently, several detection platforms based on high-throughput sequencing have been developed, such as CxBladder (Kavalieris et al., 2016) and Xpert (Valenberg et al., 2019) (multigene expression markers); Bladder EpiCheck (Mancini et al., 2020), UriFind (Ruan et al., 2021), and utMeMA (Chen et al., 2020) (DNA methylation markers); and UroCAD (Chromosomal instability) (Zeng et al., 2020). These novel markers were reported to have both high sensitivity and specificity and NPV. Valenberg et al. (2019) developed the Xpert Bladder Cancer Monitor (Xpert) and measured five mRNA targets (ABL1, CRH, IGF2, UPK1B, and ANXA10) that are frequently overexpressed in BC. The overall sensitivity was 74% (63% for LG, 83% for HG) and specificity was 80%. Ruan et al. (2021) developed and validated a urine-based PCR DNA methylation assay for early detection of BC, which showed a sensitivity of 88.1%–91.2%, a specificity of 89.7–85.7%, and superior sensitivity in detecting low-grade (66.7%–77.8%) and Ta tumors (83.3%). Compared with these detection platforms based on the high-throughput sequencing, nano-cytology showed similar sensitivity for low-grade (79.1%) and Ta tumors (78.3%). However, these liquid biopsy methods are still not widely used in clinical practice; further studies with a larger sample size in multiple centers and longer follow-up are warranted.

Nanotechnology has widely been developed for the management of cancers from diagnosis to treatment (Tomlinson et al., 2015). However, nanotechnology applied on the noninvasive detection of BC is limited. Eissa et al. (2014) described a gold nanoparticle assay in which target RNA was purified using magnetic nanoparticles (Fe_2O_3) and then detected with standard molecular techniques. This approach reached a sensitivity of 88.5% and a specificity of 94%. Hyaluronanase was detected in urine based on the agglomeration characteristics of cationic gold nanoparticles to diagnose BC in 40 participants; this study showed that the sensitivity was 90% and the specificity was 80.8% when the threshold value was 93.5 μU/ng protein (Nossier et al., 2013). Nossier et al. (2016) developed a simple colorimetric gold nanoparticle assay for the detection of urinary total gelatinase activity (MMP-2 and MMP-9) to differentiate BC patients, and resulted in a sensitivity of 87.5% and a specificity of 86.4%.

Based on the fact that the tumor cell membrane is negatively charged, nanoparticles with positive electricity are more conducive to bind to the cell membrane (Chen et al., 2016; Hla et al., 2021). Inspired by unlike electric charges attract, we utilized the positively charged mNPs to capture tumor cells in urine. The morphology of low-grade tumor cells is not much different from normal urothelium. As a result, it is difficult to identify low-grade tumor cells with plenty of background cells, which leads to lower sensitivity compared to high-grade tumor cells in standard UCT (Barkan et al., 2016). The Nano-cytology method could identify tumor cells by the nano-ring phenomenon and enrich tumor cells and reduce the influence of a large number of background cells in exfoliated cell slides, thus improving the reading efficiency and accuracy of cytopathologists.

Limitations of the present study should be noted. First, mNPs are synthesized and provided by the laboratory we worked with, and nano-cytology is currently only available in our hospital. As a result, this is a single-center study. Second, only a small number of urine samples were included in the present study, and the value of nano-cytology should be confirmed *via* a larger cohort and multicenter study in the future. Third, Nano-cytology was the combination of the "nano-ring" phenomenon and the cytology test of the mNP-enriched cells. Compared with UCT, the cytology test of mNP enrichment lost some of the urine exfoliated cells. Fourth, nano-ring is essential to capture tumor cells, but we have found that mNPs could also be absorbed by few leukocytes such as granulocytes in a previous study (Chen et al., 2016). In the present study, five patients with a false-positive result (nano-ring phenomenon on white blood cells) were found to have a high level

of white blood cells in urine (at least 280 cells/HPF). Predictably, the diagnostic accuracy can be influenced in patients with severe urinary tract infection, and nano-cytology should be conducted after infection is under control. Fourth, although mNPs are specific for tumor cells, they cannot capture tumor cells less than 50/50 ml; the lack of sufficient exfoliative cells in urine from patients may be the major technique limitation. So, the combination of nano-cytology and UCT will help to improve detection sensitivity. Fifth, we did not compare the diagnostic performance of nano-cytology with FISH assay, because urine sample collected at one urination is not enough for three urine tests, and urine collected at different times may further introduce bias.

CONCLUSION

Compared with standard UCT, the Nano-cytology assay showed significantly improved sensitivity and comparable specificity for detecting BC. Nano-cytology may be a promising novel approach adjunct to cystoscopy for diagnosis of BC in clinical practice.

DATA AVAILABILITY STATEMENT

The original contributions presented in the study are included in the article/supplementary material. Further inquiries can be directed to the corresponding authors.

ETHICS STATEMENT

The studies involving human participants were reviewed and approved by Shanghai Changhai Hospital. The patients/participants provided their written informed consent to participate in this study. The animal study was reviewed and approved by Shanghai Changhai Hospital.

AUTHOR CONTRIBUTIONS

JX: Conceptualization, resources, data curation, supervision, funding acquisition, writing—original draft, writing—review and editing. SZ: Resources, data curation, investigation, writing—original draft, writing—review and editing. JL: Conceptualization, data curation, investigation. LG: Resources, supervision, data curation. WL: Conceptualization, data curation, supervision, methodology. XH: Conceptualization, supervision, methodology. GW: Data curation. BC: Conceptualization, data curation, supervision, funding acquisition. ZZ: Conceptualization, data curation, supervision, funding acquisition, investigation. CX: Conceptualization, data curation, supervision, funding acquisition, writing—original draft, writing—review and editing.

FUNDING

This research was financed by grants from Precision Medicine Translational application Research Project of Naval Medical University (2017JZ16 and 2017JZ33), grants from the Qihang program of Naval Medical University, Discipline development plan in Changhai Hospital (2019YXK041), Medical innovation research special project of Shanghai (20Y11904800), Shanghai Health Commission health industry clinical research project (201940177), and the National Natural Science Foundation of China (81572509, 81772720, 81802515, 81972391, and 82172871).

ACKNOWLEDGMENTS

We thank YanLei Chu, the secretary of the Department of Urology in Changhai Hospital, for her assistance in collecting and sending urine samples used in the study.

REFERENCES

Babjuk, M., Burger, M., Compérat, E. M., Gontero, P., Mostafid, A. H., Palou, J., et al. (2019). European Association of Urology Guidelines on Non-Muscle-Invasive Bladder Cancer (TaT1 and Carcinoma *In Situ*) - 2019 Update. *Eur. Urol.* 76 (5), 639–657. doi:10.1016/j.eururo.2019.08.016

Babjuk, M., Burger, M., Compérat, E. M., Gontero, P., Mostafid, A. H., Palou, J., et al. (2022). European Association of Urology Guidelines on Non-Muscle-Invasive Bladder Cancer (Ta, T1, and Carcinoma *In Situ*). *Eur. Urol.* 81 (1), 75–94.

Barkan, G. A., Wojcik, E. M., Nayar, R., Savic-Prince, S., Quek, M. L., Kurtycz, D. F. I., et al. (2016). The Paris System for Reporting Urinary Cytology: The Quest to Develop a Standardized Terminology. *J. Am. Soc. Cytopathol.* 5 (3), 177–188. doi:10.1016/j.jasc.2016.04.005

Birkhahn, M., Mitra, A. P., Williams, A. J., Barr, N. J., Skinner, E. C., Stein, J. P., et al. (2013). A Novel Precision-Engineered Microfiltration Device for Capture and Characterisation of Bladder Cancer Cells in Urine. *Eur. J. Cancer* 49 (15), 3159–3168. doi:10.1016/j.ejca.2013.04.033

Chen, B., Le, W., Wang, Y., Li, Z., Wang, D., Ren, L., et al. (2016). Targeting Negative Surface Charges of Cancer Cells by Multifunctional Nanoprobes. *Theranostics* 6 (11), 1887–1898.

Chen, X., Zhang, J., Ruan, W., Huang, M., Wang, C., Wang, H., et al. (2020). Urine DNA Methylation Assay Enables Early Detection and Recurrence Monitoring for Bladder Cancer. *J. Clin. Invest.* 130 (12), 6278–6289. doi:10.1172/JCI139597

Compérat, E., Larré, S., Roupret, M., Neuzillet, Y., Pignot, G., Quintens, H., et al. (2015). Clinicopathological Characteristics of Urothelial Bladder Cancer in Patients Less Than 40 Years Old. *Virchows Arch.* 466 (5), 589–594. doi:10.1007/s00428-015-1739-2

Dimashkieh, H., Wolff, D. J., Smith, T. M., Houser, P. M., Nietert, P. J., and Yang, J. (2013). Evaluation of Urovysion and Cytology for Bladder Cancer Detection: a Study of 1835 Paired Urine Samples with Clinical and Histologic Correlation. *Cancer Cytopathol* 121 (10), 591–597. doi:10.1002/cncy.21327

Eissa, S., Shawky, S. M., Matboli, M., Mohamed, S., and Azzazy, H. M. (2014). Direct Detection of Unamplified Hepatoma Upregulated Protein RNA in Urine Using Gold Nanoparticles for Bladder Cancer Diagnosis. *Clin. Biochem.* 47 (1–2), 104–110. doi:10.1016/j.clinbiochem.2013.10.022

Grossman, H. B., Messing, E., Soloway, M., Tomera, K., Katz, G., Berger, Y., et al. (2005). Detection of Bladder Cancer Using a point-of-care Proteomic Assay. *JAMA* 293 (20), 810–816. doi:10.1001/jama.293.7.810

Miyake, M., Nakai, Y., Nishimura, N., Ohnishi, S., Oda, Y., Fujii, T., et al. (2021). Hexylaminolevulinate-Mediated Fluorescent Urine Cytology with a Novel Automated Detection Technology for Screening and Surveillance of Bladder Cancer. *BJU Int.* 128 (2), 244–253. doi:10.1111/bju.15368

Hla, B., Cma, B., and Xd, B. (2021). Rapid Visualizing and Pathological Grading of Bladder Tumor Tissues by Simple Nanodiagnostics. *Biomaterials*, 264 120434 doi:10.1016/j.biomaterials.2020.120434

International Agency for Research on Cancer (2021). *Estimated Number of New 959 Cases in 2020, Worldwide, Both Sexes, All Ages*. Geneva, Switzerland: World Health Organization.

Kavalieris, L., O'Sullivan, P., Frampton, C., Guilford, P., Darling, D., Jacobson, E., et al. (2016). Performance Characteristics of a Multigene Urine Biomarker Test for Monitoring for Recurrent Urothelial Carcinoma in a Multicenter Study. *J. Urol.* 197, 1419–1426. doi:10.1016/j.juro.2016.12.010

Mancini, M., Righetto, M., Zumerle, S., Montopoli, M., and Zattoni, F. (2020). The Bladder EpiCheck Test as a Non-invasive Tool Based on the Identification of DNA Methylation in Bladder Cancer Cells in the Urine: A Review of Published Evidence. *Int. J. Mol. Sci.* 21 (18). 6542 doi:10.3390/ijms21186542

Nossier, A. I., Eissa, S., Ismail, M. F., Hamdy, M. A., and Azzazy, H. M. (2013). Direct Detection of Hyaluronidase in Urine Using Cationic Gold Nanoparticles: a Potential Diagnostic Test for Bladder Cancer. *Biosens. Bioelectron.* 54 (8), 7–14. doi:10.1016/j.bios.2013.10.024

Meilleroux, J., Daniel, G., Aziza, J., d'Aure, D. M., Quintyn-Ranty, M. L., Basset, C. M., et al. (2018). One Year of Experience Using the Paris System for Reporting Urinary Cytology. *Cancer Cytopathol.* 126 (6), 430–436. doi:10.1002/cncy.21999

Nossier, A. I., Mohammed, O. S., Fakhr El-Deen, R. R., Zaghloul, A. S., and Eissa, S. (2016). Gelatin-modified Gold Nanoparticles for Direct Detection of Urinary Total Gelatinase Activity: Diagnostic Value in Bladder Cancer. *Talanta* 161, 511–519. doi:10.1016/j.talanta.2016.09.015

Ruan, W., Chen, X., Huang, M., Wang, H., Chen, J., Liang, Z., et al. (2021). A Urine-Based DNA Methylation Assay to Facilitate Early Detection and Risk Stratification of Bladder Cancer. *Clin. Epigenetics* 13 (1), 91. doi:10.1186/s13148-021-01073-x

Sahoo, S. K., Parveen, S., and Panda, J. J. (2007). The Present and Future of Nanotechnology in Human Health Care. *Nanomedicine*. 3 (1), 20–31. doi:10.1016/j.nano.2006.11.008

Tomlinson, B., Lin, T.-y., Dall'Era, M., and Pan, C.-X. (2015). Nanotechnology in Bladder Cancer: Current State of Development and Clinical Practice. *Nanomedicine* 10 (7), 1189–1201. doi:10.2217/nnm.14.212

Valenberg, F. J. P. v., Hiar, A. M., Wallace, E., Bridge, J. A., Mayne, D. J., Beqaj, S., et al. (2019). Prospective Validation of an mRNA-Based Urine Test for Surveillance of Patients with Bladder Cancer. *Eur. Urol.* 75 (5), 853–860. doi:10.1016/j.eururo.2018.11.055

Witjes, J. A., Bruins, H. M., Cathomas, R., Compérat, E. M., Cowan, N. C., Gakis, G., et al. (2021). European Association of Urology Guidelines on Muscle-Invasive and Metastatic Bladder Cancer: Summary of the 2020 Guidelines. *Eur. Urol.* 79 (1), 82–104. doi:10.1016/j.eururo.2020.03.055

Xu, C., Xu, W., Ren, S., Wu, C., Wang, F., Lu, J., et al. (2013). Establishment of a Chinese Bladder Cancer Cell Line (T921) with High Metastatic Activity. In Vitro *Cell Dev. Biol. Anim.* 499, 668–678. doi:10.1007/s11626-013-9651-z

Yafi, F. A., Brimo, F., Steinberg, J., Aprikian, A. G., Tanguay, S., and Kassouf, W. (2015). Prospective Analysis of Sensitivity and Specificity of Urinary Cytology and Other Urinary Biomarkers for Bladder Cancer. *Urol. Oncol.* 33 (2), 66e25–31. doi:10.1016/j.urolonc.2014.06.008

Zeng, S., Ying, Y., Xing, N., Wang, B., Qian, Z., Zhou, Z., et al. (2020). Noninvasive Detection of Urothelial Carcinoma by Cost-Effective Low-Coverage Whole-Genome Sequencing from Urine-Exfoliated Cell DNA. *Clin. Cancer Res.* 26 (21), 5646–5654. doi:10.1158/1078-0432.ccr-20-0401

Conflict of Interest: The authors declare that the research was conducted in the absence of any commercial or financial relationships that could be construed as a potential conflict of interest.

Publisher's Note: All claims expressed in this article are solely those of the authors and do not necessarily represent those of their affiliated organizations, or those of the publisher, the editors, and the reviewers. Any product that may be evaluated in this article, or claim that may be made by its manufacturer, is not guaranteed or endorsed by the publisher.

frontiers in Cell and Developmental Biology

ORIGINAL RESEARCH
published: 31 January 2022
doi: 10.3389/fcell.2021.800967

TNF Family–Based Signature Predicts Prognosis, Tumor Microenvironment, and Molecular Subtypes in Bladder Carcinoma

Huihuang Li[1,2†], Siyuan Liu[3†], Chenxuan Li[4], Zicheng Xiao[1,2], Jiao Hu[1,2] and Cheng Zhao[1,2]*

[1]Department of Urology, Xiangya Hospital, Central South University, Changsha, China, [2]National Clinical Research Center for Geriatric Disorders, Xiangya Hospital, Central South University, Changsha, China, [3]Department of General Surgery, The Second Xiangya Hospital, Central South University, Changsha, China, [4]Xiangya School of Medicine, Central South University, Changsha, China

OPEN ACCESS

Edited by:
Yongwen Luo,
Wuhan University, China

Reviewed by:
Enchong Zhang,
ShengJing Hospital of China Medical University, China
Guangdi Chu,
Affiliated Hospital of Qingdao University, China

***Correspondence:**
Cheng Zhao
webshaq@163.com

[†]These authors have contributed equally to this work

Specialty section:
This article was submitted to Molecular and Cellular Pathology, a section of the journal Frontiers in Cell and Developmental Biology

Received: 24 October 2021
Accepted: 01 December 2021
Published: 31 January 2022

Citation:
Li H, Liu S, Li C, Xiao Z, Hu J and Zhao C (2022) TNF Family–Based Signature Predicts Prognosis, Tumor Microenvironment, and Molecular Subtypes in Bladder Carcinoma. Front. Cell Dev. Biol. 9:800967. doi: 10.3389/fcell.2021.800967

Background: Tumor necrosis factor (TNF) family members play vital roles in cancer development and antitumor immune responses. However, the expression patterns, prognostic values, and immunological characteristics of TNF members in bladder carcinoma (BLCA) remain unclear.

Methods: The training cohort, TCGA-BLCA, was downloaded from The Cancer Genome Atlas; another two Gene Expression Omnibus datasets (GSE13507 and GSE32894) and the Xiangya cohort (RNA-sequencing cohort collected from our hospital) were used as the external validation cohort. The least absolute shrinkage and selection operator (LASSO) algorithm and cross-validation were used to screen variables. Cox regression model and random survival forest (RSF) were used to develop the risk score, respectively. Then, we systematically correlated the TNF risk score with the tumor microenvironment (TME) cell infiltration, molecular subtypes of BLCA, and the potential value for predicting the efficacy of immunotherapy.

Results: We developed two TNF-based patterns, named TNF cluster 1 and TNF cluster 2. TNF cluster 1 exhibited poorer survival outcome and an inflamed TME characteristic compared with TNF cluster 2. We then filtered out 196 differentially expressed genes between the two TNF clusters and applied the LASSO algorithm and cross-validation to screen out 22 genes to build the risk score. For risk score, we found that RSF exhibited higher efficacy than the Cox regression model, and we chose the risk score developed by RSF for the following analysis. BLCA patients in the higher risk score group showed significantly poorer survival outcomes. Moreover, these results could be validated in the external validation cohorts, including the GSE13507, GSE32894, and Xiangya cohorts. Then, we systematically correlated the risk score with TME cell infiltration and found that it was positively correlated with the infiltration of a majority of immune cells. Also, a higher risk score indicated a basal subtype of BLCA. Notably, the relationship between risk score, TME cell infiltration, and molecular subtypes could be validated in the Xiangya cohort.

Conclusion: We developed and validated a robust TNF-based risk score, which could predict prognostic outcomes, TME, and molecular subtypes of BLCA. However, the value of risk score predicting the efficacy of immunotherapy needs further research.

Keywords: bladder carcinoma, prognosis, tumor microenvironment, immunotherapy, molecular subtype

INTRODUCTION

Bladder carcinoma (BLCA) is the 11th most common carcinomas globally, with nearly 550,000 new cases and 200,000 new deaths every year (Bray et al., 2018). BLCA can be divided into muscle-invasive bladder carcinoma (MIBC) and non–muscle-invasive bladder carcinoma (NMIBC) based on whether the tumors invade the detrusor muscle (Sanli et al., 2017). MIBCs account for approximately 20% of newly diagnosed BLCA, and 15% to 20% of NMIBC cases tend to progress to MIBC, which is a more aggressive form of cancer with extremely poor survival outcomes (Patel et al., 2020). Moreover, 10% of diagnosed BLCA cases are spread beyond the bladder, with only 5% to 30% 5-year overall survival (OS) rate (Siegel et al., 2018). Therefore, discovering specific prognostic methods for the OS of BLCA is needed to choose the most suitable treatment options for distinct subsets of BLCA patients.

Because of the poor prognosis, the US Food and Drug Administration has approved five immune checkpoint inhibitors (ICIs) for the treatment of metastatic BLCA (Patel et al., 2020). As a result, the immune component of the tumor microenvironment (TME) has reinvigorated the interest of researchers. ICIs can reinvigorate anticancer immune responses by targeting inhibitory receptors on T cells, and they have achieved remarkable success in treating different types of carcinomas (Havel et al., 2019). However, only a subset of patients benefits from ICI treatment. Engaging costimulatory receptors is another promising way for promoting T-cell responsiveness (Tran and Theodorescu, 2020). Tumor necrosis factor (TNF) family members, which contain 29 TNF receptors (TNFRSF) and 19 TNF ligands (TNFSF), play a vital role in the immune system through either coinhibited or costimulated ways (Dostert et al., 2019). Therefore, regulating the comprehensive interactions between TNF members is a promising carcinoma treatment option. However, the expression patterns, prognostic values, and immunological characteristics of TNF family members in BLCA remain unclear. In this study, we conducted a comprehensive analysis of TNF family members regarding prognosis, TME, and molecular subtypes of BLCA.

MATERIALS AND METHODS

Sources of BLCA Datasets and Preprocessing

We enrolled 932 BLCA cases from three public datasets and an RNA-sequencing (RNA-seq) cohort collected from Xiangya hospital. For The Cancer Genome Atlas (TCGA) database, the fragments per kilobase per million mapped fragments (FPKM) and the count value of 408 BLCA samples were downloaded from Genomic Data Commons (GDC, https://portal.gdc.cancer.gov/) (Colaprico et al., 2016), and then we transformed the FPKM value into transcripts per kilobase million value. After filtering duplicated patients and patients lacking full follow-up information, 403 patients from TCGA-BLCA were finally enrolled. Another two Gene Expression Omnibus (GEO) (https://www.ncbi.nlm.nih.gov/geo/) datasets with clinical and survival information were also enrolled. There are 308 cases in GSE32894 (Sjödahl et al., 2012), and we excluded 84 cases without survival information. There are 188 tumor cases and 67 normal cases in GSE13507 (Lee et al., 2010), and we excluded 23 tumor cases without survival information. Finally, for GEO databases, we included 224 cases from GSE32894 and 165 cases from GSE13507. As our previous study reported (Hu et al., 2021), we developed an RNA-seq cohort based on Xiangya hospital (Xiangya cohort) and uploaded it on the GEO database (GSE188715), which included 56 patients with survival information. The clinical information of these four datasets is summarized in **Supplementary Table S1**.

Consensus Clustering

Forty-seven TNF family genes, including 18 TNFSF and 29 TNFRSF genes, were collected from a previous study (**Supplementary Table S2**) (Zhang et al., 2020). We excluded TNFRSF6B because of its zero expression in TCGA-BLCA and included 46 TNF family genes for further analysis. We applied the consensus clustering algorithm (maxK = 5, reps = 100, pItem = 0.8, distance = "manhattan," clusterAlg = "pam") implemented in the "ConsensusClusterPlus" R package to identify distinct TNF-related patterns based on these 46 TNF family genes (Wilkerson and Hayes, 2010).

Depicting Tumor Immune Microenvironment of BLCA

In summary, the tumor immune microenvironment (TIME) of BLCA in this study included the activation of the anti–cancer-immunity cycle, infiltration of immune cells, and expression of ICI genes, effector genes of immune cells, and T cell–associated inflammatory signature (TIS). The activation levels of seven-step anti–cancer-immunity cycles were downloaded from the tracking tumor immunophenotype (TIP) (http://biocc.hrbmu.edu.cn/TIP/) (Xu et al., 2018), which is a web-based analytical platform. Then, the single-sample gene set enrichment analysis (ssGSEA) algorithm was applied to calculate individual immune cells in the TME, and the gene set for calculating is summarized in **Supplementary Table S3** (Charoentong et al., 2017). In addition, we summarized 22 ICI genes, 18 TIS genes, and effector genes of immune cells, including $CD8^+$ T cells, dendritic cells (DCs),

macrophages, natural killer (NK) cells, and type 1 T helper (T_H1) cells from our previous study (**Supplementary Table S4**) (Hu et al., 2021).

Gene Set Variation Analysis and Molecular Subtypes of BLCA

Gene signatures that had a close association with the clinical response to immune checkpoint blockade (ICB) therapy and molecular subtypes of BLCA were summarized from the studies by Mariathasan et al. and Kamoun et al., respectively (**Supplementary Table S5**) (Mariathasan et al., 2018; Kamoun et al., 2020). We then performed enrichment gene set variation analysis (GSVA) based on these signatures using the "GSVA" R package (Hänzelmann et al., 2013). In addition, seven independent molecular subtype classifications were developed using the "ConsensusMIBC" and "BLCAsubtyping" R packages as our previous study described (Hu et al., 2021). Based on the classification methods reported in consensus subtype, we renamed different names of molecular subtypes into "basal" and "luminal" subtypes (Kamoun et al., 2020).

Differentially Expressed Genes Filtering and Functional Annotation

We applied empirical Bayesian algorithm implemented in the "limma" R package to identify differentially expressed genes (DEGs). The genes with absolute log2 fold change greater than 2 and adjusted $p < 0.01$ were considered as DEGs. We then conducted Gene Ontology (GO) and Kyoto Encyclopedia of Genes and Genomes (KEGG) analyses using the "ClusterProfiler" R package.

The Development and Validation of a Risk Score Based on DEGs

We first applied univariate Cox analysis to identify the genes with prognostic value based on the DEGs using the "survival" R package. We then selected the prognostic genes to perform the least absolute shrinkage and selection operator (LASSO) regression using the "glmnet" R package. We filtered 24 genes to develop a risk score; among these genes, IL9R and TSPAN8 were ruled out because of nonexpression in the validation cohort. Finally, 22 TNF-associated genes were enrolled, and a TNF-based risk score was developed using the "rfsrc" function implemented in the "randomForestSRC" R package. In addition, we also developed a risk score using Cox proportional hazard regression analysis implemented in the "glmnet" R package:

$$\text{Risk score} = \sum \beta i^{*}\text{RNAi}.$$

We set the median value of the TNF-based risk score as the cutoff value and divided the patients into high and low TNF risk score groups. The Kaplan–Meier (K-M) method and log-rank test implemented in the "survminer" R package were used to plot the survival curves, and the timeROC function implemented in the "tROC" R package was used to assess the predictive accuracy of the risk score.

Statistical Analysis

Pearson or Spearman correlation coefficients were applied to evaluate the correlations among the variables, and *t* test or Mann-Whitney *U* test was applied to evaluate the differences between binary groups with continuous variables. The K-M method and log-rank test were applied to plot the survival curves, and univariate Cox analysis and LASSO algorithm were applied to narrow down the candidate genes for developing risk score. The values of hazard ratio for the candidate genes were calculated by univariate Cox regression model. Both random survival forest (RSF) and Cox proportional hazard regression analysis were applied to develop the risk score, and the predictive accuracy of the TNF-based risk score was assessed using time-dependent receiver operating characteristic (ROC) analysis. Multivariate Cox regression model was chosen for calculating independent prognostic value of the TNF-based risk score. $p < 0.05$ was set as the significant criteria, and the two-sided statistical tests were applied. R software (4.0.3) was used for all analyses.

RESULTS

Development of TNF-Based Patterns and Association With TIME

Figure 1Ashows the comprehensive landscape of 46 TNF family genes connection, interaction, and prognostic roles. TNF family genes had a close relationship with each other, and most of the genes had prognostic roles. So, we conducted an unsupervised clustering analysis using the "ConsensuClusterPlus" R package based on these 46 TNF family genes and found that dividing the TCGA-BLCA patients into two patterns was most suitable (**Supplementary Figure S1**). We named these two patterns as TNF cluster 1 and TNF cluster 2 and found that TNF cluster 1 exhibited significantly poorer survival outcome compared with cluster 2 ($p = 0.02$, **Figure 1B**).

We then wondered if these TNF-based patterns had regulation roles in the TME. A series of stepwise actions should be activated, proceeded, and expanded to effectively kill carcinoma cells; these series of steps were named cancer-immunity cycles and consisted of seven steps (Chen and Mellman, 2013). We found that a majority of these steps were activated significantly higher in the TNF cluster 1 than cluster 2, including T-cell recruiting, CD8 T-cell recruiting, NK cell recruiting, infiltration of immune cells into tumors, and killing of cancer cells (**Figure 1C**). This result indicated that TNF cluster 1 might represent an inflamed TME of BLCA and could be more sensitive to ICB therapy (Gajewski, 2015; Zemek et al., 2019). We then directly figured out the infiltration levels of 28 immune cells in the TME using ssGSEA algorithm and confirmed that TNF cluster 1 could be an inflamed phenotype with higher infiltration of immune cells, including activated CD4 T cells, activated CD8 T cells, macrophages, NK cells, and T_H1 cells (**Figure 1D**). Mariathasan et al. developed gene signatures that are closely associated with clinical response to ICB therapy (Mariathasan et al., 2018). As shown in **Figure 1E**, all these 21 gene signatures were significantly activated in TNF cluster 1, indicating that patients in TNF cluster 1 could be more sensitive to ICB therapy.

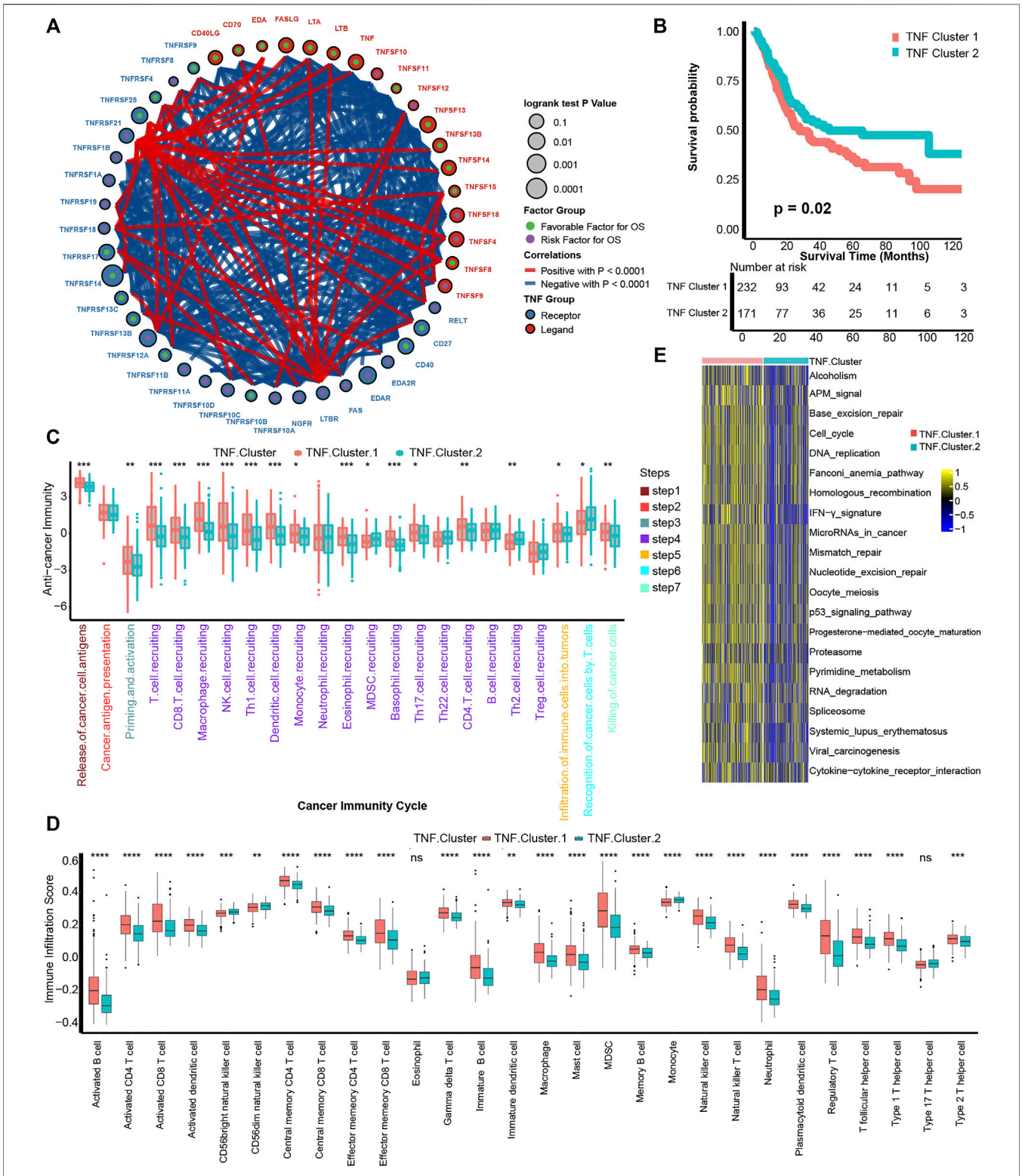

FIGURE 1 | Development of TNF-based patterns and association with TIME. **(A)** The interaction between TNF family members in bladder carcinomas. The size of the circle represents the *p* value for overall survival (OS) calculated using log-rank test. The green and purple dots in the circle represent the favorable and risk factors for OS, respectively; red and blue lines represent positive and negative correlations between TNF family members, respectively. **(B)** K-M plot of OS between two TNF-based patterns; red and azure lines represent TNF clusters 1 and 2, respectively. **(C)** The different levels of anticancer immunity between two TNF-based patterns; red and azure lines represent TNF cluster 1 and 2, respectively. **(D)** The different infiltration levels of 28 immune cells in the TME using ssGSEA algorithm between two TNF-based patterns; red and azure lines represent TNF clusters 1 and 2, respectively. **(E)** The different activated levels of gene signatures associated with ICB response between two TNF-based patterns. Red and azure lines represent TNF clusters 1 and 2, respectively. **p* < 0.05, ***p* < 0.01, ****p* < 0.001, *****p* < 0.0001; ns, not statistically significant.

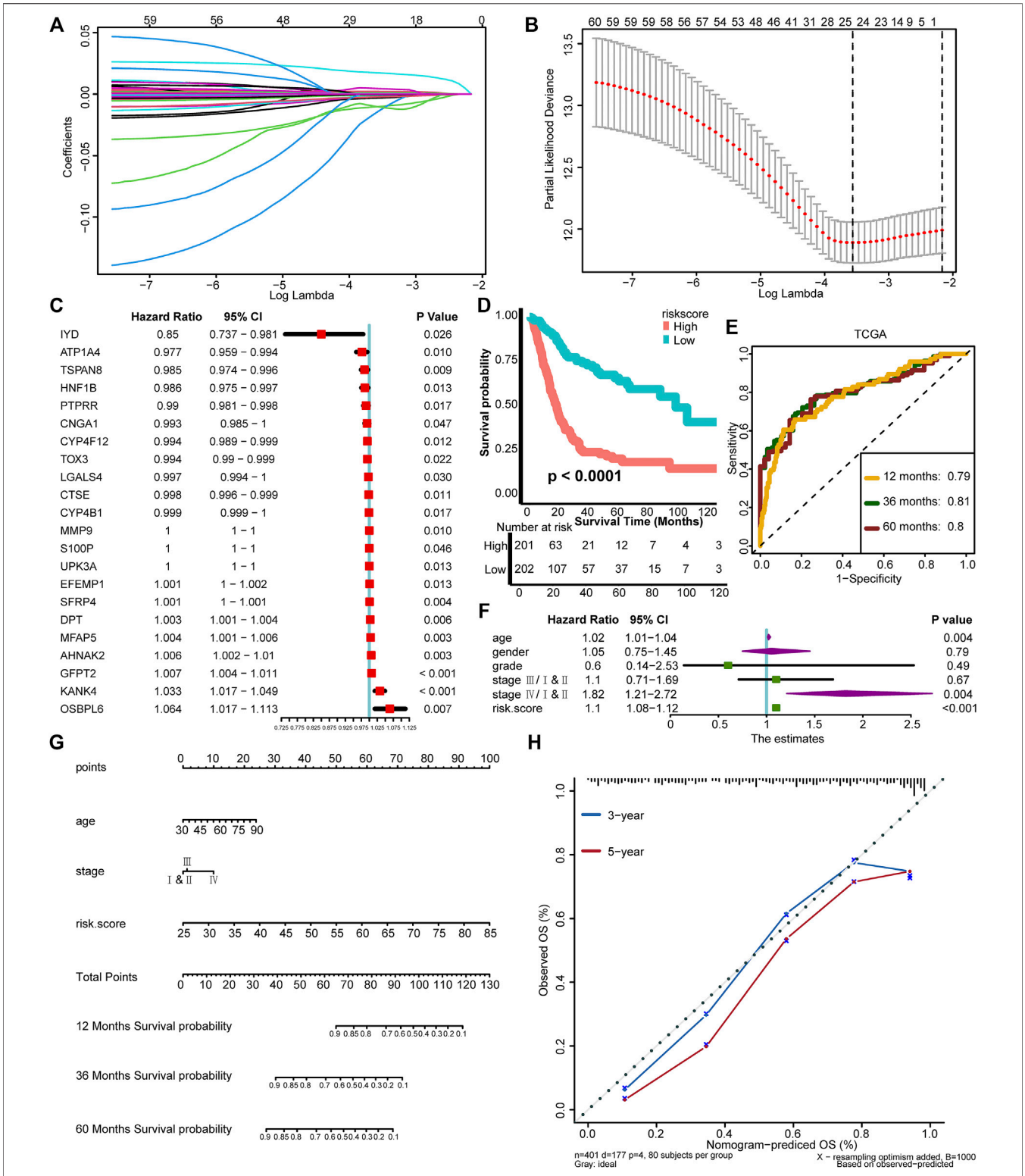

FIGURE 2 | Development of a TNF family–based risk score in the TCGA-BLCA cohort. **(A)** Coefficients of TNF-related DEGs with prognostic value are shown by lambda parameter. **(B)** Partial likelihood deviance versus log (lambda) drawn by LASSO algorithm and cross-validation. **(C)** The univariate analysis of 22 TNF-associated genes selected for developing risk score is shown in forest plots. **(D)** K-M plot of OS between TNF-based risk score groups; red and azure lines represent high and low TNF-based risk score groups, respectively. **(E)** The area under the curve (AUC) plot of TNF-based risk score in TCGA training cohort. **(F)** Forest plots of multivariate Cox analysis of TNF-based risk score combined with age, gender, tumor grade, and stage of BLCA. **(G)** Nomogram developed by using age, tumor stage, and TNF-based risk score. **(H)** Calibration curves of the nomogram.

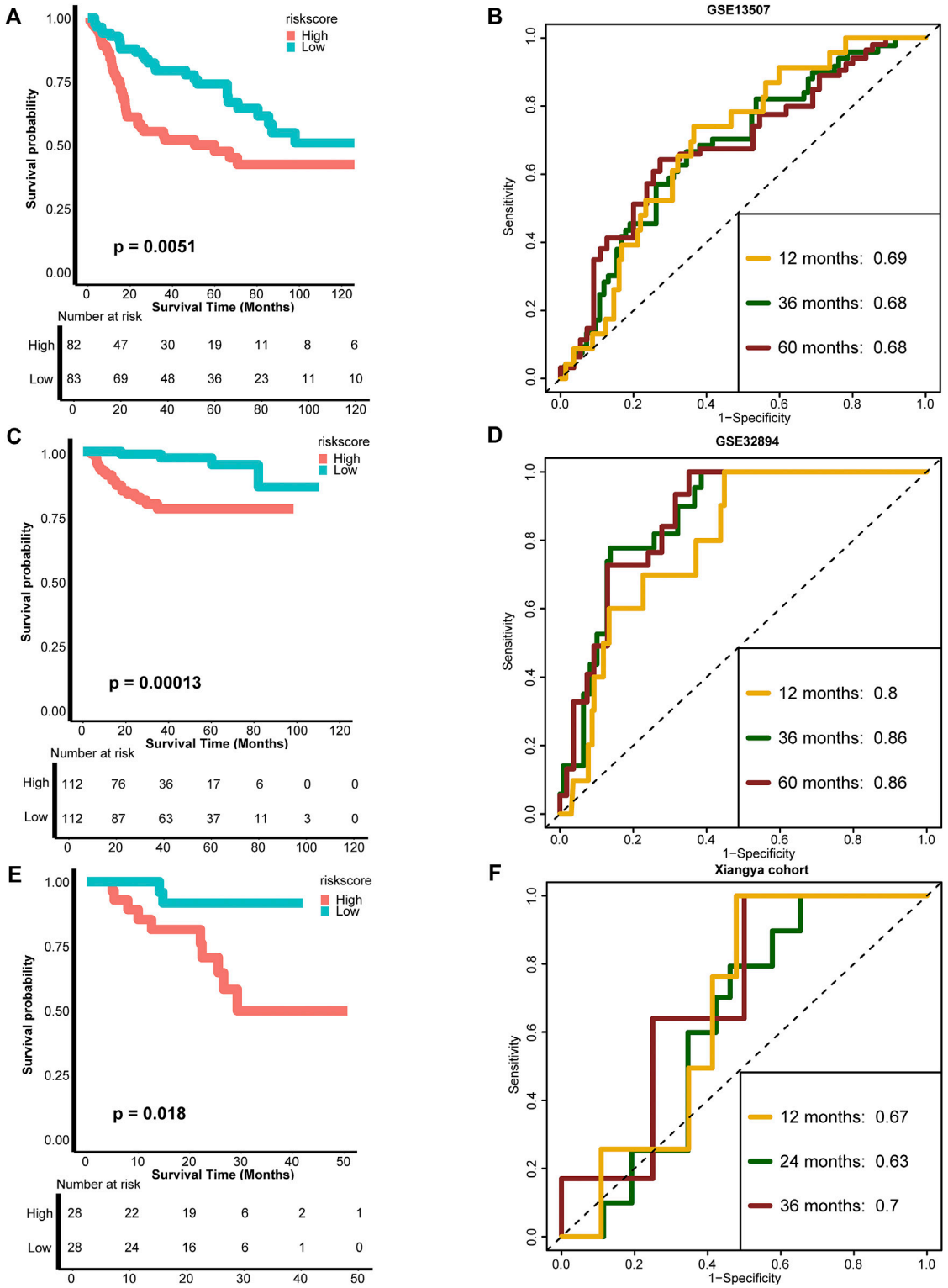

FIGURE 3 | External validation of the TNF-based risk score. **(A,B)** K-M plot of OS between TNF-based risk score groups and AUC plot of the risk score in the GSE13507 validation cohort, respectively. **(C,D)** K-M plot of OS between TNF-based risk score groups and AUC plot of the risk score in the GSE32894 validation cohort, respectively. **(E,F)** K-M plot of OS between TNF-based risk score groups and AUC plot of the risk score in Xiangya validation cohort, respectively. Red and azure lines represent high and low TNF-based risk score groups, respectively.

Development of a TNF Family–Based Risk Score in the TCGA-BLCA Cohort

We have depicted two TNF-based patterns and correlated them with survival outcome and TIME. In order to conduct a personalized evaluation of the role of TNF family genes in BLCA, we further developed a TNF family–based risk score. First, we filtered out 196 DEGs between TNF cluster 1 and cluster 2 using the "limma" R package (**Supplementary Figures S2A, B**, **Supplementary Table S6**). GO and KEGG analysis revealed that these 196 DEGs could be enriched in some immune-related pathways, like collagen-containing extracellular matrix and cytokine activity (**Supplementary Figures S2C–F**, **Supplementary Table S7**), which had driven us to correlate the risk score with TIME and ICB response in the next step. Among these 196 DEGs, 60 genes possessed prognostic values using univariate Cox analysis (**Supplementary Table S8**). We further narrowed down these genes using LASSO and 10-fold cross-validation. We identified 24 candidate genes with minimal lambda (0.11), and IL9R and TSPAN8 were ruled out because of nonexpression in the validation cohort (**Figures 2A, B**). Finally, 22 TNF-associated genes were enrolled, and a TNF-based risk score was developed using the "rfsrc" function implemented in the "randomForestSRC" R package. The prognostic values of these genes are shown in **Figure 2C**. As shown in **Figure 2D**, the patients with high TNF-based risk score exhibited significantly poorer survival outcomes ($p < 0.0001$), and the predictive accuracy for 12, 36, and 60 months were 0.79, 0.81, and 0.80, respectively (**Figure 2E**), indicating relatively high predictive accuracy. However, the accuracy of the risk score developed using Cox proportional hazard regression analysis was lower than the RSF developed risk score (**Supplementary Figures S3A, B**). Therefore, we chose the risk score developed using RSF for further analysis. Combined with age, gender, tumor grade, and stage of BLCA, TNF-based risk score still remained an independent risk factor ($p < 0.001$) in multivariate Cox analysis (**Figure 2F**). We then developed a nomogram by combining the TNF-based risk score and other clinicopathological characteristics with independent prognostic values in multivariate Cox analysis, including age and tumor stage (**Figure 2G**). The OS predicted by the nomogram was generally consistent with the actual OS, indicating the potentiality in the clinical application of this nomogram (**Figure 2H**).

External Validation of the Risk Score

To test the extrapolation of our risk score, we validated the risk score using external cohorts, including GSE13507, GSE32894, and Xiangya cohort. As shown in **Figures 3A, B**, the patients with higher risk score in GSE13507 also exhibited significantly poorer survival outcomes ($p = 0.0051$), and the predictive accuracies for 12, 36, and 60 months were 0.69, 0.68, and 0.68, respectively. For GSE32894, the survival outcomes in the high-risk group were still poorer ($p = 0.00013$), and the predictive accuracies for 12, 36, and 60 months were 0.80, 0.86, and 0.86, respectively, indicating relatively high predictive accuracy of our risk score (**Figures 3C, D**). The same for Xiangya cohort, the patients in the high-risk score group exhibited poorer survival outcomes ($p = 0.018$), and the predictive accuracies for 12, 24, and 36 months were 0.67, 0.63, and 0.70, respectively (**Figures 3E, F**). The risk score developed using Cox proportional hazard regression analysis was not satisfied as developed using RSF (**Supplementary Figures S3B–H**). All these results indicated that our risk score could be a robust predictive tool for OS of BLCA.

Association Between TNF Family–Based Risk Score and TIME and ICB Response

One of the main obstacles in understanding and treating carcinoma is the high heterogeneity of the TME (Duan et al., 2020). So, we correlated our TNF family–based risk score with TIME and detected its potential biomarker role for ICB response. For cancer-immunity cycles, TNF-based risk score was significantly positively correlated with the majority of these seven steps, including T-cell recruiting, CD8 T-cell recruiting, macrophage recruiting, T_H1 cell recruiting, and killing of cancer cells (**Figure 4A**, left, **Supplementary Table S9**). Moreover, the risk score was significantly positively associated with immune cells in the TME, such as activated CD4 and CD8 T cells, macrophages, and T_H1 cells (**Figure 4A**, right, **Supplementary Table S9**). Unlike TNF-based patterns, our TNF-based risk score could evaluate the patients' individual TME phenotypes and guide treatment options. We further found that the risk score was positively correlated with the TIS score (**Figure 4B**). As shown in **Figures 4C, D**, the risk score was positively correlated with most of the ICI genes and TIS genes (**Supplementary Table S10**). The patients in the high-risk score group expressed higher effector genes of immune cells, including $CD8^+$ T cells, DCs, macrophages, NK cells, and T_H1 cells (**Figure 4E**). We further evaluated the level of ICB response–associated pathways between high- and low-risk score groups and found that almost all these pathways were activated in the high-risk score group. These results indicated that patients with higher risk score represented an inflamed phenotype and might be more sensitive to ICB therapy.

TNF Family–Based Risk Score Stratified Molecular Subtypes of BLCA

Molecular subtypes were extensively researched topics that could predict the prognosis and treatment response of BLCA (Warrick et al., 2019). There are seven reported BLCA molecular classifications (Kamoun et al., 2020). However, the different numbers, sizes, and names of molecular subtypes, as well as the complicated detected methods, impeded their clinical application. In this study, we found that the high-risk score group represented the basal subtype of BLCA across seven molecular classifications, including TCGA subtype (Robertson et al., 2017), MDAnderson Cancer Center (MDA) subtype (Choi et al., 2014), Lund subtype (Marzouka et al., 2018), Cartes d'Identité des Tumeurs-Curie (CIT) subtype (Rebouissou et al., 2014), University of North Carolina (UNC) subtype (Damrauer et al., 2014), Baylor subtype (Mo et al., 2018), and consensus subtype (Kamoun et al., 2020) (**Figure 5A**). The high-risk score group was characterized by the activation of basal differentiation, epithelial–mesenchymal transition

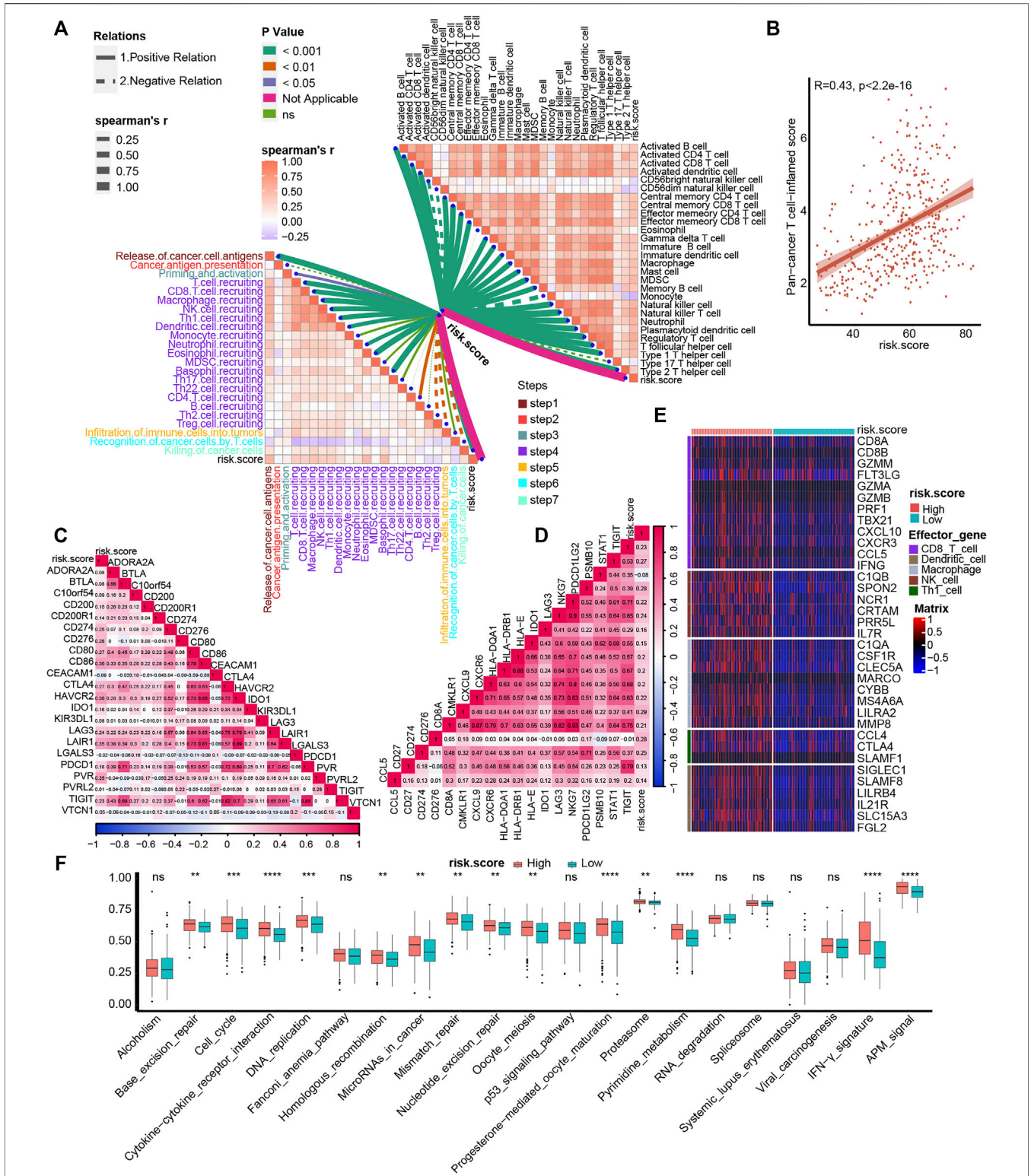

FIGURE 4 | Association between TNF family–based risk score and TIME and ICB response. **(A)** The association between TNF-based risk score and cancer-immunity cycles **(left)** and immune cells in the TME **(right)**. The different types of lines represent the positive or negative relations. The different colors of the lines represent the *p* values of the relations, and the thickness of the lines represents the strength of the relations. **(B)** The association between TNF-based risk score and T cell–associated inflammatory signature (TIS) score. **(C, D)** The association between TNF-based risk score and immune checkpoint inhibitor (ICI) genes and TIS genes, respectively. **(E)** The different expression patterns of effector genes of immune cells between different TNF-based risk score groups. **(F)** The different activated levels of gene signatures associated with ICB response between different TNF-based risk score groups. Red and azure lines represent high and low TNF-based risk score, respectively. $^{**}p < 0.01$, $^{***}p < 0.001$, $^{****}p < 0.0001$; ns, not statistically significant.

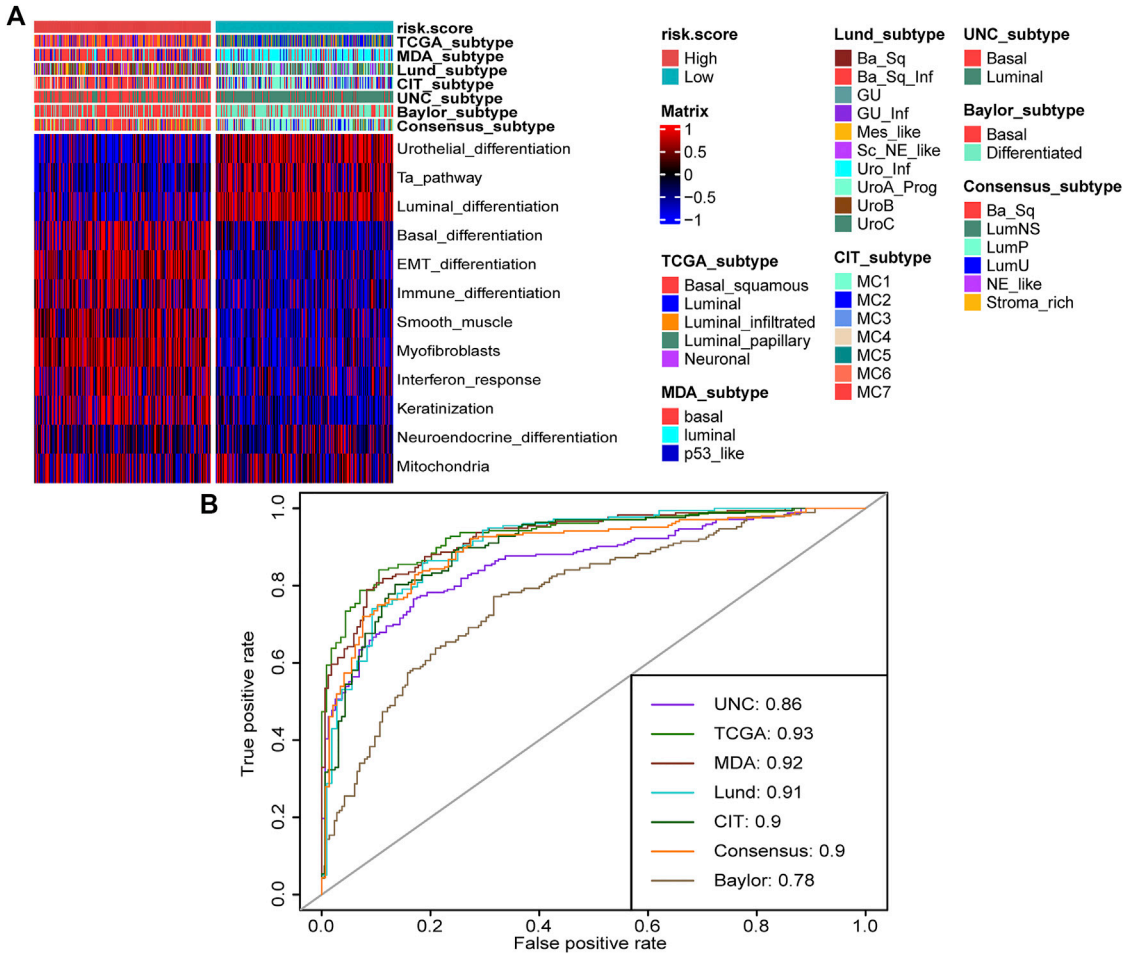

FIGURE 5 | TNF family–based risk score stratified molecular subtypes of BLCA in TCGA cohort. **(A)** The heat map of different TNF-based risk score groups, seven molecular subtype classifications, and bladder cancer–associated signatures in BLCA. Activated or inhibited pathways are marked as red or blue, respectively. **(B)** AUC plot of the risk score for predicting seven molecular subtype classifications in BLCA.

differentiation, immune differentiation, interferon response, and so on (**Figure 5A**) and might be more sensitive to neoadjuvant chemotherapy (NAC) and immune therapy. On the contrary, the low-risk score group represented the luminal subtypes and was characterized by urothelial differentiation, Ta pathway, and luminal differentiation (**Figure 5A**). Importantly, the risk score's predictive accuracy for molecular subtypes was extremely high, with a majority of ROCs being more than 0.90 (**Figure 5B**). The basal subtype has the features of more immune cell infiltration and higher response rates to immunotherapy, whereas the luminal subtype has the opposite features (Kamoun et al., 2020). The ability of TNF family–based risk score stratifying molecular subtypes of BLCA-revalidated risk score could predict TIME and ICB response from the aspect of molecular subtypes.

Validation of the TNF Family–Based Risk Score Roles in the Xiangya Cohort

We validated the relationship between TNF family–based risk score and TME and molecular subtypes in the Xiangya cohort. As expected, the TNF-based risk score was positively correlated with most steps of cancer-immunity cycles and immune cells in the TME in the Xiangya cohort (**Figure 6A**, **Supplementary Table S11**). For the effector genes of immune cells, patients with high-risk score expressed them higher than the low-risk score group (**Figure 6B**). Moreover, the risk score in the Xiangya cohort was also positively correlated with most of the ICI genes and TIS genes (**Figures 6C, D**, **Supplementary Table S12**). For molecular subtypes of BLCA, the patients with a high-risk score represented basal subtypes, whereas patients with a low-risk score represented luminal subtypes in the Xiangya cohort (**Figure 6E**). All ROCs for molecular subtypes were more than 0.90 (**Figure 6F**).

DISCUSSION

Our study was the first comprehensive investigation of the expression patterns and clinical and immunological roles of TNF family members in BLCA. We developed TNF-based patterns and correlated these patterns with prognosis and

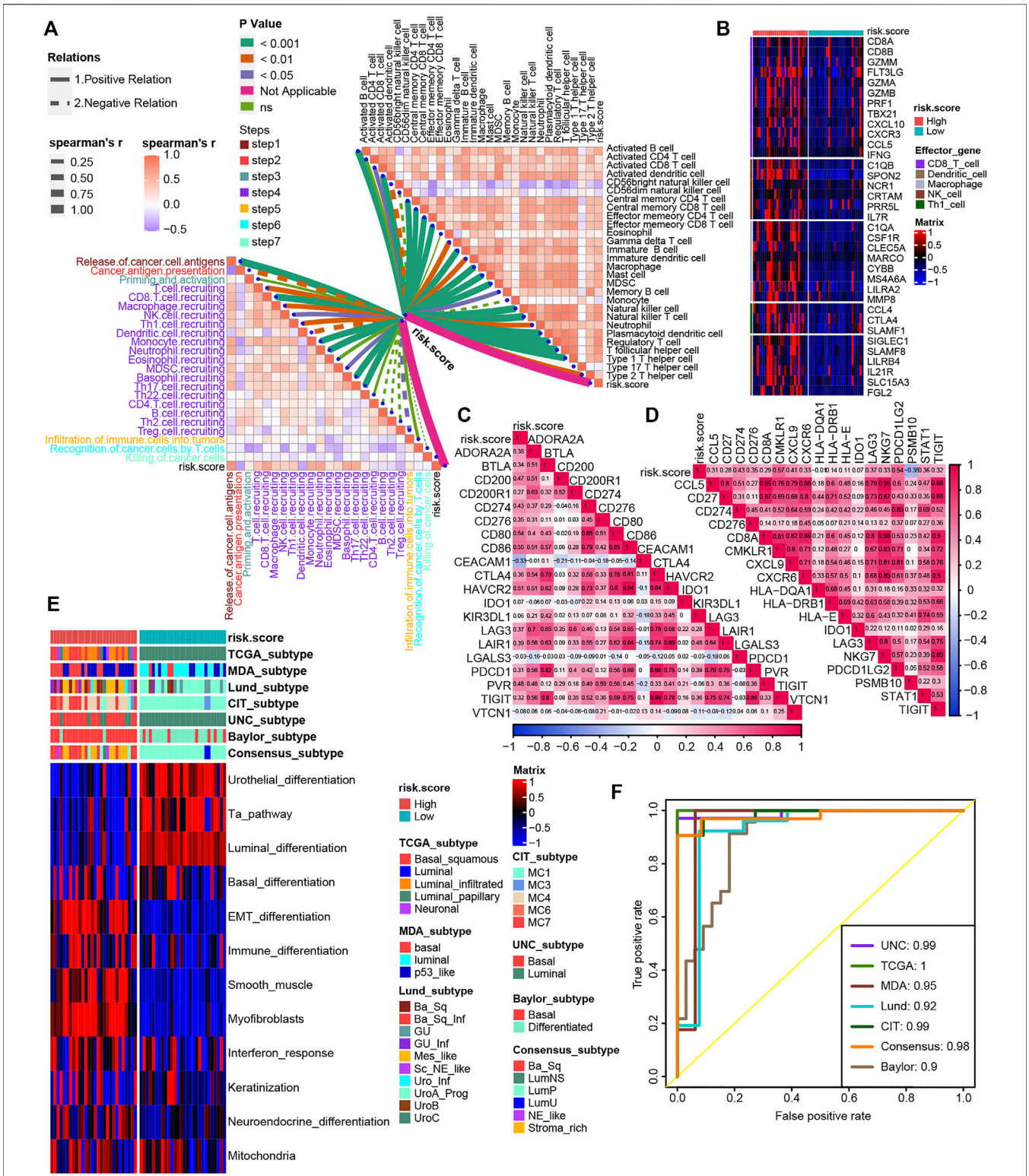

FIGURE 6 | Validation of the TNF family–based risk score roles in the Xiangya cohort. **(A)** The association between TNF-based risk score, cancer-immunity cycles **(left)**, and immune cells in the TME **(right)** in the Xiangya cohort. The different types of lines represent the positive or negative relations. The different colors of the lines represent the *p* values of the relations, and the thickness of the lines represents the strength of the relations. **(B)** The different expression patterns of effector genes of immune cells between different TNF-based risk score groups in the Xiangya cohort. **(C,D)** The association between TNF-based risk score and ICI genes and TIS genes, respectively, in the Xiangya cohort. **(E)** The heat map of different TNF-based risk score groups, seven molecular subtype classifications, and bladder cancer–associated signatures in Xiangya cohort. Activated or inhibited pathways are marked as red or blue, respectively. **(F)** AUC plot of the risk score for predicting seven molecular subtype classifications in the Xiangya cohort.

immune cell infiltration. In order to conduct a personalized evaluation of the role of TNF family members in BLCA, we have also developed and validated a TNF family–based risk score, which could be a robust tool for predicting prognosis. We further explored the relationship between the risk score and immune phenotypes and immunotherapy response of BLCA based on the specific role of TNF family members in TME. Moreover, TNF-based risk score could accurately stratify BLCA patients into basal and luminal subtypes, which reclarified the potential role for predicting the immune phenotypes and immunotherapy response from the aspect of molecular subtypes.

TNF family members, including 19 TNFSF ligands and 29 TNFRSF receptors, have a comprehensive shared ligand and receptor usage system. This system makes the TNF family members vital regulators of immunity through either coinhibited or costimulated ways (Dostert et al., 2019). TNFRSF6 can mediate the process of removing activated effector T cells, preventing immune damage by an over-long immune response (Dostert et al., 2019). Moreover, TNFRSF6 is essential for the process of cytotoxic T and NK cells killing tumor cells (Berke, 1995), whereas in its ligand, the expression of TNFSF6 in carcinoma cells could eliminate the infiltration of T cells and promote tumor proliferation and progression (Hahne et al., 1996; O'Connell et al., 1996). The higher expression of TNFRSF25 in activated T cells can promote T-cell proliferation and inflammatory cytokine production (Meylan et al., 2011; Ward-Kavanagh et al., 2016). TNFRSF4, as a costimulatory receptor, could be upregulated in $CD8^+$ T cells, $CD4^+$ T cells, and T_H1 cells after antigen recognition (Willoughby et al., 2017). Interferon-γ could upregulate the expression of TNFSF10 in T cells, NK cells, and DCs, which could induce the death of numerous carcinoma cells (Pitti et al., 1996; Dostert et al., 2019). Zhang et al. conducted comprehensive analyses of TNF family members and correlated them with prognosis, immune phenotypes, and immunotherapy in lung adenocarcinoma (LUSC) (Zhang et al., 2020). In their study, they also developed a TNF-based risk score correlated with prognosis and immune cell infiltration in LUSC. However, their predictive accuracy remained unclear. In our study, we developed two risk scores using RSF and Cox proportional hazard regression analysis, respectively. We found that the risk score developed by RSF possessed higher predictive accuracy. Li et al. compared the RSF with other prediction models and found that RSF performed best with the highest AUC (Yang et al., 2020). The reasons could be that RSF could deal with regression and classification problems at the same time and accept dirty data. As far as we know, this is the first TNF-based risk score predicting the prognosis of BLCA.

ICB therapies, including programmed cell death-1, its ligand, and cytotoxic T-lymphocyte associated protein-4, have been approved for the treatment of multiple carcinoma types, such as advanced melanoma, renal cell carcinoma, non–small cell lung cancer, and BLCA (Reck et al., 2016; Motzer et al., 2018; Jenkins and Fisher, 2021). However, response rates to ICB therapies are approximately only 15% to 20% across different carcinomas (Osipov et al., 2019). TME, consisting of carcinoma cells, immune cells, stromal cells, and extracellular molecules, plays a key role in the efficacy of immunotherapy (Son et al., 2017). The TME can be divided into noninflamed (cold) and inflamed (hot) phenotypes based on the levels of T-cell infiltration and inflammatory cytokine (Duan et al., 2020). The inflamed phenotype of TME is reported to be more sensitive to ICB therapy as the preexisting T cells in the TME are a vital determinant for immunotherapy response (Liu et al., 2020). Distinguishing the immune phenotypes of BLCA is a promising way for improving ICB response rates in BLCA. Many efforts are committing to developing a risk score for immune phenotypes (Wang et al., 2020; Liu et al., 2021), and this is the first TNF-based risk score for predicting immune phenotypes in BLCA. We not only correlated the risk score with TME immune cell infiltration in pubic databases, but also validated its role in TME using the RNA-seq cohort developed by our hospital (Xiangya cohort), which made our risk score a more robust and reliable tool for predicting immune phenotypes. Moreover, we found that the TNF-based risk score could predict the ICB response rate using 21 gene signatures closely associated with clinical response to ICB therapy from the study by Mariathasan et al. (Mariathasan et al., 2018).

BLCA is a biologically heterogeneous disease and has different clinical outcomes and responses to therapies. Besides the conventional staging system using clinicopathological features, more and more studies are focusing on dividing BLCA into molecular subtypes using gene expression profiling and unsupervised analyses (Choi et al., 2014; Kamoun et al., 2020). Until now, there are seven reported BLCA molecular classifications, including TCGA, MDA, Lund, CIT, UNC, Baylor, and consensus subtypes (Kamoun et al., 2020). Generally, the basal subtype of BLCA patients possesses more immune cell infiltration and could be more sensitive to immunotherapy and NAC. However, the different numbers, sizes, and names of molecular subtypes and the complicated detected methods impeded the clinical application of all these seven classifications. The TNF-based risk score developed by us could distinguish basal and luminal subtypes of BLCA with high predictive accuracy, which could advance the clinical application of the molecular subtypes. Interestingly, although more immune cells are infiltrating into TME in the basal subtype of patients, this subtype is associated with poorer survival outcomes (Choi et al., 2014; Warrick et al., 2019). This could explain why the TNF risk score represented an inflamed phenotype of BLCA and was associated with poorer survival outcomes.

It should be acknowledged that there are some limitations. First, although we validated our risk score in two public databases and our Xiangya cohort, all these cohorts were retrospective cohorts, and prospective cohorts are still needed for further validation. Second, immune profiles in the TME are complicated and regulated by numerous factors. We did not validate the TNF family members' role in TME *in vivo* and *in vitro*. Third, our training cohort (TCGA) was developed using RNA-seq, whereas two of our validation cohorts (GSE32894 and GSE13507) were developed using microarray. We could not correct for the batch effects. However, our risk score could be robustly validated in validation cohort

regardless of batch effects caused by different sequencing platforms, indicating that our risk score was reliable.

CONCLUSION

We developed and validated a robust TNF-based risk score, which could predict prognostic outcomes, TME, and molecular subtypes of BLCA. However, the value of risk score predicting the efficacy of immunotherapy needs further research.

DATA AVAILABILITY STATEMENT

The datasets presented in this study can be found in online repositories. The names of the repository/repositories and accession number(s) can be found in the article/**Supplementary Material**.

AUTHOR CONTRIBUTIONS

HL, SL, CL, ZX performed analyses and drafted the manuscript. HL, SL, JH, and ZX searched and downloaded the original datasets from TCGA and GEO. HL, SL, and CZ contributed to statistical analyses. HL, SL, CL, ZX, and CZ edited the pictures. CZ conceived and supervised the study. All authors contributed to writing the manuscript. All authors reviewed and approved the final manuscript.

FUNDING

This research is supported by grant of Natural Science Foundation of Hunan Province (No. 2021JJ41055) and Natural Science Foundation of Xiangya hospital (No. 2020Q19) to CZ.

ACKNOWLEDGMENTS

We sincerely thank Belaydi Othmane for revising the language of this article. We sincerely thank all participants in the study.

SUPPLEMENTARY MATERIAL

The Supplementary Material for this article can be found online at: https://www.frontiersin.org/articles/10.3389/fcell.2021.800967/full#supplementary-material

REFERENCES

Berke, G. (1995). The CTL's Kiss of Death. *Cell* 81 (1), 9–12. doi:10.1016/0092-8674(95)90365-8

Bray, F., Ferlay, J., Soerjomataram, I., Siegel, R. L., Torre, L. A., and Jemal, A. (2018). Global Cancer Statistics 2018: GLOBOCAN Estimates of Incidence and Mortality Worldwide for 36 Cancers in 185 Countries. *CA Cancer J. Clinic.* 68 (6), 394–424. doi:10.3322/caac.21492

Charoentong, P., Finotello, F., Angelova, M., Mayer, C., Efremova, M., Rieder, D., et al. (2017). Pan-cancer Immunogenomic Analyses Reveal Genotype-Immunophenotype Relationships and Predictors of Response to Checkpoint Blockade. *Cel Rep.* 18 (1), 248–262. doi:10.1016/j.celrep.2016.12.019

Chen, D. S., and Mellman, I. (2013). Oncology Meets Immunology: the Cancer-Immunity Cycle. *Immunity* 39 (1), 1–10. doi:10.1016/j.immuni.2013.07.012

Choi, W., Porten, S., Kim, S., Willis, D., Plimack, E. R., Hoffman-Censits, J., et al. (2014). Identification of Distinct Basal and Luminal Subtypes of Muscle-Invasive Bladder Cancer with Different Sensitivities to Frontline Chemotherapy. *Cancer Cell* 25 (2), 152–165. doi:10.1016/j.ccr.2014.01.009

Colaprico, A., Silva, T. C., Olsen, C., Garofano, L., Cava, C., Garolini, D., et al. (2016). TCGAbiolinks: an R/Bioconductor Package for Integrative Analysis of TCGA Data. *Nucleic Acids Res.* 44 (8), e71. doi:10.1093/nar/gkv1507

Damrauer, J. S., Hoadley, K. A., Chism, D. D., Fan, C., Tiganelli, C. J., Wobker, S. E., et al. (2014). Intrinsic Subtypes of High-Grade Bladder Cancer Reflect the Hallmarks of Breast Cancer Biology. *Proc. Natl. Acad. Sci.* 111 (8), 3110–3115. doi:10.1073/pnas.1318376111

Dostert, C., Grusdat, M., Letellier, E., and Brenner, D. (2019). The TNF Family of Ligands and Receptors: Communication Modules in the Immune System and beyond. *Physiol. Rev.* 99 (1), 115–160. doi:10.1152/physrev.00045.2017

Duan, Q., Zhang, H., Zheng, J., and Zhang, L. (2020). Turning Cold into Hot: Firing up the Tumor Microenvironment. *Trends Cancer* 6 (7), 605–618. doi:10.1016/j.trecan.2020.02.022

Gajewski, T. F. (2015). The Next Hurdle in Cancer Immunotherapy: Overcoming the Non-T-cell-inflamed Tumor Microenvironment. *Semin. Oncol.* 42 (4), 663–671. doi:10.1053/j.seminoncol.2015.05.011

Hahne, M., Rimoldi, D., Schröter, M., Romero, P., Schreier, M., French, L. E., et al. (1996). Melanoma Cell Expression of Fas(Apo-1/CD95) Ligand: Implications for Tumor Immune Escape. *Science* 274 (5291), 1363–1366. doi:10.1126/science.274.5291.1363

Hänzelmann, S., Castelo, R., and Guinney, J. (2013). GSVA: Gene Set Variation Analysis for Microarray and RNA-Seq Data. *BMC Bioinformatics* 14, 7. doi:10.1186/1471-2105-14-7

Havel, J. J., Chowell, D., and Chan, T. A. (2019). The Evolving Landscape of Biomarkers for Checkpoint Inhibitor Immunotherapy. *Nat. Rev. Cancer* 19 (3), 133–150. doi:10.1038/s41568-019-0116-x

Hu, J., Yu, A., Othmane, B., Qiu, D., Li, H., Li, C., et al. (2021). Siglec15 Shapes a Non-inflamed Tumor Microenvironment and Predicts the Molecular Subtype in Bladder Cancer. *Theranostics* 11 (7), 3089–3108. doi:10.7150/thno.53649

Jenkins, R. W., and Fisher, D. E. (2021). Treatment of Advanced Melanoma in 2020 and beyond. *J. Invest. Dermatol.* 141 (1), 23–31. doi:10.1016/j.jid.2020.03.943

Kamoun, A., de Reyniès, A., Allory, Y., Sjödahl, G., Robertson, A. G., Seiler, R., et al. (2020). A Consensus Molecular Classification of Muscle-Invasive Bladder Cancer. *Eur. Urol.* 77 (4), 420–433. doi:10.1016/j.eururo.2019.09.006

Lee, J.-S., Leem, S.-H., Lee, S.-Y., Kim, S.-C., Park, E.-S., Kim, S.-B., et al. (2010). Expression Signature ofE2F1and its Associated Genes Predict Superficial to Invasive Progression of Bladder Tumors. *J. Clin. Oncol.* 28 (16), 2660–2667. doi:10.1200/jco.2009.25.0977

Liu, X., Hoft, D. F., and Peng, G. (2020). Senescent T Cells within Suppressive Tumor Microenvironments: Emerging Target for Tumor Immunotherapy. *J. Clin. Invest.* 130 (3), 1073–1083. doi:10.1172/jci133679

Liu, Z., Tang, Q., Qi, T., Othmane, B., Yang, Z., Chen, J., et al. (2021). A Robust Hypoxia Risk Score Predicts the Clinical Outcomes and Tumor Microenvironment Immune Characters in Bladder Cancer. *Front. Immunol.* 12, 725223. doi:10.3389/fimmu.2021.725223

Mariathasan, S., Turley, S. J., Nickles, D., Castiglioni, A., Yuen, K., Wang, Y., et al. (2018). TGFβ Attenuates Tumour Response to PD-L1 Blockade by Contributing to Exclusion of T Cells. *Nature* 554 (7693), 544–548. doi:10.1038/nature25501

Marzouka, N.-a. -d., Eriksson, P., Rovira, C., Liedberg, F., Sjödahl, G., and Höglund, M. (2018). A Validation and Extended Description of the Lund Taxonomy for Urothelial Carcinoma Using the TCGA Cohort. *Sci. Rep.* 8 (1), 3737. doi:10.1038/s41598-018-22126-x

Meylan, F., Richard, A. C., and Siegel, R. M. (2011). TL1A and DR3, a TNF Family Ligand-Receptor Pair that Promotes Lymphocyte Costimulation, Mucosal Hyperplasia, and Autoimmune Inflammation. *Immunol. Rev.* 244 (1), 188–196. doi:10.1111/j.1600-065X.2011.01068.x

Mo, Q., Nikolos, F., Chen, F., Tramel, Z., Lee, Y.-C., Hayashi, K., et al. (2018). Prognostic Power of a Tumor Differentiation Gene Signature for Bladder Urothelial Carcinomas. *J. Natl. Cancer Inst.* 110 (5), 448–459. doi:10.1093/jnci/djx243

Motzer, R. J., Tannir, N. M., McDermott, D. F., Arén Frontera, O., Melichar, B., Choueiri, T. K., et al. (2018). Nivolumab Plus Ipilimumab versus Sunitinib in Advanced Renal-Cell Carcinoma. *N. Engl. J. Med.* 378 (14), 1277–1290. doi:10.1056/NEJMoa1712126

O'Connell, J., O'Sullivan, G. C., Collins, J. K., and Shanahan, F. (1996). The Fas Counterattack: Fas-Mediated T Cell Killing by colon Cancer Cells Expressing Fas Ligand. *J. Exp. Med.* 184 (3), 1075–1082. doi:10.1084/jem.184.3.1075

Osipov, A., Saung, M. T., Zheng, L., and Murphy, A. G. (2019). Small Molecule Immunomodulation: the Tumor Microenvironment and Overcoming Immune Escape. *J. Immunother. Cancer* 7 (1), 224. doi:10.1186/s40425-019-0667-0

Patel, V. G., Oh, W. K., and Galsky, M. D. (2020). Treatment of Muscle-invasive and Advanced Bladder Cancer in 2020. *CA Cancer J. Clin.* 70 (5), 404–423. doi:10.3322/caac.21631

Pitti, R. M., Marsters, S. A., Ruppert, S., Donahue, C. J., Moore, A., and Ashkenazi, A. (1996). Induction of Apoptosis by Apo-2 Ligand, a New Member of the Tumor Necrosis Factor Cytokine Family. *J. Biol. Chem.* 271 (22), 12687–12690. doi:10.1074/jbc.271.22.12687

Rebouissou, S., Bernard-Pierrot, I., de Reyniès, A., Lepage, M.-L., Krucker, C., Chapeaublanc, E., et al. (2014). EGFR as a Potential Therapeutic Target for a Subset of Muscle-Invasive Bladder Cancers Presenting a Basal-like Phenotype. *Sci. Transl. Med.* 6 (244), 244ra91. doi:10.1126/scitranslmed.3008970

Reck, M., Rodríguez-Abreu, D., Robinson, A. G., Hui, R., Csőszi, T., Fülöp, A., et al. (2016). Pembrolizumab versus Chemotherapy for PD-L1-Positive Non-small-cell Lung Cancer. *N. Engl. J. Med.* 375 (19), 1823–1833. doi:10.1056/NEJMoa1606774

Robertson, A. G., Kim, J., Al-Ahmadie, H., Bellmunt, J., Guo, G., Cherniack, A. D., et al. (2017). Comprehensive Molecular Characterization of Muscle-Invasive Bladder Cancer. *Cell* 171 (3), 540. doi:10.1016/j.cell.2017.09.007

Sanli, O., Dobruch, J., Knowles, M. A., Burger, M., Alemozaffar, M., Nielsen, M. E., et al. (2017). Bladder Cancer. *Nat. Rev. Dis. Primers* 3, 17022. doi:10.1038/nrdp.2017.22

Siegel, R. L., Miller, K. D., and Jemal, A. (2018). Cancer Statistics, 2018. *CA Cancer J. Clinic.* 68 (1), 7–30. doi:10.3322/caac.21442

Sjödahl, G., Lauss, M., Lövgren, K., Chebil, G., Gudjonsson, S., Veerla, S., et al. (2012). A Molecular Taxonomy for Urothelial Carcinoma. *Clin. Cancer Res.* 18 (12), 3377–3386. doi:10.1158/1078-0432.Ccr-12-0077-t

Son, B., Lee, S., Youn, H., Kim, E., Kim, W., and Youn, B. (2017). The Role of Tumor Microenvironment in Therapeutic Resistance. *Oncotarget* 8 (3), 3933–3945. doi:10.18632/oncotarget.13907

Tran, L., and Theodorescu, D. (2020). Determinants of Resistance to Checkpoint Inhibitors. *Int. J. Mol. Sci.* 21 (5), 1594. doi:10.3390/ijms21051594

Wang, Y., Chen, L., Yu, M., Fang, Y., Qian, K., Wang, G., et al. (2020). Immune-related Signature Predicts the Prognosis and Immunotherapy Benefit in Bladder Cancer. *Cancer Med.* 9 (20), 7729–7741. doi:10.1002/cam4.3400

Ward-Kavanagh, L. K., Lin, W. W., Šedý, J. R., and Ware, C. F. (2016). The TNF Receptor Superfamily in Co-stimulating and Co-inhibitory Responses. *Immunity* 44 (5), 1005–1019. doi:10.1016/j.immuni.2016.04.019

Warrick, J. I., Sjödahl, G., Kaag, M., Raman, J. D., Merrill, S., Shuman, L., et al. (2019). Intratumoral Heterogeneity of Bladder Cancer by Molecular Subtypes and Histologic Variants. *Eur. Urol.* 75 (1), 18–22. doi:10.1016/j.eururo.2018.09.003

Wilkerson, M. D., and Hayes, D. N. (2010). ConsensusClusterPlus: a Class Discovery Tool with Confidence Assessments and Item Tracking. *Bioinformatics* 26 (12), 1572–1573. doi:10.1093/bioinformatics/btq170

Willoughby, J., Griffiths, J., Tews, I., and Cragg, M. S. (2017). OX40: Structure and Function - what Questions Remain? *Mol. Immunol.* 83, 13–22. doi:10.1016/j.molimm.2017.01.006

Xu, L., Deng, C., Pang, B., Zhang, X., Liu, W., Liao, G., et al. (2018). TIP: A Web Server for Resolving Tumor Immunophenotype Profiling. *Cancer Res.* 78 (23), 6575–6580. doi:10.1158/0008-5472.Can-18-0689

Yang, L., Wu, H., Jin, X., Zheng, P., Hu, S., Xu, X., et al. (2020). Study of Cardiovascular Disease Prediction Model Based on Random forest in Eastern China. *Sci. Rep.* 10 (1), 5245. doi:10.1038/s41598-020-62133-5

Zemek, R. M., De Jong, E., Chin, W. L., Schuster, I. S., Fear, V. S., Casey, T. H., et al. (2019). Sensitization to Immune Checkpoint Blockade through Activation of a STAT1/NK axis in the Tumor Microenvironment. *Sci. Transl. Med.* 11 (501), eaav7816. doi:10.1126/scitranslmed.aav7816

Zhang, C., Zhang, G., Sun, N., Zhang, Z., Zhang, Z., Luo, Y., et al. (2020). Comprehensive Molecular Analyses of a TNF Family-Based Signature with Regard to Prognosis, Immune Features, and Biomarkers for Immunotherapy in Lung Adenocarcinoma. *EBioMedicine* 59, 102959. doi:10.1016/j.ebiom.2020.102959

Conflict of Interest: The authors declare that the research was conducted in the absence of any commercial or financial relationships that could be construed as a potential conflict of interest.

Publisher's Note: All claims expressed in this article are solely those of the authors and do not necessarily represent those of their affiliated organizations, or those of the publisher, the editors and the reviewers. Any product that may be evaluated in this article, or claim that may be made by its manufacturer, is not guaranteed or endorsed by the publisher.

GLOSSARY

TNF tumor necrosis factor
BLCA bladder carcinoma
TCGA the cancer genome atlas
GEO gene expression omnibus
LASSO least absolute shrinkage and selection operator
RSF random survival forest
TME tumor microenvironment
DEG differentially expressed gene
MIBC muscle-invasive bladder carcinoma
NMIBC non–muscle-invasive bladder carcinoma
OS overall survival
FDA US food and drug administration
ICI immune checkpoint inhibitor
TNFRSF TNF receptor
TNFSF TNF ligand
RNA-seq RNA-sequencing
FPKM fragments per kilobase per million mapped fragments
GDC Genomic Data Commons
TPM transcripts per kilobase million
TIME tumor immune microenvironment
TIS T cell–associated inflammatory signature
TIP tracking tumor immunophenotype
ssGSEA single-sample gene set enrichment analysis
DC dendritic cell
NK cell natural killer cell
T_H1 cell Type 1 T helper cell
GSVA gene set variation analysis
ICB immune checkpoint blockade
FC fold change
GO Gene Ontology
KEGG Kyoto Encyclopedia of Genes and Genomes
K-M Kaplan–Meier
ROC receiver operating characteristic
MDA MDAnderson Cancer Center
CIT Cartes d'Identité des Tumeurs-Curie
UNC University of North Carolina
NAC neoadjuvant chemotherapy
LUSC lung adenocarcinoma

frontiers in Cell and Developmental Biology

ORIGINAL RESEARCH
published: 21 February 2022
doi: 10.3389/fcell.2022.810272

Identification and Quantification of Iron Metabolism Landscape on Therapy and Prognosis in Bladder Cancer

Xiaodong Song[1†], Sheng Xin[1†], Yucong Zhang[2], Jiaquan Mao[1], Chen Duan[1], Kai Cui[1], Liang Chen[1], Fan Li[1], Zheng Liu[1], Tao Wang[1], Jihong Liu[1], Xiaming Liu[1] and Wen Song[1]**

[1]Department of Urology, Tongji Hospital, Tongji Medical College, Huazhong University of Science and Technology, Wuhan, China, [2]Department of Geriatric, Tongji Hospital, Tongji Medical College, Huazhong University of Science and Technology, Wuhan, China

The morbidity of bladder cancer (BLCA) is high and has gradually elevated in recent years. BLCA is also characterized by high recurrence and high invasiveness. Due to the drug resistance and lack of effective prognostic indicators, the prognosis of patients with BLCA is greatly affected. Iron metabolism is considered to be a pivot of tumor occurrence, progression, and tumor microenvironment (TME) in tumors, but there is little research in BLCA. Herein, we used univariate COX regression analysis to screen 95 prognosis-related iron metabolism-related genes (IMRGs) according to transcription RNA sequencing and prognosis information of the Cancer Genome Atlas (TCGA) database. TCGA-BLCA cohort was clustered into four distinct iron metabolism patterns (C1, C2, C3, and C4) by the non-negative matrix factorization (NMF) algorithm. Survival analysis showed that C1 and C3 patterns had a better prognosis. Gene set variant analysis (GSVA) revealed that C2 and C4 patterns were mostly enriched in carcinogenic and immune activation pathways. ESTIMATE and single sample gene set enrichment analysis (ssGSEA) also confirmed the level of immune cell infiltration in C2 and C4 patterns was significantly elevated. Moreover, the immune checkpoint genes in C2 and C4 patterns were observably overexpressed. Studies on somatic mutations showed that the tumor mutation burden (TMB) of C1 and C4 patterns was the lowest. Chemotherapy response assessment revealed that C2 pattern was the most sensitive to chemotherapy, while C3 pattern was the most insensitive. Then we established the IMRG prognosis signature (IMRGscore) by the least absolute shrinkage and selection operator (LASSO), including 13 IMRGs (TCIRG1, CTSE, ATP6V0A1, CYP2C8, RNF19A, CYP4Z1, YPEL5, PLOD1, BMP6, CAST, SCD, IFNG, and ASIC3). We confirmed IMRGscore could be utilized as an independent prognostic indicator. Therefore, validation and quantification of iron metabolism landscapes will help us comprehend the formation of the BLCA immunosuppressive microenvironment, guide the selection of chemotherapeutic drugs and immunotherapy, and predict the prognosis of patients.

Keywords: bladder cancer, iron metabolism, tumor microenvionment, prognostic signature, nomogram, bioinformactics

OPEN ACCESS

Edited by:
Yongwen Luo,
Wuhan University, China

Reviewed by:
Qingping Jiang,
Third Affiliated Hospital of Guangzhou Medical University, China
Dong Ren,
The First Affiliated Hospital of Sun Yat-sen University, China
Man-Li Luo,
Sun Yat-sen Memorial Hospital, China
Liang Liang,
Xi'an Jiaotong University, China

***Correspondence:**
Xiaming Liu
xmliu77@hust.edu.cn
Wen Song
songwen922@163.com

†These authors have contributed equally to this work

Specialty section:
This article was submitted to Molecular and Cellular Pathology, a section of the journal Frontiers in Cell and Developmental Biology

Received: *06 November 2021*
Accepted: *17 January 2022*
Published: *21 February 2022*

Citation:
Song X, Xin S, Zhang Y, Mao J, Duan C, Cui K, Chen L, Li F, Liu Z, Wang T, Liu J, Liu X and Song W (2022) Identification and Quantification of Iron Metabolism Landscape on Therapy and Prognosis in Bladder Cancer. Front. Cell Dev. Biol. 10:810272. doi: 10.3389/fcell.2022.810272

INTRODUCTION

Bladder cancer (BLCA) is one of the most familiar malignant tumors in the urinary system, with about 81400 new cases and 17900 deaths in the United States in 2020 (Siegel et al., 2020). Approximately 75% of BLCA was found to be non-muscle invasive bladder cancer (NMIBC), which was characterized by a high recurrence rate (45% 5-year recurrence rate) (Berdik, 2017; Babjuk et al., 2019). Transurethral resection of bladder tumor (TURBT), chemotherapy, BCG vaccine, radiotherapy, and radical cystectomy are the main treatments for BLCA patients (Berdik, 2017). Chemotherapy and immunotherapy are also important strategies for conservative treatment of BLCA (Yin et al., 2016; Rouanne et al., 2018). However, some patients are not sensitive to these drug therapies. Due to the high recurrence rate, high metastatic risk, and patient's dissatisfaction with the treatment effect, it is of great significance to identify and quantify some molecular landscapes that have impacts on the choice of drug treatment, and explore a novel indicator that predicts the prognosis of BLCA patients.

Iron is a vital trace element for cell proliferation and growth in the human body (Torti and Torti, 2013). In cancer, the absorbability, effusion, storage, and regulation of iron are entirely disturbed, which indicates that the reprogramming of iron metabolism would induce the dysregulation in tumor cells division and survival (Andrews, 2008; Manz et al., 2016; Wang et al., 2018; Jung et al., 2019). Iron plays a dual role in cancer (Thévenod, 2018). Epidemiological investigations revealed that excess iron was a hazard factor of carcinogenesis (Stevens et al., 1994; Wu et al., 2004; Fonseca-Nunes et al., 2014). The accumulation of iron supports tumor worsening in proliferation, metabolism, and metastasis (Torti et al., 2018). Cancer cells exhibit a phenotype search for iron through disordering regulation of iron-binding proteins (Dufès et al., 2013; Bialasek et al., 2019). On the other hand, iron dependence of cancer cells affects many cell death modes, including ferroptosis, a form of iron-dependent cell death (Mou et al., 2019; Battaglia et al., 2020). Inducing ferroptosis of cancer cells has become a new hotspot in the research and development of cancer treatment (Hassannia et al., 2019; Xu et al., 2019).

There has been little research on iron metabolism in BLCA. The study was conducted to confirm whether iron metabolism had an effect on the molecular microenvironment of BLCA, as well as its ability to predict the clinical prognosis. We first clustered the TCGA-BLCA cohort into different iron metabolic patterns on the basis of the expression of iron metabolism-related genes (IMRGs). Then the survival prognosis, GSVA analysis, tumor immune microenvironment (TIME), somatic mutations chemotherapy, and immunotherapy response among different patterns were analyzed. Eventually, we established a prognostic signature associated with iron metabolism and confirmed that it is an effective independent predictor in BLCA patients.

TABLE 1 | Characteristics of patients included in the study.

Variable	TCGA-BLCA cohort (n = 400)	GSE13507 cohort (n = 165)
	Number (%)	Number (%)
Age		
≤70	228 (57.00)	109 (66.06)
>70	172 (43.00)	56 (33.94)
Gender		
MALE	296 (74.00)	135 (81.82)
FEMALE	104 (26.00)	30 (18.18)
T stage		
TX	1 (0.25)	0
T0	1 (0.25)	0
Ta	0	24 (14.55)
T1	3 (0.75)	80 (48.48)
T2	117 (29.25)	31 (18.79)
T3	190 (47.5)	19 (11.52)
T4	57 (14.25)	11 (6.67)
Unknow	31 (7.75)	0
N stage		
NX	36 (9.00)	1 (0.61)
N0	233 (58.25)	149 (90.30)
N1	44 (11.00)	8 (4.85)
N2	75 (18.75)	6 (3.64)
N3	7 (1.75)	1 (0.61)
Unknow	5 (1.25)	0
M stage		
MX	194 (48.50)	0
M0	193 (48.25)	158 (95.76)
M1	11 (2.75)	7 (4.24)
Unknow	2 (0.50)	0
Pathologic stage		
Stage 0	0	23 (13.94)
Stage I	2 (0.50)	80 (48.48)
Stage II	127 (31.75)	26 (15.76)
Stage III	138 (34.50)	29 (17.58)
Stage IV	131 (32.75)	7 (4.24)
unknow	2 (0.50)	0
Histologic grade		
Low grade	20 (5.00)	105 (63.64)
High grade	377 (94.25)	60 (36.36)
unknow	3 (0.75)	0

MATERIALS AND METHODS

Retrieval of Iron Metabolism-Related Genes

A set of IMRGs was sorted from multiple gene sets from Molecular Signatures Database (MSigDB) (http://www.gsea-msigdb.org/gsea/msigdb/index.jsp), including GOMF_IRON_ION_BINDING, GOBP_IRON_ION_TRANSPORT, GOBP_RESPONSE_TO_IRON_ION, GOBP_IRON_ION_METABOLISM, GOBP_IRON_IMPORT_INTO_CELL, GOBP_IRON_ION_IMPORT_ACROSS_PLASMA_MEMBRANE, GOMF_2_IRON_2_SULFUR_CLUSTER_BINDING, GOMF_4_IRON_4_SULFUR_CLUSTER_BINDING, GOBP_IRON_COORDINATION_ENTITY_TRANSPORT, GOBP_CELLULAR_IRON_ION_METABOLISM, GOBP_HEME_METABOLIC_PROCESS, HEME_BIOSYNTHETIC_PROCESS, MODULE_540, HALLMARK_HEME_METABOLISM and REACTOME_IRON_UPTAKE_AND_TRANSPORT. After removing the duplicate genes from all gene sets, a total of 515 IMRGs were retrieved.

TABLE 2 | Prognosis-related IMRGs selected by univariate COX regression analysis.

Gene	HR	z	*p*-value
AIFM3	0.73913	−3.0568	0.00224
ALKBH2	0.71241	−2.4545	0.01411
ALKBH3	1.35869	2.1987	0.02790
ALOX5	0.85793	−2.8965	0.00377
ASIC3	0.68739	−2.2624	0.02367
ATP5IF1	0.71955	−2.1818	0.02913
ATP6V0A1	1.81787	3.6315	0.00028
ATP6V0D1	1.45896	2.7342	0.00625
ATP6V1A	1.37125	2.0984	0.03587
ATP6V1C2	1.28480	2.2647	0.02353
ATP6V1G3	2.54732	2.9203	0.00350
BMP6	1.30778	2.9345	0.00334
CAST	1.33555	2.8334	0.00460
CDO1	1.25977	2.3200	0.02034
CIAO3	0.64021	−2.3552	0.01851
CIR1	0.52578	−3.1615	0.00157
CISD1	1.28174	2.0195	0.04343
CLTC	1.52718	3.0834	0.00205
CROCCP2	0.66104	−2.9905	0.00278
CTSE	0.84792	−3.9943	0.00006
CUL1	1.46334	2.1223	0.03381
CYBRD1	1.13803	2.1286	0.03329
CYP19A1	1.82637	3.2558	0.00113
CYP1B1	1.12555	2.3874	0.01697
CYP26B1	1.22486	2.8893	0.00386
CYP27B1	0.76528	−2.0634	0.03908
CYP2C8	0.48055	−3.2681	0.00108
CYP2D6	0.53783	−2.5791	0.00991
CYP2D7	0.39076	−3.3122	0.00093
CYP2F1	1.47375	2.3839	0.01713
CYP2R1	0.68076	−2.2516	0.02434
CYP2W1	1.14759	2.2957	0.02169
CYP3A5	0.88535	−2.1530	0.03132
CYP4A22	0.01075	−2.3088	0.02095
CYP4F12	0.85576	−3.1193	0.00181
CYP4F8	0.89174	−2.6547	0.00794
CYP4Z1	0.51083	−3.0875	0.00202
CYP4Z2P	0.71692	−3.1295	0.00175
CYP51A1	1.54962	3.0788	0.00208
CYP7B1	1.25543	2.0346	0.04189
DNM2	0.72877	−2.6658	0.00768
ENDOD1	1.36254	3.4875	0.00049
EPOR	0.79640	−2.2602	0.02381
FA2H	0.86757	−2.3261	0.02001
FECH	1.29593	2.0714	0.03832
FTO	1.44207	2.1268	0.03344
G6PD	1.18156	2.4243	0.01534
GCLM	1.19098	2.5395	0.01110
HJV	0.00736	−2.2164	0.02667
HRG	0.28674	−1.9665	0.04924
IFNG	0.72938	−2.4603	0.01388
ISCU	0.69174	−2.1696	0.03004
LAMP2	1.22151	2.0780	0.03771
MBOAT2	1.31363	3.5807	0.00034
MKRN1	0.66446	−2.3893	0.01688
MYC	1.14183	2.4370	0.01481
NARF	0.73477	−2.3869	0.01699
NDUFV2	0.71090	−2.3388	0.01934
NFE2	1.25892	2.0291	0.04244
NUBPL	1.71372	2.1941	0.02823
OGFOD1	1.56046	2.0597	0.03943
P3H1	1.27676	2.5856	0.00972
P3H3	1.16777	2.4532	0.01416
P4HA2	1.33888	2.9448	0.00323
P4HA3	1.28168	2.8335	0.00460
PGLS	0.75124	−1.9790	0.04782
PHF8	0.73442	−2.3199	0.02034
PLOD1	1.32204	2.9487	0.00319
PPEF1	1.96121	2.6470	0.00812
PTGIS	1.13599	2.9572	0.00310
RAB11B	0.67495	−2.4727	0.01341
RBM5	0.73620	−2.2846	0.02234
REV3L	1.40219	2.3541	0.01857
RNF19A	0.71735	−3.2263	0.00125
RSAD1	0.73571	−2.1465	0.03184
SCD	1.14688	2.6027	0.00925
SIDT2	1.45914	2.4669	0.01363
SLC25A28	0.75484	−2.0647	0.03895
SLC25A38	0.71371	−2.4859	0.01292
SLC39A14	1.24303	2.5771	0.00996
SLC6A9	1.23132	2.3060	0.02111
SLC7A11	1.16394	2.7767	0.00549
SRI	0.78060	−1.9652	0.04939
STEAP4	1.17801	2.3779	0.01741
TCIRG1	0.70379	−4.0200	0.00006
TET1	2.00528	2.6694	0.00760
TFRC	1.16560	2.2608	0.02377
TMCC2	1.38726	2.8966	0.00377
TNS1	1.11924	2.0886	0.03674
TSPO	0.79418	−2.8037	0.00505
TYW5	0.46331	−2.2249	0.02609
UCP2	0.89329	−2.0547	0.03991
UGT1A1	0.76531	−2.2396	0.02512
UGT1A4	6.38284	2.1260	0.03350
YPEL5	0.62817	−3.0093	0.00262

(Continued in next column)

(*Continued*)

HR, hazard ratio.

Acquisition and Process of Original Data

Transcription RNA sequencing, clinical data, and somatic mutation data for patients with BLCA were obtained from the Cancer Genome Atlas (TCGA) database (https://portal.gdc.cancer.gov/). The cohort included 411 BLCA tissues and 19 normal bladder tissues. The TCGA-BLCA level 3 RNA-sequencing data was downloaded as fragments per kilobase of transcript per million mapped reads (FPKM), and when multiple Ensembl IDs were mapped to a single gene symbol in the RNA sequencing data, gene expression is annotated in an average expression. The GSE13507 dataset was analyzed as an external validation cohort. The gene expression profile and clinical information for the microarray dataset came from the Gene Expression Synthesis (GEO) database (https://www.ncbi.nlm.nih.gov/geo/). All sequencing data were processed with log two transformation, background adjustment, normalization, final summarization through the "Affy" package in R. The clinical information of all BLCA patients included in this study is shown in **Tables 1**, **2**.

NMF Clustering for Iron Metabolism Patterns

We matched IMRGs' RNAseq data and overall survival (OS) information of the TCGA-BLCA dataset. A univariate Cox

regression analysis was carried out to determine the prognosis-related IMRGs in BLCA, with a screening criterion of $p < 0.05$. Non-negative matrix factorization (NMF) is applied to determine distinct iron metabolism-related patterns with the help of the "NMF" R package. NMF algorithm decomposes the original matrix into two non-negative matrices to identify the potential features in the gene expression profile (Brunet et al., 2004). Repeat the deposition and aggregate the results to obtain consistent clustering. According to the cophenetic coefficient, contour, and sample size, k = 4 was determined as the best cluster number.

GSVA

Gene set variant analysis (GSVA), is a nonparametric, unsupervised algorithm. GSVA transforms the isolate gene expression matrix to an expression matrix of particular gene sets as features. The algorithm is implemented based on the "GSVA" R package. The difference of expression matrix after transformation was analyzed by the "limma" package to find the difference of enriched functions among different iron metabolic patterns.

Evaluation of Tumor Immune Microenvironment

In order to assess the TIME status of BLCA, we used single sample gene set enrichment analysis (ssGSEA), ESTIMATE, and CIBERSORT in R. ssGSEA investigated congenital and adaptive immune cells as well as a variety of immune-related functions. The Normalized Enrichment Score (NES) was to embody the relative amount of each TIME infiltration unit in patients. ESTIMATE predicted the level of infiltrating matrix and immune cells by calculating stromal and immune scores, comprehensively obtained the ESTIMATE score for evaluating the TIME. We also evaluated the relative fraction of 22 tumor-infiltrating immune cells (TIICs), including B cells, T cells, natural killer (NK) cells, macrophages, dendritic cells (DCs), eosinophils, neutrophils, and so on in each cancer sample with CIBERSORT algorithm. $p < .05$ was the threshold of a credible sample for estimating the proportion of immune cells.

Evaluation of Immunotherapy and Chemotherapy on Iron Metabolism Patterns

Tumor Immune Dysfunction and Exclusion (TIDE) score is a computational framework developed based on the analysis and modeling of characteristic genes for T cell exclusion and T cell dysfunction in immunosuppression at high levels of cytotoxic T lymphocytes (CTL) (Jiang et al., 2018). We applied four indicators to predict the efficacy of immunotherapy, including exclusion score, dysfunction score, microsatellite instability (MSI), and TIDE. The chemotherapeutic response of BLCA patients was evaluated by Genomics of Drug Sensitivity in Cancer (GDSC) (https://www.cancerRxgene.org). Six chemotherapeutic drugs in BLCA treatment were chosen, including Gemcitabine, Cisplatin, Docetaxel, Mitomycin-C, Doxorubicin, and Paclitaxel. The ridge regression algorithm was used to calculate the half-maximal inhibitory concentration (IC50), and satisfactory prediction accuracy was obtained through 10 times cross-validation (Geeleher et al., 2014). The calculation process was completed by the "pRRophetic" R package.

Construction and Validation of IMRG Prognostic Signature

According to the prognosis-related IMRGs in the univariate Cox regression model, the "glmnet" package in R performed the least absolute shrinkage and selection operator (LASSO) to identify important prognostic IMRGs and select one standard error (SE) above the minimum criteria. The multivariate Cox regression model made it more optimized and practical. Finally, the IMRGscore formula was obtained:

$$\begin{aligned} \textit{Risk score} = {} & (\textit{exp Gene1} \times \textit{coefficient gene1}) \\ & + (\textit{exp Gene2} \times \textit{coefficient gene2}) + \ldots \\ & + (\textit{exp GeneN} \times \textit{coefficient GeneN}) \end{aligned}$$

On the basis of the optimal cut-off of IMRGscore obtained by the "surv_cutpoint" function in R, we divided BLCA patients into high-risk and low-risk groups. With the help of Kaplan-Meier analysis ("survival" package) and receiver operating characteristic (ROC) curve ("timeROC" package), the predictive ability of the prognostic signature was evaluated. The diagnostic accuracy was estimated by the area under the curve (AUC). The same IMRGscore calculation formula, cut-off value and, analysis methods were applied in the GSE13507 cohort to validate the signature.

Establishment and Evaluation of the Nomogram

Nomogram is an intuitive clinical prognosis prediction model integrating a variety of clinicopathological features related to prognosis. We established a nomogram model to provide a more accurate prediction of prognosis for clinical patients based on IMRGscore and clinical pathological characteristics. First, univariate Cox regression analysis was utilized to assess the predicted values of variables. Then further determined the coefficient via multivariate Cox regression analysis. The "rms" R package then established a nomogram for predicting the operating system. Concordance index (C-index) and calibration analysis were applied to estimate the accuracy and consistency. Finally, the clinical application value of the nomogram is evaluated using Decision Curve Analysis (DCA). These analyses were performed with "survival" package.

Statistical Analysis

All statistical analyses were completed with R software (version 4.0.4) in this study. Before establishing and verifying the prognostic signature, the batch differences between the TCGA dataset and GEO datasets were removed through the "sva" package. Wilcoxon rank-sum test was to verify the significance of the difference in two groups. When comparing more than two

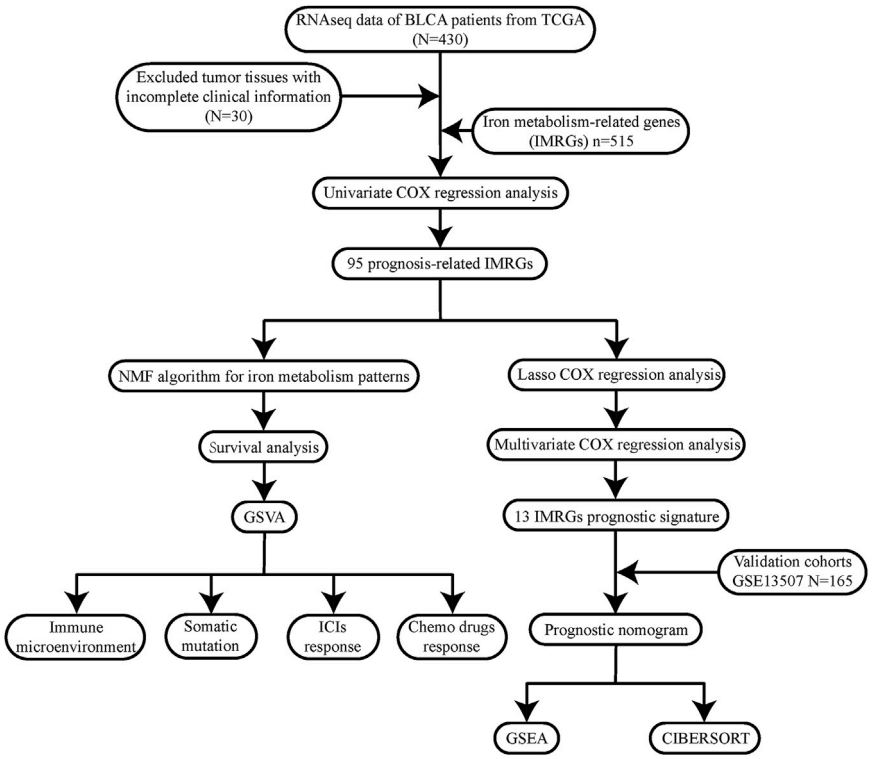

FIGURE 1 | Flow chart of our study.

groups, the Kruskal Wallis test was selected to verify the difference. Set p-value <.05 as a statistically significant standard.

RESULTS

To describe our research intuitively and systematically, we showed the research process in **Figure 1**.

Characterization of Iron Metabolism Patterns in BLCA

Through the univariate COX regression analysis ($p < .05$) of the TCGA-BLCA patients with integrated survival information and cancer tissue expression profile, 95 IMRGs were selected as prognosis-related genes (**Table 1**). Then we clustered the TCGA-BLCA cohort by NMF algorithm based on these genes. According to cophenetic coefficients, we decided k = 4 as the best cluster number (**Figure 2A**). **Figure 2B** was the NMF matrix heatmap when k = 4, including C1 subtype 89 cases, C2 subtype 141 cases, C3 subtype 91 cases, and C4 subtype 79 cases. Kaplan-Meier survival curves showed that the prognosis of patients in C1 and C3 patterns was better than that of C1 and C2 patterns (p = .020) (**Figure 2C**).

Figure 2D shows the expression of prognosis-related IMRGs in iron metabolic patterns. We also analyzed the clinicopathological differences among distinct iron metabolism patterns (**Figure 2E**). It was found that the proportion of TNM stages, pathologic stage, histologic grade, OS, DSS, and PFI events was dissimilar among patterns, and the incidence of advanced clinicopathological results in C2 and C4 patterns tended to increase.

Through GSVA analysis, we obtained the rich-concentration pathways among iron metabolism patterns (**Figure 2F**). We found that C4 pattern was positively related to multiple stromal, carcinogenic, and immune activation related pathways, including TGF-β signaling pathway, WNT signaling pathway, MAPK signaling pathway, JAK-STAT signaling pathway, T cell receptor signaling pathway, chemokine signaling pathway, B cell receptor signaling pathway, cytokine–cytokine receptor interaction, NOD-like receptor signaling pathway, TOLL-like receptor signaling pathway and so on. C2 pattern showed a similar trend to C4 pattern, but C2 was also significantly expressed in a variety of DNA damage repair related pathways. The correlation score of most carcinogenic and immune activation-related pathways was reduced in C1 and C3 patterns. While C3 pattern was also found to exhibit an enriched trend in DNA damage repair related pathways.

Tumor Immune Microenvironment of Iron Metabolism Patterns

In order to investigate whether there are differences in TIME among distinct iron metabolism patterns, we used ESTIMATE and ssGSEA scores for evaluation. ESTIMATE showed that there

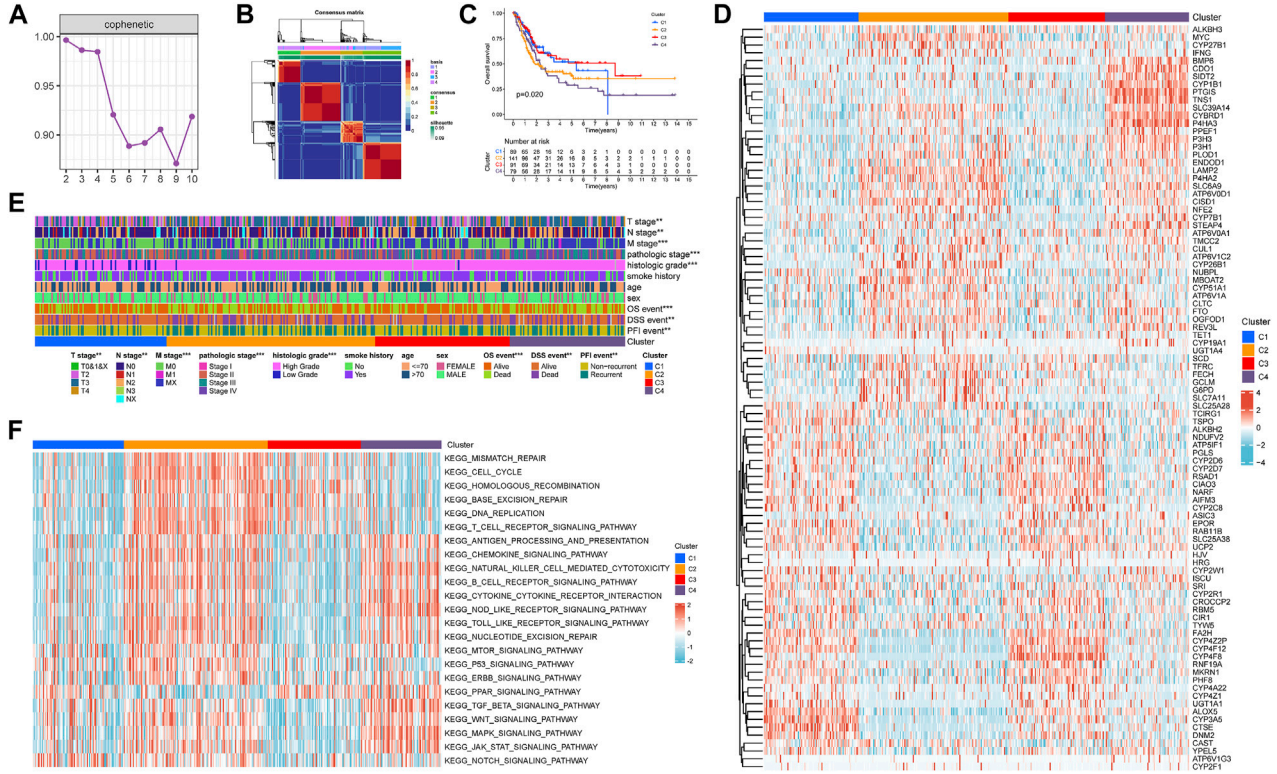

FIGURE 2 | Non-negative matrix factorization clustering of iron metabolism patterns in TCGA-BLCA cohort. **(A)** Cophenetic coefficients of NMF algorithm clustering number from 2–10 **(B)** NMF matrix heatmap when k = 4. **(C)** Kaplan-Meier survival analysis of iron metabolism patterns. **(D)** Expression Heatmap of prognosis-related IMRGs. **(E)** Correlation between iron metabolism pattern and clinicopathological characteristics. **(F)** Heatmap of GSVA analysis among iron metabolism patterns. $^{*}p < 0.05$; $^{**}p < 0.01$; $^{***}p < 0.001$.

were significant differences in the stromal score ($p < .001$), immune score ($p < .001$), and ESTIMATE score ($p < .001$) among the three patterns, of which C4 was the highest, C1 and C3 were the lowest (**Figure 3A**). Then we analyzed the infiltration differences in immune cells among iron metabolism patterns. The ssGSEA score suggested that the infiltration of all 22 TIICs in iron metabolism patterns was significantly different, among which, the ssGSEA score of TIICs in C1 and C3 patterns was lower and C2 and C4 patterns were higher (**Figure 3B**). And the enrichment trend of immune-related functions in iron metabolism patterns was similar to that of immune cell infiltration (**Figure 3C**). Additionally, the expression levels of major histocompatibility complex (MHC) molecules, costimulatory molecules, and adhesion molecules roundly decreased in C1 and C3 patterns (**Figure 3D**).

Tumor Somatic Mutation in Iron Metabolism Patterns

The tumorigenesis frequently occurs after the accumulation of gene mutations (Martincorena and Campbell, 2015). It is also reported that tumor mutation burden (TMB) can be used as a potential prognostic indicator for BLCA (Chan et al., 2019). Consequently, we used the "maftools" R package to show the distribution of somatic mutations and the differences of TMB in various iron metabolism patterns. Through the simple nucleotide variation information of TCGA-BLCA, the mutation spectrum and TMB of each sample was obtained. In BLCA samples, the 20 genes with the highest mutation rate were TP53, TTN, KMT2D, MUC16, ARID1A, KDM6A, PIK3CA, SYNE1, RB1, HMCN1, FGFR3, RYR2, KMT2C, MACF1, EP300, FLG, FAT4, STAG2, ATM and OBSCN (**Figures 4A–D**). C2 pattern had the highest mutation rate of TP53, while the mutation of TTN and KMT2D mostly happened in C3 pattern. The mutation rates of these three genes in C1 and C4 patterns were significantly reduced. Most gene mutations were missense-mutation. In patients with BLCA, high TMB indicated a better prognosis (hazard ratio [HR] = .65 (.48–.88), $p = .005$) (**Figure 4E**). Additionally, we found that the TMB of C2 and C3 patterns was significantly upper than that of C1 and C4 patterns (**Figure 4F**).

Evaluation of Immunotherapy in Iron Metabolism Patterns

Lately, immune checkpoint inhibitors (ICIs) have gradually become the second-line treatment for advanced BLCA. Therefore, we analyzed the expression of some immune checkpoints (PDCD1 (PD-1), CD274 (PD-L1), PDCD1LG2 (PD-L2), LAG3, TIGIT, IDO1, and CTLA4) among different iron metabolism patterns to predict the efficacy of immunotherapy (**Figure 5A**). The expression

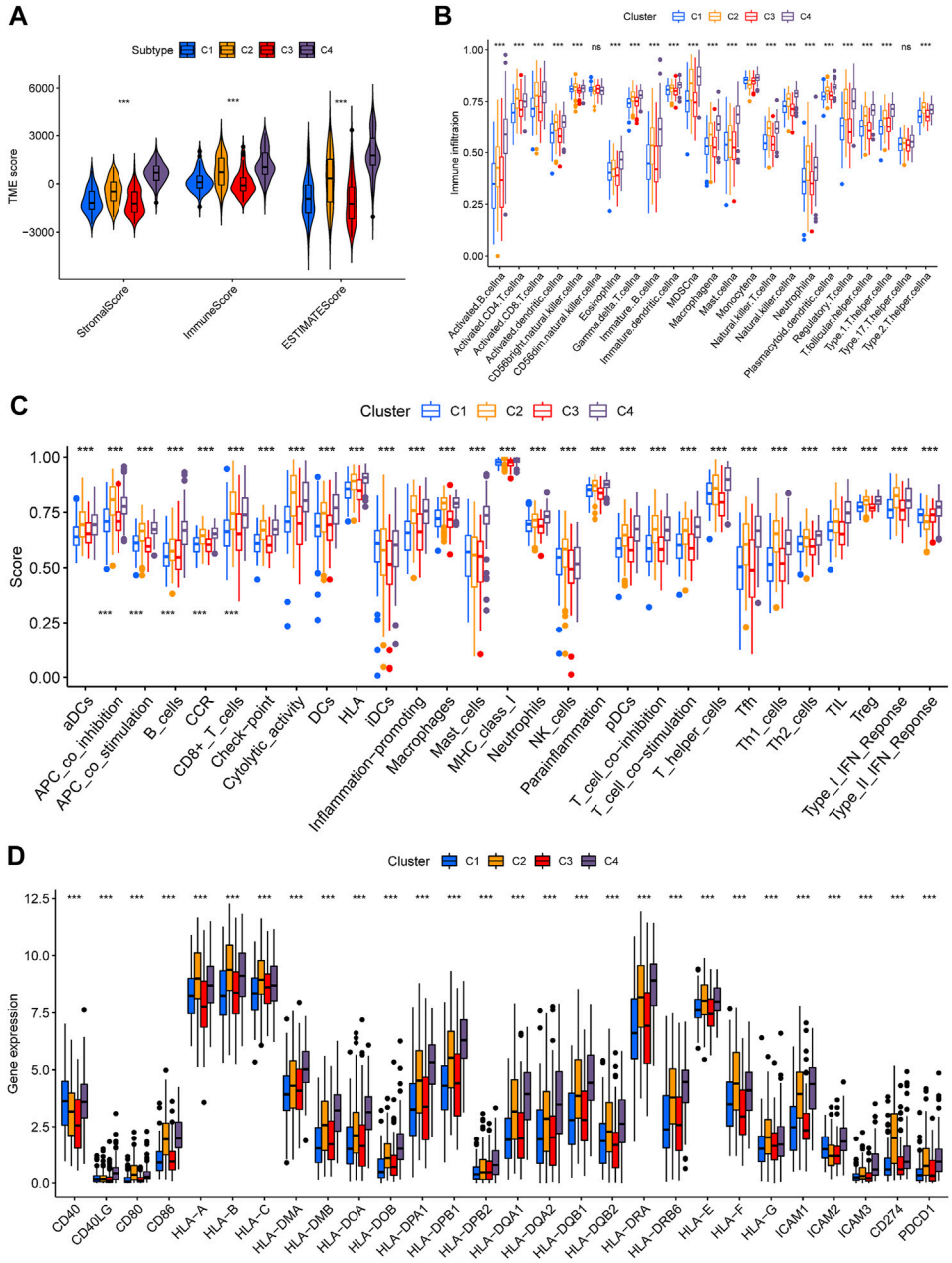

FIGURE 3 | Tumor immune microenvironment of iron metabolism patterns. **(A)** Differences of stromal, immune, and ESTIMATE scores among iron metabolism patterns **(B)** Infiltration of 22 TIICs in iron metabolism patterns. **(C)** Immune-related functions in iron metabolism patterns. **(D)** Difference analysis in MHC molecules, costimulatory molecules, and adhesion molecules of iron metabolism patterns. *$p < 0.05$; **$p < 0.01$; ***$p < 0.001$.

of all immune checkpoints in C2 and C4 patterns was signally higher than that in the other two patterns. This suggested that C2 and C4 might be more suitable for ICIs treatment. However, the high expression level of immune checkpoints may be related to the formation of the immunosuppressive microenvironment (Dunn et al., 2002). This conclusion was confirmed in **Figures 5B,C**. C4 immune exclusion score was observably higher than other iron metabolism patterns. The immune dysfunction score of C4 pattern also increased signally, while C3 was the lowest. Moreover, we used the TIDE algorithm to evaluate ICIs response, in which the MSI of C1 and the TIDE of C4 were the highest (**Figures 5D,E**).

Chemotherapeutics Drugs Response in Iron Metabolism Patterns

Chemotherapeutics drugs are widely used in the treatment of BLCA, including intravesical instillation and systemic chemotherapy. Consequently, we evaluated the IC50 values of

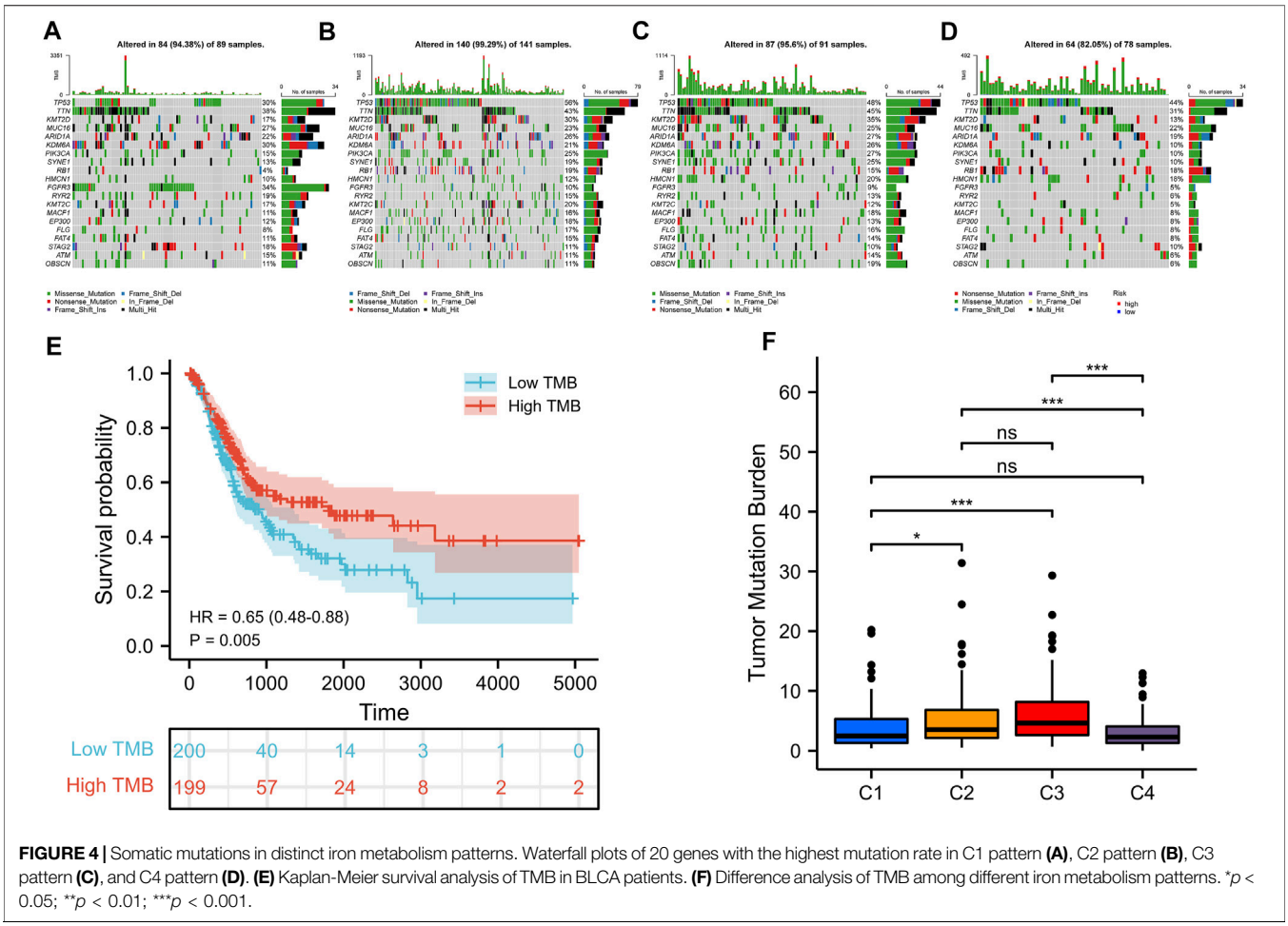

FIGURE 4 | Somatic mutations in distinct iron metabolism patterns. Waterfall plots of 20 genes with the highest mutation rate in C1 pattern **(A)**, C2 pattern **(B)**, C3 pattern **(C)**, and C4 pattern **(D)**. **(E)** Kaplan-Meier survival analysis of TMB in BLCA patients. **(F)** Difference analysis of TMB among different iron metabolism patterns. $*p < 0.05$; $**p < 0.01$; $***p < 0.001$.

six commonly used chemotherapeutic drugs (Gemcitabine, Cisplatin, Docetaxel, Mitomycin-C, Doxorubicin, and Paclitaxel) in each sample (**Figures 6A–F**). Among the six drugs, C2 patterns showed the lowest IC50 value. In Gemcitabine, Cisplatin, Docetaxel, and Paclitaxel, the IC50 value of C4 pattern was also lower than that of C1 and C3 patterns. As for C3 pattern, the IC50 value in Gemcitabine, Doxorubicin, and Paclitaxel was higher than that of C1 pattern. The above results strongly indicated that C2 was the most sensitive to chemotherapeutic drugs, C4 was the second, while C3 was more insensitive to chemotherapeutic drugs.

Establishment of the IMRG Prognostic Signature in the TCGA-BLCA Cohort

We selected 400 BLCA patients with explicit, non-zero OS and survival status to establish an IMRG signature from the TCGA database. Then used the LASSO Cox regression model to calculate, and selected an SE higher than the minimum standard to further screen the prognostic genes. Finally, through the multivariate COX regression analysis, we obtained the optimal prognostic signature containing 13 IMRGs, including TCIRG1, CTSE, ATP6V0A1, CYP2C8, RNF19A, CYP4Z1, YPEL5, PLOD1, BMP6, CAST, SCD, IFNG, and ASIC3 (**Figures 7A,B**). And constructed a formula to evaluate the IMRGscore of each patient: IMRGscore = −(.18775 × TCIRG1 expression) − (.073 × CTSE expression) + (.33856 × ATP6V0A1 expression) − (.37089 × CYP2C8 expression) − (.30306 × RNF19A expression) − (.27636 × CYP4Z1 expression) − (.35016 × YPEL5 expression) + (.17559 × PLOD1 expression) + (.25065 × BMP6 expression) + (.23398 × CAST expression) + (.13313 × SCD expression) − (.52087 × IFNG expression) − (.57726 × ASIC3 expression). And according to the optimal cut-off value (cut point = 1.78265), samples were decomposed into low- and high-risk groups. Kaplan-Meier survival analysis showed that the OS of the low-risk group was longer (hazard ratio [HR] = 4.49 (3.29–6.14), $p < .001$) (**Figure 7C**). And the AUCs for the 1-, 3-, and 5-year OS survival rates were .741, .772, and .755, respectively (**Figure 7D**). The risk score distribution, survival status graph, and expression profile heatmap were shown in **Figures 7E–G**. The proportion of patient deaths was observably positively correlated with the IMRGscore. The expression of ATP6V0A1, PLOD1, BMP6, CAST, and SCD were up-regulated in the high-risk group, while TCIRG1, CTSE, CYP2C8, RNF19A, CYP4Z1, YPEL5, IFNG, and ASIC3 were down-regulated.

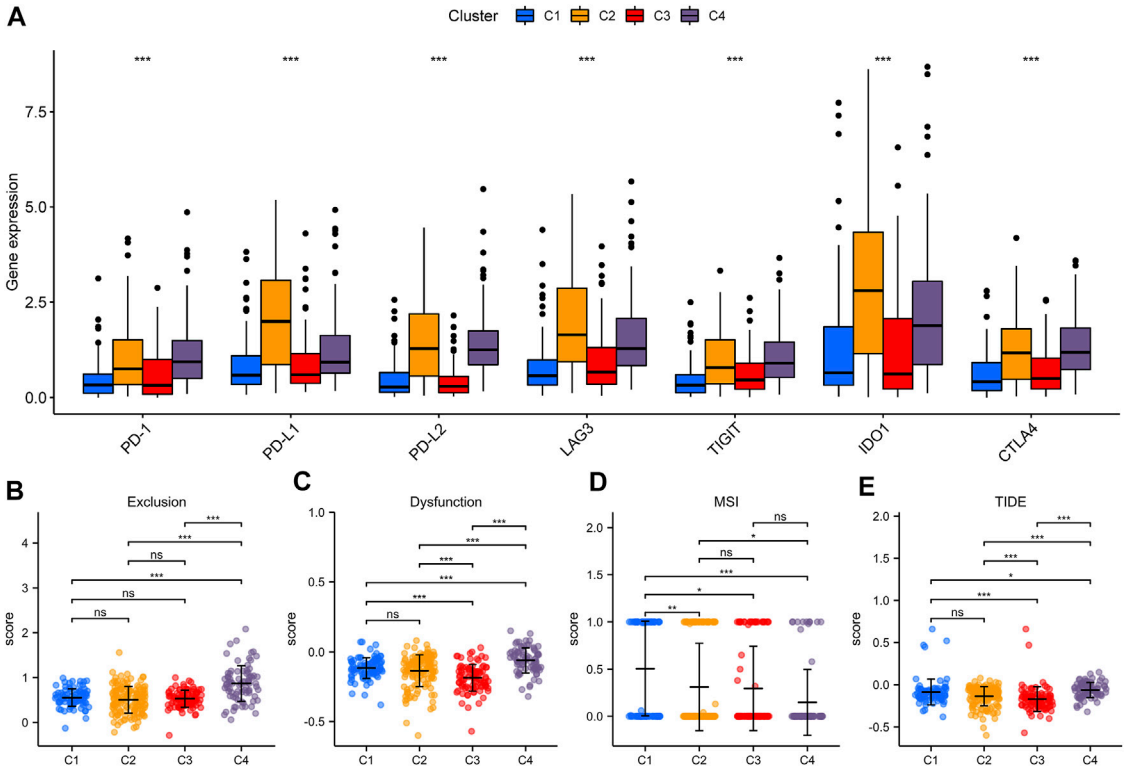

FIGURE 5 | Evaluation of immunotherapeutic therapy in iron metabolism patterns. **(A)** The expression of immune checkpoints in iron metabolism patterns. The comparisons of exclusion score **(B)**, dysfunction score **(C)**, MSI **(D)** and TIDE **(E)** among iron metabolism patterns. *$p < 0.05$; **$p < 0.01$; ***$p < 0.001$.

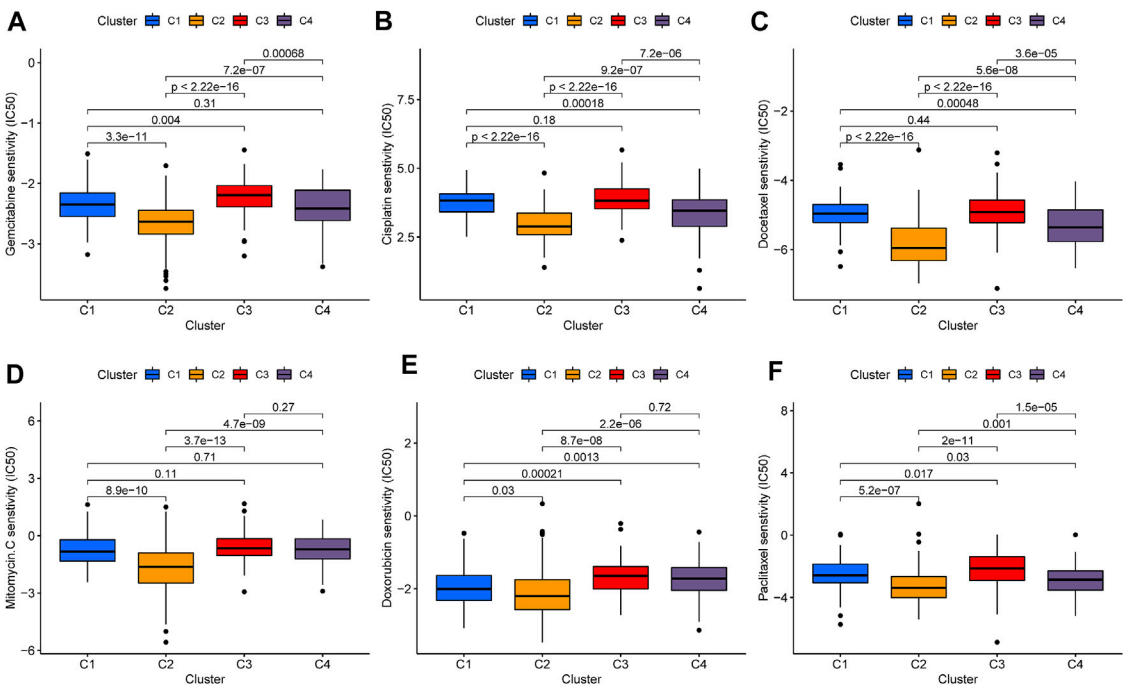

FIGURE 6 | Evaluation of chemotherapy in iron metabolism patterns. The comparisons in IC50 value of Gemcitabine **(A)**, Cisplatin **(B)**, Docetaxel **(C)**, Mitomycin-C **(D)**, Doxorubicin **(E)**, and Paclitaxel **(F)** among iron metabolism patterns.

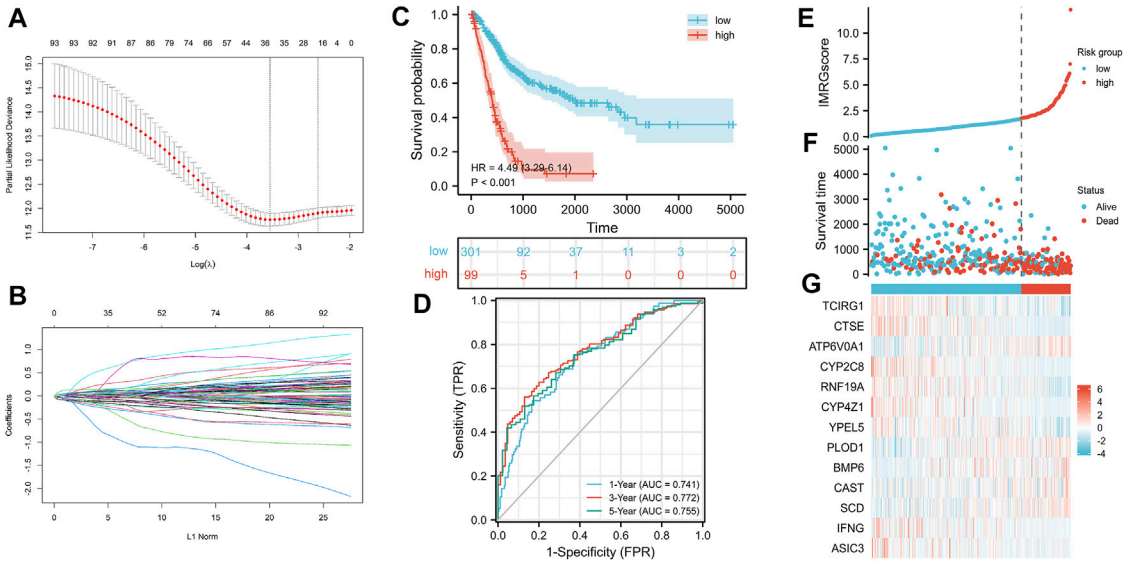

FIGURE 7 | Construction of IMRG signature and prognosis analysis based on the training set. **(A,B)** LASSO regression identified 13 IMRGs. **(C)** Kaplan-Meier survival analysis between IMRGscore-defined groups. **(D)** Time-dependent ROC curves of IMRG signature. **(E)** IMRGscore distribution. **(F)** Survival status map. **(G)** IMRGs expression profiles heatmap.

Confirmation of the IMRG Signature in the GSE13507 Cohort

As the test set, 165 BLCA samples in the GSE13507 cohort were grouped using the same IMRGscore calculation formula and cut-off value of the train set to validate the applicability and stability of the IMRG signature. Consistent with the above conclusion, patients in the low-risk group had a better OS (hazard ratio [HR] = 2.65 (1.52–4.60), $p = .001$) in the GSE13507 cohort (**Figure 8A**). The AUCs for the 1-, 3-, and 5-year OS survival rates were .753, .630, and .552, respectively (**Figure 8B**). The conclusions of the risk score distribution, survival status graph, and expression profile heatmap were consistent with the training set (**Figures 8C–E**).

Clinical Relevance of the IMRG Signature

To further supplement the clinical application value of the IMRG prognostic signature, we integrated the significant differences in IMRGscore among distinct subgroups of BLCA patients with clinicopathological characteristics (**Figure 9A**). Heatmap indicated that the advanced TNM stages, pathologic stage, histologic grade, aging, and worse OS, DSS, and PFI events had an elevated trend in IMRGscore.

Since the significant correlation between signature and clinicopathological stage, we determined whether the IMRGscore was a clinically independent predictor of BLCA patients (**Figures 9B,C**). Univariate Cox regression analysis showed that advanced pathologic stage ($p < .001$), aging ($p = .005$), and higher IMRGscore ($p < .001$) were unfavorable factors for OS. After performing the multivariate Cox regression analysis, we confirmed that the IMRGscore was an independent prognostic parameter.

Establishment of a Nomogram Based on the IMRG Signature

According to the above result from univariate Cox regression analysis of the TCGA-BLCA cohort, we established a nomogram model containing pathologic stage, age, and IMRGscore (**Figure 10A**). After removing the patients without complete information and the subgroups of variables with few samples, a total of 362 patients were included. We standardized each variable with a score from 0 to 100 and summed the scores to obtain the total number of points for each BLCA patient. The predicted 1-, 3-, and 5-year survival probabilities of each patient were standardized according to the relationship between the positions along with the prognosis and total points axes. The C-index reached 0.694 (95% CI: 0.653–0.735). **Figures 10B–D** suggested that the nomogram model predicted that the prognosis results of TCGA-BLCA patients would fit well with the actual prognosis results. Besides, DCA curves revealed that the signature provided patients with a stable and significant net benefit in BLCA patients (**Figures 10E–G**). Then based on the nomogram model, we built the Kaplan-Meier survival curve and the time-dependent ROC curves. In the TCGA-BLCA cohort, we divided samples into high- and low-risk groups with the optimal cut-off value (cut point = −.122532). Patients in the high-risk group showed a significantly poor OS (hazard ratio [HR] = 4.22 (2.92–6.10), $p < .001$, **Figure 10H**). The AUCs for the 1-, 3-, and 5-year OS survival rates were .764, .769, and .760, respectively (**Figure 10I**). Additionally, we verified the nomogram model in the GSE13507 cohort. The cut-off value was consistent with the train set. Kaplan-Meier survival analysis showed that patients in the low-risk group had a better OS than those in the high-risk group (hazard ratio [HR] = 6.47 (2.89–14.49), $p < .001$,

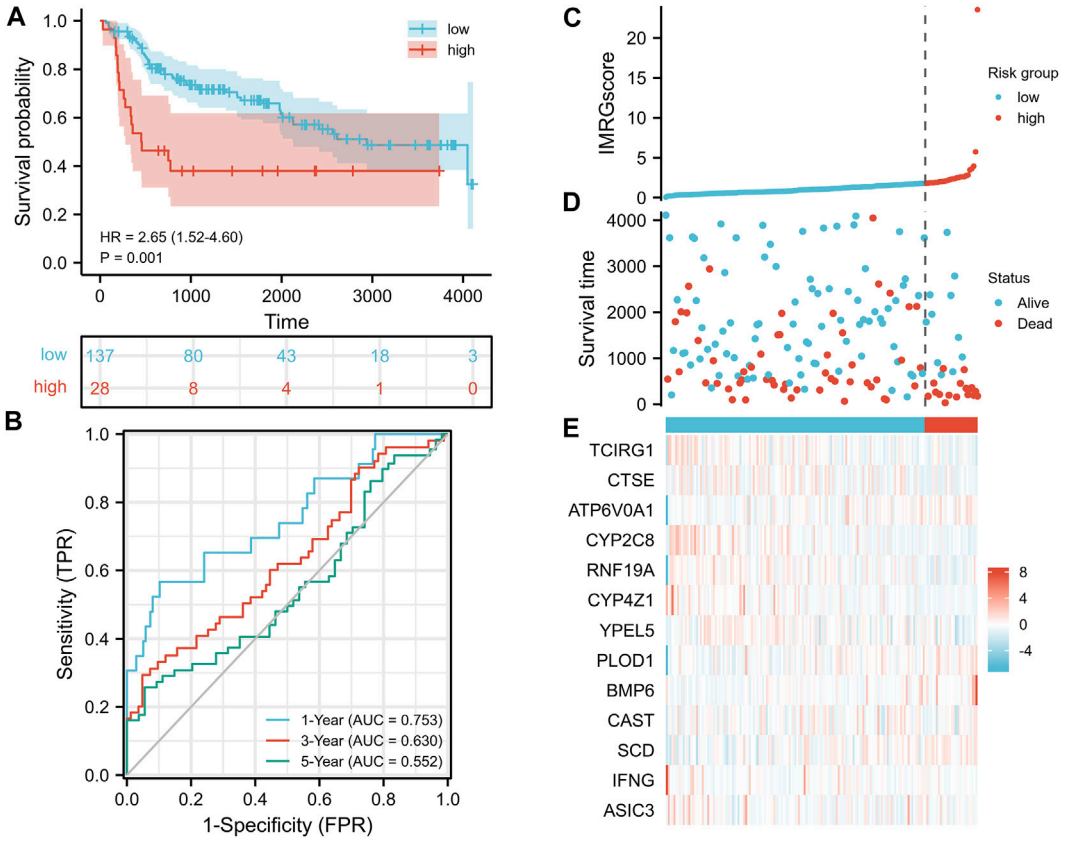

FIGURE 8 | Validation of IMRG signature based on the test set. **(A)** Kaplan-Meier survival analysis between IMRGscore-defined groups. **(B)** Time-dependent ROC curves of IMRG signature. **(C)** IMRGscore distribution. **(D)** Survival status map. **(E)** IMRGs expression profiles heatmap.

Figure 10J), and the AUCs were .896, .906, and .915 (**Figure 10K**).

GSEA

To further comprehend the effect of IMRGs expression on the biological characteristics of BLCA, we carried on GSEA analysis in IMRGscore-defined groups (**Figures 11A,B**). The Kyoto Encyclopedia of Genes and Genomes (KEGG) results revealed that in the high-risk group, the main enrichment pathways were ECM receptor interaction, regulation of actin cytoskeleton, MAPK signaling pathway, WNT signaling pathway, pathways in cancer. While the low-risk group is mainly concentrated in allograft rejection, asthma, primary immunodeficiency, and so on. Furthermore, **Figures 11C,D** showed the enrichment of the high- and low-risk groups in the Gene Ontology biological process (GOBP). We found that the low-risk group was enriched in multiple immune functions, such as activation of immune response, adaptive immune response, B cell-mediated immunity, and so on.

Correlation Between Tumor Immune Microenvironment and IMRG Signature

As we mentioned before, iron metabolism is closely related to TIME. Based on the CIBERSORT algorithm, we calculated the proportion of 22 TIICs in each TCGA-BLCA sample (**Figure 12A**). After selecting samples with significant immune cell fraction results ($p < .05$), 195 samples were included in the difference analysis, including 141 cases in the low-risk group and 54 cases in the high-risk group. Then the difference in the proportion of TIICs between the IMRGscore-defined groups was shown in **Figure 12B**. It was found that the fraction of CD8 T cells, activated CD4 memory T cells, follicular helper T cells (TFH) and regulatory T cells (Treg) in the low-risk group was significantly higher. In contrast, the fraction of M0 macrophages was upper in the high-risk group. Furthermore, high levels of CD8 T cells ($p = .004$), activated CD4 memory T cells ($p = .013$) and TFH ($p = .041$) were observably associated with better OS (**Figures 12C–E**), while increased M0 macrophages ($p = .035$) indicated a poor OS (**Figure 12F**).

DISCUSSION

Bladder cancer is a heterogeneous malignancy. Patients with BLCA generally show different prognoses because of the molecular discrepancy (Knowles and Hurst, 2015; Guo and Czerniak, 2019). At present, it is generally believed that clinical or pathological stages were insufficient to predict the

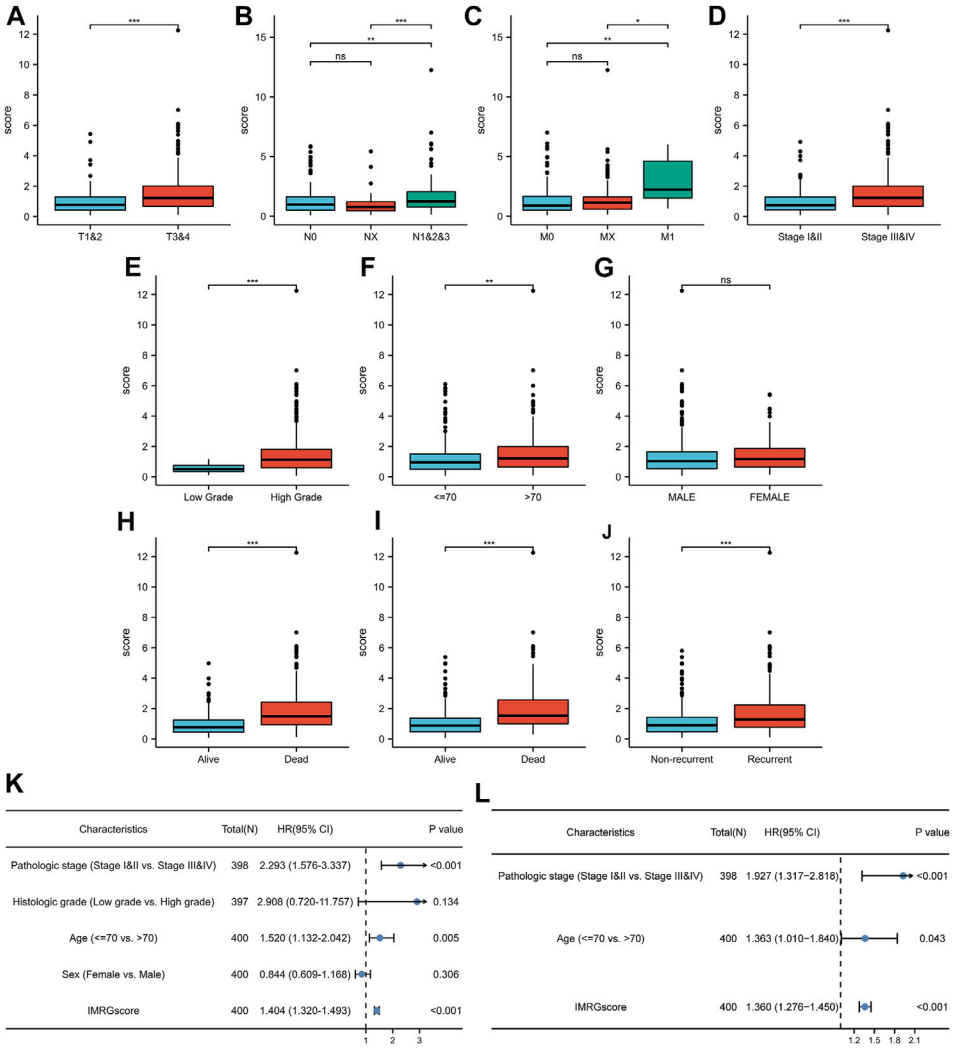

FIGURE 9 | Clinical relevance of IMRG signature. Correlation between IMRGscore and clinicopathological characteristics, including T stage **(A)**, N stage **(B)**, M stage **(C)**, pathologic stage **(D)**, histologic grade **(E)**, age **(F)**, gender **(G)**, OS event **(H)**, DSS event **(I)**, and PFI event **(J)**. Univariate **(K)** and multivariate **(L)** Cox regression analysis of risk-group and clinicopathological characteristics. *$p < 0.05$; **$p < 0.01$; ***$p < 0.001$.

prognosis of patients with BLCA (Konety, 2006; Rosenberg et al., 2013). Therefore, it is essential to develop a more accurate and efficient model to predict the survival prognosis for patients. In recent years, some studies have found iron involvement in the appearance and progression of cancers. Abundant researches have revealed that iron metabolism is involved in the entire process of cancer progression. Murata M. demonstrated that iron released from the damaged transferrin could mediate the Fenton reaction and produce ROS, which contributes to the carcinogenic process in multiple ways (Murata, 2018). A cross-sectional study found that the serum iron concentration in patients with BLCA was lower than that in the control group (Mazdak et al., 2010). However, studies on the potential function of iron metabolism in the treatment and prognosis of BLCA are scarce.

In this study, patients in the TCGA-BLCA cohort were divided into four iron metabolism patterns based on the expression of prognosis-related IMRGs. Survival analysis suggested that C1 and C3 had a better prognosis. Our results also showed that C2 and C4 patterns have higher enrichment scores in multiple carcinogenic and immune activation-related pathways. For instance, abnormal activation of NOD-like receptors (NLRs) occurs in various cancers, coordinates the tumor immune microenvironment, and promotes angiogenesis, cancer cell stem cells, and chemotherapy resistance, thereby enhancing tumor risk (Liu et al., 2019). Toll-like receptor (TLR) is a transmembrane pattern recognition receptor that detects and defends microbial pathogens through the innate immune response (Brennan and Gilmore, 2018). The activation of the Notch signaling pathway can be seen in most components of the tumor microenvironment (TME), such as angiogenesis, tumor stem cell maintenance, immune infiltration, or therapeutic resistance (Meurette and Mehlen, 2018). Besides, C2 and C4 iron metabolism patterns were highly infiltrated by immune cells,

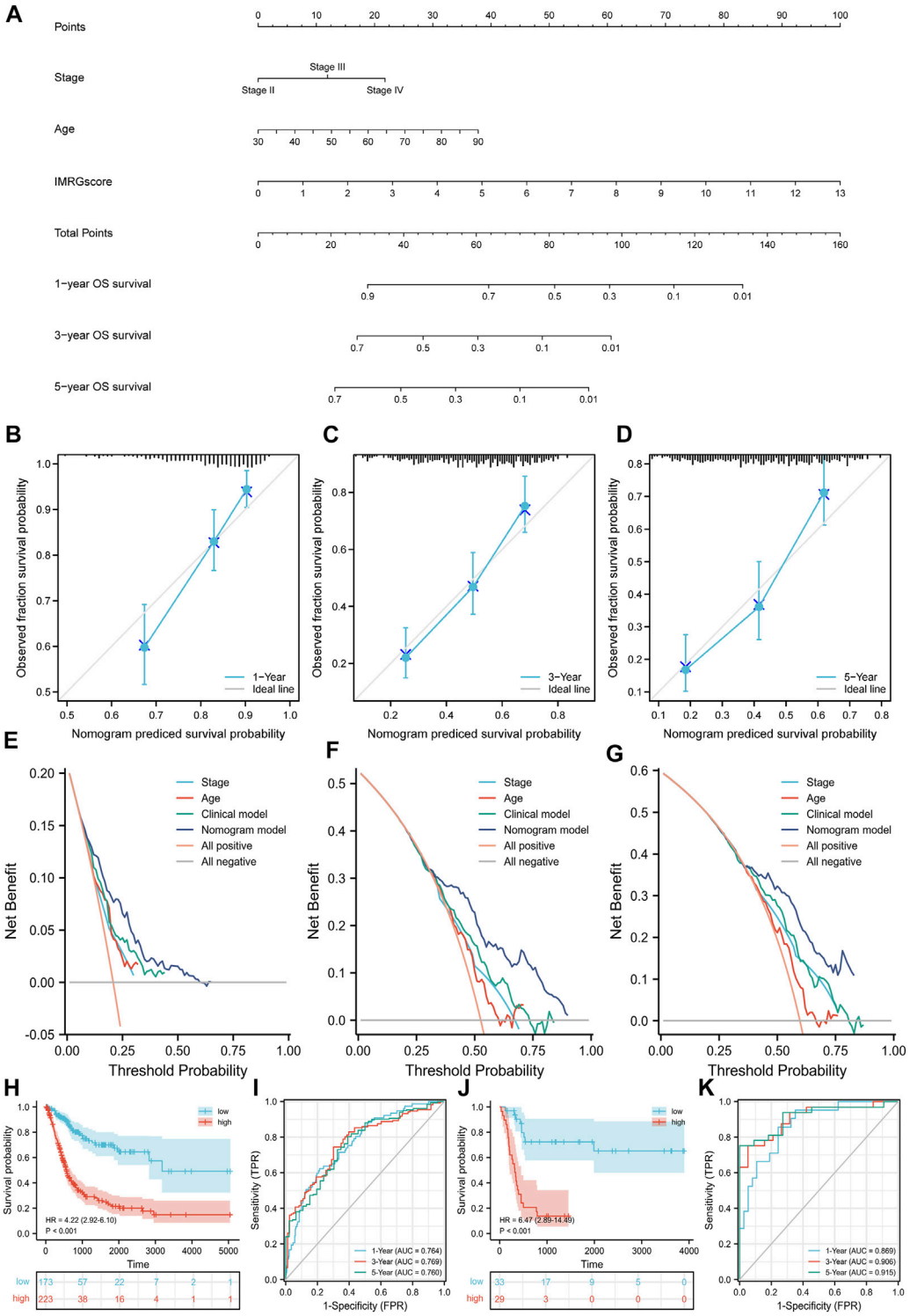

FIGURE 10 | Nomogram model based on clinicopathological characteristics and IMRGscore. **(A)** Nomogram for predicting the probability of OS over 1, 3, and 5 years. **(B–D)** Calibration curves for predicting the fitness of the nomogram model in 1, 3, and 5 years. **(E–G)** DCA curves based on three predictors of 1, 3, and 5 years. **(H)** Kaplan-Meier analysis of nomogram model in the TCGA-BLCA cohort. **(I)** Time-dependent ROC curves of nomogram model in the TCGA-BLCA cohort. **(J)** Kaplan-Meier analysis of nomogram model in the GSE13507 cohort. **(K)** Time-dependent ROC curves of nomogram model in the GSE13507 cohort.

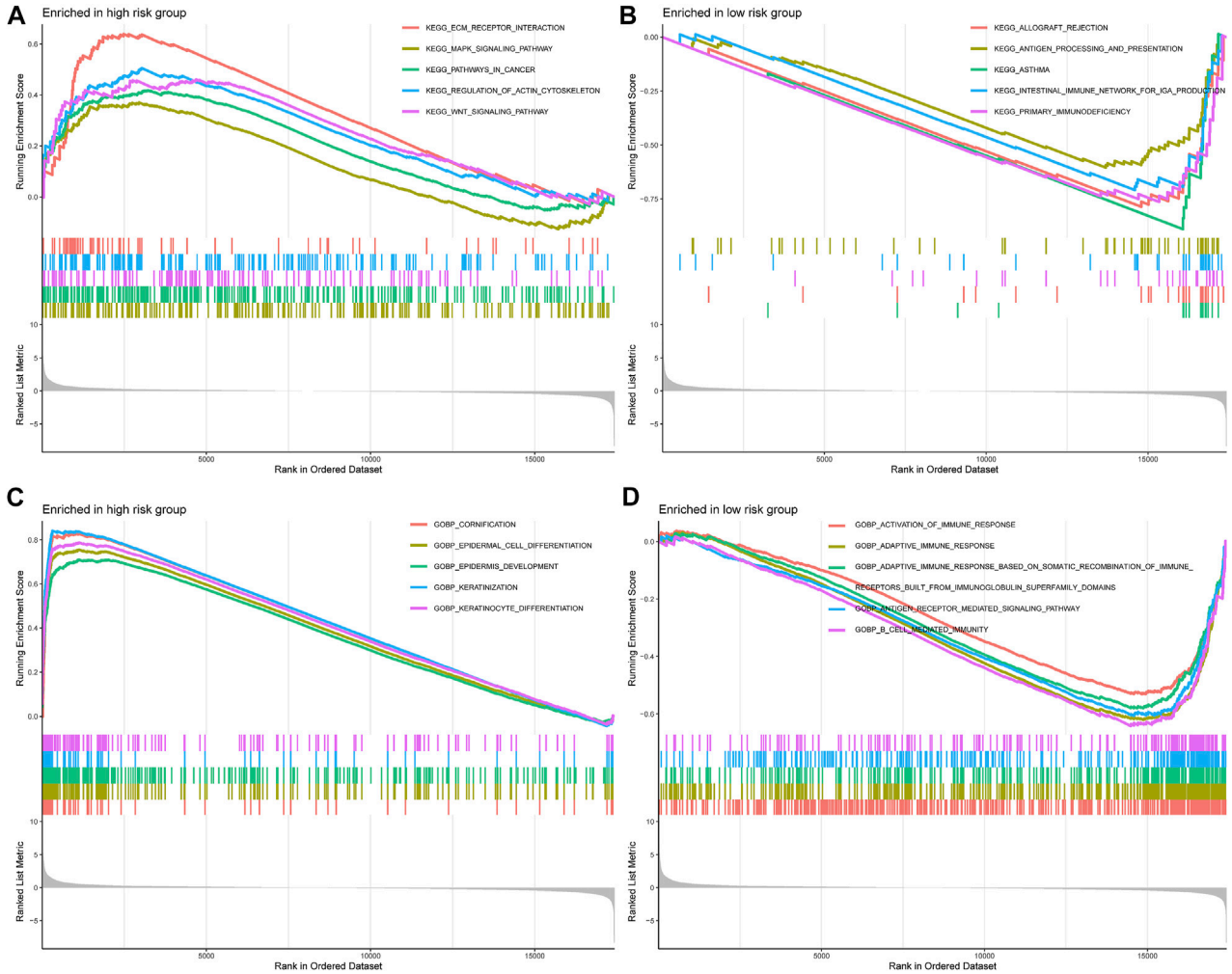

FIGURE 11 | Correlation between IMRG signature and biological functions. KEGG results of the high-risk group **(A)** and low-risk group **(B)**. GOBP results of the high-risk group **(C)** and low-risk group **(D)**.

and the expression of MHC genes was highly elevated. These characteristics are consistent with an immune-inflamed phenotype. On the other hand, C1 and C3 are suspected to be immune-desert phenotypes due to lack of immune infiltration and antigen presentation. Additionally, we found that multiple immune checkpoints (PD-1, PD-L1, PD-L2, LAG3, TIGIT, IDO1, and CTLA4) were highly expressed in C2 and C4 patterns, which might indicate that immunotherapy has a better effect on them. Furthermore, studies have shown that the high-level expression of immune checkpoint genes might be a stimulative to the immunosuppressive microenvironment and led to the immune escape of tumor cells (Dunn et al., 2002). The TIDE algorithm confirmed this conclusion. Therefore, we speculate that the reason why C2 and C4 patterns do not show a better prognosis of immunoinflammatory phenotype is that the antitumor effect based on the activated immune pathway and high infiltration level of T cells were eliminated by the formation of the immunosuppressive microenvironment. The above evidence proved that iron metabolism is of great significance in shaping various TME landscapes in BLCA.

Somatic mutation is not only the driving factor of cancer, but also the guiding basis for diagnosis and treatment. The three genes with the highest mutation rate in BLCA were TP53, TTN, and KMT2D. The mutation rate of TP53 in C2 iron metabolism pattern was the highest, while in C1 pattern was the lowest. In C2 and C3 patterns, the incidence of TTN and KMT2D mutations was significantly higher. Detection of TP53 mutation was conducive to estimating the high risk of early lesions (Olivier et al., 2010). Single TTN gene mutation often indicated high TMB (Oh et al., 2020). The mutation of epigenetic regulator KMT2D was a biomarker of poor prognosis in some cancers (Ferrero et al., 2020). Additionally, we found that high TMB suggested that patients with BLCA had a better prognosis through the TCGA database. Consistently, the TMB of C1 and C4 patterns was observably decreased. These results show that iron metabolism has a complex interaction with somatic mutation.

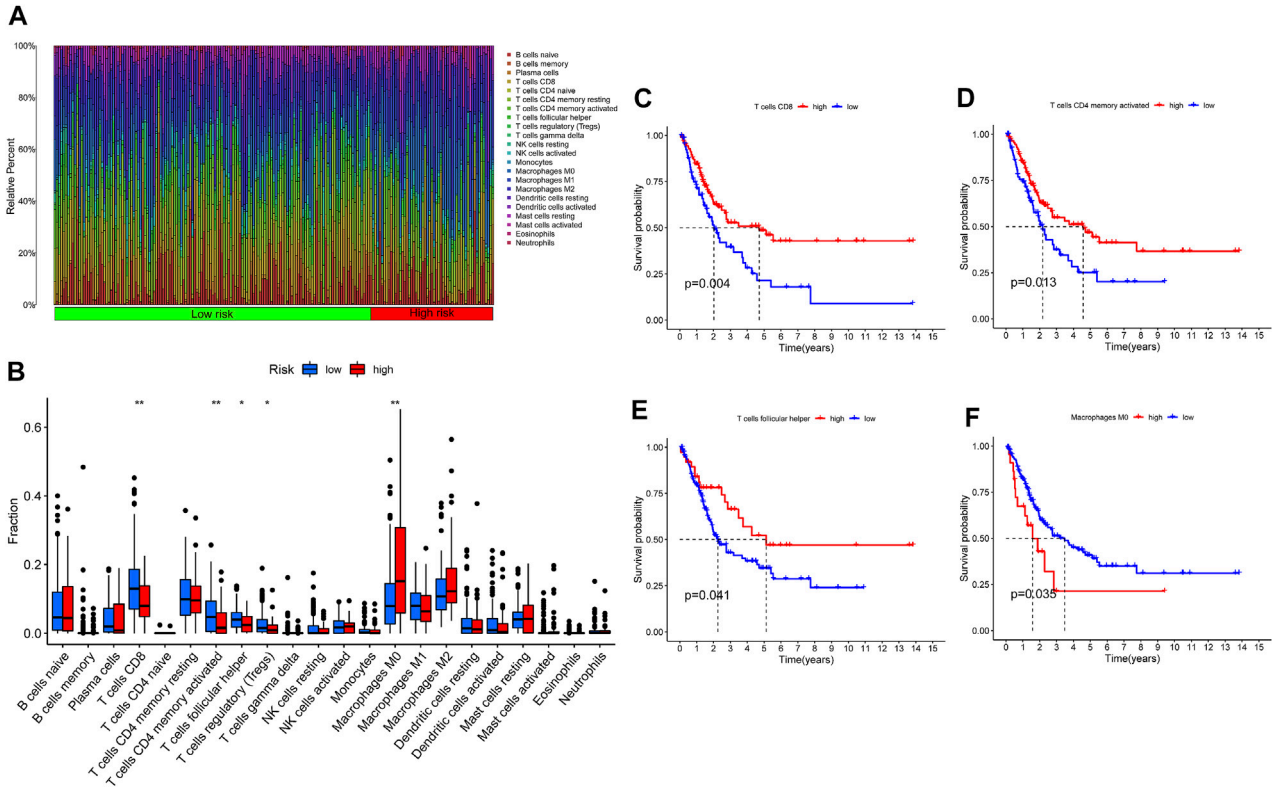

FIGURE 12 | Tumor immune microenvironment of IMRG signature. **(A)** The proportion of 22 TIICs in BLCA. **(B)** Infiltration of 22 TIICs in low- and high-risk groups. Correlation between the infiltration level of TIICs (CD8 T cells **(C)**, activated CD4 memory T cells **(D)**, follicular helper T cells **(E)**, and M0 macrophages **(F)** and prognosis of patients with BLCA. $^{*}p < 0.05$; $^{**}p < 0.01$.

Chemotherapy is still one of the main treatments for BLCA. According to the latest guidelines of the European Association of Urology (EAU), all muscle-invasive bladder cancer (MIBC) patients with physical conditions can apply platinum-based neoadjuvant chemotherapy before operation (Witjes et al., 2021). This study investigated the efficacy of six common chemotherapeutic drugs on iron metabolism mode, including Gemcitabine, Cisplatin, Docetaxel, Mitomycin-C, Doxorubicin, and Paclitaxel. The results showed that C2 pattern was the most sensitive to these chemotherapeutic drugs, while C3 pattern was the most insensitive. This provided a reference basis for the selection of clinical chemotherapy drugs.

Due to the effect of iron metabolism on the tumorigenesis and progression of cancer, it is of great importance to establish an IMRG signature for predicting the prognosis of patients with BLCA. Herein, we applied stepwise regression analysis to compose a clinical prognostic signature for BLCA patients with 13 IMRGs (TCIRG1, CTSE, ATP6V0A1, CYP2C8, RNF19A, CYP4Z1, YPEL5, PLOD1, BMP6, CAST, SCD, IFNG, and ASIC3). A test set was utilized to confirm its accuracy and stability. Moreover, the IMRGscore was elevated in multiple advanced clinicopathological stages. And multivariate Cox regression analysis verified that IMRGscore was an independent prognostic index of BLCA patients. Finally, we combined some clinicopathological features, including pathologic stage, age, and IMRGscore to construct a nomogram that accurately predicted the prognosis of patients with BLCA. The accuracy and clinical contributions were verified by calibration analysis and DCA.

Several studies have shown that these 13 IMRGs are closely related to cancers, and some of these genes have been confirmed about BLCA. TCIRG1, one of the V-ATPase subunits, is abnormally overexpressed in patients with recurrent hepatocellular carcinoma, and enhances the ability of metastasis by regulating the growth, death, and epithelial to mesenchymal transition of cancer cells (Yang et al., 2018). A retrospective study suggests that CTSE can be used as an independent prognostic marker for NMIBC, so as to guide the treatment of patients (Lin et al., 2001). ATP6V0A1was demonstrated that it could enhance the fusion of autophagosomes and lysosomes, up-regulate autophagy volume accumulation, and finally induce autophagic cell death (Hsin et al., 2012). CYP2C8 can be regulated by GAS5/miR-382-3p in hepatocellular carcinoma and play an anticancer role (Li and Chen, 2020). RNF19A was confirmed to be overexpressed in non-small cell lung cancer, which plays a carcinogenic role by destroying the function of p53 (Cheng et al., 2021). CYP4Z1 was confirmed to be highly expressed in BLCA and positively correlated with the progression of histologic grade and pathologic stage (Al-Saraireh et al., 2021). YPEL5 was found

to be inhibited by METTL3-m6A (N6-methyladenosine)-YTHDF2 axis in colorectal cancer, promoting the growth and metastasis of tumor (Zhou et al., 2021). The expression of PLOD1 was an independent prognostic factor in BLCA patients, and downregulated by inhibitor could significantly reduce the invasiveness of BLCA cells (Yamada et al., 2019). The expression of BMP6, a key endogenous regulator of iron metabolism, was affected by Med19, which could promote bone metastasis and invasiveness of bladder cancer (Andriopoulos Jr et al., 2009; Wen et al., 2013). Public clinical data also confirm that BMP6 is a prognostic marker for bladder cancer (Yuen et al., 2012). Calpastatin (CAST) is involved in many important physiological processes, including cell cycle, ECM, cancer cell proliferation, metastasis, and apoptosis (Nian and Ma, 2021). SCD can protect cancer cells from oxidative stress and ferroptosis through mediated lipogenesis in prostate cancer with over-activation of PI3K-AKT-mTOR signaling (Yi et al., 2020). SCD has also been shown to reduce proliferation and invasion of BLCA cells when inhibited (Piao et al., 2019). Iron metabolism can affect innate immune response by affecting IFNG mediated immune response pathway in macrophages (Nairz et al., 2014). And IFNG was demonstrated to inhibit the activity of bladder cancer stem cells (Qiu et al., 2020). ASIC3 has an H+ gating function, which promotes the acid-induced epithelial-mesenchymal transition in pancreatic cancer cells (Zhu et al., 2017).

GSEA analysis showed that several cancer-related pathways were enriched in the high-risk group. The unique biochemical and biophysical properties of ECM when it is dysregulated are the key drivers of cancer progression (Walker et al., 2018). The MAPK signaling pathway is considered to be related to cell proliferation, differentiation, migration, aging, and apoptosis (Sun et al., 2015). The Wnt signaling pathway is an important driving factor to maintain tissue development and homeostasis. Abnormal Wnt signaling will cause the occurrence and progression of many cancers by affecting cancer stem cells (Duchartre et al., 2016). Furthermore, CIBERSORT analysis indicated that several TIICs with differential infiltration levels had significant correlations between the prognosis of BLCA patients, and played a regulatory role in the balance of iron metabolism. After being activated by immunotherapy, CD8 T cells can enhance ferroptosis-specific lipid peroxidation and increase ferroptosis in tumor cells, which contributes to the anti-tumor effect (Wang et al., 2019). Macrophages are the regulatory hub of iron metabolism. Macrophages phagocytize and degrade aging and damaged erythrocytes to recover iron, and also have the ability to release iron. The accumulation of M2 macrophages is often associated with poor prognosis, and M2 macrophages possess iron release characteristics (Recalcati et al., 2010). Therefore, the accumulation of M2 macrophages may further aggravate the disorder of iron metabolism.

Our research has obvious advantages in the study of iron metabolism characteristics and the clinical application of BLCA. First, we divided BLCA patients into distinct iron metabolism landscapes to further confirm the relationship between iron metabolism and TME and somatic mutations. At the same time, we also verified that iron metabolism landscapes had guiding significance for chemotherapy drugs and immunotherapy selection. Next, we established the IMRG prognostic signature and proved IMRGscore was an independent prognostic factor for BLCA patients, and it also had the predictive ability for clinicopathological characteristics. At present, our research is still insufficient. First, it is a retrospective study. Deviations in variables such as clinicopathological characteristics of patients most likely exist. Second, our prognostic signature depends on gene expression and does not take into account the effects of gene mutation, methylation, or other factors on the prognosis of BLCA patients. Finally, the prognostic signature can be incorporated into large sample prospective studies to further verify its clinical value.

DATA AVAILABILITY STATEMENT

Raw data for this study were generated at the TCGA database with the cancer type of BLCA. The datasets used and/or analyzed during the current study are available from the GEO database (GSE13507). Derived data supporting the findings are available from the corresponding author (WS) on reasonable request.

AUTHOR CONTRIBUTIONS

XL and WS designed and guided the work. XS and SX participated in data collecting, data processing, figures preparation, and manuscript writing. YZ, JM, and CD contributed to statistical analysis. KC, LC, and FL contributed to manuscript writing and article publishment. ZL and TW contributed to manuscript draft writing. JL revised the manuscript critically. All authors provided critical advice for the final manuscript.

FUNDING

This work was supported by the National Natural Science Foundation of China (Grant Number: 82072838), Tongji Outstanding Young Researcher Funding (Grant number: 2020YQ13), Huazhong University of Science and Technology (Grant Number: 2019kfyXKJC06), Natural Science Foundation of Hubei Province (Grant Number: ZRMS2020002466).

ACKNOWLEDGMENTS

The authors thank the members of the Urology Department of Tongji Hospital of Huazhong University of science and technology for their valuable support and useful discussion. We also thank TCGA, GEO, and MSigDB databases for the availability of the data.

REFERENCES

Al-Saraireh, Y. M., Alshammari, F. O. F. O., Youssef, A. M. M., Al-Sarayreh, S., Almuhaisen, G. H., Alnawaiseh, N., et al. (2021). Profiling of CYP4Z1 and CYP1B1 Expression in Bladder Cancers. *Sci. Rep.* 11 (1), 5581. doi:10.1038/s41598-021-85188-4

Andrews, N. C. (2008). Forging a Field: the golden Age of Iron Biology. *Blood* 112 (2), 219–230. doi:10.1182/blood-2007-12-077388

Andriopoulos Jr, B., Jr., Corradini, E., Xia, Y., Faasse, S. A., Chen, S., Grgurevic, L., et al. (2009). BMP6 Is a Key Endogenous Regulator of Hepcidin Expression and Iron Metabolism. *Nat. Genet.* 41 (4), 482–487. doi:10.1038/ng.335

Babjuk, M., Burger, M., Compérat, E. M., Gontero, P., Mostafid, A. H., Palou, J., et al. (2019). European Association of Urology Guidelines on Non-muscle-invasive Bladder Cancer (TaT1 and Carcinoma *In Situ*) - 2019 Update. *Eur. Urol.* 76 (5), 639–657. doi:10.1016/j.eururo.2019.08.016

Battaglia, A. M., Chirillo, R., Aversa, I., Sacco, A., Costanzo, F., and Biamonte, F. (2020). Ferroptosis and Cancer: Mitochondria Meet the "Iron Maiden" Cell Death. *Cells* 9 (6), 1505. doi:10.3390/cells9061505

Berdik, C. (2017). Unlocking Bladder Cancer. *Nature* 551 (7679), S34–s35. doi:10.1038/551S34a

Bialasek, M., Kubiak, M., Gorczak, M., Braniewska, A., Kucharzewska-Siembieda, P., Krol, M., et al. (2019). Exploiting Iron-Binding Proteins for Drug Delivery. *J. Physiol. Pharmacol.* 70 (5). doi:10.26402/jpp.2019.5.03

Brennan, J. J., and Gilmore, T. D. (2018). Evolutionary Origins of Toll-like Receptor Signaling. *Mol. Biol. Evol.* 35 (7), 1576–1587. doi:10.1093/molbev/msy050

Brunet, J.-P., Tamayo, P., Golub, T. R., and Mesirov, J. P. (2004). Metagenes and Molecular Pattern Discovery Using Matrix Factorization. *Proc. Natl. Acad. Sci.* 101 (12), 4164–4169. doi:10.1073/pnas.0308531101

Chan, T. A., Yarchoan, M., Jaffee, E., Swanton, C., Quezada, S. A., Stenzinger, A., et al. (2019). Development of Tumor Mutation burden as an Immunotherapy Biomarker: Utility for the Oncology Clinic. *Ann. Oncol.* 30 (1), 44–56. doi:10.1093/annonc/mdy495

Cheng, Y., Hu, Y., Wang, H., Zhao, Z., Jiang, X., Zhang, Y., et al. (2021). Ring finger Protein 19A Is Overexpressed in Non-small Cell Lung Cancer and Mediates P53 Ubiquitin-Degradation to Promote Cancer Growth. *J. Cel Mol Med* 25 (16), 7796–7808. doi:10.1111/jcmm.16674

Duchartre, Y., Kim, Y.-M., and Kahn, M. (2016). The Wnt Signaling Pathway in Cancer. *Crit. Rev. Oncology/Hematology* 99, 141–149. doi:10.1016/j.critrevonc.2015.12.005

Dufès, C., Al Robaian, M., and Somani, S. (2013). Transferrin and the Transferrin Receptor for the Targeted Delivery of Therapeutic Agents to the Brain and Cancer Cells. *Ther. Deliv.* 4 (5), 629–640. doi:10.4155/tde.13.21

Dunn, G. P., Bruce, A. T., Ikeda, H., Old, L. J., and Schreiber, R. D. (2002). Cancer Immunoediting: from Immunosurveillance to Tumor Escape. *Nat. Immunol.* 3 (11), 991–998. doi:10.1038/ni1102-991

Ferrero, S., Rossi, D., Rinaldi, A., Bruscaggin, A., Spina, V., Eskelund, C. W., et al. (2020). KMT2D Mutations and TP53 Disruptions Are Poor Prognostic Biomarkers in Mantle Cell Lymphoma Receiving High-Dose Therapy: a FIL Study. *Haematologica* 105 (6), 1604–1612. doi:10.3324/haematol.2018.214056

Fonseca-Nunes, A., Jakszyn, P., and Agudo, A. (2014). Iron and Cancer Risk-A Systematic Review and Meta-Analysis of the Epidemiological Evidence. *Cancer Epidemiol. Biomarkers Prev.* 23 (1), 12–31. doi:10.1158/1055-9965.Epi-13-0733

Geeleher, P., Cox, N., and Huang, R. S. (2014). pRRophetic: an R Package for Prediction of Clinical Chemotherapeutic Response from Tumor Gene Expression Levels. *PLoS One* 9 (9), e107468. doi:10.1371/journal.pone.0107468

Guo, C. C., and Czerniak, B. (2019). Bladder Cancer in the Genomic Era. *Arch. Pathol. Lab. Med.* 143 (6), 695–704. doi:10.5858/arpa.2018-0329-RA

Hassannia, B., Vandenabeele, P., and Vanden Berghe, T. (2019). Targeting Ferroptosis to Iron Out Cancer. *Cancer Cell* 35 (6), 830–849. doi:10.1016/j.ccell.2019.04.002

Hsin, I.-L., Sheu, G.-T., Jan, M.-S., Sun, H.-L., Wu, T.-C., Chiu, L.-Y., et al. (2012). Inhibition of Lysosome Degradation on Autophagosome Formation and Responses to GMI, an Immunomodulatory Protein fromGanoderma Microsporum. *Br. J. Pharmacol.* 167 (6), 1287–1300. doi:10.1111/j.1476-5381.2012.02073.x

Jiang, P., Gu, S., Pan, D., Fu, J., Sahu, A., Hu, X., et al. (2018). Signatures of T Cell Dysfunction and Exclusion Predict Cancer Immunotherapy Response. *Nat. Med.* 24 (10), 1550–1558. doi:10.1038/s41591-018-0136-1

Jung, M., Mertens, C., Tomat, E., and Brüne, B. (2019). Iron as a Central Player and Promising Target in Cancer Progression. *Int. J. Mol. Sci.* 20 (2), 273. doi:10.3390/ijms20020273

Knowles, M. A., and Hurst, C. D. (2015). Molecular Biology of Bladder Cancer: New Insights into Pathogenesis and Clinical Diversity. *Nat. Rev. Cancer* 15 (1), 25–41. doi:10.1038/nrc3817

Konety, B. R. (2006). Molecular Markers in Bladder Cancer: a Critical Appraisal. *Urol. Oncol. Semin. Original Invest.* 24 (4), 326–337. doi:10.1016/j.urolonc.2005.11.023

Li, K., and Chen, Y. (2020). CYP2C8 Regulated by GAS5/miR-382-3p Exerts Anti-cancerous Properties in Liver Cancer. *Cancer Biol. Ther.* 21 (12), 1145–1153. doi:10.1080/15384047.2020.1840886

Lin, C. K., Lai, K. H., Lo, G. H., Cheng, J. S., Hsu, P. I., Mok, K. T., et al. (2001). Cathepsin E and Subtypes of Intestinal Metaplasia in Carcinogenesis of the Human Stomach. *Zhonghua Yi Xue Za Zhi (Taipei)* 64 (6), 331–336.

Liu, P., Lu, Z., Liu, L., Li, R., Liang, Z., Shen, M., et al. (2019). NOD-like Receptor Signaling in Inflammation-Associated Cancers: From Functions to Targeted Therapies. *Phytomedicine* 64, 152925. doi:10.1016/j.phymed.2019.152925

Manz, D. H., Blanchette, N. L., Paul, B. T., Torti, F. M., and Torti, S. V. (2016). Iron and Cancer: Recent Insights. *Ann. N.Y. Acad. Sci.* 1368 (1), 149–161. doi:10.1111/nyas.13008

Martincorena, I., and Campbell, P. J. (2015). Somatic Mutation in Cancer and normal Cells. *Science* 349 (6255), 1483–1489. doi:10.1126/science.aab4082

Mazdak, H., Yazdekhasti, F., Movahedian, A., Mirkheshti, N., and Shafieian, M. (2010). The Comparative Study of Serum Iron, Copper, and Zinc Levels between Bladder Cancer Patients and a Control Group. *Int. Urol. Nephrol.* 42 (1), 89–93. doi:10.1007/s11255-009-9583-4

Meurette, O., and Mehlen, P. (2018). Notch Signaling in the Tumor Microenvironment. *Cancer Cell* 34 (4), 536–548. doi:10.1016/j.ccell.2018.07.009

Mou, Y., Wang, J., Wu, J., He, D., Zhang, C., Duan, C., et al. (2019). Ferroptosis, a New Form of Cell Death: Opportunities and Challenges in Cancer. *J. Hematol. Oncol.* 12 (1), 34. doi:10.1186/s13045-019-0720-y

Murata, M. (2018). Inflammation and Cancer. *Environ. Health Prev. Med.* 23 (1), 50. doi:10.1186/s12199-018-0740-1

Nairz, M., Haschka, D., Demetz, E., and Weiss, G. (2014). Iron at the Interface of Immunity and Infection. *Front. Pharmacol.* 5, 152. doi:10.3389/fphar.2014.00152

Nian, H., and Ma, B. (2021). Calpain-calpastatin System and Cancer Progression. *Biol. Rev.* 96 (3), 961–975. doi:10.1111/brv.12686

Oh, J.-H., Jang, S. J., Kim, J., Sohn, I., Lee, J.-Y., Cho, E. J., et al. (2020). Spontaneous Mutations in the Single TTN Gene Represent High Tumor Mutation burden. *Npj Genom. Med.* 5, 33. doi:10.1038/s41525-019-0107-6

Olivier, M., Hollstein, M., and Hainaut, P. (2010). TP53 Mutations in Human Cancers: Origins, Consequences, and Clinical Use. *Cold Spring Harbor Perspect. Biol.* 2 (1), a001008. doi:10.1101/cshperspect.a001008

Piao, C., Cui, X., Zhan, B., Li, J., Li, Z., Li, Z., et al. (2019). Inhibition of Stearoyl CoA Desaturase-1 Activity Suppresses Tumour Progression and Improves Prognosis in Human Bladder Cancer. *J. Cel Mol Med* 23 (3), 2064–2076. doi:10.1111/jcmm.14114

Qiu, Y., Qiu, S., Deng, L., Nie, L., Gong, L., Liao, X., et al. (2020). Biomaterial 3D Collagen I Gel Culture Model: A Novel Approach to Investigate Tumorigenesis and Dormancy of Bladder Cancer Cells Induced by Tumor Microenvironment. *Biomaterials* 256, 120217. doi:10.1016/j.biomaterials.2020.120217

Recalcati, S., Locati, M., Marini, A., Santambrogio, P., Zaninotto, F., De Pizzol, M., et al. (2010). Differential Regulation of Iron Homeostasis during Human Macrophage Polarized Activation. *Eur. J. Immunol.* 40 (3), 824–835. doi:10.1002/eji.200939889

Rosenberg, E., Baniel, J., Spector, Y., Faerman, A., Meiri, E., Aharonov, R., et al. (2013). Predicting Progression of Bladder Urothelial Carcinoma Using microRNA Expression. *BJU Int.* 112 (7), a–n. doi:10.1111/j.1464-410X.2012.11748.x

Rouanne, M., Roumiguié, M., Houédé, N., Masson-Lecomte, A., Colin, P., Pignot, G., et al. (2018). Development of Immunotherapy in Bladder Cancer: Present and Future on Targeting PD(L)1 and CTLA-4 Pathways. *World J. Urol.* 36 (11), 1727–1740. doi:10.1007/s00345-018-2332-5

Siegel, R. L., Miller, K. D., and Jemal, A. (2020). Cancer Statistics, 2020. *CA A. Cancer J. Clin.* 70 (1), 7–30. doi:10.3322/caac.21590

Stevens, R. G., Graubard, B. I., Micozzi, M. S., Neriishi, K., and Blumberg, B. S. (1994). Moderate Elevation of Body Iron Level and Increased Risk of Cancer Occurrence and Death. *Int. J. Cancer* 56 (3), 364–369. doi:10.1002/ijc.2910560312

Sun, Y., Liu, W.-Z., Liu, T., Feng, X., Yang, N., and Zhou, H.-F. (2015). Signaling Pathway of MAPK/ERK in Cell Proliferation, Differentiation, Migration, Senescence and Apoptosis. *J. Receptors Signal Transduction* 35 (6), 600–604. doi:10.3109/10799893.2015.1030412

Thévenod, F. (2018). 15. Iron and its Role in Cancer Defense: A Double-Edged Sword. *Met. Ions Life Sci.* 18, 437–468. doi:10.1515/9783110470734-021

Torti, S. V., Manz, D. H., Paul, B. T., Blanchette-Farra, N., and Torti, F. M. (2018). Iron and Cancer. *Annu. Rev. Nutr.* 38, 97–125. doi:10.1146/annurev-nutr-082117-051732

Torti, S. V., and Torti, F. M. (2013). Iron and Cancer: More Ore to Be Mined. *Nat. Rev. Cancer* 13 (5), 342–355. doi:10.1038/nrc3495

Walker, C., Mojares, E., and del Río Hernández, A. (2018). Role of Extracellular Matrix in Development and Cancer Progression. *Int. J. Mol. Sci.* 19 (10), 3028. doi:10.3390/ijms19103028

Wang, Y., Yu, L., Ding, J., and Chen, Y. (2018). Iron Metabolism in Cancer. *Int. J. Mol. Sci.* 20 (1), 95. doi:10.3390/ijms20010095

Wang, W., Green, M., Choi, J. E., Gijón, M., Kennedy, P. D., Johnson, J. K., et al. (2019). CD8+ T Cells Regulate Tumour Ferroptosis during Cancer Immunotherapy. *Nature* 569 (7755), 270–274. doi:10.1038/s41586-019-1170-y

Wen, H., Feng, C.-c., Ding, G.-x., Meng, D.-l., Ding, Q., Fang, Z.-j., et al. (2013). Med19 Promotes Bone Metastasis and Invasiveness of Bladder Urothelial Carcinoma via Bone Morphogenetic Protein 2. *Ann. Diagn. Pathol.* 17 (3), 259–264. doi:10.1016/j.anndiagpath.2012.11.004

Witjes, J. A., Bruins, H. M., Cathomas, R., Compérat, E. M., Cowan, N. C., Gakis, G., et al. (2021). European Association of Urology Guidelines on Muscle-Invasive and Metastatic Bladder Cancer: Summary of the 2020 Guidelines. *Eur. Urol.* 79 (1), 82–104. doi:10.1016/j.eururo.2020.03.055

Wu, T., Sempos, C. T., Freudenheim, J. L., Muti, P., and Smit, E. (2004). Serum Iron, Copper and Zinc Concentrations and Risk of Cancer Mortality in US Adults. *Ann. Epidemiol.* 14 (3), 195–201. doi:10.1016/s1047-2797(03)00119-4

Xu, T., Ding, W., Ji, X., Ao, X., Liu, Y., Yu, W., et al. (2019). Molecular Mechanisms of Ferroptosis and its Role in Cancer Therapy. *J. Cel Mol Med* 23 (8), 4900–4912. doi:10.1111/jcmm.14511

Yamada, Y., Kato, M., Arai, T., Sanada, H., Uchida, A., Misono, S., et al. (2019). Aberrantly Expressed PLOD 1 Promotes Cancer Aggressiveness in Bladder Cancer: a Potential Prognostic Marker and Therapeutic Target. *Mol. Oncol.* 13 (9), 1898–1912. doi:10.1002/1878-0261.12532

Yang, H. D., Eun, J. W., Lee, K.-B., Shen, Q., Kim, H. S., Kim, S. Y., et al. (2018). T-cell Immune Regulator 1 Enhances Metastasis in Hepatocellular Carcinoma. *Exp. Mol. Med.* 50 (1), e420. doi:10.1038/emm.2017.166

Yi, J., Zhu, J., Wu, J., Thompson, C. B., and Jiang, X. (2020). Oncogenic Activation of PI3K-AKT-mTOR Signaling Suppresses Ferroptosis via SREBP-Mediated Lipogenesis. *Proc. Natl. Acad. Sci. USA* 117 (49), 31189–31197. doi:10.1073/pnas.2017152117

Yin, M., Joshi, M., Meijer, R. P., Glantz, M., Holder, S., Harvey, H. A., et al. (2016). Neoadjuvant Chemotherapy for Muscle-Invasive Bladder Cancer: A Systematic Review and Two-step Meta-Analysis. *Oncologist* 21 (6), 708–715. doi:10.1634/theoncologist.2015-0440

Yuen, H.-F., McCrudden, C. M., Grills, C., Zhang, S.-D., Huang, Y.-H., Chan, K.-K., et al. (2012). Combinatorial Use of Bone Morphogenetic Protein 6, Noggin and SOST Significantly Predicts Cancer Progression. *Cancer Sci.* 103 (6), 1145–1154. doi:10.1111/j.1349-7006.2012.02252.x

Zhou, D., Tang, W., Xu, Y., Xu, Y., Xu, B., Fu, S., et al. (2021). METTL3/YTHDF2 m6A axis Accelerates Colorectal Carcinogenesis through Epigenetically Suppressing YPEL5. *Mol. Oncol.* 15 (8), 2172–2184. doi:10.1002/1878-0261.12898

Zhu, S., Zhou, H.-Y., Deng, S.-C., Deng, S.-J., He, C., Li, X., et al. (2017). ASIC1 and ASIC3 Contribute to Acidity-Induced EMT of Pancreatic Cancer through Activating Ca2+/RhoA Pathway. *Cell Death Dis* 8 (5), e2806. doi:10.1038/cddis.2017.189

Conflict of Interest: The authors declare that the research was conducted in the absence of any commercial or financial relationships that could be construed as a potential conflict of interest.

Publisher's Note: All claims expressed in this article are solely those of the authors and do not necessarily represent those of their affiliated organizations, or those of the publisher, the editors and the reviewers. Any product that may be evaluated in this article, or claim that may be made by its manufacturer, is not guaranteed or endorsed by the publisher.

frontiers in Cell and Developmental Biology

ORIGINAL RESEARCH
published: 23 February 2022
doi: 10.3389/fcell.2022.814735

Integrated Analysis of Energy Metabolism Signature-Identified Distinct Subtypes of Bladder Urothelial Carcinoma

Fan Zhang[1†], Jiayu Liang[1†], Dechao Feng[1], Shengzhuo Liu[1], Jiapei Wu[1], Yongquan Tang[2], Zhihong Liu[1], Yiping Lu[1], Xianding Wang[1] and Xin Wei[1]**

[1]Department of Urology, Institute of Urology, West China Hospital, Sichuan University, Chengdu, China, [2]Department of Pediatric Urology, West China Hospital, Sichuan University, Chengdu, China

OPEN ACCESS

Edited by:
Fang-Ming Deng,
New York University, United States

Reviewed by:
Yu Fu,
Southwest University, China
Juan Huang,
Chinese Academy of Medical Sciences and Peking Union Medical College, China

***Correspondence:**
Xianding Wang
xiandingwang@qq.com
Xin Wei
weixinscu@scu.edu.cn

[†]*These authors have contributed equally to this work and share first authorship*

Specialty section:
This article was submitted to Molecular and Cellular Pathology, a section of the journal Frontiers in Cell and Developmental Biology

Received: *14 November 2021*
Accepted: *03 February 2022*
Published: *23 February 2022*

Citation:
Zhang F, Liang J, Feng D, Liu S, Wu J, Tang Y, Liu Z, Lu Y, Wang X and Wei X (2022) Integrated Analysis of Energy Metabolism Signature-Identified Distinct Subtypes of Bladder Urothelial Carcinoma. Front. Cell Dev. Biol. 10:814735. doi: 10.3389/fcell.2022.814735

Background: Bladder urothelial carcinoma (BLCA) is the most common type of bladder cancer. In this study, the correlation between the metabolic status and the outcome of patients with BLCA was evaluated using data from the Cancer Genome Atlas and Gene Expression Omnibus datasets.

Methods: The clinical and transcriptomic data of patients with BLCA were downloaded from the Cancer Genome Atlas and cBioPortal datasets, and energy metabolism-related gene sets were obtained from the Molecular Signature Database. A consensus clustering algorithm was then conducted to classify the patients into two clusters. Tumor prognosis, clinicopathological features, mutations, functional analysis, ferroptosis status analysis, immune infiltration, immune checkpoint-related gene expression level, chemotherapy resistance, and tumor stem cells were analyzed between clusters. An energy metabolism-related signature was further developed and verified using data from cBioPortal datasets.

Results: Two clusters (C1 and C2) were identified using a consensus clustering algorithm based on an energy metabolism-related signature. The patients with subtype C1 had more metabolism-related pathways, different ferroptosis status, higher cancer stem cell scores, higher chemotherapy resistance, and better prognosis. Subtype C2 was characterized by an increased number of advanced BLCA cases and immune-related pathways. Higher immune and stromal scores were also observed for the C2 subtype. A signature containing 16 energy metabolism-related genes was then identified, which can accurately predict the prognosis of patients with BLCA.

Conclusion: We found that the energy metabolism-associated subtypes of BLCA are closely related to the immune microenvironment, immune checkpoint-related gene expression, ferroptosis status, CSCs, chemotherapy resistance, prognosis, and progression of BLCA patients. The established energy metabolism-related gene signature was able to predict survival in patients with BLCA.

Keywords: bladder cancer, prognosis, metabolic status, nonogram, signature

INTRODUCTION

Bladder cancer (BC) is one of the most prevalent cancers, accounting for approximately 200,000 deaths per year worldwide, with preponderance in men compared with women (4:1) (Bray et al., 2018). More than 90% of BC cases are transitional cell carcinomas, also known as bladder urothelial carcinoma (BUC or BLCA), accounting for the majority of primary BC cases (Potts et al., 2017). BC can be divided into muscle invasive bladder cancer (MIBC) and non-muscle invasive bladder cancer (NMIBC) based on whether it invades the muscle layer of the bladder (Babjuk et al., 2017). At the time of initial diagnosis, NMIBC accounts for approximately 75% of BC cases (Hollenbeck et al., 2007). In NMIBC patients, carcinoma *in situ* (CIS), high-grade T1, and high-grade Ta tumors are considered to have a high risk of tumor recurrence and disease progression. In the clinical management of BLCA, the prognosis of tumors often depends on the histopathology and stage of cancer (Kamat et al., 2016; Babjuk et al., 2017), which provides a simple risk stratification but cannot explain the different prognoses and outcomes of patients with the same histopathology and tumor stage. Thus, it is imperative to determine new biomarkers correlated with the prognosis of patients with BLCA at an early stage.

Alterations in the energy metabolism of cancer cells compared with normal cells are an emerging hallmark of most cancers (Hanahan and Weinberg, 2011; Fumarola et al., 2018). In the different types of energy metabolism reprogramming that cancer cells may rely on, glycolysis is the most common pathway that many cancer cells may utilize, even in the presence of oxygen, to generate ATP to maintain the reduction–oxidation balance and macromolecular biosynthesis, which is required to support the growth, division, and migration of cancer cells (Vander Heiden and DeBerardinis, 2017). This phenomenon of glycolysis in the presence of oxygen is also known as the Warburg effect (Dang and Semenza, 1999). While the metabolic phenotype of some tumor cells is mainly glycolytic, some other tumors have a predominantly oxidative phosphorylation (OXPHOS) metabolic phenotype (Sonveaux et al., 2008). There is growing evidence that metabolic reprogramming of cancer cells is heterogeneous. Furthermore, it has been reported that tumor cells can also absorb free fatty acids and ketones secreted by adjacent catabolic cells, which provide energy for mitochondrial OXPHOS (Bonuccelli et al., 2010; Nieman et al., 2011). In addition, a previous study reported that glutamine-driven mitochondrial OXPHOS, rather than glycolysis, takes up most of the ATP production under hypoxic conditions (Fan et al., 2013). Concerns regarding the possibility that cancer-related energy metabolic reprogramming may provide new targeted therapies are emerging, which may have fewer side effects and higher antitumor efficiency than conventional cytotoxic chemotherapy (Tennant et al., 2010; DeBerardinis and Chandel, 2016; Luengo et al., 2017).

In this study, the energy metabolic profile and clinical value in patients with BLCA were investigated using the Cancer Genome Atlas (TCGA) and cBioPortal online sequencing data. Based on the consensus clustering analysis of the gene expression profile, patients could be classified into two robust clusters with significant differences in molecular features and tumor prognosis. Furthermore, an energy metabolism-related signature was developed to assess the prognosis of patients with BLCA in the TCGA dataset, which was then verified using data from the cBioPortal database. We found a significant association between the prognosis of patients with BLCA and the energy metabolism-related signature, which could serve as an independent clinicopathological prognostic factor. In summary, our study revealed a strong correlation between energy metabolism status and clinical prognosis of patients with BLCA.

METHODS

Dataset Collection

Data from bladder cancer patients containing clinicopathological and transcriptomic information were downloaded from the Cancer Genome Atlas (TCGA) data portal (https://portal.gdc.cancer.gov/). Moreover, a validation cohort ($n = 296$) was derived from the cBioPortal online database (http://www.cbioportal.org/), and it validated the results (Gao et al., 2013).

Gene Sets Containing and Consensus Clustering

The Molecular Signature Database (MSigDB, http://www.broad.mit.edu/gsea/msigdb/) was utilized to contain two energy metabolism-related gene sets (energy-requiring part of metabolism and reactome energy metabolism) (Subramanian et al., 2005; Zhou et al., 2018). After removing overlapping genes, an energy metabolism-related gene set containing 590 genes was obtained (**Supplementary Datasheet S1**). The "ConsensusClusterPlus" R package was then used to perform consensus clustering analysis, and the maximum number of clusters was set at 6. The "pheatmap" R package was utilized to visualize the results of the most differentially expressed energy metabolism-related genes in the form of a heatmap. Survival curves were generated using the R packages "survival." Comparisons of clinicopathological characteristics were performed using chi-square tests or Fisher's exact tests for categorical variables and Student's t-tests for continuous variables.

Differentially Expressed Gene Identification and Enrichment Analysis

The differentially expressed genes (DEGs) between groups characterized by consensus clustering were explored and visualized in volcano plots using the "ggplot" R package. The thresholds of the fold-change value and adjusted p value were set at 1.5 and 0.05, respectively. The top 50 upregulated and downregulated DEGs with the most differential changes are shown in the form of a heatmap. Furthermore, we used the "ClusterProfiler" R package to conduct enrichment analysis to better understand the underlying functions of the potential

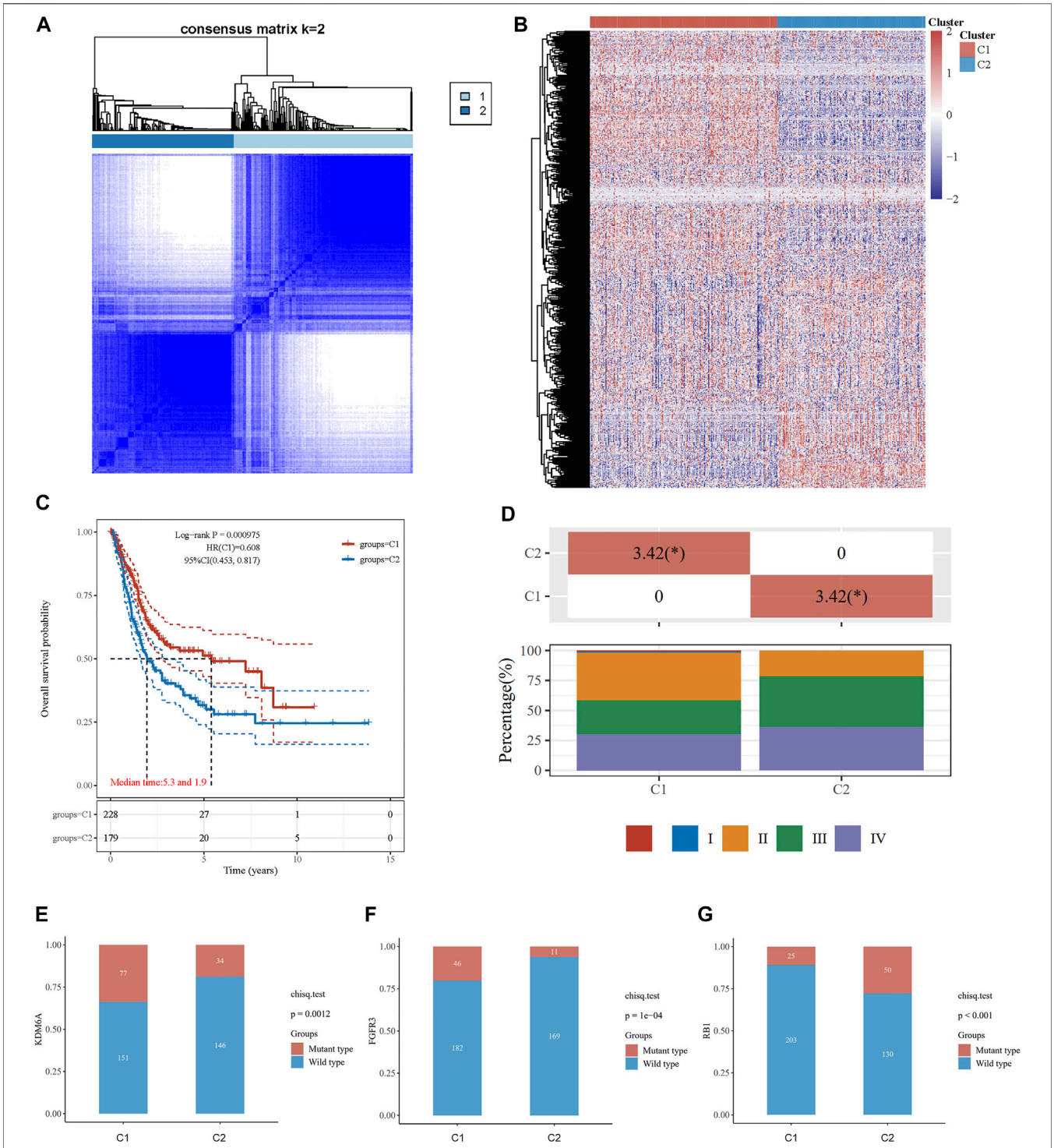

FIGURE 1 | Consensus clustering analysis to identify the genomic subtype of BLCA based on an energy metabolism-related gene set. **(A)** Consensus clustering matrix of 408 samples from the TCGA dataset for k = 2. **(B)** Heatmap of energy metabolism-related gene expression in different clusters. Red represents high gene expression, and blue represents low expression. **(C)** The Kaplan–Meier curve of overall survival of BLCA patients in two clusters. **(D)** Tumor stage distribution of BLCA patients in two clusters with different metabolic statuses. The frequency of KDM6A **(E)**, FGFR3 **(F)**, and RB1 **(G)** mutations in two clusters with different metabolic statuses.

targets. GO functions were analyzed for the DEGs between groups identified by energy metabolism-related genes, and the KEGG pathway and gene set enrichment analysis (GSEA) were enriched. In addition, the correlation between metabolic status and CSCs was evaluated using the OCLR algorithm constructed by Malta et al. (Teo and Rosenberg, 2018).

Immune Infiltration and Ferroptosis Status Analysis

Based on the cohorts grouped by consensus clustering, immune infiltration estimation was then conducted using the xCell and CIBERSORT algorithms in the "immunedeconv" R package and visualized in the form of a heatmap and boxplot. Furthermore, eight immune checkpoint-relevant genes (CD274, CTLA4, HAVCR2, LAG3, PDCD1, PDCD1LG2, TIGIT, and SIGLEC15) were selected and then explored in the different groups, and the "ggplot2" and "pheatmap" R packages were utilized to visualize the expression of these genes in the two groups. The Wilcox test was used for the analysis of significance between groups, and $p < 0.05$ was regarded as statistically significant. The ferroptosis status analysis was achieved through the "ggplot2" and "pheatmap" R packages.

Gene Signature Identification

The TCGA–BLCA dataset was analyzed to determine whether the energy metabolism-related genes were correlated with the overall survival of the patients *via* univariate Cox proportional hazards regression analysis. Simultaneously, DEGs between bladder cancer and normal tissue were determined using the online tool Gene Expression Profiling Interactive Analysis 2.0. (GEPIA2; http://gepia2.cancer-pku.cn/#index) (Tang et al., 2019). A Venn diagram was constructed to select the optimal energy metabolism-related gene set with the R package "ggplot2." Furthermore, the least absolute shrinkage and selection operator (LASSO) Cox regression algorithm was conducted through the "glmnet" R package. The nomogram and calibration curves were constructed by using the "rms" and "survival" R packages.

RESULTS

Data Collection and Consensus Clustering

To explore the role of energy metabolism status in BLCA, we obtained a cohort of 408 patients using RNA sequencing data and clinicopathological information from the TCGA database. Two energy metabolism-related gene sets were then obtained, and after removing overlapping genes, an energy metabolism-related gene set containing 590 genes was obtained (**Supplementary Datasheet S1**).

The association between energy metabolism status and prognosis of patients with BLCA was further investigated. The consensus clustering algorithm, empirical cumulative distribution function (CDF) plot, and consensus clustering matrix indicated that patients could be grouped into two groups (**Figure 1A**, **Supplementary Figure S1**). **Figure 1B** presents the clustering heatmap of the top variable expression genes with SD >0.1 in these two clusters grouped by the energy metabolism-related gene set. Survival curves revealed that patients in cluster 1 had a significantly longer overall survival [OS hazards ratio (HR): 0.608, 95% confidence interval (CI): 0.453–0.817, $p < 0.001$, **Figure 1C**] and better progression-free survival (PFS, HR: 0.691, 95% CI: 0.513–0.931, $p = 0.0151$, **Supplementary Figure S1**) than those in cluster 2.

TABLE 1 | Clinicopathological feathers between the two clusters identified by energy metabolic-related gene set.

Characteristics	C1 (*n* = 228)	C2 (*n* = 180)	*p* Value
Survive			<0.001
Alive	148 (64.9%)	81 (45%)	
Dead	80 (35.1%)	99 (55%)	
Gender			0.098
Female	52 (22.8%)	55 (30.6%)	
Male	176 (77.2%)	125 (69.4%)	
Race			<0.001
Asian	38 (16.7%)	6 (3.3%)	
Black	13 (5.7%)	10 (5.6%)	
White	166 (72.8%)	158 (87.8%)	
Metastasis			0.001
M0	129 (56.6%)	67 (37.2%)	
M1	6 (2.6%)	5 (2.8%)	
MX	92 (40.4%)	106 (58.9%)	
Stage			<0.001
I	2 (0.9%)	0	
II	91 (39.9%)	39 (21.7%)	
III	64 (28.1%)	76 (42.2%)	
IV	69 (30.3%)	65 (36.1%)	
Histologic grade			<0.001
High	205 (89.9%)	179 (99.4%)	
Low	21 (9.2%)	0	

The clinicopathological features of the two clusters were explored to investigate the differences between the clusters. Survival status and race were significantly different between the two clusters (**Table 1**). In addition, patients in cluster 1 tended to have no metastasis, relatively earlier tumor stage (**Figure 1D**), and relatively lower histologic grade, whereas more metastasis, higher tumor stage, and higher tumor grade were observed in patients from cluster 2. The top 20 most frequently mutated genes in each cluster were then compared, and we found that the frequency of KDM6A ($p = 0.001$, **Figure 1E**) and FGFR3 ($p < 0.001$, **Figure 1F**) mutations were higher in C1, whereas the frequency of RB1 mutations ($p < 0.001$, **Figure 1G**) in C2 was higher.

Enrichment Analysis

To explore the underlying mechanism of the difference between the two clusters, DEGs between the two clusters were identified. As shown in **Figure 2A**, the volcano plot indicated the upregulated genes (SNX31, VSIG2, DHRS2, HMGCS2, *etc.*) and downregulated genes (KRT6B, KRT6A, KRT14, *etc.*) in cluster 1 as compared to cluster 2. The top 50 upregulated and downregulated genes were then displayed in the form of a heatmap (**Figure 2B**).

Moreover, with the thresholds of the fold-change value and adjusted *p* value setting at 1.5 and 0.05, up- and downregulated genes were selected for functional enrichment analysis. KEGG analysis of the most relevant signaling pathways in cluster 1 was mainly associated with the energy metabolism (**Figure 2C**). The results of GO analysis showed the same trend, and the most enriched terms in the biological process (BP), molAUCecular function (MF), and cellular component (CC) were strongly correlated with the energy metabolism (**Figure 2C**), mainly

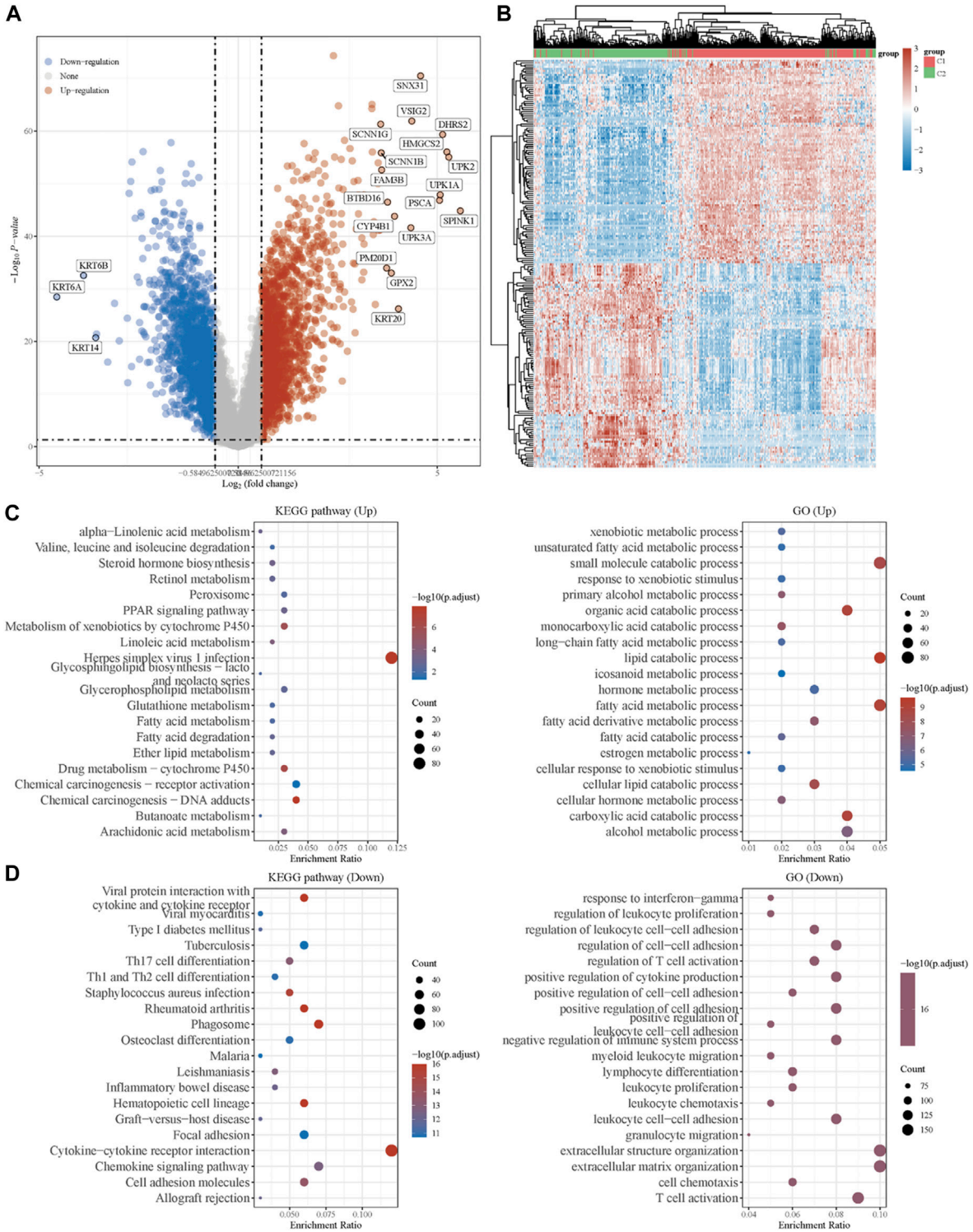

FIGURE 2 | Identification of DEGs between the two clusters grouped by energy metabolism-related gene set and functional enrichment analysis. **(A)** Volcano plot of DEGs between two clusters with different metabolic statuses. The red and blue points represent up- and downregulated genes with statistical significance, respectively. **(B)** Heatmap of the top 50 up- and downregulated genes with the most differential changes. **(C)** GO/KEGG analysis of DEGs that were upregulated in cluster 1. **(D)** GO/KEGG analysis of DEGs that were downregulated in cluster 1. DEG: differentially expressed genes.

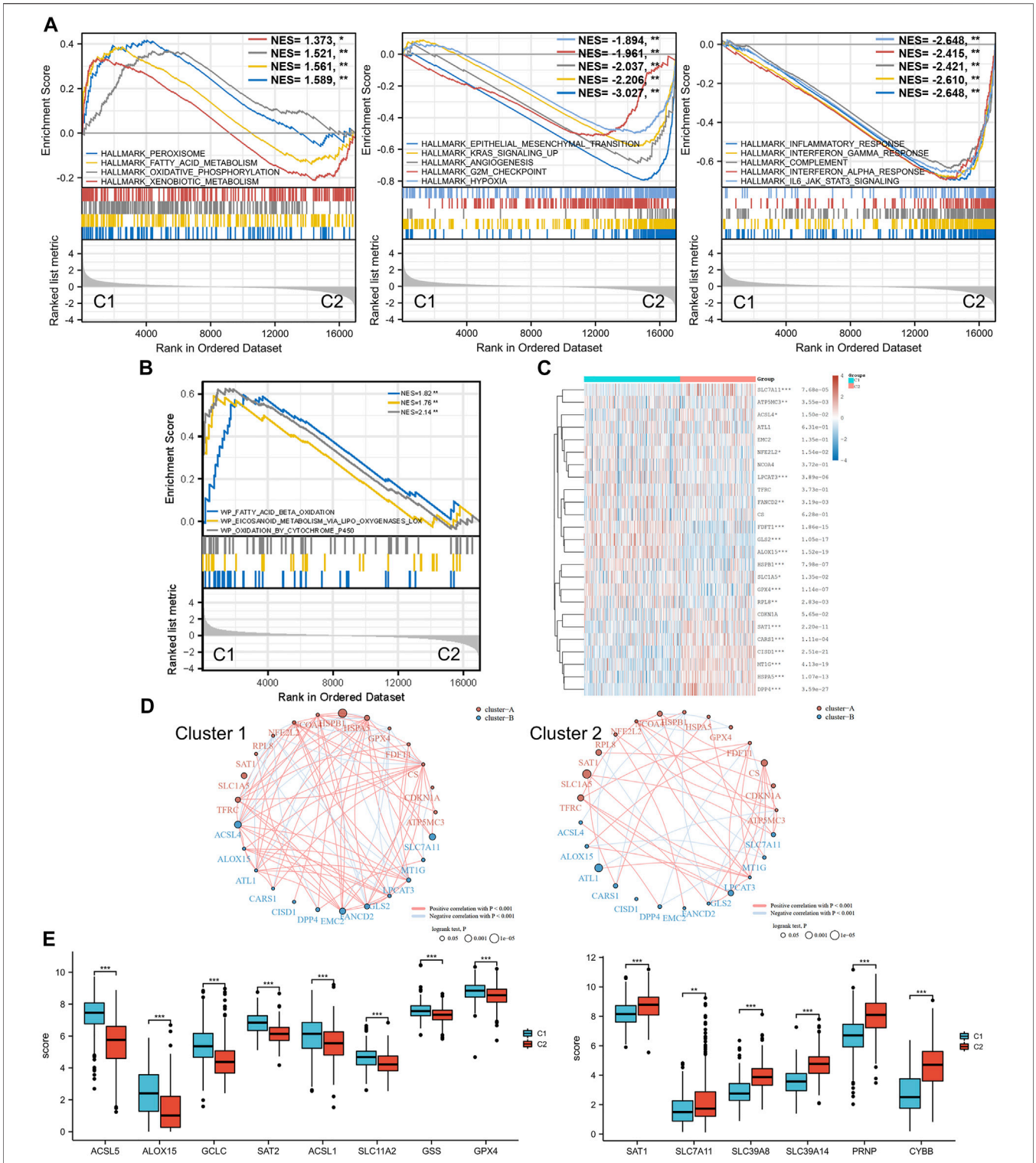

FIGURE 3 | Ferroptosis status analysis and GSEA results. **(A)** GSEA of DEGs that were upregulated in cluster 1 and cluster 2. **(B)** GSEA results of lipid oxidation metabolism terms. **(C)** Heatmap of ferroptosis-related gene expression in two different metabolic status clusters. **(D)** Ferroptosis-related gene interaction network. The red and blue lines represent the positive and negative correlation, respectively. The thickness of the line represents the correlation between the two genes. The larger circle indicates a more significant prognostic log rank *p* value. **(E)** Expression difference of ferroptosis-related genes between the two clusters. GSEA: gene set enrichment analysis. DEG: differentially expressed genes. $^{*}p < 0.05$, $^{**}p < 0.01$, $^{***}p < 0.001$.

enriched in small-molecule catabolic processes, lipid catabolic processes, and fatty acid metabolic processes. However, the GO/KEGG analysis of the downregulated genes in cluster 1, indicating that they were upregulated in cluster 2, showed different results. GO analysis of cluster 2 was mainly enriched in immune terms, including T-cell activation, leukocyte cell–cell adhesion, negative regulation of immune system process, regulation of leukocyte cell–cell adhesion, and regulation of T-cell activation. In the KEGG pathways, the results showed that the DEGs were mainly enriched in cytokine–cytokine receptor interactions, chemokine signaling pathways, and immune-related pathways, including those involving phagosomes, Th17 cell differentiation, and Th1 and Th2 cell differentiation. GSEA results of cluster 1 also showed metabolism-associated terms, while cluster 2 was mainly enriched in immune terms (**Figure 3A**, **Supplementary Figure S2**). These results indicated that cluster 1 could be characterized by the activation of oncometabolic processes, while cluster 2 may be characterized by the upregulation of tumor-related immunogenicity.

Ferroptosis Status Analysis

Ferroptosis, driven by excessive lipid peroxidation, is an iron-dependent regulated cell death that is related to the development and treatment response of various types of tumors (Chen et al., 2021). The enrichment results of the GSEA indicated that the two clusters were different in terms of fatty acid beta oxidation, eicosanoid metabolism *via* lipoxygenases lox, and oxidation by cytochrome p450 (**Figure 3B**). These lipid oxidation metabolism characteristics, which were correlated to ferroptosis, suggested that the ferroptosis status of the two clusters may differ. Analysis of ferroptosis-related genes between the two groups revealed that many ferroptosis-related genes were differentially expressed between the two clusters (**Figures 3C,E**), and the expression levels of some genes (including ACSL5, ACSL1, GSS, SLC7A11, SCL39A8, SLC39A14, and PRNP) were significantly associated with the prognosis of patients with BLCA (**Supplementary Figure S3**). In addition, the correlation between the ferroptosis-related genes was more obvious in cluster 1 and was dominated by a positive correlation, while the correlation between different genes in the ferroptosis-related gene network of C2 was weaker (**Figure 3D**). SLC7A11 was significantly downregulated in cluster 1, and the prognostic effect of SLC7A11 in cluster 1 was more significant than that in cluster 2. Similarly, SAT1 was significantly upregulated in cluster 2, and the prognostic effect in cluster 2 was more significant. This finding suggested that the metabolism status of BLCA patients was significantly associated with the expression of selected ferroptosis-related genes, some of which were correlated with the prognosis of BLCA.

Immune Infiltration Analysis

Based on the enrichment analysis results that upregulated genes in cluster 2 were correlated with tumor immune function in BLCA, the immune infiltration status of the two clusters was then examined. A heatmap of immune cell infiltration suggested that the tumor immune microenvironment was significantly different between the two clusters (**Figure 4A**). Cluster 2 had higher infiltration levels of T-cell $CD4^+$ Th1, T-cell $CD4^+$ Th2, T-cell $CD4^+$ memory, T-cell regulatory, T-cell $CD4^+$ naïve, granulocyte-monocyte progenitor, macrophage, M1 macrophage, M2 macrophage, myeloid dendritic cell, activated myeloid dendritic cells, monocytes, mast cells, plasmacytoid dendritic cells, T-cell $CD8^+$, T-cell $CD8^+$ effector memory, T-cell $CD8^+$ central memory, B-cell plasma, B-cell naïve, B cell, and B-cell memory. In addition, high infiltration levels of $CD4^+$ central memory T cells, eosinophils, and $CD8^+$ naïve T cells were observed in cluster 2. Boxplots showed similar results using the CIBERSORT algorithm (**Figure 4B**). The Spearman correlation analysis also revealed a significant association between energy metabolism-related gene set risk scores and the infiltration of $CD4^+$ T cells, $CD8^+$ T cells, neutrophils, macrophages, and myeloid dendritic cells (**Supplementary Figure S4**). This result is consistent with the conclusion of the enrichment analysis, indicating that patients with BLCA from cluster 2 had higher immune cell infiltration and that the energy metabolism-related gene set had a potential correlation with the tumor immune microenvironment.

Furthermore, we investigated the expression of immune checkpoint (IC)-related genes between the two clusters. In cluster 2, we found a relatively higher expression of IC-related genes, including CD274, CTLA4, HAVCR2, LAG3, PDCD1, PDCD1LG2, and TIGIT (**Figures 4C,D**). However, SIGLEC15 expression was higher in cluster 1. Thus, energy metabolism-related genes were significantly correlated with biomarkers of immune checkpoints and may play an important role in immunological therapy for BLCA.

Cancer Stem Cells and Drug Sensitivity Analysis

Based on the gene expression profile containing 11,774 CSC-associated genes, analysis of CSCs was conducted, and patients in cluster 1 had a higher CSC score, indicating a significant correlation between energy metabolic status and CSCs (**Figure 4E**). Next, drug sensitivity was evaluated between the two clusters. **Figures 4F,G** show that energy metabolic status was significantly associated with the IC50 scores of doxorubicin and gemcitabine for BLCA.

Energy Metabolism-Related Gene Signature Identification

Considering the close correlation between the prognosis of patients with BLCA and energy metabolism status, we suggest developing an energy metabolism-related gene signature for prognosis prediction. Based on DEGs between cluster 1 and cluster 2, Venn diagrams were constructed and showed that 162 of 590 metabolism-related genes were differentially expressed between clusters (**Supplementary Figure S5**). Then, 67 of 162 metabolism-related genes were further identified with a significant relevance to the OS of patients with BLCA ($p < 0.1$). To ensure the feasibility and stability of the clinical prognostic value of these 67 genes, LASSO analysis was conducted, and we obtained 16 energy–metabolism-correlated genes associated

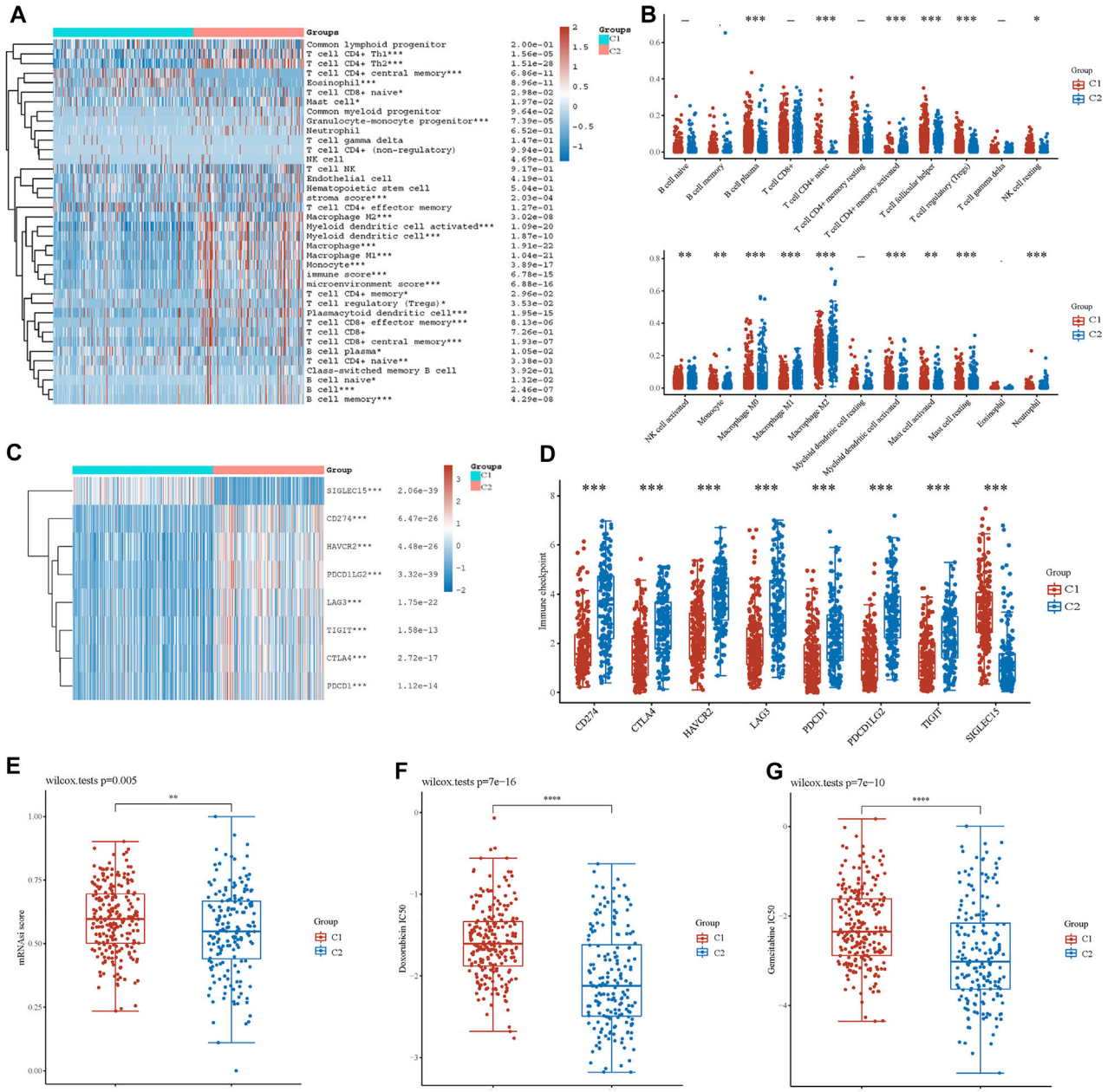

FIGURE 4 | Analysis of immune cell infiltration between two clusters. **(A)** Immune cell score heatmap by xCell algorithm. Red represents high expression/score, whereas blue represents low expression/score. **(B)** Boxplot of immune infiltration status in two clusters by the CIBERSORT algorithm. Heatmap **(C)** and boxplot **(D)** of immune checkpoint-related gene expression between two clusters. Cancer stem cell scores **(E)** and chemotherapy resistance to doxorubicin **(F)** and gemcitabine **(G)** of the two clusters. *$p < 0.05$, **$p < 0.01$, ***$p < 0.001$.

with the prognosis of patients with BLCA, including FBP1, AOC2, SLC16A8, IDUA, CYP2C8, GPC2, HS3ST1, UGT2B7, GSTM1, CSPG4, ACY3, SLC16A3, TPST1, CES1, HSPG2, and CYP1B1 (**Figures 5A,B**). Therefore, based on the Cox coefficient, the energy metabolism-related gene-based prognostic signature (EMRGPS) was calculated as follows: risk score= (−0.055 × FBP1 expression) + (−0.0085 × AOC2 expression) + (−0.0567 × SLC16A8 expression) + (−0.0351 × IDUA expression) + (−0.0444 × CYP2C8 expression) + (−0.0627 × GPC2 expression) + (−0.0885 × HS3ST1 expression) + (−0.0096 × UGT2B7 expression) + (0.0197 × GSTM1 expression) + (0.026 × CSPG4 expression) + (−0.1969 × ACY3 expression) + (0.0445 × SLC16A3 expression) + (0.117 × TPST1 expression) + (0.0421 × CES1 expression) + (0.0264 × HSPG2 expression) + (0.0051 × CYP1B1 expression).

Based on the median value of the risk score, patients with BLCA could be categorized into low-risk and high-risk groups (**Figure 5C**). The Kaplan–Meier curve indicated that patients in

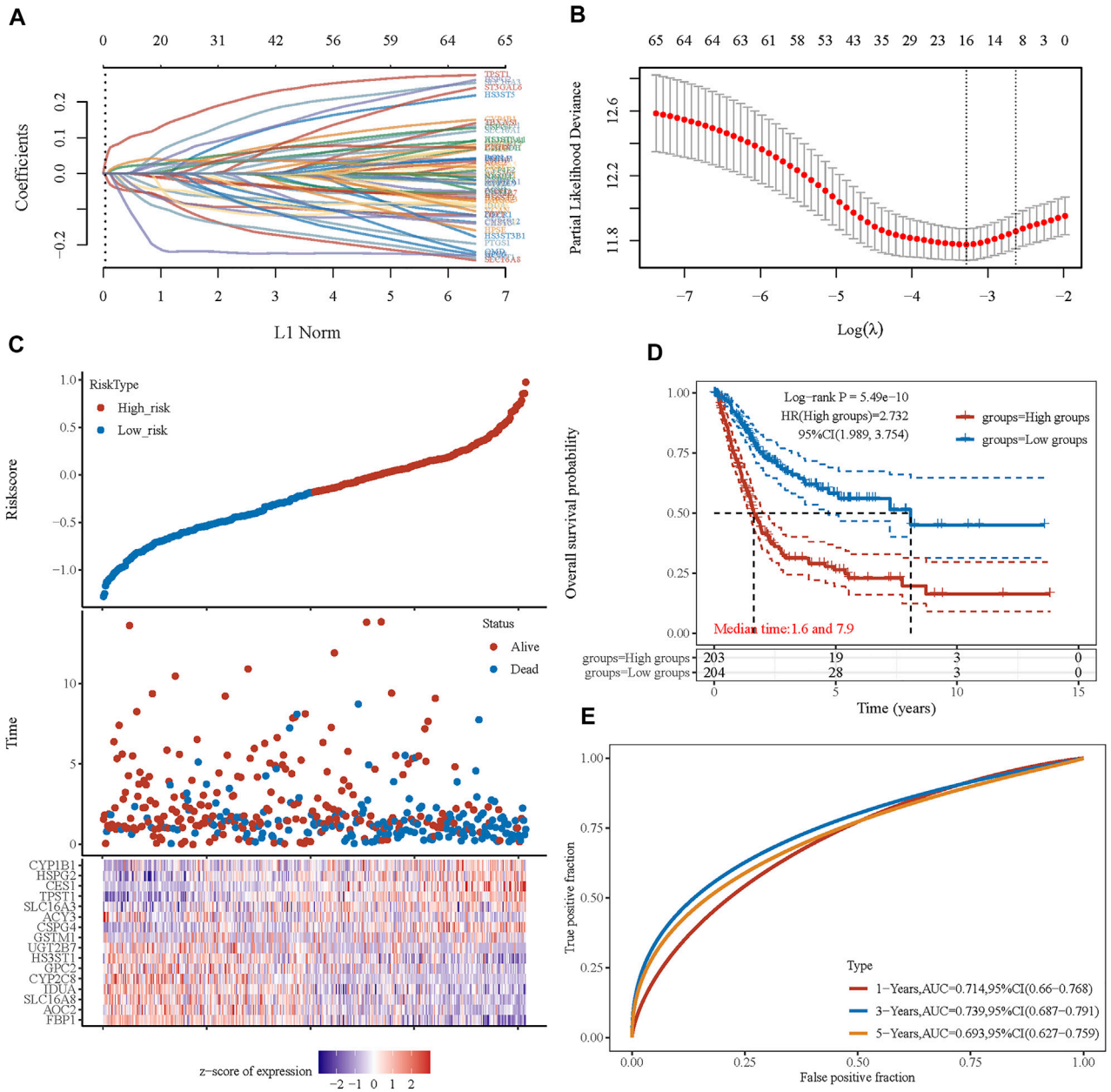

FIGURE 5 | Prognostic signature was established based on four prognostic energy metabolism-related genes. **(A)** LASSO coefficient profiles of the genes associated with the metabolism of BLCA. **(B)** Partial likelihood deviance is plotted versus log(λ). **(C)** The risk score of each sample based on the energy metabolism-related gene set. Patients were divided into low-risk and high-risk groups according to the median value of the risk score. The high/low expression levels of 16 genes which were involved in the prognostic signature are shown in red/blue in each sample. **(D)** The Kaplan–Meier curve of overall survival differences stratified by signature risk score. **(E)** The ROC curves of the signature for overall survival at 1, 3, and 5 years. LASSO: least absolute shrinkage and selection operator. ROC: receiver operating characteristic.

the high-risk group had a significantly poorer OS than those in the low-risk group (**Figure 5D**, $p < 0.001$), and the AUCs for 1-, 3-, and 5-year OS were 0.714, 0.739, and 0.693, respectively (**Figure 5E**). Furthermore, to ensure the prediction value of EMRGPS, an independent cohort from the cBioPortal online database served as a validation set to verify our results. Survival curves showed similar results, and significantly worse OS was observed in the low-risk group than in the high-risk group in patients from the cBioPortal online database (**Figure 6E**). The AUCs for 1-, 3-, and 5-year OS in the validation cohort were 0.637, 0.626, and 0.629, respectively (**Figure 6F**). The association between signature risk scores and clinicopathological characteristics of the validation cohort was presented in the form of a Sankey diagram (**Figure 6G**).

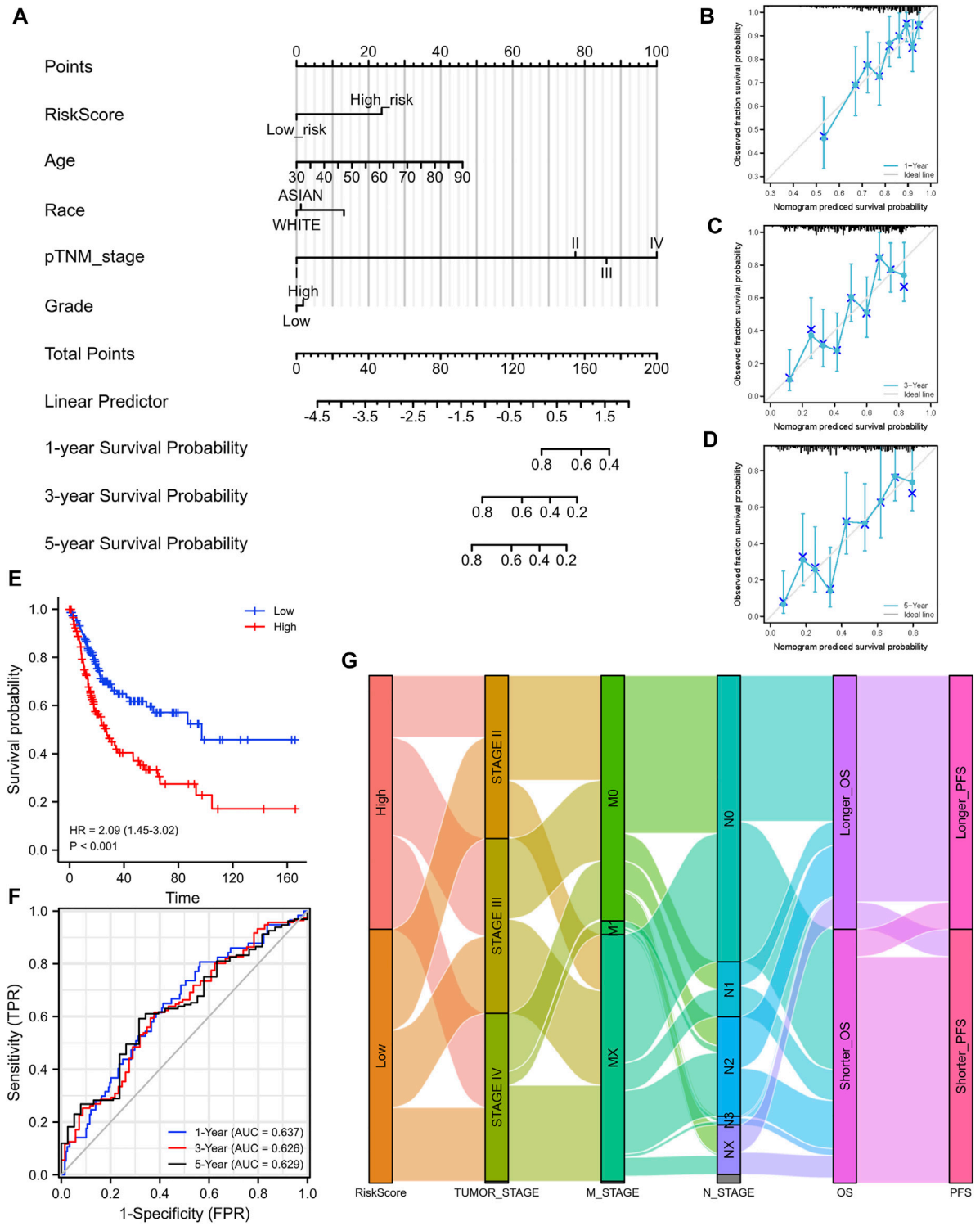

FIGURE 6 | Construction of a nomogram and the independent signature validation. **(A)** Nomogram for predicting 1-, 3-, or 5-year OS in patients with BLCA. **(B)** The calibration plots for predicting 1-year OS. **(C)** The calibration plots for predicting 3-year OS. **(D)** The calibration plots for predicting 5-year OS. **(E)** Validation of the signature in overall survival based on data from the cBioPortal online database. **(F)** The ROC curves of the signature validation for overall survival at 1, 3, and 5 years. **(G)** Sankey diagram showing the association between signature risk scores and clinicopathological characteristics based on data from the cBioPortal database. OS: overall survival. ROC: receiver operating characteristic.

TABLE 2 | Multivariate and univariate Cox regression analyses of EMRGPS and other clinicopathologic characteristics for OS in the TCGA cohort.

Overall survival	Univariate analysis			Multivariate analysis		
	HR	95% CI	*p* Value	HR	95% CI	*p* Value
TCGA cohort						
Age	1.033	1.017–1.049	<0.001	1.029	1.013–1.045	<0.001
Gender (female vs. male)	1.196	0.856–1.670	0.295			
Race			0.264			
White		Reference				
Asian	0.624	0.318–1.227	0.171			
Black	1.258	0.713–2.220	0.427			
Tumor stage (III–IV vs. I–II)	2.123	1.463–3.081	<0.001	1.819	1.250–2.646	0.002
Grade (low vs. high)	0.346	0.085–1.397	0.136			
Risk Score (high vs. low)	2.712	1.959–3.757	<0.001	2.443	1.758–3.395	<0.001

Feathers with p *value <0.1 were involved in multivariate Cox regression analyses. EMRGPS: energy metabolism-related gene-based prognostic signature.*

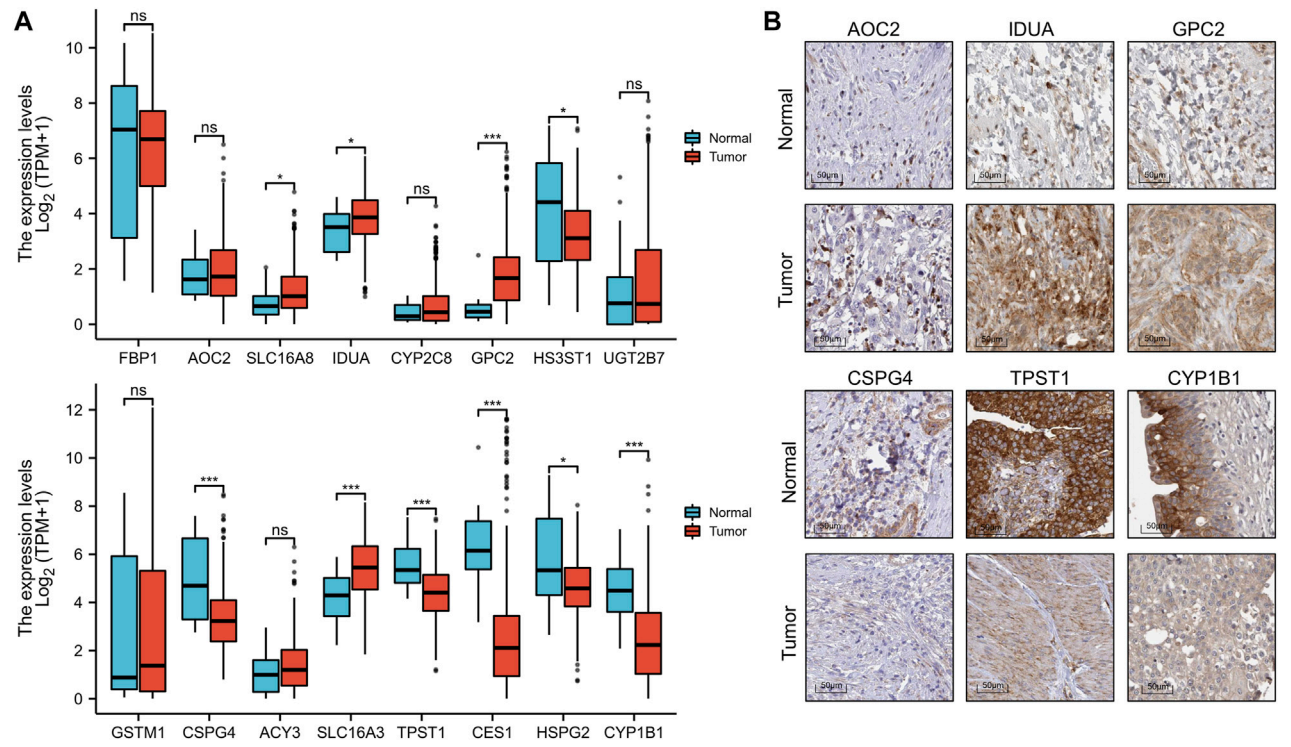

FIGURE 7 | Box plot of the expression difference of 16 genes involved in the prognostic signature between normal and BLCA tissue **(A)**. The expression difference of AOC2, IDUA, GPC2, CSPG4, TPST1, and CYP1B1 between tumor and normal tissue at the protein level according to the Human Protein Atlas (HPA) cohort. **(B)**. **p* < 0.05, ***p* < 0.01, ****p* < 0.001.

To better predict the prognostic value of EMRGPS in patients with BLCA, a nomogram using available clinicopathological parameters and the risk score of the signature was constructed (**Figure 6A**). Moreover, calibration curves using 1-, 3-, and 5-year survival rates were developed to estimate the accuracy of the nomogram (**Figures 6B–D**). The multivariate and univariate Cox regression analyses of EMRGPS and other clinicopathological characteristics for OS are presented in **Table 2**. The signature risk score was an independent factor for the prognosis of patients with BLCA (HR: 2.443, 95% CI: 1.758–3.395, $p < 0.001$). Furthermore, the survival analysis (**Supplementary Figure S6**) and the different expression patterns (**Figure 7A**) of the 16 genes involved in EMRGPS between normal and tumor tissues were explored in the TCGA cohort (**Figure 7**). Of the 16 metabolism-related genes, we found that AOC2, IDUA, GPC2, CSPG4, TPST1, and CYP1B1 were differentially expressed between tumor and normal tissue at the protein level according to the Human Protein Atlas (HPA) cohort (**Figure 7B**).

DISCUSSION

The phenomenon of cancer cells shifting their metabolic pathways from oxidative phosphorylation to glycolysis for the

production of sufficient adenosine triphosphate (ATP) and necessary macromolecular biosynthesis, also known as the Warburg effect, was first described in the 1920s (Weinhouse, 1956). Since its initial establishment, much effort has been made to better understand the potential mechanisms of cancer metabolic reprogramming. Growing evidence has shown that agents targeting cellular energetics in multiple pathways are involved in alterations in cancer metabolism (Jain et al., 2012). In this study, the association between energy metabolic status and the prognosis of patients with BLCA was evaluated based on RNA sequencing data from TCGA and cBioPortal online databases. A significant correlation between clinicopathological features and energy metabolism was observed, indicating that energy metabolism and BLCA are closely linked.

Functional enrichment analysis revealed a strong association between energy metabolic status and immune and inflammatory responses, suggesting an interface between energy metabolic status and the tumor immune microenvironment. Several recent studies have reported numerous alterations in the metabolic status of bladder cancer, indicating that tumor metabolic status may play a role in the tumor immune microenvironment (Woolbright et al., 2018). It was found that the immune system could be affected by lactic acid accumulated from the aerobic glycolysis process of tumor cells, which includes the enhancement of cytokine transcription and inhibition of the differentiation of monocytes into dendritic cells (Becker et al., 2013; Ghesquière et al., 2014). Oresta et al. found that mitochondrial metabolism is reprogrammed to control the induction of immunogenic cell death and the efficacy of chemotherapy for bladder cancer by increasing OXPHOS (Oresta et al., 2021). Our study showed a similar result, in which a significant correlation between metabolic status and resistance to chemotherapy, including doxorubicin and gemcitabine, was observed. Wang et al. reported that the inhibition of pyruvate kinase M2, a glycolytic enzyme for the Warburg effect, could significantly reduce chemoresistance to cisplatin in bladder cancer (Wang et al., 2017). We also found that energy metabolism was significantly correlated with most ICI biomarkers, which acted as biomarkers and immune checkpoint inhibitors or participated in the tumorigenesis and progression of BLCA. Checkpoint inhibitors have recently been approved as second-line treatments, which may alter the pattern of bladder cancer treatment (Teo and Rosenberg, 2018). This result indicates that energy metabolic status may affect the tumor microenvironment through immune cell infiltration and therefore mediate carcinogenesis of BLCA, and may play an important role in the sensitivity and resistance of immune therapy. A recent study found that mutations in peroxisome proliferator-activated receptor gamma (PPARγ), a transcription factor connecting glucose and fatty metabolism, led to immune suppression, such as inhibiting the infiltration of $CD8^+$ T cells in the tumor microenvironment, which may play an important role in checkpoint inhibition in BLCA (Korpal et al., 2017).

Using the OCLR algorithm constructed by Malta et al. (Malta et al., 2018), we found that BLCA metabolic status was significantly correlated with CSCs. CSCs are a population of undifferentiated cells exhibiting stem-like features, with high tumorigenic capacity to recreate the heterogeneity of the primary tumor and serve as a major culprit for recurrence in bladder cancer (Chan et al., 2010; van der Horst et al., 2012). Previous studies have reported that CSCs are resistant to conventional therapies, including chemotherapy, radiation, and immunotherapy (Bao et al., 2006; Li et al., 2008; Radvanyi, 2013). The potential mechanism of CSCs with energy metabolic status in patients with BLCA requires further investigation.

Due to the strong association between energy metabolic status and clinicopathological characteristics in patients with BLCA, a signature was established to stratify patients into high- or low-risk of poor prognosis. Von Rundstedt et al. reported a 30-gene metabolic signature that was significant in predicting survival in patients with BLCA (von Rundstedt et al., 2016). In this study, with the application of a combination of lasso regression, a signature of 16 genes showed a powerful effect on survival prediction. Of the 16 metabolism-related genes, we found AOC2, IDUA, GPC2, CSPG4, TPST1, and CYP1B1 to be differentially expressed between tumor and normal tissues at the protein level. The AOC2 gene encodes retina-specific amine oxidase, which oxidizes aromatic monoamines such as p-tyramine, tryptamine, and 2-phenylethylamine. Its physiological role is still unclear, but a previous study suggested that AOC2 plays a role in hereditary retinal diseases (Lopes de Carvalho et al., 2019). IDUA encodes an enzyme that is correlated to the degradation of two glycosaminoglycans, and mutations in this gene lead to the autosomal recessive disease mucopolysaccharidosis type I (Ghosh et al., 2017). GPC2 belongs to a six-member human glypican family of proteins and is highly expressed in neuroblastoma (Li et al., 2017). CSPG4 represents an integral membrane chondroitin sulfate proteoglycan, which is highly expressed in human malignant melanoma cells (Uranowska et al., 2021). TPST1 encodes an integral membrane glycoprotein of the trans-Golgi network, catalyzing the tyrosine O-sulfation of soluble and membrane proteins that pass through this compartment. TPST1 encodes an integral membrane glycoprotein of the trans-Golgi network, catalyzing the tyrosine O-sulfation of soluble and membrane proteins that pass through this compartment. A previous study reported that TPST1 is highly expressed in breast carcinoma, oral squamous cell carcinoma, and soft tissue sarcoma (Jiang et al., 2015). This gene encodes a member of the cytochrome P450 superfamily of enzymes. Cytochrome P450 proteins are monooxygenases that catalyze many reactions involved in drug metabolism and synthesis of cholesterol, steroids, and other lipids (Dong et al., 2021).

The main limitation of this study is that most analyses were conducted at the mRNA level; further analysis at the protein level is imperative. Moreover, our results were mainly based on the TCGA and cBioPortal datasets. Although the large number of cases from these databases may decrease the risk of bias, another independent cohort is needed to validate our results and minimize the bias.

In conclusion, we found that energy metabolic status is closely related to the immune microenvironment, IC-related genes, CSCs, chemotherapy resistance, prognosis, and recurrence in patients with BLCA. The energy metabolism-related gene signature was then developed to predict the survival of

patients with BLCA. In the era of precision medicine, this signature could provide an effective tool to meet the clinical requirements of BLCA management to some extent.

DATA AVAILABILITY STATEMENT

The original contributions presented in the study are included in the article/**Supplementary Material**, further inquiries can be directed to the corresponding authors.

AUTHOR CONTRIBUTIONS

FZ, JL, XW, YL, and XDW contributed to conception and design of the study. FZ organized the database. DF, SL, and JW performed the statistical analysis. FZ wrote the first draft of the manuscript. FZ, JL, YT, and ZL wrote sections of the manuscript. All authors contributed to manuscript revision, read, and approved the submitted version.

FUNDING

This work was supported by the China Postdoctoral Science Foundation (2021M692281), PostDoctor Research Project, West China Hospital, Sichuan University (21HXBH028), Sichuan Science and Technology Program (grant numbers 2019YJ0133 and 2021YFS0071); Chengdu Science and Technology Program (grant number 2019-YF05-00084-SN) and 1.3.5 Project for Disciplines of Excellence-Clinical Research Incubation Project, West China Hospital, Sichuan University (grant number 2018HXFH049, ZYJC18004, ZY2016104, 2021HXFH007, 20HXJS002). The funders had no role in the study design, data collection or analysis, preparation of the manuscript, or decision to publish.

SUPPLEMENTARY MATERIAL

The Supplementary Material for this article can be found online at: https://www.frontiersin.org/articles/10.3389/fcell.2022.814735/full#supplementary-material

Supplementary Datasheet S1 | An energy metabolism-related gene set containing 590 genes.

Supplementary Figure S1 | Consensus clustering matrix of 408 samples from TCGA dataset for k =3 **(A)**, 4 **(B)**, 5 **(C)**, and 6 **(D)**. Kaplan–Meier curve of progression-free survival of patients with BLCA in two clusters **(E)**. Cumulative distribution function (CDF) plot of consensus clustering for k = 2 to k = 6 **(F)**.

Supplementary Figure S2 | GSEA of cluster-correlated gene sets with the top normalized enrichment score (NES) score through Joy Plot.

Supplementary Figure S3 | Survival curves of ferroptosis-related genes on overall survival in patients with BLCA.

Supplementary Figure S4 | Spearman correlation analysis of the energy metabolism-related gene risk score and immune infiltration level, including B cells **(A)**, CD4+ T cells **(B)**, CD8+ T cells **(C)**, neutrophils **(D)**, macrophages **(E)**, and myeloid dendritic cells **(F)**.

Supplementary Figure S5 | Venn diagram identifies 162 prognostic energy metabolism-related genes that were differentially expressed between cluster 1 and cluster 2 **(A)**. Col1: 3568 genes that were differentially expressed between clusters Col2: 590 metabolism-related genes. Venn diagram identifies 67 differentially expressed energy metabolism-related genes that are significantly correlated with overall survival **(B)**. Col1: 162 metabolism-related genes that were differentially expressed between clusters 1 and 2. Col2: 157 metabolism-related genes were correlated with overall survival ($p < 0.1$).

Supplementary Figure S6 | Survival curves of 16 genes involved in the prognostic signature.

REFERENCES

Babjuk, M., Böhle, A., Burger, M., Capoun, O., Cohen, D., Compérat, E. M., et al. (2017). EAU Guidelines on Non-muscle-invasive Urothelial Carcinoma of the Bladder: Update 2016. *Eur. Urol.* 71 (3), 447–461. doi:10.1016/j.eururo.2016.05.041

Bao, S., Wu, Q., McLendon, R. E., Hao, Y., Shi, Q., Hjelmeland, A. B., et al. (2006). Glioma Stem Cells Promote Radioresistance by Preferential Activation of the DNA Damage Response. *Nature* 444 (7120), 756–760. doi:10.1038/nature05236

Becker, J. C., Andersen, M. H., Schrama, D., and Thor Straten, P. (2013). Immune-suppressive Properties of the Tumor Microenvironment. *Cancer Immunol. Immunother.* 62 (7), 1137–1148. doi:10.1007/s00262-013-1434-6

Bonuccelli, G., Tsirigos, A., Whitaker-Menezes, D., Pavlides, S., Pestell, R. G., Chiavarina, B., et al. (2010). Ketones and Lactate "fuel" Tumor Growth and Metastasis. *Cell Cycle* 9 (17), 3506–3514. doi:10.4161/cc.9.17.12731

Bray, F., Ferlay, J., Soerjomataram, I., Siegel, R. L., Torre, L. A., and Jemal, A. (2018). Global Cancer Statistics 2018: GLOBOCAN Estimates of Incidence and Mortality Worldwide for 36 Cancers in 185 Countries. *CA: A Cancer J. Clinicians* 68 (6), 394–424. doi:10.3322/caac.21492

Chan, K. S., Volkmer, J.-P., and Weissman, I. (2010). Cancer Stem Cells in Bladder Cancer: a Revisited and Evolving Concept. *Curr. Opin. Urol.* 20 (5), 393–397. doi:10.1097/mou.0b013e32833cc9df

Chen, X., Kang, R., Kroemer, G., and Tang, D. (2021). Broadening Horizons: the Role of Ferroptosis in Cancer. *Nat. Rev. Clin. Oncol.* 18 (5), 280–296. doi:10.1038/s41571-020-00462-0

Dang, C. V., and Semenza, G. L. (1999). Oncogenic Alterations of Metabolism. *Trends Biochem. Sci.* 24 (2), 68–72. doi:10.1016/s0968-0004(98)01344-9

DeBerardinis, R. J., and Chandel, N. S. (2016). Fundamentals of Cancer Metabolism. *Sci. Adv.* 2 (5), e1600200. doi:10.1126/sciadv.1600200

Dong, J., Huang, G., Cui, Q., Meng, Q., Li, S., and Cui, J. (2021). Discovery of Heterocycle-Containing α-naphthoflavone Derivatives as Water-Soluble, Highly Potent and Selective CYP1B1 Inhibitors. *Eur. J. Med. Chem.* 209, 112895. doi:10.1016/j.ejmech.2020.112895

Fan, J., Kamphorst, J. J., Mathew, R., Chung, M. K., White, E., Shlomi, T., et al. (2013). Glutamine-driven Oxidative Phosphorylation Is a Major ATP Source in Transformed Mammalian Cells in Both Normoxia and Hypoxia. *Mol. Syst. Biol.* 9, 712. doi:10.1038/msb.2013.65

Fumarola, C., Petronini, P. G., and Alfieri, R. (2018). Impairing Energy Metabolism in Solid Tumors through Agents Targeting Oncogenic Signaling Pathways. *Biochem. Pharmacol.* 151, 114–125. doi:10.1016/j.bcp.2018.03.006

Gao, J., Aksoy, B. A., Dogrusoz, U., Dresdner, G., Gross, B., Sumer, S. O., et al. (2013). Integrative Analysis of Complex Cancer Genomics and Clinical Profiles Using the cBioPortal. *Sci. Signal.* 6 (269), pl1. doi:10.1126/scisignal.2004088

Ghesquière, B., Wong, B. W., Kuchnio, A., and Carmeliet, P. (2014). Metabolism of Stromal and Immune Cells in Health and Disease. *Nature* 511 (7508), 167–176. doi:10.1038/nature13312

Ghosh, A., Mercer, J., Mackinnon, S., Yue, W. W., Church, H., Beesley, C. E., et al. (2017). IDUA Mutational Profile and Genotype-Phenotype Relationships in UK Patients with Mucopolysaccharidosis Type I. *Hum. Mutat.* 38 (11), 1555–1568. doi:10.1002/humu.23301

Hanahan, D., and Weinberg, R. A. (2011). Hallmarks of Cancer: the Next Generation. *Cell* 144 (5), 646–674. doi:10.1016/j.cell.2011.02.013

Hollenbeck, B. K., Wei, Y., and Birkmeyer, J. D. (2007). Volume, Process of Care, and Operative Mortality for Cystectomy for Bladder Cancer. *Urology* 69 (5), 871–875. doi:10.1016/j.urology.2007.01.040

Jain, M., Nilsson, R., Sharma, S., Madhusudhan, N., Kitami, T., Souza, A. L., et al. (2012). Metabolite Profiling Identifies a Key Role for glycine in Rapid Cancer Cell Proliferation. *Science* 336 (6084), 1040–1044. doi:10.1126/science.1218595

Jiang, Z., Zhu, J., Ma, Y., Hong, C., Xiao, S., and Jin, L. (2015). Tyrosylprotein Sulfotransferase 1 Expression Is Negatively Correlated with C-Met and Lymph Node Metastasis in Human Lung Cancer. *Mol. Med. Rep.* 12 (4), 5217–5222. doi:10.3892/mmr.2015.4096

Kamat, A. M., Hahn, N. M., Efstathiou, J. A., Lerner, S. P., Malmström, P.-U., Choi, W., et al. (2016). Bladder Cancer. *The Lancet* 388 (10061), 2796–2810. doi:10.1016/s0140-6736(16)30512-8

Korpal, M., Puyang, X., Jeremy Wu, Z., Seiler, R., Furman, C., Oo, H. Z., et al. (2017). Evasion of Immunosurveillance by Genomic Alterations of PPARγ/RXRα in Bladder Cancer. *Nat. Commun.* 8 (1), 103. doi:10.1038/s41467-017-00147-w

Li, N., Fu, H., Hewitt, S. M., Dimitrov, D. S., and Ho, M. (2017). Therapeutically Targeting Glypican-2 via Single-Domain Antibody-Based Chimeric Antigen Receptors and Immunotoxins in Neuroblastoma. *Proc. Natl. Acad. Sci. USA* 114 (32), E6623–e6631. doi:10.1073/pnas.1706055114

Li, X., Lewis, M. T., Huang, J., Gutierrez, C., Osborne, C. K., Wu, M.-F., et al. (2008). Intrinsic Resistance of Tumorigenic Breast Cancer Cells to Chemotherapy. *JNCI J. Natl. Cancer Inst.* 100 (9), 672–679. doi:10.1093/jnci/djn123

Lopes de Carvalho, L., Bligt-Lindén, E., Ramaiah, A., Johnson, M. S., and Salminen, T. A. (2019). Evolution and Functional Classification of Mammalian Copper Amine Oxidases. *Mol. Phylogenet. Evol.* 139, 106571. doi:10.1016/j.ympev.2019.106571

Luengo, A., Gui, D. Y., and Vander Heiden, M. G. (2017). Targeting Metabolism for Cancer Therapy. *Cel Chem. Biol.* 24 (9), 1161–1180. doi:10.1016/j.chembiol.2017.08.028

Malta, T. M., Sokolov, A., Gentles, A. J., Burzykowski, T., Poisson, L., Weinstein, J. N., et al. (2018). Machine Learning Identifies Stemness Features Associated with Oncogenic Dedifferentiation. *Cell* 173 (2), 338–e15. e15. doi:10.1016/j.cell.2018.03.034

Nieman, K. M., Kenny, H. A., Penicka, C. V., Ladanyi, A., Buell-Gutbrod, R., Zillhardt, M. R., et al. (2011). Adipocytes Promote Ovarian Cancer Metastasis and Provide Energy for Rapid Tumor Growth. *Nat. Med.* 17 (11), 1498–1503. doi:10.1038/nm.2492

Oresta, B., Pozzi, C., Braga, D., Hurle, R., Lazzeri, M., Colombo, P., et al. (2021). Mitochondrial Metabolic Reprogramming Controls the Induction of Immunogenic Cell Death and Efficacy of Chemotherapy in Bladder Cancer. *Sci. Transl Med.* 13 (575). doi:10.1126/scitranslmed.aba6110

Potts, K. G., Irwin, C. R., Favis, N. A., Pink, D. B., Vincent, K. M., Lewis, J. D., et al. (2017). Deletion of F4L (Ribonucleotide Reductase) in Vaccinia Virus Produces a Selective Oncolytic Virus and Promotes Anti-tumor Immunity with superior Safety in Bladder Cancer Models. *EMBO Mol. Med.* 9 (5), 638–654. doi:10.15252/emmm.201607296

Radvanyi, L. (2013). Immunotherapy Exposes Cancer Stem Cell Resistance and a New Synthetic Lethality. *Mol. Ther.* 21 (8), 1472–1474. doi:10.1038/mt.2013.160

Sonveaux, P., Végran, F., Schroeder, T., Wergin, M. C., Verrax, J., Rabbani, Z. N., et al. (2008). Targeting Lactate-Fueled Respiration Selectively Kills Hypoxic Tumor Cells in Mice. *J. Clin. Invest.* 118 (12), 3930–3942. doi:10.1172/JCI36843

Subramanian, A., Tamayo, P., Mootha, V. K., Mukherjee, S., Ebert, B. L., Gillette, M. A., et al. (2005). Gene Set Enrichment Analysis: a Knowledge-Based Approach for Interpreting Genome-wide Expression Profiles. *Proc. Natl. Acad. Sci.* 102 (43), 15545–15550. doi:10.1073/pnas.0506580102

Tang, Z., Kang, B., Li, C., Chen, T., and Zhang, Z. (2019). GEPIA2: an Enhanced Web Server for Large-Scale Expression Profiling and Interactive Analysis. *Nucleic Acids Res.* 47 (W1), W556–w560. doi:10.1093/nar/gkz430

Tennant, D. A., Durán, R. V., and Gottlieb, E. (2010). Targeting Metabolic Transformation for Cancer Therapy. *Nat. Rev. Cancer* 10 (4), 267–277. doi:10.1038/nrc2817

Teo, M. Y., and Rosenberg, J. E. (2018). Nivolumab for the Treatment of Urothelial Cancers. *Expert Rev. Anticancer Ther.* 18 (3), 215–221. doi:10.1080/14737140.2018.1432357

Uranowska, K., Kalic, T., Valtsanidis, V., Kitzwögerer, M., Breiteneder, H., and Hafner, C. (2021). Expression of Chondroitin Sulfate Proteoglycan 4 (CSPG4) in Melanoma Cells Is Downregulated upon Inhibition of BRAF. *Oncol. Rep.* 45 (4). doi:10.3892/or.2021.7965

van der Horst, G., Bos, L., and van der Pluijm, G. (2012). Epithelial Plasticity, Cancer Stem Cells, and the Tumor-Supportive Stroma in Bladder Carcinoma. *Mol. Cancer Res.* 10 (8), 995–1009. doi:10.1158/1541-7786.mcr-12-0274

Vander Heiden, M. G., and DeBerardinis, R. J. (2017). Understanding the Intersections between Metabolism and Cancer Biology. *Cell* 168 (4), 657–669. doi:10.1016/j.cell.2016.12.039

von Rundstedt, F.-C., Rajapakshe, K., Ma, J., Arnold, J. M., Gohlke, J., Putluri, V., et al. (2016). Integrative Pathway Analysis of Metabolic Signature in Bladder Cancer: A Linkage to the Cancer Genome Atlas Project and Prediction of Survival. *J. Urol.* 195 (6), 1911–1919. doi:10.1016/j.juro.2016.01.039

Wang, X., Zhang, F., and Wu, X.-R. (2017). Inhibition of Pyruvate Kinase M2 Markedly Reduces Chemoresistance of Advanced Bladder Cancer to Cisplatin. *Sci. Rep.* 7, 45983. doi:10.1038/srep45983

Weinhouse, S. (1956). On Respiratory Impairment in Cancer Cells. *Science* 124 (3215), 267–269. doi:10.1126/science.124.3215.267

Woolbright, B. L., Ayres, M., and Taylor, J. A., 3rd (2018). Metabolic Changes in Bladder Cancer. *Urol. Oncol. Semin. Original Invest.* 36 (7), 327–337. doi:10.1016/j.urolonc.2018.04.010

Zhou, Z., Huang, R., Chai, R., Zhou, X., Hu, Z., Wang, W., et al. (2018). Identification of an Energy Metabolism-Related Signature Associated with Clinical Prognosis in Diffuse Glioma. *Aging* 10 (11), 3185–3209. doi:10.18632/aging.101625

Conflict of Interest: The authors declare that the research was conducted in the absence of any commercial or financial relationships that could be construed as a potential conflict of interest.

Publisher's Note: All claims expressed in this article are solely those of the authors and do not necessarily represent those of their affiliated organizations, or those of the publisher, the editors, and the reviewers. Any product that may be evaluated in this article, or claim that may be made by its manufacturer, is not guaranteed or endorsed by the publisher.

frontiers in Cell and Developmental Biology

ORIGINAL RESEARCH
published: 25 February 2022
doi: 10.3389/fcell.2022.814388

Radiomics of Contrast-Enhanced Computed Tomography: A Potential Biomarker for Pretreatment Prediction of the Response to *Bacillus* Calmette-Guerin Immunotherapy in Non-Muscle-Invasive Bladder Cancer

Lei Ye[1†], Yuntian Chen[1†], Hui Xu[1], Zhaoxiang Wang[2], Haixia Li[3], Jin Qi[4], Jing Wang[4], Jin Yao[1], Jiaming Liu[2]* and Bin Song[1]*

[1]*Department of Radiology, West China Hospital, Sichuan University, Chengdu, China,* [2]*Department of Urology, Institute of Urology, West China Hospital, Sichuan University, Chengdu, China,* [3]*Philips Healthcare, Chengdu, China,* [4]*University of Electronic Science and Technology of China, Chengdu, China*

OPEN ACCESS

Edited by:
Yongwen Luo,
Wuhan University, China

Reviewed by:
David Chang,
University of Texas MD Anderson Cancer Center, United States
Faouzia Ajili,
Pasteur Institute of Tunis, Tunisia
Jian Lu,
Peking University Third Hospital, China

***Correspondence:**
Jin Yao
shelleyyao@163.com
Jiaming Liu
JM3099@163.com

†These authors have contributed equally to this work and share first authorship

Specialty section:
This article was submitted to Molecular and Cellular Pathology, a section of the journal Frontiers in Cell and Developmental Biology

Received: *13 November 2021*
Accepted: *10 January 2022*
Published: *25 February 2022*

Citation:
Ye L, Chen Y, Xu H, Wang Z, Li H, Qi J, Wang J, Yao J, Liu J and Song B (2022) Radiomics of Contrast-Enhanced Computed Tomography: A Potential Biomarker for Pretreatment Prediction of the Response to Bacillus *Calmette-Guerin Immunotherapy in Non-Muscle-Invasive Bladder Cancer. Front. Cell Dev. Biol. 10:814388. doi: 10.3389/fcell.2022.814388*

Background: *Bacillus* Calmette-Guerin (BCG) instillation is recommended postoperatively after transurethral resection of bladder cancer (TURBT) in patients with high-risk non-muscle-invasive bladder cancer (NMIBC). An accurate prediction model for the BCG response can help identify patients with NMIBC who may benefit from alternative therapy.

Objective: To investigate the value of computed tomography (CT) radiomics features in predicting the response to BCG instillation among patients with primary high-risk NMIBC.

Methods: Patients with pathologically confirmed high-risk NMIBC were retrospectively reviewed. Patients who underwent contrast-enhanced CT examination within one to 2 weeks before TURBT and received ≥5 BCG instillation treatments in two independent hospitals were enrolled. Patients with a routine follow-up of at least 1 year at the outpatient department were included in the final cohort. Radiomics features based on CT images were extracted from the tumor and its periphery in the training cohort, and a radiomics signature was built with recursive feature elimination. Selected features further underwent an unsupervised radiomics analysis using the newly introduced method, non-negative matrix factorization (NMF), to compute factor factorization decompositions of the radiomics matrix. Finally, a robust component, which was most associated with BCG failure in 1 year, was selected. The performance of the selected component was assessed and tested in an external validation cohort.

Results: Overall, 128 patients (training cohort, $n = 104$; external validation cohort, $n = 24$) were included, including 12 BCG failures in the training cohort and 11 failures in the validation cohort each. NMF revealed five components, of which component 3 was selected for the best discrimination of BCG failure; it had an area under the curve (AUC) of .79, sensitivity of .79, and specificity of .65 in the training set. In the external validation cohort, it achieved an AUC of .68, sensitivity of .73, and specificity of .69. Survival

analysis showed that patients with higher component scores had poor recurrence-free survival (RFS) in both cohorts (C-index: training cohort, .69; validation cohort, .68).

Conclusion: The study suggested that radiomics components based on NMF might be a potential biomarker to predict BCG response and RFS after BCG treatment in patients with high-risk NMIBC.

Keywords: BCG immunotherapy, NMF (nonnegative matrix factorization), NMIBC (non-muscle-invasive bladder cancer), CECT images, radiomics analysis

INTRODUCTION

Bladder cancer (BCa) is one of the most common cancers worldwide (Siegel et al., 2020). Based on the presence of muscular-invasiveness, BCa is pathologically categorized into muscular invasive BCa (MIBC) and non-muscular invasive BCa (NMIBC). Currently, the standard care for patients with NMIBC with a high-risk of recurrence is *Bacillus* Calmette-Guérin (BCG) instillation along with transurethral resection of bladder tumor (TURBT) (Babjuk et al., 2019). This therapy is effective in reducing recurrence and progression and increasing the survival of patients with high risk (Babjuk et al., 2019). However, approximately 40–60% of patients experience tumor recurrence within 2 years (Kamat and Sylvester, 2016). The earlier the tumor recurrence or BCG response is predicted, the better the patients' chances of recieving new or alternative therapies because of the high recurrence rate after BCG treatment (Lotan et al., 2017).

However, no standard method has been established for predicting responses to BCG instillation. As the outcome of BCG instillation tends to vary across molecular characteristics, how to make a quantitative pretreatment prediction on the recurrence or progression after BCG treatment for better treatment planning is still a great challenge (Tran et al., 2020). Various biochemical indicators have been proposed to predict the responses to BCG in patients with high-risk NMIBC, including urinary and serum cytokine/chemokine profiles, and peripheral blood counts, such as eosinophils, neutrophils, lymphocytes, Th1, and Th2. However, these studies had small sample sizes and were not externally validated (Kamat et al., 2018; Martínez et al., 2019; Temiz et al., 2021). No studies have applied medical imaging tests, such as ultrasound, computed tomography (CT), and magnetic resonance imaging (MRI), for predicting BCG treatment response, while they have been widely used for pretreatment prediction of other cancers, such as breast (Liu et al., 2020; Xiong et al., 2021), lung (Liu et al., 2021), and renal cancers (Rallis et al., 2021). Since diagnostic images can depict the phenotypes of bladder cancer in a non-invasive way, recent studies have illustrated that the utilization of imaging biomarkers to predict the response of MIBC with different chemotherapies is feasible (Cha et al., 2017; Hadjiiski et al., 2020; Necchi et al., 2020). Among these non-invasive imaging-based radiomics prediction or classification models, various dimensionality reduction and matrix decomposition methods have been introduced, such as vector quantization and principal component analysis. However, these methods have limited ability to capture the full message of radiomics data from a small region of interest (ROI) in patients with NMIBC, which might account for the fact that no radiomics model has been developed for predicting BCG response in such patients.

Non-negative matrix factorization (NMF), an algorithm based on decomposition by parts (Lee and Sebastian, 1999), has been introduced to identify distinct molecular patterns, while recovering meaningful biological information from tumor-related microarray data (Brunet et al., 2004; Motzer et al., 2020). In this study, we used NMF to decompose the radiomic features from small lesions on contrast-enhanced CT images, which can then be analyzed by combining different features; thus, generating all variabilities of components to represent samples, analogous to gene expression patterns in terms of the metagenes (Brunet et al., 2004). Subsequently, the most relevant component of BCG failures could be selected, which might be a potential biomarker for BCG response.

In this study, we applied NMF and our model selection criterion by factorizing the radiomic features extracted from the pretreatment contrast-enhanced CT images in NMIBC and generated different feature components representing different NMIBC subtypes. We were able to investigate whether radiomics feature components are associated with BCG failure and whether this substaging method can be used to improve patient stratification at diagnosis of NMIBC.

MATERIALS AND METHODS

Study Design

This was a two-center retrospective observational study. An unsupervised factorization algorithm named NMF, which iteratively selects the most robust pattern within pretreatment contrast-enhanced CT images, was proposed to predict the response to BCG in patients with high-risk NMIBC. Histopathological examination after TURBT was performed as per the reference standard. This study was approved by the institutional review boards of West China Hospital and Shang Jin Nan Fu Hospital, and was conducted in accordance with the Declaration of Helsinki, and the requirement for informed consent was waived.

Patients

Patients who 1) were pathologically diagnosed with HR-NMIBC (Tis or Ta/T1HG urothelial carcinoma) by TURBT; 2) received ≥5/6 BCG induction instillations after TURBT; 3) underwent TURBT or radical cystectomy when a new lesion was found during follow-up cystoscopy; and 4) underwent pretreatment contrast-enhanced CT scanning before TURBT within one to 2 weeks were included in the

study. Patients who 1) did not have pre-TURBT pathological results; 2) did not complete BCG induction or had a nonstandard instillation regimen (i.e., the number of BCG instillation less than 5); 3) had confirmative surgery at an external institution, or did not have their recurrence assessed, or had follow-up less than 12 mon; 4) did not undergo pretreatment contrast-enhanced CT scanning; and 5) had insufficient CT quality to obtain measurements (e.g., due to metal artifacts) were excluded from the study.

The primary endpoint of this study was the response status to BCG instillation therapy (BCG failure/BCG response) within 1 year. Specifically, BCG failure was defined according to the European Urology Association guidelines (Babjuk et al., 2019). The secondary endpoint was recurrence-free survival (RFS), defined as the time interval from the beginning of BCG therapy to the first high-grade disease recurrence (BCG failure) during follow-up.

Image Recognition and Feature Extraction

Contrast-enhanced CT examination of each patient was performed within 1–2 weeks before surgery. CT scanning was performed using a 128-MDCT scanner (SOMATOM Definition Flash, syngo CT 2012B medical system, Siemens, Germany) or a 160-revolution APAX MDCT scanner (Quantix 160 mm × ray cube, GEmedical system, United States). All CT examinations were performed under the following conditions: 120 KVp; 210mA; 14.17 ctdIVOL (mGy); 778.7 DLP (mGy*cm); pitch, 1.0; rotation time, .5 s; section thickness, 2.0 and 5.0 mm.

Three-dimensional region of interest (3D-ROI) was manually delineated on the CT images using ITK-SNAP software (http://www.itksnap.org), and the largest tumor was targeted for patients with multiple lesions in this study. To accurately match the targeted ROI and the pathological result, we had a coordinator to carefully review the surgery records and record the final pathological grades of targeted tumors. Radiologist 1 (4 years' experience) manually drew the 3D-ROIs along the tumor margin, and then the radiologist 2 (10 years' experience) validated these ROIs. To ensure reproducibility of ROIs, intra-class correlation (ICCs) was used for evaluating intra-observer agreement. We randomly selected 30 patients and re-delineated ROIs by radiologists 1 one month later after the initial ROI segmentation. An ICC greater than 0.75 were considered ROIs of satisfactory reproducibility. All images were resampled to a spacing of 1.0*1.0*2.0 cm. We used the image feature extraction software Python package (pyradiomics) to obtain 107 CT-based radiomic features, all of which were based on original images, including 14 shape features, 18 histogram features, and 68 texture features (**Supplementary Table S1**). All of these features have been previously reported (Aerts et al., 2014; Zhang et al., 2020; Fiz et al., 2021).

Feature Decomposition and NMF Component Construction

Radiomic features with high collinearity were excluded. Subclasses were then computed by reducing the dimensionality of the expression data from reserved radiomics features to a few meta-features using NMF (Python pakage Nimfa) (Kamat et al., 2018). This method computes multiple k-factor factorization decompositions of the feature matrix, which is the first value where the residual sum of squares curve presents an inflection point (Hutchins et al., 2008).

In traditional matrix decomposition technologies, such as feature decomposition, the decomposed matrix will have negative values, but negative values are meaningless in the actual scene. For example, in the field of image processing, radiomics features are a matrix composed of non-negative numbers, which have no practical significance for the negative values obtained by decomposition processing. Our goal is to find a small number of meta-features, each defined as a positive linear combination of the M radiomics features. Mathematically, this corresponds to factoring matrix V into two matrices with positive entries, V ~ WH. The shape of V is M × N, M equals to the number of features and N equals to the number of samples, as shown in **Figure 2A**. Matrix W has size M × k, with each of the k columns defining a meta-feature; entry Wij is the coefficient of feature i in metafeature j. Matrix H has size k × N, with each of the M columns representing the metafeature pattern of the corresponding sample; entry H_{ij} represents the level of metafeature i in sample j. For more convenient expression, we depict the level of the metafeature as the score of this component. As the NMF finds different solutions for different initial conditions, the factorizations were repeated 100 times. To select the metafeature with the most predictive ability for disease relapse, we built single-factor Cox models for each metafeature to find the metafeature with the highest C-index.

Performance Assessment

The predictive values of the NMF components were evaluated using the receiver operator characteristic and area under curve (AUC). The cutoff values for estimating sensitivity and specificity were determined using the Youden's index. The prognostic performance of the proposed components was assessed using Harrell's concordance index (C-index) and Kaplan–Meier log-rank analysis, which was also tested in the validation cohort. Furthermore, confusion matrices were constructed to evaluate the agreement between the observed outcomes and the NMF-predicted outcomes, and a calibration curve was plotted for the evaluation of predicted survival.

Statistical Analysis Workflow

Descriptive data were summarized as frequencies and percentages. Continuous parametric variables are presented as mean ± standard deviation. Nonparametric variables are shown as mean (interquartile range). Pearson's chi-square test or Fisher's exact test was used for categorical variables. Comparisons of continuous variables were conducted using Mann-Whitney U tests or Student's t-tests. Statistical significance was set at $p < .05$ was considered to be statistically different. Statistical analyses were performed using R software (version 3.8).

RESULTS

Clinical Characteristics

As shown in **Figure 1**, 413 potentially eligible patients were consecutively retrieved from the databases of two hospitals, and 128 patients were finally included in this study according

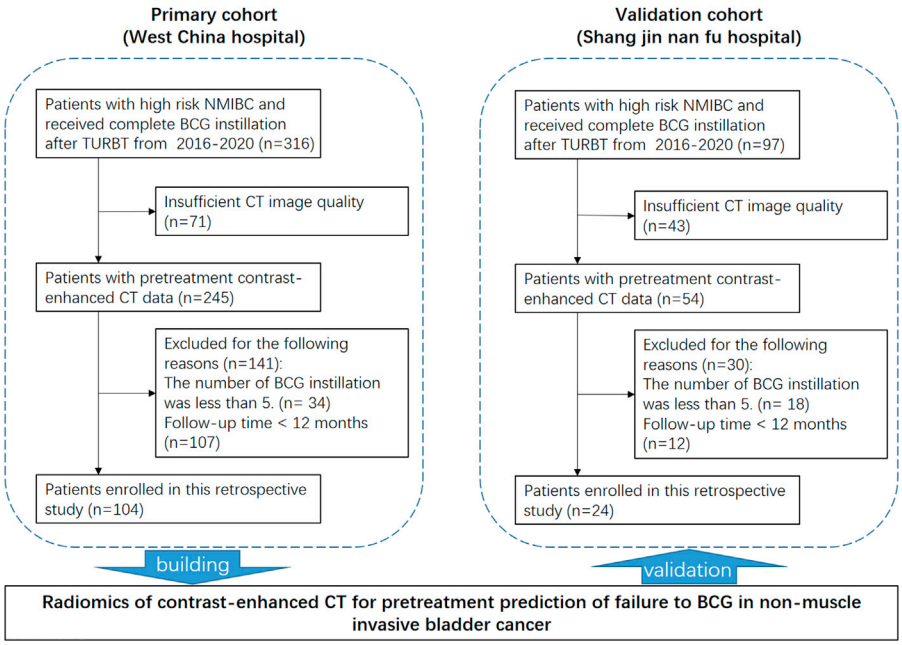

FIGURE 1 | Patient recruitment and study design.

to the inclusion and exclusion criteria. The dataset from West China Hospital had 108 eligible patients and was used to develop the model. The clinical characteristics of the patients are summarized in **Table 1**.

The cutoff date of the primary training cohort was June 19, 2021, and the median follow-up time was 24 months (IQR, 16–37 months). Twelve patients (11.1%) had BCG failure. The median RFS was 9 months (IQR, 8–10 months). The cutoff date of the validation cohort was September 30, 2021, and the median follow-up time was 12 months (IQR, 7–21 months). Eleven patients (45.8%) experienced BCG failure. The median RFS was 7 months (IQR, 5–10 months). No significant differences were detected between these two cohorts in terms of age, rate of concomitant carcinoma *in situ*, tumor focality, and size, while the

TABLE 1 | Baseline characteristics of the patients in this study.

	Primary cohort (*N* = 104)	Validation cohort (*N* = 24)	*p*
Age (years, mean ± SD)	66.0 ± 11.2	69.2 ± 10.8	.196
Gender			
Male	82 (78.8)	21 (20.2)	0.256
Female	22 (21.2)	3 (79.8)	
Concomitant CIS			.327
No	70 (67.3)	18 (75)	
Yes	34 (32.7)	6 (25)	
Tumor focality			0.522
Unifocal	51 (49.2)	12 (50)	
Multifocal	53 (50.8)	12 (50)	
Tumor size (cm)			0.418
<3	74 (71.2)	16 (66.7)	
≥3	30 (28.8)	8 (33.3)	
Stage			<.001
Ta	58 (55.8)	4 (16.7)	
T1	49 (44.2)	20 (83.3)	
BCG failure			<.001
No	96 (88.9)	13 (54.2)	
Yes	12 (11.1)	11 (45.8)	
Median total BCG instillations (IQR)	19 (19–23)	14 (9—16)	
Median total mos follow-up (IQR)	24 (16–37)	12 (7–21)	
Median mos time to BCG failure (IQR)	9 (8—10)	7 (5–10)	

BCG, Bacillus *Calmette-Guerin; CIS, carcinoma* in situ*; IQR, inter-quartile range; SD, standard deviation.*

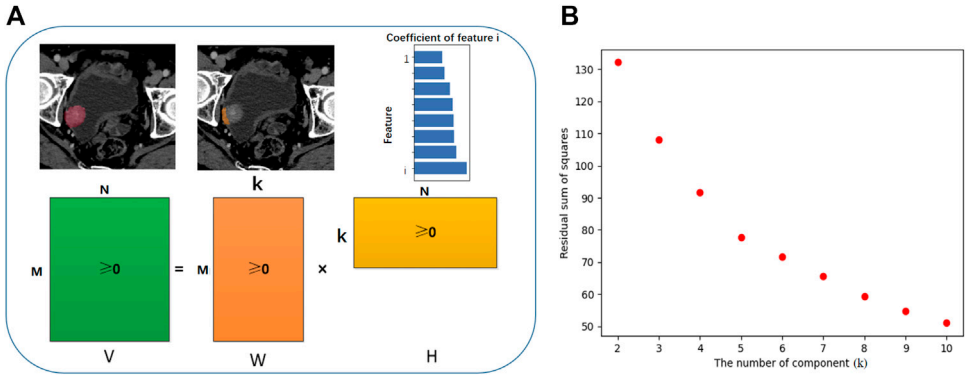

FIGURE 2 | Workflow of non-negative matrix factorization (NMF). **(A)** V represents the original data matrix as the combination of two matrices, V ~ WH. The shape of V is M × N, M equals to the number of features and N equals to the number of samples. W is a matrix which contains the reduced number of k components derive from NMF, and the sub-classified features for each component (M). Matrix H has size k × N, with each of the M columns representing the metafeature pattern of the corresponding sample. **(B)** The most robust NMF of training cohort selected and tested k = 2 to k = 10, and the turning point was identified as k = 5. That is, NMF identified five components of radiomics features in the primary training cohort.

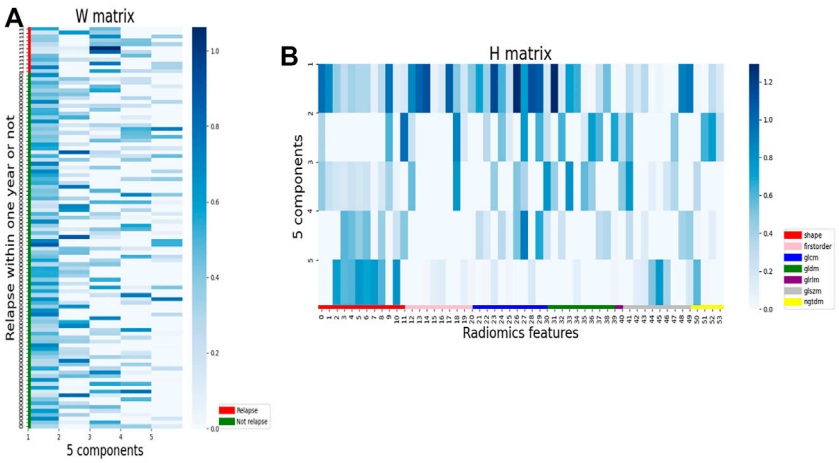

FIGURE 3 | Illustration of component selection with NMF. **(A)** Patients were aggregated by NMF component using the mean across patients for each component, and the mean Z score for each feature was calculated, resulting in one Z score per feature per NMF component. **(B)** Heatmap of radiomics features. Z scores were calculated for each features. Samples are grouped by NMF components.

validation cohort had significantly higher proportions of BCG failure ($p < .001$) and T1 stage ($p < .001$).

Construction of NMF Components

We excluded 53 radiomic features with high collinearity. To expand our understanding of the radiomics of bladder cancer, we utilized NMF to leverage the CT radiomics dataset in high-risk NMIBC and further identify predictive radiomics biomarkers of BCG failure. The most robust NMF of 108 patients selected and testing k = 2 to k = 10 was identified as k = 5 (**Figure 2B**). That is, NMF identified five components of radiomics features in the primary training cohort (as shown in the **Supplementary Table S2**). The W matrix reflects the composition of each component (**Figure 3A**), and the H matrix reflects the scores of five components for each sample (**Figure 3B**), from which we can conclude that component 3 is most associated with the failure of BCG treatment, as the level of this component is higher in the samples with the failure of BCG treatment.

Predictive and Prognostic Performance of NMF Components

The scores of NMF component 3 yielded a good prediction performance, with an AUC of .79 in the developing cohort (**Figure 4A**), and accurately predicted 9/12 BCG failures and 60/92 patients without BCG failure (**Figure 4B**). The optimal cutoff value was the component z-score of .2 with sensitivity and specificity of .75 and .65, respectively. Component 3 showed moderate performance in recurrence-free survival (RFS)

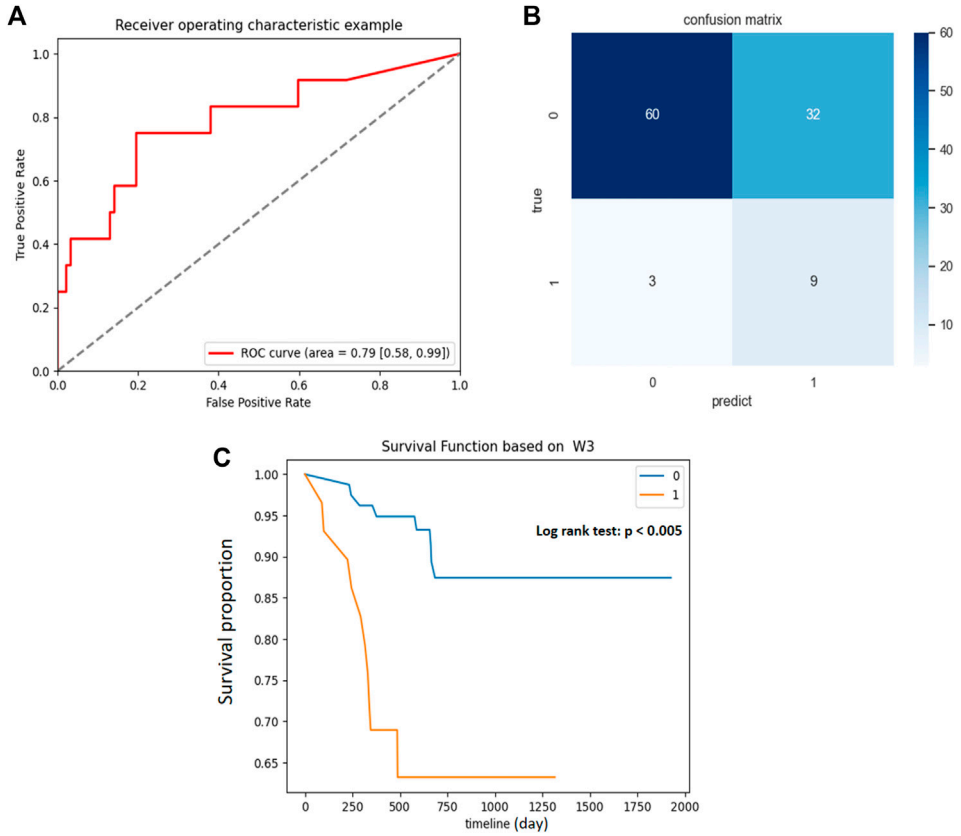

FIGURE 4 | Association between NMF component 3 and clinical outcomes in primary cohort. **(A)** ROC curve and the AUC for the predictive accuracy of NMF component 3 in predicting BCG failure in 1 year. **(B)** Confusion matrix presenting the predictive outcomes using NMF component 3 and true outcomes of BCG failure in 1 year. **(C)** With the component Z score of .2 as the cutoff, patients with scores <.2 (0) had significantly prolonged recurrence free survival (RFS) than those with scores >.2 (1), $p < .005$.

estimation in the training cohort, with a C-index of .69. Patients were divided into high-risk and low-risk groups, with a component z-score of .2 as the cutoff. Compared with patients with a z-score of less than .2, patients in the group with z-score larger than .2 had a significantly shorter RFS (**Figure 4C**, $p < .005$). The associations between the top five features in NMF component 3 and RFS were separately examined, as shown in **Supplementary Figure S1**.

Good performance was also observed for BCG failure prediction in the validation cohort. As shown in **Figure 5B**, NMF component 3 accurately predicted 8/11 BCG failures and 9/13 patients without BCG failure. Although he AUC of NMF dropped marginally in the validation cohort, the AUC approximated .70 (**Figure 5A**), and the sensitivity and specificity were .73 and .69, respectively. For prognostic performance, component 3 achieved a moderate performance in the estimation of RFS (C-index, 0.68) in the validation cohort. Compared with patients with a z-score of less than .2, patients in the group with z-score larger than .2 had a significantly shorter RFS (**Figure 5C**, $p = .04$). The calibration curve and decision curve analysis of the NMF components are shown in **Figures 5D,E**, which indicate its potential clinical usefulness.

DISCUSSION

In this two-center study, we investigated the ability of pretreatment contrast-enhanced radiomics analysis so as to predict BCG failure in patients with high-risk NMIBC. An unsupervised strategy named NMF was proposed with better performance in the primary training cohort and performed well in the external validation cohort. The outperformance of NMF indicated that the NMF-decomposed components from CT radiomics features could serve as potential biomarkers for pretreatment predicting BCG failure in patients with high-risk NMIBC.

It is of great guiding significance for the selection of treatment options and clinical decision support of patients with high-risk NMIBC to identify predictive biomarkers related to the BCG response and subsequent recurrence time (Kamat et al., 2018; Ilijazi et al., 2020; Shiota et al., 2020). Currently, most studies have focused on biomarkers in biological specimens, such as peripheral blood, urine, and tumor tissue from surgery. High levels of urine Treg cells and tumor-infiltrating dendritic cells in the pathological examination were associated with rapid recurrence following BCG therapy (Chevalier et al., 2018;

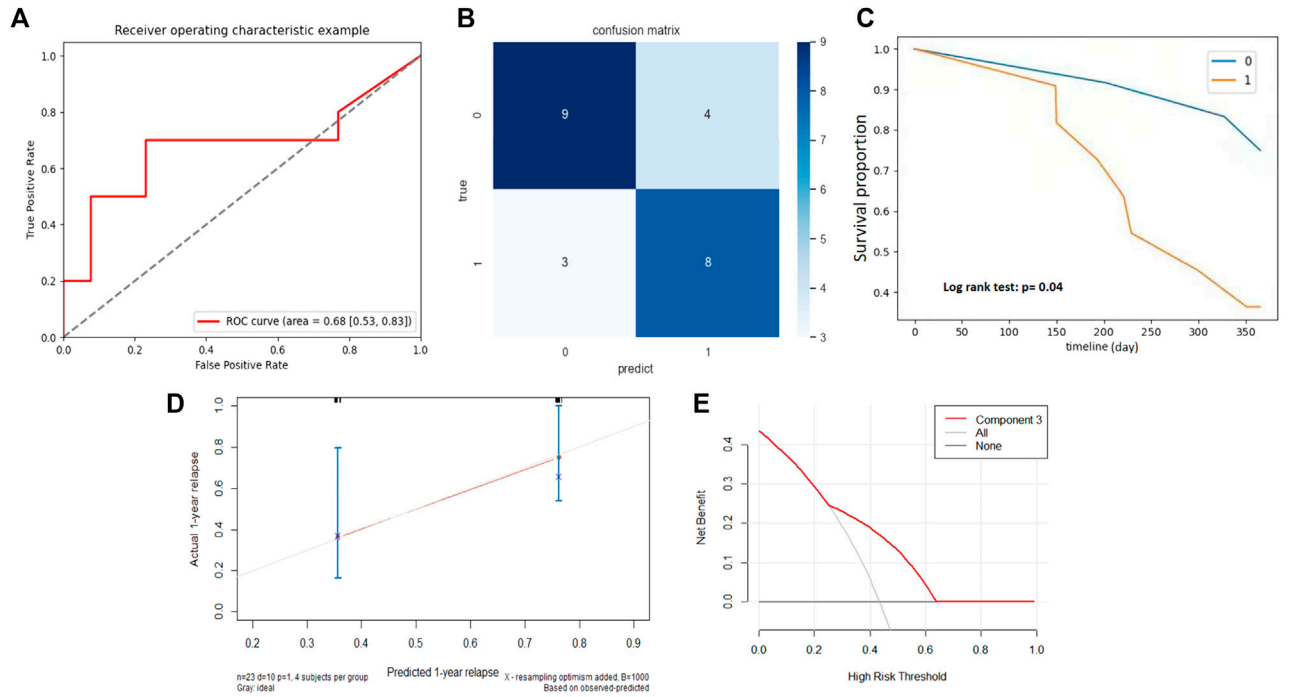

FIGURE 5 | External validation of NMF component 3. **(A)** ROC curve and the AUC for the predictive accuracy of NMF component 3 in predicting BCG failure in 1 year. **(B)** Confusion matrix presenting the predictive outcomes using NMF component 3 and true outcomes of BCG failure in 1 year. **(C)** With the component Z score of .2 as the cutoff, patients with scores <.2 (0) had significantly prolonged recurrence free survival (RFS) than those with scores >.2 (1), p = .04. **(D)** Calibration curve of the component 3. **(E)** Decision curve of component 3. The *X*-axis shows the cutoff value, while the *Y*-axis shows the net benefit.

Ayari et al., 2009). For prognostic outcome after BCG treatment, Martinez et al. found that patients with a lower T-bet$^+$/ lymphocyte ratio and higher GTR/NLR had significantly longer recurrence-free survival (Martínez et al., 2019). As to the pathological results, De Jong et al. found that T1 patients with extensive invasion of the lamina propria had a higher risk for BCG failure and an improved progression-free survival (de Jong et al., 2021). However, there are some inherent limitations for these biomarker-finding studies, such as poor specificity of biochemical factors for reacting to both inflammation and tumor, lack of external validation, and high interobserver variability in invasion extension (Babjuk et al., 2019; Del Giudice et al., 2020). The presentation of tumors on radiological images tends to be more stable than biochemistry factors, and image biomarkers extracted from medical images retain excellent stability (Zwanenburg et al., 2020) and are more easily available than pathological substaging. In our study, a non-invasive CT-based NMF component was developed and performed well in an external validation cohort.

Various imaging-based radiomics models have been proposed to predict treatment responses in different cancers (Liu et al., 2021; Rallis et al., 2021;. Zhong et al., 2021) with the hypothesis that these selected imaging features reflect specific tumor phenotypes (Lambin et al., 2012; Aerts et al., 2014). In addition, many other studies have reported the effects of imaging features on survival outcomes, but no studies have been reported regarding BCG instillation on patients diagnosed with high-risk NMIBC. In this study, the proportion of BCG failure in 1 year was too low to construct a traditional radiomics model, which we had tried on, and of which the accuracy was similar to that of flipping a coin. The main reasons for the unexpected low discrimination of traditional radiomics models might be the low proportion of BCG failure and relatively greater amount of radiomic features, which increased the difficulty of traditional machine learning methods to discover patterns of BCG failure cases (van der Ploeg et al., 2014; Gillies, Kinahan, and Hricak 2016; Moons et al., 2019). The goal of our research is similar to gene expression studies, of which a handful metagenes are selected from thousands of genes in limited samples. This can be achieved with NMF, which is an unsupervised algorithm based on decomposition by parts and a model selection mechanism. NMF has been used to iteratively select the most robust biomarkers from thousands of genes (Zhong et al., 2018; Zeng et al., 2019; Motzer et al., 2020) and to find structural covariance patterns in neuroimaging content (Nassar et al., 2019; Patel et al., 2020). In our application of NMF to radiomic features, the parts were the components of a reduced representation of the original hidden features, which may enable the recovery of biologically similar phenotypes. Considering that the molecular mode of BCG actions remains partially understood, NMF components might be a hint for potential pathways for BCG treatment failure based on

previous reports about the cellular geography associated with the poor response to BCG (Ilijazi et al., 2020; Shiota et al., 2020; Tran et al., 2020).

Compared with CT, the superiority of MRI has been documented with respect to the diagnostic performance and evaluation of treatment response of BCa, but there have been no studies on their performance in radiomics analysis (Wong et al., 2021). For MRI-based radiomics, it is quite difficult to standardize image acquisitions for numerous parameters and many variations among manufacturers with different magnetic fields (Wakabayashi et al., 2019). In addition, MRI is susceptible to many artifacts, such as image and signal distortion consequences due to contiguous gas-filled bowls and gas bubbles within the bladder (Lin and Chen, 2015) which could complicate the reproducibility of measurements. In studies on CT radiomics, automatic acquisition protocol and test-retest analysis have proven to be useful in overcoming the bias of acquisition protocols (Caruso et al., 2021). In light of the above limitations, radiomic models based on MRI are more difficult to reproduce across institutions than those based on CT images (Harding-Theobald et al., 2021). CT is recommended prior to TURBT according to the NCCN guidelines, and is still the most commonly used imaging method worldwide in diagnosing and staging BCa, mainly because CT is fast and inexpensive (Babjuk et al., 2019; Flaig et al., 2020). Considering the easily acquired CT images across hospitals, the CT radiomics model can be clinically validated on a larger sample. As expected, the NMF components from CT radiomics demonstrated a stable performance in this double-center study, and further large-scale studies are needed to determine the reproducibility and clinical utility of NMF components.

Despite these remarkable results, our study has several inherent limitations. First, although we found a robust component, which was strongly related to the risk of BCG failure in 1 year and associated with the recurrence survival after BCG instillation, we failed to uncover the underlying molecular mechanisms of these nested radiomic features. Further investigation could focus on the comparison of gene/molecular expression patterns among different subtypes defined by radiomic features. Second, owing to the retrospective design of this study, some inherent limitations were inevitable, such as the high proportion of excluded cases for missing data and those with poor quality in CT images. Besides, the retrospective design might be the main cause of inconsistent recurrence rates in the two cohorts. Given the fact that our NMF strategy performed well in both cohorts with extremely different BCG failure rates, we still have confidence in the further predictive validation of NMF strategy. Future studies should enroll more patients with standard BCG instillation with regular follow-up, so that the NMF strategy could be better validated.

In conclusion, the present preliminary study suggests that NMF could provide a potential tool for predicting BCG response and survival outcomes in patients with high-risk NMIBC. With further molecular research, NMF-based components may be useful as molecular biomarkers of treatment response.

DATA AVAILABILITY STATEMENT

The raw data supporting the conclusion of this article will be made available by the authors, without undue reservation.

ETHICS STATEMENT

The studies involving human participants were reviewed and approved by the institutional review boards of West China Hospital and Shang Jin Nan Fu Hospital. Written informed consent for participation was not required for this study in accordance with the national legislation and the institutional requirements.

AUTHOR CONTRIBUTIONS

YJ, JML, and SB: conception and design, and manuscript revision. YL and YTC: conception and design, data analysis and interpretation, and manuscript writing and revision. XH and ZXW: data acquisition. HXL, JW, and JQ: image preprocessing, and model building. All authors read and approved the final manuscript.

FUNDING

National Science Foundation of China Youth Fund (No. 31801066).

SUPPLEMENTARY MATERIAL

The Supplementary Material for this article can be found online at: https://www.frontiersin.org/articles/10.3389/fcell.2022.814388/full#supplementary-material

REFERENCES

Aerts, H. J. W. L., VelazquezLeijenaar, E. R., Leijenaar, R. T. H., Parmar, C., Grossmann, P., Carvalho, S., et al. (2014). Decoding Tumour Phenotype by Noninvasive Imaging Using a Quantitative Radiomics Approach. *Nat. Commun.* 5 (June), 4006. doi:10.1038/ncomms5006

Ayari, C., LaRue, H., Hovington, H., Decobert, M., Harel, F., Bergeron, A., et al. (2009). Bladder Tumor Infiltrating Mature Dendritic Cells and Macrophages as Predictors of Response to Bacillus Calmette-Guérin Immunotherapy. *Eur. Urol.* 55 (6), 1386–1396. doi:10.1016/j.eururo.2009.01.040

Babjuk, M., Burger, M., Compérat, E. M., Gontero, P., Mostafid, A. H., Palou, J., et al. (2019). European Association of Urology Guidelines on Non-muscle-invasive Bladder Cancer (TaT1 and Carcinoma *In Situ*) - 2019 Update. *Eur. Urol.* 76 (5), 639–657. doi:10.1016/j.eururo.2019.08.016

Brunet, J.-P., Tamayo, P., Golub, T. R., and Mesirov, J. P. (2004). Metagenes and Molecular Pattern Discovery Using Matrix Factorization. *Proc. Natl. Acad. Sci.* 101 (12), 4164–4169. doi:10.1073/pnas.0308531101

Caruso, D., Polici, M., Zerunian, M., Pucciarelli, F., Guido, G., Polidori, T., et al. (2021). Radiomics in Oncology, Part 1: Technical Principles and Gastrointestinal Application in CT and MRI. *Cancers* 13 (11), 2522. doi:10.3390/cancers13112522

Cha, K. H., Hadjiiski, L., Chan, H.-P., Weizer, A. Z., Alva, A., CohanCohanCaoili, R. H., et al. (2017). Bladder Cancer Treatment Response Assessment in CT Using Radiomics with Deep-Learning. *Sci. Rep.* 7 (August). doi:10.1038/s41598-017-09315-w

Chevalier, M. F., Schneider, A. K., Dartiguenave, V. F., Lucca, I., Jichlinski, P., Nardelli-Haefliger, D., et al. (2018). Conventional and PD-L1-Expressing Regulatory T Cells Are Enriched during BCG Therapy and May Limit its Efficacy. *Eur. Urol.* 74 (5), 540–544. doi:10.1016/j.eururo.2018.06.045

de Jong, F. C., Hoedemaeker, R. F., Kvikstad, V., Mensinkde Jong, J. T. M., de Jong, J. J., Boevévan der Schoot, E. R., et al. (2021). T1 Substaging of Nonmuscle Invasive Bladder Cancer Is Associated with bacillus Calmette-Guérin Failure and Improves Patient Stratification at Diagnosis. *J. Urol.* 205 (3), 701–708. doi:10.1097/JU.0000000000001422

Del Giudice, F., Barchetti, G., De Berardinis, E., Pecoraro, M., Salvo, V., Simone, G., et al. (2020). Prospective Assessment of Vesical Imaging Reporting and Data System (VI-RADS) and its Clinical Impact on the Management of High-Risk Non-muscle-invasive Bladder Cancer Patients Candidate for Repeated Transurethral Resection. *Eur. Urol.* 77 (1), 101–109. doi:10.1016/j.eururo.2019.09.029

Fiz, F., Costa, G., Gennaro, N., la Bella, L., Boichuk, A., Sollini, M., et al. (2021). Contrast Administration Impacts CT-Based Radiomics of Colorectal Liver Metastases and Non-tumoral Liver Parenchyma Revealing the "Radiological" Tumour Microenvironment. *Diagnostics* 11 (7), 1162. doi:10.3390/diagnostics11071162

Flaig, T. W., Spiess, P. E., Agarwal, N., Bangs, R., Boorjian, S. A., Buyyounouski, M. K., et al. (2020). Bladder Cancer, Version 3.2020, NCCN Clinical Practice Guidelines in Oncology. *J. Natl. Compr. Cancer Netw. : JNCCN* 18 (3), 329–354. doi:10.6004/jnccn.2020.0011

Gillies, R. J., Kinahan, P. E., and Hricak., H. (2016). Radiomics: Images Are More Than Pictures, They Are Data. *Radiology* 278 (2), 563–577. doi:10.1148/radiol.2015151169

Hadjiiski, L. M., Cha Cha Cohan Caoili, K. H., CohanSamala, R. H., Chan, H.-P., Caoili, E. M., Davenport, M. S., et al. (2020). Intraobserver Variability in Bladder Cancer Treatment Response Assessment with and without Computerized Decision Support. *Tomography* 6 (2), 194–202. doi:10.18383/j.tom.2020.00013

Harding-Theobald, E., Louissaint, J., Maraj, B., Cuaresma, E., Townsend, W., Mendiratta-Lala, M., et al. (2021). Systematic Review: Radiomics for the Diagnosis and Prognosis of Hepatocellular Carcinoma. *Aliment. Pharmacol. Ther.* 54 (7), 890–901. doi:10.1111/apt.16563

Hutchins, L. N., Murphy, S. M., Singh, P., and Graber, J. H. (2008). Position-Dependent Motif Characterization Using Non-negative Matrix Factorization. *Bioinformatics (Oxford, England)* 24 (23), 2684–2690. doi:10.1093/bioinformatics/btn526

Ilijazi, D., Pulverer, W., Ertl, I. E., Lemberger, U., Kimura, S., Abufaraj, M., et al. (2020). Discovery of Molecular DNA Methylation-Based Biomarkers through Genome-wide Analysis of Response Patterns to BCG for Bladder Cancer. *Cells* 9 (8), 1839. doi:10.3390/cells9081839

Kamat, A. M., Li, R., O'Donnell, M. A., Black, P. C., Roupret, M., Catto, J. W., et al. (2018). Predicting Response to Intravesical Bacillus Calmette-Guérin Immunotherapy: Are We There yet? A Systematic Review. *Eur. Urol.* 73 (5), 738–748. doi:10.1016/j.eururo.2017.10.003

Kamat, A. M., Sylvester, R. J., Böhle, A., Palou, J., Lamm, D. L., Brausi, M., et al. (2016). Andreas Böhle, Joan Palou, Donald L. Lamm, Maurizio Brausi, Mark Soloway, et alDefinitions, End Points, and Clinical Trial Designs for Non-Muscle-Invasive Bladder Cancer: Recommendations From the International Bladder Cancer Group. *Jco* 34 (16), 1935–1944. doi:10.1200/JCO.2015.64.4070

Lambin, P., Rios-Velazquez, E., Leijenaar, R., Carvalho, S., van Stiphout, R. G. P. M., Granton, P., et al. (2012). Radiomics: Extracting More Information from Medical Images Using Advanced Feature Analysis. *Eur. J. Cancer* 48 (4), 441–446. doi:10.1016/j.ejca.2011.11.036

Lee, D. D., and Seung, H. S. (1999). Learning the Parts of Objects by Non-negative Matrix Factorization. *Nature* 401 (6755), 788–791. doi:10.1038/44565

Lin, W.-C., and Chen, J.-H. (2015). Pitfalls and Limitations of Diffusion-Weighted Magnetic Resonance Imaging in the Diagnosis of Urinary Bladder Cancer. *Translational Oncol.* 8 (3), 217–230. doi:10.1016/j.tranon.2015.04.003

Liu, C., Gong, J., Yu, H., Liu, Q., Wang, S., and Wang, J. (2021). A CT-Based Radiomics Approach to Predict Nivolumab Response in Advanced Non-small-cell Lung Cancer. *Front. Oncol.* 11 (February), 544339. doi:10.3389/fonc.2021.544339

Liu, Z., Zhu, G., Jiang, X., Zhao, Y., Zeng, H., Jing, J., et al. (2020). Survival Prediction in Gallbladder Cancer Using CT Based Machine Learning. *Front. Oncol.* 10 (November), 604288. doi:10.3389/fonc.2020.604288

Lotan, Y., O'Sullivan, P., Raman, J. D., Shariat, S. F., Kavalieris, L., Frampton, C., et al. (2017). Clinical Comparison of Noninvasive Urine Tests for Ruling Out Recurrent Urothelial Carcinoma. *Urol. Oncol. Semin. Original Invest.* 35 (8), 531e15–531. doi:10.1016/j.urolonc.2017.03.008

Martínez, R., Tapia, G., De Muga, S., Hernández, A., Cao, M. G., Teixidó, C., et al. (2019). Combined Assessment of Peritumoral Th1/Th2 Polarization and Peripheral Immunity as a New Biomarker in the Prediction of BCG Response in Patients with High-Risk NMIBC. *Oncoimmunology* 8 (8), 1602460. doi:10.1080/2162402X.2019.1602460

Moons, K. G. M., Wolff, R. F., Riley, R. D., Whiting, P. F., Westwood, M., Collins, G. S., et al. (2019). PROBAST: A Tool to Assess Risk of Bias and Applicability of Prediction Model Studies: Explanation and Elaboration. *Ann. Intern. Med.* 170 (1), W1. doi:10.7326/M18-1377

Motzer, R. J., Banchereau, R., Hamidi, H., Powles, T., McDermott, D., Atkins, M. B., et al. (2020). Molecular Subsets in Renal Cancer Determine Outcome to Checkpoint and Angiogenesis Blockade. *Cancer Cell* 38 (6), 803–817. e4. doi:10.1016/j.ccell.2020.10.011

Nassar, R., Kaczkurkin, A. N., Xia, C. H., Sotiras, A., PehlivanovaMoore, M., Moore, T. M., et al. (2019). Gestational Age Is Dimensionally Associated with Structural Brain Network Abnormalities across Development. *Cereb. Cortex* 29 (5), 2102–2114. doi:10.1093/cercor/bhy091

Necchi, A., Bandini, M., Calareso, G., Raggi, D., Pederzoli, F., Farè, E., et al. (2020). Multiparametric Magnetic Resonance Imaging as a Noninvasive Assessment of Tumor Response to Neoadjuvant Pembrolizumab in Muscle-Invasive Bladder Cancer: Preliminary Findings from the PURE-01 Study. *Eur. Urol.* 77 (5), 636–643. doi:10.1016/j.eururo.2019.12.016

Patel, R., Steele, C. J., Chen, A. G. X., Patel, S., Devenyi, G. A., Germann, J., et al. (2020). Investigating Microstructural Variation in the Human Hippocampus Using Non-negative Matrix Factorization. *NeuroImage* 207 (February), 116348. doi:10.1016/j.neuroimage.2019.116348

Rallis, K. S., Kleeman, S. O., Grant, M., Ordidge, K. L., Sahdev, A., and Powles, T. (2021). Radiomics for Renal Cell Carcinoma: Predicting Outcomes from Immunotherapy and Targeted Therapies-A Narrative Review. *Eur. Urol. Focus* 7, 717–721. doi:10.1016/j.euf.2021.04.024

Shiota, M., Fujimoto, N., Yamamoto, Y., Takeuchi, A., Tatsugami, K., Uchiumi, T., et al. (2020). Genome-wide Association Study of Genetic Variations Associated with Treatment Failure after Intravesical bacillus Calmette-Guérin Therapy for Non-muscle Invasive Bladder Cancer. *Cancer Immunol. Immunother.* 69 (7), 1155–1163. doi:10.1007/s00262-020-02533-8

Siegel, R. L., Miller, K. D., and Jemal., A. (2020). Cancer Statistics, 2020. *CA A. Cancer J. Clin.* 70 (1), 7–30. doi:10.3322/caac.21590

Temiz, M. Z., Colakerol, A., Ulus, I., Kilic, E., Paslanmaz, F., Sahin, S., et al. (2021). Prediction of Non-muscle-invasive Bladder Cancer Recurrence during Intravesical BCG Immunotherapy by Use of Peripheral Blood Eosinophil Count and Percentage: A Preliminary Report. *Cancer Immunol. Immunother.* 70 (1), 245–252. doi:10.1007/s00262-020-02673-x

Tran, L., Xiao, J.-F., Agarwal, N., Duex, J. E., and Theodorescu, D. (2020). Advances in Bladder Cancer Biology and Therapy. *Nat. Rev. Cancer* 21, 104–121. doi:10.1038/s41568-020-00313-1

van der Ploeg, T., Austin, P. C., and Steyerberg, E. W. (2014). Modern Modelling Techniques Are Data Hungry: A Simulation Study for Predicting Dichotomous Endpoints. *BMC Med. Res. Methodol.* 14 (December), 137. doi:10.1186/1471-2288-14-137

Wakabayashi, T., Ouhmich, F., Gonzalez-Cabrera, C., Felli, E., Saviano, A., Agnus, V., et al. (2019). Radiomics in Hepatocellular Carcinoma: A Quantitative Review. *Hepatol. Int.* 13 (5), 546–559. doi:10.1007/s12072-019-09973-0

Wong, V. K., Ganeshan, D., Jensen, C. T., and Devine, C. E. (2021). Imaging and Management of Bladder Cancer. *Cancers* 13 (6), 1396. doi:10.3390/cancers13061396

Xiong, L., Chen, H., Tang, X., Chen, B., Jiang, X., Liu, L., et al. (2021). Ultrasound-Based Radiomics Analysis for Predicting Disease-free Survival of Invasive Breast Cancer. *Front. Oncol.* 11, 621993. doi:10.3389/fonc.2021.621993

Zeng, Z., Vo, A. H., Mao, C., Clare, S. E., Khan, S. A., and Luo, Y. (2019). Cancer Classification and Pathway Discovery Using Non-negative Matrix Factorization. *J. Biomed. Inform.* 96 (August), 103247. doi:10.1016/j.jbi.2019.103247

Zhang, G., Xu, L., Zhao, L., Mao, L., Li, X., Jin, Z., et al. (2020). CT-based Radiomics to Predict the Pathological Grade of Bladder Cancer. *Eur. Radiol.* 30 (12), 6749–6756. doi:10.1007/s00330-020-06893-8

Zhong, L., Dong, D., Fang, X., Zhang, F., Zhang, N., Zhang, L., et al. (2021). A Deep Learning-Based Radiomic Nomogram for Prognosis and Treatment Decision in Advanced Nasopharyngeal Carcinoma: A Multicentre Study. *EBioMedicine* 70 (August), 103522. doi:10.1016/j.ebiom.2021.103522

Zhong, Y., Xuan, P., Wang, X., Zhang, T., Li, J., Liu, Y., et al. (2018). A Non-negative Matrix Factorization Based Method for Predicting Disease-Associated MiRNAs in MiRNA-Disease Bilayer Network. *Bioinformatics (Oxford, England)* 34 (2), 267–277. doi:10.1093/bioinformatics/btx546

Zwanenburg, A., Vallières, M., Abdalah, M. A., Aerts, H. J. W. L., Andrearczyk, V., Apte, A., et al. (2020). The Image Biomarker Standardization Initiative: Standardized Quantitative Radiomics for High-Throughput Image-Based Phenotyping. *Radiology* 295 (2), 328–338. doi:10.1148/radiol.2020191145

Conflict of Interest: HL is employed by Philips Healthcare.

The remaining authors declare that the research was conducted in the absence of any commercial or financial relationships that could be construed as a potential conflict of interest.

Publisher's Note: All claims expressed in this article are solely those of the authors and do not necessarily represent those of their affiliated organizations, or those of the publisher, the editors and the reviewers. Any product that may be evaluated in this article, or claim that may be made by its manufacturer, is not guaranteed or endorsed by the publisher.

frontiers in Cell and Developmental Biology

ORIGINAL RESEARCH
published: 02 March 2022
doi: 10.3389/fcell.2022.833578

Dynamic Changes in Myofibroblasts Affect the Carcinogenesis and Prognosis of Bladder Cancer Associated With Tumor Microenvironment Remodeling

YiHeng Du[1,2†], YiQun Sui[3†], Jin Cao[4], Xiang Jiang[4], Yi Wang[1], Jiang Yu[1], Bo Wang[1], XiZhi Wang[1] and BoXin Xue[2]**

[1]Department of Urology, Suzhou Kowloon Hospital, Shanghai Jiaotong University School of Medicine, Suzhou, China, [2]Department of Urology, The Second Affiliated Hospital of Soochow University, Suzhou, China, [3]Department of Pathology, The Second Affiliated Hospital of Soochow University, Suzhou, China, [4]Department of Pathology, Suzhou Kowloon Hospital, Shanghai Jiaotong University School of Medicine, Suzhou, China

OPEN ACCESS

Edited by:
Yu Xiao,
Wuhan University, China

Reviewed by:
Nan Liu,
Wuhan University, China
Gurcan Gunaydin,
Hacettepe University, Turkey

***Correspondence:**
XiZhi Wang
donald81123@aliyun.com
BoXin Xue
xbxurol@163.com

[†]These authors have contributed equally to this work

Specialty section:
This article was submitted to Molecular and Cellular Pathology, a section of the journal Frontiers in Cell and Developmental Biology

Received: 11 December 2021
Accepted: 15 February 2022
Published: 02 March 2022

Citation:
Du Y, Sui Y, Cao J, Jiang X, Wang Y, Yu J, Wang B, Wang X and Xue B (2022) Dynamic Changes in Myofibroblasts Affect the Carcinogenesis and Prognosis of Bladder Cancer Associated With Tumor Microenvironment Remodeling. Front. Cell Dev. Biol. 10:833578. doi: 10.3389/fcell.2022.833578

Bladder cancer (BLCA) is a tumor that possesses significant heterogeneity, and the tumor microenvironment (TME) plays an important role in the development of BLCA. The TME chiefly consists of tumor cells and tumor-infiltrating immune cells admixed with stromal components. Recent studies have revealed that stromal components, especially cancer-associated fibroblasts (CAFs), affect immune cell infiltration and modulate the extracellular matrix in the TME of BLCA, ultimately impacting the prognosis and therapeutic efficacy of BLCA. Among the subgroups of CAFs, myofibroblasts (myCAFs) were the most abundant and were demonstrated to play an essential role in affecting the prognosis of various tumors, including BLCA. However, the dynamic changes in myCAFs during carcinogenesis and tumor progression have been less discussed previously. With the help of bioinformatics algorithms, we discussed the roles of myCAFs in the carcinogenesis and prognosis of BLCA in this manuscript. Our study highlighted the pathogenesis of BLCA was accompanied by a decrease in the abundance of myCAFs, revealing potential protective properties of myCAFs in the carcinogenesis of BLCA. Meanwhile, the reduced expressions of myCAFs marker genes were highly accurate in predicting tumorigenesis. In contrast, we also demonstrated that myCAFs regulated extracellular matrix remodeling, tumor metabolism, cancer stemness, and oncological mutations, ultimately impacting the treatment responsiveness and prognosis of BLCA patients. Thus, our research revealed the bimodal roles of myCAFs in the development of BLCA, which may be associated with the temporal change of the TME. The in-depth study of myofibroblasts and the TME may provide potential diagnostic biomarkers and therapeutic targets for BLCA.

Keywords: bladder cancer, tumor microenvironment, myofibroblasts, carcinogenesis, therapy responsiveness

INTRODUCTION

Bladder cancer (BLCA) is a common cancer of the urinary system with two distinct features, frequent recurrence and heterogeneity in tumor progression (Lokeshwar et al., 2020). Clinically, BLCA can be divided into muscle-invasive bladder cancer (MIBC) and non-muscle-invasive bladder cancer (NMIBC) (Kamoun et al., 2020). Of note, myofibroblasts are present in the vast majority of MIBC sections, suggesting that myofibroblasts play a critical role in the progression and heterogeneity of BLCA. Owing precisely to the highly heterogeneous nature of MIBC, patients with MIBC have limited treatment options and often need to undergo radical cystectomy, which significantly affects patients' quality of life (Gakis et al., 2017). With the recent development of immunotherapy, immune checkpoint blockade (ICB) therapy is now a guideline-recommended treatment for advanced BLCA when chemotherapy fails (Funt and Rosenberg, 2017). However, ICB therapy still faces many limitations, including multiple adverse effects and unpleasant therapeutic responsiveness (Lopez-Beltran et al., 2021).

The tumor microenvironment (TME) is an intricate system that mainly consists of tumor cells, stromal cells, and tumor infiltrated immune cells (Patnaik et al., 2017). Emerging evidence has shown that stromal components can shape the TME, influence chemotherapy and immunotherapy responsiveness, and promote malignant tumor progression (Yang et al., 2018). Cancer-associated fibroblasts (CAFs) occupy a dominant position in the stromal components of the TME. Recent evidence suggests that CAFs play profound roles in shaping the immune landscape of the TME *via* ECM-regulated immune cell anchorage and trafficking and via suppression of immune activation (Yu et al., 2020). In addition, CAFs-associated remodeling of the TME also plays a crucial role in the chemosensitivity of tumors (Zhang et al., 2020). Thus, the functions of CAFs in the tumor microenvironment are complicated, and further studies on CAFs are critical in the field of cancer research.

With the rapid development of single-cell RNA sequencing (scRNA-seq) techniques, CAFs are now considered to be classified into different subgroups, including inflammatory CAFs (iCAFs), myofibroblasts (myCAFs), and antigen-presenting CAFs (apCAFs) (Elyada et al., 2019). myCAFs have been shown to promote a more aggressive cancer cell phenotype by both *in vivo* and *in vitro* experiments (Otranto et al., 2012). Meanwhile, myCAFs have been demonstrated to greatly impact patients' prognosis among various types of human cancers (Liu et al., 2016). However, controversy remains, with some studies confirming that animal models of pancreatic cancer after removal of myCAFs exhibit significantly worse prognosis, suggesting that fibroblast reactions could also play a protective role (Özdemir et al., 2014). Therefore, it is essential to investigate the dynamics of myCAFs to study the temporal alterations in the tumor microenvironment.

In the present study, we comprehensively discussed the roles of myCAFs in the carcinogenesis and progression of BLCA with the help of bioinformatics algorithms and immunohistochemical validations. Our research revealed dual functions of myCAFs that crucially affected the carcinogenesis, prognosis, and therapy responsiveness of BLCA. Further studies on myCAFs may provide potential diagnostic biomarkers and therapeutic targets for BLCA.

MATERIALS AND METHODS

Raw Data Acquisition

The gene transcriptome data of 408 patients with BLCA were downloaded from the TCGA portal (https://portal.gdc.cancer.gov/), 406 patients with complete clinical information were further selected. The average gene expression of the samples from the same patient was calculated using the "limma" package of R software version 4.0.3. Gene expression was transformed into TPM for further analysis. Meanwhile, GEO cohorts (GSE13507 and GSE32894) were obtained from the Gene Expression Omnibus (https://www.ncbi.nlm.nih.gov/geo/). Gene expression of the TCGA and GEO cohorts was transformed by log2 (expression+1) before normalization by the "Combat" algorithm of the "SVA" package. The integrated cohort (TCGA, GSE13507, and GSE32894) was used for subsequent analysis. The IMvigor210 cohort was obtained from the R package "IMvigor210CoreBiologies" for external validation (Mariathasan et al., 2018). (http://researchpub.gene.com/IMvigor210CoreBiologies/IMvigor210CoreBiologies.tar.gz). The information of the cohorts used in this manuscript was provided in **Table 1**.

Weighted Gene Co-Expression Network Analysis (WGCNA) and Differentially Expressed Genes (DEGs) Analysis

The "WGCNA" R package was used to identify the genes correlated with normal and tumor tissues for co-expression network analysis. A heatmap displays the values of the correlation between each module and the normal and tumor tissues. The genes with the highest correlations in the modules were selected for subsequent analysis. DEGs were calculated using the Limma package of R software between different groups and were defined as genes with adjusted p-value < 0.05 and |Log2 (Fold Change)| >1.

Survival Analysis and Independent Prognostic Factor Screening

Kaplan–Meier (KM) survival analysis with the log-rank test was used to compare the survival differences in the present study. Figures were plotted using the R packages "survival" and "survminer." The Univariate and multivariate Cox regression analyses were performed to screen the independent risk factors for patients' overall survival (OS) and disease-free survival (DFS). Due to the different survival information in the integrated BLCA cohort, the survival analysis for OS in this study collected patients from the TCGA and GSE13507 cohorts. The analysis for DFS included patients from the GSE32894 cohort.

TABLE 1 | Information for the BLCA cohorts used in the present study.

Cohort	GSE13507	GSE32894	TCGA-BLCA	IMvigor210
Type (Number)	NMIBC(103), MIBC(62)	NMIBC(215), MIBC(93)	NMIBC(5), MIBC(401)	
Gender	Female:30, Male:135	Female:80, Male:228	Female:107, Male:299	Female:65, Male:233
Survival outcome	OS	DFS	OS	

Consensus Cluster

Consistency analysis of all the samples was conducted using the 'ConsensusClusterPlus' package of R software version 4.0.3. The maximum number of clusters was 9, and 80% of the total sample was drawn 50 times, clusterAlg = "km," distance = "euclidean." In this study, BLCA patients were clustered into three distinct subgroups based on the gene expression levels of myCAF marker genes, including ACTA2, TAGLN, MYL9, TPM1, and TPM2.

Gene Ontology and Kyoto Encyclopedia of Genes and Genomes Pathway Enrichment Analysis

Gene Ontology (GO), which included molecular function (MF), biological pathways (BP), and cellular components (CC), was used for functional annotation. Kyoto Encyclopedia of Genes and Genomes (KEGG) pathway analysis was used to obtain an analytical study based on DEGs. The "ClusterProfiler" package of R software was used to annotate GO functions and enrich the KEGG pathways.

Calculation of the Cancer Stemness Index

The OCLR algorithm was constructed by Malta et al. to calculate cancer stemness based on mRNA expression and DNA methylation levels (Malta et al., 2018). In this manuscript, we used EREG-mRNAsi and EREG-DNAsi to represent the stemness of each sample. We further corrected the stem cell index by adjusting to the tumor purity and obtained the corrected stem cell index (mRNAsi or DNAsi/TumorPurity). The cancer stemness results of TCGA patients were obtained from the UCSC Xena database (https://xenabrowser.net/datapages/).

Gene Set Variation Analysis and Single-Sample Gene Set Enrichment Analysis (ssGSEA)

Gene set variation analysis (GSVA) is a pathway-based analysis method that provides each sample with an overall pathway or gene set activity score (Hänzelmann et al., 2013). The pathways of the hallmark gene sets were used for GSVA to identify their comprehensive activities. The ssGSEA algorithm is a rank-based method defining a score representing the degree of absolute enrichment of a particular gene set in each sample. We constructed the myCAFs score based on the combined expression of myCAFs marker genes, including ACTA2, TAGLN, MYL9, TPM1, and TPM2. The GSVA and ssGSEA processes were conducted by the R Bioconductor package Gene Set Variation Analysis version 3.5. The high and low myCAFs groups were classified based on the medium value of the myCAFs score.

Bladder Cancer Molecular Subtyping

The molecular subtype of BLCA was obtained from previously published articles, which classified BLCA into five subtypes (Robertson et al., 2017) according to molecular expression, mutation, and immune infiltration.

Estimation of Tumor-Infiltrating Immune Cells and Biological Functions

The abundance of the TME components was estimated by the 'immunedeconv' (Sturm et al., 2019) R package. The results of four different algorithms, including TIMER (Li et al., 2016), CIBERSORT (Newman et al., 2015), xCELL (Aran et al., 2017), and MCP-COUNTER (Becht et al., 2016), are displayed. Subsequently, scores of biological functions, including lipid metabolism (Wu et al., 2019), energy metabolism (Zhou et al., 2018), DNA repair (Jinjia et al., 2019), senescence-associated secreting phenotype (SASP) (Birch and Gil, 2020), and ageing (Cardoso et al., 2018), were acquired through the ssGSEA algorithm.

Calculation of Tumor Immune Dysfunction and Exclusion and Prediction of ICB Treatment Reactiveness

The tumor dysfunction and exclusion scores of each patient were calculated using the TIDE algorithm. Potential ICB response was predicted based on the dysfunction and exclusion score. TIDE uses various gene expression markers to assess two distinct tumor immune escape mechanisms, including tumor-infiltrating cytotoxic T lymphocyte (CTL) dysfunction and exclusion by immunosuppressive factors. Higher TIDE scores indicated poorer efficacy of ICB therapy (Jiang et al., 2018).

Prediction of the Chemotherapeutic Response

We predicted the chemotherapeutic response for each TCGA sample based on the largest publicly available pharmacogenomics database, the Genomics of Drug Sensitivity in Cancer (GDSC), (https://www.cancerrxgene.org). The prediction process was implemented by the R package "pRRophetic," where the half-maximal inhibitory concentration (IC50) of the samples was estimated by ridge regression (Geeleher et al., 2014; Lu et al., 2019).

TABLE 2 | Clinical information for BLCA patients with IHC analysis.

Characteristics	Age		Gender		T Stage		N stage		M Stage		Grade	
	≤65	>65	Male	Female	Ta-T1	T2-T4	N–	N+	M–	M+	High	Low
Number	19	21	30	10	26	14	38	2	37	3	32	8

Gene Mutation Analysis

Somatic mutation information was downloaded from the TCGA database and subsequently visualized using the R package "maftools." The waterfall plot showed mutation data of each gene. The specific mutation types were annotated with different colors at the bottom left of the waterfall plot. The tumor mutation burden (TMB) was estimated as (total mutation/total covered bases) × 10^6.

Immunohistochemical Analysis and Scoring

Forty postoperative BLCA sections from 2016 to 2021 were recruited for IHC analysis with the approval of the institutional ethics committee. The patients' clinical information is listed in the following table (**Table 2**). The BenchMark GX automatic immunohistochemical staining system (Roche, Switzerland) with the Opti View DAB Detection Kit (Ventana, USA) was used to detect ACTA2 (Abcam, catalog number: ab7817, 1:250) expression in this study. The primary antibodies were visualized using a horseradish peroxidase-labeled secondary antibody. Hematoxylin was applied for counterstaining, whereas Bluing Reagent was applied for post counterstaining. The mean integrated optical density (IOD) values of positive protein expression was calculated by Image-Pro Plus 6.0.

Statistical Analysis

Principal component analysis (PCA) confirmed the distinct distribution of the clusters gained from the consensus analysis. The Wilcoxon test was used to examine the differences between variables of the two groups. Furthermore, the Kruskal–Wallis test (non-normal distribution) or one-way ANOVA (normal distribution) was used to analyze statistically significant differences for the variables of more than two groups. The Spearman correlation test examined the relationship between two different elements. The Receiver operating characteristic (ROC) curves were used to determine the predictive accuracy of myCAFs marker genes for bladder carcinogenesis. A two-sided p value < 0.05 was considered statistically significant. All statistical analyses were performed using R language v4.0.3.

RESULTS

Five myCAFs Marker Genes Were Identified to Be Associated With the Pathogenesis and Prognosis of BLCA

We applied WGCNA and DEGs analysis between normal and BLCA samples to screen for genes potentially associated with bladder carcinogenesis. The yellow module of WGCNA was identified as the most related module with tumorigenesis (**Figure 1A**). A total of 325 up-regulated and 722 down-regulated DEGs were identified by differential analysis (**Figure 1B**). After intersecting genes in the yellow module of WGCNA with DEGs, we identified five myCAFs marker genes defined by previous single-cell sequencing (Elyada et al., 2019) that were significantly down-regulated in tumor tissues, including ACTA2, MYL9, TAGLN, TPM1, and TPM2 (**Figures 1C,D**). To clarify the impact of these genes on the prognosis of BLCA, we applied the KM survival analysis, with the results showing that high expression of these genes impaired the OS (**Figure 1E**) and DFS (**Figure 1F**) of BLCA patients. These results indicated the dual roles of myCAFs marker genes in tumorigenesis and BLCA prognosis.

Consistent Clustering Arranged BLCA Patients Into Three Distinct Subgroups Based on the Expression of the Five myCAF Marker Genes

We subsequently integrated the gene expression data of BLCA patients from the TCGA, GSE13507, and GSE32894 cohorts. Consistent clustering classified the BLCA patients from the integrated cohort into three subgroups based on these five myCAFs marker genes (**Figure 2A**). Patients' OS (p = 0.002) and DFS (p < 0.001) significantly differed between the three clusters (**Figures 2B,C**), suggesting that the different abundance of myCAFs may impact the prognosis of BLCA patients. By analyzing the clinical characteristics of patients in different subgroups, we found that the proportion of more advanced BLCA was higher in the cluster with higher myCAFs content (p < 0.001), suggesting a potential association of myCAFs abundance with the T-stage of BLCA (**Figure 2D**; **Table 3**). Subsequently, we confirmed the different expression levels of myCAFs-related genes in these three groups using PCA (**Figure 2E**). By screening the DEGs among the three subgroups, we further identified a total of 60 common DEGs (**Figure 2F**) that were significantly involved in extracellular matrix remodeling, further confirming that the abundance of myCAFs may indeed confer different clinical and TME features to these three subgroups of BLCA patients (**Figure 2G**).

myCAFs Abundance Was an Independent Risk Factor for Patients' OS and DFS

To better quantify the abundance of myCAFs, we constructed a myCAF score by the ssGSEA algorithm based on the combined expression levels of the five myCAF marker genes. High myCAFs

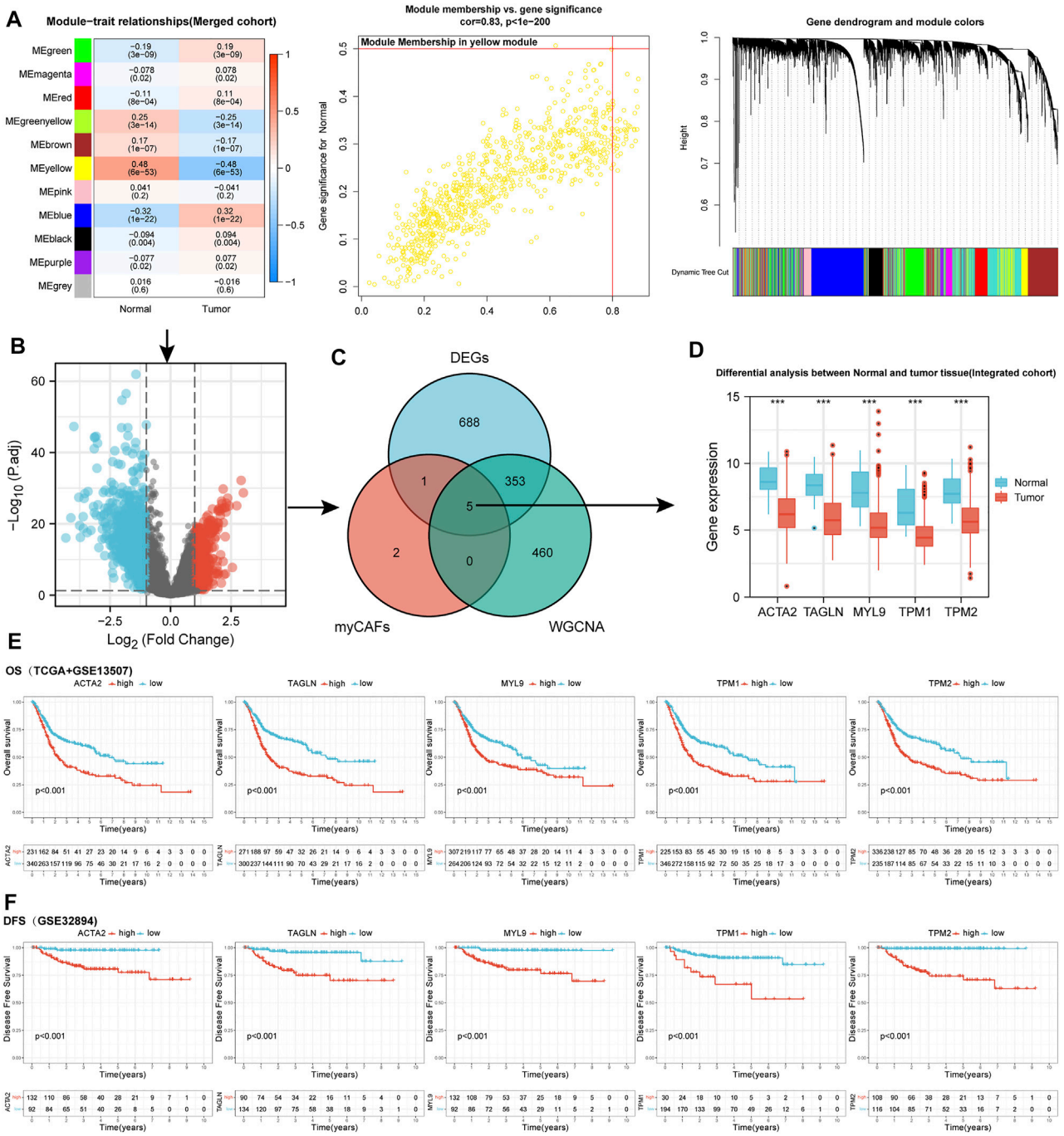

FIGURE 1 | WGCNA and DEGs analysis identified five marker genes of myCAFs that showed bimodal functions on bladder cancer carcinogenesis and prognosis. **(A)** WGCNA indicated the yellow module was the most correlated module with bladder carcinogenesis, with a correlation efficiency (Gene significance to module membership) of 0.83. **(B)** Volcano plot displayed the differentially expressed genes between normal and tumor samples with adjusted *p*-value<0.05 and |Log2(Fold Change)|>1. **(C,D)** The intersection of WGCNA and DEG analysis in the integrated cohort identified the expression of five myCAFs related genes, including ACTA2, TAGLN, MYL9, TPM1, and TPM2, were significantly down-regulated in tumor tissue ($p < 0.001$). **(E,F)** KM survival analysis revealed that patients with high expression of ACTA2, TAGLN, MYL9, TPM1, and TPM2 owned shortened OS ($p < 0.001$) (panel **E**) and DFS ($p < 0.001$) (panel **F**). ***$p < 0.001$.

score significantly shortened patients' OS (high vs. low, $p < 0.001$) and DFS (high vs. low, $p < 0.001$) (**Figure 3A**) and acted as an independent risk factor for OS (multivariate Cox regression, $p = 0.049$) (**Figure 3B**) and DFS (multivariate Cox regression, $p = 0.031$) (**Table 4**). The correlation analysis between myCAFs scores and clinical characteristics of BLCA patients revealed significant differences in myCAFs scores between subgroups of myCAFs, between BLCA patients with

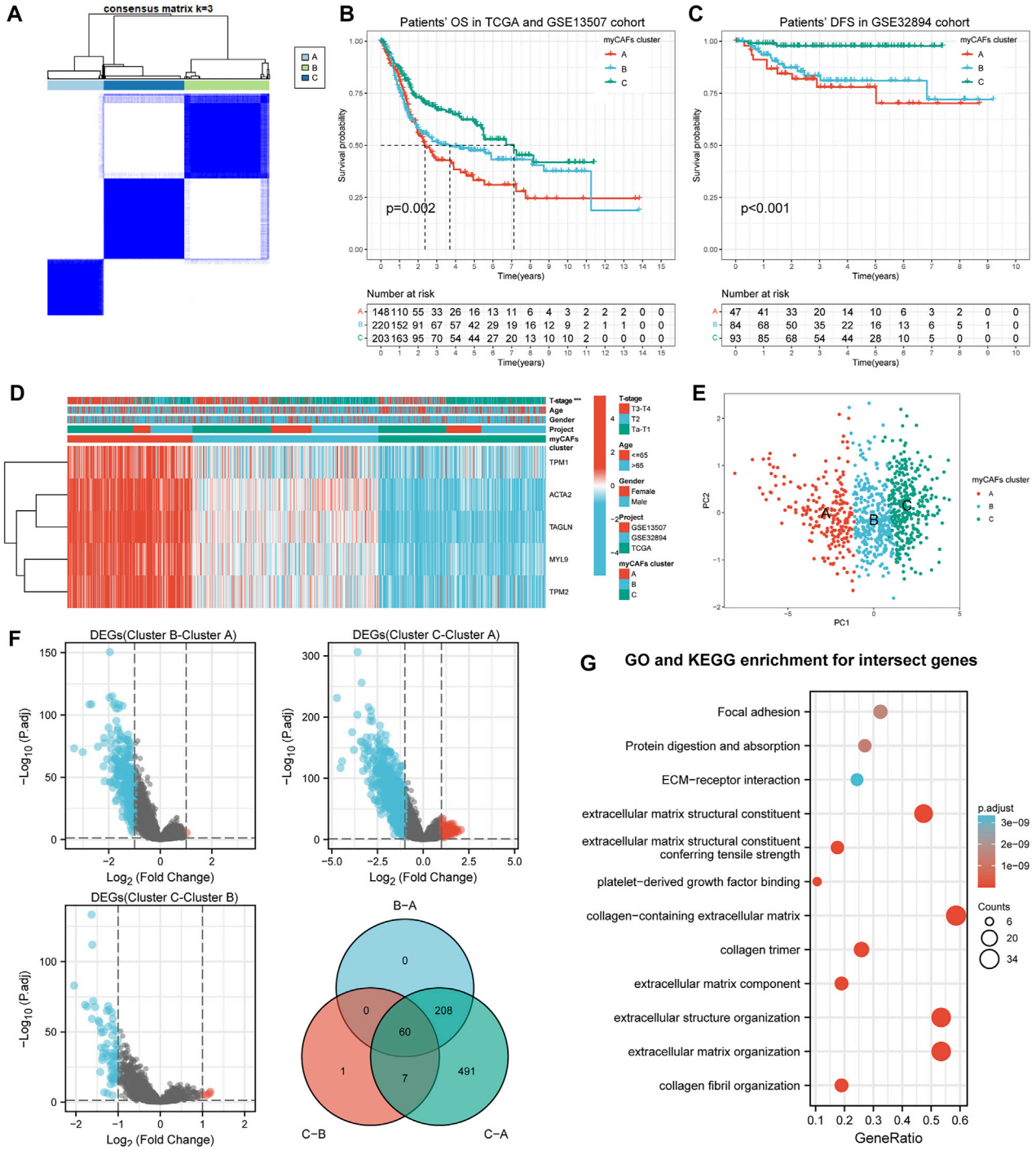

FIGURE 2 | Consensus clusters identified three subgroups of BLCA patients showing significant differences in clinical pathological and tumor microenvironment features. **(A)** BLCA patients in the integrated cohort were classified into three distinct clusters based on the myCAFs related gene expressions. **(B)** KM survival analysis indicated a significant OS difference between the three clusters ($p = 0.002$), with patients of cluster A showing the lowest medium survival interval. **(C)** Patients' DFS was significantly lower in cluster A and B than that in cluster C ($p < 0.001$). **(D)** The heatmap demonstrated the association of BLCA subgroups with T-stage, age, and gender, suggesting that subgroups with high levels of myCAFs have a higher proportion of more advanced BLCA patients ($p < 0.001$). **(E)** Principal component analysis confirmed the scattered distribution of CAFs related gene expressions between the three clusters. **(F,G)** The 60 common differentially expressed genes between the three clusters were significantly enriched in extracellular matrix remodeling related processes, including extracellular structure organization, ECM-receptor interaction, and Focal adhesion.

TABLE 3 | Different invasive features among distinct BLCA subgroups.

Cluster	T3-T4	T2	Ta-T1
Cluster A	107 (48.4%)	70 (31.7%)	44 (19.9%)
Cluster B	121 (36.8%)	83 (24.2%)	125 (38.0%)
Cluster C	62 (20.9%)	82 (27.7%)	152 (51.4%)

Chi-square test p-*value* < *0.001.*

different ages and T-stages (**Figure 3C**). These results suggested that advanced BLCA tended to own higher myCAFs abundance. Meantimes, we found that the subtypes with higher myCAFs scores took a higher proportion in T3-T4 patients than in T2 patients, laterally suggesting the potential correlation of myCAFs abundance with the T-stage of BLCA patients (**Figure 3D**). We also observed that the patient's age crucially altered the myCAFs score, indicating that senescence impacts the abundance of myCAFs. To further discuss the effect of myCAFs on survival in different subgroups of BLCA patients, we conducted subgroup survival analysis and found that the myCAFs level had a significant impact on the OS and DFS of BLCA patients in several subgroups, especially in young (age <65) and male patients (**Figures 3E,F**).

myCAFs regulated in T Cell Infiltration and Immune Response, Further Influencing the Immunotherapy Responsiveness of BLCA Patients

With the TIMER, CIBERSORT, and MCP-COUNTER algorithms, we found that tumors with high myCAFs scores had higher $CD8^+$ T cell infiltration and possessed elevated levels of immunosuppressive cells such as M2 macrophages (**Figure 4A**). myCAFs scores were also correlated with tumor microenvironment scores provided by xCEll, especially stromal scores. These results suggest that the abundance of myCAFs in stromal components may increase the infiltration of $CD8^+$ T cells and affect the M2 polarization of macrophages. Further analysis of the immune processes associated with myCAFs revealed that myCAFs scores were significantly positively correlated with the levels of various immune checkpoint molecules (**Figure 4B**). Tumors with high myCAFs scores had higher CCR, checkpoint, cytotoxicity, HLA, MHC, and proinflammatory activities (**Figure 4C**). The TIDE algorithm further revealed that myCAFs scores significantly correlated with T cell exclusion and dysfunction (**Figure 4D**). These results indicated that myCAFs could induce and sequester $CD8^+$ T cells in the tumor microenvironment, hinder their infiltration into the tumor tissue, and ultimately lead to T cell dysfunction, resulting in immune evasion. Subsequent predictions of response to immune checkpoint inhibitor therapy by the TIDE algorithm confirmed these inferences, showing that patients with high myCAFs scores exhibited lower responsiveness to immune checkpoint therapy (**Figure 4E**). Immune checkpoint responsiveness results from the IMvigor210 cohort further confirmed the predictions of the TIDE algorithm (**Figure 4F**). We also validated the characteristics of myCAFs scores in patients with different T cell infiltration features in the IMvigor210 cohort. Specifically, myCAFs scores were higher in the inflamed and excluded phenotypes than in the desert phenotype (**Figure 4G**).

myCAFs Were Correlated With Tumor Metabolic Features, Senescence-Associated Secreting Phenotype, and Cancer Stemness, Influencing the Responsiveness of BLCA Patients to Chemotherapy

We further analyzed the metabolic characteristics associated with myCAFs. We found that energy, lipid metabolism, fatty acid metabolism, and adipogenesis activities were significantly reduced in tumors with high myCAFs. In contrast, SASP and senescence-related gene expression were significantly more active in tumors with high myCAFs. After GSVA, we found that tumors with high myCAFs exhibited stronger angiogenesis and myogenesis, more elevated hypoxia, and lower oxidative phosphorylation levels. These results fully suggested that remodeling of the tumor microenvironment by myCAFs could occur through multiple pathways and finally result in a hypoxia- and nutrition-deprived tumor microenvironment. In addition, myCAFs could also affect several signaling pathways related to tumor cell stemness, such as the STAT3 (Wang et al., 2018), KRAS (Yoon et al., 2019), and Notch (Yang et al., 2020) signaling pathways, suggesting that the abundance of myCAFs may affect tumor stemness (**Figures 5A,B**). We then performed correlation analysis between myCAFs and tumor stemness by two different scoring algorithms, the mRNA stemness index (EREG-mRNAsi) and the DNA stemness index (EREG-DNAsi). We corrected the above index based on tumor purity, considering the influence of stromal components (Stemcell index/TumorPurity). The results showed that the myCAFs score had a significant positive correlation with the tumor stemness index, suggesting that tumor stemness was more robust in patients with higher myCAFs scores (**Figure 5C**). Among the sensitivity of chemotherapeutic drugs obtained by the "pRRophetic" package, we found that patients with higher myCAFs scores tended to respond to cisplatin-based chemotherapy. In contrast, myCAFs abundance significantly impacted patient sensitivity to two commonly used chemotherapeutic drugs for BLCA, gemcitabine and methotrexate (**Figure 5D**).

myCAFs Were Associated With Tumor Mutation Burden and Oncogenic Mutations, Especially FGFR3 and the RTK-RAS Signaling Pathway

After analyzing the gene mutation profile of the TCGA BLCA cohort by the "maftools" package, we combined the gene mutation information with myCAFs scores and found that myCAFs scores conformed to show a significant negative correlation with tumor mutation burden (TMB) (**Figure 6A**).

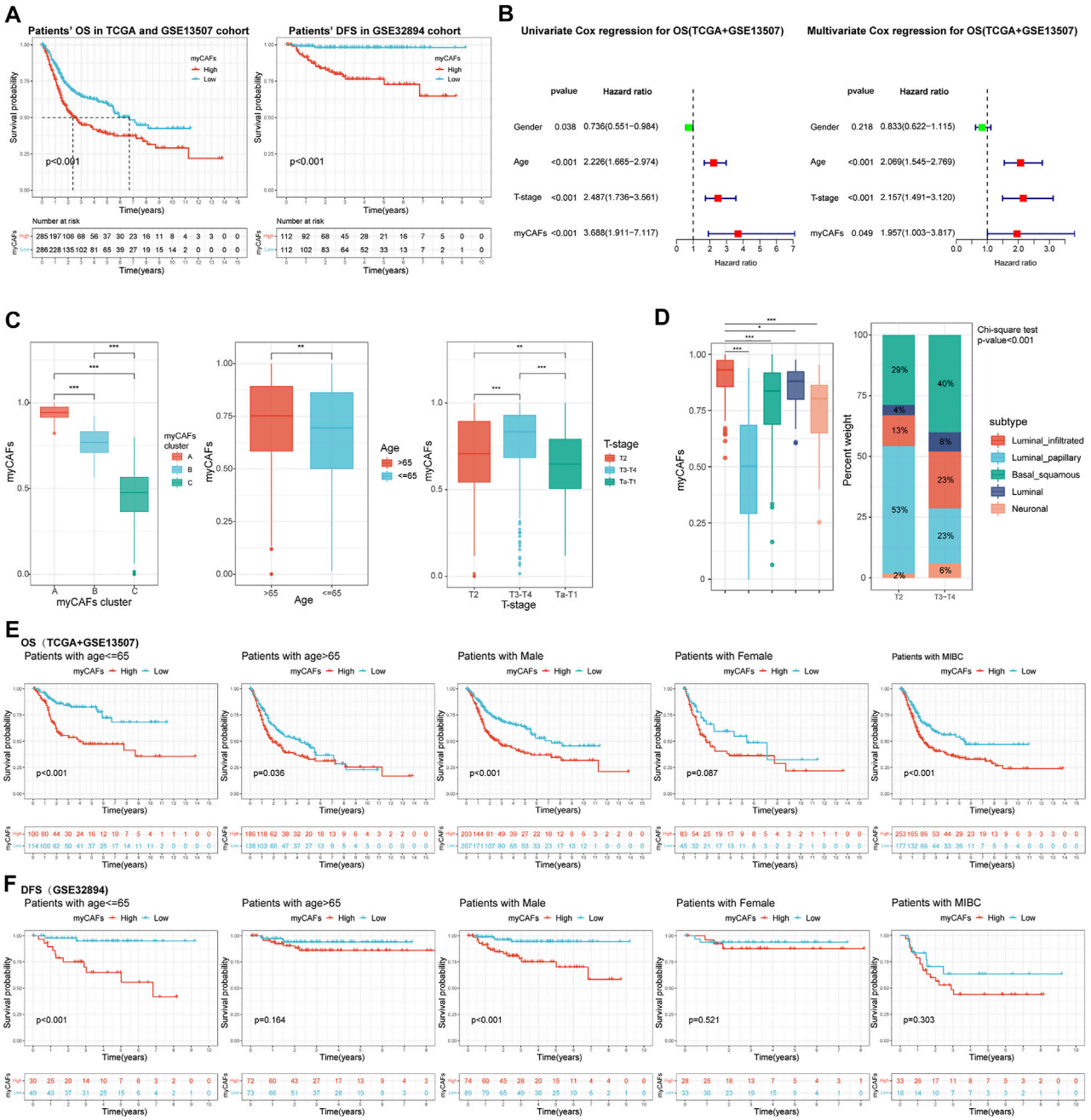

FIGURE 3 | The myCAFs score was significantly correlated with patients' prognosis and clinical-pathological features. **(A)** Patients with high myCAFs scores showed significant impaired OS ($p < 0.001$) and DFS ($p < 0.001$). **(B)** The myCAFs score acted as an independent risk factor for patients' OS revealed by multivariate Cox regression analysis ($p = 0.049$). **(C)** The myCAFs score was significantly correlated with patients' myCAFs cluster, age, and T-stage. **(D)** Significant differences in myCAFs scores were found among molecular subtypes of BLCA, with a higher proportion of myCAFs-rich molecular subtypes in more advanced BLCA ($p < 0.001$). **(E)** Subgroup survival analysis in TCGA and GSE13507 cohorts showed that patients with high myCAFs scores tended to own impaired OS, especially patients with male ($p < 0.001$) and age less than 65 ($p < 0.001$). **(F)** Subgroup survival analysis on patients' DFS in the GSE32894 cohort also confirmed high myCAFs score shortened DFS in patients with male ($p < 0.001$) and age less than 65 ($p < 0.001$). ***$p < 0.001$, **$p < 0.01$, *$p < 0.05$.

In addition, myCAFs score combined with TMB had a more substantial effect on patients' OS (**Figure 6B**), and the mutation information of the IMvigor210 cohort further confirmed the negative correlation between myCAFs abundance and TMB (**Figure 6C**). In addition, the abundance of myCAFs had a significant effect on the RTK-RAS signaling pathway (**Figure 6D**) and FGFR3 mutation frequency (**Figure 6E**), showing that tumors with high myCAFs scores often possessed lower RTK-RAS signaling pathways and FGFR3 mutation frequencies.

TABLE 4 | Univariate and multivariate Cox regression of myCAFs for patient DFS.

Characteristics	HR	HR.95 L	HR.95H	*p*-value
Univariate Cox regression				
Gender	1.538	0.577	4.100	0.389
Age	0.551	0.251	1.210	0.137
T-stage	45.087	10.617	191.473	<0.001
myCAFs	144.304	10.964	1899.241	<0.001
Multivariate Cox regression				
Gender	2.232	0.796	6.255	0.127
Age	0.636	0.276	1.464	0.287
T-stage	30.523	6.976	133.555	<0.001
myCAFs	20.181	1.320	308.566	0.031

IHC Analysis Validated the Dynamics of myCAFs During Tumor Development

Combined with the above bioinformatics analysis, we found a dynamic change in myCAFs abundance during the development of BLCA. To validate this phenomenon, we further compared the expression levels of the myCAFs marker genes in paired BLCA and normal paraneoplastic samples in the TCGA cohort (**Figure 7A**). The results confirmed the reduced expression of the myCAFs marker genes in tumor tissues. ROC analysis indicated highly diagnostic accuracy of the myCAFs marker genes in distinguishing tumors from normal bladder tissues, especially ACTA2 (**Figure 7B**). Through IHC assay, we verified the reduced ACTA2 expression levels in tumor tissues compared with the adjacent normal mucosa, indicating a decreased myCAFs abundance in BLCA tissue (**Figure 7C**). Further analysis of ACTA2 in BLCA sections with different stages revealed that ACTA2 expression levels were significantly elevated in T2 (MIBC without external bladder invasion) and T3-T4 BLCA (MIBC with external bladder invasion) (**Figure 7D**). Thus, we summarize the characteristics of changes in ACTA2 expression during BLCA carcinogenesis and progression in our recruited postoperative sections (**Figure 7E**), showing similar features to the dynamic changes in the fraction of myCAFs in our bioinformatics analysis cohorts (TCGA, GSE13507, and GSE32894) (**Figure 7F**).

DISCUSSION

BLCA is the fourth most common cancer among the male population (Kaneko and Li, 2018). The incidence rate of BLCA is higher in men, three to five times higher than that in women. It has a worldwide incidence and mortality of 330,000 and 123,000, respectively (Davis et al., 2018). Therefore, BLCA is a significant burden on global public health. Most BLCAs are urothelial carcinomas and are classified as either NMIBC or MIBC because of the distinct implications on patient management. Radical cystectomy is still the mainstay treatment for MIBC. Treatments for high-grade muscle invasive and metastatic BLCA have not advanced beyond gemcitabine and cisplatin combined chemotherapy. Recently, ICB therapy has opened the possibility of immunotherapy for BLCA, especially for muscle-invasive and metastatic BLCA, when chemotherapy fails.

While cancer originates from the accumulation of mutations within cancer cells, cancer progression and therapy responsiveness are strongly modulated by the surrounding stromal cells in the tumor microenvironment (Sahai et al., 2020). The last decades have witnessed a significant research trend towards CAFs. It is now believed that CAFs regulate cancer proliferation and metastasis through growth factor production, synthesis, and remodeling of the extracellular matrix (ECM). Recently, there has also been a growing understanding of the ability of CAFs to regulate the immune system. Targeting CAFs, by altering their number, subtype, or function is being explored to improve cancer therapy (Sahai et al., 2020). With the advancement of research techniques in recent years, many controversies have emerged in the study of CAFs, including the different effects of CAFs on tumors.

While most previous reports showed a significant tumor-promoting effect of CAFs, studies of CAFs have also identified the antitumor roles of CAFs (Özdemir et al., 2014). Evidence proposed that tumor stroma played a bimodal role in cancer development, impeding neoplastic growth in normal tissue while encouraging migration and tumor growth during tumor progression. The heterogeneity of CAFs allows them to comprise multiple subgroups, including tumor-promoting and tumor-suppressing CAFs (Schauer et al., 2011). As the fibroblasts are very heterogeneous and highly plastic, temporal changes of the tumor microenvironment could dramatically affect the dynamics of fibroblasts during cancer development. It has been demonstrated that there is a process of interconversion between different subgroups of CAFs and that the conversion of cancer-inhibiting to cancer-promoting CAFs may accompany the development of BLCA (Li B. et al., 2021). A recent study also demonstrated that CAFs in lung metastases are transcriptionally dynamic and plastic, revealing stage-specific gene signatures of CAFs that imply functional tasks to remodel the tumor microenvironment, including extracellular matrix remodeling, stress response, and shaping the inflammatory microenvironment (Shani et al., 2021). By investigating the effects of myofibroblasts in early lesions in breast cancer development and progression, Betul G et al. revealed the phenotypic and functional characteristics of CAFs in preneoplastic lesions, further underlining the importance of temporal changes in CAFs during cancer progression (Gok Yavuz et al., 2018). Freja A et al. demonstrated that multiple subpopulations of CAFs co-exist in murine breast cancer and that the abundance and dynamics for each marker differ depending on tumor type and time (Venning et al., 2021). In the present article, we also found evidence with the bioinformatics analysis supporting that myCAFs played dual functions within the carcinogenesis and progression of BLCA, further emphasizing the significance of the temporal change in tumor microenvironment on both the tumor and stromal cells. Meanwhile, Our study also found that the pathogenesis of epithelial tumors like BLCA was accompanied by a significant decrease in fibroblast content, resulting in significantly lower expression levels of marker genes for myCAFs such as ACTA2.

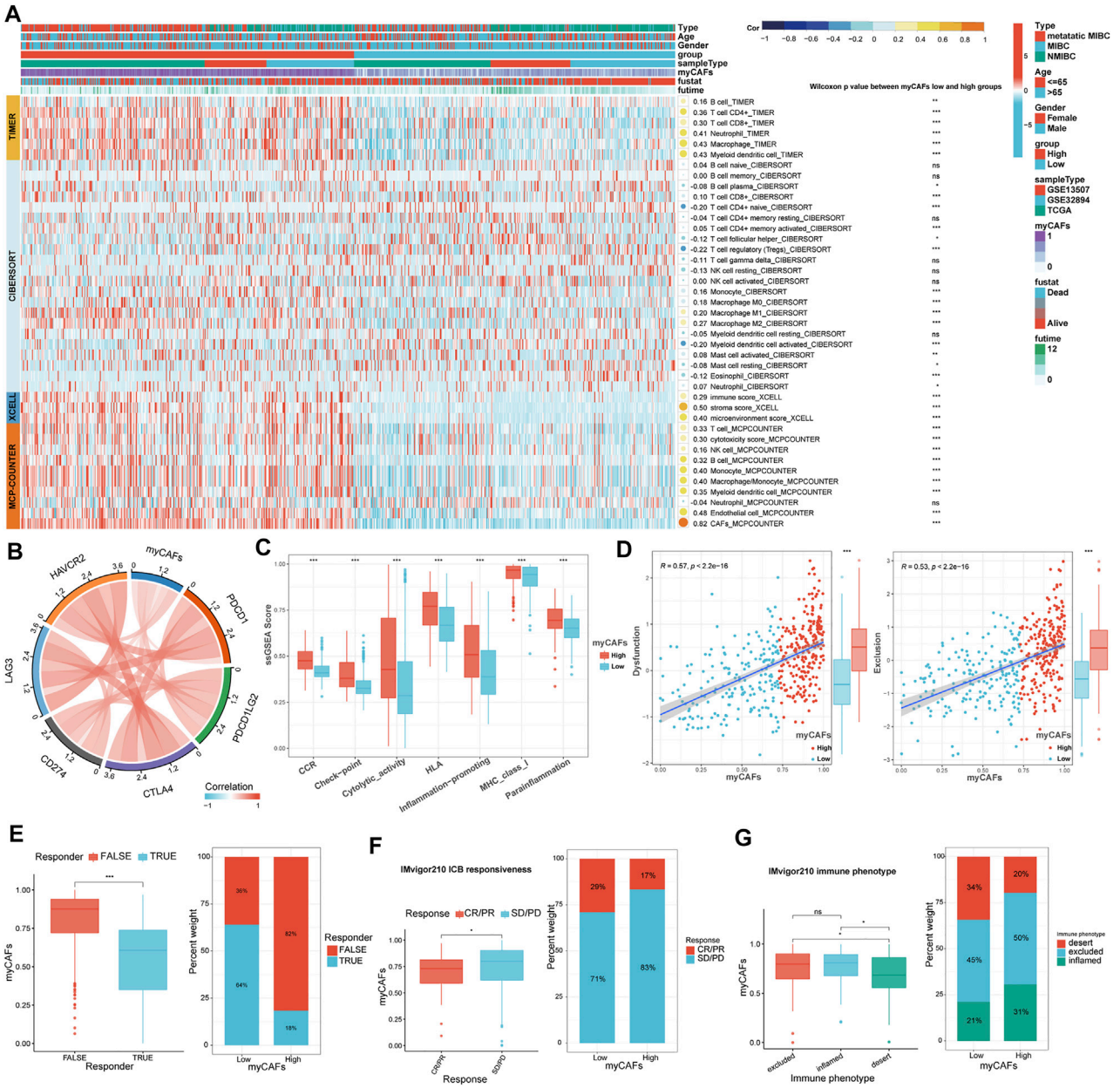

FIGURE 4 | Relationship between myCAFs score and the immune landscape of BLCA patients. **(A)** The TIMER, CIBERSORT, xCELL, and MCP-COUNTER algorithms showed significantly higher $CD8^+$ T cells ($p < 0.001$) and M2 macrophages ($p < 0.001$) in the high myCAFs group. **(B)** The myCAFs score was significantly positively correlated with the expression levels of multiple immune checkpoint-related genes, including CD274 (R = 0.21, $p < 0.001$), PDCD1 (R = 0.28, $p < 0.001$), CTLA4 (R = 0.40, $p < 0.001$), PDCD1LG2 (R = 0.45, $p < 0.001$), HAVCR2 (R = 0.47, $p < 0.001$), and LAG3 (R = 0.33, $p < 0.001$). **(C)** Immune-related functions, including CCR ($p < 0.001$), checkpoint ($p < 0.001$), cytotoxic activity ($p < 0.001$), HLA ($p < 0.001$), inflammation-promoting ($p < 0.001$), MHC_class_I ($p < 0.001$), and para inflammation ($p < 0.001$) were significantly higher in patients with high myCAFs scores. **(D)** The myCAFs score was positively correlated with T cell dysfunction (R = 0.57, $p < 0.001$) and exclusion score (R = 0.53, $p < 0.001$) gained from the TIDE algorithm. **(E)** TIDE algorithm predicts that patients with high myCAFs scores are more likely to be unresponsive to ICB treatment ($p < 0.001$). **(F)** The results of the IMvigor210 immunotherapy cohort confirmed the lower responsive rate of high myCAFs score patients. **(G)** myCAFs scores were higher in excluded ($p < 0.05$) and inflamed ($p < 0.05$) phenotype than that in desert phenotype. ***$p < 0.001$, **$p < 0.01$, *$p < 0.05$, ns: not significant.

However, it does not mean that activated fibroblasts are more deficient in BLCA than normal tissues. Previous studies have confirmed that the proportion of myCAFs in BLCA was still elevated compared to normal paraneoplastic tissues (Li B. et al., 2021). Therefore, it is critical to discuss the changes in fibroblasts during the development of BLCA in terms of their absolute content and the ratio of different CAFs subpopulations.

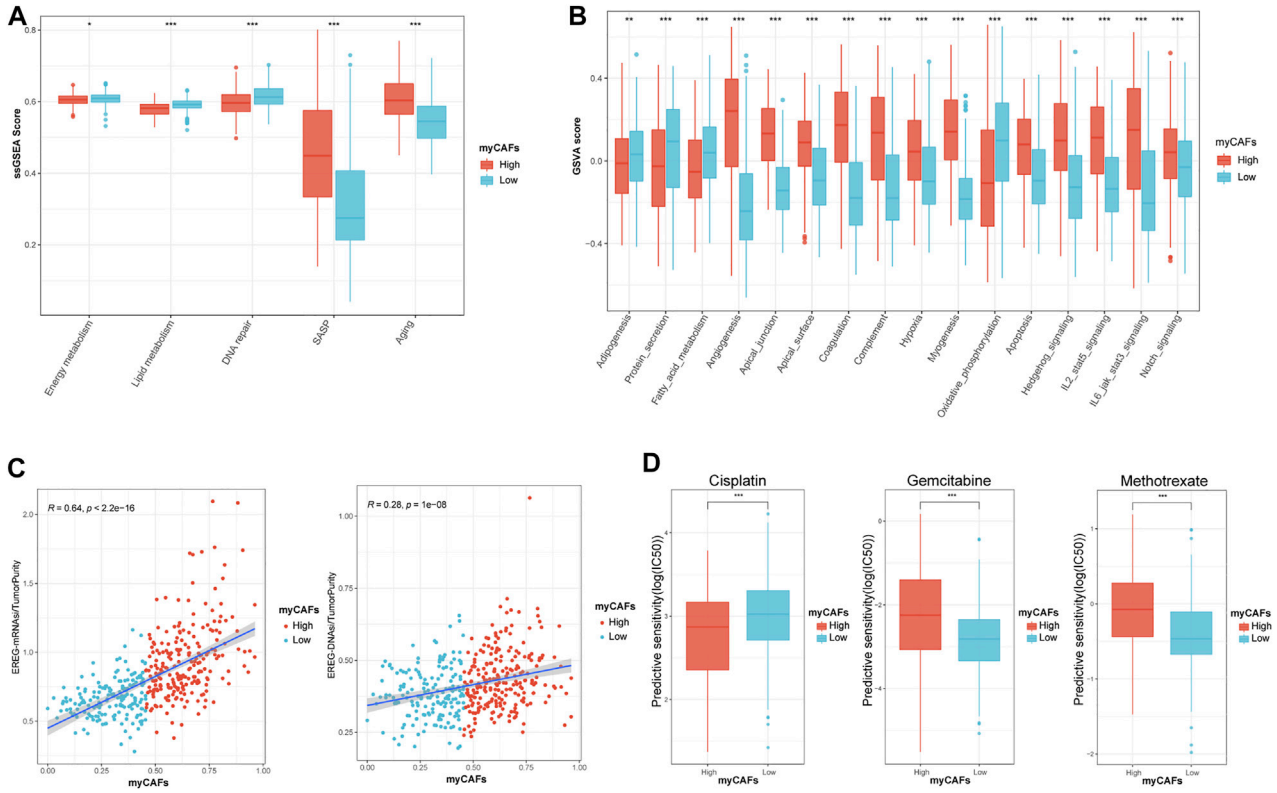

FIGURE 5 | myCAFs score was correlated with tumor metabolic activities, senescence, tumor stemness, and chemotherapy responsiveness in BLCA patients. **(A,B)** myCAFs are closely associated with energy ($p < 0.05$), lipid ($p < 0.001$), fatty acid ($p < 0.001$) metabolic activities, senescence-related secretory phenotypes ($p < 0.001$), tumor microenvironment remodeling-related processes ($p < 0.001$), and cancer stemness-related pathways ($p < 0.001$). **(C)** The myCAFs score was positively correlated with EREG mRNAsi ($R = 0.64$, $p < 0.001$) and EREG DNAsi ($R = 0.28$, $p < 0.001$), indicating that the myCAFs score was positively correlated with cancer stemness. **(D)** The responsiveness of chemotherapy predicted by the "pRRophetic" package highlighted patients with high myCAFs scores tend to benefit from cisplatin chemotherapy ($p < 0.001$) but are resistant to gemcitabine ($p < 0.001$) and methotrexate ($p < 0.001$). ***$p < 0.001$, **$p < 0.01$, *$p < 0.05$.

This present article identified five myCAFs marker genes that showed highly similar expression patterns and impact on BLCA patients' prognosis, including ACTA2, TAGLN, MYL9, TPM1, and TPM2. Three different subgroups of BLCA patients based on the expression of these genes were revealed through systematic bioinformatics analysis. Patients with distinct myCAFs levels exhibited diverse tumor microenvironment features with altered infiltration of CD8 T cells and the polarization of M2 macrophages, further bringing differences in patients' prognosis and treatment responses. With further verification of the TIDE algorithm and the IMvigor210 immunotherapy cohort, our results highlighted that the therapy targeting myCAFs might benefit patients' therapy responsiveness and prognosis. Meantime, our study also indicated a crucial effect of senescence on the extracellular matrix and fibroblasts with elder patients possessing higher myCAFs abundances (Fane and Weeraratna, 2020), suggesting that aging-related factors also need to be adequately addressed in the study of CAFs.

In the present study, we also found that myCAFs were significantly correlated with the mutation frequency of FGFR3 in TCGA BLCA patients, showing that patients with high FGFR3 mutations possessed lower myCAFs abundance. We further revealed a negative correlation between myCAFs content and tumor mutation burden, suggesting that BLCA with high myCAFs content has a lower TMB. Since previous studies indicated that a low TMB is detrimental to the immune system's recognition of tumor cells and affects the immunotherapeutic response, our results suggested that the effect of myCAFs on therapeutic responsiveness might also be related to tumor mutations (Sholl et al., 2020).

Predictive models based on bioinformatics analysis are widely available in the field of BLCA research, and many of them show high predictive accuracy (Abudurexiti et al., 2019; Li Z. et al., 2021; Du et al., 2021). However, there are still fewer diagnostic models for predicting the carcinogenesis of BLCA. In the present study, we constructed a myCAFs score that showed potential in distinguishing the pathogenesis of bladder cancer. Meanwhile, our myCAFs score has a significant predictive value for OS and DFS in BLCA. However, our prediction model did not show a considerable advantage in predictive accuracy on patients' prognoses compared with other prognostic models. The main reason is that our myCAFs score was not constructed by the Cox regression model but by the ssGSEA algorithm. Precisely on this basis,

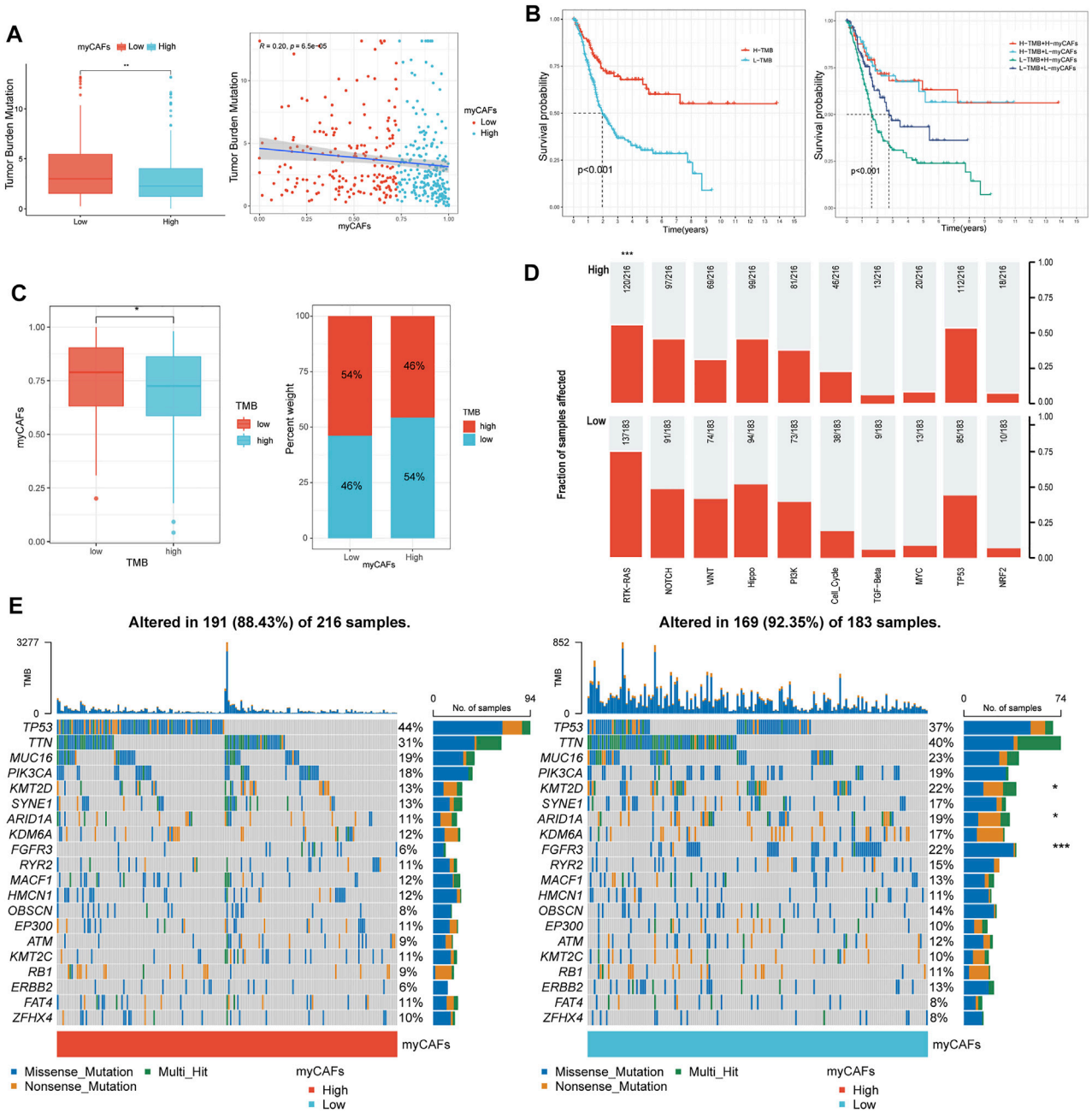

FIGURE 6 | myCAFs score was related to the TMB and mutation frequency of FGFR3 and the RTK-RAS pathway. **(A–C)** myCAFs were negatively correlated with TMB (R = 0.20, $p < 0.001$), and the combination of myCAFs and TMB better differentiated patients' OS ($p < 0.001$). The IMvigor210 cohort validated the negative correlation between myCAFs and TMB in the TCGA cohort ($p < 0.05$). **(D)** the mutation frequency of the RTK-RAS signaling pathway was higher in the low myCAFs score group ($p < 0.001$). **(E)** the waterfall plot showed lower FGFR3 ($p < 0.001$), ARID1A ($p < 0.05$), KMT2D ($p < 0.05$) mutation frequency in high myCAFs score patients. ***$p < 0.001$, **$p < 0.01$, *$p < 0.05$.

our myCAFs can reflect the myCAFs content in each tumor sample more realistically than other prediction models, validated by the high correlation of our myCAFs score with the CAFs score calculated by the MCP-COUNTER algorithm (**Figure 4A**). At the same time, the ssGSEA algorithm integrates the combined expression of the five genes used for myCAFs score construction, leading to a high correlation of the myCAFs score with the expression levels of these five genes. In clinical applications, we can even detect one of these genes, especially ACTA2, to represent the myCAFs score, which is convenient for clinical applications and confirmed by our immunohistochemical experiments.

With our myCAFs score, we deeply explored the dynamic change of myCAFs during BLCA carcinogenesis and

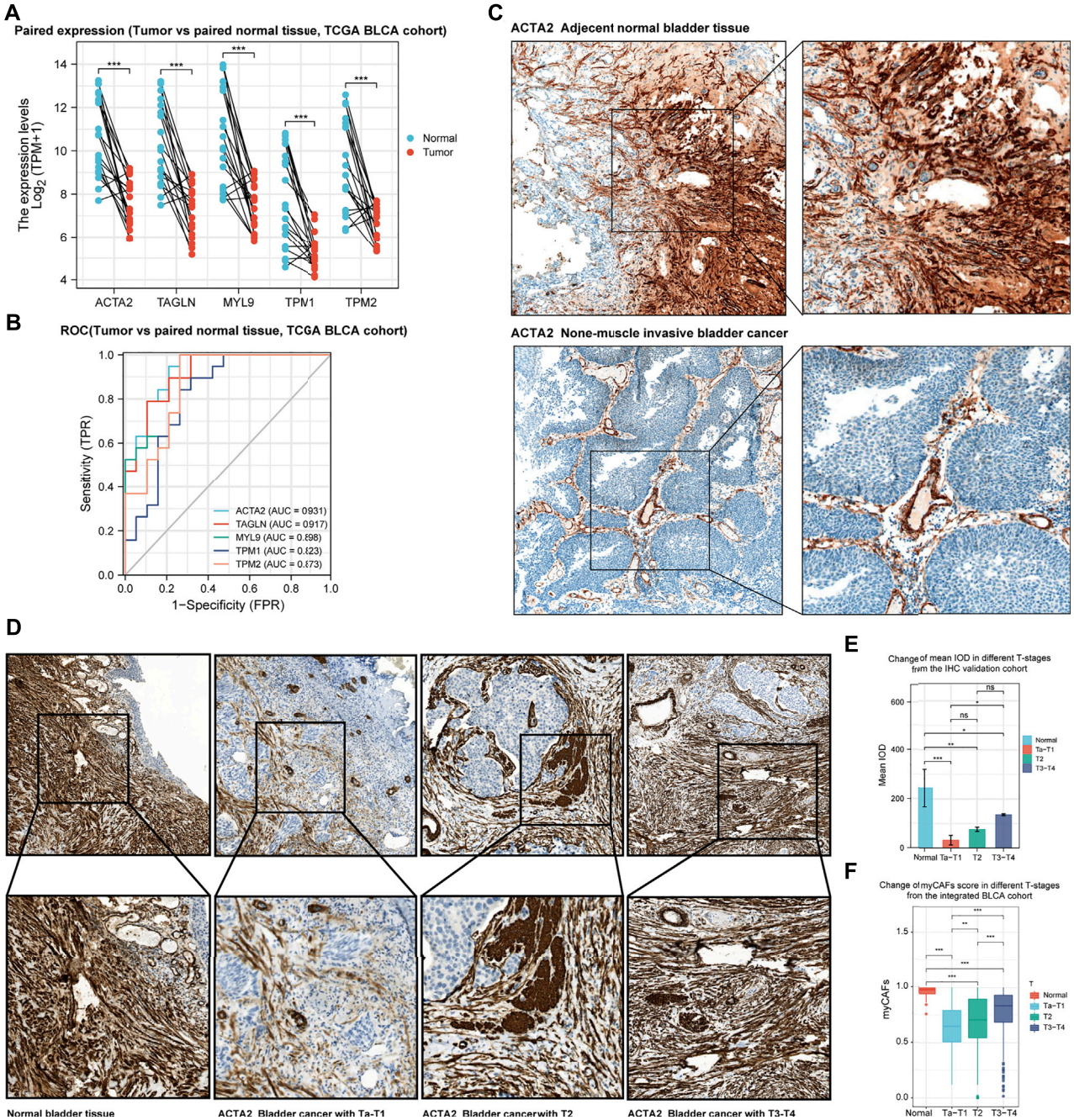

FIGURE 7 | The development of bladder cancer is accompanied by dynamic changes in the abundance of myCAFs. **(A)** myCAFs related gene expressions were significantly reduced in BLCA samples compared with adjacent normal tissue ($p < 0.001$) in the TCGA BLCA cohort. **(B)** The ROC curve demonstrated that decreased expression of the five myCAFs marker genes was highly accurate in predicting bladder carcinogenesis. **(C)** IHC analysis confirmed the reduction of myCAFs in BLCA tissue compared with paired normal tissue. **(D,E)**. IHC with IOD analysis suggested a significant decrease of myCAFs abundance in tumor samples (normal to Ta-T1, $p < 0.001$; normal to T2, $p < 0.01$; normal to T3-T4, $p < 0.05$), while high myCAFs abundance was observed in advanced BLCA sections (T3-T4 to Ta-T1, $p < 0.05$). **(F)** ssGSEA generated myCAFs score in the integrated BLCA cohort confirmed the dynamic change of myCAFs abundance in the development of BLCA. ***$p < 0.001$, **$p < 0.01$, *$p < 0.05$, ns: not significant.

progression, suggesting that fibroblasts may play multiple roles in the process of tumor development in reaction to the time-dependent tumor microenvironment. However, our results were limited by the lack of deconvoluting algorithms that could precisely identify the accurate subgroups of CAFs in bulk sequencing. Further verification by scRNA-seq and experimental assays are required for discussing the temporal change of CAFs.

Meantime, the prediction of therapy responsiveness in this manuscript mainly depended on bioinformatics algorithms and should be verified by further experimental and clinical research. In addition, we need a larger sample size of BLCA sections to validate the immunohistochemical results of this study.

CONCLUSION

Our results revealed the dynamic changes in myCAFs abundance in the development of BLCA and highlighted the TME remodeling property of myCAFs, which further impacted BLCA patients' therapy responsiveness and prognosis. The in-depth study of myofibroblasts can help explore the role of fibroblasts in the development of BLCA and provide possible diagnostic markers for predicting bladder carcinogenesis and potential therapeutic targets for BLCA treatment.

DATA AVAILABILITY STATEMENT

The datasets presented in this study can be found in online repositories. The names of the repository/repositories and accession number(s) can be found in the article/supplementary material.

ETHICS STATEMENT

The studies involving human participants were reviewed and approved by the Medical Ethics Committee of Suzhou Kowloon Hospital. The patients/participants provided their written informed consent to participate in this study.

AUTHOR CONTRIBUTIONS

YD and YS contributed equally to this manuscript. YD and BX designed the whole study. YD participated in bioinformatics and statistical analysis. YS, XJ, and JC performed the immunohistochemistry analysis and the corresponding statistical analysis. YW and JY made the manuscript and figure editing. BW and XW revised the manuscript. XW and BX provided administrative support. All the authors read and approved the final version of the manuscript.

FUNDING

This study was funded by the Basic Research on Medical and Health Application of Suzhou Municipal Science and Technology Bureau (Grant number: SYSD2020076 and SKJY2021031) and the Pre research Fund of the Second Affiliated Hospital of Soochow University (Grant number: SDFEYQN 1901).

REFERENCES

Abudurexiti, M., Xie, H., Jia, Z., Zhu, Y., Zhu, Y., Shi, G., et al. (2019). Development and External Validation of a Novel 12-Gene Signature for Prediction of Overall Survival in Muscle-Invasive Bladder Cancer. *Front. Oncol.* 9, 856. doi:10.3389/fonc.2019.00856

Aran, D., Hu, Z., and Butte, A. J. (2017). xCell: Digitally Portraying the Tissue Cellular Heterogeneity Landscape. *Genome Biol.* 18 (1), 220. doi:10.1186/s13059-017-1349-1

Becht, E., Giraldo, N. A., Lacroix, L., Buttard, B., Elarouci, N., Petitprez, F., et al. (2016). Estimating the Population Abundance of Tissue-Infiltrating Immune and Stromal Cell Populations Using Gene Expression. *Genome Biol.* 17 (1), 218. doi:10.1186/s13059-016-1070-5

Birch, J., and Gil, J. (2020). Senescence and the SASP: many Therapeutic Avenues. *Genes Dev.* 34 (23-24), 1565–1576. doi:10.1101/gad.343129.120

Cardoso, A. L., Fernandes, A., Aguilar-Pimentel, J. A., de Angelis, M. H., Guedes, J. R., Brito, M. A., et al. (2018). Towards Frailty Biomarkers: Candidates from Genes and Pathways Regulated in Aging and Age-Related Diseases. *Ageing Res. Rev.* 47, 214–277. doi:10.1016/j.arr.2018.07.004

Davis, R. M., Kiss, B., Trivedi, D. R., Metzner, T. J., Liao, J. C., and Gambhir, S. S. (2018). Surface-Enhanced Raman Scattering Nanoparticles for Multiplexed Imaging of Bladder Cancer Tissue Permeability and Molecular Phenotype. *ACS Nano* 12 (10), 9669–9679. doi:10.1021/acsnano.8b03217

Du, Y., Wang, B., Jiang, X., Cao, J., Yu, J., Wang, Y., et al. (2021). Identification and Validation of a Stromal EMT Related LncRNA Signature as a Potential Marker to Predict Bladder Cancer Outcome. *Front. Oncol.* 11, 620674. doi:10.3389/fonc.2021.620674

Elyada, E., Bolisetty, M., Laise, P., Flynn, W. F., Courtois, E. T., Burkhart, R. A., et al. (2019). Cross-Species Single-Cell Analysis of Pancreatic Ductal Adenocarcinoma Reveals Antigen-Presenting Cancer-Associated Fibroblasts. *Cancer Discov.* 9 (8), 1102–1123. doi:10.1158/2159-8290.cd-19-0094

Fane, M., and Weeraratna, A. T. (2020). How the Ageing Microenvironment Influences Tumour Progression. *Nat. Rev. Cancer* 20 (2), 89–106. doi:10.1038/s41568-019-0222-9

Funt, S. A., and Rosenberg, J. E. (2017). Systemic, Perioperative Management of Muscle-Invasive Bladder Cancer and Future Horizons. *Nat. Rev. Clin. Oncol.* 14 (4), 221–234. doi:10.1038/nrclinonc.2016.188

Gakis, G., Black, P. C., Bochner, B. H., Boorjian, S. A., Stenzl, A., Thalmann, G. N., et al. (2017). Systematic Review on the Fate of the Remnant Urothelium after Radical Cystectomy. *Eur. Urol.* 71 (4), 545–557. doi:10.1016/j.eururo.2016.09.035

Geeleher, P., Cox, N. J., and Huang, R. (2014). Clinical Drug Response Can Be Predicted Using Baseline Gene Expression Levels and *In Vitro* Drug Sensitivity in Cell Lines. *Genome Biol.* 15 (3), R47. doi:10.1186/gb-2014-15-3-r47

Gok Yavuz, B., Gunaydin, G., Kosemehmetoglu, K., Karakoc, D., Ozgur, F., and Guc, D. (2018). The Effects of Cancer-Associated Fibroblasts Obtained from Atypical Ductal Hyperplasia on Anti-tumor Immune Responses. *Breast J.* 24 (6), 1099–1101. doi:10.1111/tbj.13139

Hänzelmann, S., Castelo, R., and Guinney, J. (2013). GSVA: Gene Set Variation Analysis for Microarray and RNA-Seq Data. *BMC Bioinformatics* 14, 7. doi:10.1186/1471-2105-14-7

Jiang, P., Gu, S., Pan, D., Fu, J., Sahu, A., Hu, X., et al. (2018). Signatures of T Cell Dysfunction and Exclusion Predict Cancer Immunotherapy Response. *Nat. Med.* 24 (10), 1550–1558. doi:10.1038/s41591-018-0136-1

Jinjia, C., Xiaoyu, W., Hui, S., Wenhua, L., Zhe, Z., Xiaodong, Z., et al. (2019). The Use of DNA Repair Genes as Prognostic Indicators of Gastric Cancer. *J. Cancer* 10 (20), 4866–4875. doi:10.7150/jca.31062

Kamoun, A., de Reyniès, A., Allory, Y., Sjödahl, G., Robertson, A. G., Seiler, R., et al. (2020). A Consensus Molecular Classification of Muscle-Invasive Bladder Cancer. *Eur. Urol.* 77 (4), 420–433. doi:10.1016/j.eururo.2019.09.006

Kaneko, S., and Li, X. (2018). X Chromosome Protects against Bladder Cancer in Females via a KDM6A-dependent Epigenetic Mechanism. *Sci. Adv.* 4, eaar5598. doi:10.1126/sciadv.aar5598

Li, B., Pei, G., Yao, J., Ding, Q., Jia, P., and Zhao, Z. (2021). Cell-type Deconvolution Analysis Identifies Cancer-Associated Myofibroblast Component as a Poor

Prognostic Factor in Multiple Cancer Types. *Oncogene* 40 (28), 4686–4694. doi:10.1038/s41388-021-01870-x

Li, B., Severson, E., Pignon, J.-C., Zhao, H., Li, T., Novak, J., et al. (2016). Comprehensive Analyses of Tumor Immunity: Implications for Cancer Immunotherapy. *Genome Biol.* 17 (1), 174. doi:10.1186/s13059-016-1028-7

Li, Z., Li, Y., Zhong, W., and Huang, P. (2021). m6A-Related lncRNA to Develop Prognostic Signature and Predict the Immune Landscape in Bladder Cancer. *J. Oncol.* 2021, 7488188. doi:10.1155/2021/7488188

Liu, L., Liu, L., Yao, H. H., Zhu, Z. Q., Ning, Z. L., and Huang, Q. (2016). Stromal Myofibroblasts Are Associated with Poor Prognosis in Solid Cancers: A Meta-Analysis of Published Studies. *PLoS One* 11, e0159947. doi:10.1371/journal.pone.0159947

Lokeshwar, V. B., Morera, D. S., Hasanali, S. L., Yates, T. J., Hupe, M. C., Knapp, J., et al. (2020). A Novel Splice Variant of HYAL-4 Drives Malignant Transformation and Predicts Outcome in Patients with Bladder Cancer. *Clin. Cancer Res.* 26 (13), 3455–3467. doi:10.1158/1078-0432.ccr-19-2912

Lopez-Beltran, A., Cimadamore, A., Blanca, A., Massari, F., Vau, N., Scarpelli, M., et al. (2021). Immune Checkpoint Inhibitors for the Treatment of Bladder Cancer. *Cancers (Basel)* 13 (1), 131. doi:10.3390/cancers13010131

Lu, X., Jiang, L., Zhang, L., Zhu, Y., Hu, W., Wang, J., et al. (2019). Immune Signature-Based Subtypes of Cervical Squamous Cell Carcinoma Tightly Associated with Human Papillomavirus Type 16 Expression, Molecular Features, and Clinical Outcome. *Neoplasia* 21 (6), 591–601. doi:10.1016/j.neo.2019.04.003

Malta, T. M., Sokolov, A., Gentles, A. J., Burzykowski, T., Poisson, L., Weinstein, J. N., et al. (2018). Machine Learning Identifies Stemness Features Associated with Oncogenic Dedifferentiation. *Cell.* 173 (2), 338–354.e15. doi:10.1016/j.cell.2018.03.034

Mariathasan, S., Turley, S. J., Nickles, D., Castiglioni, A., Yuen, K., Wang, Y., et al. (2018). TGFβ Attenuates Tumour Response to PD-L1 Blockade by Contributing to Exclusion of T Cells. *Nature* 554 (7693), 544–548. doi:10.1038/nature25501

Newman, A. M., Liu, C. L., Green, M. R., Gentles, A. J., Feng, W., Xu, Y., et al. (2015). Robust Enumeration of Cell Subsets from Tissue Expression Profiles. *Nat. Methods* 12 (5), 453–457. doi:10.1038/nmeth.3337

Otranto, M., Sarrazy, V., Bonté, F., Hinz, B., Gabbiani, G., and Desmouliere, A. (2012). The Role of the Myofibroblast in Tumor Stroma Remodeling. *Cell Adhes. Migration* 6 (3), 203–219. doi:10.4161/cam.20377

Özdemir, B. C., Pentcheva-Hoang, T., Carstens, J. L., Zheng, X., Wu, C.-C., Simpson, T. R., et al. (2014). Depletion of Carcinoma-Associated Fibroblasts and Fibrosis Induces Immunosuppression and Accelerates Pancreas Cancer with Reduced Survival. *Cancer Cell.* 25 (6), 719–734. doi:10.1016/j.ccr.2014.04.005

Patnaik, A., Swanson, K. D., Csizmadia, E., Solanki, A., Landon-Brace, N., Gehring, M. P., et al. (2017). Cabozantinib Eradicates Advanced Murine Prostate Cancer by Activating Antitumor Innate Immunity. *Cancer Discov.* 7 (7), 750–765. doi:10.1158/2159-8290.cd-16-0778

Robertson, A. G., Kim, J., Al-Ahmadie, H., Bellmunt, J., Guo, G., Cherniack, A. D., et al. (2017). Comprehensive Molecular Characterization of Muscle-Invasive Bladder Cancer. *Cell.* 171 (3), 540–556.e25. doi:10.1016/j.cell.2017.09.007

Sahai, E., Astsaturov, I., Cukierman, E., DeNardo, D. G., Egeblad, M., Evans, R. M., et al. (2020). A Framework for Advancing Our Understanding of Cancer-Associated Fibroblasts. *Nat. Rev. Cancer* 20 (3), 174–186. doi:10.1038/s41568-019-0238-1

Schauer, I. G., Sood, A. K., Mok, S., and Liu, J. (2011). Cancer-associated Fibroblasts and Their Putative Role in Potentiating the Initiation and Development of Epithelial Ovarian Cancer. *Neoplasia* 13 (5), 393–405. doi:10.1593/neo.101720

Shani, O., Raz, Y., Monteran, L., Scharff, Y., Levi-Galibov, O., Megides, O., et al. (2021). Evolution of Fibroblasts in the Lung Metastatic Microenvironment Is Driven by Stage-specific Transcriptional Plasticity. *Elife* 10, e60745. doi:10.7554/eLife.60745

Sholl, L. M., Hirsch, F. R., Hwang, D., Botling, J., Lopez-Rios, F., Bubendorf, L., et al. (2020). The Promises and Challenges of Tumor Mutation Burden as an Immunotherapy Biomarker: A Perspective from the International Association for the Study of Lung Cancer Pathology Committee. *J. Thorac. Oncol.* 15 (9), 1409–1424. doi:10.1016/j.jtho.2020.05.019

Sturm, G., Finotello, F., Petitprez, F., Zhang, J. D., Baumbach, J., Fridman, W. H., et al. (2019). Comprehensive Evaluation of Transcriptome-Based Cell-type Quantification Methods for Immuno-Oncology. *Bioinformatics* 35 (14), i436–i445. doi:10.1093/bioinformatics/btz363

Venning, F. A., Zornhagen, K. W., Wullkopf, L., Sjölund, J., Rodriguez-Cupello, C., Kjellman, P., et al. (2021). Deciphering the Temporal Heterogeneity of Cancer-Associated Fibroblast Subpopulations in Breast Cancer. *J. Exp. Clin. Cancer Res.* 40 (1), 175. doi:10.1186/s13046-021-01944-4

Wang, T., Fahrmann, J. F., Lee, H., Li, Y.-J., Tripathi, S. C., Yue, C., et al. (2018). JAK/STAT3-Regulated Fatty Acid β-Oxidation Is Critical for Breast Cancer Stem Cell Self-Renewal and Chemoresistance. *Cel Metab.* 27 (1), 136–150. e5. doi:10.1016/j.cmet.2017.11.001

Wu, F., Zhao, Z., Chai, R. C., Liu, Y. Q., Li, G. Z., Jiang, H. Y., et al. (2019). Prognostic Power of a Lipid Metabolism Gene Panel for Diffuse Gliomas. *J. Cel Mol Med* 23 (11), 7741–7748. doi:10.1111/jcmm.14647

Yang, L., Shi, P., Zhao, G., Xu, J., Peng, W., Zhang, J., et al. (2020). Targeting Cancer Stem Cell Pathways for Cancer Therapy. *Sig Transduct Target. Ther.* 5 (1), 8. doi:10.1038/s41392-020-0110-5

Yang, Y., Bai, Y., He, Y., Zhao, Y., Chen, J., Ma, L., et al. (2018). PTEN Loss Promotes Intratumoral Androgen Synthesis and Tumor Microenvironment Remodeling via Aberrant Activation of RUNX2 in Castration-Resistant Prostate Cancer. *Clin. Cancer Res.* 24 (4), 834–846. doi:10.1158/1078-0432.ccr-17-2006

Yoon, C., Till, J., Cho, S.-J., Chang, K. K., Lin, J.-x., Huang, C.-m., et al. (2019). KRAS Activation in Gastric Adenocarcinoma Stimulates Epithelial-To-Mesenchymal Transition to Cancer Stem-like Cells and Promotes Metastasis. *Mol. Cancer Res.* 17 (9), 1945–1957. doi:10.1158/1541-7786.mcr-19-0077

Yu, M., Guo, G., Huang, L., Deng, L., Chang, C.-S., Achyut, B. R., et al. (2020). CD73 on Cancer-Associated Fibroblasts Enhanced by the A2B-Mediated Feedforward Circuit Enforces an Immune Checkpoint. *Nat. Commun.* 11 (1), 515. doi:10.1038/s41467-019-14060-x

Zhang, H., Deng, T., Liu, R., Ning, T., Yang, H., Liu, D., et al. (2020). CAF Secreted miR-522 Suppresses Ferroptosis and Promotes Acquired Chemo-Resistance in Gastric Cancer. *Mol. Cancer* 19 (1), 43. doi:10.1186/s12943-020-01168-8

Zhou, Z., Huang, R., Chai, R., Zhou, X., Hu, Z., Wang, W., et al. (2018). Identification of an Energy Metabolism-Related Signature Associated with Clinical Prognosis in Diffuse Glioma. *Aging* 10 (11), 3185–3209. doi:10.18632/aging.101625

Conflict of Interest: The authors declare that the research was conducted in the absence of any commercial or financial relationships that could be construed as a potential conflict of interest.

Publisher's Note: All claims expressed in this article are solely those of the authors and do not necessarily represent those of their affiliated organizations, or those of the publisher, the editors and the reviewers. Any product that may be evaluated in this article, or claim that may be made by its manufacturer, is not guaranteed or endorsed by the publisher.

frontiers in Cell and Developmental Biology

ORIGINAL RESEARCH
published: 02 March 2022
doi: 10.3389/fcell.2022.809747

Development and Validation of Ferroptosis-Related LncRNA Biomarker in Bladder Carcinoma

Yiru Wang[1†], Shijie Zhang[2†], Yang Bai[2†], Gen Li[2], Siyu Wang[2], Jiayi Chen[2], Xin Liu[3,4*] and Hang Yin[2,3,4*]*

[1]Department of Gynecologic Oncology, Harbin Medical University Cancer Hospital, Harbin, China, [2]Department of Radiation Oncology, Harbin Medical University Cancer Hospital, Harbin, China, [3]Department of Pharmacology, State-Province Key Laboratories of Biomedicine-Pharmaceutics of China, Ministry of Education, College of Pharmacy, Harbin Medical University, Harbin, China, [4]Key Laboratory of Cardiovascular Medicine Research, Ministry of Education, College of Pharmacy, Harbin Medical University, Harbin, China

OPEN ACCESS

Edited by:
Yongwen Luo,
Wuhan University, China

Reviewed by:
Li Liu,
Huazhong University of Science and Technology, China
Haiqing Zheng,
Third Affiliated Hospital of Sun Yat-sen University, China

***Correspondence:**
Hang Yin
yinhang@hrbmu.edu.cn
Xin Liu
freyaliuxin@163.com
Jiayi Chen
xhl9588@163.com

[†]These authors have contributed equally to this work and share first authorship

Specialty section:
This article was submitted to Molecular and Cellular Pathology, a section of the journal Frontiers in Cell and Developmental Biology

Received: 05 November 2021
Accepted: 24 January 2022
Published: 02 March 2022

Citation:
Wang Y, Zhang S, Bai Y, Li G, Wang S, Chen J, Liu X and Yin H (2022) Development and Validation of Ferroptosis-Related LncRNA Biomarker in Bladder Carcinoma. Front. Cell Dev. Biol. 10:809747. doi: 10.3389/fcell.2022.809747

Bladder cancer (BC) is a highly prevalent cancer form of the genitourinary system; however, the effective biomarkers are still ambiguous and deserve deeper investigation. Long non-coding RNA (lncRNA) occupies a prominent position in tumor biology and immunology, and ferroptosis-related genes participate in regulatory processes of cancer. In this study, 538 differentially expressed ferroptosis-related lncRNAs were identified from the The Cancer Genome Atlas database through co-expression method and differential expression analysis. Then, the samples involved were equally and randomly divided into two cohorts for the construction of gene model and accuracy verification. Subsequently, a prediction model containing five ferroptosis-related lncRNAs was constructed by LASSO and Cox regression analysis. Furthermore, in terms of predictive performance, consistent results were achieved in the training set, testing set, and entire set. Kaplan–Meier curve, receiver operating characteristic area under the curve, and principal component analysis results verified the good predictive ability of model, and the gene model was confirmed as an independent prognostic indicator. To further investigate the mechanism, we explored the upstream of five lncRNAs and found that they may be modified by m6A to increase or decrease their expression in BC. Importantly, the low-risk group displayed higher mutation burden of tumors and lower Tumor Immune Dysfunction and Exclusion score, which may be predicted to have a higher response rate to immunotherapy. Interestingly, the patients in the high-risk group appeared to have a higher sensitivity to traditional chemotherapeutic agents through pRRophetic analysis. In general, our research established a five-ferroptosis-related lncRNA signature, which can be served as a promising prognostic biomarker for BC.

Keywords: bladder cancer, long non-coding RNA, immune, ferroptosis, biomarkers

Abbreviations: AUC, Area under the curve; BC, Bladder cancer; DE, Differentially expressed; GO, Gene Ontology; KEGG, Kyoto Encyclopedia of Genes and Genomes; PCA, Principal Component Analysis; ROC, Receiver operating characteristic; TIDE, Tumor Immune Dysfunction and Exclusion; TMB, Tumor mutation burden.

BACKGROUND

Bladder cancer (BC) is one of the main human malignant tumors, which has high morbidity and mortality. There were approximately 81,400 newly diagnosed cases and 17,980 deaths in United States in 2020 (Siegel et al., 2020). BC can be classified into muscle-invasive bladder cancer (MIBC) and non-muscle-invasive bladder cancer (NMIBC) according to the extent of tumor invasion (Thompson 2006). Approximately 75% of newly diagnosed urothelial BC is NMIBC (Burger et al., 2013). The main diagnostic modalities for NMIBC is transurethral resection and cystoscopy (Babjuk et al., 2017; Sefik et al., 2019). In addition, most patients are diagnosed as late-stage cancer with postoperative drug resistance and rapid progression (Dreicer 2017; Robertson et al., 2018). Because of the high recurrence rate of BC, continuous surveillance strategies and treatment were necessary (Svatek et al., 2014). The biomarkers related to early diagnosis and prognosis prediction are especially important and urgently need.

Whether immune escape or immune response, the occurrence and development of tumor is inseparable from the immunity. Immunotherapy has a good therapeutic effect in many tumors and brought hope to many patients with cancer (Sharma and Allison 2015). *Bacillus* Calmette Guerin (BCG) is the main drug for intravesical instillation of BC because of the enhanced immune response (Kamat et al., 2016). Nevertheless, tumor immune escape brings challenges to immunotherapy (Tang et al., 2020). It is necessary to analyze the relationship between BC and immunity.

Long non-coding RNA (lncRNA) is a special class of non-coding RNAs longer than 200 nucleotides in length (Mendell 2016). Many lncRNAs recruit regulatory protein complexes to regulate transcription (Engreitz et al., 2016). Our previous studies have shown that some lncRNAs were different from that in normal tissues, which could be prognostic factors in many cancers including head and neck squamous cell, clear cell renal, and endometrium (Yin et al., 2018; Xu et al., 2019; Wang et al., 2020). Furthermore, the lncRNA *LNMAT2* and *SNHG16* enhanced tumor lymphangiogenesis and lymph node (LN) metastasis, which may be attractive therapeutic targets for BC with LN metastasis (Chen et al., 2020; Chen C. et al., 2021). However, the role of lncRNAs in BC has not fully understood and merit further work.

As a new star in cancer, ferroptosis is a kind of programmed cell death differed from cell necrosis, apoptosis, and autophagy. The characteristic of ferroptosis is accumulation of heavy ROS and iron (Dixon et al., 2012). In addition, ferroptosis is closely related to tumor that affects tumor-related signaling pathways and plays an important role in chemotherapy, radiotherapy, and immunotherapy (Chen X. et al., 2021). There are many ferroptosis regulators consist of GPX4 (Yang et al., 2014), SLC7A11 (Koppula et al., 2021), ACSL4 (Doll et al., 2017), etc. According to many current works, lncRNAs may regulate the ferroptosis as an epigenetic regulator. *LINC00336* could regulate the expression of cystathionine-β-synthase and inhibit ferroptosis combined with ELAV-like RNA-binding protein 1 (ELAVL1) (Wang M. et al., 2019). The cytosolic *lncRNA P53RRA* activate the p53 pathway to promote ferroptosis and apoptosis (Jiang et al., 2015). Nevertheless, the regulator role of some ferroptosis-related lncRNAs in BC has not been fully understood.

Therefore, we analyzed BC genes from The Cancer Genome Atlas (TCGA) and screen out differentially expressed (DE) ferroptosis-prognosis–related lncRNAs. The five ferroptosis-prognosis–related lncRNAs were screened out. Furthermore, we built a prediction model that had been tested the strong prediction ability. The result of survival analysis confirmed that the risk score was inversely correlated with the survival of patients. Cox regression analysis showed that the risk score is an independent risk factor for BC. Then, we compared the differences in clinical stage, immunity, and methylation between the two risk groups and carried out depth immunoassay. Thus, it is confirmed that the five-ferroptosis-related lncRNA signature that closely related to tumor immunity has great significance for the prognosis prediction of BC.

MATERIALS AND METHODS

Data Collection and lncRNAs Screening

We downloaded clinical and RNA sequencing data of BC from TCGA (https://portal.gdc.cancer.gov/). Samples with insufficient clinical information were excluded. Hence, there are 406 BC tissues and 19 normal tissues with mRNA sequencing and lncRNA sequencing. Ferroptosis genes were acquired from FerrDb (www.zhounan.org/ferrdb/). A total of 1,752 ferroptosis-related lncRNAs were selected by the co-expression analysis between ferroptosis genes and BC lncRNAs ($|cor| > 0.4$ and $p < 0.001$). We explored the significantly DE BC genes, ferroptosis genes, and ferroptosis-related lncRNAs between cancer and normal samples using the limma package. The cutoff value was $|log2FC| > 1$ and FDR <0.05 (FC, fold change; FDR, false discovery rate).

Function and Pathway Enrichment of DE Ferroptosis Genes

We used the clusterProfler package to analyze the Gene Ontology (GO) and Kyoto Encyclopedia of Genes and Genomes (KEGG) pathways of DE ferroptosis genes to further explore the underlying molecular functions (MFs) and cellular components (CCs) ($p < 0.05$).

Identification and Selection of Ferroptosis-Prognosis–Related lncRNAs

The ferroptosis-prognosis–related lncRNAs were screened by univariate Cox regression analysis. The LASSO regression analysis was used on the screened genes and establishes the risk model. Then, we studied the lncRNAs that can affect BC alone by multivariate regression analysis.

All 406 BC samples were randomly divided into two sets. The risk score for each sample was calculated using the formula Risk score (RS) = $\sum_{i=1}^{N}(Expi*Coei)$ (N is the number of prognostic lncRNA genes, Expi is the expression value of

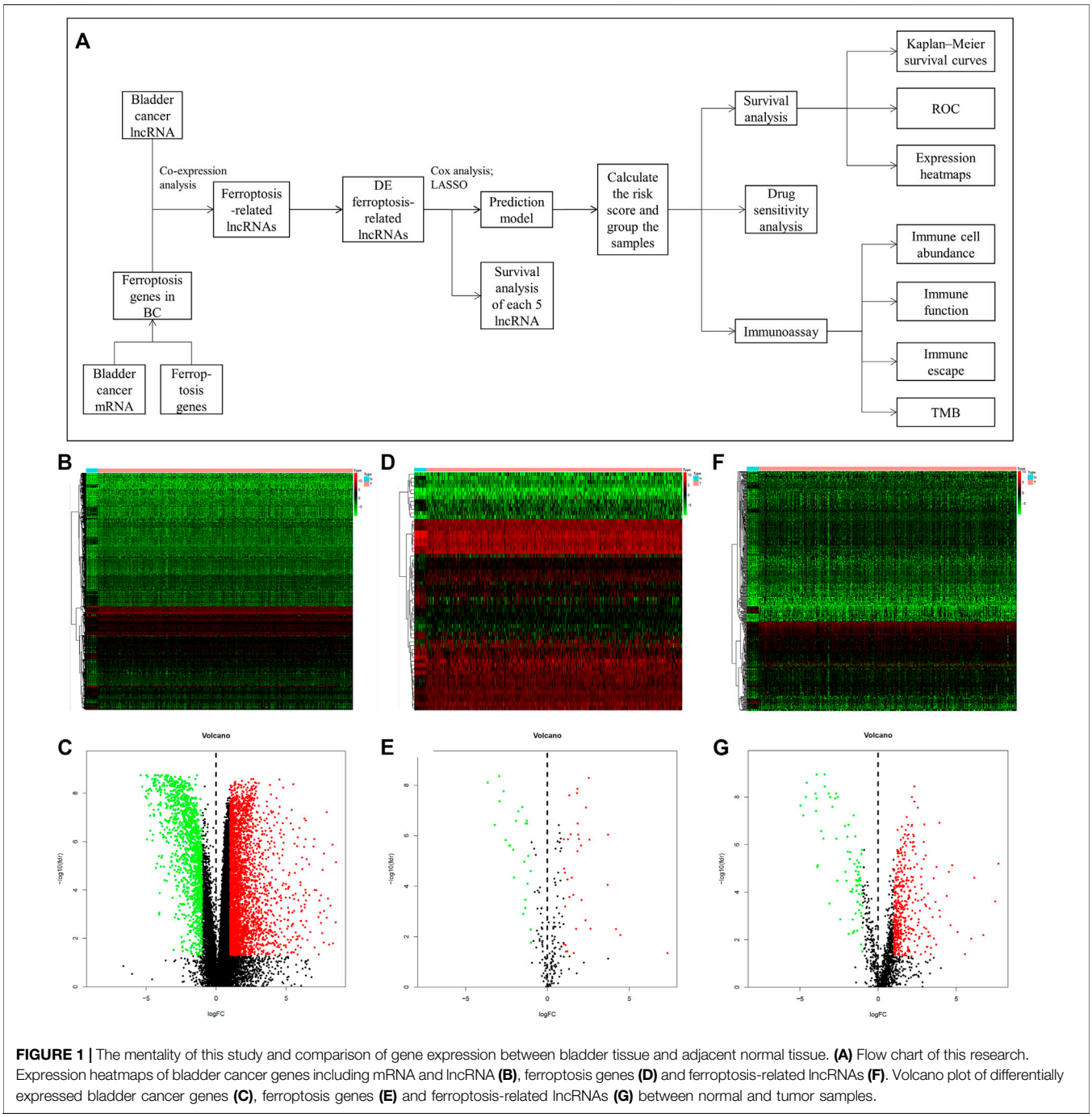

FIGURE 1 | The mentality of this study and comparison of gene expression between bladder tissue and adjacent normal tissue. **(A)** Flow chart of this research. Expression heatmaps of bladder cancer genes including mRNA and lncRNA **(B)**, ferroptosis genes **(D)** and ferroptosis-related lncRNAs **(F)**. Volcano plot of differentially expressed bladder cancer genes **(C)**, ferroptosis genes **(E)** and ferroptosis-related lncRNAs **(G)** between normal and tumor samples.

lncRNA, and Coei is the estimated regression coefficient of lncRNA in the multivariable Cox regression analysis), which could predict the prognosis risk of patients with BC. According to the median risk score, the patients in each group were divided into high- and low-risk groups. Overall survival (OS) was compared between the two risk groups. The receiver operating characteristic (ROC) was carried out with the R package to test predictive ability of our model. Principal component analysis (PCA) was used to explore the distribution of samples in different risk group. Survival analysis and Cox regression analysis were performed on the clinical variables (age, gender, grade, and stage) and the risk scores.

Construct the Network of Ferroptosis-Prognosis–Related lncRNAs

To explore the connections of these ferroptosis-related lncRNAs that can predict prognosis of BC, co-expression analysis was performed to construct the network. We used the database to

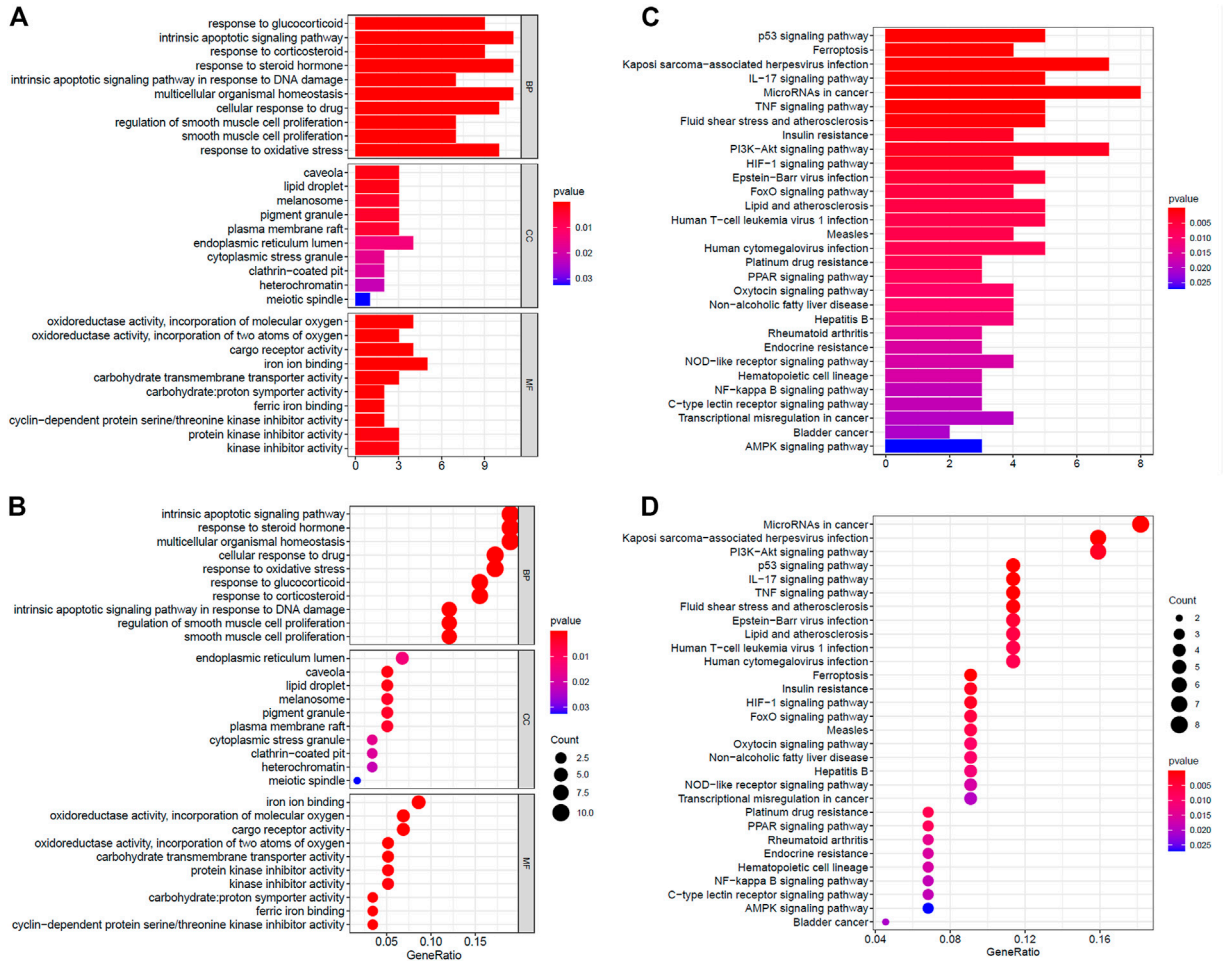

FIGURE 2 | Functional enrichment analysis of ferroptosis-related genes. **(A,B)** The GO analysis of DE ferroptosis genes. **(C,D)** The KEGG analysis revealed that DE ferroptosis genes were associated with microRNAs, Kaposi's sarcoma-associated herpesvirus infection, PI3K-Akt signaling pathway, etc.

explore the interaction between and distinguished genes according to *p* value.

Comparative Analysis of High- and Low-Risk Group

Previous studies have confirmed that methylation is of great significance in tumors (Yin et al., 2021). To further explore the relationship between our risk grouping, clinical variables and m6A methylation, we compared the differences in TNM staging system, age, gender, grade, stage, and m6A methylation genes between the high- and low-risk groups.

Immunoassay

We used different algorithms to evaluate the immune cell abundance of the high- and low-risk groups including and studied the correlation between immune cell content and the risk score in BC samples. Furthermore, the differences of immune function, immune checkpoints, and molecular typing of immune subtypes between the two risk groups were studied. Moreover, to explore the significance of our risk model in immune escape and immunotherapy, we used VarScan to discuss the tumor mutation burden (TMB) and calculated the Tumor Immune Dysfunction and Exclusion (TIDE) score. To further explore the effect of immunity on BC, tumor samples were divided into two groups according to the quantity of memory B cells, T cells, macrophages, neutrophils, etc., and Kaplan–Meier survival curve was drawn. Similarly, we evaluated the immune function of BC samples and divided them into two groups according to the median immune score. Survival analysis was performed for different groups.

Drug Sensitivity Analysis

In addition, drug resistance is a bottleneck in tumor treatment. To explore the relationship between the risk score and the sensitivity of antineoplastic agents, we used an R package to calculate the 50% inhibiting concentration (IC50) of commonly used drugs for BC.

Statistical Analysis

R software package limma selected the DE genes between tumor tissues and normal tissues. LASSO regression analysis was carried

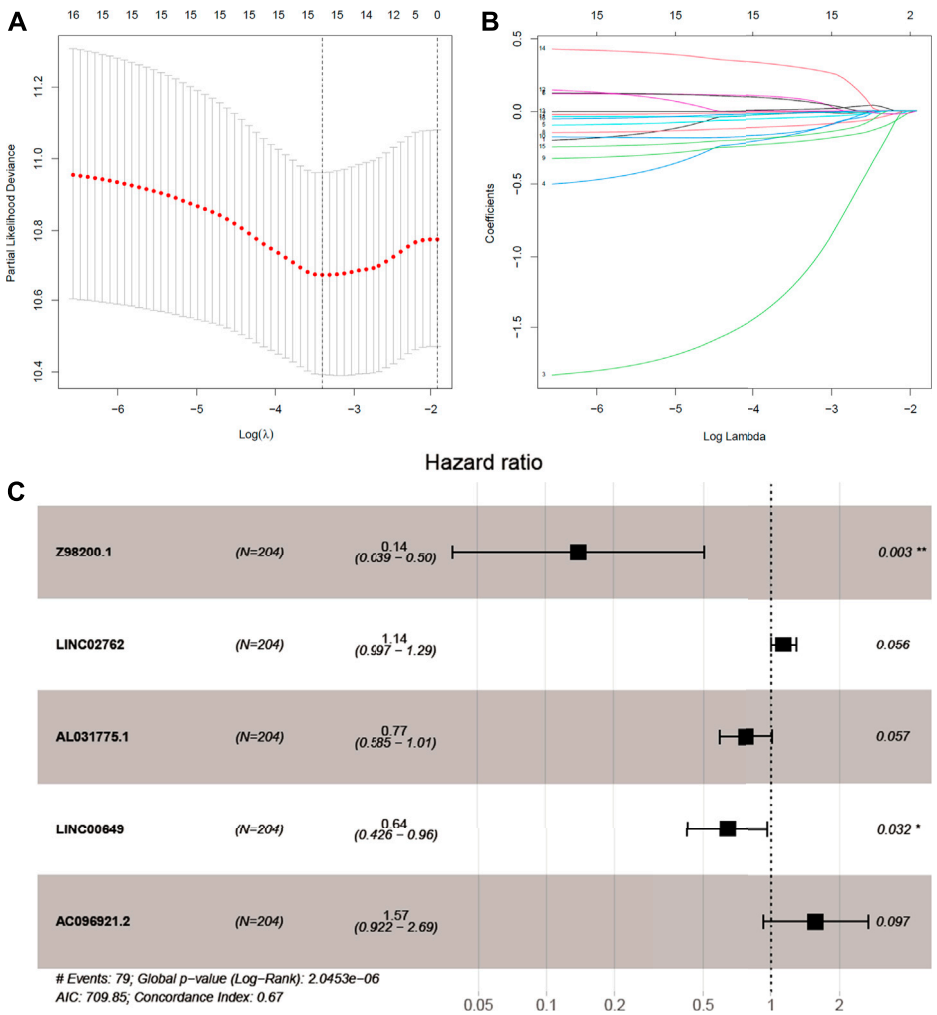

FIGURE 3 | Identifcation of ferroptosis-prognosis–related lncRNAs. **(A,B)** LASSO regression analysis selected ferroptosis-prognosis–related lncRNAs. **(C)** Multivariate Cox regression analysis to identify independent risk factors for bladder cancer.

out with glmnet package. We used Cox regression analysis to identify prognostic factors for BC. Survival curves were plotted by the survival package for R. To further confirmed prediction ability of the risk score, PCA was used to describe the distribution of the high- and low-risk groups.

RESULTS

Differentially Expressed Gene in BC

The flow chart of this study is shown in **Figure 1A**. We first acquired the data from TCGA and identified 4,847 DE genes (including mRNAs and lncRNAs) of BC. There were 3,429 upregulated and 1,418 downregulated genes in tumor samples compared to normal samples (**Figures 1B,C**). In addition, 61 DE ferroptosis genes (36 elevated and 25 downregulated; **Figures 1D,E**) were distinguished. Co-expression analysis was used to find ferroptosis-related lncRNAs. Among them, 538 DE ferroptosis-related lncRNAs (463 elevated and 75 downregulated; **Figures 1F,G**) were screened out between tumor tissues and normal tissues (|log2FC| > 1 and FDR <0.05).

GO and KEGG Pathway Enrichment Analysis

The GO analysis revealed that DE ferroptosis genes is related to intrinsic apoptotic, multicellular organismal homeostasis, and response to some stimulus including steroid hormone, drug, and oxidative stress, at the biological process (BP) category. The relationship between some DE genes and BP is shown in **Supplementary Figure S1A**. For the MF category, the DE genes were involved in iron ion binding, oxidoreductase activity, acting on single donors with incorporation of molecular oxygen, cargo receptor activity, etc. What is more, they mainly enriched in endoplasmic reticulum lumen, caveola, lipid droplet, melanosome, pigment granule, etc., at the CC category (**Figures 2A,B**). The KEGG analysis revealed that DE ferroptosis genes were associated with microRNAs, Kaposi's

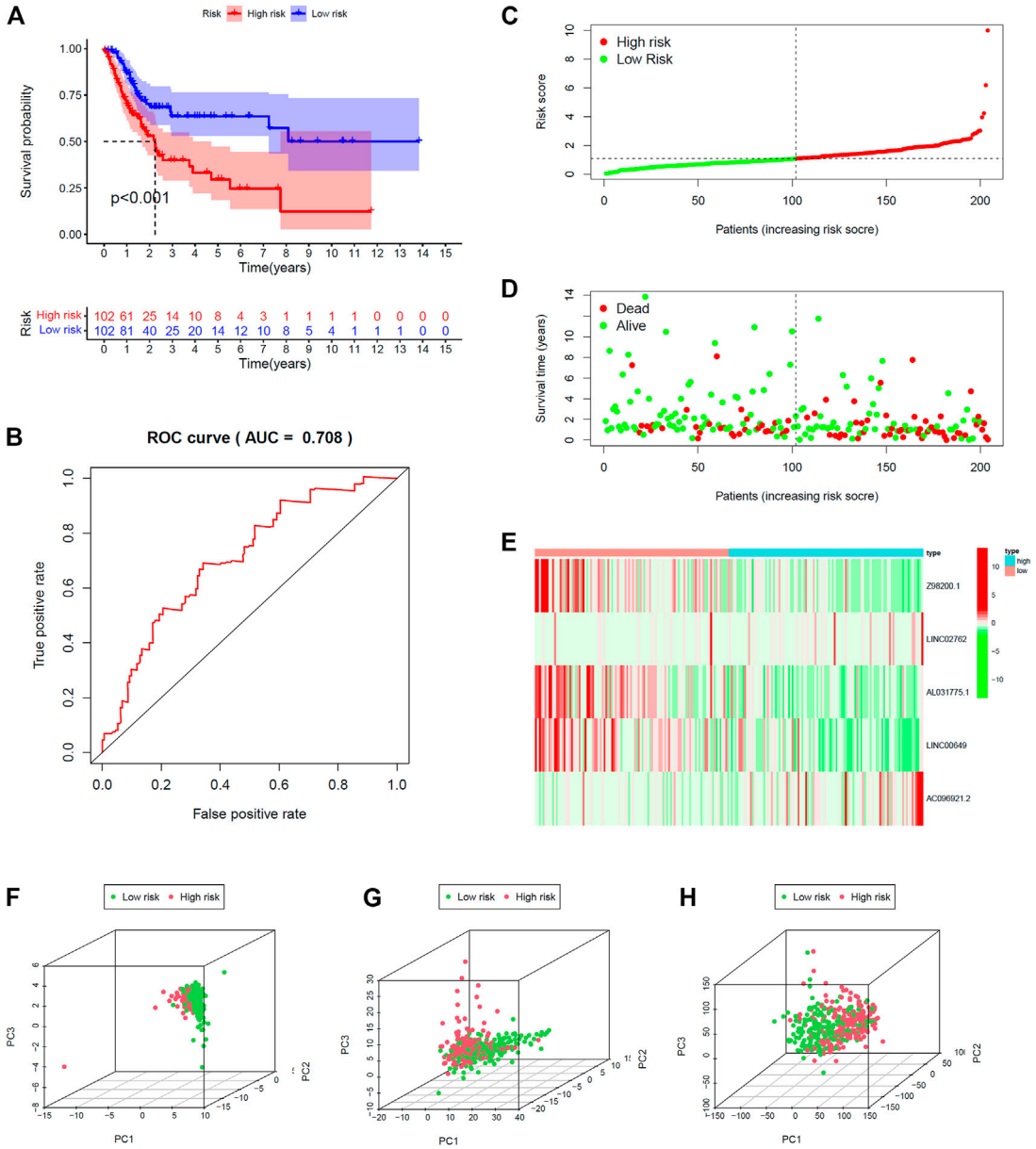

FIGURE 4 | Validation of prediction model in training set. **(A)** Kaplan–Meier survival curves revealed OS comparison of the high- and low-risk groups. **(B)** Receiver operating characteristic (ROC). Distribution of risk scores **(C)** and survival status **(D)**. **(E)** Expression heatmaps of the five ferroptosis-prognosis–related lncRNAs. **(F,G,H)** Principal component analysis (PCA) was used to explore the distribution of samples in different risk group.

sarcoma-associated herpesvirus infection, PI3K-Akt signaling pathway, etc. (**Figures 2C,D**).

Establish and Verify the Prediction Model

We try to discuss the relationship between ferroptosis-related lncRNAs and survival. As a result, 16 ferroptosis-related lncRNAs were closely related with OS in the univariate Cox regression analysis (**Supplementary Figure S1B**). We build the risk signature of the five ferroptosis-related lncRNAs by the LASSO regression analysis (**Figures 3A,B**). Then, the further research result showed that two of the five ferroptosis-related lncRNAs genes with hazard ratio (HR) > 1 (*AC096921.2* and *LINC02762*) could be poor prognostic markers for BC and other three genes with a HR < 1 (*Z98200.1*, *LINC00649*, and *AL031775.1*) may be protective markers (**Figure 3C**).

All 406 BC samples were then divided into training set and testing set by the complete randomization method. The training set included 204 samples, which were divided into high-risk group (n = 102) and the low-risk group (n = 102) according to the calculated median risk score. Kaplan–Meier survival curve

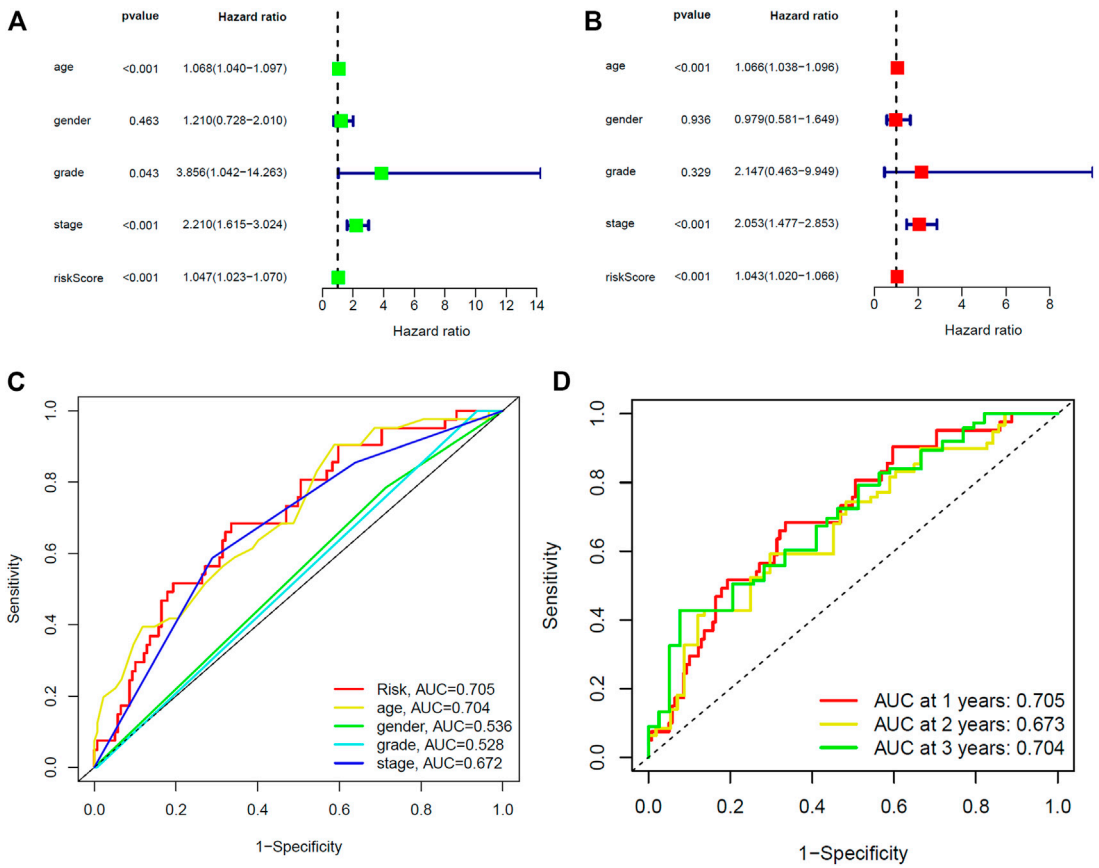

FIGURE 5 | Identification of prognostic indicators for bladder cancer in training set. **(A)** Univariate Cox regression analysis showed that age, stage and the risk score were prognostic factors of bladder cancer. **(B)** Age, stage, and the risk score are independent risk factors for bladder cancer. **(C)** ROC curve of prognostic indicators for bladder cancer. **(D)** Time-dependent ROC curve of the risk score.

revealed that the OS in the high-risk group was significantly lower than that in the low-risk group ($p < 0.001$; **Figure 4A**). We plotted ROC and the area under the curve (AUC) was 0.708 (**Figure 4B**). The differences between the two risk groups in the distribution of risk score and survival status were further explored. (**Figures 4C,D**). Patients with BC in the high-risk group had high expression of *AC096921.2* and *LINC02762* but low expression of *Z98200.1*, *LINC00649*, and *AL031775.1* (**Figure 4E**).

The testing set and entire set were divided into high-risk group ($n = 109$ in the testing set, $n = 211$ in the entire set) and low-risk group ($n = 93$ in the testing set, $n = 195$ in the entire set) by the same way as training set. There was significant difference in the OS rate between the two groups according to the risk score. Patients in the high-risk group had poorer OS than the low-risk group ($p < 0.012$, $p < 0.001$; **Supplementary Figures 2A**, **3A**). The AUC was 0.656 and 0.683 in the testing set and the entire set, respectively (**Supplementary Figures S2B, 3B**). The distributions of the risk score and survival state were shown in **Supplementary Figures S2C,D** and **Supplementary Figures S3C,D**. The expression plotted of the five ferroptosis-related lncRNAs is demonstrated in **Supplementary Figures S2E, 3E**. To explore the function of the five ferroptosis-related lncRNAs in BC, we performed PCA that showed that the whole genome expression, DE ferroptosis-related lncRNAs, and the above risk genes in the model could separate the high- and low-risk groups (**Figures 4F–H**). The results showed that samples in the two risk groups generally had different ferroptosis states and may be identified by the lncRNA signature.

Furthermore, we compared the prognostic relevance of BC between the risk score and clinical variables (age, gender, grade, and stage). Univariate Cox regression analysis in the training and entire sets revealed that age, stage, and the risk score were directly related to the prognosis of BC (**Figure 5A**, **Supplementary Figure S5A**; $p < 0.001$). In addition, the multivariate Cox regression analysis showed that age, stage, and the risk score were independent prognostic indictors in BC (**Figure 5B**, **Supplementary Figure S5B**; $p < 0.001$). The AUC corresponding to the risk score (training set, 0.705; testing set, 0.652; entire set, 0.680) was higher than that for age (training set, 0.704; testing set, 0.610; entire set, 0.660), gender (training set, 0.536; testing set, 0.411; entire set, 0.479), grade (training set, 0.528; testing set, 0.527; entire set, 0.528), and stage (training set, 0.672; testing set, 0.600; entire set, 0.639) (**Figure 5C**, **Supplementary Figures S4C, 5C**). This risk score was an independent risk factor for BC prognosis and had good predictive power at 1, 2, and 3 years (**Figure 5D**, **Supplementary**

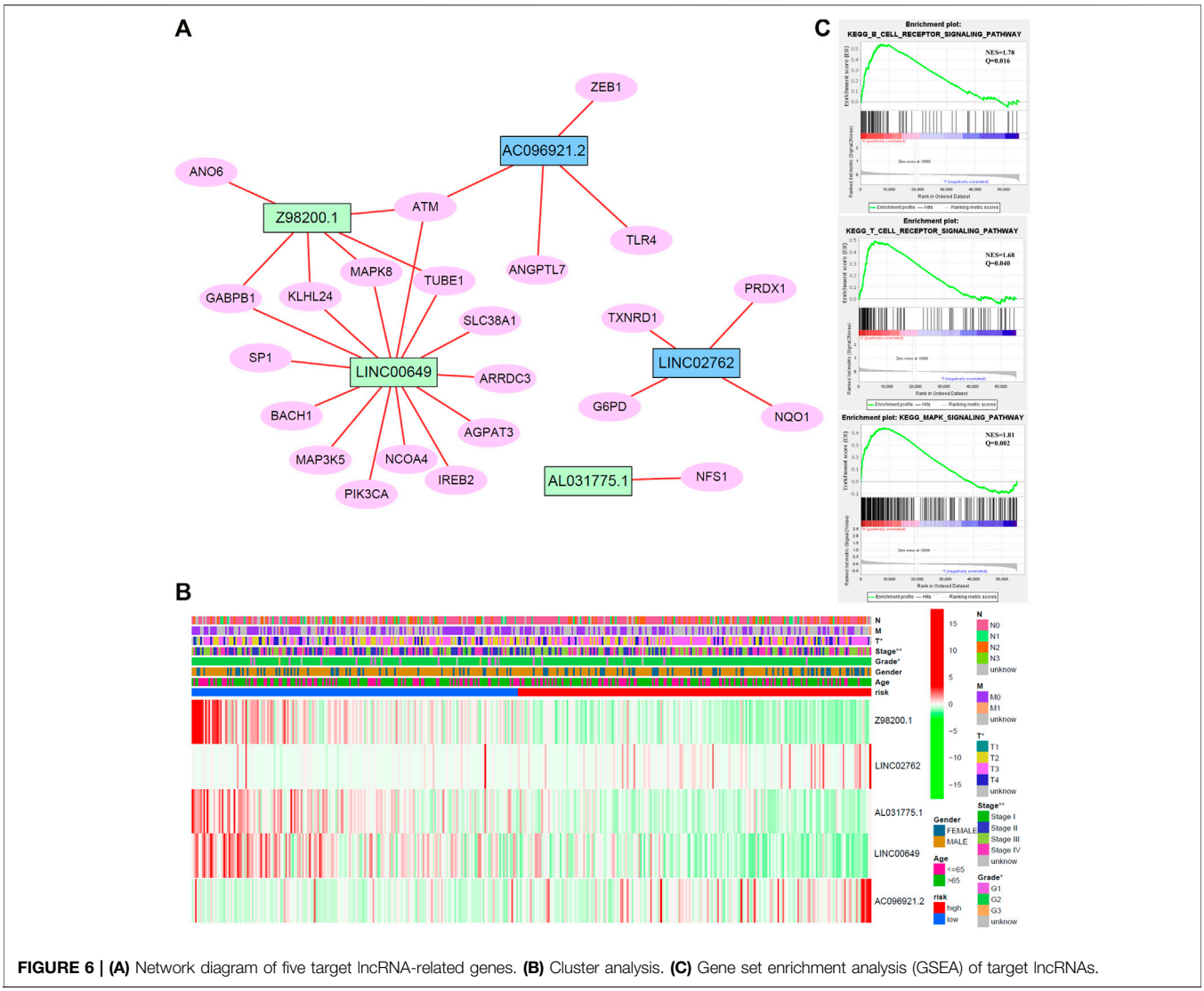

FIGURE 6 | (A) Network diagram of five target lncRNA-related genes. **(B)** Cluster analysis. **(C)** Gene set enrichment analysis (GSEA) of target lncRNAs.

Figures S4D, 5D). The results demonstrated that the risk score based on five lncRNAs may predict the OS rate of patients with BC.

Interaction Network

To enhance the understanding of potential interactions among the five ferroptosis-related lncRNAs, a total of 23 related genes were obtained by gene coexpression analysis. Furthermore, Cytoscape software was used to construct the network (|cor|>0.3, $p < 0.05$; **Figure 6A**). *ATM* may be a junction of the genes network, which connected *Z98200.1*, *LINC00649*, and *AC096921.2*.

Comparative Analysis of Different Risk Groups

Cluster analysis of stage, grade, TNM stage, age, gender distribution, and target gene showed that patients with worse pathological stage, higher grade, and later stage had higher risk score, higher expression of *AC096921.2* and *LINC02762*, and lower expression of *Z98200.1*, *LINC00649*, and *AL031775.1* (**Figure 6B**). Patients in the high-risk group had a later clinical stage than those in the low-risk group. T stage, gender, and stage were closely related to the risk score.

In addition, our previous work revealed that m6A played an important role in lung cancer (Yin et al., 2021). Hence, we explored the expression of m6A methylation gene in patients with BC. There were obvious differences between the high- and low-risk groups. Expression of *YTHDF1*, *YTHDF2*, *YTHDC1*, and *METTL3* in the low-risk group was significantly high compared with the high-risk group, which suggests that m6A modification may affect the progression of BC (**Supplementary Figure S6A**).

The Target lncRNAs May Be Bound up With Immunity

To study the biological pathways and functions involved in the pathogenesis of BC, we performed gene set enrichment analysis. The

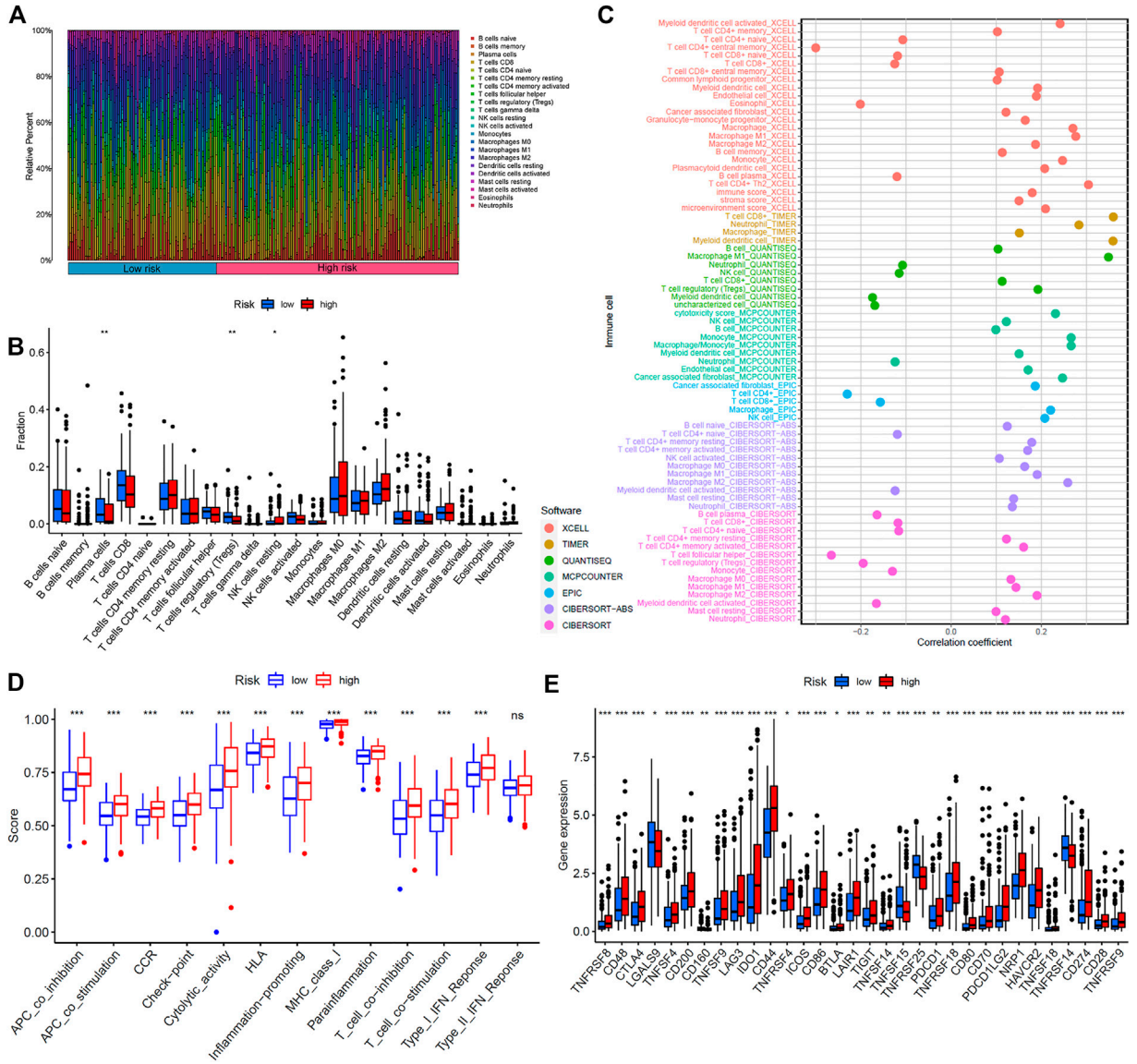

FIGURE 7 | Immunoassay showed that the five ferroptosis-prognosis–related lncRNAs were closely related to the immune system. **(A)** Proportion of immune cells in the high- and low-risk groups. **(B)** Immune cell abundance in the high- and low-risk groups. **(C)** Correlation analysis between immune cell abundance and the risk score. **(D)** Immune function analysis showed that there were significant differences between the high- and low-risk groups. **(E)** Comparison of immune checkpoints between two risk groups.

five lncRNAs may participate in B-cell receptor signaling pathway, T-cell receptor signaling pathway, and MAPK signaling pathway (**Figure 6C**).

The immune response to tumor affects the progress of tumor to a great extent. Immune cell infiltration in tumor microenvironment (TME) can reflect the immune response to tumor. The proportion of immune cells in the two risk groups is shown in **Figures 7A,B**. There were distinct differences in immune response between the high- and low-risk groups. The immune cell abundance was significantly correlated with the risk score (**Figure 7C**). In addition, the analysis of immune score showed that the immune function of the high-risk group was stronger than that of the low-risk group (**Figure 7D**). We further explored the immune checkpoint genes in these groups. The results revealed that the genes were generally highly expressed in the high-risk group except *LGALS9*, *TNFSF15*, *TNFRSF25*, and *TNFRSF14* (**Figure 7E**). The mechanism of the five lncRNAs may be related to immune response. Furthermore, type C1 (wound healing) immunization is the main immunization mode in the low-risk group, whereas type C2 [interferon-γ (IFN-γ) dominant] immunization accounts for a high proportion in the high-risk group (**Figure 8A**). The proportion of type C3 (inflammatory) and type C4 (lymphocyte depleted) immunization

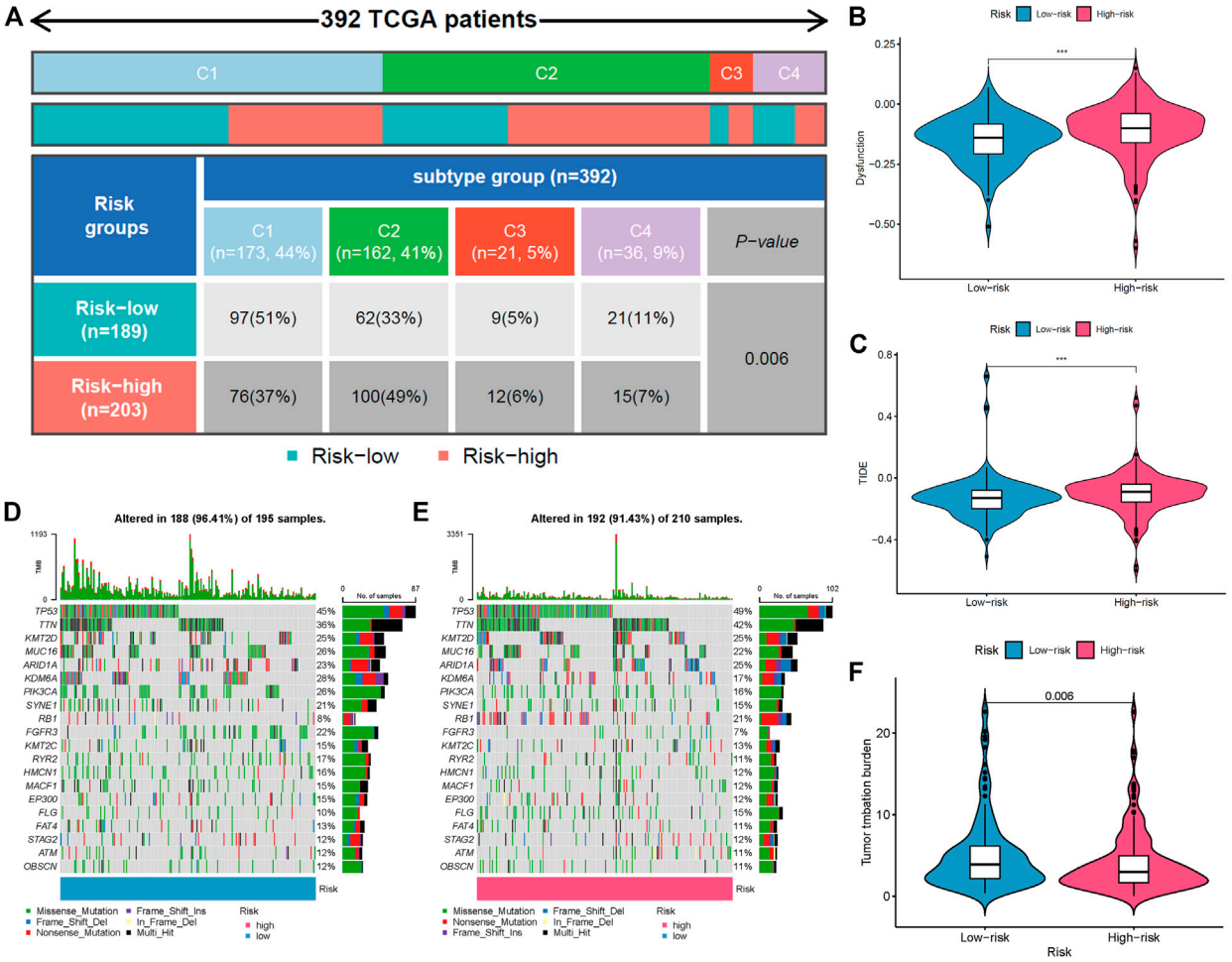

FIGURE 8 | Comparison of two risk groups in molecular typing of immune subtypes, tumor mutation burden (TMB), and immune escape. **(A)** Proportion of molecular typing of immune subtypes. **(B)** The high-risk group had more immune dysfunction. **(C)** Compared with the low-risk group, the high-risk group had higher Tumor Immune Dysfunction and Exclusion (TIDE) score and greater potential of immune escape. **(D)** TMB of the low-risk group. **(E)** TMB of the high-risk group. **(F)** Statistical analysis of TMB in two risk groups.

was low in the two groups. The difference of molecular typing of immune subtypes between the two risk groups was statistically significant. Moreover, the high-risk group had higher TIDE prediction scores and patients may not benefit from immune checkpoint inhibitor (ICI; **Figures 8B,C**). Programmed death inhibitor-1 (PD-1) protein or its ligand (PD-L1) plays an important role in many tumor treatments. TMB is an index to evaluate the efficacy of PD-1 antibody therapy. The analysis showed that the low-risk group has a lower TMB as a whole (**Figures 8D,E**). Therefore, its immunotherapy response rate may be higher. The difference of TMB was statistically significant (**Figure 8F**).

The low-content group of memory B cells ($p = 0.012$), macrophages (M0: $p = 0.014$; M2: $p < 0.001$), resting mast cells ($p = 0.018$), neutrophils ($p < 0.001$), and activated natural killer cells ($p = 0.032$) had better OS. For plasma cells ($p < 0.001$), activated $CD4^+$ memory T cells ($p = 0.001$), and $CD8^+$ T cells ($p < 0.001$) (**Supplementary Figures S7A–F**), better survival appeared in the high-content group (**Supplementary Figures S7G–I**). In addition, the survival analysis of immune function showed that there were significant differences in survival between immune score groups, and the high–immune score group had better OS than the low–immune score group (**Supplementary Figure S8**).

Significance of the Risk Model in Routine Chemotherapy

We explored the response of patients with BC with different risk scores to conventional chemotherapy drugs including cisplatin, paclitaxel, doxorubicin, mitomycin, gemcitabine, and docetaxel (**Figure 9**). The difference of drug sensitivity between the high- and low-risk groups was statistically significant. Patients in the high-risk group had higher drug sensitivity than those in the low-risk group. The findings suggest that this risk model may be helpful for clinical treatment and prevention of drug resistance in patients with BC.

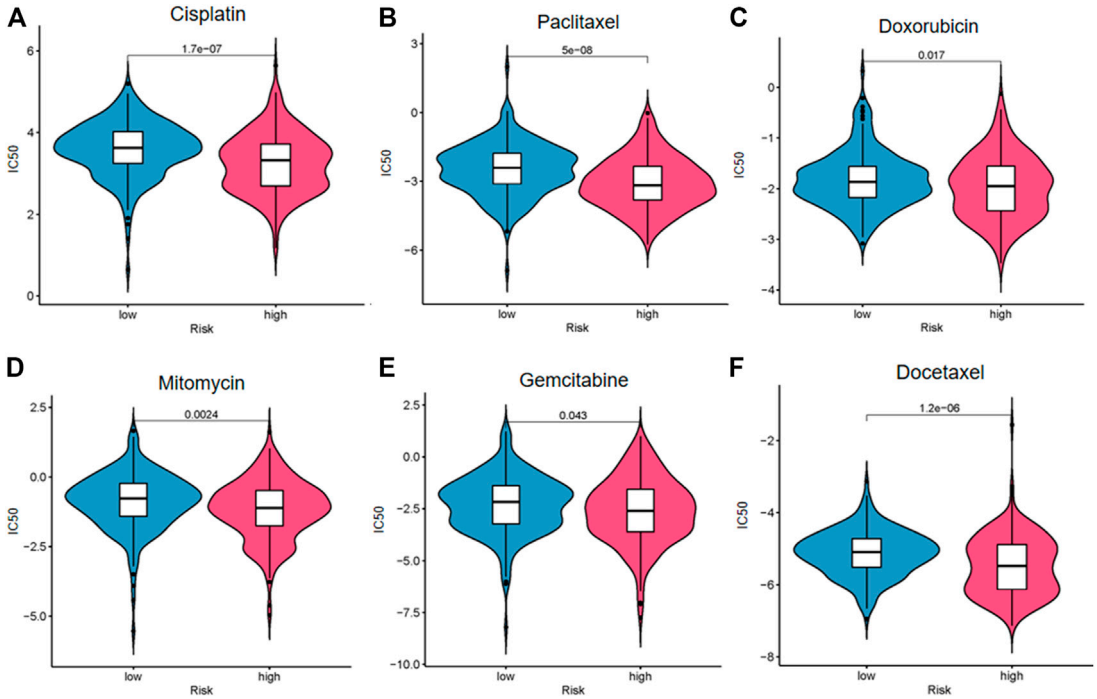

FIGURE 9 | Drug sensitivity analysis of cisplatin **(A)**, paclitaxel **(B)**, doxorubicin **(C)**, mitomycin **(D)**, gemcitabine **(E)**, and docetaxel **(F)**.

Single Gene Risk Analysis

The diversity in expression of the five ferroptosis-related lncRNAs genes between BC tissues and normal tissues was shown in **Figure 10A**. The 406 patients with BC were divided into high- and low-expression groups according to the median expression level of each lncRNA. The Kaplan–Meier curve of the high- and low-expression groups showed that *Z98200.1*, *LINC00649*, and *AL031775.1* were positively correlated with the prognosis of BC and that *LINC02762* was negatively correlated with the prognosis of BC (**Figure 10B**).

DISCUSSION

Some research studies reported the change characteristics of morbidity and mortality of BC from 1990 to 2016 and predicted that the morbidity will continue to rise by 2030, especially in the high social population index countries (Cai et al., 2020). European Organization for Research and Treatment of Cancer divided patients with BC into low-, medium-, and high-risk groups according to tumor size, number, T category, recurrence rate, *in situ* cancer, and grading (Sylvester et al., 2006). Hence, the discovery and application of more prognostic predictors in BC may improve the survival rate of patients.

Increasing studies have confirmed that lncRNAs potentially participate in cancer progression. Our current study explored the differential expression of ferroptosis-related ncRNA genes in patients with BC and found 463 upregulated genes and 75 downregulated genes. LncRNAs may affect the occurrence and progression of BC through ferroptosis. The results indicate that lncRNAs could regulate development of cancer on many levels such as the TME, tumor growth, invasion, metastasis, and recurrence (Statello et al., 2021). Focally amplified lncRNA on chromosome 1 (*FAL1*) repressed P21 to regulate the cell proliferation (Hu et al., 2014). Gastric cancer–associated lncRNA1 (*GClnc1*) may promote progression of BC *via* activation of *MYC* (Zhuang et al., 2019). Although many studies have been devoted to the role of lncRNAs in tumors, further research in the prognosis of BC is still extremely needed.

Further analysis showed that these genes may play a role by affecting microRNAs and PI3K-Akt signaling pathway. The PI3K pathway was widely activated in BC, which could be the potential therapeutic targets (Cancer Genome Atlas Research 2014). Pictilisib (an effective PI3K inhibitor) synergized with cisplatin and/or gemcitabine could significantly delay the growth of BC compared with single-drug treatment (Zeng et al., 2017). The inhibitor of PI3K acted synergistically with fibroblast growth factor receptor inhibitors in BC, which plays a significant role of targeted therapeutics (Wang et al., 2017). Inhibition of PI3K pathway may activate the corresponding feedback pathway and affect the therapeutic effect. How to prevent drug resistance deserves further study.

Our research showed that the five ferroptosis-related lncRNAs may act on the immune system. There were significant differences between the two risk groups in immune cell abundance, immune function, immune escape, and TMB. Patients with high risk of BC may have a stronger immune response. It was found that the

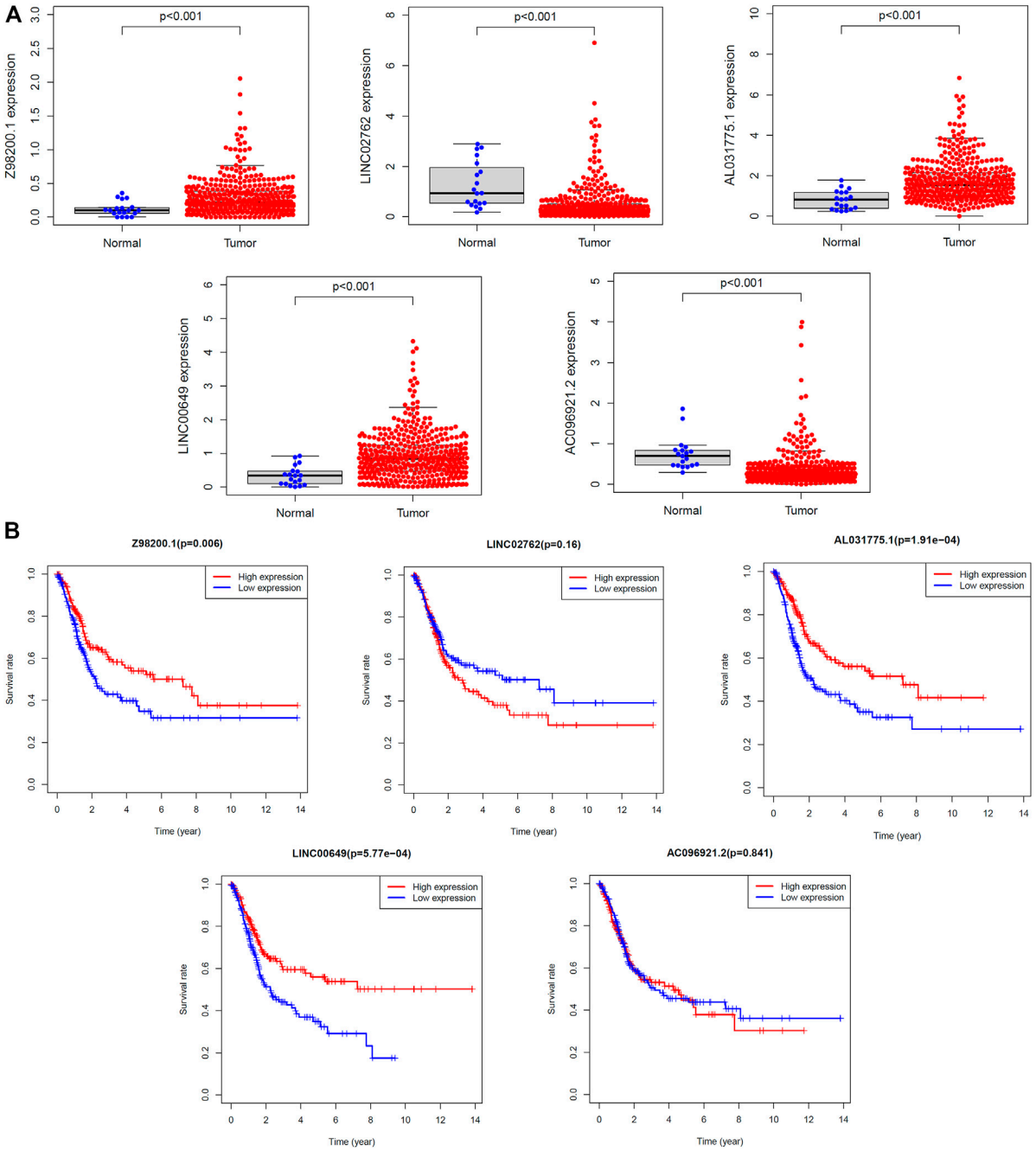

FIGURE 10 | Survival analysis of single lncRNA. **(A)** The expression levels of five target lncRNAs in tumor tissues and normal tissues were compared. **(B)** The samples were grouped according to the median expression size for survival analysis, and the survival analysis was carried out.

degree of immune infiltration and immune molecules is related to prognosis (Efstathiou et al., 2019; Seo et al., 2021). In recent years, immunotherapy has developed rapidly and is widely used in the treatment of a variety of tumors. From the BCG, which is the first approved immunotherapy drug of BC approved by the Food and Drug Administration to adoptive immunotherapy, immune checkpoint blockades, cancer vaccines, bispecific antibodies, and oncolytic viruses, more and more immunotherapy has been used in the field of BC (Wu et al., 2021). The research of immunotherapy combined with chemotherapy is emerging one after another. Maintenance avelumab plus chemotherapy with gemcitabine plus cisplatin or carboplatin significantly prolonged the progression-free survival and the OS of patients with unresectable urothelial carcinoma (Galsky et al., 2020; Powles et al., 2020). Whether primary or metastatic tumors, ICI is beneficial to the treatment of BC (Grobet-Jeandin et al., 2021).

This research suggests that, using the model to predict the risk score of patients with BC, can reflect the effect of ICI and immune response rate to some extent. Immunoassays for BC may provide more diagnostic and therapeutic options for patients. In addition, the difference between the two risk groups in the treatment response of commonly used chemotherapeutic agents for BC suggests that this model may be helpful in the selection of chemotherapy regimen and the judgment of curative effect.

Interestingly, ferroptosis plays an important role in preventing drug resistance and tumor immunity, which is perceived as a major breakthrough (Viswanathan et al., 2017; Wang W. et al., 2019). Furthermore, ferroptosis can occur in a variety of immune cells and affect the immune response, among which, T cells have an effect on ferroptosis of tumors (Xu et al., 2021). Immunotherapy activated $CD8^+$ T cells downregulate SLC3A2 and SLC7A11 by releasing IFN-γ, which reduces the uptake of cystine and promotes ferroptosis. In addition, ferroptosis can enhance the antitumor effect mediated by T cells (Wang W. et al., 2019). Detecting specific ferroptosis-related biomarkers may help us diagnose and treat tumors. Some scholars have proposed that gene modification can be used to enhance immunity to tumors.

Tracing upstream of the target genes, we found that they might be modified by m6A to increase or decrease their expression in BC. M6A is a base modification behavior widely existing in mRNAs. This reversible methylation occurs at the sixth nitrogen atom of adenylate. Its regulatory factors include methyltransferase (METTL3, METTL14, WTAP, and KIAA1492), demethylase [fat mass and obesity-associated protein (FTO) and ALKBH5] and methylated reading protein (YTHDC1-2, YTHDF1-3, HNRNPA2B1, and eIF). Gene methylation occurs widely in tumors. FTO mediates m6A modification of MALAT/miR-384/MAL2 axis to promote tumorigenesis of BC (Tao et al., 2021). Studies have shown that m6A modification and PI3K-Akt signaling pathway also play a role in epithelial–mesenchymal transition (EMT) (Lin et al., 2019). Primary epithelial tumor cells mainly develop type three EMT, which enhances cell invasiveness and migration, resulting in tumor progression and metastasis (Kalluri. 2009).

Our research started with ferroptosis-related lncRNAs and explored some new biomarkers for BC. It expands the layout of BC gene expression study and provides more abundant and comprehensive support for the diagnosis and treatment of BC. Early identification and risk stratification of patients with BC at the gene level is conducive to the development of precision medicine. We can also use the ferroptosis gene specifically expressed in BC as a breakthrough to inhibit tumor resistance and relapse and explore new therapeutic targets. Tumor-related research is changing with each passing day, and its mystery is gradually revealed. In the experiment, there may be some differences between reality and expectation in terms of the comparison results of the target genes expression in tumor samples and normal samples, which may due to the insufficient sample size of normal tissues. We tried to validate our risk model with another independent database of BC data, but the database with complete information was not found.

In a word, we identified some novel biomarkers closely related to survival rate of patients with BC and generated a prediction model that has positive significance in predicting prognosis of BC. The more in-depth and detailed research of ferroptosis in BC was required, and the specific pathway of target gene on each system is still unclear. Moreover, whether the treatment targeting the five lncRNAs can improve the therapeutic effect on related chemotherapeutic drugs and immunotherapy such as ICI and reduce drug resistance deserves further study.

DATA AVAILABILITY STATEMENT

The datasets presented in this study can be found in online repositories. The names of the repository/repositories and accession number(s) can be found in the article/ **Supplementary Material**.

AUTHOR CONTRIBUTIONS

HY supervised and designed the project. HY, YW, SZ, and YB performed the research, analyzed the data and wrote the manuscrip. GL, SW, XL, and JC contributed to the analyses, provided scientific advice, and revised the manuscript.

FUNDING

This study was supported by the National Natural Science Foundation of China (81903120 to HY), Young Innovative Talents Training Program of Higher Education Institutions in Heilongjiang Province (UNPYSCT-2020161 to HY), Special Support for Postdoctoral in Heilongjiang Province (LBH-TZ2115 to HY), Haiyan Foundation of Harbin Medical University Cancer Hospital (JJZD2021-13 to HY), Postdoctoral Foundation of Heilongjiang Province (LBH-Z20076 to HY), the Natural science funding of Heilongjiang (YQ2021H024 to HY), China Postdoctoral Science Foundation (2020M681117 and 2021T140170 to HY), and Young Talents Foundation of Harbin Medical University Cancer Hospital (No. BJQN2020-01 to HY).

ACKNOWLEDGMENTS

We thank for using TCGA database for free.

SUPPLEMENTARY MATERIAL

The Supplementary Material for this article can be found online at: https://www.frontiersin.org/articles/10.3389/fcell.2022.809747/full#supplementary-material

Supplementary Figure S1 | (A) GO analysis of ferroptosis-related genes at biological process (BP) category. **(B)** Univariate Cox regression analysis of differentially expressed ferroptosis-related lncRNAs.

Supplementary Figure S2 | Validation of prediction model in testing set. **(A)** Kaplan–Meier survival curves. **(B)** Receiver operating characteristic (ROC). Distribution of risk scores **(C)** and survival status **(D)**. **(E)** Expression heatmaps of the five ferroptosis-prognosis–related lncRNAs.

Supplementary Figure S3 | Validation of prediction model in entire set. **(A)** Kaplan–Meier survival curves. **(B)** Receiver operating characteristic (ROC). Distribution of risk scores **(C)** and survival status **(D)**. **(E)** Expression heatmaps of the five ferroptosis-prognosis–related lncRNAs.

Supplementary Figure S4 | Identification of prognostic indicators in testing set. **(A)** Univariate Cox regression analysis. **(B)** Multivariate Cox regression analysis. **(C)** ROC curve of prognostic indicators for bladder cancer. **(D)** Time-dependent ROC curve of the risk score.

Supplementary Figure S5 | Identification of prognostic indicators in entire set. **(A)** Univariate Cox regression analysis. **(B)** Multivariate Cox regression analysis. **(C)** ROC curve of prognostic indicators for bladder cancer. **(D)** Time-dependent ROC curve of the risk score.

Supplementary Figure S6 | Analysis of m6A-related gene expression in two risk groups.

Supplementary Figure S7 | The samples were grouped according to the abundance of immune cells, and the overall survival rate between grades was compared. Memory B cells **(A)**, M0 macrophages **(B)**, M2 macrophages **(C)**, resting mast cells **(D)**, neutrophils **(E)**, activated NK cells **(F)**, plasma cells **(G)**, activated $CD4^+$ memory T cells **(H)**, and $CD8^+$ T cells **(I)**.

Supplementary Figure S8 | The different immune function scores of the samples were calculated, and the overall survival of the high rating group and the low rating group were compared. APC co-inhibition **(A)**, checkpoint **(B)**, cytolytic activity **(C)**, HLA **(D)**, inflammation-promoting **(E)**, MHC class I **(F)**, T-cell co-inhibition **(G)**, T-cell co-stimulation **(H)**, and type I IFN response **(I)**.

REFERENCES

Babjuk, M., Böhle, A., Burger, M., Capoun, O., Cohen, D., Compérat, E. M., et al. (2017). EAU Guidelines on Non-Muscle-invasive Urothelial Carcinoma of the Bladder: Update 2016. *Eur. Urol.* 71 (3), 447–461. doi:10.1016/j.eururo.2016.05.041

Burger, M., Catto, J. W. F., Dalbagni, G., Grossman, H. B., Herr, H., Karakiewicz, P., et al. (2013). Epidemiology and Risk Factors of Urothelial Bladder Cancer. *Eur. Urol.* 63 (2), 234–241. doi:10.1016/j.eururo.2012.07.033

Cai, Q., Chen, Y., Xin, S., Zhang, D., Pan, J., Xie, Z., et al. (2020). Temporal Trends of Bladder Cancer Incidence and Mortality from 1990 to 2016 and Projections to 2030. *Transl Androl. Urol.* 9 (2), 153–165. doi:10.21037/tau.2020.02.24

Cancer Genome Atlas Research, N. (2014). Comprehensive Molecular Characterization of Urothelial Bladder Carcinoma. *Nature* 507 (7492), 315–322. doi:10.1038/nature12965

Chen, C., Luo, Y., He, W., Zhao, Y., Kong, Y., Liu, H., et al. (2020). Exosomal Long Noncoding RNA LNMAT2 Promotes Lymphatic Metastasis in Bladder Cancer. *J. Clin. Invest.* 130 (1), 404–421. doi:10.1172/JCI130892

Chen, C., Zheng, H., Luo, Y., Kong, Y., An, M., Li, Y., et al. (2021). SUMOylation Promotes Extracellular Vesicle-Mediated Transmission of lncRNA ELNAT1 and Lymph Node Metastasis in Bladder Cancer. *J. Clin. Invest.* 131 (8). doi:10.1172/jci146431

Chen, X., Kang, R., Kroemer, G., and Tang, D. (2021). Broadening Horizons: the Role of Ferroptosis in Cancer. *Nat. Rev. Clin. Oncol.* 18 (5), 280–296. doi:10.1038/s41571-020-00462-0

Dixon, S. J., Lemberg, K. M., Lamprecht, M. R., Skouta, R., Zaitsev, E. M., Gleason, C. E., et al. (2012). Ferroptosis: an Iron-dependent Form of Nonapoptotic Cell Death. *Cell* 149 (5), 1060–1072. doi:10.1016/j.cell.2012.03.042

Doll, S., Proneth, B., Tyurina, Y. Y., Panzilius, E., Kobayashi, S., Ingold, I., et al. (2017). ACSL4 Dictates Ferroptosis Sensitivity by Shaping Cellular Lipid Composition. *Nat. Chem. Biol.* 13 (1), 91–98. doi:10.1038/nchembio.2239

Dreicer, R. (2017). Chemotherapy for Advanced Urothelial Cancer: End of the Beginning? *Lancet Oncol.* 18 (5), 567–569. doi:10.1016/s1470-2045(17)30241-3

Efstathiou, J. A., Mouw, K. W., Gibb, E. A., Liu, Y., Wu, C.-L., Drumm, M. R., et al. (2019). Impact of Immune and Stromal Infiltration on Outcomes Following Bladder-Sparing Trimodality Therapy for Muscle-Invasive Bladder Cancer. *Eur. Urol.* 76 (1), 59–68. doi:10.1016/j.eururo.2019.01.011

Engreitz, J. M., Ollikainen, N., and Guttman, M. (2016). Long Non-coding RNAs: Spatial Amplifiers that Control Nuclear Structure and Gene Expression. *Nat. Rev. Mol. Cell Biol* 17 (12), 756–770. doi:10.1038/nrm.2016.126

Galsky, M. D., Arija, J. Á. A., Bamias, A., Davis, I. D., De Santis, M., Kikuchi, E., et al. (2020). Atezolizumab with or without Chemotherapy in Metastatic Urothelial Cancer (IMvigor130): a Multicentre, Randomised, Placebo-Controlled Phase 3 Trial. *The Lancet* 395 (10236), 1547–1557. doi:10.1016/s0140-6736(20)30230-0

Grobet-Jeandin, É., Pinar, U., Loriot, Y., and Roupret, M. (2021). Treatment of Bladder Cancer with Immune Checkpoints Inhibitors. *Rev. Prat* 71 (4), 391–395.

Hu, X., Feng, Y., Zhang, D., Zhao, S. D., Hu, Z., Greshock, J., et al. (2014). A Functional Genomic Approach Identifies FAL1 as an Oncogenic Long Noncoding RNA that Associates with BMI1 and Represses P21 Expression in Cancer. *Cancer Cell* 26 (3), 344–357. doi:10.1016/j.ccr.2014.07.009

Jiang, L., Hickman, J. H., Wang, S.-J., and Gu, W. (2015). Dynamic Roles of P53-Mediated Metabolic Activities in ROS-Induced Stress Responses. *Cell Cycle* 14 (18), 2881–2885. doi:10.1080/15384101.2015.1068479

Kalluri, R. (2009). EMT: when Epithelial Cells Decide to Become Mesenchymal-like Cells. *J. Clin. Invest.* 119 (6), 1417–1419. doi:10.1172/jci39675

Kamat, A. M., Hahn, N. M., Efstathiou, J. A., Lerner, S. P., Malmström, P.-U., Choi, W., et al. (2016). Bladder Cancer. *The Lancet* 388 (10061), 2796–2810. doi:10.1016/s0140-6736(16)30512-8

Koppula, P., Zhuang, L., and Gan, B. (2021). Cystine Transporter SLC7A11/xCT in Cancer: Ferroptosis, Nutrient Dependency, and Cancer Therapy. *Protein Cell* 12 (8), 599–620. doi:10.1007/s13238-020-00789-5

Lin, X., Chai, G., Wu, Y., Li, J., Chen, F., Liu, J., et al. (2019). RNA m6A Methylation Regulates the Epithelial Mesenchymal Transition of Cancer Cells and Translation of Snail. *Nat. Commun.* 10 (1), 2065. doi:10.1038/s41467-019-09865-9

Mendell, J. T. (2016). Targeting a Long Noncoding RNA in Breast Cancer. *N. Engl. J. Med.* 374 (23), 2287–2289. doi:10.1056/nejmcibr1603785

Powles, T., Park, S. H., Voog, E., Caserta, C., Valderrama, B. P., Gurney, H., et al. (2020). Avelumab Maintenance Therapy for Advanced or Metastatic Urothelial Carcinoma. *N. Engl. J. Med.* 383 (13), 1218–1230. doi:10.1056/nejmoa2002788

Robertson, A. G., Kim, J., Al-Ahmadie, H., Bellmunt, J., Guo, G., Cherniack, A. D., et al. (2018). Comprehensive Molecular Characterization of Muscle-Invasive Bladder Cancer. *Cell* 174 (4), 1033. doi:10.1016/j.cell.2018.07.036

Sefik, E., Bozkurt, I. H., Basmaci, I., and Celik, S. (2019). Re: Perioperative Oral Nutrition Supplementation Reduces Prevalence of Sarcopenia Following Radical Cystectomy: Results of a Prospective Randomized Controlled Trial. *J. Urol.* 202 (4), 819. doi:10.1097/ju.0000000000000373

Seo, W. I., Lee, C. H., Jung, S. J., Lee, D. S., Park, H. Y., Jeong, D. H., et al. (2021). Expression of VISTA on Tumor-Infiltrating Immune Cells Correlated with Short Intravesical Recurrence in Non-muscle-invasive Bladder Cancer. *Cancer Immunol. Immunother.* 70 (11), 3113–3122. doi:10.1007/s00262-021-02906-7

Sharma, P., and Allison, J. P. (2015). Immune Checkpoint Targeting in Cancer Therapy: toward Combination Strategies with Curative Potential. *Cell* 161 (2), 205–214. doi:10.1016/j.cell.2015.03.030

Siegel, R. L., Miller, K. D., and Jemal, A. (2020). Cancer Statistics, 2020. *CA A. Cancer J. Clin.* 70 (1), 7–30. doi:10.3322/caac.21590

Statello, L., Guo, C.-J., Chen, L.-L., and Huarte, M. (2021). Gene Regulation by Long Non-coding RNAs and its Biological Functions. *Nat. Rev. Mol. Cell Biol* 22 (2), 96–118. doi:10.1038/s41580-020-00315-9

Svatek, R. S., Hollenbeck, B. K., Holmäng, S., Lee, R., Kim, S. P., Stenzl, A., et al. (2014). The Economics of Bladder Cancer: Costs and Considerations of Caring for This Disease. *Eur. Urol.* 66 (2), 253–262. doi:10.1016/j.eururo.2014.01.006

Sylvester, R. J., van der Meijden, A. P. M., Oosterlinck, W., Witjes, J. A., Bouffioux, C., Denis, L., et al. (2006). Predicting Recurrence and Progression in Individual Patients with Stage Ta T1 Bladder Cancer Using EORTC Risk Tables: a

Combined Analysis of 2596 Patients from Seven EORTC Trials. *Eur. Urol.* 49 (3), 466–477. doi:10.1016/j.eururo.2005.12.031

Tang, S., Ning, Q., Yang, L., Mo, Z., and Tang, S. (2020). Mechanisms of Immune Escape in the Cancer Immune Cycle. *Int. Immunopharmacology* 86, 106700. doi:10.1016/j.intimp.2020.106700

Tao, L., Mu, X., Chen, H., Jin, D., Zhang, R., Zhao, Y., et al. (2021). FTO Modifies the m6A Level of MALAT and Promotes Bladder Cancer Progression. *Clin. Transl Med.* 11 (2), e310. doi:10.1002/ctm2.310

Thompson, L. D. R. (2006). World Health Organization Classification of Tumours: Pathology and Genetics of Head and Neck Tumours. *Ear Nose Throat J.* 85 (2), 74. doi:10.1177/014556130608500201

Viswanathan, V. S., Ryan, M. J., Dhruv, H. D., Gill, S., Eichhoff, O. M., Seashore-Ludlow, B., et al. (2017). Dependency of a Therapy-Resistant State of Cancer Cells on a Lipid Peroxidase Pathway. *Nature* 547 (7664), 453–457. doi:10.1038/nature23007

Wang, L., Šuštić, T., Leite de Oliveira, R., Lieftink, C., Halonen, P., van de Ven, M., et al. (2017). A Functional Genetic Screen Identifies the Phosphoinositide 3-kinase Pathway as a Determinant of Resistance to Fibroblast Growth Factor Receptor Inhibitors in FGFR Mutant Urothelial Cell Carcinoma. *Eur. Urol.* 71 (6), 858–862. doi:10.1016/j.eururo.2017.01.021

Wang, M., Mao, C., Ouyang, L., Liu, Y., Lai, W., Liu, N., et al. (2019). Long Noncoding RNA LINC00336 Inhibits Ferroptosis in Lung Cancer by Functioning as a Competing Endogenous RNA. *Cell Death Differ* 26 (11), 2329–2343. doi:10.1038/s41418-019-0304-y

Wang, W., Green, M., Choi, J. E., Gijón, M., Kennedy, P. D., Johnson, J. K., et al. (2019). CD8+ T Cells Regulate Tumour Ferroptosis during Cancer Immunotherapy. *Nature* 569 (7755), 270–274. doi:10.1038/s41586-019-1170-y

Wang, Y., Liu, Y., Guan, Y., Li, H., Liu, Y., Zhang, M., et al. (2020). Integrated Analysis of Immune-Related Genes in Endometrial Carcinoma. *Cancer Cell Int* 20, 477. doi:10.1186/s12935-020-01572-6

Wu, Z., Liu, J., Dai, R., and Wu, S. (2021). Current Status and Future Perspectives of Immunotherapy in Bladder Cancer Treatment. *Sci. China Life Sci.* 64 (4), 512–533. doi:10.1007/s11427-020-1768-y

Xu, Q., Yin, H., Ao, H., Leng, X., Liu, M., Liu, Y., et al. (2019). An 11-lncRNA Expression Could Be Potential Prognostic Biomarkers in Head and Neck Squamous Cell Carcinoma. *J. Cell Biochem* 120 (10), 18094–18103. doi:10.1002/jcb.29113

Xu, S., Min, J., and Wang, F. (2021). Ferroptosis: an Emerging Player in Immune Cells. *Sci. Bull.* 66 (22), 2257–2260. doi:10.1016/j.scib.2021.02.026

Yang, W. S., SriRamaratnam, R., Welsch, M. E., Shimada, K., Skouta, R., Viswanathan, V. S., et al. (2014). Regulation of Ferroptotic Cancer Cell Death by GPX4. *Cell* 156 (1-2), 317–331. doi:10.1016/j.cell.2013.12.010

Yin, H., Chen, L., Piao, S., Wang, Y., Li, Z., Lin, Y., et al. (2021). M6A RNA Methylation-Mediated RMRP Stability Renders Proliferation and Progression of Non-small Cell Lung Cancer through Regulating TGFBR1/SMAD2/SMAD3 Pathway. *Cell Death Differ*. doi:10.1038/s41418-021-00888-8

Yin, H., Wang, X., Zhang, X., Wang, Y., Zeng, Y., Xiong, Y., et al. (2018). Integrated Analysis of Long Noncoding RNA Associated-Competing Endogenous RNA as Prognostic Biomarkers in clear Cell Renal Carcinoma. *Cancer Sci.* 109 (10), 3336–3349. doi:10.1111/cas.13778

Zeng, S.-X., Zhu, Y., Ma, A.-H., Yu, W., Zhang, H., Lin, T.-Y., et al. (2017). The Phosphatidylinositol 3-Kinase Pathway as a Potential Therapeutic Target in Bladder Cancer. *Clin. Cancer Res.* 23 (21), 6580–6591. doi:10.1158/1078-0432.ccr-17-0033

Zhuang, C., Ma, Q., Zhuang, C., Ye, J., Zhang, F., and Gui, Y. (2019). LncRNA GClnc1 Promotes Proliferation and Invasion of Bladder Cancer through Activation of MYC. *FASEB j.* 33 (10), 11045–11059. doi:10.1096/fj.201900078rr

Conflict of Interest: The authors declare that the research was conducted in the absence of any commercial or financial relationships that could be construed as a potential conflict of interest.

Publisher's Note: All claims expressed in this article are solely those of the authors and do not necessarily represent those of their affiliated organizations or those of the publisher, the editors, and the reviewers. Any product that may be evaluated in this article, or claim that may be made by its manufacturer, is not guaranteed or endorsed by the publisher.

frontiers in Cell and Developmental Biology

ORIGINAL RESEARCH
published: 21 March 2022
doi: 10.3389/fcell.2022.832892

Ferroptosis Patterns and Tumor Microenvironment Infiltration Characterization in Bladder Cancer

Qi-Dong Xia†, Jian-Xuan Sun†, Chen-Qian Liu, Jin-Zhou Xu, Ye An, Meng-Yao Xu, Zheng Liu‡, Jia Hu*‡ and Shao-Gang Wang*‡*

Department and Institute of Urology, Tongji Hospital, Tongji Medical College, Huazhong University of Science and Technology, Wuhan, China

OPEN ACCESS

Edited by:
Yu Xiao,
Wuhan University, China

Reviewed by:
Emanuele Giurisato,
University of Siena, Italy
Lifeng Zhang,
Changzhou No.2 People's Hospital, China

***Correspondence:**
Zheng Liu
lz2013tj@163.com
Jia Hu
jiahutjm@163.com
Shao-Gang Wang
sgwang0701@hust.edu.cn

†*These authors have contributed equally to this work and share first authorship*

‡*These authors have contributed equally to this work*

Specialty section:
This article was submitted to Molecular and Cellular Pathology, a section of the journal Frontiers in Cell and Developmental Biology

Received: *10 December 2021*
Accepted: *24 February 2022*
Published: *21 March 2022*

Citation:
Xia Q-D, Sun J-X, Liu C-Q, Xu J-Z, An Y, Xu M-Y, Liu Z, Hu J and Wang S-G (2022) Ferroptosis Patterns and Tumor Microenvironment Infiltration Characterization in Bladder Cancer. Front. Cell Dev. Biol. 10:832892. doi: 10.3389/fcell.2022.832892

Background: Ferroptosis is a unique iron-dependent form of cell death and bladder cancer (BCa) is one of the top ten most common cancer types in the world. However, the role of ferroptosis in shaping the tumor microenvironment and influencing tumor clinicopathological features remains unknown.

Methods: Using the data downloaded from The Cancer Genome Atlas (TCGA) and Gene Expression Omnibus (GEO), we comprehensively evaluated the ferroptosis patterns of 570 BCa samples based on 234 validated ferroptosis genes reported in the FerrDb database and systematically correlated these ferroptosis patterns with tumor microenvironment (TME) cell-infiltrating characteristics. The ferroptosis score was constructed to quantify ferroptosis patterns of individuals using principal component analysis (PCA) algorithms.

Results: Four distinct ferroptosis patterns and two gene clusters were finally determined. Significant differences in clinical characteristics and the prognosis of patients were found among different ferroptosis patterns and gene clusters, so were in the mRNA transcriptome and the landscape of TME immune cell infiltration. We also established a set of scoring system to quantify the ferroptosis pattern of individual patients with BCa named the ferroptosis score, which was discovered to tightly interact with clinical signatures such as the TNM category and tumor grade and could predict the prognosis of patients with BCa. Moreover, tumor mutation burden (TMB) was positively correlated to the ferroptosis score, and the low ferroptosis score was related to a better response to immunotherapy using PD-1 blockade. Finally, we also found there existed a positive correlation between the sensitivity to cisplatin chemotherapy and ferroptosis score.

Conclusions: Our work demonstrated and interpreted the complicated regulation mechanisms of ferroptosis on the tumor microenvironment and that better understanding and evaluating ferroptosis patterns could be helpful in guiding the clinical therapeutic strategy and improving the prognosis of patients with BCa.

Keywords: ferroptosis, tumor microenvironment, tumor mutation burden, bladder cancer, immunotherapy

INTRODUCTION

Ferroptosis is a unique iron-dependent form of cell death and is morphologically, biochemically, and genetically distinct from apoptosis, necrosis, pyroptosis, and autophagy (Dixon et al., 2012). Abundant and accessible cellular iron is necessary to induce ferroptosis (Dixon et al., 2012). The first discovered ferroptosis inducers are erastin (Dolma et al., 2003) and RSL3 (Yang and Stockwell, 2008), and then, a variety of ferroptosis inducers have been found in succession such as sorafenib, sulfasalazine, FIN56, and so on (Liang et al., 2019). System Xc^- inhibition and glutathione (GSH) peroxidase 4 (GPX4) inhibition are the two main mechanisms that induce ferroptosis (Liang et al., 2019). System Xc^- is the glutamate/cystine antiporter which can facilitate the exchange of cystine and glutamate across the plasma membrane (Bridges et al., 2012). The inhibition of system Xc^- can decrease the intracellular cysteine level, which is the precursor for glutathione synthesis (Yang et al., 2014). GPX4 is an indispensable enzyme which catalyzes the reduction of lipid hydroperoxide within a complex cellular membrane environment, which utilizes glutathione as an essential cofactor for its enzymatic activity (Brigelius-Flohé and Maiorino, 2013). Therefore, the inhibition of both system Xc^- and GPX4 will result in the accumulation of iron-dependent lipid hydroperoxides and increased level of reactive oxygen species (ROS), and finally, lead to cell death (Chan et al., 2019). Ferroptosis is regulated by several molecular pathways such as the transsulfuration pathway and mevalonate pathway (Yang and Stockwell, 2016), and a variety of ferroptosis regulators participate in these pathways (Liang et al., 2019). In recent years, ferroptosis has been discovered to be related to many human diseases such as acute kidney injury, Huntington disease, periventricular leukomalacia, and so on, among which cancer was the one that researchers paid most attention to (Liang et al., 2019). Different cancers seem to exhibit significantly different susceptibility to ferroptosis (Mou et al., 2019); therefore, increasing the sensitivity to ferroptosis and developing new therapies targeted at ferroptosis could be an intriguing and challenging research field in the future.

Bladder cancer (BCa) is one of the top ten most common cancer types in the world and accounted for approximately 550,000 new cases and 200,000 deaths in 2018 (Richters et al., 2020). In the United States alone, in 2019, the number of new cases and deaths were 80,470 and 17,670, respectively (Siegel et al., 2019). Advanced age, male sex, tobacco smoking, and occupational exposure to some chemical agents are the main risk factors for the incidence of BCa (Sylvester et al., 2021). According to the depth of tumor invasion and infiltration, BCa can be divided into non-muscle invasive bladder cancer (NMIBC) and muscle invasive bladder cancer (MIBC). Patients with NMIBC are treated with endoscopic resection and adjuvant intravesical therapy, including intravesical chemotherapy and intravesical bacillus Calmette–Guérin (BCG) immunotherapy (Sylvester et al., 2021). Patients with MIBC can choose radical cystectomy (RC) and lymphadenectomy, pre- and post-operative radiotherapy, neoadjuvant immunotherapy, as well as chemotherapy depending on the risk classification (Witjes et al., 2021). However, the efficacy of various treatments for BCa remains unideal and new therapeutic strategies need to be developed.

Recently, several studies have focused on the interaction between ferroptosis and BCa. A variety of ferroptosis-related signatures were established based on ferroptosis regulator genes (FRGs) to predict the landscape of the epithelial-mesenchymal transition (EMT) status, the tumor microenvironment (TME), and the prognosis of patients with BCa, and it seems that these signatures had their unique roles in evaluating their response to chemotherapy and immunotherapy (Cui et al., 2021; Sun et al., 2021; Yan et al., 2021). However, the establishment of these signatures was confined to limited ferroptosis regulator genes and many other novel validated ferroptosis-related genes were ignored. So, in this article, we evaluated the genetic variation of 23 ferroptosis regulators in BCa among a total of 412 samples from the TCGA-BLCA cohort, explored the FerrDb database to find validated ferroptosis genes (VFGs), divided the patients with BCa into four ferroptosis patterns according to the expression levels of VFGs and performed survival analysis, and then we further explored the TME cell infiltration characteristics in distinct VFG patterns and surprisingly found VFG patterns were tightly connected with TME. Next, we discovered 367 VFG cluster-related differentially expressed genes (DEGs), classified the patients into two distinct genomic subgroups, and explored the interaction between VFG patterns and gene patterns. Finally, we established a set of scoring system termed the ferroptosis score to quantify the ferroptosis pattern in individual patients and explored the characteristics of ferroptosis in tumor somatic mutation, immunotherapy, and chemotherapy.

MATERIALS AND METHODS

Data Retrieval and Processing

Ferroptosis regulator genes (FRGs) were obtained from Liu et al. (2020). Ferroptosis-related genes with validated evidences were obtained from FerrDb (http://www.zhounan.org/ferrdb/). RNA-sequencing data of BCa patients were searched from The Cancer Genome Atlas (TCGA database, https://portal.gdc.cancer.gov/) and the Gene Expression Omnibus (GEO database, https://www.ncbi.nlm.nih.gov/gds/?term=). Notably, datasets without detailed corresponding survival information or with a small sample size were excluded. Finally, two eligible high-quality bulk-seq cohorts, TCGA_BLCA and GSE13507, were enrolled in this study. Among them, transcriptome profiles in TCGA_BLCA datasets were downloaded in the fragments per kilobase of transcript per million mapped reads (FPKM) format. Then, we transformed the FPKM values of each sample into transcripts per kilobase million (TPM) values. Normalized matrix files with corresponding clinical information of GSE13507 were downloaded. We merged these two datasets and used the combat algorithm to eliminate the batch effects by R package "sva". The mutation atlas was also downloaded from the TCGA database. The copy number variation matrix was obtained from UCSC-Xena (http://xena.ucsc.

edu/). All the original data were processed and analyzed by the R program version 4.1.1.

Differential Expression Status, Mutation Atlas, and Copy Number Variation of FRGs

We first systematically investigated the expression, mutant, copy number variant status of the FRGs. Differentially expressed analysis was performed between normal tissue and tumor tissue in both TCGA_BLCA and GSE13507. The mutation atlas of these FRGs was extracted from the original matrix and visualized. The copy number variation atlas was annotated and visualized in the genome cycle plot.

Role of FRGs in Bladder Cancer and the Unsupervised Cluster of VFGs

Having merged the gene matrix and eliminating the batch effects, we performed both univariate cox regression and log-rank test to check the prognostic value of the FRGs. Then, we performed the Spearman correlation test between every two FRGs to investigate the co-expression status between FRGs. Subsequently, we conducted an unsupervised cluster of all the VFGs in FerrDb, and the number of clusters was determined according to the algorithm of consensus clustering. Notably, this unsupervised clustering was conducted by R package "ConsensusClusterPlus", and all the procedures were repeated 1,000 times to ensure and verify the stability of the unsupervised cluster.

Survival Differences, Potential Functions, and Immune Infiltrations of the VFG Clusters

Having obtained the classification clustered by the VFG, we performed survival analysis to investigate the survival differences between VFG clusters. Kaplan–Meier survival curves were plotted, and the log-rank test was conducted. Principle components analysis (PCA) was applied to check the discrimination between different VFG clusters. In addition, gene set variation analysis (GSVA) was used to compare the differential enhanced functions or pathways between different VFG clusters. Finally, single sample gene set enrichment analysis (ssGSEA) was used to estimate the immune infiltration and immune-related functions of each sample. The Wilcoxon test was applied to compare the differential immune infiltration and immune-related functions between VFG clusters.

Differentially Expressed Genes Between VFG Clusters and the Establishment of the Ferroptosis Score

Differentially expressed analysis was performed between every two VFG clusters to seek the DEGs. Subsequently, we took an intersect of these DEGs in different comparisons and obtained the final DEGs. GO enrichment analysis and KEGG enrichment analysis were conducted to further investigate the potential functions and mechanisms of these DEGs. Subsequently, univariate cox regression was carried out to seek those DEGs with prognostic value. Following this, an unsupervised cluster was performed again based on the left DEGs to quantify the detailed ferroptosis patterns in BCa patients. Then, we performed principal component analysis (PCA) to distinguish the molecular characteristics of these DEGs with prognostic value and obtained a ferroptosis score formula according to the PCA:

$$Ferroptosis\ score = \sum (PC1 + PC2).$$

Among the formula, PC1 and PC2 separately mean the expression score in two dimensions of the DEGs. Thus, the sum of these two scores was named the ferroptosis score, which can represent the ferroptosis patterns to some extent.

Further Verification and Functional Investigation of the Ferroptosis Score

In all included samples with detailed survival information, we set the threshold according to the best cut-off value in the TCGA_BLCA cohort calculated by the "surv_cutpoint" function in R package "survminer". Here, the best cut-off is -0.0410544, and then all patients including TCGA_ BLCA and GSE13507 cohorts were divided into high or low ferroptosis score groups. Cohorts that are higher than -0.0410544 are defined as the high ferroptosis score group and those that are lower are the low ferroptosis score group. Survival analysis in all patients, TCGA_BLCA cohort, and GSE13507 cohort, was separately conducted to check whether this ferroptosis score was associated with survival. Then we divided all patients into several sub-groups according to their clinicopathological characteristics, including age, gender, grade, T stage, N stage, and M stage. Then survival analysis was applied in each sub-group to investigate the universality of this ferroptosis score. In addition, in the TCGA_BLCA cohort, we calculated the tumor mutation burden (TMB) of each patient according to its somatic mutation profiles. Then we further investigated the correlation between TMB and the ferroptosis score, and combined these two factors to predict the survival of patients with BCa. Following this, we separately summarized the mutation atlas of the patients with low-/high ferroptosis scores and compared the mutant frequencies of each gene between the high ferroptosis score group and low ferroptosis score group by the χ^2 test.

More importantly, as the biological process of ferroptosis is associated with both chemotherapy and immunotherapy, we further explored the association between the drug sensitivity to chemotherapy (cisplatin, doxorubicin, methotrexate, vinblastine) which was predicted by the R package "pRRophetic" (Geeleher et al., 2014). Notably, here we performed three methods to predict the response to immunotherapy: TCIA (Charoentong et al., 2017), TIDE (Jiang et al., 2018), and submap (Hoshida et al., 2007). The drug response to chemotherapy and immunotherapy was compared between the high- or low-ferroptosis score groups by the Wilcoxon test or χ^2 test. In addition, we calculated the ferroptosis score of each patient in IMvigor-210 cohort to externally validate the predicted response to immunotherapy. Response to anti-PD-L1 immunotherapy in IMvigor-210

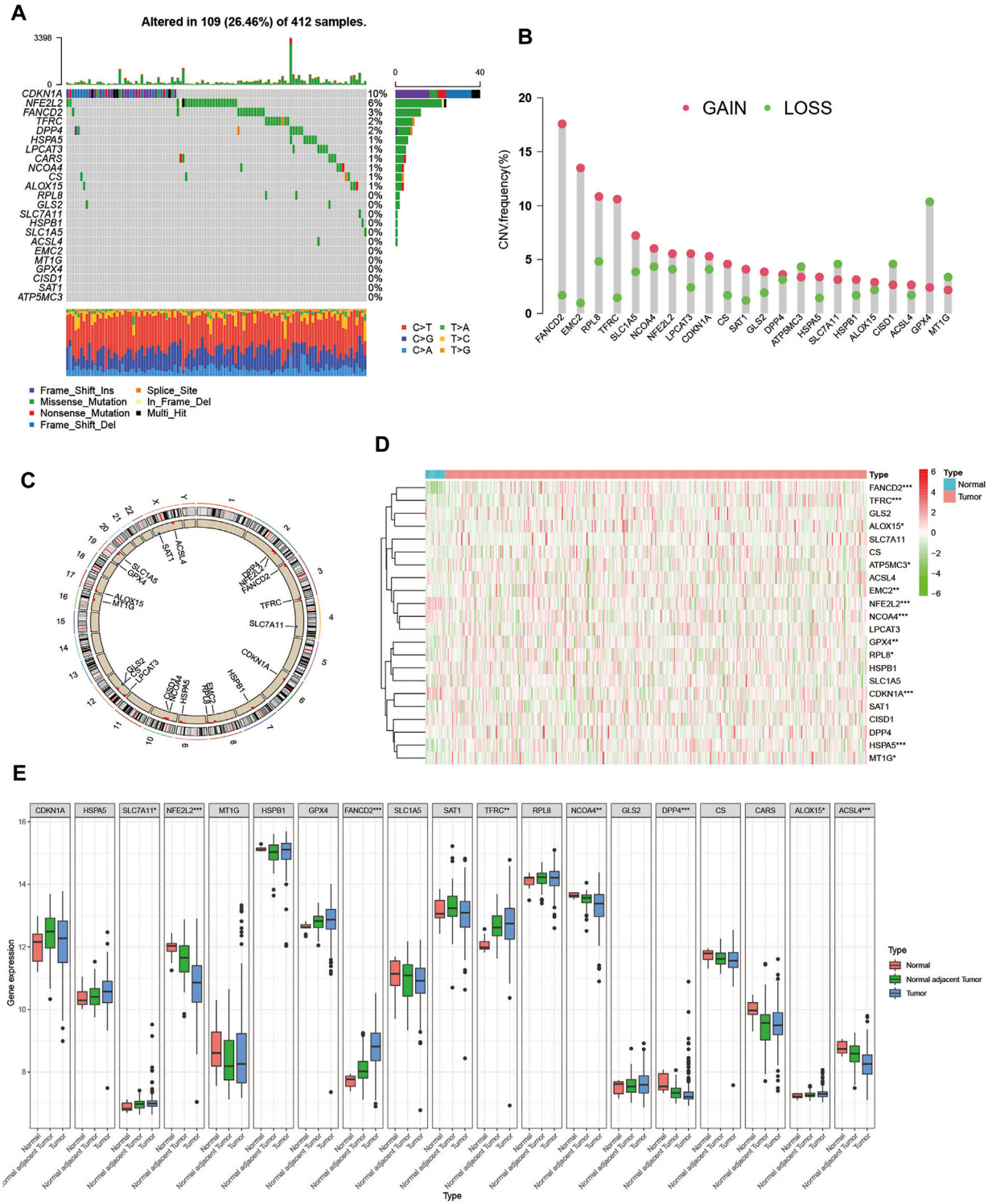

FIGURE 1 | Landscape of genetic and expression variation of ferroptosis regulators in BCa. **(A)** Mutation frequency of 23 ferroptosis regulator genes in 412 patients with BCa from the TCGA-BLCA cohort. Each column represented individual patients. The upper barplot showed TMB. The number on the right indicated the mutation frequency in each regulator gene. The right barplot showed the proportion of each variant type. The stacked barplot below showed a fraction of conversions in each sample. **(B)** CNV variation frequency of ferroptosis regulator genes in GSE13507 cohort. The height of the column represented the alteration frequency. The deletion frequency, green dot; The amplification frequency, red dot. **(C)** Location of CNV alteration of ferroptosis regulator genes on 23 chromosomes using GSE13507 cohort. **(D)** Expression of 22 ferroptosis regulator genes between normal bladder tissues and tumor tissues in the TCGA-BLCA cohort. Tumor, red; Normal, blue. Each

(*Continued*)

FIGURE 1 | column represented individual samples. The upper line represented the type of tissues. The color of each pane represented the expression level. **(E)** Expression of 19 ferroptosis regulator genes between normal bladder tissues, normal adjacent tumor tissues and tumor tissues in GSE13507 cohort. Tumor, blue; Normal adjacent tumor, green; Normal, red. The upper and lower ends of the boxes represented interquartile range of values. The lines in the boxes represented median value, and black dots showed outliers. The asterisks represented the statistical *p* value (*$p < 0.05$; **$p < 0.01$; ***$p < 0.001$).

cohort was also compared between the high- or low-ferroptosis score groups.

Statistical Analysis

All the data processing and statistical analysis were conducted by R software version 4.1.1. All the *p*-values were on two sides, and *p*-value< 0.05 was considered with statistical significance.

RESULTS

Landscape of Genetic Variation of Ferroptosis Regulators in Bladder Cancer

In this study, 23 genes were identified to play critical roles in regulating ferroptosis and were defined as ferroptosis regulator genes (FRGs), including cyclin-dependent kinase inhibitor 1 (CDKN1A), nuclear factor, erythroid 2 like 2 (NFE2L2), Fanconi anemia complementation group D2 (FANCD2), transferrin receptor (TFRC), dipeptidyl-dippeptidase-4 (DPP4), heat shock protein family A member 5 (HSPA5), lysophosphatidylcholine acyltransferase 3 (LPCAT3), cysteinyl tRNA synthetase (CARS), nuclear receptor coactivator 4 (NCOA4), citrate synthase (CS), arachidonate 15-lipoxygenase (ALOX15), ribosomal protein L8 (RPL8), glutaminase 2 (GLS2), solute carrier family 7 member 11 (SLC7A11), heat shock protein beta 1 (HSPB1), solute carrier family 1 member 5 (SLC1A5), acyl-CoA synthetase long-chain family member 4 (ACSL4), ER membrane protein complex subunit 2 (TTC35/EMC2), metallothionein-1G (MT1G), glutathione peroxidase 4 (GPX4), CDGSH iron sulfur domain 1 (CISD1), spermidine/spermine N1-acetyl-transferase 1 (SAT1), and ATP synthase membrane subunit C locus 3 (ATP5MC3/ATP5G3) (Stockwell et al., 2017). Among the 23 FRGs, 10 are negative regulators, including CDKN1A, HSPA5, EMC2, SLC7A11, NFE2L2, MT1G, HSPB1, GPX4, FANCD2, and CISD1, and 13 are positive regulators, including SLC1A5, SAT1, TFRC, RPL8, NCOA4, LPCAT3, GLS2, DPP4, CS, CARS, ATP5MC3, ALOX15, and ACSL4.

First, we summarized the incidence of copy number variations (CNV) and somatic mutations of the 23 FRGs in BCa. Mutations of FRGs occurred in 109 samples among a total of 412 samples from the TCGA-BLCA cohort with a frequency of 26.46%. We found that CDKN1A exhibited the highest mutation frequency followed by NFE2L2 and FANCD2, while EMC2, MT1G, GPX4, CISD1, SAT1, and ATP5MC3 showed no mutation in BCa samples (**Figure 1A**). Since CDKN1A had the highest mutation frequency, we then explored whether mutations in CDKN1A would influence the expression of other FRGs. As shown in **Supplementary Figure S1**, the expression levels of other FRGs were remarkably different between CDKN1A mutation and wild samples, among which GLS2 and TFRC expression were higher in CDKN1A mutation samples while MT1G and RPL8 were just opposite (**Supplementary Figures S1A–D**). Then, we investigated the CNV alteration in 23 FRGs and found a prevalent CNV alteration in 22 FRGs, among which most alterations were gained in copy number, while ATP5MC3, SLC7A11, CISD1, GPX4, and MT1G had a greater frequency of CNV loss (**Figure 1B**). The location of CNV alteration of FRGs on chromosomes was shown in **Figure 1C**. Next, we searched the GEO and TCGA databases for public gene expression data in tumor, normal adjacent tumor tissue, and normal tissue to find whether the above genetic variations could influence the FRGs' expression in BCa patients. We discovered that both mutation and CNV alteration contributed to the difference in expression levels of FRGs but CNV alteration might play a more critical role. Most FRGs with gain of CNV exhibited significantly higher expression in BCa tumor tissues compared to normal adjacent tumor tissues or normal bladder tissues, such as FANCD2, EMC2, and TFRC. But when it came to FRGs with loss of CNV, the differences between tumor tissue and normal adjacent tumor tissue or normal bladder tissue were inconsistent with the variation in CNV, which indicated that there existed other ways of regulating the expression of FRGs except for CNV variation (**Figures 1D,E**). The above analyses showed the high heterogeneity of the genetic and expression alteration

TABLE 1 | Annotation of 23 FRGs in the FerrDb database.

FRG	Type	Confidence
CDKN1A	Suppressor	Validated
HSPA5	Suppressor	Validated
EMC2	Driver	Validated
SLC7A11	Suppressor/Marker	Validated
NFE2L2	Suppressor/Marker	Validated
MT1G	Suppressor	Validated
HSPB1	Suppressor/Marker	Validated
GPX4	Suppressor/Marker	Validated
FANCD2	Suppressor	Validated
CISD1	Suppressor	Validated
SLC1A5	Driver	Validated
SAT1	Driver/Marker	Validated
TFRC	Driver/Marker	Validated
RPL8	Driver/Marker	Validated
NCOA4	Driver	Validated
LPCAT3	Driver	Validated
GLS2	Driver	Validated
DPP4	Driver	Validated
CS	Driver	Validated
CARS	Driver	Validated
ATP5MC3	Driver/Marker	Validated/Deduced
ALOX15	Driver/Marker	Validated/Deduced
ACSL4	Driver	Validated

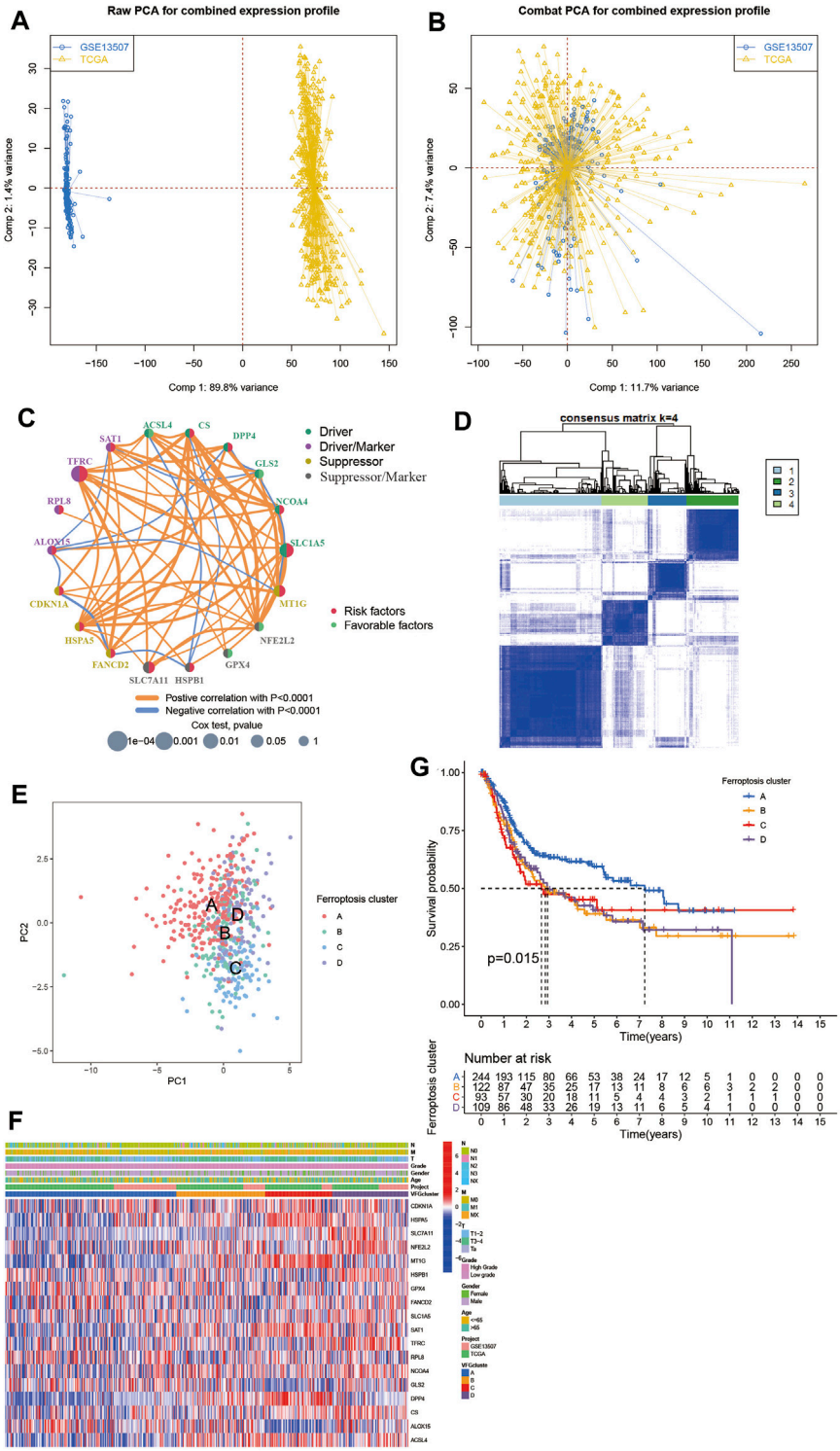

FIGURE 2 | Patterns of ferroptosis and biological characteristics of each pattern. **(A,B)** Principal component analysis for the expression profiles of common genes before and after combination of GSE13507 and the TCGA-BLCA cohort. Before processing, two subgroups without intersection were identified, indicating the GSE13507 and TCGA-BLCA samples were well distinguished based on the expression profiles of their common genes, while the two datasets merged together well after processing. Samples from GSE13507 were marked with blue and samples from TCGA-BLCA marked with yellow. **(C)** Interaction between FRGs in BCa. The circle size represented the effect of each ferroptosis regulator gene on the prognosis, and the range of values calculated by Log-rank test was $p < 0.0001$, $p < 0.001$, $p < 0.01$, $p < 0.05$ and $p < 0.1$, respectively. Red dots in the circle, risk factors of prognosis; Light green dots in the circle, protective factors of prognosis. The lines linking

(*Continued*)

FIGURE 2 | regulators showed their interactions, and their thickness showed the correlation strength between regulator genes. Negative correlation was marked with blue and positive correlation with orange. The driver, driver/marker, suppressor, suppressor/marker were marked with dark green, purple, yellow, and gray, respectively. **(D)** Consensus matrices of the meta-cohort for k = 4. **(E)** Principal component analysis for the transcriptome profiles of four ferroptosis patterns, showing a remarkable difference on transcriptome between different ferroptosis patterns. **(F)** Unsupervised clustering of 234 validated ferroptosis genes in the meta-cohort. The VFGcluster, project, age, gender, grade, and TNM category were used as patient annotations. Red represented high expression of regulators and blue represented low expression. **(G)** Kaplan–Meier curves indicated ferroptosis patterns were markedly related to overall survival of 568 patients in meta-cohort, of which 244 cases were in VFGcluster A, 122 cases in VFGcluster B, 93 cases in VFGcluster C, and 109 cases in VFGcluster D (p = 0.015, Log-rank test).

TABLE 2 | Basic characteristics of the included patients.

	Overall	GSE13507	TCGA	*p*
n	568	165	403	
Status = Alive/Dead (%)	323/245 (56.9/43.1)	96/69 (58.2/41.8)	227/176 (56.3/43.7)	0.755
Age (mean (SD))	67.22 (11.08)	65.18 (11.97)	68.06 (10.60)	0.005
Gender = Female/Male (%)	135/433 (23.8/76.2)	30/135 (18.2/81.8)	105/298 (26.1/73.9)	0.058
Grade (%)				<0.001
High Grade	440 (77.5)	60 (36.4)	380 (94.3)	
Low Grade	125 (22.0)	105 (63.6)	20 (5.0)	
Unknown	3 (0.5)	0 (0.0)	3 (0.7)	
T (%)				<0.001
T1	83 (14.6)	80 (48.5)	3 (0.7)	
T2	149 (26.2)	31 (18.8)	118 (29.3)	
T3	210 (37.0)	19 (11.5)	191 (47.4)	
T4	69 (12.1)	11 (6.7)	58 (14.4)	
Ta	24 (4.2)	24 (14.5)	0 (0.0)	
Unknown	33 (5.8)	0 (0.0)	33 (8.2)	
M (%)				<0.001
M0	351 (61.8)	158 (95.8)	193 (47.9)	
M1	18 (3.2)	7 (4.2)	11 (2.7)	
MX	197 (34.7)	0 (0.0)	197 (48.9)	
Unknown	2 (0.4)	0 (0.0)	2 (0.5)	
N (%)				<0.001
N0	385 (67.8)	151 (91.5)	234 (58.1)	
N1	54 (9.5)	8 (4.8)	46 (11.4)	
N2	79 (13.9)	4 (2.4)	75 (18.6)	
N3	8 (1.4)	1 (0.6)	7 (1.7)	
NX	37 (6.5)	1 (0.6)	36 (8.9)	
Unknown	5 (0.9)	0 (0.0)	5 (1.2)	
Ferroptosis.scores (median [IQR])	1.47 [–5.53, 5.78]	2.61 [–1.80, 4.84]	–0.19 [–6.56, 7.11]	0.384
Group = High/Low (%)	314/254 (55.3/44.7)	115/50 (69.7/30.3)	199/204 (49.4/50.6)	<0.001

landscape of FRGs between normal and BCa samples, indicating that the expression imbalance of FRGs played a crucial role in the occurrence and progression of BCa.

Validated Ferroptosis Gene Patterns Classified According to the Expression of Validated Ferroptosis Genes

To further investigate the interaction between ferroptosis genes and tumor characteristics, we explored the FerrDb database established by Zhou et al. which collected nearly all the ferroptosis regulators and markers reported in published articles from PubMed up to 20 February 2020 (Zhou and Bao, 2020). In this database, genes were annotated as drivers, suppressors, and markers according to their function reported in the original article. And the confidence level was divided into four categories sorted by experimental reliability and reproducibility: validated, screened, predicted, and deduced (Zhou and Bao, 2020). In **Table 1**, we summarized the 23 FRGs according to their annotations in the FerrDb database. Next, we used Combat R packages to eliminate the heterogeneity between the GEO dataset GSE13507 and TCGA-BLCA cohort and enrolled them into a new meta-cohort. Before processing, we could easily distinguish the two datasets by principal component analysis (PCA) (**Figure 2A**), while the two datasets merged well together after processing (**Figure 2B**). The detailed characteristics of the included patients were shown in **Table 2**. Then we divided the meta-cohort into two subgroups according to the expression level of every FRG and performed survival analysis (**Supplementary Figures S2A–N**). As shown in the figures, the survival outcomes were significantly associated with the expression levels of the fourteen FRGs, among which higher expression level of ACSL4 and GPX4 predicted a better prognosis while lower expression level of ALOX15, CDKN1A, DPP4, FANCD2, HSPA5, HSPB1, MT1G, NCOA4, RPL8, SLC1A5, SLC7A11, and TFRC revealed a survival advantage. The

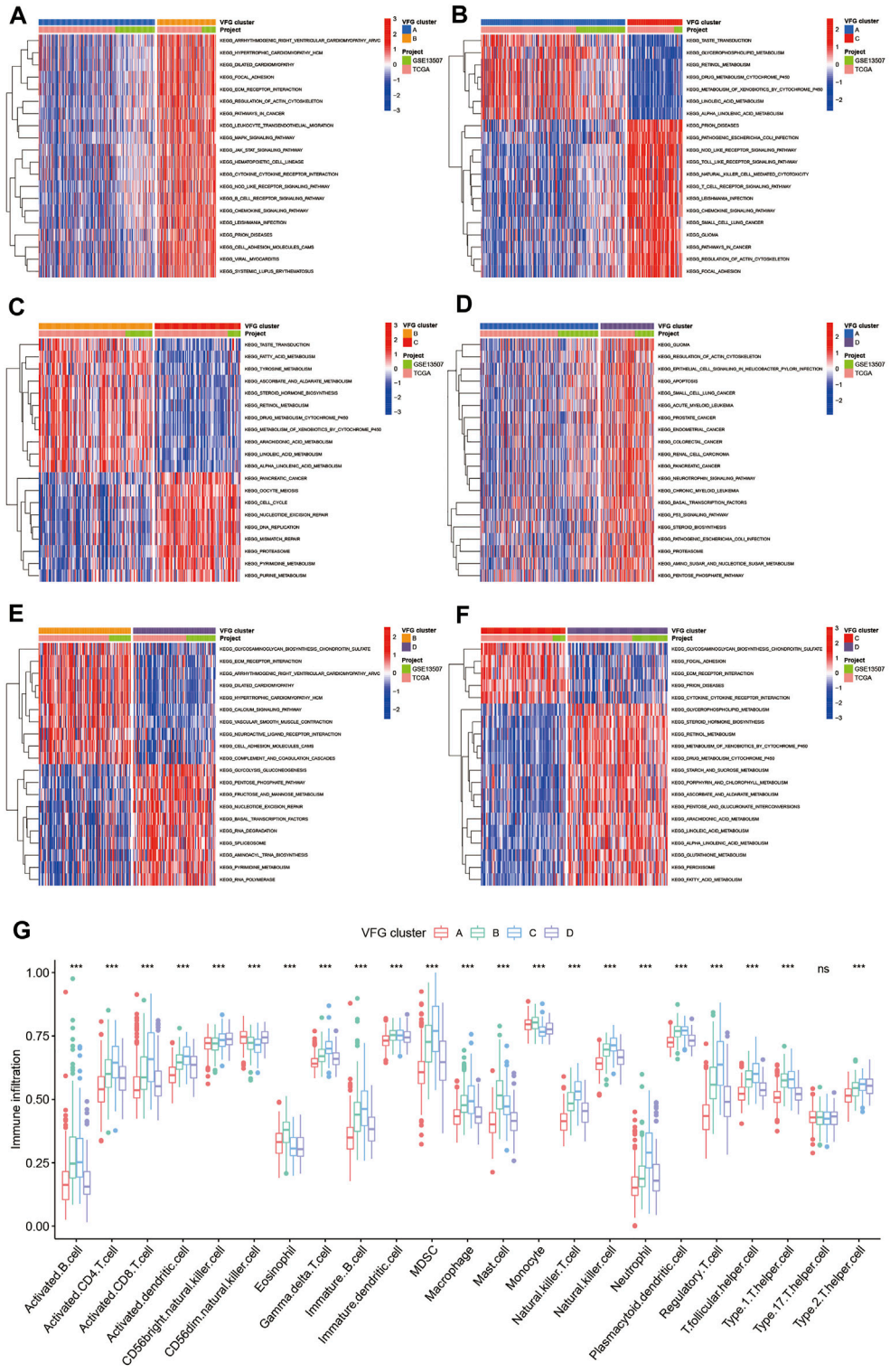

FIGURE 3 | TME cell infiltration characteristics in distinct VFG patterns. **(A–F)** GSVA enrichment analysis showing the activation states of biological pathways in distinct ferroptosis patterns. The heatmap was used to visualize these biological processes, and red represented activated pathways and blue represented inhibited pathways. The project and VFGclusters were used as sample annotations. **(A)** VFGcluster A vs. VFGcluster B; **(B)** VFGcluster A vs. VFGcluster C; **(C)** VFGcluster B vs. VFGcluster C; **(D)** VFGcluster A vs. VFGcluster D; **(E)** VFGcluster B vs. VFGcluster D; **(F)** VFGcluster C vs. VFGcluster D. **(G)** The abundance of each TME infiltrating cell in four ferroptosis patterns. The upper and lower ends of the boxes represented interquartile range of values. The lines in the boxes represented median value, and black dots showed outliers. The asterisks represented the statistical *p* value (*$p < 0.05$; **$p < 0.01$; ***$p < 0.001$).

comprehensive landscape of FRGs' interactions, connections, and their prognostic significance for BCa patients was described in the FRG network (**Figure 2C**). In the network we could find that not only FRGs in the same categories (e.g., drivers and drivers, suppressors and suppressors) exhibited a significant correlation, but also a remarkable correlation was shown between drivers, suppressors, and markers. The results uncovered the latent cross-talk among the FRGs which might play a crucial role in the prognosis of BCa patients and needed to be further studied.

In order to dig deep into the relationship between ferroptosis genes and tumor characteristics, we explored all 382 ferroptosis genes reported in the FerrDb database, including 150 drivers, 123 markers, and 109 suppressors (**Supplementary Tables S1–S4**). Then we screened out the 234 validated ferroptosis genes (VFGs) from them to improve credibility. We used the ConsensusClusterPlus R package to classify patients with qualitatively different ferroptosis patterns based on the expression levels of 234 validated ferroptosis genes, and four distinct validated ferroptosis gene patterns were identified using unsupervised clustering (**Figure 2D**, **Supplementary Figures S3A–H**), including 244 cases in pattern A, 123 cases in pattern B, 93 cases in pattern C and 110 cases in pattern D. Then the cumulative distribution function (CDF) curve and scree plot were used to verify the rationality of the grouping (**Supplementary Figure S3I, J**). The track plot showed the details of grouping (**Supplementary Figure S3K**). We named these patterns as VFGcluster A-D, respectively. A dramatic difference was found on the FRG transcriptional profile among the four different VFG clusters (**Figure 2E**). VFGcluster A was characterized by decreased expression level of HSPA5, SLC7A11, NFE2L2, SAT1, NCOA4, MT1G, and DPP4, and presented variable increase in other FRGs; VFGcluster B exhibited a remarkable decrease in SLC7A11, RPL8, and GLS2 and an increase in NFE2L2, NCOA4, DPP4, ACSL4, and SAT1; VFGcluster C showed a significant increase in CDKN1A, HSPA5, MT1G, SAT1, DPP4, and ACSL4, and decrease in GLS2, ALOX15, and HSPB1; and VFGcluster D was characterized by increased expression of NFE2L2, HSPB1, SLC1A5, TFRC, NCOA4, and CS. We also noticed that VFGcluster B-C had higher TNM categories compared with VFGcluster A, but there existed no significant differences in gender and age among the four VFGclusters (**Figure 2F**). Survival analyses for the four VFGclusters revealed the particularly prominent survival advantage in patients from VFGcluster A (**Figure 2G**).

TME Cell Infiltration Characteristics in Distinct VFG Patterns

In order to further explore the latent differences in biological behaviors behind the distinct VFG patterns, we performed GSVA enrichment analysis. As shown in **Figures 3A,B**, VFGcluster A was dramatically enriched in pathways associated with metabolism, such as glycerophospholipid metabolism, linolenic metabolism, and drug metabolism mediated by cytochrome P450. VFGcluster B showed enrichment in stromal and carcinogenic activation pathways such as MAPK signaling pathway, focal adhesion, and ECM receptor interaction (**Figure 3A**), and it also exhibited relative enrichment in pathways associated with metabolism compared to VFGcluster C (**Figure 3C**). VFGcluster C was related to pathways about stroma, tumorigenesis, and infectious immunity (**Figures 3B, 3C, 3F**), while VFGcluster D was remarkably enriched in metabolic and carcinogenic activation pathways (**Figures 3D–F**). Then we analyzed the TME cell infiltration and were surprised to find that VFGcluster B and C were significantly enriched in nearly all kinds of immune cells such as activated $CD4^+$ T cell, activated $CD8^+$ T cell, activated dendritic cell, macrophage, MDSC, and natural killer cell (**Figure 3G**). However, patients with these VFG patterns did not show a corresponding survival advantage (**Figure 2F**). It has been reported that the innate immune cells as well as adaptive immune cells in TME could contribute to tumor progression (Hinshaw and Shevde, 2019). Previous studies have suggested that TME could be classified into three distinguished immune phenotypes based on the basic immune profiles: immune-inflamed phenotype, immune-excluded phenotype, and immune-desert phenotype. The immune-inflamed phenotype was characterized by abundant immune cells presented in the tumor parenchyma as well as many proinflammatory and effector cytokines. The immune-excluded phenotype was also abundant in various immune cells, however, the immune cells did not penetrate the tumor parenchyma and were retained in the stroma surrounding the tumor nests. The stroma could limit T-cell migration and their normal function of anti-tumor. However, the immune-desert phenotype was characterized by a lack of T cells in both the parenchyma and the stroma of the tumor (Chen and Mellman, 2017). The results of GSVA analyses have displayed that VFGcluster B and VFGcluster C were tightly connected with stroma activation. Therefore, we speculated that VFGclsuter B and VFGcluster C belonged to immune-excluded phenotype, in which the stroma activation significantly suppressed the immune cells' normal anti-tumor function.

Generation of Ferroptosis Gene Signatures and Functional Annotation

To further investigate the latent biological behavior of each VFG pattern, we used limma R package to discover 367 VFG cluster-related DEGs (**Figure 4E**). We performed GO and KEGG enrichment analyses for the DEGs by using the clusterProfiler R package. To our surprise, the results of GO enrichment analysis showed a remarkable relationship with stroma and immunity in all cellular component (CC), molecular function (MF), and biological process (BP) patterns (**Figures 4A,B**). The genes in KEGG analysis also exhibited enrichment in pathways related to immunity, which was consistent with previous results (**Figures 4C,D**). The above results further proved that ferroptosis was an indispensable component in modification of immunity and TME. Then we performed unsupervised clustering analyses based on the 367 VFG cluster-related DEGs to find out the potential regulation mechanism. We successfully classified the patients into two distinct genomic subgroups using the unsupervised

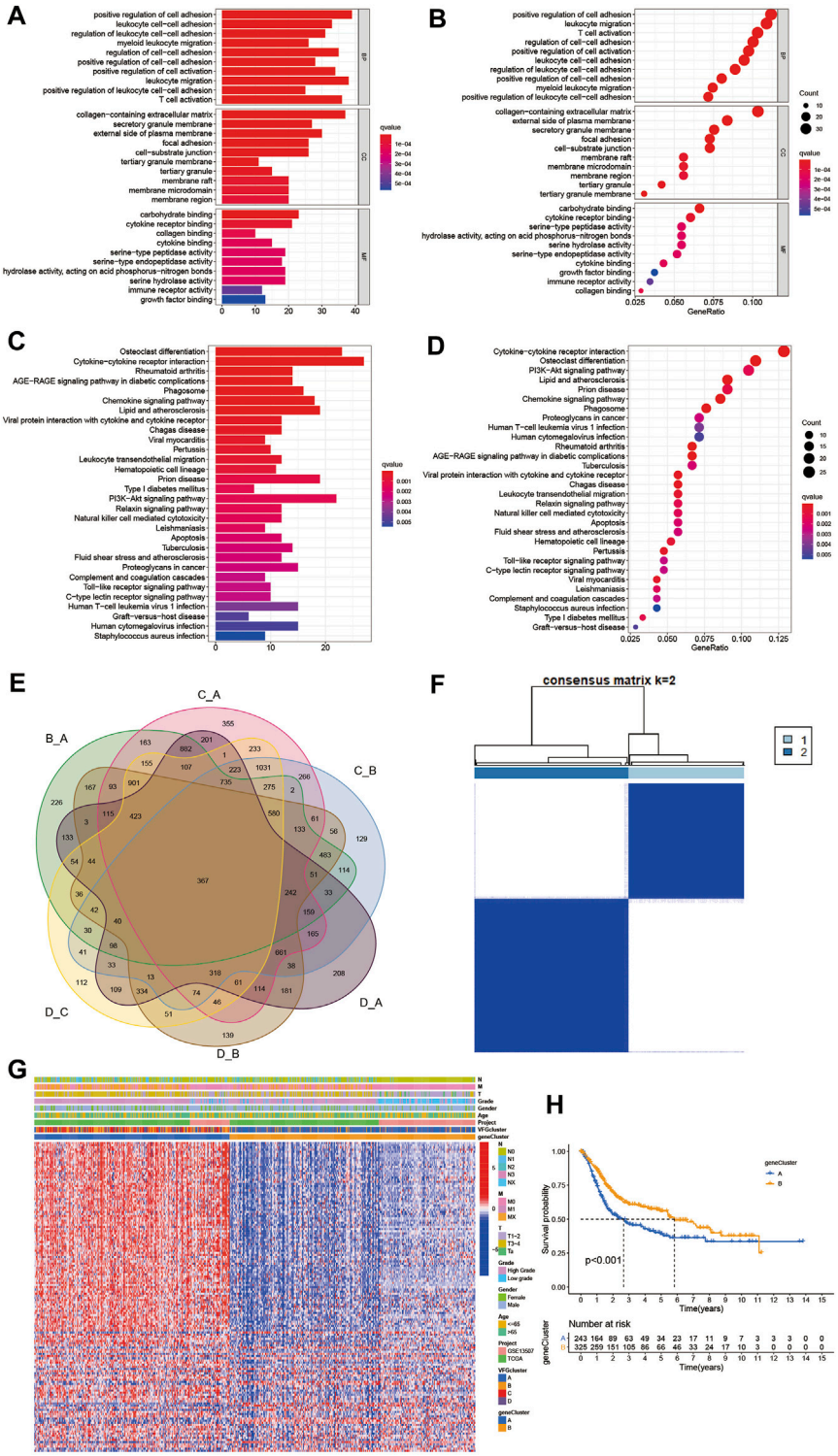

FIGURE 4 | Generation of ferroptosis gene signatures and functional annotation. **(A,B)** Functional annotation for VFG cluster-related DEGs using GO enrichment analysis. The color depth of the barplots and plots represented the number of genes enriched. The pathways were grouped by cellular component (CC), molecular function (MF) and biological process (BP). **(C,D)** Functional annotation for VFG cluster-related DEGs using KEGG enrichment analysis. The color depth of the barplots and plots represented the number of genes enriched. **(E)** 367 VFG cluster-related DEGs shown in the Venn diagram. **(F)** Unsupervised clustering of 367 VFG cluster-related DEGs in meta-cohort and consensus matrices for $k = 2$. **(G)** Unsupervised clustering of overlapping 367 VFG cluster-related DEGs in meta-cohort to classify patients into different genomic subtypes, termed as gene cluster A-B, respectively. The gene clusters, VFGclusters, project, age, gender, grade, and TNM category were used as patient annotations. **(H)** Kaplan–Meier curves indicated ferroptosis genomic phenotypes were markedly related to overall survival of 568 patients in meta-cohort, of which 243 cases were in gene cluster A and 325 cases in gene cluster B ($p < 0.001$, Log-rank test).

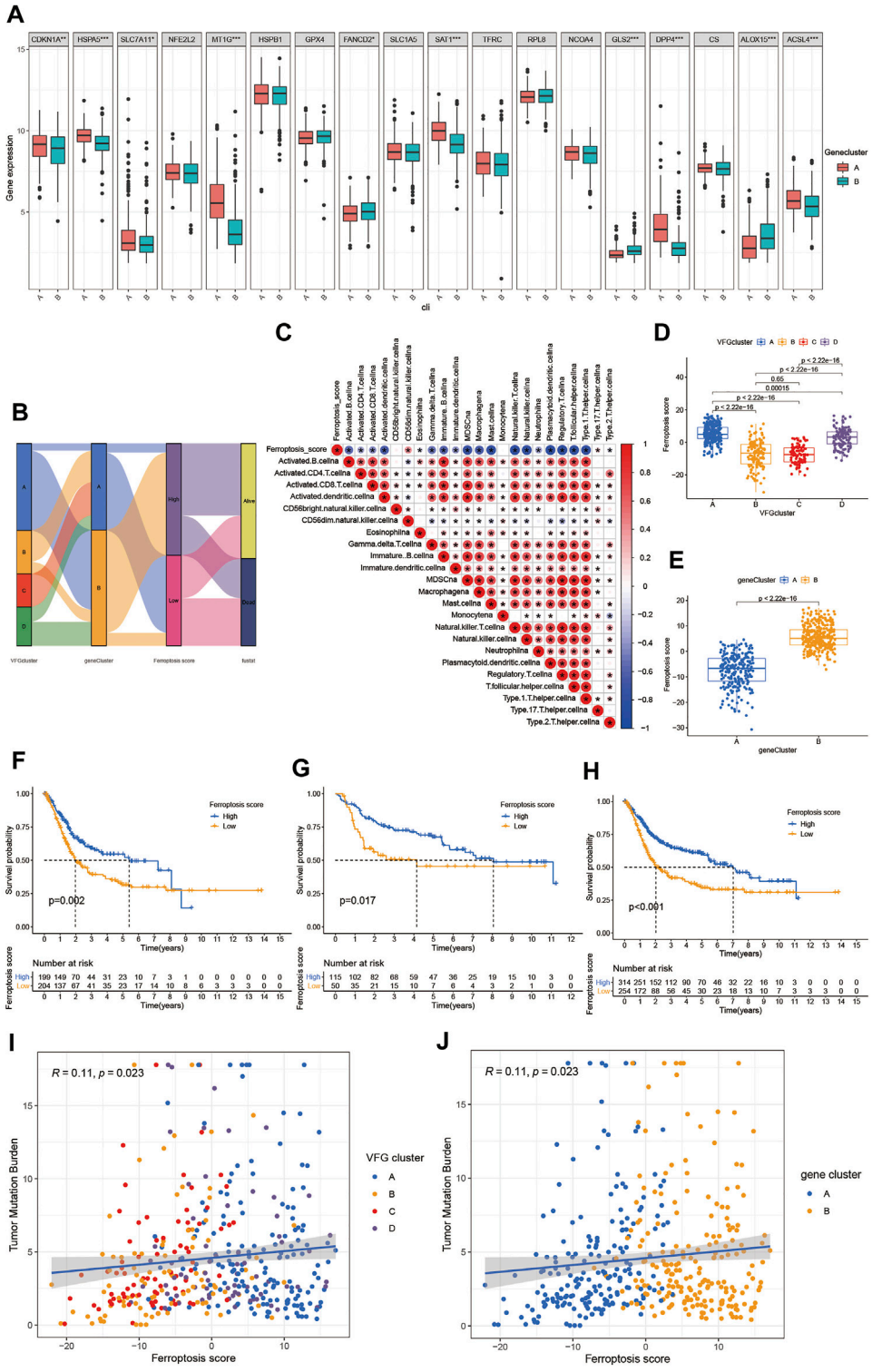

FIGURE 5 | Establishment of the ferroptosis score and its interaction with tumor clinicopathological characteristics. **(A)** Expression of 18 FRGs in two gene clusters. The upper and lower ends of the boxes represented interquartile range of values. The lines in the boxes represented median value, and black dots showed outliers. The asterisks represented the statistical *p* value (*$p < 0.05$; **$p < 0.01$; ***$p < 0.001$). The student's t test was used to test the statistical differences between two gene clusters. **(B)** Sankey diagram showing the changes of VFGclusters, survival status, gene cluster, and ferroptosis score. **(C)** Correlations between the ferroptosis score and the known immune cells in meta-cohort using Spearman analysis. Negative correlation was marked with blue and positive correlation with red. **(D)** Differences in the ferroptosis score among four VFGclusters in meta-cohort. The Kruskal Wallis H test was used to compare the statistical difference between four VFGclusters (*p* <

(*Continued*)

FIGURE 5 | 0.001). **(E)** Differences in the ferroptosis score among two gene clusters in meta-cohort ($p < 0.001$, Wilcoxon test). **(F)** Survival analyses for low (204 cases) and high (199 cases) ferroptosis score patient groups in the TCGA-BLCA cohort using Kaplan–Meier curves ($p = 0.002$, Log-rank test). **(G)** Survival analyses for low (50 cases) and high (115 cases) ferroptosis score patient groups in GSE13507 cohort using Kaplan–Meier curves ($p = 0.017$, Log-rank test). **(H)** Survival analyses for low (254 cases) and high (314 cases) ferroptosis score patient groups in meta-cohort using Kaplan–Meier curves ($p < 0.001$, Log-rank test). **(I)** Linear regression analysis for TMB and ferroptosis score. The dot represented each sample, and the color of the dot represented the VFGcluster. Blue, VFGcluster A; orange, VFGcluster B; red, VFGcluster C; purple, VFGcluster D ($R = 0.11$, $p = 0.023$). **(J)** Linear regression analysis for TMB and ferroptosis score. The dot represented each sample, and the color of the dot represented the gene cluster. Blue, gene cluster A; orange, gene cluster B ($R = 0.11$, $p = 0.023$).

clustering algorithm (**Figures 4F,G**, **Supplementary Figures S4A–H**). The cumulative distribution function (CDF) curve and screen plot also validated the rationality of the grouping (**Supplementary Figures S4I–K**). We named the two different subgroups as gene cluster A and B, respectively. In total, 243 patients were assigned to gene cluster A while 325 patients were classified into gene cluster B. We observed that gene cluster B was mainly composed of patients from VFGcluster A, and tumors in gene cluster B had a better TNM category and were enriched in low grade compared to gene cluster A (**Figure 4G**). Thus, it is not difficult to explain the phenomenon that patients in gene cluster B had a better prognosis (**Figure 4H**). We also found that the two gene clusters were characterized by different signature genes (**Figure 4G**). We also discovered a significant difference in expression level among the majority of FRGs, which was consistent with VFGclusters (**Figure 5A**).

Characteristics of Clinical Traits in Ferroptosis Related Phenotypes

The above analyses revealed a remarkable correlation between TME and ferroptosis based on the patient population. Therefore, we next explored the latent ferroptosis pattern in individual patients considering the individual heterogeneity and complexity of ferroptosis. Based on these phenotype-related genes, we constructed a set of scoring system named the ferroptosis score to quantify the ferroptosis pattern of individual patients with BCa. The Sankey diagram was used to visualize the attribute changes of individual patients (**Figure 5B**). To better understand the relationship between ferroptosis signature and TME, we also tested the correlation between the known immune cells and ferroptosis score (**Figure 5C**). We found significant difference in the ferroptosis score between VFGclusters using the Kruskal Wallis H test (**Figure 5D**). VFGcluster A showed the highest median score while VFGcluster B and C shared the lowest median score, which indicated that the low ferroptosis score might be related to stroma activation signatures. Moreover, gene cluster B also exhibited a higher median ferroptosis score compared to gene cluster A and the difference was of statistical significance (**Figure 5E**). Next, we further explored whether the ferroptosis score had a predictive significance for the prognosis of patients. We used survminer R package to determine the cut off value -0.041 and divided the patients into two subgroups with high and low ferroptosis score. We found a significant survival advantage among patients with high ferroptosis score in all of the GSE13507 cohort (**Figure 5G**), TCGA-BLCA cohort (**Figure 5F**), and the meta-cohort (**Figure 5H**). In the meta-cohort, the 5 year survival rate with high ferroptosis score is almost twice than those with low ferroptosis score (22.29% vs. 11.81%). Then, we investigated the interaction between the ferroptosis score and clinical signatures and found the ferroptosis score was significantly related to the grade, TNM category, and final survival status (**Figures 6E–6N**). We also found significant differences of the ferroptosis score in the molecular subtypes of BCa (**Figure 6O**). However, the distribution difference of the ferroptosis score in age and gender did not show a statistical significance (**Supplementary Figures S5A–D**). In addition, we performed subgroup analyses and found the ferroptosis score was a good predictor of survival especially for patients who were male, with high grade and low TNM category (T1-T2, N0-N3, M0) (**Supplementary Figures S5E–S**).

Characteristics of Ferroptosis in Tumor Somatic Mutation, Immunotherapy and Chemotherapy

Next, we sought to explore the relationship between the ferroptosis score and TMB. We discovered that TMB was positively correlated to the ferroptosis score. Compared to other clusters, VFGcluster A had a higher ferroptosis score, so did gene cluster B, which was consistent to above results (**Figures 5I,J**). Then, we analyzed the distribution differences of somatic mutation between the low and high ferroptosis scores in the TCGA-BLCA cohort using maftools R package. As shown in **Figures 6C,D**, in general, there were no obvious distribution differences of TMB between the low and high ferroptosis scores, but for some popular genes in BCa studies such as FGFR3, the high ferroptosis score group exhibited more extensive TMB than the low ferroptosis score group. The previous studies have demonstrated that TMB was tightly related to the results of immunotherapy and the prognosis of patients (Chan et al., 2019; Valero et al., 2021). Therefore, we first preformed survival analyses to validate the linkage between TMB and clinical outcome and were excited to find that patients with high ferroptosis score and high TMB had a better prognosis, which indicated the combination of ferroptosis score and TMB had a considerable prognostic value for BCa patients (**Figures 6A,B**).

Then, we further explored whether the ferroptosis score had a predictive significance for the outcome of immunotherapy. As shown in **Figures 7A–D**, the expression of the main immunotherapy targets PD-1, PD-L1, LAG-3, and CTLA-4 were significantly lower in patients with high ferroptosis score

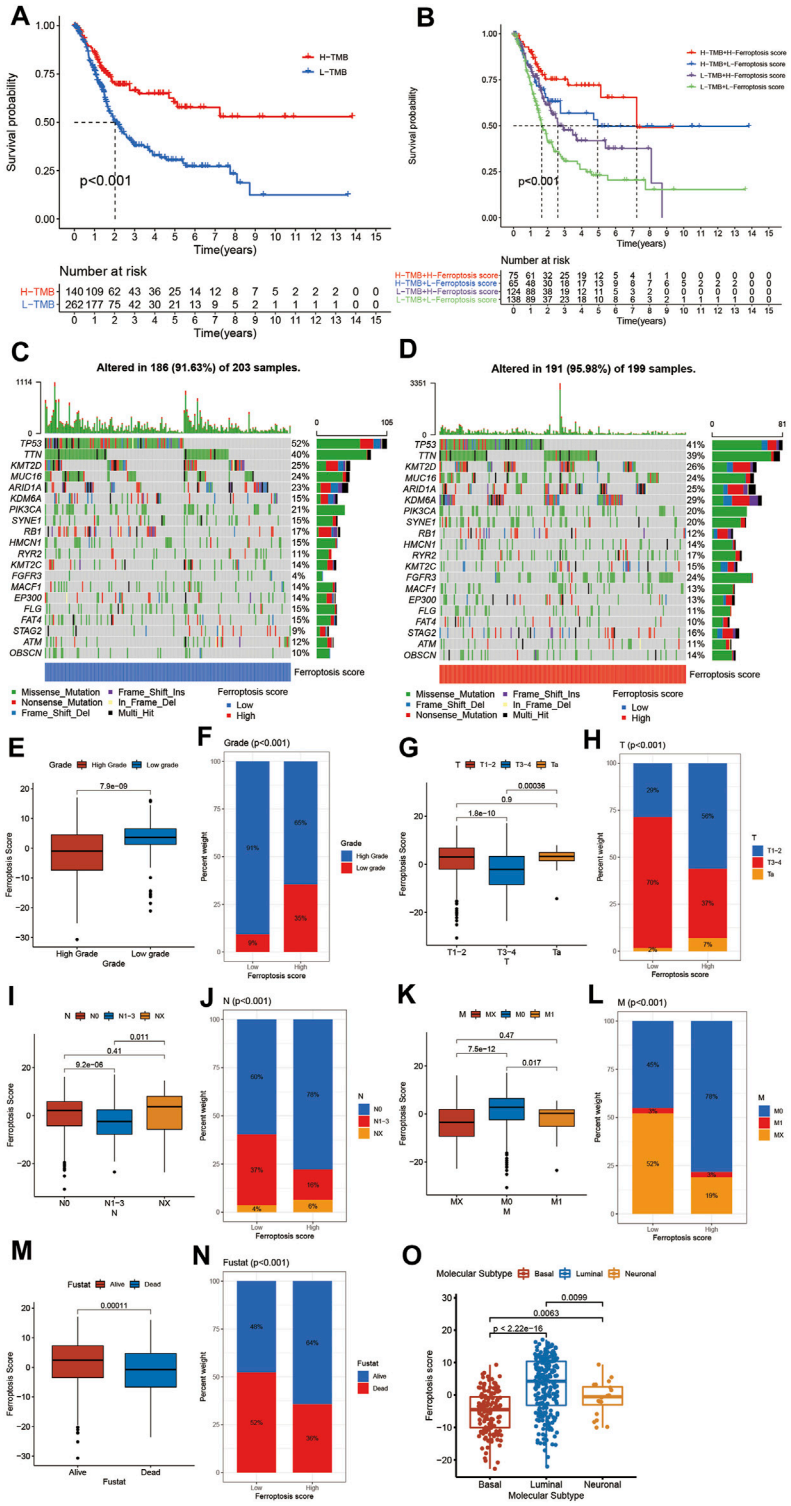

FIGURE 6 | Characteristics of ferroptosis in tumor somatic mutation and tumor stage. **(A)** Survival analyses for low (262 cases) and high (140 cases) TMB patient groups in the TCGA-BLCA cohort using Kaplan–Meier curves ($p < 0.001$, Log-rank test). **(B)** Survival analyses for four groups grouped according to TMB and ferroptosis score in the TCGA-BLCA cohort using Kaplan–Meier curves including 75 cases in the high TMB and high ferroptosis score group, 65 cases in the high TMB and low ferroptosis score groups, 124 cases in the low TMB and high ferroptosis score group, and 138 cases in the low TMB and low ferroptosis score group. The high TMB and high ferroptosis score group showed significantly better overall survival than the other three groups ($p < 0.001$, Log-rank test). **(C,D)** Waterfall plot of tumor somatic mutation established by those with low ferroptosis score **(C)** and high ferroptosis score **(D)**. Each column represented individual patients. The upper barplot

(*Continued*)

FIGURE 6 | showed TMB. The number on the right indicated the mutation frequency in each gene. The right barplot showed the proportion of each variant type. **(E)** Differences in the ferroptosis score between high and low tumor grade groups in meta-cohort ($p < 0.001$, Wilcoxon test). **(F)** Proportion of patients with different tumor grade in low or high ferroptosis score groups. High grade/low grade: 91%/9% in the low ferroptosis score groups and 65%/35% in the high ferroptosis score groups. **(G)** Differences in the ferroptosis score among Ta, T1-T2, and T3-T4 groups in meta-cohort ($p < 0.001$, Kruskal Wallis H test). **(H)** Proportion of patients with Ta, T1-T2, and T3-T4 stage tumor in the low or high ferroptosis score groups. **(I)** Differences in the ferroptosis score among N0, N1-N3, and NX groups in meta-cohort ($p < 0.001$, Kruskal Wallis H test). **(J)** Proportion of patients with N0, N1-N3, and NX stage tumor in low or high ferroptosis score groups. **(K)** Differences in the ferroptosis score among M0, M1, and MX groups in meta-cohort ($p < 0.001$, Kruskal Wallis H test). **(L)** Proportion of patients with M0, M1, and MX stage tumor in the low or high ferroptosis score groups. **(M)** Differences in the ferroptosis score between alive and dead groups in meta-cohort ($p < 0.001$, Wilcoxon test). **(N)** Proportion of alive patients in the low or high ferroptosis score groups. **(O)** Differences in the ferroptosis score among three subtypes of BCa including basal, luminal and neuronal subtypes (Kruskal Wallis H test).

compared to those with low ferroptosis score. Next, we evaluated the interaction between the ferroptosis score and the response to immune checkpoint inhibitors treatment. We found that the low ferroptosis score was related to a better response to anti-PD-1 and anti-CTLA-4 immunotherapy. After Bonferroni correction, there still existed a remarkable correlation between the low ferroptosis score and response to anti-PD-1 immunotherapy although there was a lack of statistical significance (**Figure 7E**). Then we divided the patients into four subgroups according to the use of anti-CTLA-4 and anti-PD-1 immunotherapy: CTLA-4 positive PD-1 positive, CTLA-4 positive PD-1 negative, CTLA-4 negative PD-1 positive, and CTLA-4 negative PD-1 negative. As shown in **Figures 7F–I**, in CTLA-4 positive PD-1 negative and CTLA-4 negative PD-1 negative subgroups, the high ferroptosis score was related to a better immunotherapy response, while in CTLA-4 positive PD-1 positive and CTLA-4 negative PD-1 positive subgroups the results were exactly opposite, which further proved that ferroptosis had a tighter relationship with immunotherapy targeted at PD-1 compared to other immune checkpoint inhibitors. Anti-PD-L1 immunotherapy has also been proven effective for patients with metastatic urothelial carcinoma in a multicenter, single-arm phase 2 trial using atezolizumab (IMvigor 210, NCT02108652) (Rosenberg et al., 2016). Using the data acquired from IMvigor 210 cohort, we further verified the interaction between the ferroptosis score and immune phenotypes. We found there existed significant differences in the proportion of three immune phenotypes between low and high ferroptosis groups (**Supplementary Figure S6A**). The immune-desert phenotype exhibited the highest ferroptosis score, whereas the immune-inflamed phenotype showed the lowest ferroptosis score (**Supplementary Figures S6B**), which was in accordance with the previous results. In general, a lower ferroptosis score predicted a better immunotherapy response, and vice versa (**Figure 7J–M**). Next, we would like to find out whether the ferroptosis score was also connected with response to chemotherapy. We screened out several commonly used chemotherapy drugs in BCa and explored the interaction between the half maximal inhibitory concentration (IC50) and ferroptosis score. We found that the low ferroptosis score was related to low IC50 in cisplatin, doxorubicin, and vinblastine (**Figures 7N, O, Q**), which means a higher sensitivity to chemotherapy. While methotrexate was just the reverse (**Figure 7P**). Then we further discovered that IC50 for cisplatin was positively correlated to the ferroptosis score (**Figure 7R**). In summary, the above results showed the unique role of the ferroptosis score in predicting the efficacy of immunotherapy and chemotherapy.

DISCUSSION

Nowadays, increasing evidences have demonstrated that ferroptosis could play a vital role in cancer therapy and predicting the prognosis of patients with cancer (Mou et al., 2019), including BCa. For example, Yan et al. has established a prognostic signature based on 6 ferroptosis regulator genes which could not only predict the progression of BCa patients but also the landscape of macrophage infiltration and EMT status (Yan et al., 2021). Moreover, a ferroptosis-related long non-coding RNA (FRlncRNA) signature comprising 13 prognostic FRlncRNAs established by Cui and his colleagues also had an independent prognostic significance for the overall survival of BCa patients. However, previous studies paid more attention to limited ferroptosis regulator genes and did not go deep into the comprehensive effect of ferroptosis in BCa as well as interaction between TME cell infiltration and ferroptosis, which were necessary to guide more effective immunotherapy strategies or therapies targeted at ferroptosis.

In this article, we first summarized the landscape of genetic variation of 23 FRGs in BCa among 412 samples from the TCGA-BLCA cohort, then we explored the FerrDb database to collect all 382 ferroptosis genes ever reported, screened out 234 validated ferroptosis genes, combined the GEO dataset GSE13507 and TGCA-BLCA cohort into a new meta-cohort, and divided the patients in the meta-cohort into four ferroptosis patterns named VFGcluster A-D using unsupervised clustering according to the expression levels of these validated ferroptosis genes. To our surprise, we not only found significant differences in clinical characteristics and the prognosis of patients among the four distinct VFG clusters, but also found remarkable differences in TME immune cell infiltration. TME comprises both cancer cells and immune cells including T cells, B cells, natural killer cells (NK cells), macrophages, dendritic cells (DCs), and myeloid-derived suppressor cells (MDSCs) (Binnewies et al., 2018). It was intriguing that VFGcluster B and C were abundant in almost all kinds of immune cells but did not exhibit consistent survival advantage. Therefore we classified the VFGcluster B and C into immune-excluded phenotype, also called 'cold' tumor, in which the majority of cytotoxic T lymphocytes (CTLs) were arrested in the margin of the tumor mass instead of the core region, thus

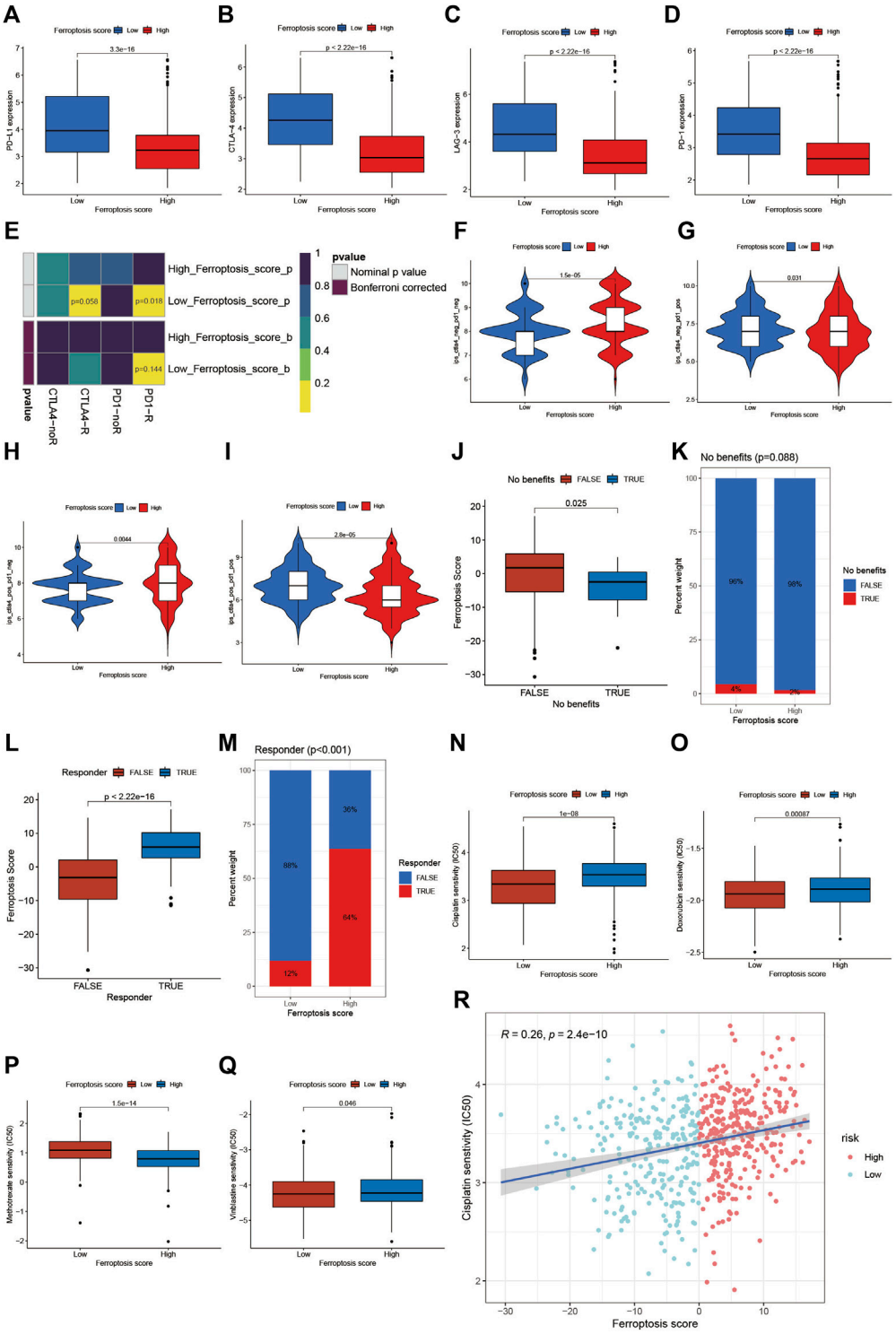

FIGURE 7 | Role of ferroptosis patterns in immunotherapy and chemotherapy. **(A)** Differences in the expression of PD-L1 between the high and low ferroptosis score groups in meta-cohort ($p < 0.001$, Wilcoxon test). **(B)** Differences in the expression of CTLA-4 between high and low ferroptosis score groups in meta-cohort ($p < 0.001$, Wilcoxon test). **(C)** Differences in the expression of LAG-3 between high and low ferroptosis score groups in meta-cohort ($p < 0.001$, Wilcoxon test). **(D)** Differences in the expression of PD-1 between high and low ferroptosis score groups in meta-cohort ($p < 0.001$, Wilcoxon test). **(E)** The similarity of gene expression profiles between ferroptosis score and BCa patients treated with immune checkpoint blockade (ICB). CTLA4-noR, patients no respond to anti-CTLA4 treatment, CTLA4-R, patients respond to anti-CTLA4 treatment, PD1-noR, patients no respond to anti-PD-1 treatment, PD1-R, patients respond to anti-PD-1 treatment. **(F–I)** Violin diagram showed the differences of response index between high and low ferroptosis score groups in four subgroups. **(F)** If no immunotherapy was conducted, the

(*Continued*)

FIGURE 7 | high ferroptosis score resulted in a better prognosis compared to low ferroptosis score ($p < 0.001$, Wilcoxon test). **(G)** If only anti-PD1 immunotherapy was used, the high ferroptosis score resulted in a worse prognosis compared to low ferroptosis score ($p = 0.031$, Wilcoxon test). **(H)** If only anti-CTLA4 immunotherapy was used, the higher ferroptosis score group tended to get a better therapeutic response compared to low ferroptosis score group ($p = 0.0044$, Wilcoxon test). **(I)** When anti-PD1 and anti-CTLA4 immunotherapy methods were simultaneously adopted, the high ferroptosis score group might get significantly worse prognosis compared to low ferroptosis score group ($p < 0.001$, Wilcoxon test). **(J)** Differences in ferroptosis score between immunotherapy benefit and no benefit groups in meta-cohort ($p = 0.025$, Wilcoxon test). **(K)** The proportion of patients benefit from immunotherapy in low or high ferroptosis score groups. **(L)** Differences in ferroptosis score between immunotherapy response and nonresponse groups in meta-cohort ($p < 0.001$, Wilcoxon test). **(M)** The proportion of patients who response to immunotherapy in low or high ferroptosis score groups. **(N–Q)** Differences in IC50 of chemotherapy drugs between high and low ferroptosis score groups in meta-cohort. **N** cisplatin ($p < 0.001$, Wilcoxon test). **(O)** doxorubicin ($p < 0.001$, Wilcoxon test). **(P)** methotrexate ($p < 0.001$, Wilcoxon test). **(Q)** vinblastine ($p = 0.046$, Wilcoxon test). **(R)** Linear regression analysis for cisplatin sensitivity and ferroptosis score. The dot represented each sample, and the color of the dot represented the level of risk. Blue, low risk; red, high risk ($R = 0.26$, $p < 0.001$).

having poor response to immunotherapy (Binnewies et al., 2018). Although both the immune cells and cancer cells in the TME share similar growth signals and metabolic properties, there still exist differences in the sensitivity to ferroptosis among these cells. For example, it seems that anti-tumor T cells are sensitive to ferroptosis while MDSCs exhibit resistance to ferroptosis, and M1 macrophages show higher resistance to ferroptosis than M2 phenotypes (Xu et al., 2021). Therefore, it is conceivable that the TME immune cell infiltration is tightly related to the VFG patterns. We also performed GSVA enrichment analysis and found the pathways related to tumorigenesis and stroma activation were remarkably enriched in VFGcluster B and C. Various studies have demonstrated that stroma could prevent CTL from entering the tumor core and suppress their anti-tumor function. Cells in the stroma such as fibroblasts could not only synthesize and secret collagen to form mechanical separation, but also secretes signaling molecular like transforming growth factor β (TGF-β), which was proved immunosuppressive. The combination of TGF-β blocking antibody and anti-PD-L1 reduced TGF-β signaling in stromal cells, facilitated T-cell penetration into the center of the tumor, and significantly restored anti-tumor immunity and suppressed tumor progression (Mariathasan et al., 2018). Therefore, the results of GSVA enrichment analysis were consistent with VFGcluster patterns.

Further, in this study, we explored the mRNA transcriptome differences between distinct VFG patterns and also found a remarkable relationship with stroma and immunity-related pathways. These differentially expressed genes were considered as ferroptosis-related signature genes. Then we classified the patients into two distinct genomic subtypes based on the 367 VFG cluster-related DEGs and found the gene clusters were tightly connected with VFGcluster patterns. These results demonstrated again that ferroptosis was an important signature to distinguish different TME landscapes. Therefore, a comprehensive assessment of the ferroptosis patterns will enhance our understanding of TME cell-infiltrating characterization.

Next, considering the individual heterogeneity and complexity of ferroptosis, it was necessary for us to explore the latent ferroptosis pattern in individual patients. Thus, we constructed a set of scoring system named the ferroptosis score to quantify the ferroptosis pattern of individuals with BCa. We found immune cells in TME were significantly related to the ferroptosis score and there also existed differences in the ferroptosis score among distinct VFG clusters. VFGcluster A showed the highest median score while VFGcluster B and C shared the lowest median score, which suggested the ferroptosis score was a reliable and effective tool to assess the individual ferroptosis patterns and could also be used to evaluate the landscape of TME immune cell infiltration. Moreover, we also discovered that the ferroptosis score was tightly interacted with clinical signatures such as the TNM category and tumor grade and could predict the prognosis of patients with BCa, especially for patients who were male, with high grade and low TNM category.

Our study also found that TMB was positively correlated to the ferroptosis score. The previous studies have reported that TMB could serve as a latent biomarker of the response to immunotherapy using checkpoint inhibitors in multiple cancers such as lung cancer and mesothelioma (Harber et al., 2021; Sholl, 2021). Therefore, we would like to figure out whether the ferroptosis score could predict the response to immunotherapy and guide clinical treatment strategies. Many patients have benefited from immunotherapy using immune checkpoint inhibitors such as PD-1, PD-L1, and CTLA-4 blockade, but many more patients did not see pronounced clinical response to immunotherapeutic intervention (Binnewies et al., 2018). PD-1/PD-L1 blockade has demonstrated a significant benefit in patients with unresectable and metastatic BCa in the second-line setting, either as monotherapy or in combination with chemotherapy or CTLA-4 checkpoint inhibition (Witjes et al., 2021). The results of the phase II trial using the PD-1 inhibitor pembrolizumab reported a complete pathological remission (pT0) in 42% and pathological response (<pT2) in 54% of patients (Necchi et al., 2018), whereas another single-arm phase II trial with atezolizumab showed a pathologic complete response rate of 31% (Powles et al., 2019). These results suggested that the response rate still needed to be improved and it was important to screen out patients who were appropriate for immunotherapy. Our results found that the lower ferroptosis score was connected with higher expression of main immunotherapy targets like PD-1, PD-L1, LAG-3, and CTLA-4 and a better response to immunotherapy using PD-1 blockade. Therefore, we showed that ferroptosis patterns played a non-negligible role in distinguishing different TME and ferroptosis signature integrated with various biomarkers comprising TMB, immune checkpoint expression, landscape of TME immune cell infiltration and stromal activation, and could be an effective predictive strategy for immunotherapy.

Many drugs used for cancer treatment have been confirmed to work as ferroptosis inducer in their anti-tumor function, such as cisplatin and sorafenib (Liang et al., 2019). Therefore, in our

study, we evaluated the relationship between the ferroptosis score and sensitivity to different chemotherapy drugs and found IC50 for all these drugs exhibited a significant difference between the high and low ferroptosis score groups, which indicated that the ferroptosis score could also be a feasible indicator for the response to chemotherapy. Since cisplatin-based chemotherapy was a conventional treatment for patients with BCa (Sylvester et al., 2021; Witjes et al., 2021), we further performed regression analysis for the ferroptosis score and IC50 for cisplatin and confirmed that there really existed a positive correlation between the sensitivity to cisplatin chemotherapy and ferroptosis score. Overall, the ferroptosis score could also be an effective predictive strategy for chemotherapy, which could help in selecting drug resistant patients before treatment.

In general, our study provided a comprehensive insight into the interaction between ferroptosis, TMB, TME immune cell infiltration, chemotherapy, and immunotherapy. We demonstrated that different VFG patterns could help in distinguishing the landscape of TME immune cell infiltration and clinical characteristics among patients, which was further verified using the ferroptosis score within individuals. We also demonstrated that the ferroptosis score could be used to evaluate the clinicopathological features including the TNM category, tumor grade, TMB, and genetic variation. Moreover, the ferroptosis score could also function as a predictive indicator for the survival of patients. Finally, we also evaluated the ability of the ferroptosis score to predict the response to immunotherapy using immune checkpoint inhibitor and chemotherapy, which might help in improving therapeutic strategies, screening patients eligible for immunotherapy or chemotherapy and guiding individual precision therapy in the future.

However, we also realize that there still exist several shortcomings and limitations in our study. First, the current omics data only provide the level of mRNA but the ferroptosis process relies on proteins, which will bring in some inaccuracies. Second, although we have used the data acquired from IMvigor 210 cohort to further verify the role of ferroptosis patterns in immunotherapy, the number of clinical samples is limited and our study is a lack of verification from other clinical data sets apart from the public data which will be helpful to further confirm our conclusions, and whether ferroptosis has a similar role in other types of cancer hasn't been verified. Therefore, we are prepared to collect some clinical samples to further verify our conclusions, and assess the role of ferroptosis in other urinary system tumors. Third, since some new studies were published and novel ferroptosis-related genes were reported recently, the ferroptosis-related genes we used for analyses could not be comprehensive enough, which might bring a bias into our study. Finally, the specific mechanisms behind the interaction between ferroptosis patterns and TMB immune cell infiltration remain unclear, so cell biological experiments should be performed for further validation in the future.

In conclusion, our work demonstrated and interpreted the complicated regulation mechanisms of ferroptosis on the tumor microenvironment. The differences in ferroptosis patterns in population or individual patients could significantly influence the heterogeneity in tumor clinicopathological features and TME, thus influencing the response to immunotherapy and chemotherapy. Therefore, better understanding and evaluating ferroptosis patterns could be helpful in guiding the clinical therapeutic strategy and improving the prognosis of patients with BCa.

DATA AVAILABILITY STATEMENT

The original contributions presented in the study are included in the article/**Supplementary Material**, further inquiries can be directed to the corresponding author.

AUTHOR CONTRIBUTIONS

Q-DX and J-XS analyzed the data, wrote the manuscript, and drew the figures; S-GW, ZL, and JH designed the study; C-QL, J-ZX, YA, and M-YX contributed to the critical revision of the manuscript.

FUNDING

This work was supported by the Natural Science Foundation of China (81772729).

ACKNOWLEDGMENTS

We sincerely thank Professor Jun Yang for his contribution to the revision of this article. We also thank all the R programming package developers.

SUPPLEMENTARY MATERIAL

The Supplementary Material for this article can be found online at: https://www.frontiersin.org/articles/10.3389/fcell.2022.832892/full#supplementary-material

REFERENCES

Binnewies, M., Roberts, E. W., Kersten, K., Chan, V., Fearon, D. F., Merad, M., et al. (2018). Understanding the Tumor Immune Microenvironment (TIME) for Effective Therapy. *Nat. Med.* 24 (5), 541–550. doi:10.1038/s41591-018-0014-x

Bridges, R. J., Natale, N. R., and Patel, S. A. (2012). System Xc- Cystine/glutamate Antiporter: an Update on Molecular Pharmacology and Roles within the CNS. *Br. J. Pharmacol.* 165 (1), 20–34. doi:10.1111/j.1476-5381.2011.01480.x

Brigelius-Flohé, R., and Maiorino, M. (2013). Glutathione Peroxidases. *Biochim. Biophys. Acta (Bba) - Gen. Subjects* 1830 (5), 3289–3303. doi:10.1016/j.bbagen.2012.11.020

Chan, T. A., Yarchoan, M., Jaffee, E., Swanton, C., Quezada, S. A., Stenzinger, A., et al. (2019). Development of Tumor Mutation burden as an Immunotherapy Biomarker: Utility for the Oncology Clinic. *Ann. Oncol.* 30 (1), 44–56. doi:10.1093/annonc/mdy495

Charoentong, P., Finotello, F., Angelova, M., Mayer, C., Efremova, M., Rieder, D., et al. (2017). Pan-cancer Immunogenomic Analyses Reveal Genotype-Immunophenotype Relationships and Predictors of Response to Checkpoint Blockade. *Cel Rep.* 18 (1), 248–262. doi:10.1016/j.celrep.2016.12.019

Chen, D. S., and Mellman, I. (2017). Elements of Cancer Immunity and the Cancer-Immune Set point. *Nature* 541 (7637), 321–330. doi:10.1038/nature21349

Cui, Y., Zhou, Z., Chai, Y., Che, X., and Zhang, Y. (2021). Identification of a Nomogram from Ferroptosis-Related Long Noncoding RNAs Signature to Analyze Overall Survival in Patients with Bladder Cancer. *J. Oncol.* 2021, 8533464. doi:10.1155/2021/8533464

Dixon, S. J., Lemberg, K. M., Lamprecht, M. R., Skouta, R., Zaitsev, E. M., Gleason, C. E., et al. (2012). Ferroptosis: an Iron-dependent Form of Nonapoptotic Cell Death. *Cell* 149 (5), 1060–1072. doi:10.1016/j.cell.2012.03.042

Dolma, S., Lessnick, S. L., Hahn, W. C., and Stockwell, B. R. (2003). Identification of Genotype-Selective Antitumor Agents Using Synthetic Lethal Chemical Screening in Engineered Human Tumor Cells. *Cancer Cell* 3 (3), 285–296. doi:10.1016/s1535-6108(03)00050-3

Geeleher, P., Cox, N., and Huang, R. S. (2014). pRRophetic: an R Package for Prediction of Clinical Chemotherapeutic Response from Tumor Gene Expression Levels. *PLoS One* 9 (9), e107468. doi:10.1371/journal.pone.0107468

Harber, J., Kamata, T., Pritchard, C., and Fennell, D. (2021). Matter of TIME: the Tumor-Immune Microenvironment of Mesothelioma and Implications for Checkpoint Blockade Efficacy. *J. Immunother. Cancer* 9 (9), 3032. doi:10.1136/jitc-2021-003032

Hinshaw, D. C., and Shevde, L. A. (2019). The Tumor Microenvironment Innately Modulates Cancer Progression. *Cancer Res.* 79 (18), 4557–4566. doi:10.1158/0008-5472.can-18-3962

Hoshida, Y., Brunet, J.-P., Tamayo, P., Golub, T. R., and Mesirov, J. P. (2007). Subclass Mapping: Identifying Common Subtypes in Independent Disease Data Sets. *PLoS One* 2 (11), e1195. doi:10.1371/journal.pone.0001195

Jiang, P., Gu, S., Pan, D., Fu, J., Sahu, A., Hu, X., et al. (2018). Signatures of T Cell Dysfunction and Exclusion Predict Cancer Immunotherapy Response. *Nat. Med.* 24 (10), 1550–1558. doi:10.1038/s41591-018-0136-1

Liang, C., Zhang, X., Yang, M., and Dong, X. (2019). Recent Progress in Ferroptosis Inducers for Cancer Therapy. *Adv. Mater.* 31 (51), e1904197. doi:10.1002/adma.201904197

Liu, Z., Zhao, Q., Zuo, Z.-X., Yuan, S.-Q., Yu, K., Zhang, Q., et al. (2020). Systematic Analysis of the Aberrances and Functional Implications of Ferroptosis in Cancer. *iScience* 23 (7), 101302. doi:10.1016/j.isci.2020.101302

Mariathasan, S., Turley, S. J., Nickles, D., Castiglioni, A., Yuen, K., Wang, Y., et al. (2018). TGFβ Attenuates Tumour Response to PD-L1 Blockade by Contributing to Exclusion of T Cells. *Nature* 554 (7693), 544–548. doi:10.1038/nature25501

Mou, Y., Wang, J., Wu, J., He, D., Zhang, C., Duan, C., et al. (2019). Ferroptosis, a New Form of Cell Death: Opportunities and Challenges in Cancer. *J. Hematol. Oncol.* 12 (1), 34. doi:10.1186/s13045-019-0720-y

Necchi, A., Anichini, A., Raggi, D., Briganti, A., Massa, S., Lucianò, R., et al. (2018). Pembrolizumab as Neoadjuvant Therapy before Radical Cystectomy in Patients with Muscle-Invasive Urothelial Bladder Carcinoma (PURE-01): An Open-Label, Single-Arm, Phase II Study. *J. Clin. Oncol.* 36 (34), 3353–3360. doi:10.1200/jco.18.01148

Powles, T., Kockx, M., Rodriguez-Vida, A., Duran, I., Crabb, S. J., Van Der Heijden, M. S., et al. (2019). Clinical Efficacy and Biomarker Analysis of Neoadjuvant Atezolizumab in Operable Urothelial Carcinoma in the ABACUS Trial. *Nat. Med.* 25 (11), 1706–1714. doi:10.1038/s41591-019-0628-7

Richters, A., Aben, K. K. H., and Kiemeney, L. A. L. M. (2020). The Global burden of Urinary Bladder Cancer: an Update. *World J. Urol.* 38 (8), 1895–1904. doi:10.1007/s00345-019-02984-4

Rosenberg, J. E., Hoffman-Censits, J., Powles, T., van der Heijden, M. S., Balar, A. V., Necchi, A., et al. (2016). Atezolizumab in Patients with Locally Advanced and Metastatic Urothelial Carcinoma Who Have Progressed Following Treatment with Platinum-Based Chemotherapy: a Single-Arm, Multicentre, Phase 2 Trial. *Lancet* 387 (10031), 1909–1920. doi:10.1016/S0140-6736(16)00561-4

Sholl, L. M. (2021). Biomarkers of Response to Checkpoint Inhibitors beyond PD-L1 in Lung Cancer. *Mod. Pathol.* 35, 66. doi:10.1038/s41379-021-00932-5

Siegel, R. L., Miller, K. D., and Jemal, A. (2019). Cancer Statistics, 2019. *CA A. Cancer J. Clin.* 69 (1), 7–34. doi:10.3322/caac.21551

Stockwell, B. R., Friedmann Angeli, J. P., Bayir, H., Bush, A. I., Conrad, M., Dixon, S. J., et al. (2017). Ferroptosis: A Regulated Cell Death Nexus Linking Metabolism, Redox Biology, and Disease. *Cell* 171 (2), 273–285. doi:10.1016/j.cell.2017.09.021

Sun, J., Yue, W., You, J., Wei, X., Huang, Y., Ling, Z., et al. (2021). Identification of a Novel Ferroptosis-Related Gene Prognostic Signature in Bladder Cancer. *Front. Oncol.* 11, 730716. doi:10.3389/fonc.2021.730716

Sylvester, R. J., Rodríguez, O., Hernández, V., Turturica, D., Bauerová, L., Bruins, H. M., et al. (2021). European Association of Urology (EAU) Prognostic Factor Risk Groups for Non-muscle-invasive Bladder Cancer (NMIBC) Incorporating the WHO 2004/2016 and WHO 1973 Classification Systems for Grade: An Update from the EAU NMIBC Guidelines Panel. *Eur. Urol.* 79 (4), 480–488. doi:10.1016/j.eururo.2020.12.033

Valero, C., Lee, M., Hoen, D., Wang, J., Nadeem, Z., Patel, N., et al. (2021). The Association between Tumor Mutational burden and Prognosis Is Dependent on Treatment Context. *Nat. Genet.* 53 (1), 11–15. doi:10.1038/s41588-020-00752-4

Witjes, J. A., Bruins, H. M., Cathomas, R., Compérat, E. M., Cowan, N. C., Gakis, G., et al. (2021). European Association of Urology Guidelines on Muscle-Invasive and Metastatic Bladder Cancer: Summary of the 2020 Guidelines. *Eur. Urol.* 79 (1), 82–104. doi:10.1016/j.eururo.2020.03.055

Xu, H., Ye, D., Ren, M., Zhang, H., and Bi, F. (2021). Ferroptosis in the Tumor Microenvironment: Perspectives for Immunotherapy. *Trends Mol. Med.* 27 (9), 856–867. doi:10.1016/j.molmed.2021.06.014

Yan, Y., Cai, J., Huang, Z., Cao, X., Tang, P., Wang, Z., et al. (2021). A Novel Ferroptosis-Related Prognostic Signature Reveals Macrophage Infiltration and EMT Status in Bladder Cancer. *Front. Cel Dev. Biol.* 9, 712230. doi:10.3389/fcell.2021.712230

Yang, W. S., SriRamaratnam, R., Welsch, M. E., Shimada, K., Skouta, R., Viswanathan, V. S., et al. (2014). Regulation of Ferroptotic Cancer Cell Death by GPX4. *Cell* 156 (1-2), 317–331. doi:10.1016/j.cell.2013.12.010

Yang, W. S., and Stockwell, B. R. (2016). Ferroptosis: Death by Lipid Peroxidation. *Trends Cel Biol.* 26 (3), 165–176. doi:10.1016/j.tcb.2015.10.014

Yang, W. S., and Stockwell, B. R. (2008). Synthetic Lethal Screening Identifies Compounds Activating Iron-dependent, Nonapoptotic Cell Death in Oncogenic-RAS-Harboring Cancer Cells. *Chem. Biol.* 15 (3), 234–245. doi:10.1016/j.chembiol.2008.02.010

Zhou, N., and Bao, J. (2020). *FerrDb: A Manually Curated Resource for Regulators and Markers of Ferroptosis and Ferroptosis-Disease Associations*. Oxford: Database, 2020.

Conflict of Interest: The authors declare that the research was conducted in the absence of any commercial or financial relationships that could be construed as a potential conflict of interest.

Publisher's Note: All claims expressed in this article are solely those of the authors and do not necessarily represent those of their affiliated organizations, or those of the publisher, the editors, and the reviewers. Any product that may be evaluated in this article, or claim that may be made by its manufacturer, is not guaranteed or endorsed by the publisher.

frontiers in Cell and Developmental Biology

ORIGINAL RESEARCH
published: 31 March 2022
doi: 10.3389/fcell.2022.725024

Construction and Validation of a 15-Top-prognostic-gene-based Signature to Indicate the Dichotomized Clinical Outcome and Response to Targeted Therapy for Bladder Cancer Patients

Hongbing Gu[1,2] *and Chaozhao Liang*[1]*

[1]Department of Urology, The First Affiliated Hospital of Anhui Medical University, Institute of Urology, Anhui Medical University and Anhui Province Key Laboratory of Genitourinary Diseases, Anhui Medical University, Hefei, China, [2]Department of Urology, East District of First Affiliated Hospital of Anhui Medical University, Feidong People's Hospital, Hefei, China

OPEN ACCESS

Edited by:
Yongwen Luo,
Wuhan University, China

Reviewed by:
Wenjie Luo,
Fudan University, China
Le Qu,
Nanjing University, China
Lifeng Zhang,
Changzhou No. 2 People's Hospital, China

***Correspondence:**
Chaozhao Liang
liang_chaozhao@ahmu.edu.cn

Specialty section:
This article was submitted to Molecular and Cellular Pathology, a section of the journal Frontiers in Cell and Developmental Biology

Received: 14 June 2021
Accepted: 17 February 2022
Published: 31 March 2022

Citation:
Gu H and Liang C (2022) Construction and Validation of a 15-Top-prognostic-gene-based Signature to Indicate the Dichotomized Clinical Outcome and Response to Targeted Therapy for Bladder Cancer Patients. Front. Cell Dev. Biol. 10:725024. doi: 10.3389/fcell.2022.725024

The clinical outcome of heterogeneous bladder cancer (BCa) is impacted by varying molecular characteristics and clinical features, and new molecular classification is necessary to recognize patients with dichotomized prognosis. We enrolled a total of 568 BCa patients from the TCGA-BLCA and GSE13507 cohorts. A total of 107 candidate genes, which were mostly involved in the extracellular matrix-associated pathway, were first selected through the consensus value of the area under the receiver operating characteristic curve (AUC). Furthermore, absolute shrinkage and selection operation regression analysis was implemented to reveal the 15 genes and establish the prognostic signature. The newly defined prognostic signature could precisely separate BCa patients into subgroups with favorable and poor prognosis in the training TCGA-BLCA cohort ($p < 0.001$, HR = 2.41, and 95% CI: 1.76–3.29), as well as the testing GSE13507 cohort ($p < 0.001$, HR = 7.32, and 95% CI: 1.76–3.29) and external validation E-MTAB-4321 cohort ($p < 0.001$, HR = 10.56, 95% CI: 3.208–34.731). Multivariate Cox analysis involving the signature and clinical features indicated that the signature is an independent factor for the prediction of BCa prognosis. We also explored potential targeted therapy for BCa patients with high- or low-risk scores and found that patients with high risk were more suitable for chemotherapy with gemcitabine, doxorubicin, cisplatin, paclitaxel, and vinblastine (all $p < 0.05$), but anti-PD-L1 therapy was useless. We knocked down HEYL with siRNAs in T24 and 5,637 cells, and observed the decreased protein level of HEYL, and inhibited cell viability and cell invasion. In summary, we proposed and validated a 15-top-prognostic gene-based signature to indicate the dichotomized prognosis and response to targeted therapy.

Keywords: bladder cancer, target therapy, signature, prognosis, PDL1

Abbreviations: BCa, Bladder cancer; DEG, Differentially expressed gene; GEO, Gene Expression Omnibus; KM, Kaplan–Meier; ROC, Receiver operating characteristic; TCGA, The Cancer Genome Atlas.

INTRODUCTION

Bladder cancer (BCa), a common disease in the world with an estimated 430,000 new cases diagnosed in 2012, is the ninth most frequent tumor globally. Men have a higher incidence than women, accounting for 75% of patients. European male mortality rates were by far the highest recorded worldwide, especially in Eastern Europe (Antoni et al., 2017). In China, its morbidity and mortality are rising. According to the 2015 National Central Cancer Registry in China, the incidence of BCa ranked sixth in male cancers, with $7.68/10^5$ new cases diagnosed in 2011 (Pang et al., 2016). A total of $3.56/10^5$ persons died of BCa in 2014 (Chen et al., 2018). Among the risk factors, smoking occupies the most important position, and approximately two-thirds of men and one-third of women with BCa are related to smoking (Farling, 2017). There are two types of BCa, muscle invasive BCa (MIBC) and non-muscle invasive BCa (NMIBC). NMIBC is also known as early-stage bladder cancer, and MIBC is an advanced stage with a high recurrence rate (Hautmann et al., 2006; Chamie et al., 2013).

As a heterogeneous disease, the clinical outcome of BCa is impacted by various characteristics in different patients, such as gene mutations, neoantigens, gene copy number alterations, and infiltration of immunocytes. Low-grade tumors have a low progression rate and a low short-term recurrence rate and can be removed easily by transurethral resection (TUR) or intravesical therapy with *Bacillus* Calmette-Guérin (BCG). However, 15.0%–20.0% of NMIBCs ultimately develop into invasive MIBCs (Hedegaard et al., 2016). At the other end of the spectrum, with a high short-term recurrence rate and a high malignant potential leading to tumor progression, high-grade tumors always have a poor prognosis (Kirkali et al., 2005). Therefore, it is important to establish an efficient and concise novel method to discriminate high-risk and low-risk BCa patients. Many teams have attempted to establish a novel classification of BCa at the molecular level. Mo et al. generated an 18-gene signature model to divide MIBC and NMIBC into two subgroups: basal and differentiated. The basal subgroup expressed a low signature gene level, and the differentiated subgroups expressed a high signature gene level. Further study showed a significant difference in overall survival time between the basal and differentiated subgroups. Compared with the differentiated subgroup, the basal subgroup had a worse overall survival outcome (Mo et al., 2018). Sjödahl et al. defined five major urothelial cancer subtypes using 308 cases, and 11 signature genes were identified. They broke the limitation of pathological staging and grading, adding more valuable information for pathological classification (Sjödahl et al., 2012). Kim et al. generated a progression-related gene classifier to predict the disease outcome of NMIBC patients (Kim W. J et al., 2010). Although many prognostic signatures and molecular subtypes have been found, they are still not mature enough to guide clinical therapy such as HER2 for breast cancer (Tsang and Tse, 2020).

Molecular classification is a novel, objectively assessed, individual, and functions as a complement to the classification system. Some genetic events, such as genetic or epigenetic changes that can cause aberrant gene expression, occur in the early stage of BCa (Kim and Quan, 2005; Kim and Bae, 2008). Thus, classification based on gene expression profiling represents a potentially useful way to discriminate different prognosis. In our novel molecular classification module, a total of 1,155 genes from TCGA and GSE13507 cohorts were enrolled and finally generated a 17-gene signature classifier.

MATERIALS AND METHODS

Data Collection

All expression profiles were derived from The Cancer Genome Atlas (TCGA, https://portal.gdc.cancer.gov/) and the Gene Expression Omnibus (GEO, www.ncbi.nlm.nih.gov/gds), and corresponding clinical information was obtained from the TCGA Bladder-cancer Clinical Data Resource dataset and GEO clinical data resource. After matching the available gene expression data and clinical features, a total of 403 patients from the TCGA-BLCA cohort and 165 patients from the GSE13507 cohort were recorded for the utilization of the current study.

Identification of Candidate Genes

Taking the intersection of the expression files of the TCGA-BLCA and GSE13507 cohorts, we finally enrolled 11,255 genes for the subsequent analysis. The receiver operating characteristic (ROC) curve and area under the curve (AUC) were calculated by the "pROC" package to assess the prognostic ability of all included genes and screen the genes included in the analysis with optimal cutoff values (TCGA-BLCA: 0.60; GSE13507: 0.65). Furthermore, to construct an accurate prognostic model, the least absolute shrinkage and selector operation (LASSO) regression analysis was implemented for screening candidate genes by using the "glmnet" package. The minimum lambda value was defined as a cutoff point to minimize the mean cross-validated error. These genes selected *via* LASSO analysis were used to calculate the risk score of each patient with the gene expression value and coefficient. The process of the current study is shown in **Figure 1**.

Enrichment Analysis of Selected Genes

The genes with the top mean AUC in both TCGA-BLCA and GSE13507 cohorts were visualized with a heatmap using the R function "barplot". GO (Gene Ontology), KEGG (Kyoto Encyclopedia of Genes and Genomes), and HALLMARK enrichment analyses of genes were implemented by R package "ClusterProfiler" (Yu et al., 2012) and "msigdbr" (Subramanian et al., 2005). Dot plots of biological processes, molecular function, and cellular components were visualized using the R function "enrichGO"; the connections between biological processes were shown using the R function "emapplot", the correlation between intersection genes and the top 5 biological process GO terms was demonstrated using the R function "cnetplot", KEGG pathways were drawn using the R function "enrichKEGG", and HALLMARK pathways were illustrated using the function "msigdbr" in "clusterProfiler". Adjusted $p < 0.05$ was set as the cutoff threshold.

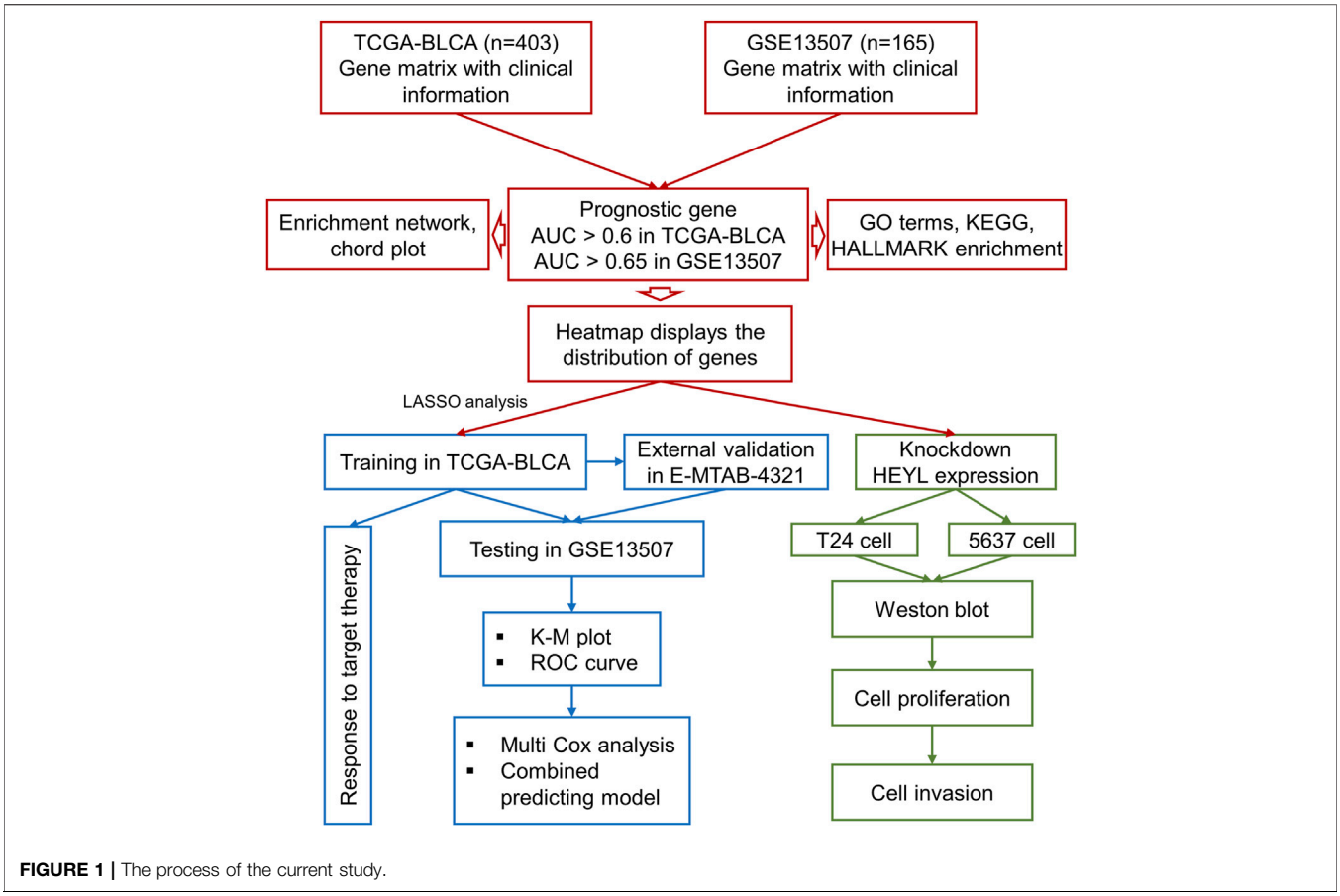

FIGURE 1 | The process of the current study.

Overall Survival Analysis and Cox Survival Analysis

Kaplan–Meier (K-M) survival analysis and a log-rank test were performed based on the data of candidate gene expression profiles and corresponding clinical parameters to evaluate survival rates by using the "survival" package. The Cox model was established to calculate hazard ratios (HRs) and 95% confidence intervals (CIs). Multivariate Cox regression curves were generated to explore the independent prognostic effect of risk scores after adjusting for several clinical characteristics, including age, sex, and grade. The results were illustrated with multiforest plots. To further explore the impact of the classifier on the prognosis of different subgroups, we conducted a subgroup analysis based on clinical features related to prognosis, including age (≤70 or >70), tumor stage (≤Stage II or >Stage II), sex (male or female), and grade (low or high).

Prediction of the Response to Targeted Therapy

We predicted the chemotherapeutic response for each sample based on the Genomics of Drug Sensitivity in Cancer (GDSC). Six commonly used chemotherapy drugs, cisplatin, doxorubicin, mitomycin, paclitaxel, vinblastine, and gemcitabine, were selected for assessment. We compared the response to the above six drugs *via* the estimation of the samples' half-maximal inhibitory concentration (IC_{50}) conducted by ridge regression. To evaluate the individual likelihood of responding to immunotherapy, a subclass analysis was performed in response to anti-PD-L1 therapy based on the clinical response of 248 patients with BCa who underwent immunotherapy (Meng, 2021).

Cell Culture, Proliferation, Invasion, and Western Blotting

We cultured the T24 and 5,637 BCa cell lines in RPMI-1640 medium supplemented with 10% fetal bovine serum at 37°C with 5% CO_2. The BCa cell lines 5,637 and T24 were respectively transfected with 50 pmol negative control, si-HEYL-1#, and si-HEYL-2# inhibitors *via* Lipofectamine 3,000 (Invitrogen; Thermo Fisher Scientific, Inc.) transfer system. The siRNAs were purchased from Guangzhou Ribobio Co., Ltd., and the sequences are listed in **Supplementary Table S1**.

We evaluated cell viability *via* the MTT assay. A total of 5,000 cells were seeded into a 24-well plate and cultured for 0, 1, 2, and 3 days. Then, 50 μl of 0.5% MTT reagent was added to each well, and the cells were further cultured for 1.5 h at 37°C and then detected on a microplate reader. The optical density (OD) values were measured at 450 nm.

For cell invasion, we seeded 20,00 cells in the upper Transwell chamber (8 μm; Corning, Inc.); Matrigel at a 1:20 concentration was precoated and cultured at 37°C for 2 h. The lower chamber

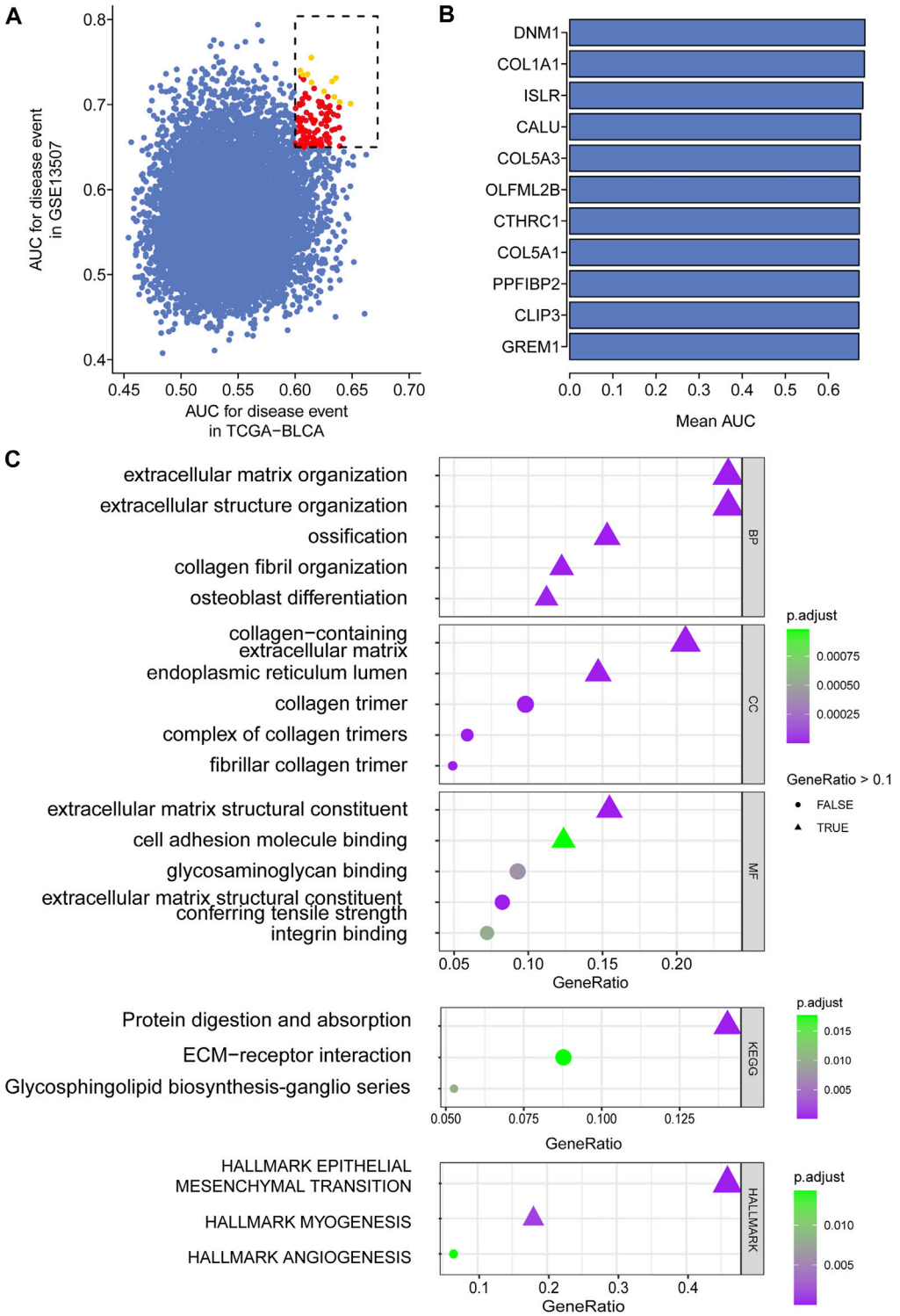

FIGURE 2 | Top prognostic gene selection in both TCGA-BLCA and GSE13507 cohorts. **(A)** AUC evaluation of the prognostic value of candidate genes involved in overall survival based on datasets TCGA and GSE10816. **(B)** The average AUC value of the top 11 candidate genes. **(C)** Annotation of enriched signaling pathways by GO, KEGG, and HALLMARK.

TABLE 1 | The details of the enriched signaling pathways of the 107 prognostic genes.

ONTOLOGY BP				
Terms	***p*-value**	***p*.adjust**	***q*-value**	**geneID**
Extracellular matrix organization	1.16E-18	1.26E-15	1.06E-15	PLOD1/MMP11/COL16A1/COL18A1/ADAM12/COL5A2/COL3A1/COL5A3/BGN/FAP/COMP/TNC/GREM1/SULF1/COL5A1/VCAN/LOX/ITGA5/ADAMTS2/COL1A1/COL8A1/AEBP1/ITGA11
Extracellular structure organization	1.23E-18	1.26E-15	1.06E-15	PLOD1/MMP11/COL16A1/COL18A1/ADAM12/COL5A2/COL3A1/COL5A3/BGN/FAP/COMP/TNC/GREM1/SULF1/COL5A1/VCAN/LOX/ITGA5/ADAMTS2/COL1A1/COL8A1/AEBP1/ITGA11
Collagen fibril organization	6.24E-17	4.27E-14	3.59E-14	PLOD1/MMP11/COL5A2/COL3A1/COL5A3/COMP/GREM1/COL5A1/LOX/ADAMTS2/COL1A1/AEBP1
Ossification	2.40E-09	1.23E-06	1.03E-06	CTHRC1/DCHS1/GLI2/COL5A2/COMP/TNC/GREM1/VCAN/LOX/COL1A1/RRBP1/ASPN/TWIST1/ITGA11/FAM20C
Osteoblast differentiation	2.73E-08	1.12E-05	9.41E-06	CTHRC1/GLI2/TNC/GREM1/VCAN/LOX/COL1A1/RRBP1/TWIST1/ITGA11/FAM20C
ONTOLOGY CC				
collagen-containing extracellular matrix	1.63E-15	3.32E-13	2.86E-13	CTHRC1/COL16A1/COL18A1/COL5A2/COL3A1/COL5A3/BGN/COMP/TNC/GREM1/SULF1/COL5A1/VCAN/NCAM1/ADAMTS2/CDH2/COL1A1/COL8A1/AEBP1/ASPN/SERPINE2
collagen trimer	2.52E-11	2.57E-09	2.21E-09	CTHRC1/COL16A1/COL18A1/COL5A2/COL3A1/COL5A3/COL5A1/LOX/COL1A1/COL8A1
endoplasmic reticulum lumen	6.16E-11	4.19E-09	3.61E-09	RCN3/COL16A1/COL18A1/COL5A2/COL3A1/COL5A3/TNC/COL5A1/VCAN/PDIA5/CDH2/COL1A1/COL8A1/FAM20C/CALU
complex of collagen trimers	4.24E-10	2.16E-08	1.86E-08	COL5A2/COL3A1/COL5A3/COL5A1/COL1A1/COL8A1
fibrillar collagen trimer	1.51E-09	5.14E-08	4.43E-08	COL5A2/COL3A1/COL5A3/COL5A1/COL1A1
ONTOLOGY MF				
extracellular matrix structural constituent	1.22E-14	3.35E-12	3.03E-12	CTHRC1/COL16A1/COL18A1/COL5A2/COL3A1/COL5A3/BGN/COMP/TNC/COL5A1/VCAN/COL1A1/COL8A1/AEBP1/ASPN
extracellular matrix structural constituent conferring tensile strength	5.00E-11	6.85E-09	6.19E-09	COL16A1/COL18A1/COL5A2/COL3A1/COL5A3/COL5A1/COL1A1/COL8A1
glycosaminoglycan binding	4.63E-06	0.000423	0.000382	TNFAIP6/COL5A3/BGN/COMP/NRP2/SULF1/COL5A1/VCAN/SERPINE2
integrin binding	8.05E-06	0.000552	0.000498	COL16A1/COL3A1/FAP/COMP/THY1/COL5A1/ITGA5
cell adhesion molecule binding	1.79E-05	0.000983	0.000887	PVR/COL16A1/COL3A1/FAP/COMP/THY1/COL5A1/ITGA5/CALD1/CDH2/CNN3/FLNA
KEGG				
Protein digestion and absorption	5.22E-07	7.57E-05	6.65E-05	COL16A1/COL18A1/COL1A1/COL3A1/COL5A1/COL5A2/COL5A3/COL8A1
Glycosphingolipid biosynthesis—ganglio series	0.000143	0.010337	0.00908	B4GALNT1/ST3GAL5/ST6GALNAC5
ECM–receptor interaction	0.000366	0.017704	0.015551	COL1A1/COMP/ITGA11/ITGA5/TNC
HALLMARK				
HALLMARK_EPITHELIAL_MESENCHYMAL_TRANSITION	2.29E-22	6.86E-21	6.26E-21	ACTA2/ADAM12/BGN/CALD1/CALU/CDH2/COL16A1/COL1A1/COL3A1/COL5A1/COL5A2/COL5A3/COMP/CTHRC1/FAP/FLNA/GEM/GREM1/ITGA5/LOX/PLOD1/PRRX1/PVR/SERPINE2/TAGLN/THY1/TNC/VCAN
HALLMARK_MYOGENESIS	7.61E-05	0.001142	0.001041	ACTC1/ADAM12/AEBP1/CNN3/COL1A1/COL3A1/DTNA/MAPK12/NCAM1/SPHK1/TAGLN
HALLMARK_ANGIOGENESIS	0.001434	0.01434	0.013082	COL3A1/COL5A2/KCNJ8/VCAN

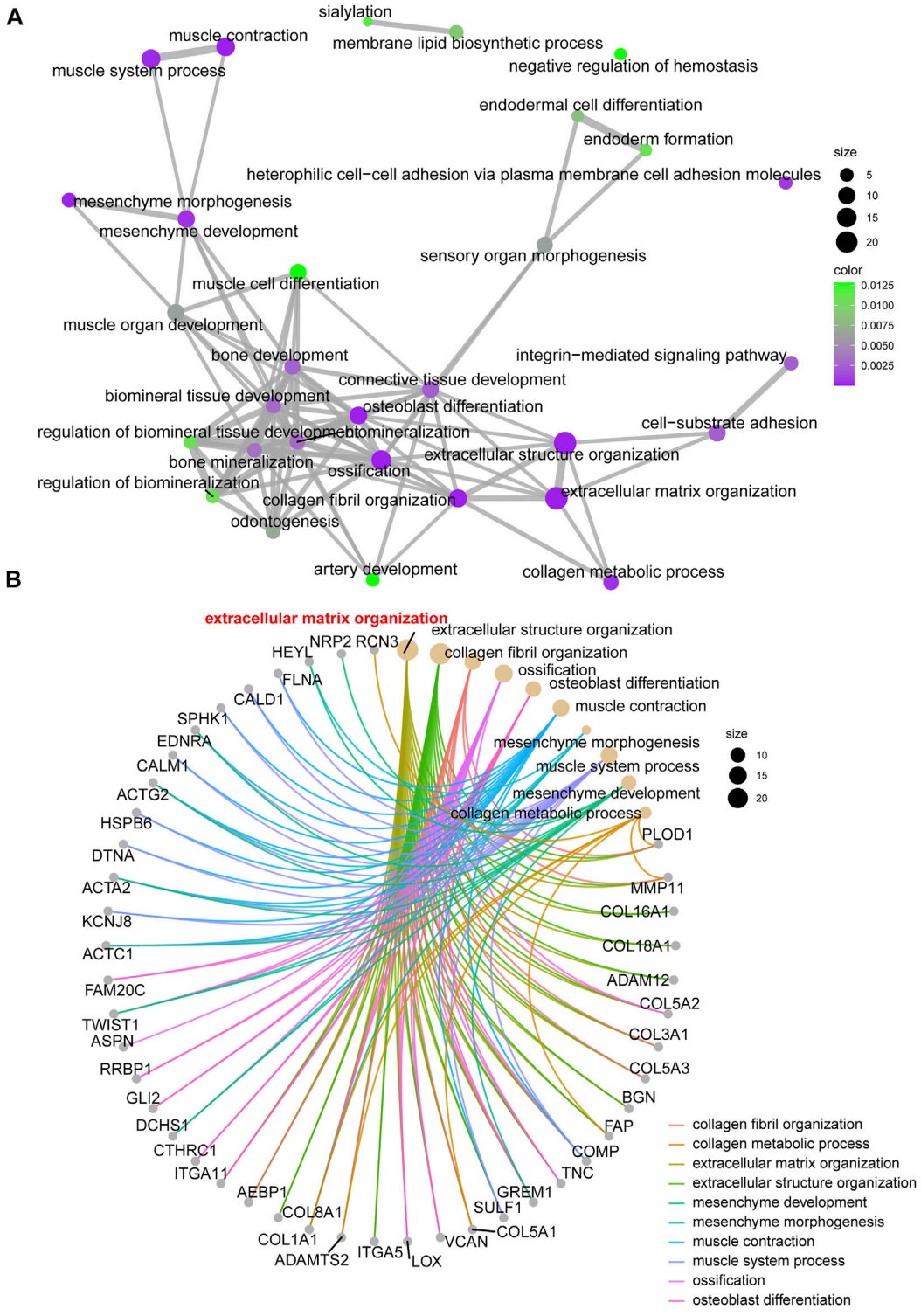

FIGURE 3 | The network and chord graph shows the most important pathways. **(A)** Network of enriched signaling pathways; **(B)** Chord graph of the enriched signaling pathways.

was filled with complete medium as a chemoattractant. After culturing the coculture system at 37°C for 24 h, the chamber and cells were mixed with formalin for 15 min and further stained with 1% crystal violet. The invaded cells were counted in 3 repeated groups (magnification, ×200) under a light microscope (Nikon Corporation).

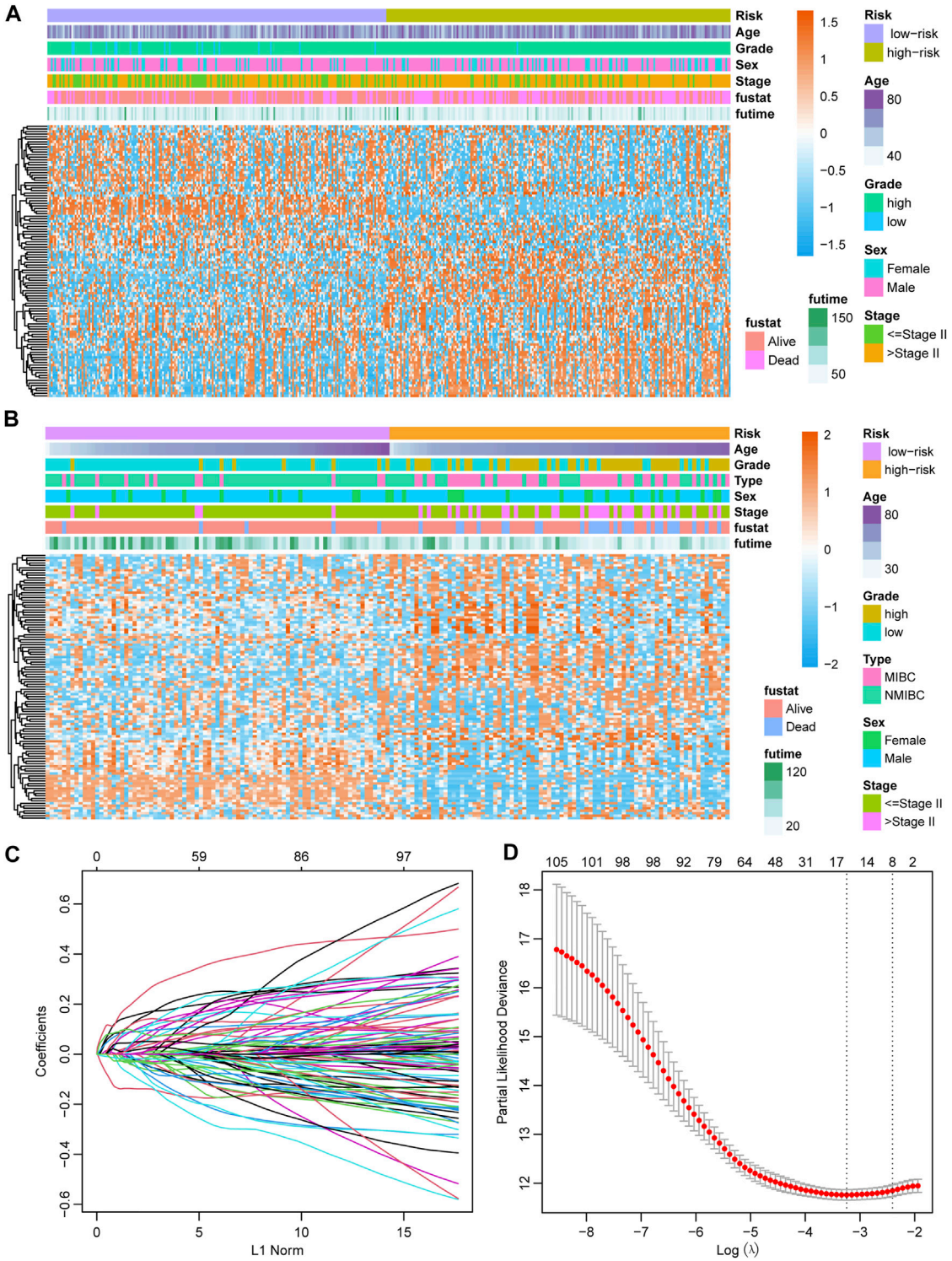

FIGURE 4 | Establishment of the prognostic model **(A)** Heatmap showing the expression of 107 candidate genes in the TCGA-BLCA cohort. **(B)** Heatmap showing the expression of 107 candidate genes in the GSE13507 cohort. **(C)** The optimal tuning parameter (lambda) in the LASSO analysis selected with 5-fold cross-validation and one standard error rule. **(D)** LASSO coefficient profiles of the 107 candidate genes.

Western blotting was performed to confirm the knockdown of HEYL at the protein level. Anti-HEYL and anti-tubulin antibodies were used to detect the protein lanes.

Statistical Analysis

All analyses were completed by R software v4.0.3 (http://www.r-project.org). The risk score of each BCa patient was calculated with the sum of the selected 15 gene coefficients by LASSO regression. The high-risk group and low-risk group were discriminated by the median value of the risk score. Heatmap and enrichment analyses were applied to the visualized expression files. K-M survival analysis was performed to explore the survival difference between the high-risk and low-risk score groups. A log-rank test was used to estimate the survival analysis. HR and 95% CI were calculated by the Cox model. The independent prognostic effect of the risk score was calculated by multivariate Cox regression analysis. $p < 0.05$ was considered a statistically significant difference.

RESULT

Gene Selection

In total, 403 patients with 14,163 genes in TCGA-BLCA and 165 patients with 18,561 genes in GSE13507 were first enrolled, and the corresponding clinical information was also downloaded. Following preprocessing of raw data, 11,255 intersecting genes were subjected to the calculation of AUC to estimate the prediction of the prognosis of BCa patients in those two cohorts (**Figure 2A**). Genes with the top mean AUC are shown in **Figure 2B**, including "GREM1", "CLIP3", "PPFIBP2", "COL5A1", "CTHRC1", "OLFML2B″, "COL5A3", "CALU", "ISLR", "COL1A1", and "DNM1". With the preset cutoff value of AUC (TCGA-BLCA: 0.60; GSE13507: 0.65), we finally enrolled 107 genes for the subsequent analysis.

Intersection Gene Enrichment and Annotation

For the enrolled 107 candidate genes, we performed enrichment analysis to reveal their potential function in BCa. The results demonstrated the top five biological process, cellular component, and molecular function GO terms, KEGG terms, and HALLMARK terms (**Figure 2C**). We concluded that the extracellular matrix structural process, cell adhesion molecule binding, ECM–receptor interaction, and hallmark epithelial–mesenchymal transition signaling pathways play pivotal roles in the tumorigenesis of BCa. The details of the enriched pathways and genes are displayed in **Table 1**. The interrelation of the top 30 enriched biological processes is presented in **Figure 3A**, and the correlation between intersected genes and extracellular matrix-associated signaling is also illustrated in **Figure 3B**.

Construction of the Prognostic Signature

The gene expression of 107 genes and associated clinical features for the TCGA-BLCA cohort are shown in **Figure 4A**, and those for the GSE13507 cohort are shown in **Figure 4B**. LASSO regression was performed to identify candidate genes and evaluate the corresponding coefficients in the TCGA-BLCA training cohort (**Figures 4C,D**). Based on the minimum lambda value of 0.032, a total of 15 genes were enrolled for the calculation of the prognostic signature, with the formula risk score = 0.109 × expression of PHGDH − 0.117 × expression of CD96 + 0.007 × expression of SETBP1 + 0.077 × expression of GALK1 + 0.019 × expression of DTNA +0.064 × expression of SERPINB2 + 0.018 × expression of COMP +0.043 × expression of CALM1 + 0.111 × expression of HEYL +0.022 × expression of CCRN4L + 0.032 × expression of FADS2 + 0.083 × expression of TMEM109 − 0.013 × expression of CTSE +0.021 × expression of FAM43A − 0.022 × expression of IL9R. The risk score for each patient in both TCGA-BLCA and GSE13507 cohorts was calculated along with the above-mentioned formula. For the subsequent analysis, the prognostic value of each single gene is displayed in **Supplementary Figure S1**.

Prognostic Value of the Newly Defined Signature

With the median risk score as the cutoff point, patients in the TCGA-BLCA cohort were divided into the high-risk class (n = 201) and low-risk class (n = 198) (**Supplementary Figure S2A**), and the results of the risk map showed a significant survival difference between the two classes (**Supplementary Figure S2A**). K-M curves demonstrated that the low-risk class had a better overall survival time than the high-risk class ($p < 0.001$, HR = 2.41, 95% CI: 1.76–3.29) (**Figure 5A**), and the ROC curve showed that the AUC of this classification strategy could be 0.727, with a 95% CI of 0.678–0.776, which indicated an outstanding prognostic value (**Figure 5B**). The distribution of the clinical features in the high-risk and low-risk groups of TCGA-BLCA are listed in **Table 2**. We also assessed the prognostic value in different subgroups of patients. The signature was meaningful for BCa patients in the subgroups of age ≤ 70 years old ($p < 0.01$), age >70 years old ($p < 0.01$), Stage I + II ($p = 0.02$), Stage III + IV ($p < 0.01$), male sex ($p < 0.01$), and high grade ($p < 0.01$) in the TCGA-BLCA cohort (**Supplementary Figure S3**).

Assessing the Prognostic Value of the Signature in the Testing GSE13507 Cohort

To validate the 15-gene signature predictive values in other BCa cohorts, the same formula was conducted in the GSE13507 dataset to generate the risk score of each patient. Similarly, patients were divided into a high-risk group and a low-risk group based on the median risk score as the cutoff point (**Supplementary Figure S2B**). Consistent with the results in the TCGA-BLCA cohort, the low-risk group exhibited a shorter overall survival time than the high-risk group ($p < 0.001$, HR = 7.32, and 95% CI: 1.76–3.29, **Figure 5C**), and the AUC was 0.786, with a 95% CI of 0.703–0.869 (**Figure 5D**). The distribution of the clinical features in the high-risk and low-risk groups of GSE13507 is listed in **Table 3**. We also assessed the

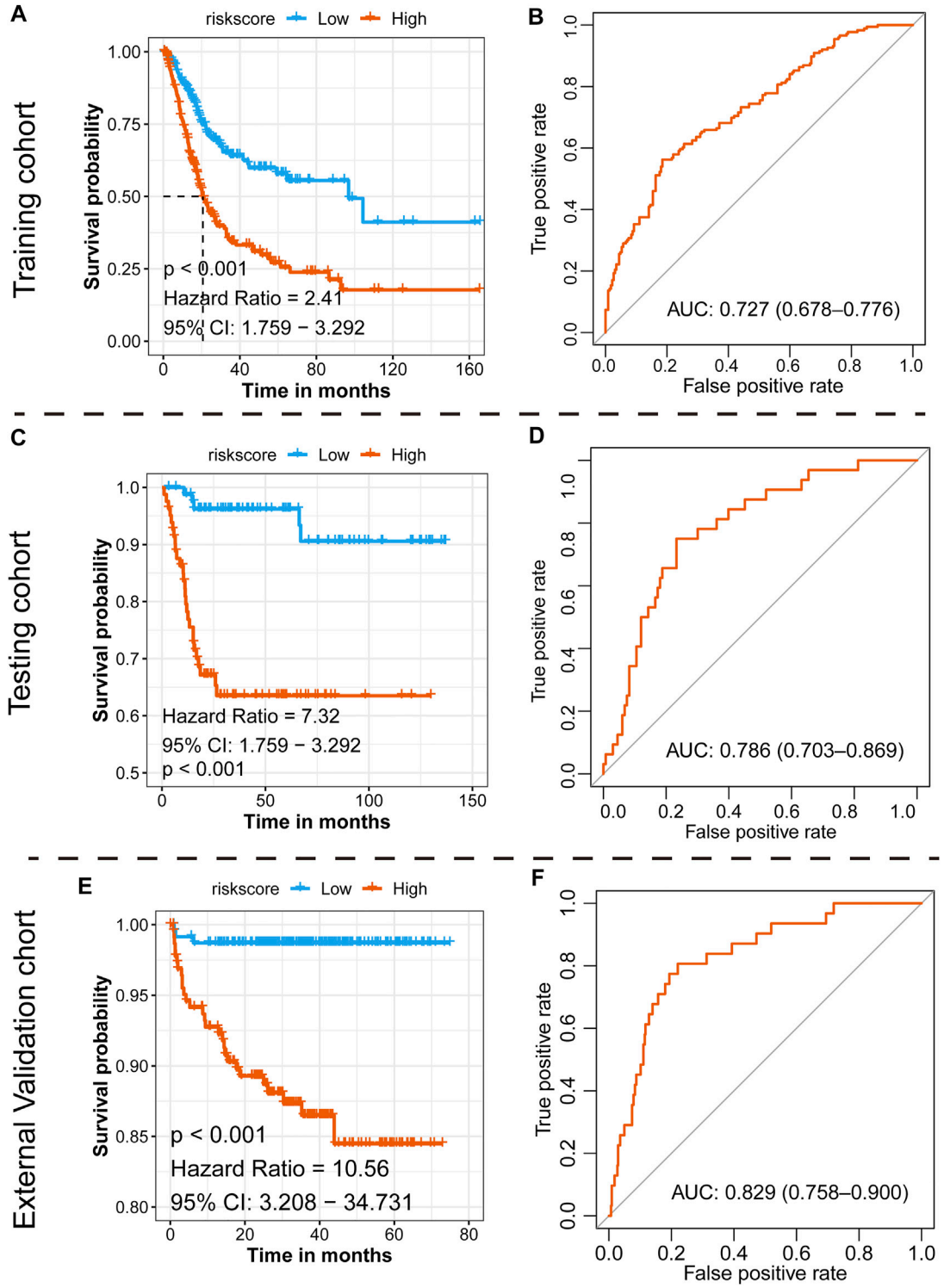

FIGURE 5 | Prognostic value of the newly defined signature. **(A)** K-M plot showing the separated clinical outcome of patients belonging to the high-risk and low-risk subgroups in the training TCGA-BLCA cohort **(A)**, testing GSE13507 cohort **(C)**, and external validation cohort **(E)**; ROC curve showing the prognostic value of the signature in the training TCGA-BLCA cohort **(B)**, testing GSE13507 cohort **(D)**, and external validation cohort **(F)**.

prognostic value in different subgroups of patients. The signature was meaningful for BCa patients in the subgroups of age ≤ 70 years old ($p < 0.01$), age >70 years old ($p < 0.01$), Stage I + II ($p = 0.027$), male ($p < 0.01$), female ($p < 0.01$), low grade ($p = 0.018$), and high grade ($p < 0.01$) in the GSE13507 cohort (**Supplementary Figure S4**).

TABLE 2 | Summary of clinical features in the TCGA-BLCA cohort.

	Level	Low risk	High risk	*p*
Survival time		29.43 ± 28.66	23.79 ± 25.37	0.038
Survival status (%)	0	140 (70.7)	84 (41.8)	<0.001
	1	58 (29.3)	117 (58.2)	
Stage (%)	≤Stage II	84 (42.4)	45 (22.4)	<0.001
	>Stage II	114 (57.6)	156 (77.6)	
Sex (%)	Female	44 (22.2)	61 (30.3)	0.084
	Male	154 (77.8)	140 (69.7)	
Grade (%)	High	179 (90.4)	200 (99.5)	<0.001
	Low	19 (9.6)	1 (0.5)	
Age		66.62 ± 10.64	69.08 ± 10.24	0.019
Signature		1.92 ± 0.33	2.69 ± 0.26	<0.001

TABLE 3 | Summary of clinical features in the GSE13507 cohort.

	Level	Low risk	High risk	*p*
Survival time		55.60 ± 37.87	29.70 ± 30.42	<0.001
Survival status (%)	0	108 (90.8)	25 (54.3)	<0.001
	1	11 (9.2)	21 (45.7)	
Stage (%)	≤Stage II	106 (89.1)	23 (50.0)	<0.001
	>Stage II	13 (10.9)	23 (50.0)	
Sex (%)	Female	17 (14.3)	13 (28.3)	0.063
	Male	102 (85.7)	33 (71.7)	
Type (%)	MIBC	25 (21.0)	37 (80.4)	<0.001
	NMIBC	94 (79.0)	9 (19.6)	
Grade (%)	High	27 (22.7)	33 (71.7)	<0.001
	Low	92 (77.3)	13 (28.3)	
Age		64.59 ± 12.65	66.72 ± 9.98	0.258
Signature		4.57 ± 0.26	5.26 ± 0.19	<0.001

Assessing the Prognostic Value of the Signature in the External Validation E-MTAB-4321 Cohort

To validate the 15-gene signature predictive values in other BCa cohorts, the same formula was conducted in the E-MTAB-4321 dataset to generate the risk score of each patient. Similarly, patients were divided into a high-risk group and a low-risk group based on the median risk score as the cutoff point (**Supplementary Figure S2C**). Consistent with the results in the TCGA-BLCA cohort, the low-risk group exhibited a shorter overall survival time than the high-risk group ($p < 0.001$, HR = 10.56, and 95% CI: 3.21–34.73, **Figure 5E**), and the AUC was 0.829, with a 95% CI of 0.758–0.900 (**Figure 5F**). We also assessed the prognostic value in different subgroups of patients. The signature was meaningful for BCa patients in the subgroups of age < = 70 years old ($p = 0.004$), age >70 years old ($p < 0.001$), stage CIS and Ta ($p = 0.004$), stage T1–T4 ($p = 0.019$), male sex ($p < 0.001$), low grade ($p < 0.001$), and high grade ($p = 0.045$) in the E-MTAB-4321 cohort (**Supplementary Figure S5**).

Independent Prognostic Value of the Risk Score

To further explore the signature usage, multivariate Cox regression analysis was performed in the TCGA-BLCA cohort, and as the results showed, age, stage, and risk score were independent prognostic factors ($p < 0.001$). Even after adjusting for the impact of other clinical features, the signature defined high-risk patients as having an approximately 2.22-fold higher risk of death than low-risk patients (**Figure 6A**). A combined nomogram enrolling both the signature classifier and other clinical features demonstrated a better prognostic value (AUC: 0.740, 95% CI: 0.683–0.796, **Figure 6B**). For the GSE13507 cohort, we also revealed similar findings. The prognostic signatures defined as high-risk patients had a 2.90-fold higher risk of death than low-risk patients, which acted as an independent prognostic factor after adjusting for the features of age, tumor stage, sex, and grade (**Figure 6C**). Moreover, the combined nomogram illustrated a prognostic AUC value as high as 0.960, with a 95% CI of 0.928–0.992 (**Figure 6D**). For the E-MTAB-4321 cohort, the prognostic signatures defined as high-risk patients had a 6.13-fold risk of BCa recurrence compared with low-risk patients, which acted as an independent prognostic factor after adjusting for the features of age, T stage, sex, and grade (**Figure 6E**). The combined nomogram illustrated a prognostic AUC value as high as 0.912, with a 95% CI of 0.866–0.959 (**Figure 6F**).

Exploring the Appropriate Targeted Therapy for BCa Patients

Six chemotherapy drugs, cisplatin, doxorubicin, mitomycin, paclitaxel, vinblastine, and gemcitabine, are commonly used for the clinical treatment of BCa. We compared the response of the six drugs by assessing the IC50 after comparison with the GDSC data. We found that patients in the high-risk group were more suitable for treatment with gemcitabine, doxorubicin, cisplatin, paclitaxel, and vinblastine (all $p < 0.05$), but not mitomycin ($p = 0.06$, **Figure 7A**). For immunotherapy, especially anti-PD-L1 therapy, we employed the gene expression data of the IMvigor210 cohort. After comparing the similarity of the gene expression profile of responders with the patients in both the high-risk and low-risk groups, we found that both patients in the two subgroups were not suitable for treatment with anti-PD-L1 therapy (**Figure 7B**).

Knockdown of HEYL Inhibited the Proliferation and Invasion of BCa Cells

To evaluate the functions of the newly defined signature, we evaluated the phenotypic alterations of BCa cells after knockdown HEYL, due to the fact that HEYL was given a large weight of 0.111 in the risk score formula. We transferred the control, si-HEYL-1#, and si-HEYL-2# by the Lipofectamine 3,000 system to both T24 and 5,637 cells and observed decreased protein levels of HEYL (**Figures 8A,B)**. Cell viability was also inhibited after knockdown by two siRNAs (**Figures 8A,B**). For cell invasion, which represents tumor malignancy, we observed similar results: the invaded cell numbers significantly decreased

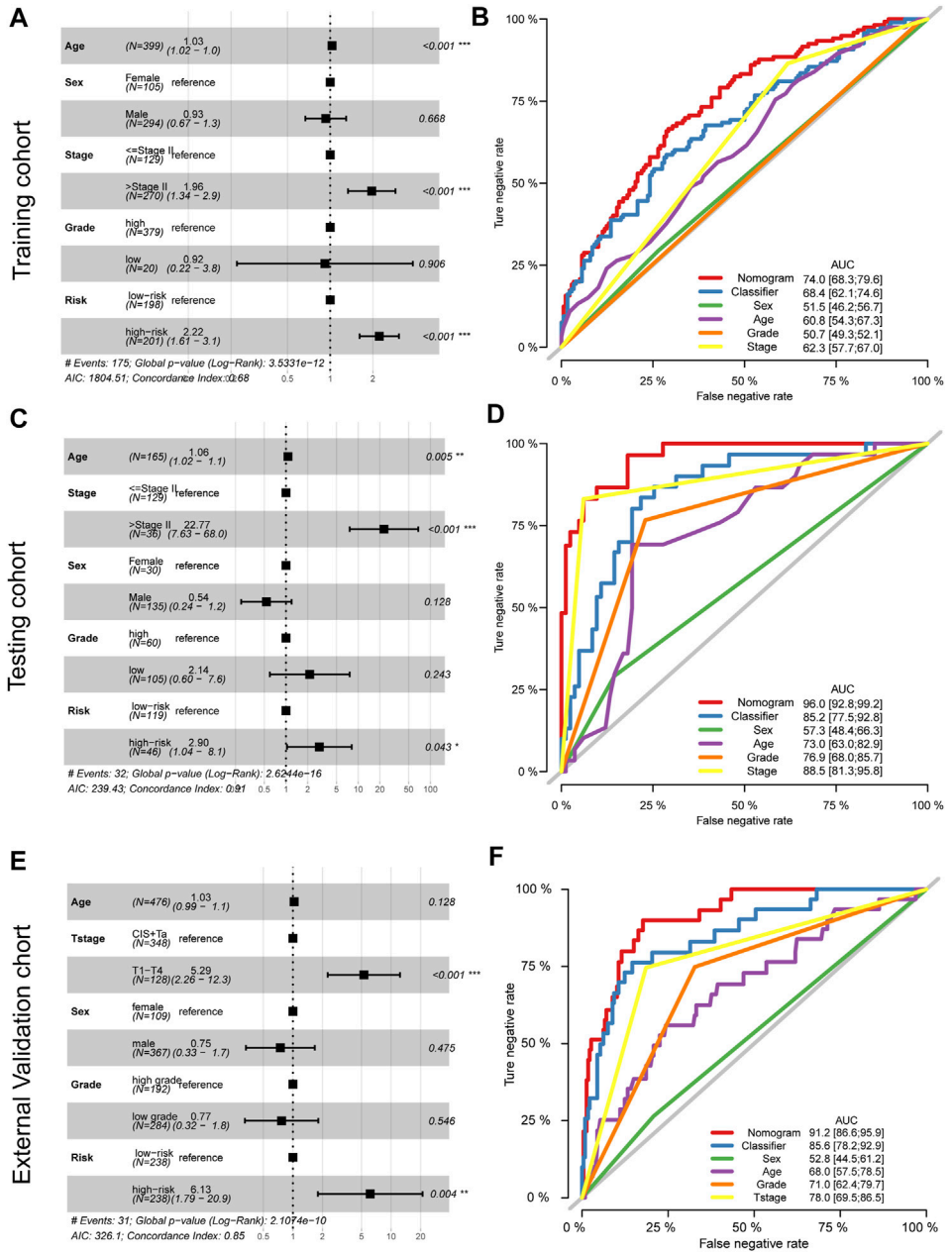

FIGURE 6 | Adjustment and combination of the clinical features with the prognostic signature. Multivariate Cox analysis and forest plot revealed the independent prognostic value of the signature in the training TCGA-BLCA cohort **(A)**, testing GSE13507 cohort **(C)**, and external validation cohort **(E)**. The combination nomogram of the signature and clinical features displays a preferred prognostic value in the training TCGA-BLCA cohort **(B)**, testing GSE13507 cohort **(D)**, and external validation cohort **(F)**.

in the si-HEYL-1# (all $p < 0.001$, **Figure 8C**) and si-HEL-2# (all $p < 0.01$, **Figure 8D**) groups compared with the control group in both T24 and 5,637 cells.

DISCUSSION

BCa ranks as the fourth most common malignant cancer among men in the Western world (Kirkali et al., 2005). BCa is a type of tumor with a strong correlation between age and sex. The median age at diagnosis is approximately 65–70 years old. The incidence rate in men is 3–4 times that in women (Chen et al., 2018). However, according to the Global Cancer Incidence and Mortality Survey, the age-standardized rates (ASRs per 100,000) of women are 5.7, and the ASRs of men are 9.6, suggesting that the stage-adjusted survival of BCa in women is poorer than that in men (Ferlay et al., 2019). There is a detectable difference among variant races and regions or countries. For

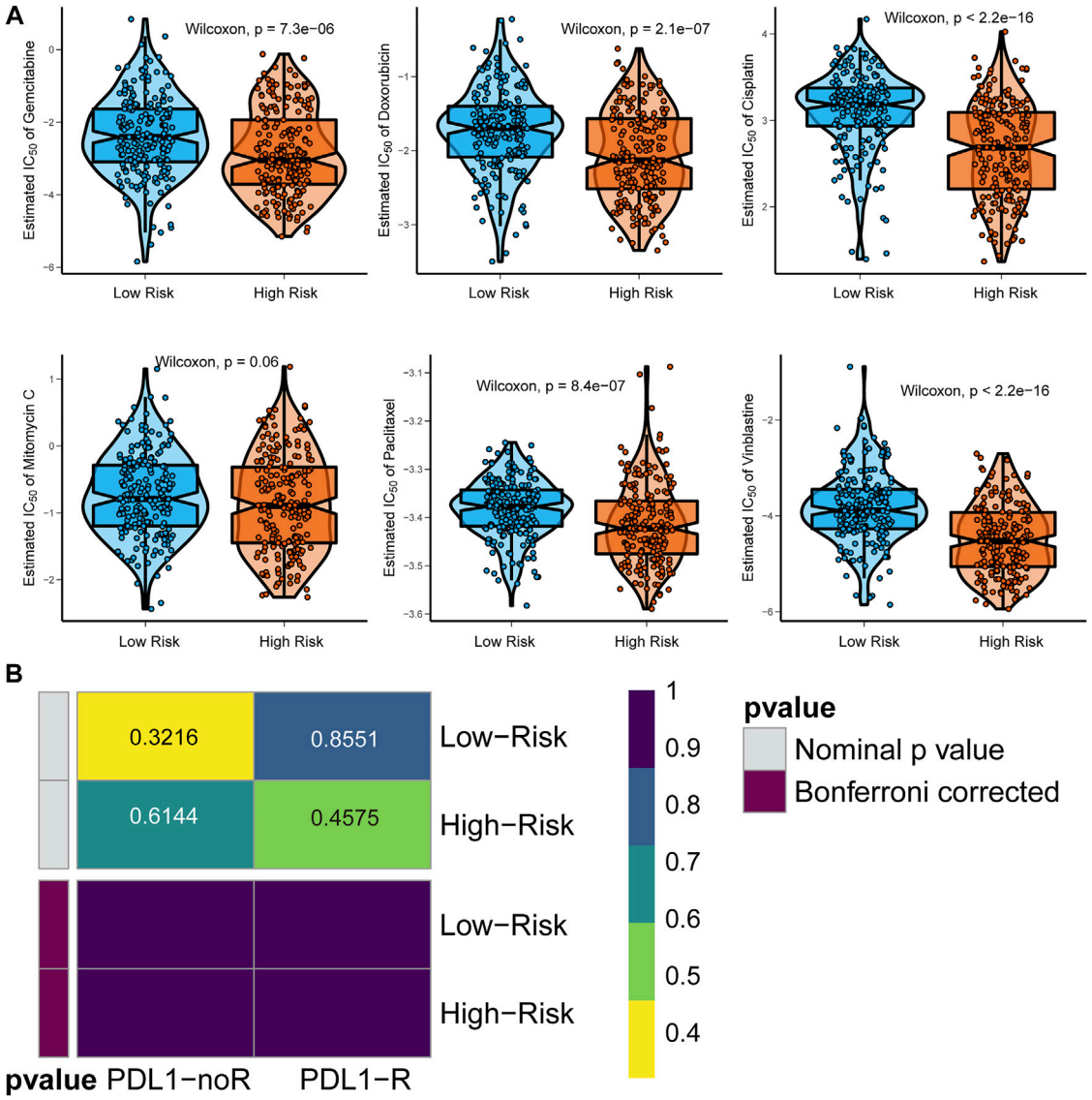

FIGURE 7 | Identification of appropriate targeted therapy for BCa patients. **(A)** Appropriate chemotherapy for signature-defined high-risk and low-risk patients. **(B)** Appropriate anti-PD-L1 immunotherapy for signature-defined high-risk and low-risk patients.

instance, white Americans are more susceptible to BCa than African Americans. On the other hand, white Americans are more likely to evolve into invasive tumors and have a higher mortality rate than African Americans (Uno et al., 2000). With the development of sequencing and complementary technologies, molecular classification methods based on genes have been increasingly studied. Compared to the traditional pathology-based classification, a novel subtyping strategy involves more tumor biological information and is expected to have broad application prospects.

Great progress has been made in the study of gene expression profiles and cancer prognosis. For instance, patients with HER2-enriched breast cancer have poor clinical outcomes, but they are sensitive to neoadjuvant chemotherapy, which can greatly benefit this group (Ross et al., 2003). However, only limited data are available for predicting BCa and prognosis to date. Different teams generate a distinct subtyping system, and each has its own characteristics and validity. Either they were created to cater to a specific clinical therapy project or relied on a robust statistical method without considering the cancer biological process at data analysis (Zhu et al., 2020). In our study, we downloaded two data sets from different sources, and a total of 107 prognostic genes were identified for LASSO analysis. To further explore the functions of the 107 candidate genes, GO enrichment analysis was performed. As the results showed, the candidate gene expression was mainly involved in five pathways, including extracellular matrix organization, extracellular structure organization, ossification, collagen fibril organization, and osteoblast differentiation. Moreover, we established the prognostic signature by LASSO analysis of selected genes and

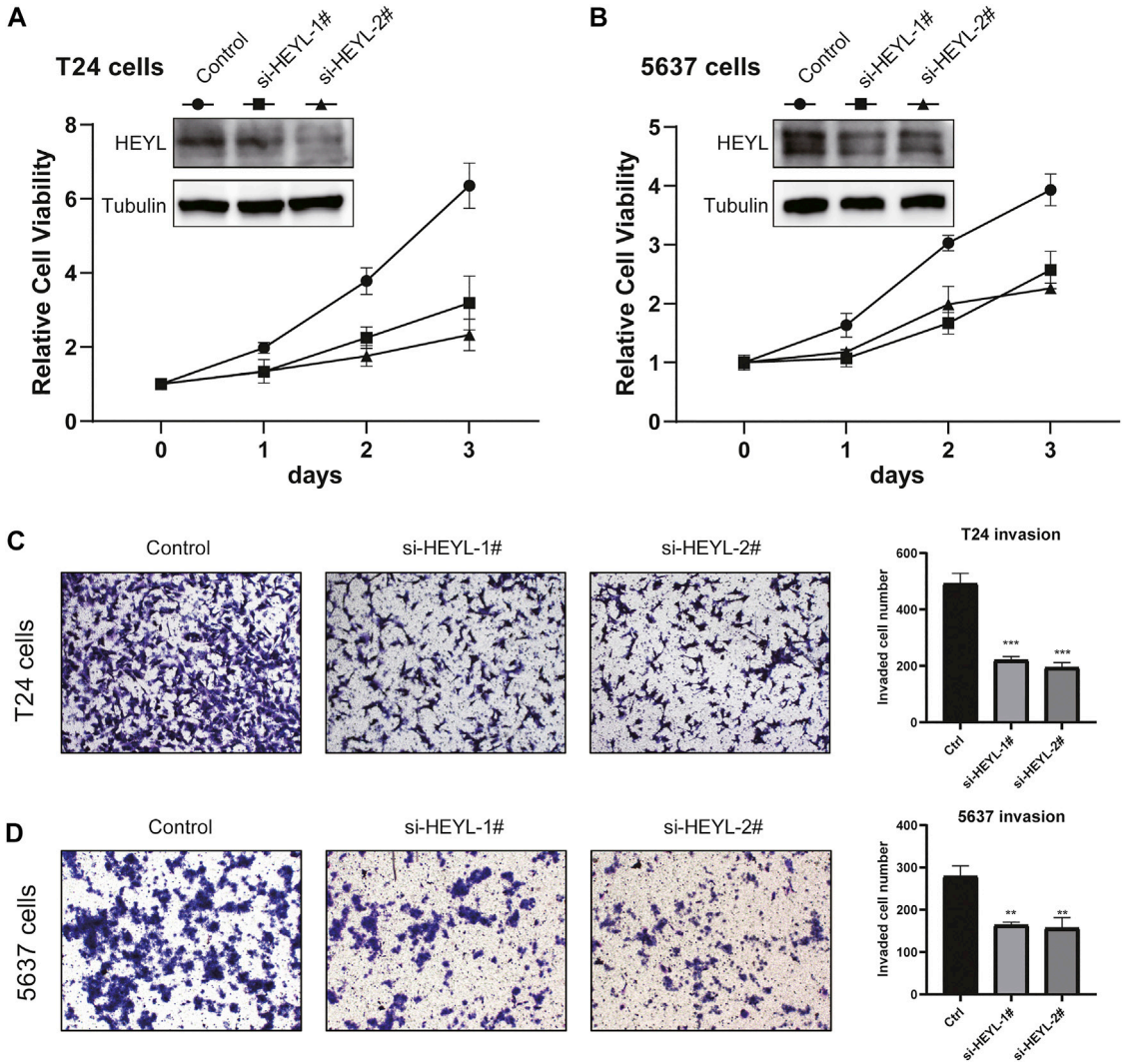

FIGURE 8 | Phenotypic validation of HEYL knockdown in BCa cell lines. **(A)** Knockdown of HEYL inhibited the viability of T24 cells. **(B)** Knockdown of HEYL inhibited the viability of 5,637 cells. **(C)** Knockdown of HEYL inhibited the invasion of T24 cells. **(D)** Knockdown of HEYL inhibited the invasion of 5,637 cells.

generated a risk predictive model with one of them. The formula risk score = $\sum_{i=1}^{n} \alpha * Xi$ (αrepresent coef. min) was used to calculate the risk score of each patient. Selecting an optimal cutoff point, the high-risk group and low-risk group were separated. With a robust statistical method, we found that patients in the high-risk group exhibited a worse prognosis than those in the low-risk group. Independently, the same formula and statistical strategy were performed on the testing GSE13507 cohort and external validation E-MTAB-4321 cohort to assess the efficacy of the model, and the result was similar to that in the TCGA-BLCA cohort. Furthermore, we also realized that the newly defined signature is an independent prognostic signature after adjusting for the clinical features of age, tumor stage, sex, and grade.

For the 15 genes enrolled for the calculation of the prognostic signature, several basic experiments have already demonstrated their function in the tumorigenesis of BCa. DNTA plays a role in cell signal transduction and mediates the Notch1 pathway axis. This pathway was reported to be an essential regulator in cell proliferation, differentiation, and apoptosis (Kim M. Y et al., 2010), and the Notch1 pathway has also been proven to contribute to the metastasis of various malignancies, including ovarian, breast, lung, and renal cancer (Kong et al., 2016). HEYL is the target gene of the Notch1 pathway, and there is limited information on the impact of its target gene HEYL. The results of Weber et al. showed that an enhanced expression level of HEYL decreased cancer cell dissemination and the absolute number of metastases formed, while the capacity of cell metastasis remained good, indicating that HEYL can function as a negative regulator by inhibiting the infiltration of metastasis-initiating cells (Weber et al., 2019). At the same time, we found two other tumor suppression genes, SETBP1 and SULF1 (Lai et al., 2008; Li et al., 2020). It was reported that decreased expression of SETBP1 contributed to the development of non-small-cell lung

cancer cells by increasing tumor cell proliferation, migration, and invasion and was associated with poor prognosis. In addition, other studies have claimed that SETBP1 expression is associated with acute myeloid leukemia and that microRNA-211-5p directly targets SETBP1 to inhibit triple-negative breast cancer cell proliferation, migration and metastasis (Chen et al., 2017). SULF1 is increasingly considered for its tumor suppressor effect. The target pathways related to the effect of SULF1 include hedgehog, Wnt, and multiple heparan sulfate-dependent receptor tyrosine kinase pathways, which may prove to be an important method to prevent and treat cancer (Lai et al., 2008).

We also revealed six oncogenes that have been validated to be related to the poor prognosis of patients with cancer: CTSE, CALM1, PHGDH, IL9R, and CD96 (Boulay et al., 2001; Possemato et al., 2011; Yan et al., 2011; Pontious et al., 2019; Salazar et al., 2020; Zhao et al., 2020; Liu et al., 2021). CTSE is an intracellular hydrolytic aspartic protease that has been found to be overexpressed in cancer tissues. With the help of endoscopy and immunosorbent assay (ELISA) and Western blot, CTSE was considered a better biomarker than CA19-9 for detecting pancreatic cancer. CALM1, a calcium ion (Ca2+) receptor protein, is responsible for mediating various signaling processes. Overexpression of CALM1 in cancer is significantly related to clinical stage, T classification, and poor prognosis. The function of CALM1 depends on the synergy of ERGF, and similar to anti-EGFR antibodies, CALM1 inhibitors play an essential role in cancer chemotherapy (Liu et al., 2021). PHGDH is a key enzyme in the serine synthesis pathway. Serine is an intermediate of other amino acids and lipid and nucleic acid synthesis pathways (Locasale et al., 2011) and thus promotes cancer progression. Studies have shown that PHGDH is a reliable biomarker and independent factor predicting prognosis (Song et al., 2018). IL9 is a multifunctional cytokine involved in many pathways in the cell and plays opposite roles in different tumors. For instance, IL9 inhibited the proliferation of the gastric cancer cell line SGC-7901 *in vitro* (Cai et al., 2019) through the activation of adaptive or innate immune responses. However, IL9 can act as a tumorigenic factor or an enhancing factor to promote the proliferation of hematological tumors and some solid tumors (Chen and Wang, 2014; Hu et al., 2017). CD96 is mainly involved in immune function, especially the immune response mediated by T cells. CD96 can promote cancer metastasis by enhancing NK cell-target adhesion and inhibiting the NK-mediated cytokine response (Liu et al., 2020). Interestingly, high expression of CD96 inhibits IL9 production in Th9 cells (Stanko et al., 2018).

The expression level of SERPINB2 was consistent with carcinogen exposure, indicating that SEPRINB2 may provide sensitive and accurate information for the beginning of tumorigenic events (Lee et al., 2019). SERPINB2 was also reported as a regulator or biomarker for predicting the malignant progression of colorectal and bladder cancer (Ganesh et al., 1994; Champelovier et al., 2002). Importantly, an increase in SERPINB2 was detected with most of the additional tested tumorigenic substances, which adds more evidence for SEPRINB2 as a potential biomarker. Liu et al. found that COMP was an excellent prognostic factor and biomarker of colon cancer equivalent to noninvasive biomarker performance, such as CA-199 (Liu et al., 2018). Studies have shown that COMP contributes to the development and metastasis of breast cancer. The enhanced expression level of COMP in tumor cells is significantly related to the reduced breast cancer-specific survival rate and recurrence-free survival rate of patients, while the expression level of COMP in the stroma has a poor connection with prognosis (Englund et al., 2016). CCRN4L, a type of clock-control gene, is a key component in the regulation of circadian rhythms (Filipski and Lévi, 2009). It was considered that the expression of clock-control genes changed in some cancer groups, and polymorphisms in the CCRN4L gene may contribute to the genesis of NSCLC in Brazilian patients (Couto et al., 2014). FADS2 is a potential oncogene (Tian et al., 2020). Several cancers have been validated to utilize FADS2 to desaturate palmitate to the unusual fatty acid sapienate, which can be applied to the biosynthesis of the membrane. Sapienate biosynthesis is an alternative method for fatty acid desaturation metabolism in cancer cells (Vriens et al., 2019).

As we know, this is the first study that concerned the top prognosis prediction genes to construct the signature; we selected the top prognostic genes with the high AUC values in both TCGA-BLCA and GSE13507 cohorts, and the highly prognostic efficacy of the 15-gene signature was displayed in both TCGA-BLCA and GSE13507 cohorts, as well as the external validation E-MTAB-4321 cohort. Meanwhile, several limitations of the current study should be illustrated. First, real-world patient cohort is needed to further validate the prognostic value of the 15-gene signature. Second, experimental studies of the enrolled 15 genes are necessary to further reveal the potential mechanisms of them in BCa tumorigenesis. Third, the strength of evidence for the significance of therapy is not enough, and further mechanism study and clinical experiment should be conducted to evaluate the targeted therapy efficacy.

CONCLUSION

As gene mutation events accumulate, tumor cells gradually develop. Molecular changes occur earlier than clinical symptom onset and overt radiographic evidence. Therefore, molecular classifiers are considered promising tools for the early prediction of tumors. BCa is a disease with multiple factors and heterogeneity, and traditional classification cannot reflect the actual situation and prognosis. In the current study, we enrolled 15 genes that can delineate BCa from multiple angles, and the 15-gene classifier was validated to be associated with the clinical outcome and response to targeted therapy of patients with BCa.

DATA AVAILABILITY STATEMENT

The datasets presented in this study can be found in online repositories. The names of the repository/repositories and accession number(s) can be found in the article/**Supplementary Material**.

AUTHOR CONTRIBUTIONS

HG designed the study; HG and CL analyzed the data, made the figures, and drafted the manuscript; CL revised the whole paper and approved the final paper. All authors read and approved the final manuscript.

SUPPLEMENTARY MATERIAL

The Supplementary Material for this article can be found online at: https://www.frontiersin.org/articles/10.3389/fcell.2022.725024/full#supplementary-material

REFERENCES

Antoni, S., Ferlay, J., Soerjomataram, I., Znaor, A., Jemal, A., and Bray, F. (2017). Bladder Cancer Incidence and Mortality: A Global Overview and Recent Trends. *Eur. Urol.* 71 (1), 96–108. doi:10.1016/j.eururo.2016.06.010

Boulay, A., Masson, R., Chenard, M. P., El Fahime, M., Cassard, L., Bellocq, J. P., et al. (2001). High Cancer Cell Death in Syngeneic Tumors Developed in Host Mice Deficient for the Stromelysin-3 Matrix Metalloproteinase. *Cancer Res.* 61, 2189.

Cai, L., Zhang, Y., Zhang, Y., Chen, H., and Hu, J. (2019). Effect of Th9/IL-9 on the Growth of Gastric Cancer in Nude Mice. *Ott* 12, 2225–2234. doi:10.2147/ott.S197816

Chamie, K., Litwin, M. S., Bassett, J. C., Daskivich, T. J., Lai, J., Hanley, J. M., et al. (2013). Recurrence of High-Risk Bladder Cancer: a Population-Based Analysis. *Cancer* 119 (17), 3219–3227. doi:10.1002/cncr.28147

Champelovier, P., Boucard, N., Levacher, G., Simon, A., Seigneurin, D., and Praloran, V. (2002). Plasminogen- and colony-stimulating Factor-1-Associated Markers in Bladder Carcinoma: Diagnostic Value of Urokinase Plasminogen Activator Receptor and Plasminogen Activator Inhibitor Type-2 Using Immunocytochemical Analysis. *Urol. Res.* 30 (5), 301–309. doi:10.1007/s00240-002-0270-5

Chen, L.-l., Zhang, Z.-j., Yi, Z.-b., and Li, J.-j. (2017). MicroRNA-211-5p Suppresses Tumour Cell Proliferation, Invasion, Migration and Metastasis in Triple-Negative Breast Cancer by Directly Targeting SETBP1. *Br. J. Cancer* 117 (1), 78–88. doi:10.1038/bjc.2017.150

Chen, N., and Wang, X. (2014). Role of IL-9 and STATs in Hematological Malignancies (Review). *Oncol. Lett.* 7 (3), 602–610. doi:10.3892/ol.2013.1761

Chen, W., Sun, K., Sun, K., Zheng, R., Zeng, H., Zhang, S., et al. (2018). Cancer Incidence and Mortality in China, 2014. *Chin. J. Cancer Res.* 30 (1), 1–12. doi:10.21147/j.issn.1000-9604.2018.01.01

Couto, P., Miranda, D., Vieira, R., Vilhena, A., De Marco, L., and Bastos-Rodrigues, L. (2014). Association between CLOCK, PER3 and CCRN4L with Non-small Cell Lung Cancer in Brazilian Patients. *Mol. Med. Rep.* 10 (1), 435–440. doi:10.3892/mmr.2014.2224

Englund, E., Bartoschek, M., Reitsma, B., Jacobsson, L., Escudero-Esparza, A., Orimo, A., et al. (2016). Cartilage Oligomeric Matrix Protein Contributes to the Development and Metastasis of Breast Cancer. *Oncogene* 35 (43), 5585–5596. doi:10.1038/onc.2016.98

Farling, K. B. (2017). Bladder Cancer: Risk Factors, Diagnosis, And Management. *Nurse Pract.* 42 (3), 26–33. doi:10.1097/01.NPR.0000512251.61454.5c

Ferlay, J., Colombet, M., Soerjomataram, I., Mathers, C., Parkin, D. M., Piñeros, M., et al. (2019). Estimating the Global Cancer Incidence and Mortality in 2018: GLOBOCAN Sources and Methods. *Int. J. Cancer* 144 (8), 1941–1953. doi:10.1002/ijc.31937

Filipski, E., and Lévi, F. (2009). Circadian Disruption in Experimental Cancer Processes. *Integr. Cancer Ther.* 8 (4), 298–302. doi:10.1177/1534735409352085

Ganesh, S., Sier, C. F., Griffioen, G., Vloedgraven, H. J., de Boer, A., Welvaart, K., et al. (1994). Prognostic Relevance of Plasminogen Activators and Their Inhibitors in Colorectal Cancer. *Cancer Res.* 54 (15), 4065–4071.

Hautmann, R. E., Gschwend, J. E., de Petriconi, R. C., Kron, M., and Volkmer, B. G. (2006). Cystectomy for Transitional Cell Carcinoma of the Bladder: Results of a Surgery Only Series in the Neobladder Era. *J. Urol.* 176 (2), 486–492. doi:10.1016/j.juro.2006.03.038

Hedegaard, J., Lamy, P., Nordentoft, I., Algaba, F., Høyer, S., Ulhøi, B. P., et al. (2016). Comprehensive Transcriptional Analysis of Early-Stage Urothelial Carcinoma. *Cancer Cell* 30 (1), 27–42. doi:10.1016/j.ccell.2016.05.004

Hu, B., Qiu-Lan, H., Lei, R. E., Shi, C., Jiang, H. X., and Qin, S. Y. (2017). Interleukin-9 Promotes Pancreatic Cancer Cells Proliferation and Migration via the miR-200a/Beta-Catenin Axis. *Biomed. Res. Int.* 2017, 2831056. doi:10.1155/2017/2831056

Kim, M.-Y., Ann, E.-J., Mo, J.-S., Dajas-Bailador, F., Seo, M.-S., Hong, J.-A., et al. (2010). JIP1 Binding to RBP-Jk Mediates Cross-Talk between the Notch1 and JIP1-JNK Signaling Pathway. *Cell Death Differ* 17 (11), 1728–1738. doi:10.1038/cdd.2010.50

Kim, W.-J., and Bae, S.-C. (2008). Molecular Biomarkers in Urothelial Bladder Cancer. *Cancer Sci.* 99 (4), 646–652. doi:10.1111/j.1349-7006.2008.00735.x

Kim, W.-J., Kim, E.-J., Kim, S.-K., Kim, Y.-J., Ha, Y.-S., Jeong, P., et al. (2010). Predictive Value of Progression-Related Gene Classifier in Primary Non-muscle Invasive Bladder Cancer. *Mol. Cancer* 9, 3. doi:10.1186/1476-4598-9-3

Kim, W.-J., and Quan, C. (2005). Genetic and Epigenetic Aspects of Bladder Cancer. *J. Cel. Biochem.* 95 (1), 24–33. doi:10.1002/jcb.20412

Kirkali, Z., Chan, T., Manoharan, M., Algaba, F., Busch, C., Cheng, L., et al. (2005). Bladder Cancer: Epidemiology, Staging and Grading, and Diagnosis. *Urology* 66 (6), 4–34. doi:10.1016/j.urology.2005.07.062

Kong, R., Feng, J., Ma, Y., Zhou, B., Li, S., Zhang, W., et al. (2016). Silencing NACK by siRNA Inhibits Tumorigenesis in Non-small Cell Lung Cancer via Targeting Notch1 Signaling Pathway. *Oncol. Rep.* 35 (4), 2306–2314. doi:10.3892/or.2016.4552

Lai, J. P., Sandhu, D. S., Shire, A. M., and Roberts, L. R. (2008). The Tumor Suppressor Function of Human Sulfatase 1 (SULF1) in Carcinogenesis. *J. Gastrointest. Cancer* 39 (1-4), 149–158. doi:10.1007/s12029-009-9058-y

Lee, N. H., Park, S. R., Lee, J. W., Lim, S., Lee, S. H., Nam, S., et al. (2019). SERPINB2 Is a Novel Indicator of Cancer Stem Cell Tumorigenicity in Multiple Cancer Types. *Cancers (Basel)* 11 (4), 499. doi:10.3390/cancers11040499

Li, H. R., Gao, J., Jin, C., Jiang, J. H., and Ding, J. Y. (2020). Downregulation of SETBP1 Promoted Non-small Cell Lung Cancer Progression by Inducing Cellular EMT and Disordered Immune Status. *Am. J. Transl Res.* 12 (2), 447–462.

Liu, F., Huang, J., He, F., Ma, X., Fan, F., Meng, M., et al. (2020). CD96, a New Immune Checkpoint, Correlates with Immune Profile and Clinical Outcome of Glioma. *Sci. Rep.* 10 (1), 10768. doi:10.1038/s41598-020-66806-z

Liu, T.-t., Liu, X.-s., Zhang, M., Liu, X.-n., Zhu, F.-x., Zhu, F.-m., et al. (2018). Cartilage Oligomeric Matrix Protein Is a Prognostic Factor and Biomarker of colon Cancer and Promotes Cell Proliferation by Activating the Akt Pathway. *J. Cancer Res. Clin. Oncol.* 144 (6), 1049–1063. doi:10.1007/s00432-018-2626-4

Liu, T., Han, X., Zheng, S., Liu, Q., Tuerxun, A., Zhang, Q., et al. (2021). CALM1 Promotes Progression and Dampens Chemosensitivity to EGFR Inhibitor in Esophageal Squamous Cell Carcinoma. *Cancer Cel Int* 21 (1), 121. doi:10.1186/s12935-021-01801-6

Locasale, J. W., Grassian, A. R., Melman, T., Lyssiotis, C. A., Mattaini, K. R., Bass, A. J., et al. (2011). Phosphoglycerate Dehydrogenase Diverts Glycolytic Flux and Contributes to Oncogenesis. *Nat. Genet.* 43 (9), 869–874. doi:10.1038/ng.890

Meng, J., Lu, X., Zhou, Y., Zhang, M., Ge, Q., Zhou, J., et al. (2021). Tumor Immune Microenvironment-Based Classifications of Bladder Cancer for Enhancing the Response Rate of Immunotherapy. *Mol. Ther. - Oncolytics* 20 (2021), 410–421. doi:10.1016/j.omto.2021.02.001

Mo, Q., Nikolos, F., Chen, F., Tramel, Z., Lee, Y.-C., Hayashi, K., et al. (2018). Prognostic Power of a Tumor Differentiation Gene Signature for Bladder Urothelial Carcinomas. *JNCI: J. Natl. Cancer Inst.* 110 (5), 448–459. doi:10.1093/jnci/djx243

Pang, C., Guan, Y., Li, H., Chen, W., and Zhu, G. (2016). Urologic Cancer in China. *Jpn. J. Clin. Oncol.* 46 (6), 497–501. doi:10.1093/jjco/hyw034

Pontious, C., Kaul, S., Hong, M., Hart, P. A., Krishna, S. G., Lara, L. F., et al. (2019). Cathepsin E Expression and Activity: Role in the Detection and Treatment of Pancreatic Cancer. *Pancreatology* 19 (7), 951–956. doi:10.1016/j.pan.2019.09.009

Possemato, R., Marks, K. M., Shaul, Y. D., Pacold, M. E., Kim, D., Birsoy, K., et al. (2011). Functional Genomics Reveal that the Serine Synthesis Pathway Is Essential in Breast Cancer. *Nature* 476 (7360), 346–350. doi:10.1038/nature10350

Ross, J. S., Fletcher, J. A., Linette, G. P., Stec, J., Clark, E., Ayers, M., et al. (2003). The Her-2/neu Gene and Protein in Breast Cancer 2003: Biomarker and Target of Therapy. *Oncologist* 8 (4), 307–325. doi:10.1634/theoncologist.8-4-307

Salazar, Y., Zheng, X., Brunn, D., Raifer, H., Picard, F., Zhang, Y., et al. (2020). Microenvironmental Th9 and Th17 Lymphocytes Induce Metastatic Spreading in Lung Cancer. *J. Clin. Invest.* 130 (7), 3560–3575. doi:10.1172/JCI124037

Sjödahl, G., Lauss, M., Lövgren, K., Chebil, G., Gudjonsson, S., Veerla, S., et al. (2012). A Molecular Taxonomy for Urothelial Carcinoma. *Clin. Cancer Res.* 18 (12), 3377–3386. doi:10.1158/1078-0432.Ccr-12-0077-t

Song, Z., Feng, C., Lu, Y., Lin, Y., and Dong, C. (2018). PHGDH Is an Independent Prognosis Marker and Contributes Cell Proliferation, Migration and Invasion in Human Pancreatic Cancer. *Gene* 642, 43–50. doi:10.1016/j.gene.2017.11.014

Stanko, K., Iwert, C., Appelt, C., Vogt, K., Schumann, J., Strunk, F. J., et al. (2018). CD96 Expression Determines the Inflammatory Potential of IL-9-producing Th9 Cells. *Proc. Natl. Acad. Sci. USA* 115 (13), E2940–e2949. doi:10.1073/pnas.1708329115

Subramanian, A., Tamayo, P., Mootha, V. K., Mukherjee, S., Ebert, B. L., Gillette, M. A., et al. (2005). Gene Set Enrichment Analysis: a Knowledge-Based Approach for Interpreting Genome-wide Expression Profiles. *Proc. Natl. Acad. Sci.* 102 (43), 15545–15550. doi:10.1073/pnas.0506580102

Tian, J., Lou, J., Cai, Y., Rao, M., Lu, Z., Zhu, Y., et al. (2020). Risk SNP-Mediated Enhancer-Promoter Interaction Drives Colorectal Cancer through Both FADS2 and AP002754.2. *Cancer Res.* 80 (9), 1804–1818. doi:10.1158/0008-5472.CAN-19-2389

Tsang, J. Y. S., and Tse, G. M. (2020). Molecular Classification of Breast Cancer. *Adv. Anat. Pathol.* 27 (1), 27–35. doi:10.1097/pap.0000000000000232

Uno, K., Azuma, T., Nakajima, M., Yasuda, K., Hayakumo, T., Mukai, H., et al. (2000). Clinical Significance of Cathepsin E in Pancreatic Juice in the Diagnosis of Pancreatic Ductal Adenocarcinoma. *J. Gastroenterol. Hepatol.* 15 (11), 1333–1338. doi:10.1046/j.1440-1746.2000.02351.x

Vriens, K., Christen, S., Parik, S., Broekaert, D., Yoshinaga, K., Talebi, A., et al. (2019). Evidence for an Alternative Fatty Acid Desaturation Pathway Increasing Cancer Plasticity. *Nature* 566 (7744), 403–406. doi:10.1038/s41586-019-0904-1

Weber, S., Koschade, S. E., Hoffmann, C. M., Dubash, T. D., Giessler, K. M., Dieter, S. M., et al. (2019). The Notch Target Gene HEYL Modulates Metastasis Forming Capacity of Colorectal Cancer Patient-Derived Spheroid Cells *In Vivo*. *BMC Cancer* 19 (1), 1181. doi:10.1186/s12885-019-6396-4

Yan, D., Dai, H., and Liu, J.-W. (2011). Serum Levels of MMP-11 Correlate with Clinical Outcome in Chinese Patients with Advanced Gastric Adenocarcinoma. *BMC Cancer* 11, 151. doi:10.1186/1471-2407-11-151

Yu, G., Wang, L.-G., Han, Y., and He, Q.-Y. (2012). clusterProfiler: an R Package for Comparing Biological Themes Among Gene Clusters. *OMICS: A J. Integr. Biol.* 16 (5), 284–287. doi:10.1089/omi.2011.0118

Zhao, X., Fu, J., Du, J., and Xu, W. (2020). The Role of D-3-Phosphoglycerate Dehydrogenase in Cancer. *Int. J. Biol. Sci.* 16 (9), 1495–1506. doi:10.7150/ijbs.41051

Zhu, S., Yu, W., Yang, X., Wu, C., and Cheng, F. (2020). Traditional Classification and Novel Subtyping Systems for Bladder Cancer. *Front. Oncol.* 10, 102. doi:10.3389/fonc.2020.00102

Conflict of Interest: The authors declare that the research was conducted in the absence of any commercial or financial relationships that could be construed as a potential conflict of interest.

Publisher's Note: All claims expressed in this article are solely those of the authors and do not necessarily represent those of their affiliated organizations, or those of the publisher, the editors, and the reviewers. Any product that may be evaluated in this article, or claim that may be made by its manufacturer, is not guaranteed or endorsed by the publisher.

frontiers | Frontiers in Cell and Developmental Biology

MINI REVIEW
published: 02 May 2022
doi: 10.3389/fcell.2022.892067

Urinary Markers for Bladder Cancer Diagnosis and Monitoring

Seung-Hwan Jeong[1] *and Ja Hyeon Ku*[1,2]*

[1]Department of Urology, Seoul National University Hospital, Seoul, South Korea, [2]Department of Urology, Seoul National University College of Medicine, Seoul, South Korea

Hematuria is a typical symptom of bladder cancer which enables early detection of bladder cancer. However, reliable diagnostic tools for bladder cancer using urine samples or other non-invasive methods are lacking. Tremendous attempts have been tried and revealed fancy works to convey definitive diagnostic power using urine samples. In this paper, we reviewed urinary markers for bladder cancer and compared their efficacies.

Keywords: bladder cancer, urine marker, diagnosis, Hematuria, screening

INTRODUCTION

Bladder cancer is the 6th most common cancer in men and 17th most common cancer in women. The incidence of bladder cancer is relatively high in developed countries, and because of rapid industrialization, its worldwide incidence is increasing (Saginala et al., 2020). As bladder cancer results in gross or microscopic hematuria, approximately 80% of bladder cancers are diagnosed as non-muscle invasive bladder cancer (NMIBC) (Zhu et al., 2019). However, the recurrence rate of NMIBC is as high as 60% within 1 year of the first diagnosis (Mancini et al., 2020). The gold standard for the confirmative diagnosis of bladder cancer is cystoscopic examination, but its invasiveness hinders its early utilization requiring non-invasive diagnostic marker (Zhu et al., 2019). The bladder is a hollow organ that preserves urine; thus, tremendous attempts have been made to facilitate non-invasive diagnostic tools using urine for bladder cancer. Nevertheless, there have been limitations to these attempts due to the restricted efficacy reflecting the current status, which warrants skipping further cystoscopic examinations. In this review, we summarize the representative tests for bladder cancer using urine and suggest future directions.

URINE CYTOLOGY

Urine cytology examines the morphological changes in exfoliated cells from the urinary tract to assess abnormalities (Woldu et al., 2017). The sensitivity of urine cytology varies with cancer grade. In high-grade urothelial cancer, the sensitivity is as high as 86%, but 20–50% in low-grade cancers (Zhu et al., 2019). Furthermore, urine cytology suffers from subjective results upon examination and variables related to low cellularity, infections, and artifacts. The Paris Working Group released a standardized reporting system for urine cytology to improve the objectivity of results (Barkan et al., 2016). To yield more cellularity, catheterization and washing methods can be attempted in some situations, but are limited because of the invasiveness and artifacts caused by the maneuvers (Sullivan et al., 2010). However, the specificity of urine cytology is 90–100%, empowering its diagnostic value in addition to cystoscopy in high-risk bladder cancer. In bladder cancer patients managed with transurethral resection, urine cytology and cystoscopy examinations are recommended every 3–6 months by the National Comprehensive Cancer Network guidelines (Flaig et al., 2020). Abnormal urine cytology results imply the presence of a tumor, but negative results do not ensure normal conditions.

OPEN ACCESS

Edited by:
Xiaogang Wu,
University of Texas MD Anderson Cancer Center, United States

Reviewed by:
Tao Liu,
Wuhan University, China

***Correspondence:**
Ja Hyeon Ku
kuuro70@snu.ac.kr

Specialty section:
This article was submitted to Cancer Cell Biology, a section of the journal Frontiers in Cell and Developmental Biology

Received: *08 March 2022*
Accepted: *20 April 2022*
Published: *02 May 2022*

Citation:
Jeong S-H and Ku JH (2022) Urinary Markers for Bladder Cancer Diagnosis and Monitoring. Front. Cell Dev. Biol. 10:892067. doi: 10.3389/fcell.2022.892067

OVERVIEW OF URINARY MOLECULAR MARKERS

Molecular Markers

Considering that the purpose of urine testing is to avoid unnecessary cystoscopic examinations, a high negative predictive value is required for molecular marker tests. Unfortunately, the reported markers only provided higher sensitivity with lower specificity compared to urine cytology, hampering their negative predictive value. Thus, none of them is in use with recommendations from the guidelines.

Nuclear Matrix Protein-22

Borderline results from urine cytology, such as atypical cells, are confusing for follow-up and diagnosis. Nuclear matrix protein-22 (NMP-22) mediates the appropriate distribution of chromatin in cellular proliferation and exists at a low level in normal cells but at a level as high as 25 fold in tumorous conditions (Têtu, 2009). NMP-22 improves the positive predictive value of urine cytology from 30 to 60% (Ahn et al., 2011). The NMP-22 Bladder Cancer ELISA Test Kit quantifies the level of NMP-22 in urine to provide a sensitivity of 50–70% and a specificity of 60–90% for cancer detection. However, the variable results between individuals and institutions restrict their use in clinical settings (Murakami et al., 2021). NMP22 BladderChek delivers an easy and direct result within 30 min at the point-of-care, with a sensitivity of 56% and specificity of 88%. These values are especially higher in more advanced-stage cancers. The pooled positive and negative likelihood ratio were 4.36 and 0.51, respectively (Wang et al., 2017). Thus, NMP22 BladderChek can be used in high-risk patients but has limited clinical applications.

Bladder Tumor Antigen (BTA), BTAstat and BTA-TRAK

The bladder tumor antigen (BTA) assay detects complement factor H-related protein released from bladder cancer. BTA stat is a point-of-care form, and BTA-TRAK is an ELISA kit that shares similar sensitivity and specificity of 58 and 73%, respectively (Têtu, 2009; Villicana et al., 2009). BTA analysis is approved by the FDA for monitoring bladder cancer with cystoscopy, but not for initial screening.

UroVysion in Fluorescence *in situ* Hybridization

Bladder cancer exhibits aneuploidy of chromosomes (3, 7, and 17) and deletion of the 9p21 locus. UroVysion uses fluorescence *in situ* hybridization (FISH) to detect chromosomal abnormalities (Villicana et al., 2009). The sensitivity of UroVysion varies depending on the disease status from low to high T stage and tumor grade. The overall sensitivity was approximately 72% and the specificity was 83%, providing a higher diagnostic AUC of 0.867 compared with 0.626 for urine cytology (Villicana et al., 2009). Because of the complicated procedures required by cytopathology experts and expensive equipment, the expansion of this method is restricted.

Urine miRNA

MicroRNAs (miRNAs) are small non-coding RNAs consisting of 20–22 nucleotides, which regulate protein expression through post-transcriptional gene regulation via RNA silencing. The miRNA is transcribed in the nucleus by RNA polymerase II, reading the long primary transcript, and matured by Drosha and Dicer to form a single-stranded structure pairing with the 3' untranslated region of messenger RNAs (mRNAs) (Kuehbacher et al., 2007). miRNAs are relatively stable in body fluids, including blood and urine, compared to mRNA, which allows miRNAs to be an appropriate diagnostic target for bladder cancer. Although the alteration of miRNA has not been fully elucidated in the bladder, miRNA is dysregulated in bladder cancer to promote proliferation and progression through epithelial to mesenchymal transition and inhibit apoptosis (Enokida et al., 2016; Hofbauer et al., 2018). Hofbauer et al. reported a diagnostic model using six miRNAs (let-7c, miR-135a, miR-135b, miR-148a, miR-204, miR-345) to provide a diagnostic AUC of 88.3% (Hofbauer et al., 2018). In a meta-analysis of urine miRNA for bladder cancer detection, a combination test with multiple miRNAs was found to be superior to the single miRNA test (Kutwin et al., 2018). Urinary miRNAs have implications not only for diagnosis, but also for prognosis. For an instance, miR-9, miR-182, and miR-200b have been associated with muscle invasiveness and poor prognosis (Braicu et al., 2015). Huang et al. reported that miR-125b acts as a tumor suppressor and is downregulated in bladder cancer (Ahn et al., 2011). Wang et al. found that the urinary miR-200 family, miR-192, and miR-155 are downregulated in bladder cancer compared with controls (Ahn et al., 2011). The ratio of urinary miR-126 to miR-152 is elevated in bladder cancer, with a sensitivity and specificity of 72 and 82%, respectively (Hanke et al., 2010). Otherwise miR-126, miR-96 show similar sensitivities and specificity of 71–72% and 82–89% (Enokida et al., 2016). The six-miRNA panel of miR-152, miR-148b-3p, miR-3187-3p, miR-15b-5p, miR-27a-3p, and miR-30a-5p had a high diagnostic yield, represented by an AUC of 0.899. Furthermore, high levels of miR-152 and miR-3187-3p were associated with poor recurrence-free survival in NMIBC (Jiang et al., 2015).

Urine Cell-free DNA

Urine cell-free DNA (cfDNA) originates from several sources, including urothelial cells, transrenal circulating DNA, and bacteria (Tse et al., 2021). The majority of urine cfDNAs is from urothelial cells lining the urinary tract, which can be shed off and undergo necrosis or apoptosis to release DNA from the cells. Unlike normal cells, tumor cells release longer DNA segments with higher integrity (Casadio et al., 2013). Thus, a higher proportion of cfDNA to cellular DNA reflects the presence of tumor cells (Ou et al., 2020). Detection of urine cfDNA integrity and mutations is available for assessing bladder cancer. The integrity of urine cfDNA is much higher in bladder cancer than under normal conditions (Brisuda et al., 2016). Furthermore, the length of DNA fragments is relatively longer in bladder cancer, implying that it originates from the necrotic debris of cancer cells (Tse et al., 2021). Urine cfDNA tests can detect bladder cancer with a sensitivity of 57–86% and specificity

of 72–84% (Salvi et al., 2016). The amount of urine cfDNA depends on the volume and concentration of the urine. Thus, urine creatinine-adjusted DNA concentrations can be used for normalization. Notably, urine cfDNA of 400-bp was much more abundant than that of the control, whereas the median concentration was only higher by 1.5 fold in bladder cancers (Tse et al., 2021). Additionally, a urine cfDNA concentration over 250 ng/ml was indicated as the threshold value to predict bladder cancers (Tse et al., 2021). Urine cfDNA sequencing has revealed valuable genetic mutations for the detection of bladder cancer. For an instance, the frequently detected mutations in bladder cancers such as TERT, FGFR3, TP53, PIK3CA, and KRAS were significantly altered in urine cfDNAs showing cancer detection rate using these five gene panel with a AUC confidence interval of 0.94 (Ou et al., 2020). Telomerase reverse transcriptase (TERT) mutations are observed in 60–85% of bladder cancers with frequently mutated promoter regions C228T and C250T (Avogbe et al., 2019). TERT promoter mutations in urinary cell-free and cellular DNA can be detected in urothelial cancer with a sensitivity of 86%, up to 93.9% when combined with urine cytology, and with a specificity of 94.7%. The fibroblast growth factor receptor3 (FGFR3) mutation is one of the most commonly detected mutations in bladder cancer, occurring in approximately 12% of all cases and in 70% of low-grade NMIBC (Zuiverloon et al., 2010; Weinstein et al., 2014). Urinary FGFR3 mutation analysis has a sensitivity of 73% and a specificity of 87%, with positive results implying shorter recurrence periods (Ahn et al., 2011). In another study, urine cfDNA for droplet digital polymerase chain reaction of the TERT promoter and FGFR3 provided a sensitivity of 68.9% and specificity of 100%, with an enhanced sensitivity of 85.9% when combined with urine cytology (Hayashi et al., 2020). Moreover, patients with TERT mutations in urine cfDNA showed worse prognosis compared with negative patients.

Tumors shed off DNA and the mutations harbor distinct alterations of DNA sequences according to tumor type and development, but the sensitivity of the cfDNA test is relatively low, making it a more appropriate method with improvements. DNA methylation is highly preserved throughout species and organs, which vary in tumor cells, implying its utilization for cancer detection (Lee et al., 2020). The detection of cfDNA mutations targeting single nucleotide variants and copy number alterations has caveats due to confounding signals of white blood cells and clonal hematopoiesis of indeterminate potential. Methylation sequencing of cfDNA surpasses targeted or whole-genome sequencing in the Circulating Cell-free Genome Atlas study (Liu et al., 2020). Epigenetic changes in urine cfDNA have diagnostic value for urothelial cancers. Anouk et al. reported that DNA methylation of urine samples and tumor tissues is significantly correlated, which allows the utilization of urine DNA methylation analysis for the diagnosis of bladder cancer. Among the nine genes reported in their previous study to be associated with bladder cancer according to the methylation status, the GHSR/MAL panel achieved a significant value with an AUC of 0.87 (95% CI, 0.73–1.00) (Hentschel et al., 2020). Yu et al. demonstrated that bladder cancer patients harbor methylation of 11 genes, including SALL3, CFTR, ABCC6, HPR1, RASSF1A, MT1A, ALX4, CDH13, RPRM, MINT1, and BRCA1, in urine samples. Bladder EpiCHeck detects DNA methylation in urine with a panel designed with 15 markers to diagnose bladder cancer with a sensitivity of 68.2% and a specificity of 88.0% (Witjes et al., 2018; Chen et al., 2020). A 2-marker based methylation assay, utMeMA, revealed a superior detection rate in early stage bladder cancer, with a better association with tumor burden (Chen et al., 2020). Furthermore, DNA methylation of urine samples is useful for detecting the recurrence of bladder cancer. Notably, TWIST and NID2 methylation are associated with bladder cancer recurrence with 84 and 96% sensitivity and specificity, respectively. In addition, another study reported that methylation of APC, RASSF1A, and CDK2AP2 is associated with bladder cancer recurrence with a sensitivity and specificity of 87 and 100%, respectively (Kandimalla et al., 2013). Further investigation is required to provide concrete evidence for the clinical use of these examinations.

DISCUSSION/CONCLUSION

In bladder cancer, the diagnostic utilization of urine has enormous potential because cancer cells shed materials directly into the urine. Nonetheless, no other urine tests, except for urine cytology, are recommended for the initial diagnosis or follow-up of bladder cancer because of their low sensitivity and specificity. In addition to traditional urinary marker tests, miRNA and cfDNA tests have been investigated and have shown promising results. Next-generation sequencing has enabled deeper analysis of molecular markers in urine, and comprehensive analysis can be achieved in accordance with artificial intelligence to deduce the fundamental assembly of molecular markers. In this regard, further studies are expected to reveal key molecular panels that facilitate accurate diagnosis and reduce invasive procedures.

AUTHOR CONTRIBUTIONS

Conceptualization: S-HJ; Data collection: S-HJ and JK; Data analysis: S-HJ and JK; Data interpretation: S-HJ and JK; Manuscript writing: S-HJ; Supervision: S-HJ and JK.

FUNDING

This research was supported by a Basic Science Research Program through National Research Foundation of Korea (NRF), funded by the Ministry of Education (NRF-2018R1D1A1B07041191) and by Seoul National University Hospital (0320202190).

ACKNOWLEDGMENTS

We would like to thank Editage (www.editage.co.kr) for editing and reviewing this manuscript for English language.

REFERENCES

Ahn, J. S., Kim, H.-S., Chang, S.-G., and Jeon, S. H. (2011). The Clinical Usefulness of Nuclear Matrix Protein-22 in Patients with Atypical Urine Cytology. *Korean J. Urol.* 52, 603–606. doi:10.4111/kju.2011.52.9.603

Avogbe, P. H., Manel, A., Vian, E., Durand, G., Forey, N., Voegele, C., et al. (2019). Urinary TERT Promoter Mutations as Non-Invasive Biomarkers for the Comprehensive Detection of Urothelial Cancer. *EBioMedicine* 44, 431–438. doi:10.1016/j.ebiom.2019.05.004

Barkan, G. A., Wojcik, E. M., Nayar, R., Savic-Prince, S., Quek, M. L., Kurtycz, D. F. I., et al. (2016). The Paris System for Reporting Urinary Cytology: The Quest to Develop a Standardized Terminology. *Acta Cytol.* 60, 185–197. doi:10.1159/000446270

Braicu, C., Cojocneanu-Petric, R., Chira, S., Truta, A., Floares, A., Achimas-Cadariu, P., et al. (2015). Clinical and Pathological Implications of miRNA in Bladder Cancer. *Ijn* 10, 791–800. doi:10.2147/ijn.s72904

Brisuda, A., Pazourkova, E., Soukup, V., Horinek, A., Hrbáček, J., Capoun, O., et al. (2016). Urinary Cell-free DNA Quantification as Non-invasive Biomarker in Patients with Bladder Cancer. *Urol. Int.* 96, 25–31. doi:10.1159/000438828

Casadio, V., Calistri, D., Tebaldi, M., Bravaccini, S., Gunelli, R., Martorana, G., et al. (2013). Urine Cell-free DNA Integrity as a Marker for Early Bladder Cancer Diagnosis: Preliminary Data. *Urol. Oncol. Seminars Orig. Investig.* 31, 1744–1750. doi:10.1016/j.urolonc.2012.07.013

Chen, X., Zhang, J., Ruan, W., Huang, M., Wang, C., Wang, H., et al. (2020). Urine DNA Methylation Assay Enables Early Detection and Recurrence Monitoring for Bladder Cancer. *J. Clin. Invest.* 130, 6278–6289. doi:10.1172/JCI139597

Enokida, H., Yoshino, H., Matsushita, R., and Nakagawa, M. (2016). The Role of microRNAs in Bladder Cancer. *Investig. Clin. Urol.* 57, S60–S76. doi:10.4111/icu.2016.57.S1.S60

Flaig, T. W., Spiess, P. E., Agarwal, N., Bangs, R., Boorjian, S. A., Buyyounouski, M. K., et al. (2020). Bladder Cancer, Version 3.2020, NCCN Clinical Practice Guidelines in Oncology. *J. Natl. Compr. Cancer Netw.* 18, 329–354. doi:10.6004/jnccn.2020.0011

Hanke, M., Hoefig, K., Merz, H., Feller, A. C., Kausch, I., Jocham, D., et al. (2010). A Robust Methodology to Study Urine microRNA as Tumor Marker: MicroRNA-126 and microRNA-182 Are Related to Urinary Bladder Cancer. *Urologic Oncol. Seminars Orig. Investig.* 28, 655–661. doi:10.1016/j.urolonc.2009.01.027

Hayashi, Y., Fujita, K., Matsuzaki, K., Eich, M.-L., Tomiyama, E., Matsushita, M., et al. (2020). Clinical Significance of Hotspot Mutation Analysis of Urinary Cell-free DNA in Urothelial Bladder Cancer. *Front. Oncol.* 10, 1–8. doi:10.3389/fonc.2020.00755

Hentschel, A. E., Nieuwenhuijzen, J. A., Bosschieter, J., van Splunter, A. P., Lissenberg-Witte, B. I., van der Voorn, J. P., et al. (2020). Comparative Analysis of Urine Fractions for Optimal Bladder Cancer Detection Using Dna Methylation Markers. *Cancers* 12, 859–911. doi:10.3390/cancers12040859

Hofbauer, S. L., de Martino, M., Lucca, I., Haitel, A., Susani, M., Shariat, S. F., et al. (2018). A Urinary microRNA (miR) Signature for Diagnosis of Bladder Cancer. *Urologic Oncol. Seminars Orig. Investig.* 36, 531.e1–531.e8. doi:10.1016/j.urolonc.2018.09.006

Jiang, X., Du, L., Wang, L., Li, J., Liu, Y., Zheng, G., et al. (2015). Serum microRNA Expression Signatures Identified from Genome-wide microRNA Profiling Serve as Novel Noninvasive Biomarkers for Diagnosis and Recurrence of Bladder Cancer. *Int. J. Cancer* 136, 854–862. doi:10.1002/ijc.29041

Kandimalla, R., Van Tilborg, A. A., and Zwarthoff, E. C. (2013). DNA Methylation-Based Biomarkers in Bladder Cancer. *Nat. Rev. Urol.* 10, 327–335. doi:10.1038/nrurol.2013.89

Kuehbacher, A., Urbich, C., Zeiher, A. M., and Dimmeler, S. (2007). Role of Dicer and Drosha for Endothelial microRNA Expression and Angiogenesis. *Circul. Res.* 101, 59–68. doi:10.1161/CIRCRESAHA.107.153916

Kutwin, P., Konecki, T., Borkowska, E. M., Traczyk-Borszyńska, M., and Jabłonowski, Z. (2018). Urine miRNA as a Potential Biomarker for Bladder Cancer Detection - a Meta-Analysis. *Ceju* 71, 177–185. doi:10.5173/ceju.2018.1605

Lee, C.-J., Ahn, H., Jeong, D., Pak, M., Moon, J. H., and Kim, S. (2020). Impact of Mutations in DNA Methylation Modification Genes on Genome-wide Methylation Landscapes and Downstream Gene Activations in Pan-Cancer. *BMC Med. Genomics* 13, 1–14. doi:10.1186/s12920-020-0659-4

Liu, M. C., Oxnard, G. R., Klein, E. A., Swanton, C., Seiden, M. V., Liu, M. C., et al. (2020). Sensitive and Specific Multi-Cancer Detection and Localization Using Methylation Signatures in Cell-free DNA. *Ann. Oncol.* 31, 745–759. doi:10.1016/j.annonc.2020.02.011

Mancini, M., Righetto, M., Zumerle, S., Montopoli, M., and Zattoni, F. (2020). The Bladder Epicheck Test as a Non-invasive Tool Based on the Identification of DNA Methylation in Bladder Cancer Cells in the Urine: A Review of Published Evidence. *Ijms* 21, 6542–6549. doi:10.3390/ijms21186542

Murakami, K., Pagano, I., Chen, R., Sun, Y., Goodison, S., Rosser, C. J., et al. (2021). Influencing Factors on the Oncuria Urinalysis Assay: An Experimental Model. *Diagnostics* 11, 1023. doi:10.3390/diagnostics11061023

Ou, Z., Li, K., Yang, T., Dai, Y., Chandra, M., Ning, J., et al. (2020). Detection of Bladder Cancer Using Urinary Cell-free DNA and Cellular DNA. *Clin. Transl. Med.* 9, 4. doi:10.1186/s40169-020-0257-2

Saginala, K., Barsouk, A., Aluru, J. S., Rawla, P., Padala, S. A., and Barsouk, A. (2020). Epidemiology of Bladder Cancer. *Med. Sci.* 8, 15–25. doi:10.3390/medsci8010015

Salvi, S., Gurioli, G., De Giorgi, U., Conteduca, V., Tedaldi, G., Calistri, D., et al. (2016). Cell-free DNA as a Diagnostic Marker for Cancer: Current Insights. *Ott* 9, 6549–6559. doi:10.2147/OTT.S100901

Sullivan, P. S., Chan, J. B., Levin, M. R., and Rao, J. (2010). Urine Cytology and Adjunct Markers for Detection and Surveillance of Bladder Cancer. *Am. J. Transl. Res.* 2, 412–440.

Têtu, B. (2009). Diagnosis of Urothelial Carcinoma from Urine. *Mod. Pathol.* 22, S53–S59. doi:10.1038/modpathol.2008.193

Tse, R. T.-H., Zhao, H., Wong, C. Y.-P., Cheng, C. K.-L., Kong, A. W., Peng, Q., et al. (2021). Urinary Cell-Free Dna in Bladder Cancer Detection. *Diagnostics* 11, 306. doi:10.3390/diagnostics11020306

Villicana, P., Whiting, B., Goodison, S., and Rosser, C. J. (2009). Urine-based Assays for the Detection of Bladder Cancer. *Biomark. Med.* 3, 265–274. Available at: http://www.embase.com/search/results?subaction=viewrecord&from=export&id=L355023326%0Ahttp://www.futuremedicine.com/doi/pdf/10.2217/bmm.09.23%0A. doi:10.2217/bmm.09.23

Wang, Z., Que, H., Suo, C., Han, Z., Tao, J., Huang, Z., et al. (2017). Evaluation of the NMP22 BladderChek Test for Detecting Bladder Cancer: A Systematic Review and Meta-Analysis. *Oncotarget* 8, 100648–100656. doi:10.18632/oncotarget.22065

Weinstein, J. N., Akbani, R., Broom, B. M., Wang, W., Verhaak, R. G. W., McConkey, D., et al. (2014). Comprehensive Molecular Characterization of Urothelial Bladder Carcinoma. *Nature* 507, 315–322. doi:10.1038/nature12965

Witjes, J. A., Morote, J., Cornel, E. B., Gakis, G., van Valenberg, F. J. P., Lozano, F., et al. (2018). Performance of the Bladder EpiCheckTM Methylation Test for Patients under Surveillance for Non–muscle-invasive Bladder Cancer: Results of a Multicenter, Prospective, Blinded Clinical Trial. *Eur. Urol. Oncol.* 1, 307–313. doi:10.1016/j.euo.2018.06.011

Woldu, S. L., Bagrodia, A., and Lotan, Y. (2017). Guideline of Guidelines: Non-muscle-invasive Bladder Cancer. *BJU Int.* 119, 371–380. doi:10.1111/bju.13760

Zhu, C.-Z., Ting, H.-N., Ng, K.-H., and Ong, T.-A. (2019). A Review on the Accuracy of Bladder Cancer Detection Methods. *J. Cancer* 10, 4038–4044. doi:10.7150/jca.28989

Zuiverloon, T. C. M., Van Der Aa, M. N. M., Van Der Kwast, T. H., Steyerberg, E. W., Lingsma, H. F., Bangma, C. H., et al. (2010). Fibroblast Growth Factor Receptor 3 Mutation Analysis on Voided Urine for Surveillance of Patients with Low-Grade Non-Muscle-invasive Bladder Cancer. *Clin. Cancer Res.* 16, 3011–3018. doi:10.1158/1078-0432.CCR-09-3013

Conflict of Interest: The authors declare that the research was conducted in the absence of any commercial or financial relationships that could be construed as a potential conflict of interest.

Advantages of publishing in Frontiers

OPEN ACCESS
Articles are free to read for greatest visibility and readership

FAST PUBLICATION
Around 90 days from submission to decision

HIGH QUALITY PEER-REVIEW
Rigorous, collaborative, and constructive peer-review

TRANSPARENT PEER-REVIEW
Editors and reviewers acknowledged by name on published articles

Frontiers
Avenue du Tribunal-Fédéral 34
1005 Lausanne | Switzerland

Visit us: www.frontiersin.org
Contact us: frontiersin.org/about/contact

REPRODUCIBILITY OF RESEARCH
Support open data and methods to enhance research reproducibility

DIGITAL PUBLISHING
Articles designed for optimal readership across devices

FOLLOW US
@frontiersin

IMPACT METRICS
Advanced article metrics track visibility across digital media

EXTENSIVE PROMOTION
Marketing and promotion of impactful research

LOOP RESEARCH NETWORK
Our network increases your article's readership